ABSTRACT

Title of dissertation: IMPROVING ANALYTICAL TEMPLATES AND SEARCHING FOR GRAVITATIONAL WAVES FROM COALESCING BLACK HOLE BINARIES

Evan Ochsner
Doctor of Philosphy, 2010

Dissertation directed by: Professor Alessandra Buonanno
Department of Physics

The Laser Interferometer Gravitational-wave Observatory (LIGO) and Virgo are taking data at design sensitivity. They will be upgraded to Advanced LIGO and Virgo within the next 5 years and the detection of gravitational waves will be very likely. Binaries of two compact objects which inspiral and coalesce are one of the most promising sources for LIGO and Virgo. Most searches have focused solely on the inspiral portion of the waveform, and are consequently limited to low total mass. Recent breakthroughs in numerical relativity allow one to construct complete inspiral-merger-ringdown waveforms and search for the whole signal. This thesis will review some of the basic characteristics of gravitational waves from compact binaries and methods of searching for them. Analytical template waveforms for such systems will be presented including a comparison of different families of analytical waveforms, a study on the inclusion of spin effects in such waveforms, and a study of inspiral-

merger-ringdown waveforms with amplitude corrections and the importance of these effects for parameter estimation. The thesis will culminate with a presentation of the first gravitational wave search to use inspiral-merger-ringdown templates, which was performed on data from the fifth science run of LIGO.

IMPROVING ANALYTICAL TEMPLATES AND SEARCHING FOR GRAVITATIONAL WAVES FROM COALESCING BLACK HOLE BINARIES

by

Evan Ochsner

Dissertation submitted to the Faculty of the Graduate School of the
University of Maryland, College Park in partial fulfillment
of the requirements for the degree of
Doctor of Philosophy
2010

Advisory Committee:
Professor Alessandra Buonanno, Chair/Advisor
Professor Ted Jacobson
Professor Cole Miller
Professor Peter Shawhan
Professor Manuel Tiglio

Preface

The work presented in Ch. 7 and Sec. 2.3.2 of Ch. 2 of this thesis was carried out within the LIGO Scientific Collaboration (LSC) using data taken by the LSC and the Virgo Collaboration. The methods and results presented there are under review and are potentially subject to change. The opinions expressed there are those of the author and not necessarily those of the LSC or the Virgo Collaboration. The author gratefully acknowledges the support of the United States National Science Foundation for the construction and operation of the LIGO Laboratory and the Italian Istituto Nazionale di Fisica Nucleare and the French Centre National de la Recherche Scientifique for the construction and operation of the Virgo detector, which provided support for this work.

To Susan and my parents, for all your love and support.

Acknowledgments

I would like to thank my advisor, Alessandra Buonanno, for all of her guidance and advice during my research, teaching me about EOB waveforms, spin effects and many other things, not to mention for sending me all over the world.

I owe a great debt to everyone in the LSC and Virgo collaborations, without all of your hard work, none of this would be possible. To single out a few people, I must begin with Peter Shawhan for getting me interested in the subject as a SURF student at Caltech. I would like to thank everyone at the University of Wisconsin at Milwaukee, in particular Patrick Brady, Rahul Biswas and Jessica Clayton for teaching me about the LAL code and running search pipelines, and also for your hospitality during my visit. Duncan Brown was also very helpful in teaching me how the LAL code works. I would like to thank B.S. Sathyaprakash, Craig Robinson, Chris Van Den Broeck, Dave McKechan, Ian Harry, Gareth Jones, Thomas Cokelaer, Steve Fairhurst, Patrick Sutton and everyone else who was at Cardiff University for your hospitality during my stay to write the LAL EOB code. I would especially like to thank B.S. Sathyaprakash for teaching me a great deal about how to write, test and debug computer code. I would like to thank everyone involved in the S5 high mass search for all of your work, including Chad Hanna, Craig Robinson, Alan Weinstein, Ilya Mandel, Riccardo Sturani, John Whelan, everyone who ran the pipeline on part of the data, the followup team and many, many others.

I would like to thank all of the co-authors on the various papers which make up chapters of this work: K.G. Arun, Alessandra Buonanno, Guillaume Faye, Bala

Iyer, Yi Pan, B.S. Sathyaprakash, and everyone in the NINJA collaboration. I look forward to working with you again in the future.

I owe a very special thank you to Sean McWilliams for all of his help on applying the Fisher matrix to EOB waveforms, advice on how to improve the results, and generally reassuring me of my sanity.

Lastly, I would like to thank Jane Hessing for all of her help with administrative matters. Without her help, I couldn't keep track of all the paperwork to stay enrolled and graduate.

I'm sure I have neglected to mention many people, and I apologize to anyone I missed!

Table of Contents

List of Tables

List of Figures

List of Abbreviations

GW	Gravitational Wave
TT	Transverse-Traceless
LIGO	Laser Interferometer Gravitational-wave Observatory
LSC	LIGO Scientific Collaboration
LAL	LSC Algorithm Library
LCGT	Large-scale Cryogenic Gravitational-wave Telescope
ET	Einstein Telescope
LISA	Laser Interferometer Space Antenna
NINJA	Numerical INJection Analysis
CBC	Compact Binary Coalescence
BH	Black Hole
NS	Neutron Star
BBH	Binary Black Hole
BNS	Binary Neutron Star
IMBH	Intermediate-Mass Black Hole
PN	Post-Newtonian
NR	Numerical Relativity
SPA	Stationary-Phase Approximation
EOB	Effective-One-Body
IMR	Inspiral Merger Ringdown
QNM	QuasiNormal Mode
NR-AR	Numerical-Relativity–Analytical-Relativity
SO	Spin-Orbit
SS	Spin-Spin
ISCO	Innermost Stable Circular Orbit
PSD	Power Spectral Density
MCMC	Markov-Chain Monte-Carlo
ERD	Effective RingDown
WRD	Weighted RingDown
DQ	Data Quality
IFAR	Inverse False Alarm Rate
S5	LIGO's Fifth Science Run
VSR1	Virgo Science Run 1

Notational Conventions

- We will use boldface to denote vectors, as in $\mathbf{L}$
- Unit vectors will be denoted with boldface and a hat, as in $\widehat{\mathbf{L}}$
- In the context of the effective-one-body formalism, a hat (without boldface) will be used to denote dimensionless time and frequency variables, as in

$$\hat{t} \equiv \frac{t}{GMc^3}\,, \qquad\qquad \hat{\omega} \equiv GM\omega c^3\ .$$

Chapter 1

Preamble

General Relativity posits that what we observe as the gravitational attraction between any two bodies is in fact a manifestation of the curvature of spacetime. In this theory, the Universe is described as a four-dimensional manifold of space and time. The manifold is characterized by a metric tensor, $g_{\mu\nu}$, which allows one to calculate the separation between any two events (points in space and time). The geometry of spacetime determines the behavior of the matter and energy within it; matter and energy move along geodesics (extremal paths between two events) of the spacetime.

In Newtonian gravity, space and time are an absolute, immutable framework within which all physical processes play out. General relativity is a dramatic paradigm shift away from this conception of the Universe. General relativistic spacetime is a dynamical structure that is affected by the matter and energy within it. Matter and energy curve spacetime, and the geometry of spacetime determines the behavior of the matter and energy. Mathematically, this is described by Einstein's equation:

$$R_{\mu\nu} - \frac{1}{2} R\, g_{\mu\nu} = 8\,\pi\, T_{\mu\nu} \ . \tag{1.1}$$

Here $g_{\mu\nu}$ is the metric tensor, $R_{\mu\nu}$ is the Ricci tensor (a function of the metric

and its first and second derivatives) and R is the Ricci scalar, the contraction of the Ricci tensor. Thus, the left hand side of the equation represents the curvature of spacetime. On the right hand side, $T_{\mu\nu}$ is the stress-energy tensor, which describes the distribution of matter and energy within the spacetime. This tensor equation describes the interaction between matter, energy and spacetime. If the distribution of matter and energy varies in time, then the curvature, as described by the metric $g_{\mu\nu}$, can also vary in time. This variation in the metric will propagate outward from the varying matter and energy distribution throughout the rest of spacetime as gravitational waves (GWs) which stretch and squeeze spacetime itself, causing the measured distance between two points to grow and shrink at different times.

The strain, or fractional change in length, is used to quantify the effect of gravitational waves. Suppose the proper distance between some two freely falling reference points at rest with respect to each other is L, and a gravitational wave of strain h passes by. The wave will produce a time-dependent variation in L, $\Delta L(t) = h(t)\, L$. So, if we can measure the distance between two points to high enough precision, and we find that the distance varies in time, this may be evidence of a gravitational wave. Of course, we must be sure that the change in distance is not caused by some other factor. For instance, if our reference points are on the surface of the Earth, seismic activity could cause their separation to vary in time. The most important way to rule out such "noise" sources is to perform these distance measurement experiments at two or more widely separated locations. We then require that multiple sites measure a strain at the same time (within some coincidence window to allow for the fact that a gravitational wave can arrive at the

different locations at slightly different times), and that the measured strains are all of consistent strength and functional form $h(t)$.

In electrodynamics, one can describe the electromagnetic waves emitted from a source electromagnetic potential by expanding the potential in multipoles. If these multipoles vary in time, they can create electromagnetic radiation. Because electromagnetic charge is conserved, the electric monopole (i.e. the total charge) will not vary and cannot produce electromagnetic waves. However, if the electric dipole of the potential varies in time, this will produce electromagnetic waves. Higher time derivatives of higher order multipoles can also contribute to electromagnetic radiation. In general relativity, we can use an analogous approach to describe gravitational waves in terms of multipoles of the stress-energy tensor (which represents the distribution of mass-energy and mass-energy "currents") of a source. Because mass-energy (mass monopole), linear momentum (mass dipole) and angular momentum (current dipole) are conserved, they cannot contribute to gravitational waves. It turns out that the second time derivative of the mass quadrupole is the lowest order contribution to gravitational radiation. This represents the dominant contribution to gravitational waves, with higher time derivatives of higher order multipoles giving smaller corrections. Since the dominant contribution to gravitational waves is related to the second time derivative of the mass distribution of a source, this means that one must have a mass undergoing acceleration to produce gravitational waves.

Now, because gravity is much weaker than the other fundamental forces of Nature, one must have very large masses undergoing extreme accelerations to produce

detectable gravitational waves. One of the classic examples is a binary of two compact objects (neutron stars and/or black holes) undergoing centripetal acceleration as they orbit one another.

The Hulse-Taylor binary system of two neutron stars provides compelling (although indirect) evidence for the existence of gravitational waves [1]. Discovered in 1974, it is observed as a pulsar which emits bursts of radio waves approximately every 59 ms. This emission comes from a magnetic hot spot on a rotating neutron star that beams radiation every time the bright spot faces Earth. The period of these bursts is Doppler shifted by a pattern consistent with a 1.441 $M_\odot$ pulsar in a binary orbit with a 1.387 $M_\odot$ companion with an eccentricity of 0.617131 and an orbital period of about 7.75 hours. This period has slowly decreased over the years at a rate that agrees very well with the energy loss (thus shrinking radius and decreased period) predicted by general relativity. After a few years of observation, the rate of change in the period was measured accurately enough to show that it agreed with the prediction of general relativity to within a few percent [2]. Further years of observation allowed a more precise measurement of the rate of change of the period, so that after 30 years of observation, it is found to agree with general relativity to within 0.2% [3, 4]. So, although gravitational waves from this binary have not been observed directly, the observations strongly support their existence, as there is no other explanation for the changing orbital period that can fit the data so precisely.

Gravitational waves from this binary have not been detected because their observable effect is extremely weak, and they are at frequencies well below the

sensitive band of any current gravitational wave detector. Just before the Hulse-Taylor binary merges in roughly 300 million years, the two neutron stars will orbit each other many times a second, and their gravitational waves will be of a high enough frequency that current detectors could observe them. Thus, if other binaries in the Universe consisting of two neutron stars and/or black holes are merging right now, we may be able to detect them if they are not too far away.

To see just how difficult it is to detect gravitational waves directly, and why we do not notice them in our everyday lives, consider the well-known quadrupole formula (see e.g. Ref. [5]), which gives this leading order expression for the strain of gravitational waves emitted from a compact binary such as the Hulse-Taylor binary:

$$h(t) \sim 2.36\,10^{-22} \left(\frac{M}{10\,M_\odot}\right)^{5/3} \left(\frac{\eta}{0.25}\right) \left(\frac{F_{\rm orb}}{100\,{\rm Hz}}\right)^{2/3} \left(\frac{100\,{\rm Mpc}}{D_{\rm eff}}\right) . \tag{1.2}$$

In this equation, $M = m_1 + m_2$ is the total mass of the binary, $0 < \eta = m_1 m_2 / M^2 \leq 0.25$ is the symmetric mass ratio, $F_{\rm orb}$ is the orbital frequency of the binary, and $D_{\rm eff}$ is the effective distance between the binary and detector (the distance adjusted to take into account the relative orientation between the binary and detector). For the example binary in the above equation, we get a strain $\mathcal{O}(10^{-22})$. If a ~ 2 m long freely falling test apparatus is impinged upon by a gravitational wave from our example source, it will be stretched and squeezed by $\mathcal{O}(10^{-22})$ m. Now, the closest extra-solar stars are ~ 1 pc away, so if we moved this same binary to their location, the gravitational waves would still only warp our apparatus by $\mathcal{O}(10^{-14})$ m. This should make it quite clear that gravitational waves from astrophysical sources

are very weak and can only be detected by precision experiments. However, if we were much closer to a source, the strain would be much stronger. Perhaps there is some experiment we could perform in a laboratory on Earth to produce gravitational waves that are easily detectable near the source? By converting the units of Eq. (1.2) into laboratory scale units, it becomes quite apparent that producing detectable gravitational waves in a laboratory would be exceedingly difficult.

$$h(t) \sim 7.35\,10^{-42} \left(\frac{M}{20,000\,\mathrm{kg}}\right)^{5/3} \left(\frac{\eta}{0.25}\right) \left(\frac{F_{\mathrm{orb}}}{100\,\mathrm{Hz}}\right)^{2/3} \left(\frac{0.1\,\mathrm{m}}{D_{\mathrm{eff}}}\right) . \tag{1.3}$$

This tells us that if we can rotate a 20-ton barbell-shaped weight 100 times a second, a freely falling ~ 1 m object located 10 cm from the system would only be stretched by $\mathcal{O}(10^{-42})$ m. The effect could be made somewhat stronger by changing the geometry and mass of the rotating weight, by spinning it faster, or by measuring the effect at closer distances. However, one would need a system that is many orders of magnitude heavier, more compact, faster and closer to get an easily measurable effect. As with astrophysical sources, GWs produced in a laboratory on Earth have a very tiny effect that could only be detected by a very precise measurement. Sadly, it seems college freshmen will never see a classroom demonstration of gravitational waves in an introductory physics lab.

Despite the challenges, the detection of gravitational waves could reap handsome benefits. First of all, it would allow us to test general relativity. The predictions of general relativity have been confirmed by numerous experiments, including the perihelion precession of Mercury, bending of light by the Sun, the gravita-

tional redshift of electromagnetic radiation, the "time-dilation" corrections needed for global positioning satellites to work correctly and many others. For a general discussion of these and other tests of general relativity, see Ref. [6]. However, all of these tests occur where gravity is relatively weak. They do not test general relativity in regimes where gravity is strongest, such as near the surface of a black hole. Since the sources of gravitational waves are systems experiencing strong gravity, observing GWs could tell whether strong-field gravity obeys general relativity. GW observations could also provide a wealth of astrophysical information. Much as radio astronomy opened a whole new window on the Universe by detecting objects such as pulsars which emit radio waves rather than visible light, GW observations could shed new light on electromagnetically dark objects. It could also offer a complementary view of objects which are electromagnetically visible. One promising scenario is if both gravitational and electromagnetic waves are observed from the same event (such as a compact binary coalescence). Then, one can determine both the physical distance and the redshift of the object rather accurately and thus get a precise measurement of the rate of expansion of the Universe and Hubble's constant, as proposed in Ref. [7].

The rest of this thesis is organized as follows: In Chapter 2, we will begin by deriving some of the basic properties of gravitational waves. Then, we will give an overview of work by the author and collaborators related to building analytic template waveforms for gravitational waves from compact binaries, and how these waveforms can be applied to search for and analyze gravitational waves. Chapter 3 will present a comparison of various families of post-Newtonian waveforms to assess

their reliability. Chapter 4 will present post-Newtonian waveforms for inspiralling compact binaries in which one or both of the bodies is rapidly spinning and study the consequences of these spin effects. Some of the lengthier expressions from this chapter will appear in Appendices A-D. Chapter 5 will present a study which used effective one-body template waveforms to search for numerical relativity waveforms injected into simulated data. Chapter 6 will present effective one-body waveforms with amplitude corrections for the inspiral, merger and ringdown of compact binaries and study the implications of the merger-ringdown and amplitude corrections on the precision with which the parameters of the compact binary can be recovered. Chapter 7 will present the results of a search for gravitational waves from compact binaries in LIGO's fifth science run (S5). This search attempted to find gravitational waves from binaries with a total mass between $(25-100)\,M_{\odot}$ with individual masses in the range $(1-99)\,M_{\odot}$, and is the first search to use complete inspiral-merger-ringdown waveforms. Finally, we have some brief concluding remarks in Ch. 8.

Chapter 2

Introduction

2.1 Basic properties of gravitational waves

We now set about to derive some of the basic properties of gravitational waves propagating far from their source within the framework of linearized gravity. This means that we will treat gravitational waves as a small perturbation to a flat background spacetime. Einstein performed such a calculation and predicted the existence and basic properties of gravitational waves [8]. The derivation of the properties of gravitational waves in this section is modelled after the presentation in the first chapter of the excellent text book on gravitational waves by Maggiore [9].

2.1.1 Linearized gravity metric

As we have argued in the preamble, any gravitational waves that we might hope to observe here on Earth will be very tiny and difficult to detect. Because of this, it should be reasonable to treat them as a small perturbation of a background spacetime metric. For simplicity, we will begin by assuming a flat, Minkowski background spacetime, $\eta_{\mu\nu}$, and the effect of the gravitational wave will be described by $h_{\mu\nu}$. For the gravitational waves to be a "small perturbation", this means that there exists a frame in which the components of $h_{\mu\nu}$ are small. So, we will decompose our

spacetime metric as

$$g_{\mu\nu} = \eta_{\mu\nu} + h_{\mu\nu}, \qquad |h_{\mu\nu}| \ll 1 \tag{2.1}$$

and only keep terms that are linear in $h_{\mu\nu}$. One consequence of this is that we can raise and lower tensor indices by contracting with the flat spacetime metric $\eta_{\mu\nu}$.

Now, general relativity is invariant under any diffeomorphic (smooth mapping with a smooth inverse mapping) coordinate transformation. It turns out that if we specify a coordinate frame which satisfies Eq. (2.1), we still have a remaining gauge freedom. To see this, note that if we perform a coordinate transformation $x^\mu \to x'^\mu$, then our spacetime metric will transform as

$$g_{\mu\nu} \to \frac{\partial x^\alpha}{\partial x'^\mu} \frac{\partial x^\beta}{\partial x'^\nu} g_{\alpha\beta} \ . \tag{2.2}$$

So, if we consider a transformation of the form $x^\mu \to x^\mu + \xi^\mu(x)$, our metric will transform as $g_{\mu\nu} \to \eta_{\mu\nu} + h_{\mu\nu} - \partial_\mu \xi_\nu - \partial_\nu \xi_\mu$. Thus, the tensor describing the gravitational waves has transformed as

$$h_{\mu\nu} \to h_{\mu\nu} - \partial_\mu \xi_\nu - \partial_\nu \xi_\mu \tag{2.3}$$

and so we are allowed to perform any such transformation so long as $|\partial_\mu \xi_\nu + \partial_\nu \xi_\mu| \leq |h_{\mu\nu}|$. In fact, we will find such transformations useful to simplify our equations and expressions [9].

2.1.2 Describing curvature

In differential geometry, the curvature of a manifold (spacetime) can be described in terms of parallel transport of a vector. To parallel transport a vector means to move a vector along a curve so that it remains tangent to that curve at all times. On a flat manifold, parallel transport is path independent, or equivalently if a vector is invariant when parallel transported along a closed path. If the direction of the final vector depends upon the path over which it was parallel transported, then this is a sign that the manifold is curved.

A sphere such as the Earth provides a classic example to illustrate this concept. Let us start with a vector at 0° longitude at the equator. If we transport it to the north pole along the line of 0° longitude, it will point in the direction of 180° longitude at the north pole. If instead we first transport our vector along the equator to 90° east longitude, and then transport it to the north pole along the line of 90° east longitude, it will then point in the direction of 90° west longitude at the north pole. Equivalently, we could also travel along one curve and then backwards along the other to arrive back at the equator at 0° longitude and we would find our vector rotated 90° relative to it's initial orientation. So, the curvature of the sphere means that a vector will not be invariant when parallel transported over a closed loop.

This concept can be used to describe the curvature of a generic manifold (spacetime) via the Riemann tensor. Given a spacetime metric $g_{\mu\nu}$, the covariant

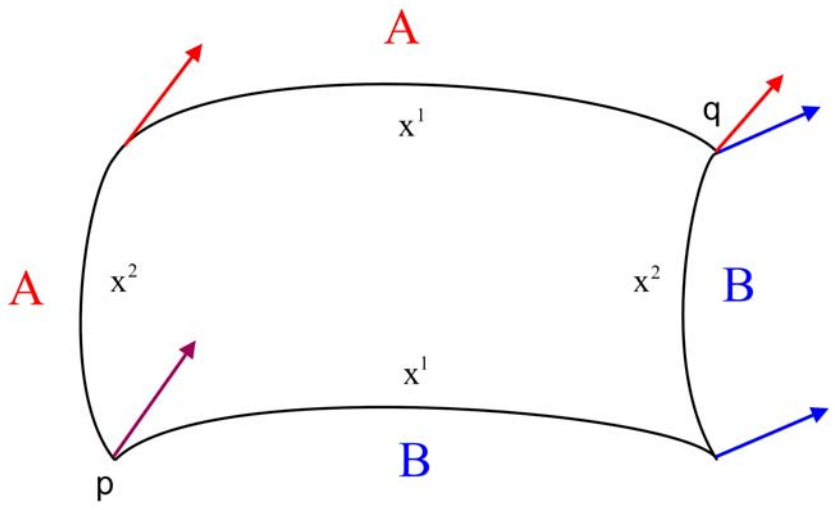

Figure 2.1: Depiction of measuring curvature with the path dependence of parallel transport. We have a vector at point p and parallel transport it along either path A (red) or B (blue). The direction of the vector at q depends on the path taken.

derivative of a vector is defined as

$$\nabla_\mu x^\nu = \partial_\mu + \Gamma^\nu_{\mu\lambda}\, x^\lambda \tag{2.4}$$

where $\Gamma^\nu_{\mu\lambda}$ is the Christoffel symbol (or connection coefficient) defined as

$$\Gamma^\nu_{\mu\lambda} = \frac{1}{2}\, g^{\nu\rho} \left(\frac{\partial g_{\rho\mu}}{\partial x^\lambda} + \frac{\partial g_{\rho\lambda}}{\partial x^\mu} - \frac{\partial g_{\mu\lambda}}{\partial x^\rho} \right) \ . \tag{2.5}$$

The covariant derivative can be used to parallel transport a vector. Given a curve C with tangent vector y^μ, a vector x^ν will parallel transported if $y^\mu \nabla_\mu x^\nu = 0$ everywhere along C.

The path dependence of parallel transport is related to the non-commutation of covariant derivatives. To get an intuitive feel for why this is, let us consider

parallel transport of a vector from point p to q over an infinitesimally small distance (so the metric does not change appreciably) of a curved spacetime, as depicted in Fig. 2.1. If we parallel transport along curve A where we first go in the direction of x^2 and then x^1, the final direction of the vector is depicted in red. If we parallel transport along curve B, which first goes in the direction of x^1 and then x^2, the final direction of the vector is depicted in blue. Now, curves A and B only differ in the order in which they traverse the x^1 and x^2 segments. So, the fact that we obtain a different result depending on the order in which the segments are traversed means that the covariant derivative along the x^1 direction does not commute with the covariant derivative along the x^2 direction. Recalling, Eq. (2.4), it is clear that the non-commutation is caused by the presence of the Christoffel symbols (which are zero in flat spacetimes) in the covariant derivatives.

Guided by this intuition, we will define the Riemann tensor in terms of the commutator of covariant derivatives

$$R^{\lambda}{}_{\sigma\mu\nu} x^{\sigma} = \left(\nabla_{\mu}\nabla_{\nu} - \nabla_{\nu}\nabla_{\mu}\right) x^{\lambda} \ . \tag{2.6}$$

Using the definition of the covariant derivative, Eq. (2.4), this leads to

$$R^{\lambda}{}_{\sigma\mu\nu} = \frac{\partial \Gamma^{\lambda}_{\sigma\nu}}{\partial x^{\mu}} - \frac{\partial \Gamma^{\lambda}_{\sigma\mu}}{\partial x^{\nu}} + \Gamma^{\lambda}_{\gamma\mu}\,\Gamma^{\gamma}_{\sigma\nu} - \Gamma^{\lambda}_{\gamma\nu}\,\Gamma^{\gamma}_{\sigma\mu} \ . \tag{2.7}$$

From this definition, one finds that the Riemann tensor has several symmetries

$$R_{\lambda\sigma\mu\nu} = -R_{\sigma\lambda\mu\nu} = -R_{\lambda\sigma\nu\mu} \ , \tag{2.8}$$

$$R_{\lambda\sigma\mu\nu} = R_{\mu\nu\lambda\sigma} \ , \tag{2.9}$$

$$0 = R_{\lambda\sigma\mu\nu} + R_{\lambda\mu\nu\sigma} + R_{\lambda\nu\sigma\mu} \ , \tag{2.10}$$

$$0 = \nabla_\gamma R^{\lambda}{}_{\sigma\mu\nu} + \nabla_\mu R^{\lambda}{}_{\sigma\nu\gamma} + \nabla_\nu R^{\lambda}{}_{\sigma\gamma\mu} \ . \tag{2.11}$$

The Ricci tensor and scalar are defined from contractions of the Riemann tensor with the metric

$$R_{\mu\nu} = g^{\lambda\sigma} R_{\lambda\sigma\mu\nu} \ , \tag{2.12}$$

$$R = g^{\mu\nu} R_{\mu\nu} \ . \tag{2.13}$$

We have now defined the Riemann tensor, Ricci tensor, and Ricci scalar which describe the curvature of a spacetime with a generic metric $g_{\mu\nu}$ [10]. In linearized gravity, with a metric of the form Eq. (2.1) and keeping only terms linear in $h_{\mu\nu}$, we find [11]

$$\Gamma^{\nu}_{\mu\lambda} = \frac{1}{2}\,\eta^{\nu\rho}\left(\frac{\partial h_{\rho\mu}}{\partial x^\lambda} + \frac{\partial h_{\rho\lambda}}{\partial x^\mu} - \frac{\partial h_{\mu\lambda}}{\partial x^\rho}\right) \ , \tag{2.14}$$

$$R_{\lambda\sigma\mu\nu} = \frac{1}{2}\left(\partial_\mu\partial_\sigma h_{\lambda\nu} + \partial_\nu\partial_\lambda h_{\sigma\mu} - \partial_\mu\partial_\lambda h_{\sigma\nu} - \partial_\nu\partial_\sigma h_{\lambda\mu}\right) \ . \tag{2.15}$$

2.1.3 Wave equation for gravitational waves and the TT gauge

Recall that Einstein's equation is given by

$$R_{\mu\nu} - \frac{1}{2} R\, g_{\mu\nu} = 8\,\pi\, T_{\mu\nu} \ . \tag{2.16}$$

Here $T_{\mu\nu}$ is the stress-energy tensor for the matter and energy in the spacetime. Since we are working at linear order in $h_{\mu\nu}$, we can obtain expressions for the Ricci tensor and scalar by contracting the linearized Riemann tensor of Eq. (2.15) with the flat spacetime metric $\eta_{\mu\nu}$. Doing this, Eq. (2.16) can be greatly simplified by expressing it in terms of the trace-reversed tensor

$$\bar{h}_{\mu\nu} = h_{\mu\nu} - \frac{1}{2}\eta_{\mu\nu} h \ , \tag{2.17}$$

where $h = \eta^{\mu\nu} h_{\mu\nu}$ and so $\bar{h} = -h$. Then, Einstein's equation, Eq. (2.16), becomes

$$\Box \bar{h}_{\mu\nu} + \eta_{\mu\nu} \partial^{\lambda} \partial^{\sigma} \bar{h}_{\lambda\sigma} - \partial^{\lambda} \partial_{\nu} \bar{h}_{\mu\lambda} - \partial^{\lambda} \partial_{\mu} \bar{h}_{\nu\lambda} = 16\,\pi\, T_{\mu\nu} \ . \tag{2.18}$$

Note that $\Box = \partial^{\mu}\partial_{\mu}$ is the D'Alembertian operator. At this point, it is very convenient to exploit our gauge freedom and impose the Lorenz gauge condition

$$\partial^{\nu} \bar{h}_{\mu\nu} = 0 \ . \tag{2.19}$$

In this gauge, all but the first term on the left hand side vanish and we are left with

$$\Box \bar{h}_{\mu\nu} = -16\,\pi\, T_{\mu\nu}\ . \tag{2.20}$$

This is a nice concise wave equation with a source term given by the stress-energy tensor, and therefore the matter and energy distribution in the spacetime.

Note that our wave equation, Eq. (2.20) coupled with our gauge condition, Eq. (2.19) and the fact that partial derivatives commute gives us a simple conservation law for energy-momentum in the linearized theory

$$\partial^{\mu} T_{\mu\nu} = 0\ . \tag{2.21}$$

Now, we will be interested in detecting gravitational waves of astrophysical origin far away from the source. Therefore, we will set the source term $T_{\mu\nu} = 0$ and our wave equation becomes

$$\Box \bar{h}_{\mu\nu} = 0\ . \tag{2.22}$$

First, since (restoring c) $\Box = -\frac{1}{c^2}\partial_t^2 + \boldsymbol{\nabla^2}$, this equation means that we expect gravitational waves to propagate at the speed of light. Next, we note that since Eq. (2.22) is an equation for a symmetric rank-2 tensor, it has 10 independent components. However, the gauge condition of Eq. (2.19) fixes 4 of those components, and so we are left with 6. However, there is still a remaining gauge freedom. Let us perform a coordinate transformation $x^{\mu} \to x^{\mu} + \xi^{\mu}$. Then, from Eq. (2.3) and Eq.

(2.17), the trace-reversed tensor transforms as

$$\bar{h}_{\mu\nu} \to \bar{h}_{\mu\nu} + \xi_{\mu\nu} \quad \xi_{\mu\nu} = \partial_\mu \xi_\nu + \partial_\nu \xi_\mu - \eta_{\mu\nu} \partial_\lambda \xi^\lambda \ . \tag{2.23}$$

Now, if ξ_μ satisfies $\Box \xi_\mu = 0$, then it follows that $\Box \xi_{\mu\nu} = 0$ also. So, we can perform any coordinate transformation so long as $\Box \xi_\mu = 0$. In particular, we can choose ξ^0 such that $\bar{h} = 0$. Therefore, from Eq. (2.17) we have $\bar{h}_{\mu\nu} = h_{\mu\nu}$. We will also choose the ξ^i so that $h_{0i} = 0$. The Lorenz gauge condition, Eq. (2.19) now implies $\partial^0 h_{00} + \partial^i h_{0i} = 0$ and given our choice of ξ^i, this implies $\partial^0 h_{00} = 0$. Since a time-independent h_{00} corresponds to a static contribution to the gravitational field, and gravitational waves are time-dependent fluctuations, we can set $h_{00} = 0$. So, with our gauge choices, only the spatial components h_{ij} can be non-zero. This gauge is known as the transverse-traceless (TT) gauge, the gravitational wave strain in this gauge is often denoted h_{ij}^{TT}, and it is given by the constraints

$$h_{0\mu} = 0, \quad h^i{}_i = 0, \quad \partial^j h_{ij} = 0 \ . \tag{2.24}$$

Note that this gauge admits plane wave solutions. If a plane wave is traveling along the z-axis with angular frequency ω, the strain takes the form

$$h_{ij}^{TT} = \begin{pmatrix} h_+ & h_\times & 0 \\ h_\times & -h_+ & 0 \\ 0 & 0 & 0 \end{pmatrix}_{ij} \cos\left(\omega(t - z/c)\right) \ . \tag{2.25}$$

Suppose that we have the strain in some harmonic gauge coordinate system, but not in the TT gauge for propagation along some direction $\widehat{\mathbf{N}}$. Then, we can transform into the TT gauge using the Lambda tensor [9],

$$\Lambda_{ij,kl}(\widehat{\mathbf{N}}) = P_{ik}\, P_{jl} - \frac{1}{2}\, P_{ij}\, P_{kl}\ , \tag{2.26}$$

where $P_{ij}(\widehat{\mathbf{N}}) = \delta_{ij} - N_i\, N_j$ is a projector along $\widehat{\mathbf{N}}$. Then, if h_{kl} is the strain is some arbitrary harmonic coordinate frame, we have

$$h_{ij}^{\rm TT} = \Lambda_{ij,kl}(\widehat{\mathbf{N}})\, h_{kl}\ . \tag{2.27}$$

Equivalently, we can construct an orthonormal basis $\left(\widehat{\mathbf{N}}, \widehat{\mathbf{P}}, \widehat{\mathbf{Q}}\right)$ (where $\widehat{\mathbf{N}}$ is the direction of propagation) and construct the two polarizations h_+ and $h_\times$ appearing in Eq. (2.25) directly as

$$h_+ \;=\; \frac{1}{2}(P^i\, P^j - Q^i\, Q^j)\, h_{ij}\,, \tag{2.28}$$

$$h_\times \;=\; \frac{1}{2}(P^i\, Q^j + Q^i\, P^j)\, h_{ij}\,. \tag{2.29}$$

Let us consider a rotation by an angle Ψ about the z-axis. This coordinate transformation can be described with the rotation matrix

$$\mathcal{R}(\Psi)^i{}_j = \begin{pmatrix} \cos\Psi & \sin\Psi & 0 \\ -\sin\Psi & \cos\Psi & 0 \\ 0 & 0 & 1 \end{pmatrix}\ . \tag{2.30}$$

According to the tensor transformation law [12], the GW strain tensor will transform as $h'_{ij} = \mathcal{R}(\Psi)^k{}_i \, \mathcal{R}(\Psi)^l{}_j \, h_{kl}$, and so

$$h_{ij}^{\prime TT} = \begin{pmatrix} h_+ \cos 2\,\Psi + h_\times \sin 2\,\Psi & -h_+ \sin 2\,\Psi + h_\times \cos 2\,\Psi & 0 \\ -h_+ \sin 2\,\Psi + h_\times \cos 2\,\Psi & -h_+ \cos 2\,\Psi - h_\times \sin 2\,\Psi & 0 \\ 0 & 0 & 0 \end{pmatrix}_{ij} , \quad (2.31)$$

where we have dropped the factor $\cos(\omega(t - z/c))$ above for brevity. Note that when we apply a coordinate rotation by the angle Ψ, the components of the gravitational wave strain are rotated by an angle $2\,\Psi$. This shows that gravitational waves are a spin-2 field [9].

2.1.4 Interactions with gravitational waves

The equation of motion for a freely falling test mass in a curved spacetime is given by the geodesic equation

$$\frac{d^2 x^\mu}{d\tau^2} + \Gamma^\mu_{\nu\lambda} \frac{dx^\nu}{d\tau} \frac{dx^\lambda}{d\tau} = 0 \ , \quad (2.32)$$

where τ is proper time (or some other affine parameter) parametrizing the location of the test mass along the geodesic [12, 9]. Let us work in the TT gauge and consider a gravitational wave propagating along the z-axis, which at proper time $\tau = 0$ passes three test particles which are all at rest in the TT gauge with (x, y, z) coordinates of $(0, 0, 0)$, $(L, 0, 0)$ and $(0, L, 0)$. We can use the geodesic equation to find the motion of each test particle. Since they are all initially at rest, each test particle will have

$dx^i/d\tau = 0$ and $dx^0/d\tau = c$. Therefore, at the instant the gravitational wave reaches the test particles, we have

$$\left.\frac{d^2x^\mu}{d\tau^2}\right|_{\tau=0} = -c^2\,\Gamma^\mu_{00}\Big|_{\tau=0} \quad . \tag{2.33}$$

Using Eq. (2.14), we find

$$\Gamma^\mu_{00} = \frac{1}{2}\,\left(2\,\partial_0\,h_{0\mu} - \partial_\mu\,h_{00}\right) \quad . \tag{2.34}$$

Note that Eq. (2.33) is identically zero, since in the TT gauge we have $h_{0\mu} = 0$. Therefore, if a particle is initially at rest with respect to the TT frame, it will remain at rest with respect to this frame as a gravitational wave passes. However, this is a statement about the *coordinate* distance between the test particle, while what is physically observable is the *proper* distance between the particles. Using the TT gravitational strain of Eq. (2.25), we have

$$\begin{aligned} ds^2 &= -c^2\,dt^2 + \left[1 + h_+\,\cos\left(\omega(t - z/c)\right)\right]\,dx^2 + \left[1 - h_+\,\cos\left(\omega(t - z/c)\right)\right]\,dy^2 \\ &\quad +2\,h_\times\,\cos\left(\omega(t - z/c)\right)\,dx\,dy \ , \end{aligned} \tag{2.35}$$

and we can compute the proper distance between the test particles on the x- or y-axis by integrating along that axis. These proper distances are [11, 9]

$$s = L\,\sqrt{1 \pm h_+\,\cos\left(\omega(t - z/c)\right)} \simeq L\,\left[1 \pm \frac{h_+}{2}\,\cos\left(\omega(t - z/c)\right)\right] \ , \tag{2.36}$$

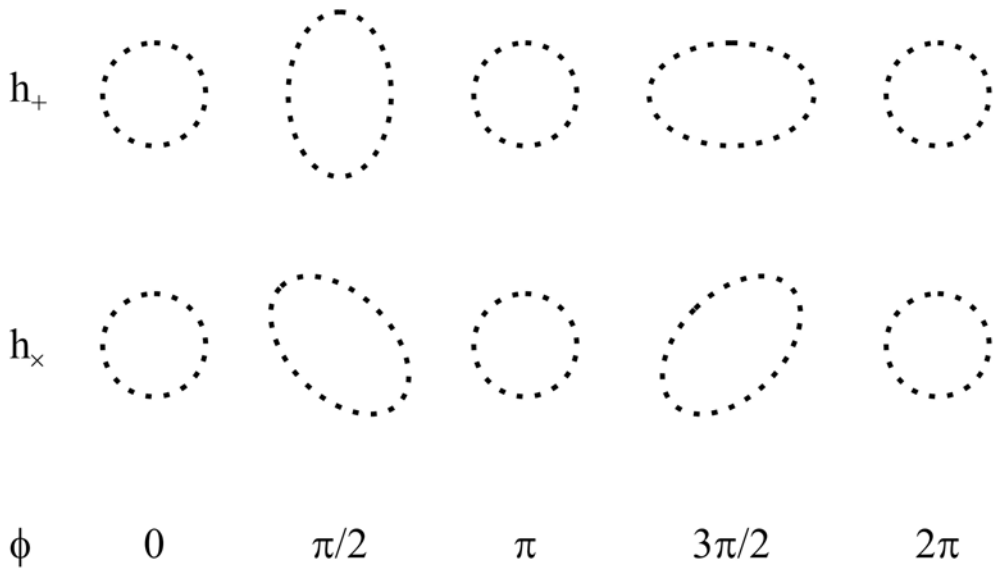

Figure 2.2: A ring of test particles in the x-y plane will be stretched and squeezed by a gravitational wave travelling along the z-axis. The effect of the polarization modes h_+ and $h_\times$ is shown at each quarter gravitational wave cycle.

where the upper sign is for the x-axis and the lower sign is for the y-axis. Therefore, the proper separations along the x- and y-axes undergo an oscillatory fractional change proportional to h_+. When one is stretched, the other is squeezed. Similarly, the diagonal directions are stretched and squeezed proportionally to $h_\times$. Fig 2.2 depicts the effect of each gravitational wave strain on a ring of test particles.

2.1.5 Detecting gravitational waves

The basic idea of a laser interferometer gravitational wave detector like LIGO is to measure the distance along two perpendicular directions to a very high precision to detect a differential change in length from a passing gravitational wave. We have seen how the polarizations of a passing gravitational wave will warp the plane perpendicular to the direction of propagation. The effect of a gravitational

wave from an arbitrary direction can be described with the aid of *antenna pattern functions*. These depend on the geometry of the detector. For an interferometer with arms at right angles, they are given by [5]

$$F_+ = \frac{1}{2}\left(1+\cos^2\bar{\theta}\right)\cos 2\bar{\phi}\cos 2\,\psi - \cos\bar{\theta}\sin 2\bar{\phi}\sin 2\psi\ , \tag{2.37}$$

$$F_\times = \frac{1}{2}\left(1+\cos^2\bar{\theta}\right)\cos 2\bar{\phi}\sin 2\psi + \cos\bar{\theta}\sin 2\bar{\phi}\cos 2\psi\ . \tag{2.38}$$

where $(\bar{\theta},\bar{\phi})$ are the spherical coordinates from which the gravitational wave propagates (measured relative to directly above the center of the detector), and the polarization angle ψ describes the angle of the vector P^i appearing in Eqs. (2.28)-(2.29) relative to the plane of constant sky azimuthal angle $\bar{\phi}$. The measured strain (the fractional differential change in arm length) is then

$$h(t) = F_+\,h_+(t) + F_\times\,h_\times(t)\ . \tag{2.39}$$

A basic schematic for a LIGO-type interferometer is depicted in Fig. 2.3. A laser is fired at a beam splitter, which sends the light down each arm in equal parts. The beams travel down the arms and return to the beam splitter, where they interfere with one another, and this combined light is monitored at the "dark port". The dark port is so named because the interferometer is designed so that when the instrument is locked the arm lengths will differ by a half wavelength (plus some integral number of wavelengths) and the beams from each arm will interfere destructively and cancel. If some light is observed at the dark port, this means there

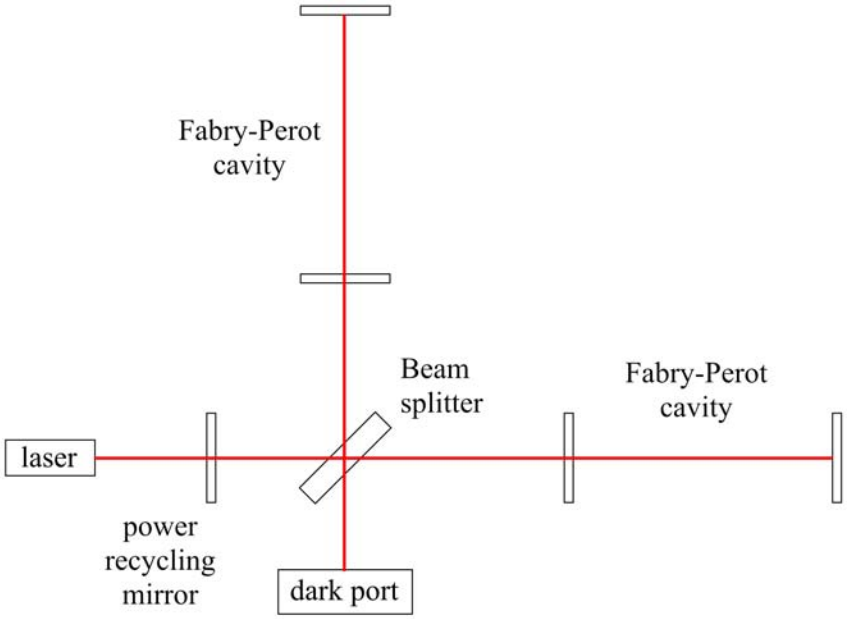

Figure 2.3: Basic schematic of a ground-based interferometer such as LIGO. A laser impinges upon a beam splitter which splits the light equally along two arms perpendicular to one another. Each arm consists of a Fabry-Perot cavity, where the light reflects several times before returning to the beam splitter. Light which heads back towards the laser is reflected back to the beam splitter by a power recycling mirror, increasing the laser power in the instrument. The superposition of light from both arms is measured at the dark port, and perturbations to the arm lengths will change the measured intensity of light.

has been a relative phase shift in the two beams, and thus a differential change in the path length of each beam.

Since a gravitational wave will produce a fractional change in length, while the phase shift (and hence the change in light intensity at the dark port) is proportional to the absolute change in path length of the light, one should make each of the arms of the interferometer as long as possible. For this reason, the main LIGO interferometers have 4 km arms. Furthermore, each arm of the interferometer consists of a Fabry-Perot cavity, which reflects the light several times before it escapes and returns to the beam splitter, effectively increasing the path length of the light. Such

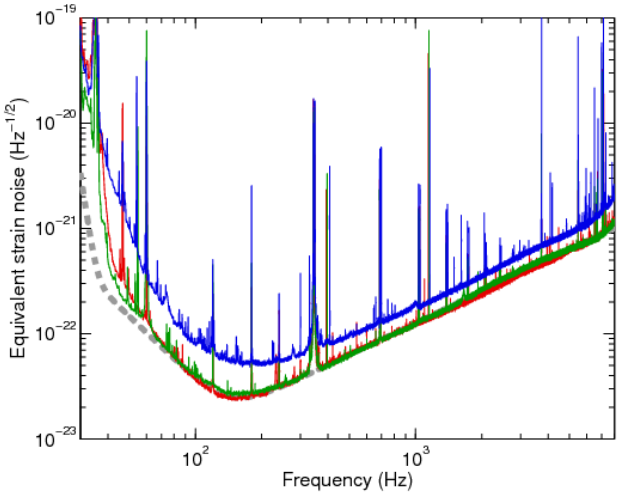

Figure 2.4: Amplitude spectral densities as a function of frequency for typical times during S5. The curves are for the H1 4km interferometer at Hanford, WA (red), the L1 4km interferometer at Livingston, LA (green), the H2 2km interferometer at Hanford (blue) and the design goal of initial LIGO (dashed grey). This plot is taken from Ref. [13].

a configuration is capable of measuring a strain of the order $\sim 10^{-22}$ at which we hope to observe gravitational waves. However, it must contend with environmental noise sources which perturb the instrument. The three main types of noise sources (at least for first generation detectors) are seismic, thermal and shot noise.

Seismic noise is caused by vibrations of the Earth and is the dominant noise source at low frequencies. It can be mitigated by isolating all of the mirrors from the ground as much as possible. The Initial LIGO interferometers suspend their mirrors from pendula attached to mass and spring "isolation stacks". This can significantly attenuate seismic noise down to ~ 40 Hz, but the noise rises very rapidly at lower frequencies, creating a "seismic wall" in the instruments' noise curve. The Advanced LIGO (and the European Virgo) detectors will suspend their mirrors from multiple pendula, which are capable of attenuating the seismic noise down to ~ 10 Hz.

Shot noise is caused by fluctuations in the number of photons which impinge upon the dark port and is the dominant noise source above frequencies of $\gtrsim 200$ Hz. The arrival of photons is a Poisson process, so if $\langle N \rangle$ is the average rate at which photons arrive at the dark port, the standard deviation is $\sqrt{\langle N \rangle}$, and so the fractional change in intensity will be less for higher intensity laser light. Thus, shot noise can be mitigated by using a more powerful laser, and using a power recycling mirror to increase the power in the interferometer.

However, a more powerful laser can increase the thermal noise, which is dominant at intermediate frequencies, roughly $40 \lesssim f \lesssim 200$ Hz. The initial LIGO design uses a 10W laser while advanced instruments will use higher powered lasers. Thermal noise is caused by thermal vibrations in the mirrors and their suspension wires. One way to address this is to use materials which have very sharp thermal peaks, so that the oscillations occur in a very narrow frequency band. The proposed (and recently funded!) Japanese Large-scale Cryogenic Gravitational-wave Telescope (LCGT) interferometer would also cryogenically cool the mirrors to reduce thermal noise [14].

Through careful design, the initial LIGO design is able to achieve sensitivities $\sim 10^{-22}$ in the frequency band of $\sim 40 - 2000$ Hz. The LIGO design sensitivity and the actual sensitivity achieved during each of LIGO's first five science runs are depicted in Fig. 2.4.

2.2 Constructing analytic templates for compact binary coalescences

Compact binary coalescences are one of the most promising sources of gravitational waves detectable by LIGO and Virgo. One of the reasons is that the waveforms from such systems can be computed analytically to create search templates which make it easier to dig weak signals out of noise. Compactness can be quantified with a so-called compactness parameter, $\gamma = G\,m/(c^2\,L) \sim 1$, where m is the mass of a body and L is its characteristic size (e.g. radius). Note that $\gamma \sim 0.5$ for a black hole (BH), $\gamma \sim 0.16$ for a neutron star (NS), while $\gamma \ll 1$ for ordinary stars. "Compact binaries" are composed of two compact objects (black holes and/or neutron stars) which orbit one another with a radial separation that is a few tens of gravitational radii (defined as $r = GM/c^2 \sim 1.5\ (M/M_\odot)$ km where $M = m_1 + m_2$ is the total mass of the binary) or less. The orbit shrinks as energy is lost to gravitational waves. At relatively large separations, the radial motion will be much slower than the orbital motion, so that the two bodies will undergo an adiabatic inspiral along slowly shrinking orbits. When the bodies are separated by only a few gravitational radii, the radial velocity will become more significant and the two bodies will plunge together and merge into a final deformed black hole, which will undergo "ringing" as it radiates away its deformations and settles into a final state.

Typically, one assumes that the binaries move along quasi-circular orbits (that is, circular apart from the slowly shrinking radius), which simplifies the waveforms greatly. This is reasonable, at least in the expected scenario of a binary star system

in which both stars produce compact objects at the end of their life cycle, because even if the binary forms on an eccentric orbit, the eccentricity will radiate away and the orbit will tend to circularize by the time it enters the sensitive band of ground-based detectors [15, 16]. However, Refs. [17, 18] proposed a scenario which could produce compact binaries on eccentric orbits that would not have time to circularize. Ref. [17] explains that four-body interactions between black holes of mass $\sim 10\,M_\odot$ in globular clusters could lead to one of the black holes being ejected, two of the black holes forming an inner binary, and a third black hole orbiting the inner binary. If the orbit of the outer object is tilted relative to the orbital plane of the inner binary, it could perturb the inner binary via the Kozai mechanism so that binary will have significant eccentricity despite the circularizing effects of GW emission. Ref. [18] finds that $\sim 30\%$ of these systems could have an eccentricity > 0.1 at a GW frequency of 10 Hz. Ref. [17] also points out that many of these systems would not have a significant "kick" from the asymmetric emission of gravitational waves, and so they would remain in the center of the globular cluster, where they could undergo further mergers. A series of such mergers could produce larger black holes of masses $\gtrsim 100\,M_\odot$. In this work we will only consider waveforms for binaries on quasicircular orbits.

If general relativity is correct, there is an upper limit on the spin (rotational angular momentum) of a black hole of a given mass. If the black hole were to exceed this maximum spin a naked singularity would form. If we write the rotational angular momentum of a black hole as $\mathbf{S} = G\,m^2\,\boldsymbol{\chi}/c$ (where m is the mass of the black hole), then this limit (known as the Kerr limit) can be written as $|\boldsymbol{\chi}| \leq 1$.

Neutron stars have spin magnitudes which are much smaller than the Kerr limit. The fastest known pulsar has a spin $|\boldsymbol{\chi}| = 0.02$. With the observed range of pulsar periods and current understanding of spindown rates, it is expected the neutron stars are likely to be born with periods of $10 - 140$ ms, corresponding to spins of $|\boldsymbol{\chi}| \lesssim 0.04$ [19]. On the other hand, there is a great deal of uncertainty in the distribution of values of $\boldsymbol{\chi}$ for black holes. However, as summarized in Ref. [19], observations of X-ray binaries have suggested that many black holes could have $|\boldsymbol{\chi}| \gtrsim 0.7$. In particular, observations suggest that one such BH in an X-ray binary has a near-extremal spin, with $|\boldsymbol{\chi}| \geq 0.98$ [20]. Therefore, it is quite possible that many black holes will have spins which are a substantial fraction of the Kerr limit. In that case, the spins can significantly affect the behavior of the binary and the observed waveform. In Sec. 2.2.1.1, we will begin by deriving inspiral waveforms for non-spinning compact binaries in the post-Newtonian (PN) formalism. In Sec. 2.2.2, we will present the basics of the effective-one-body (EOB) formalism, which can generate complete inspiral-merger-ringdown (IMR) waveforms. In Sec. 2.2.3, we will see how spin corrections can be included in the PN formalism, and the effect they have on the binary and the gravitational waveform.

2.2.1 Post-Newtonian waveforms

2.2.1.1 Post-Newtonian expansion

The PN formalism provides a framework to compute gravitational waveforms emitted by systems which are "slow-moving" ($v/c \ll 1$) and "weakly-gravitating"

($G\,M/r\,c^2 \ll 1$). One or both of these quantities is treated a small parameter, and Einstein's equations are solved iteratively. From the virial theorem, which states that the average kinetic energy equals half the average potential energy, we find the relation $v^2 \simeq G\,M/r$. When we refer to a k–PN order expression, this means that terms up to the power $(v/c)^{2k}$ and $(G\,M/r\,c^2)^k$ *beyond the leading order* have been retained and higher order terms have been discarded.

For example, the usual Kepler relation $(r\,\omega)^2 = G\,M/r$ is only true to leading order. There are general relativistic corrections, which enter as higher powers of the PN expansion parameters. The generalized Kepler relation between ω and r in PN theory takes the form

$$(r\,\omega)^2 = \frac{G\,M}{r}\left[1 + a_1\left(\frac{G\,M}{r\,c^2}\right) + a_2\left(\frac{G\,M}{r\,c^2}\right)^2 + a_3\left(\frac{G\,M}{r\,c^2}\right)^3 + \mathcal{O}\left(\frac{G\,M}{r\,c^2}\right)^4\right] . \tag{2.40}$$

Note that the above relation is currently known to 3PN order. The values of the coefficients are coordinate-dependent, and can be found in Eq. (147) of [21] for harmonic coordinates. Using Eq. (2.40), and assuming circular orbits, it is possible to compute any relevant quantity as a power series using either the orbital frequency or radius. Throughout this thesis, we shall expand in the frequency by defining the PN expansion parameter

$$v \equiv \left(\frac{G\,M\,\omega}{c^3}\right)^{1/3} , \tag{2.41}$$

with every power of v *beyond the leading order* counting as half a PN order.

2.2.1.2 Gravitational wave strain

We have shown that in linearized gravity with appropriate gauge choices, Einstein's equation can be recast as a wave equation, Eq. (2.20). As was done in Ref. [22], one can can actually express Einstein's equations in the form of a wave equation without making any simplifying assumptions such as keeping only linear terms. To do this, we can define the quantity

$$\hbar^{\mu\nu} = \eta^{\mu\nu} - \sqrt{-g}\, g^{\mu\nu} \ , \tag{2.42}$$

which is sometimes referred to as a gravitational potential, or a gravitational-field amplitude. In terms of this gravitational-field amplitude, Einstein's equations become [22, 21, 23, 9]

$$\Box \hbar^{\mu\nu} = -16\,\pi\,\tau^{\mu\nu} \ . \tag{2.43}$$

Here $\Box = \partial_\mu \partial^\mu$ is the flat spacetime D'Alembertian, $\tau^{\mu\nu} = |g|\, T^{\mu\nu} + \frac{1}{16\pi}\,\Lambda^{\mu\nu}$ is a stress-energy pseudo-tensor which is the sum of the stress-energy tensor of the matter ($T^{\mu\nu}$) plus the contribution from the gravitational waves ($\Lambda^{\mu\nu}$), which is defined in Eq. (2.6) of [23]. $\Lambda^{\mu\nu}$ is due to the non-linearity of the full theory, and contains terms quadratic in derivatives of $\hbar^{\mu\nu}$.[1] This is related to the fact that gravitational waves carry energy, and therefore can themselves be a source of gravitational waves. We can preserve the usual form of a wave equation with a source term by putting these non-linear terms on the right hand side and treating them as a source term

[1] Because this non-linear term is second order in h, it did not appear in the linearized theory.

arising from the energy in the gravitational waves themselves.

The form of Eq. (2.43) suggests that we can solve Einstein's equations for the gravitational-field amplitude $\hbar_{\mu\nu}$ by using a Green's function

$$\hbar^{\mu\nu}(t, \mathbf{x}) = 4 \int \frac{\tau^{\mu\nu}\, \delta^4(t - t' + |\mathbf{x} - \mathbf{x}'|)}{|\mathbf{x} - \mathbf{x}'|}\, d^4\mathbf{x}' \ . \tag{2.44}$$

In PN theory, one uses this Green's function representation of the solution to Eq. (2.43) and finds an approximate expression for the Green's function by expanding the integral of Eq. (2.44) in a series of multipoles, and then expanding each of the multipoles in a power series in PN expansion parameters [21, 23, 9]. This is in analogy with the computation of electromagnetic waves from a vector potential source in electrodynamics, but there are several subtle complications.

For example, we have already noted that the "source term", $\tau^{\mu\nu}$, depends explicitly on the gravitational-field amplitude, $\hbar^{\mu\nu}$, which makes the equations nonlinear and difficult to solve. Ref. [23] further explains the effect of a term $-\hbar^{\alpha\beta}\, \partial_\alpha\, \partial_\beta\, \hbar^{\mu\nu}$ appearing in $\Lambda^{\mu\nu}$. Note that the d'Alembertian operator appearing on the left hand side of Eq. (2.43) is $\Box = \eta^{\alpha\beta}\, \partial_\alpha\, \partial_\beta$, which is the wave operator for a wave travelling through flat spacetime. Although we have swept up the term $-\hbar^{\alpha\beta}\, \partial_\alpha\, \partial_\beta$ (acting on $\hbar^{\mu\nu}$) into the right hand side of Eq. (2.43), in a sense it belongs with the d'Alembertian on the left hand side, as this term is a manifestation of the fact that the gravitational waves are not propagating through a flat spacetime, but through a spacetime which is curved around the source. To deal with these and other subtleties, PN theory uses matched asymptotic expansions to calculate $\hbar^{\mu\nu}$.

In particular, one must expand with one set of "source" multipoles that are valid in the "near zone" (distances from the source that are short compared to the gravitational wavelength) and another set of "radiative" multipoles that are valid in the "far zone" (distances that are large compared to the physical size of the source) and then match the two expansions in an intermediate region where both are valid. This calculation has been carried out to 3.5PN order [24, 25, 26, 27]. The subject is also reviewed in [21, 9].

The end result of this calculation is an expression for the gravitational wave strain of the form [23]

$$h_{ij}^{\rm TT} = \Lambda_{ij,kl}\,\frac{2\,M\,\nu}{D_L}\,\left(Q_{kl} + P^{0.5}Q_{kl} + P^{1}Q_{kl} + ...\right)\ , \tag{2.45}$$

where D_L is the luminosity distance and $\Lambda_{ij,kl}$ is the Lambda tensor of Eq. (2.26), which projects into the TT gauge. The lowest order contribution to the radiation, Q_{ij} comes from the second time derivative of the mass quadrupole of the source. There are also PN corrections to the quadrupole formula, denoted as $P^n Q_{ij}$, coming from higher order multipoles. For a compact binary on a quasi-circular orbit, we have

$$Q_{ij} = 2\,v^2\,\left(\lambda_i\,\lambda_j - n_i\,n_j\right)\ , \tag{2.46}$$

where $\hat{\mathbf{n}}$ is a unit separation vector pointing from one of the bodies to the other and $\hat{\boldsymbol{\lambda}}$ is a unit vector along the instantaneous velocity of $\hat{\mathbf{n}}$. If we choose a source frame with z-axis along the orbital angular momentum of the binary, then these vectors

are given as

$$\hat{\mathbf{n}} = (\sin\Phi, -\cos\Phi, 0) \ , \tag{2.47}$$

$$\hat{\boldsymbol{\lambda}} = (\cos\Phi, \sin\Phi, 0) \ , \tag{2.48}$$

where Φ is the orbital phase of the binary. If we want to find the strain in the TT gauge for a gravitational wave propagating at some angle θ relative to the z-axis (the azimuthal angle is degenerate with the initial orbital phase, so we can set it to zero without loss of generality), i.e. along the direction

$$\widehat{\mathbf{N}} = (\sin\theta, 0, \cos\theta) \ , \tag{2.49}$$

then we can use Eq. (2.25), or equivalently Eqs. (2.28) and (2.29), to obtain the TT strain and polarizations. One finds

$$h_+(t) = \frac{2\,M\,\nu\,v(t)^2}{D_L}\left(1+\cos^2\theta\right)\cos 2\Phi(t) \ , \tag{2.50}$$

$$h_+(t) = \frac{4\,M\,\nu\,v(t)^2}{D_L}\cos\theta\,\sin 2\Phi(t) \ . \tag{2.51}$$

These polarizations are typically used to describe a gravitational wave as observed by a detector. We can insert these polarizations into Eq. (2.39) to find the strain measured by the detector.

However, the measured strain depends on the relative orientation between the source and detector through the so-called antenna pattern function F_+ and $F_\times$ of

Eqs. (2.37)-(2.37) and also through the angle θ appearing in the polarizations. In some applications, such as numerical relativity, one does not wish to specify a particular orientation between source and detector, but rather wants a more global description of the radiation emitted by a source. In this case, it is common to decompose the gravitational wave strain in terms of a set of -2 spin-weighted spherical harmonics, denoted ${}_{-2}Y^{\ell m}(\theta, \phi)$. They are a generalization of the usual spherical harmonics, and are defined in Eq. (4.41) of Chapter 4.

If we know the polarizations for a gravitational wave propagating in an arbitrary direction with spherical coordinates (θ, ϕ) relative to the source frame, then we can construct a series of harmonic modes via

$$h_{\ell m}(t) = \int d\Omega \, (h_+ - i \, h_\times)(\theta, \phi, t) \, {}_{-2}Y^{\ell m *}(\theta, \phi) \; , \tag{2.52}$$

where $2 \leq \ell < \infty$, $-\ell \leq m \leq \ell$. Alternatively, if the modes are known, one can recover the polarizations via

$$(h_+ - i \, h_\times) \, (\theta, \phi, t) = \sum_{\ell=2}^{\infty} \sum_{m=-\ell}^{\ell} h_{\ell m}(t) \, {}_{-2}Y^{\ell m}(\theta, \phi) \; . \tag{2.53}$$

Notice that the $h_{\ell m}$ do not depend on the orientation relative to the source, this is all encoded in the ${}_{-2}Y^{\ell m}$'s.

Now, if we use the leading order quadrupole expression for the strain, the only non-vanishing mode is h_{22} (and h_{2-2} because the $-m$ modes are related to the $+m$

modes by a symmetry explained in Chapter 4). At leading order, it is given by

$$h_{22}(t) = -\frac{2\,M\,\nu\,v^2(t)}{D_L}\sqrt{\frac{16\pi}{5}}\,e^{-i\,2\,\Phi(t)}\left(1+\mathcal{O}(v^2)\right)\ . \tag{2.54}$$

The $P^n Q_{ij}$ higher order corrections to the strain will contribute to other modes, as well as corrections to the h_{22} mode. Note that the $(2,2)$ mode is proportional to $\exp(-i\,m\,\Phi)$. In fact, for all ℓ and m, we have

$$h_{\ell m} \propto e^{-i\,m\,\Phi}\ , \tag{2.55}$$

so long as the mode decomposition is done in a frame in which the z-axis is along the orbital angular momentum. This can always be done for a non-spinning binary, but for a generic spinning binary the orbital angular momentum can precess, making such a decomposition impossible. We will revisit this point in the context of spin effects in Sec. 2.2.3 and in Chapter 4.

2.2.1.3 **Waveform phasing**

We have outlined how the form of the gravitational wave strain can be derived in PN theory, the various ways it can be described as a tensor, a pair of polarizations, or a series of -2 spin-weighted spherical harmonic modes. In any of these forms, it is crucial to have an accurate knowledge of the orbital phase $\Phi(t)$ and the PN expansion parameter $v(t)$. In this thesis, as is usually done, we will construct PN waveforms for binaries which move on adiabatic, quasicircular orbits. That is, the

binary moves along orbits which are circular apart from a very slowly shrinking radius, and the radial velocity is negligible compared to the circular motion. In this regime, it is common to use the PN parameter we defined in Eq. (2.41).

If the orbital radius of the binary did not shrink due to the emission of gravitational waves, the bodies would orbit one another at a constant frequency, and we could simply integrate the frequency in time to find the orbital phase at any given instant. Of course, energy loss to gravitational waves does cause the radius to shrink, and in turn the frequency increases. So, in essence, we need to find a formula for the rate of change of the orbital frequency, and integrate it twice in time to determine the evolution of the phase.

To do this, we assume that all of the energy loss of the binary goes into gravitational waves,

$$-\frac{dE}{dt} = \mathcal{F} \ . \tag{2.56}$$

This is known as the energy balance equation. Using PN expansions for the binary energy $E(v)$ and gravitational wave flux $\mathcal{F}(v)$, an application of the chain rule gives us an evolution equation for our PN expansion parameter

$$-\frac{dE}{dv}\frac{dv}{dt} = \mathcal{F} \qquad \Rightarrow \qquad \frac{dv}{dt} = -\frac{\mathcal{F}}{dE/dv} \quad . \tag{2.57}$$

So, we obtain an evolution equation for v. By using Eq. (2.57) and

$$\frac{d\Phi}{dt} \equiv \omega_{\rm orb} = \frac{v^3}{M} \ , \tag{2.58}$$

we can evolve both $\Phi(t)$ and $\omega_{\rm orb}(t)$.

There are in fact several different ways that one may solve these equations to evolve Φ and v to construct waveforms. They are all equivalent to within whichever PN order we expand E and $\mathcal{F}$, but there will be differences in the waveforms, in effect due to different (unknown) truncation errors for each method. The waveforms obtained from the various methods are called PN *approximants*.

For example, one could simply take the phasing equations, Eqs. (2.57), (2.58), and solve them numerically. This method is known as the TaylorT1 approximant. It was introduced at 2PN order in Refs. [28, 29, 23, 30], and at 3PN and 3.5PN order in Refs. [31, 32, 33]. Alternatively, note that the right hand side of Eq. (2.57) is a rational function in v. One could first re-expand it in a Taylor series polynomial in v, and then numerically integrate it along with Eq. (2.58). This is known as the TaylorT4 approximant and was introduced in Ref. [34]. There is another approximant known as TaylorEt, used in Refs. [35, 36, 37], which is analogous to the TaylorT1 except that a dimensionless energy $\zeta = -2E/(M\nu)$ is used as an expansion parameter rather than v.

One can also work with an integral form of the phasing equations by integrating Eqs. (2.57), (2.58) by dv. That is,

$$t(v) = t_{\rm ref} + \int_v^{v_{\rm ref}} dv\, \frac{dE/dv}{\mathcal{F}} \tag{2.59}$$

$$\Phi(v) = \Phi_{\rm ref} + \frac{1}{M} \int_v^{v_{\rm ref}} dv\, v^3\, \frac{dE/dv}{\mathcal{F}}\ , \tag{2.60}$$

where $v_{\rm ref}$ is an arbitrary reference frequency and $t_{\rm ref}$ and $\Phi_{\rm ref}$ are integration con-

stants. Since the integrands are rational functions of v, they can be performed analytically. The TaylorT2 approximant builds a waveform from these parametric expressions for $t(v)$ and $\Phi(v)$. One can also explicitly invert $t(v)$ to obtain an analytic expression for $v(t)$ (and $\Phi(t) = \Phi(v(t))$), which is known as the TaylorT3 approximant.

There is one last approximant, the TaylorF2, which gives the waveform in the *frequency domain* rather than the time domain. This approximant first applies the stationary-phase approximation (SPA) to the time domain gravitational wave strain to obtain an ansatz analytic frequency domain waveform

$$\tilde{h}(f) \equiv \int_{-\infty}^{\infty} h(t)\, e^{2\,\pi\, i\, f\, t}\, dt \simeq \mathcal{A}\, f^{-7/6}\, e^{i(2\,\pi\, f\, t(v) - \Phi(v) - \pi/4)}\ , \tag{2.61}$$

where $\mathcal{A}$ is a constant. Then, one plugs in the TaylorT2 expressions for $t(v)$ and $\Phi(v)$ to get an explicit analytic frequency domain PN waveform. Because it uses the stationary-phase approximation, these waveforms are often referred to as "SPA waveforms".

2.2.1.4 Limits of the post-Newtonian formalism

It is a common practice to retain only the leading order quadrupole contribution to the waveform amplitude, but to compute the waveform phase to as high a PN order as possible. This is the so-called restricted waveform approximation. This is used because it is crucial to know the waveform phasing to a very high precision, but it is not crucial to know the amplitude to the same high precision [38]. It is vital

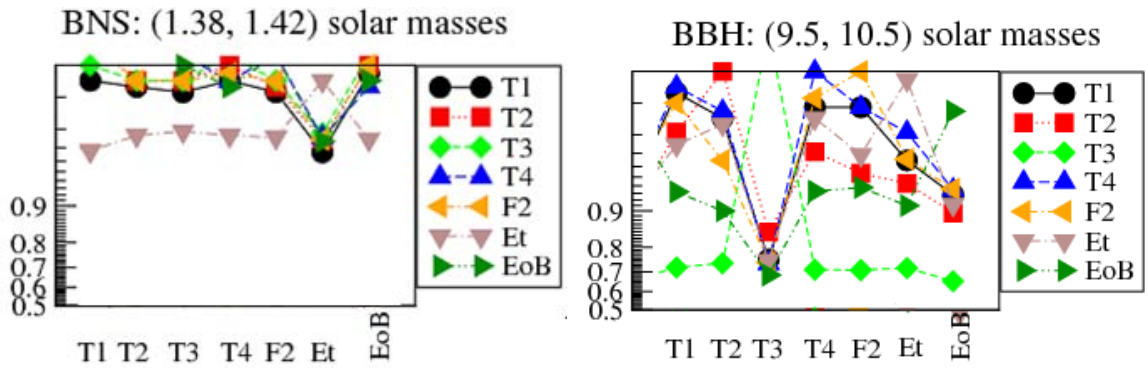

Figure 2.5: Plot of the effectualness between different PN approximants in initial LIGO for a $(1.42 + 1.38)\,M_\odot$ binary (left panel) and a $(10.5 + 9.5)\,M_\odot$ binary (right panel). As the total mass is increased, more of the large v portion of the waveform falls in the LIGO sensitive band, and the differences between the PN approximants begin to grow.

to accurately model the phasing of the waveform because one searches for binary inspirals by filtering against a bank of template waveforms. If the template gets out of phase with the actual signal, they will interfere destructively and this will degrade the ability to detect the signal. However, if the amplitude is wrong, one will simply over- or under-estimate the distance to the source, but it will not limit the ability to detect the signal.

Now, we have derived PN waveforms by assuming v is a small parameter for sources which are "slow-moving" and "weakly gravitating", but how slow and weakly gravitating must the sources be for the approximation to be valid? In addition, we have seen that there is not a single, unique prediction for the PN phasing, but several different approximants which differ by truncation errors. These factors may make one wonder if and when PN waveforms are accurate enough to be reliable detection templates. This question is addressed in detail in Chapter 3.

In short, we find that PN waveforms make good detection templates for

ground-based laser interferometers so long as the total mass of the binary is less than $M \sim 12M_\odot$. The reason that PN waveforms become inaccurate for higher mass signals is that larger values of v appear in the sensitive band as the mass is increased. Recall that $v = (M\,\omega_{\rm orb}/c^3)^{1/3} = (\pi\,M\,f_{\rm GW}/c^3)^{1/3}$. Now, ground-based laser interfometers like LIGO are most sensitive at frequencies $f_{\rm GW} \sim 150$ Hz. For a binary of total mass $1M_\odot$, this is at $v = 0.132$. For a binary of total mass $10M_\odot$, this is at $v = 0.285$. For a binary of total mass $100M_\odot$, this is at $v = 0.615$. So, our assumption that v is small begins to break down, and the PN approximants (based on Taylor series expansions in v) become less accurate.

If the total mass is much greater than $\sim 12M_\odot$, the various PN approximants start to differ significantly from one another, and also from waveforms calibrated to numerical relativity (NR) simulations. This can be quantified in terms of either faithfulness or effectualness. Faithfulness is the overlap between a signal and template waveform with the same mass parameters weighted by the noise curve of the detector normalized to be between 0 and 1. Effectualness is computed the same as faithfulness, except that the mass parameters of the template waveform are allowed to vary. Effectualness is the most appropriate measure of the performance of a template bank, since a signal would still be considered found if it matches a template with different parameters. Faithfulness is a more stringent test on the accuracy of a waveform, and quantifies the level of systematic errors in the parameters of a detected signal.

In Fig. 2.5, we illustrate the degraded effectualness among the PN approximants at 3.5PN order in initial LIGO as the total mass of the signal is increased. For

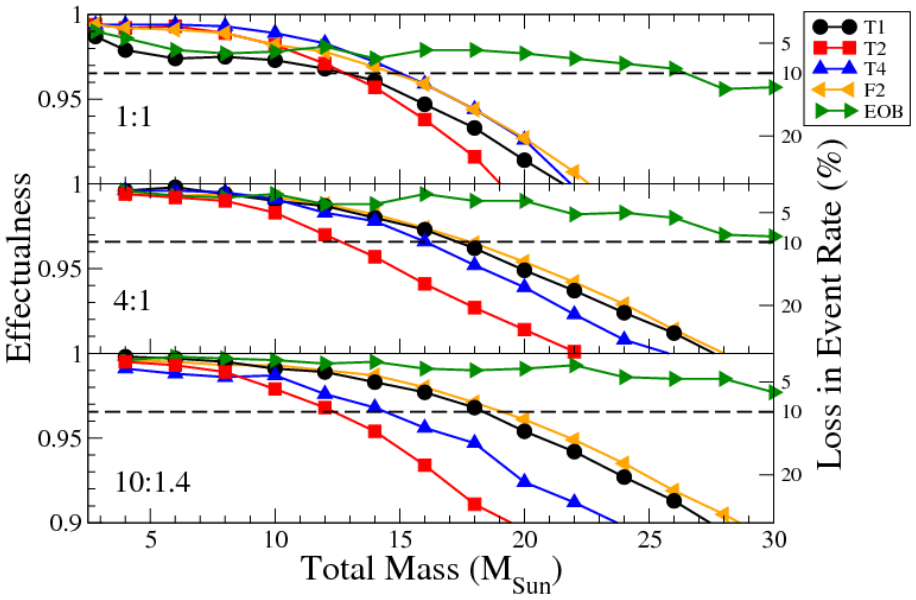

Figure 2.6: Effectualness and corresponding loss in event rate of PN templates and an EOB IMR signal for mass ratios 1:1 (top), 4:1 (center) and 10:1.4 (bottom). Note the green curve is for EOB inspiral-only templates. Beyond a total mass of $\sim 12-15\ M_{\odot}$, PN templates would lose more than 10% of IMR signals.

a $(1.42+1.38)\,M_{\odot}$ binary (left panel), all of the PN approximants (except TaylorEt) have an effectualness > 0.99, while for a $(10.5+9.5)\,M_{\odot}$ binary (right panel) the effectualness is typically $\sim 0.90-0.98$, and even lower for TaylorT3. This shows that the differences between the PN approximants grows as the total mass is increased. In Fig. 2.6, we illustrate that the PN templates become ineffectual at detecting complete IMR waveforms as the total mass is increased. We plot the effectualness of the PN approximants and an inspiral-only EOB model at 3.5PN against an EOB IMR signal which has been calibrated to NR simulations (so it is a good representation of a true, complete coalescence signal) in initial LIGO as a function of total mass for three different mass ratios. The dashed horizontal lines correspond to the effectualness at which 10% of signals are lost. Note that the PN approximants begin

to lose more than 10% of the signals once the total mass is larger than $\sim 12M_{\odot}$.

Fortunately, waveforms have been developed which improve upon the PN formalism. We will focus on the effective one-body formalism, which is described in the next section. This method employs resummation techniques to improve the PN series for large v by including the plunge-merger-ringdown signal to provide complete waveforms. By calibrating to numerical relativity simulations of the late inspiral and merger, this method can produce highly accurate IMR waveforms.

2.2.2 Effective one-body formalism

EOB dynamics and gravitational waveforms were first proposed and studied in [39, 40] to accurately describe binary black-hole systems of comparable masses. This approach was inspired by similar efforts to study two-body problems in quantum electrodynamics when the two charged bodies have comparable mass [41]. The basic idea is to create a mapping between the actual physical problem of two compact bodies interacting gravitationally and an effective problem of a single body moving in a background spacetime. A solution is found for the effective problem, and then mapped back to a solution of the actual physical problem, thereby resumming and improving the solution to the physical problem. Unlike the post-Newtonian waveforms we have discussed so far, this method does not assume an adiabatic inspiral. It can, in fact, produce a waveform up to the final plunge when the two bodies merge, at which point a ringdown waveform can be attached to create a complete inspiral-merger-ringdown waveform. Through comparison to numerical relativity

simulations, the values of certain adjustable parameters in the model describing the higher order (unknown) PN terms can be calibrated to produce analytic waveforms which agree with the numerical waveforms to a very high accuracy.

NR simulations are extremely computationally expensive to produce (a high accuracy simulation with ~ 30 GW cycles can take $\mathcal{O}(10^5$–$10^6)$ CPU-hours depending on the NR code), and have been produced for a rather small number of discrete waveform parameter values. Once the EOB waveforms have been calibrated to the NR simulations, one can interpolate and extrapolate to produce IMR waveforms for any set of waveform parameters at vastly less computational expense (a few CPU-seconds). This makes EOB waveforms very valuable for any number of data analysis tasks. In this thesis, we will use them to test the reliability of PN waveforms (Ch. 3), to predict the parameter estimation capabilities of second- and third-generation ground-based detectors (Ch. 6), and as detection templates (Ch. 5 and Ch. 7). First, we will briefly review the formalism for producing EOB waveforms.

2.2.2.1 EOB dynamics

For simplicity, we restrict the discussion to the non-spinning case, although in Sec. 2.2.2.6 we will note some more recent EOB models which include spin effects. The mapping between the real and effective problems is done within the Hamilton-Jacobi formalism. One finds a mapping between the energy levels of the two problems (that is, the two Hamiltonians) such that the total angular momentum and radial action variables are the same in both problems. If the masses of the two

compact bodies in the real problem are m_1 and m_2 (so $M = m_1 + m_2$), then the effective problem will be a single body of mass $\mu = m_1 m_2/M$ moving in a background spacetime. In the absence of radiation reaction, this background spacetime is a deformation of the usual Schwarzschild spacetime with deformation parameter $\nu = m_1 m_2/M^2$. Without loss of generality, we can assume the body moves in the equatorial plane, and describe its position with polar coordinates (R, ϕ). The Hamiltonian of the effective problem will depend on these coordinates and their conjugate momenta (P_R, P_ϕ). However, we will find it more convenient to express things in terms of "reduced" variables, which are made dimensionless by factoring out the relevant masses and constants. Therefore, we define:

$$r \equiv \frac{R}{GMc^2}\,, \quad p_r \equiv \frac{P_R}{\mu}\,, \quad p_\phi \equiv \frac{P_\phi}{GM\mu c^2}\,, \quad \hat{t} \equiv \frac{t}{GMc^3}\,, \quad \hat{\omega} \equiv GM\omega c^3\,, \tag{2.62}$$

In terms of these reduced variables, the metric of the effective spacetime is

$$ds^2 = -A(r)\,c^2\,dt^2 + \frac{D(r)}{A(r)}\,dr^2 + r^2\,\left(d\theta^2 + \sin^2\theta\,d\phi^2\right)\,, \tag{2.63}$$

and the effective Hamiltonian is

$$H^{\rm eff} \equiv \mu\,\widehat{H}^{\rm eff} = \mu\,\sqrt{A(r)\,\left[1 + \frac{A(r)}{D(r)}\,p_r^2 + \frac{p_\phi^2}{r^2} + 2\nu\,(4-3\nu)\,\frac{p_r^4}{r^2}\right]}\,. \tag{2.64}$$

The improved real Hamiltonian (and the mapping between real and effective energy levels) is given by

$$H^{\rm real} \equiv \mu\, \widehat{H}^{\rm real} = M \sqrt{1 + 2\nu \left(\frac{H^{\rm eff} - \mu}{\mu} \right)} \,. \tag{2.65}$$

We note that through 2PN order, the test particle can be considered to undergo geodesic motion within the effective spacetime, as was done in Refs [39, 40]. In this case the effective Hamiltonian would contain only terms up to quadratic order in the components of the test particle momentum (i.e. the last term in Eq. (2.64) would not be present). However, at 3PN order, requiring geodesic motion would give more constraints than free parameters and the system would be overdetermined. Therefore, Ref. [42] resolved this problem by adding a non-geodesic term to the effective Hamiltonian which is quartic in the test particle momentum. There is some freedom in the combinations of p_r and p_ϕ that appear in the quartic term. We shall only consider the simplest choice, as suggested in Ref. [42], in which we include only the quartic term proportional to p_r^4 (the last term in Eq. (2.64)).

The radial potential functions $A(r)$ and $D(r)$ appearing in the effective metric and Hamiltonian reduce to the Schwarzschild values of $1 - 2/r$ and 1 respectively in the limit $\nu \to 0$. Their Taylor series in $1/r$ are given as

$$A(r) = 1 - \frac{2}{r} + \frac{2\,\nu}{r^3} + \left(\frac{94}{3} - \frac{41\,\pi^2}{32} \right) \nu\, \frac{1}{r^4} + \frac{a_5}{r^5} \,, \tag{2.66}$$

$$D(r) = 1 - \frac{6\,\nu}{r^2} + \frac{2\,\nu\,(3\,\nu - 26)}{r^3} + \frac{d_4}{r^4} \,. \tag{2.67}$$

Both of these functions are currently known to 3PN order. The coefficients a_5 and d_4 are 4PN coefficients (because they are $\mathcal{O}(r^{-4})$ beyond the Schwarzschild values) which are not currently known. However, as we will see, one can calibrate these coefficients to mimic the behavior of all the unknown higher order PN coefficients and improve the agreement with NR simulations.

This Hamiltonian describes the *conservative* portion of the dynamics, so far we have not included the loss of energy to gravitational waves. Indeed, Hamilton's equation for the orbital angular momentum, p_ϕ, would give

$$\frac{dp_\phi}{d\hat{t}} = \frac{\partial \hat{H}^{\rm real}}{\partial \phi} = 0 \ , \tag{2.68}$$

so the orbital angular momentum would be conserved and the binary would not inspiral. This equation must be modified to include the ϕ-component of the (reduced) radiation reaction force, $\widehat{\rm F}_\phi = {\rm F}_\phi/\nu$. In principle, we should also consider the radial component of this force, but in Ref. [40], it was argued that for binaries moving along quasi-circular orbits this component is much smaller and can be neglected. Using the energy balance equation and the relation $\omega \, dL/dt = dE/dt$ one can relate the radiation reaction force, $\widehat{\rm F}_\phi$, to the gravitational wave flux, $\mathcal{F}$, by $\widehat{\rm F}_\phi = \mathcal{F}/(\nu \, v^3)$.

The EOB waveform is computed by numerically solving Hamilton's equations

for our improved real Hamiltonian augmented by our radiation reaction force:

$$\frac{dr}{d\hat{t}} = \frac{\partial \widehat{H}^{\rm real}}{\partial p_r}\,, \tag{2.69}$$

$$\frac{d\phi}{d\hat{t}} = \hat{\omega} = \frac{\partial \widehat{H}^{\rm real}}{\partial p_\phi}\,, \tag{2.70}$$

$$\frac{dp_r}{d\hat{t}} = -\frac{\partial \widehat{H}^{\rm real}}{\partial r}\,, \tag{2.71}$$

$$\frac{dp_\phi}{d\hat{t}} = \widehat{\rm F}_\phi\,. \tag{2.72}$$

Note that these waveforms compute the evolution of both ϕ and r, and so do not rely on the adiabatic approximation, i.e. that p_r will vary much more slowly than $r\,\hat{\omega}$. Using Hamilton's equations, we can calculate the waveform even when the adiabatic assumption breaks down, all the way to the final plunge before the two bodies merge.

2.2.2.2 EOB initial conditions

If we know the dynamical variables at some time, we can numerically integrate Hamilton's equations to find the values of the dynamical variables a short time later, and iterate this process to generate a waveform. However, we need a way to determine to values of the dynamical variables at the initial time. We can do this by following Ref. [40] (see also Ref. [43]) and making an adiabatic assumption for the initial conditions, i.e. that p_r is sufficiently small that we can neglect terms $\propto p_r^2$ and assume that the initial orbital angular momentum is approximately a constant, $p_\varphi^0 \equiv j$. If we start at a sufficiently large radius, this assumption will be valid.

For convenience, here we will use the variable $u = 1/r$. Then, under the adiabatic assumption, our effective Hamiltonian becomes

$$\widehat{H}^{\text{eff}}(u, j) = \sqrt{A(u)\ (1 + j^2\, u^2)}\ . \tag{2.73}$$

We can obtain a relation between j and u by solving Eq. (2.71) in the adiabatic limit,

$$\frac{dp_r}{d\hat{t}} = 0 = -\frac{\partial \widehat{H}^{\text{real}}}{\partial r}\ . \tag{2.74}$$

This will be satisfied when $\partial \widehat{H}^{\text{eff}}(u, j)/\partial u = 0$, and therefore

$$j^2(u) = -\frac{A'(u)}{(u^2\, A(u))'}\ , \tag{2.75}$$

where the prime denotes differentiation by u. Now, if we choose some initial radius r_0 (so $u_0 = 1/r_0$), then we can find the initial frequency from Eq. (2.70),

$$\hat{\omega}_0 = \left.\frac{\partial \widehat{H}^{\text{real}}(u, j(u))}{\partial j}\right|_{u=u_0}\ . \tag{2.76}$$

Conversely, if one wants to specify an initial frequency, one could invert this equation to find the initial radius corresponding to that frequency. Lastly, we need to find p_r^0, the initial value for the radial momentum. We can get this from Eq. (2.72) and the chain rule,

$$\frac{dj}{d\hat{t}} = \frac{dj}{dr}\,\frac{dr}{d\hat{t}} = \widehat{\mathrm{F}}_\phi\ . \tag{2.77}$$

This gives us dr/dt in terms of the radiation reaction force and the relation between j and r. Noting that $dj/dr = -u^2\, dj/du$ and using Eq. (2.69), we get

$$\frac{dr}{d\hat{t}} = \frac{\widehat{\mathrm{F}}_\phi}{-u^2\, dj/du} = \frac{\partial \widehat{H}^{\mathrm{real}}}{\partial p_r} \ . \tag{2.78}$$

Note that the right hand side has a term linear in p_r, and a term cubic in p_r. One can neglect the p_r^3 term, and get an explicit formula for p_r^0 as a function of u_0, $A(u_0)$ and $D(u_0)$. Alternatively, one could keep the p_r^3 and numerically solve for the value p_r^0 which satisfies Eq. (2.78).

2.2.2.3 Modeling the ringdown waveform

We have seen how the EOB formalism can be used to generate waveforms through the inspiral and plunge of the two compact bodies. We would now like to complete the waveform by including the ringdown of the merged black hole. When the two bodies merge, they will create a deformed Kerr black hole. This black hole will radiate away its deformations in a superposition of damped sinusoids [44, 45, 46]. A framework has been developed in Refs. [40, 47, 48, 49] to describe the gravitational waves emitted by a ringing Kerr black hole, in which each harmonic mode is described as a superposition of quasinormal modes (QNMs), including a fundamental ($n = 0$) and an infinite number of overtones ($n > 1$),

$$h^{\mathrm{RD}}_{\ell m}(t) = \sum_{n=0}^{\infty} A_{\ell m n}\, e^{-i\,\sigma_{\ell m n}\, t} \ . \tag{2.79}$$

Here, $A_{\ell mn}$ is an unknown complex amplitude (or real amplitude and phase constant) and $\sigma_{\ell mn} = \omega_{\ell mn} - i/\tau_{\ell mn}$ is a complex frequency containing the real frequency and decay time of the QNM. Ref. [50] provides fits to the $\sigma_{\ell mn}$ as functions of the mass and spin of the Kerr black hole.

We need to stitch the ringdown together with the inspiral-plunge to create a single IMR waveform. This can be done following the procedure of Refs. [48, 49], which is written quite concisely in Eqs. (42)-(44) of Ref. [49]. First, we will calculate the value of the inspiral waveform (i.e. harmonic mode) and its first two time derivatives $h^{\rm insp}_{\ell m}(t_{\rm match})$, $\dot{h}^{\rm insp}_{\ell m}(t_{\rm match})$, $\ddot{h}^{\rm insp}_{\ell m}(t_{\rm match})$ at some matching point $t_{\rm match}$. Then, we will approximate the ringdown waveform by including the fundamental QNM and its first two overtones,

$$h^{\rm RD}_{\ell m}(t) \simeq \sum_{n=0}^{2} A_{\ell mn}\, e^{-i\,\sigma_{\ell mn}\,(t-t_{\rm match})} \ , \tag{2.80}$$

where the $\sigma_{\ell mn}$ are given in Ref. [50]. Finally, we fix the $A_{\ell mn}$ by imposing that the inspiral and ringdown waveforms and their first two time derivatives agree at $t_{\rm match}$. which is equivalent to solving the linear system

$$\begin{pmatrix} 1 & 1 & 1 \\ -i\,\sigma_{\ell m0} & -i\,\sigma_{\ell m1} & -i\,\sigma_{\ell m2} \\ -\sigma^2_{\ell m0} & -\sigma^2_{\ell m1} & -\sigma^2_{\ell m2} \end{pmatrix} \begin{pmatrix} A_{\ell m0} \\ A_{\ell m1} \\ A_{\ell m2} \end{pmatrix} = \begin{pmatrix} h_{\ell m}(t_{\rm match}) \\ \dot{h}_{\ell m}(t_{\rm match}) \\ \ddot{h}_{\ell m}(t_{\rm match}) \end{pmatrix} \ . \tag{2.81}$$

The last thing we need is a way to determine where this $t_{\rm match}$ should occur. This is provided by Refs. [40, 51, 52]. They found that a test particle falling ra-

dially into a black hole will begin to excite the QNMs of the black hole once it crosses $r = 3\,G\,M/c^2$, the light ring (innermost unstable circular photon orbit) of a Schwarzschild black hole. This suggests that one should attach the ringdown at or near the time when the radial separation crosses the EOB light ring.

2.2.2.4 Advantages of the EOB formalism

Now that we have outlined the procedure for constructing EOB waveforms, we pause to reflect on some of the advantages of this method. We have noted that the EOB formalism does not assume an adiabatic inspiral, but rather uses a Hamiltonian to simultaneously solve for the orbital and radial motion of the binary. One could attempt to construct a non-adiabatic PN waveform model, for example by using a PN Taylor-expanded Hamiltonian. However, this will give a result which is quite different from the numerical simulations. For example, the 3PN Hamiltonian does not exhibit an innermost stable circular orbit (ISCO) (see e.g., [53]), and so the binary would never undergo a "plunge" of rapid radial motion, but would instead follow quasicircular orbits all the way down to the merger, quite unlike the numerical simulations. This suggests that the Taylor-expanded Hamiltonian is inadequate, and was a primary motivation for trying to improve the Hamiltonian by mapping onto an effective problem.

Furthermore, because the final state of coalescence is a single black hole, the effective problem of a test body orbiting a perturbed black hole spacetime is well-suited to describing the late portion of the coalescence signal. For example, the

ISCO and light ring of the perturbed spacetime arise quite naturally in the EOB formalism, and are important landmarks. The ISCO marks the onset of the plunge, while the light ring marks the beginning of excitation of ringdown QNMs. The locations of these two important landmarks are determined by the radial potential function, $A(r)$. This is very helpful in calibrating the EOB model to NR simulations, as one can adjust this radial potential with a single free parameter (the unknown 4PN coefficient a_5) to get the appropriate onset of plunge and ringdown. Compare this to the Taylor-expanded two-body Hamiltonian, where there would be many possible 4PN coefficients (corresponding to different combinations of powers of r and/or components of the momentum) and the notion of a light ring is not well-defined for a two-body spacetime.

2.2.2.5 Calibration to numerical relativity simulations

We now briefly summarize a series of improvements to the EOB model, leading up to the model of Ref. [54]. This model was compared to numerical simulations produced in 2006 by the NASA-Goddard NR group, and was found to *faithfully* represent those NR waveforms. That is, for the same mass parameters, its overlap with the NR waveforms was $\gtrsim 0.965$ and phase differences were typically $\lesssim 8\%$ of a GW cycle. This model was implemented into the LSC Algorithm Library (LAL) by the author of this thesis with the help of Yi Pan and B.S. Sathyaprakash, and is the EOB model used throughout this thesis. For convenience, we also provide all of the equations needed to generate this waveform model. Note that this model is

not a final destination, but rather a milestone along a journey. There is currently a great deal of effort to further improve the EOB model by comparing to longer, more accurate simulations, using newer resummation techniques, and including spin effects. We will briefly highlight some of these efforts in Sec. 2.2.2.6.

The first EOB model was introduced in Refs. [39, 40], and used a 2PN order EOB Hamiltonian with Taylor-expanded radial potential functions $A(r)$ and $D(r)$. It also incorporated radiation reaction force through a flux function, introduced in [55], which has a complex pole factored out and a Padé resummation is applied to the remainder. A ringdown waveform was attached analogously to the procedure described in Sec. 2.2.2.3, except that only the $(2, 2, 0)$ mode was included. A 3PN Hamiltonian was derived in Ref. [56]. Ref. [57] introduced the idea of further improving the model by applying Padé resummations to the radial potential functions $A(r)$ and $D(r)$. Padé resummation means that if one has a Taylor series for some function, this series is re-expressed as a rational function with coefficients fixed by requiring that the Taylor series of the rational function is equal to the original Taylor series [58]. Therefore, the Taylor and Padé expressions will be equivalent to the order of the Taylor series, but will differ in higher order truncation terms. The Padé resummation also provides greater freedom in the functional form of the expressions, potentially allowing for a closer approximation to the true value.

In Ref. [48], the authors compared analytic waveform models to the NR simulation of Pretorius. They found that an EOB model with a 3PN Hamiltonian with Padé-resummed radial potential functions and a 3.5PN order GW flux, Padé-resummed as in Ref. [55], gave the best agreement with the NR waveform. Ref. [48]

also proposed attaching ringdown waveforms with the dominant QNM and the first two overtones (rather than just the dominant QNM). While the first NR simulation by Pretorius had significant numerical error, the authors suggested that the agreement between EOB and numerical waveforms was quite promising, and that once more accurate NR simulations were available, it should be possible to further improve the EOB waveforms to create highly accurate analytic IMR waveforms. In Ref. [54], EOB waveforms were compared to newly available simulations by the NASA-Goddard NR group. The EOB waveforms used here were the same as in Ref. [48], except that the pseudo-4PN coefficient a_5 appearing in Eq. (2.66) was introduced to the radial potential $A(r)$ [43]. The label "pseudo" is used because the true value is not known. However, the authors introduced it to mimic the true 4PN order term (and all higher PN order terms) and searched over all possible values to find the value which gave the best agreement with the NR waveforms. In this way, the EOB model was *calibrated* to the NR simulations. One could add similar pseudo-4PN coefficients to $D(r)$ and $\mathcal{F}$ and search over their values, but a single coefficient added to $A(r)$ was found to be sufficient.

We now summarize all of the equations needed to generate the EOB waveform

model of Ref. [54]. First of all, the Padé-resummed radial potential functions are

$$\begin{aligned}
\mathrm{Num}\left[A(r)\right] &= r^3\left(32-24\nu-4a_4-a_5\right)+r^4\left(a_4-16+8\nu\right)\,, \qquad (2.82)\\
\mathrm{Den}\left[A(r)\right] &= -a_4^4-8a_5-8a_4\nu+2a_5\nu-16\nu^2+r\left(-8a_4-4a_5-2a_4\nu-16\nu^2\right)\\
&+ r^2\left(-4a_4-2a_5-16\nu\right)+r^3\left(-2a_4-a_5-8\nu\right)+r^4\left(-16+a_4+8\nu\right)\,,\\
D(r) &= \frac{r^4}{r^4+6\,\nu\,r^2+(26-3\nu)\,2\,\nu\,r+36\nu^2} \qquad (2.83)
\end{aligned}$$

where "Num" and "Den" refer to numerator and denominator, respectively and $a_4 = (91/3 - 41\,\pi^2/32)\,\nu$ is the coefficient multiplying r^{-4} in Eq. (2.66). Note that in Eq. (2.83) we have corrected a typo in Ref. [54], namely that the last term should be $36\,\nu^2$ rather than $36\,\nu$. For the Padé-resummed $A(r)$, choosing $a_5 = 60\,\nu$ was found to give the best agreement with the NR simulations to which this model was compared.

The radiation reaction force is of the form proposed in Ref. [55], where the Taylor-expanded PN GW flux (used here at 3.5PN order) has a real pole factored out and the remainder is Padé-resummed. The radiation reaction force is given as

$$\widehat{\mathrm{F}}_\phi(v) = -\frac{32}{5}\,\nu\,v^7\,\frac{f(v,\nu)}{1-v/v_{\mathrm{pole}}}\,, \qquad (2.84)$$

where the Padé-resummed portion $f(v,\nu)$ (given in continued fraction form) can be read from Eqs. (50)-(54) of Ref. [59] and the complex pole is that proposed by [55],

$$v_{\mathrm{pole}} = \frac{1}{\sqrt{3}}\sqrt{\frac{1+\frac{1}{3}\nu}{1-\frac{35}{36}\nu}}\,. \qquad (2.85)$$

With these choices of $A(r)$, $D(r)$ (inserted into the effective Hamiltonian of Eq. (2.64)) and $\widehat{\mathrm{F}}_\phi$, the inspiral waveform is generated by numerically solving Hamilton's equations, Eqs. (2.69)-(2.72). Initial conditions for the dynamical variables can be derived in the adiabatic limit, as in Ref. [40]. Here we express A and D as functions of $u = 1/r$, and a prime denotes differentiation by u. For an initial choice of $r_0 = 1/u_0$, one finds

$$\hat{\omega}_0 = u^{3/2} \sqrt{\left. \frac{-A'/2}{1 + 2\,\nu \left(\frac{A}{\sqrt{A + u\,A'/2}} - 1 \right)} \right|_{u=u_0}} , \tag{2.86}$$

$$p^0_\phi = \sqrt{\left. -\frac{A'}{u\,(2\,A + u\,A')} \right|_{u=u_0}} , \tag{2.87}$$

$$p^0_r = \left. \frac{u\,\left(2\,A + u\,A'\right)\,A'\,D}{A\,\left(2\,u\,(A')^2 + A\,A' - u\,A\,A''\right)} \right|_{u=u_0} \widehat{\mathrm{F}}_\phi(v = \hat{\omega}_0^{1/3}) \; . \tag{2.88}$$

Note that the initial value of ϕ can be chosen arbitrarily. One can also specify an initial frequency, rather than an initial radius. In this case, one inverts Eq. (2.86) to find the corresponding initial radius and plugs it into Eqs. (2.87) and (2.88).

The matching point is chosen as the time at which the reduced orbital frequency reaches the value

$$\hat{\omega}_{\rm match} = 0.133 + 0.183\,\nu + 0.161\,\nu^2 \; . \tag{2.89}$$

The ringdown waveform is attached according to Eq. (2.81), with the $\sigma_{\ell mn}$ given by Eqs. (E1)-(E2) and Table VIII of Ref. [50]. Note that these depend on the mass

and dimensionless spin of the final black hole ($j = a_{\rm final}/M_{\rm final}$). By fitting to the NR simulations, these values were chosen to be

$$M_{\rm final} = M\left(1 + (\sqrt{8/9} - 1)\,\nu - 0.498\,\nu^2\right) , \quad (2.90)$$

$$a_{\rm final}/M_{\rm final} = \sqrt{12}\,\nu - 2.900\,\nu^2 . \quad (2.91)$$

This procedure allows one to compute the harmonic modes of the EOB waveform of Ref. [54] through inspiral, merger and ringdown. One can obtain the polarizations, and thus the strain measured by a detector, by using Eq. (2.53). Note that Ref. [54] included the modes $(2,2)$, $(3,3)$ and $(4,4)$, while in Ch. 5 and Ch. 7 we include only the $(2,2)$ mode and in Ch. 6 we include the $(2,2)$, $(2,1)$, $(3,3)$ and $(3,1)$ modes (plus the $m \to -m$ modes in all cases). Each harmonic mode is constructed in the same way, so it is straightforward to include as many modes as desired.

2.2.2.6 More recent and future EOB improvements

The EOB model of Ref. [54] described in the previous section was the first attempt to faithfully match NR simulations with a complete merger and ringdown, for mass ratios $1:1$ to $1:4$. A few months after Ref. [54] appeared, other variations of the EOB model calibrated to NR simulations of the Jena and AEI groups were proposed and investigated [60, 61]. Since then, more NR simulations have been done which are longer, more accurate, and span a larger parameter space, in particular the ones from the Caltech/Cornell/CITA collaboration using a pseudo spectral code. By comparing with these NR simulations, the EOB waveforms have been improved

in a number of ways [62, 63, 64, 65], and will no doubt continue to improve as they are calibrated against more and better NR simulations.

So far, the most important improvement has been the *multiplicative* decomposition of the harmonic modes $h_{\ell m}$ and the GW flux $\mathcal{F}$ [66, 64, 67, 68] which has produced waveforms which agree in amplitude and phase to within the numerical error of the most accurate NR simulations. More recently, some of the adjustable parameters in the EOB model have been constrained [69, 70, 71, 72] using self-force calculation predictions, in particular the ISCO shift due to finite-size effect [73]. Finally, the EOB model has been also successful in modeling small-mass ratio mergers [74, 75] and extreme-mass ratio inspirals [76].

The EOB model we have described was constructed to describe *non-spinning* compact binaries. It is also possible to construct EOB models for *spinning* compact binaries. In this case, the effective problem is that of a single *spinning* body moving in a deformed *Kerr* background spacetime. The foundations of this formalism were developed in Refs. [77, 78, 79, 80, 81, 67]. Spinning EOB models have been developed and are currently being calibrated against NR simulations of binaries with spins aligned and anti-aligned with the orbital angular momentum [65]. Efforts are underway to develop EOB waveforms for generic, precessing spin configurations. One of these efforts is the numerical-relativity–analytical-relativity (NR-AR) collaboration [82], which brings together a number of NR groups as well as many waveform model builders (not only EOB, but also PN and phenomenological waveforms). The goal is to increase the interaction between these two fields, and to strategically plan which simulations are carried out, so that they will produce the simulations which

are most valuable to model builders, cover as much of the parameter space as possible, and to cross-check one another. The analytic model builders will be able to directly compare their various techniques, which will be calibrated against the same set of simulations, and share their methods and results with the collaboration. The author is working within this collaboration, and it should produce exciting new results in the near future.

2.2.3 Spin effects and precession

We began our discussion of building analytic templates for compact binary coalescences by assuming that the compact bodies were non-spinning. However, real astrophysical black holes will likely be spinning about some axis, and so we want to consider the case where one or both of the compact bodies can have a rotational angular momentum $\mathbf{S}_i$ (where $i = 1, 2$ labels either of the compact bodies). As we will see, spin effects can have a dramatic effect on the behavior of the binary and the emitted waveform, both in the amplitude and phase. We can divide spin effects into two basic categories: *spin-orbit* (SO) corrections, which come from interactions between the spins and the orbital angular momentum of the binary $\propto \mathbf{S} \cdot \mathbf{L}$, and *spin-spin* (SS) corrections which arise from interactions between the spins $\propto \mathbf{S}_1 \cdot \mathbf{S}_2$ or $\propto \mathbf{S}_i^2$.

2.2.3.1 Spin corrections to the waveform

Just as in the non-spinning case, one matches two sets of mass-energy multipoles to derive the gravitational wave strain, which will again be expressible in the form of Eq. (2.45). However, there is energy associated with the spinning of the compact bodies, and so there are spin contributions to the multipoles, which lead to spin corrections to the strain, Eq. (2.45). The first such correction is a 1PN SO term,

$$P^1 Q_{ij}^{\rm SO} = \frac{2}{M^2}\, n_{\langle i} (\boldsymbol{\Delta} \times \hat{\mathbf{N}})_{j\rangle} \ , \tag{2.92}$$

where

$$\boldsymbol{\Delta} = M \left(\frac{\mathbf{S}_2}{m_2} - \frac{\mathbf{S}_1}{m_1} \right) \ . \tag{2.93}$$

1.5PN SO and 2PN SS corrections to the strain tensor have also been computed in Refs. [23, 83]. Using Eq. (2.92), an explicit form for the 1PN SO correction to the polarizations is derived in Ref. [83]. In Ch. 4, we extend this result by providing explicitly the polarizations with SO corrections through 1.5PN order. In Ch. 4, we also provide expressions for the -2 spin-weighted spherical harmonics modes with SO corrections through 1.5PN order.

Note that both [83] and this work construct the polarizations in a different source frame than what is typically used for non-spinning binaries. This source frame, and all the angles appearing in the polarizations and modes, are depicted in Fig. 2.7. This frame is more appropriate for describing a generic spinning binary, whose orbital plane can undergo precessional motion as described in Sec. 2.2.3.2.

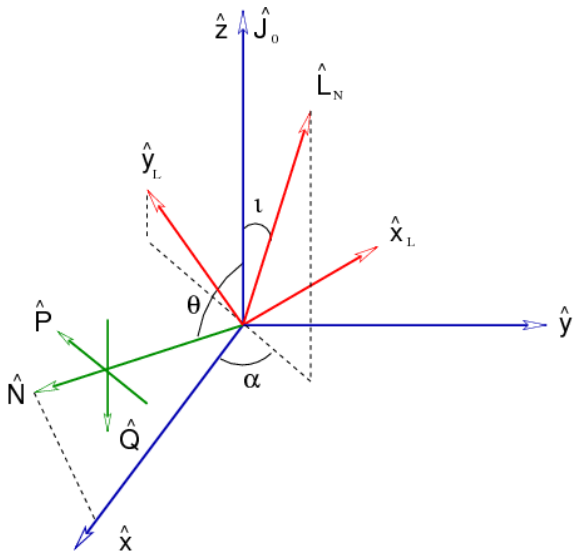

Figure 2.7: We show (i) our source frame defined by the orthonormal basis $(\hat{\mathbf{x}}, \hat{\mathbf{y}}, \hat{\mathbf{z}})$, (ii) the instantaneous orbital plane which is described by the orthonormal basis $(\hat{\mathbf{x}}_{\rm L}, \hat{\mathbf{y}}_{\rm L}, \hat{\mathbf{L}}_{\rm N})$, (iii) the polarization triad $(\hat{\mathbf{N}}, \hat{\mathbf{P}}, \hat{\mathbf{Q}})$, and (iv) the direction of the total angular momentum at initial time $\mathbf{J}_0$. Dashed lines show projections into the x–y plane.

Just as in the non-spinning case, we can obtain phasing equations for the waveform valid during the adiabatic inspiral from the energy balance equation, Eq. (2.56), but we must take into account spin corrections to the binary energy E [83, 84, 85], and the gravitational wave flux, $\mathcal{F}$ [86, 85, 87, 88]. In Eq. (8.3) of [86], the authors give an expression for $\dot{\omega}_{\rm orb}/\omega^2_{\rm orb}$ including SO effects through 2.5PN order.

This equation can be integrated twice in time to obtain the orbital frequency $\omega_{\rm orb}$ and phase Φ. If the spins are aligned or anti-aligned with the orbital angular momentum, then these integrals can be performed analytically to obtain an analytic expression for $\Phi(v)$ (or, in the notation of [86], $\Phi(x)$ where $x = v^2$). However, for any other generic spin configuration, the integrals must be done numerically to correctly include the effect of precessional motion. In Ch. 4, Eqs. (4.81)-(4.84), we explicitly

provide the SO phase corrections through 2.5PN and the 2PN SS phase correction to the TaylorF2 (SPA) approximant valid for spins aligned or anti-aligned with the orbital angular momentum. The 1.5PN SO and spin(1)-spin(2) SS corrections were previously known [89, 90], while we added the 2.5PN SO term and the spin(1)-spin(1) and spin(2)-spin(2) SS terms.

2.2.3.2 Precession

We have seen that when one or both of the objects in a compact binary is spinning, this affects the amplitude and phase of the emitted gravitational waves. In fact, the spin can have a significant impact on the motion of the binary itself. In particular, the spins will create a torque on the orbital angular momentum, causing it (and thus the orbital plane) to precess on a cone about the total angular momentum, $\mathbf{J} = \mathbf{L} + \mathbf{S_1} + \mathbf{S_2}$. We now briefly introduce the main features of precessional motion, and refer the reader to [91] for an in-depth analysis of the subject. The precessional motion is governed by the precession equations:

$$\frac{d\mathbf{S}_1}{dt} = \mathbf{\Omega}_1 \times \mathbf{S}_1 \,, \tag{2.94}$$

$$\frac{d\mathbf{S}_2}{dt} = \mathbf{\Omega}_2 \times \mathbf{S}_2 \,, \tag{2.95}$$

$$\dot{\hat{\mathbf{L}}}_{\mathrm{N}} = -\frac{v}{\nu} \left(\dot{\mathbf{S}}_1 + \dot{\mathbf{S}}_2 \right) , \tag{2.96}$$

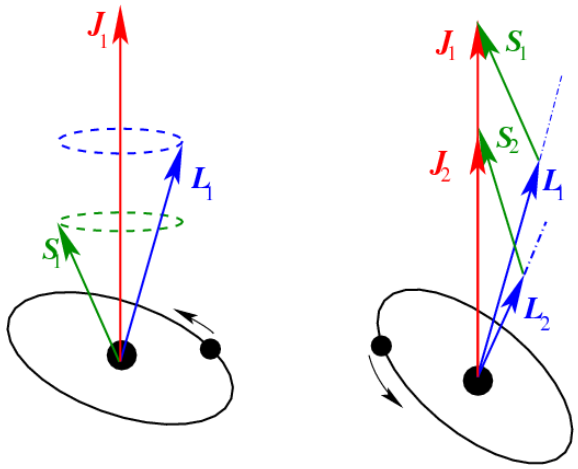

Figure 2.8: Precessional motion of **L** and **S** about **J** labeled early (1) and late (2) in the evolution. Precession causes **L** and **S** to rotate on cones about **J**. Radiation reaction will cause **L** to move away from **J** and **S** to move towards **J** as the binary evolves.

where the last equation can be obtained averaging over an orbital period (see Sec. IVB in [92]) and at 1.5PN order

$$\mathbf{\Omega}_{1,2} = \omega_{\rm orb}^{5/3} \left(\frac{3}{4} + \frac{\nu}{2} \mp \frac{3}{4}\delta \right) \hat{\mathbf{L}}_{\rm N} \,, \tag{2.97}$$

and $\mathbf{L}_{\rm N} \equiv \mu\, \mathbf{r} \times \mathbf{v}$ is the Newtonian orbital angular momentum, which is perpendicular to the instantaneous orbital plane. From these equations, we can deduce that each of $\widehat{\mathbf{L}}_{\rm N}$, $\mathbf{S}_1$ and $\mathbf{S}_2$ will rotate about a fixed direction, sweeping out a cone. Since at any instant, the change in **L** is exactly opposite to the change in the total spin $\mathbf{S} = \mathbf{S}_1 + \mathbf{S}_2$, the direction of **J** will remain fixed. So, $\hat{\mathbf{J}}$ is in fact the fixed direction about which the other vectors rotate.

We have not yet considered radiation reaction (which enters at 2.5PN order) in our discussion of the precession equations (which we have given at 1.5PN order).

If we include radiation reaction, the vectors $\widehat{\mathbf{L}}_{\rm N}$, $\mathbf{S}_1$ and $\mathbf{S}_2$ will still move according to the precession equations. However, it will cause the magnitude of $\mathbf{L}_{\rm N}$ to slowly shrink. Meanwhile, at lowest order the magnitude of the spin vectors $\mathbf{S}_1$ and $\mathbf{S}_2$ will remain constant, as will their angle relative to $\widehat{\mathbf{L}}_{\rm N}$. Thus, the only change in the magnitude of $\mathbf{J}$ will come from the shrinking of $\mathbf{L}_{\rm N}$. This means that as the system evolves, $\mathbf{L}_{\rm N}$ will contribute a smaller fraction of $\mathbf{J}$ and the spins will contribute a greater fraction of $\mathbf{J}$. Therefore, at early times, the vectors $\mathbf{J}$ and $\mathbf{L}_{\rm N}$ will be close to one another, but as the system evolves, $\mathbf{J}$ will become closer to $\mathbf{S}$. Said another way, the cone on which $\mathbf{L}_{\rm N}$ precesses about $\mathbf{J}$ will continually grow wider and the cone on which $\mathbf{S}$ precesses about $\mathbf{J}$ will continually grow tighter because of radiation reaction. This precessional motion is depicted in Fig. 2.8.

2.2.3.3 Consequences of precession

The precessional motion of the orbital plane can have a significant effect on the gravitational waveform emitted by the binary. Non-spinning corrections to the strain and phase of a gravitational waveform are constant in time, apart from the time-dependence through v. However, spin corrections such as Eq. (2.92), the leading SO correction to the strain, depend on the orientation of the spins relative to $\widehat{\mathbf{N}}$ (or other vectors such as $\widehat{\mathbf{L}}_{\rm N}$) and this orientation varies in time. So, in addition to solving the phasing equations, Eqs. (2.57)–(2.58) or (2.59)–(2.60), one must simultaneously solve the precession equations, Eq. (2.94)-(2.96), to generate the waveform. Waveforms from precessing binaries can therefore be much more feature-rich than

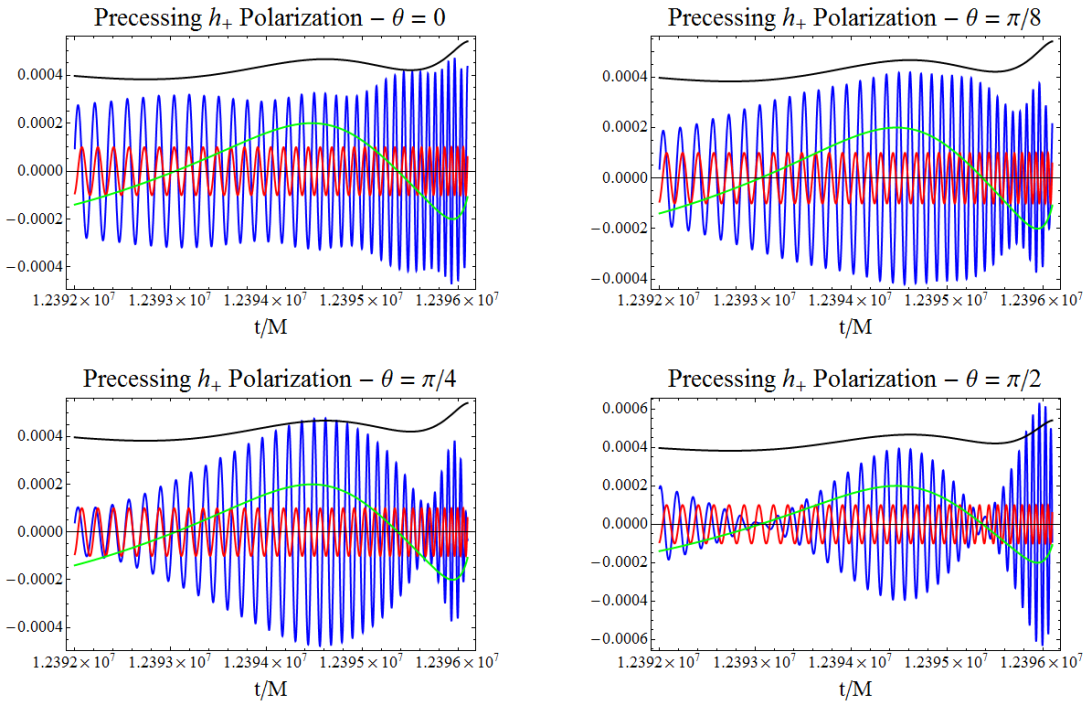

Figure 2.9: h_+ polarization for a 4:1 mass ratio binary with maximal spins perpendicular to $\widehat{\mathbf{L}}_{\rm N}$ and each other viewed from four different angles θ measured from the center of the precessional cone. The blue curve is h_+, the red curve is $\cos 2\Phi$, the green curve is $\cos\alpha$ and the black curve is ι (the latter three scaled to fit the plot). The modulation pattern changes with the viewing angle, and becomes more dramatic as the line of sight moves away from the center of the precessional cone.

waveforms from non-spinning or even spin-aligned (with the orbital angular momentum) binaries. The effects of precession on inspiral waveforms are studied in Ch. 4. We now briefly highlight some of their effects on both the waveform polarizations and harmonic modes.

The gravitational wave polarizations will be modulated in phase by 1.5PN SO, 2PN SS, and 2.5PN SO corrections (plus higher order corrections not currently known) and in amplitude by spin corrections starting at 0.5PN order for the contributions from the subdominant modes, and at 1PN for the dominant $(2,2)$ mode. However, the most striking effect of precession occurs in the leading order (non-

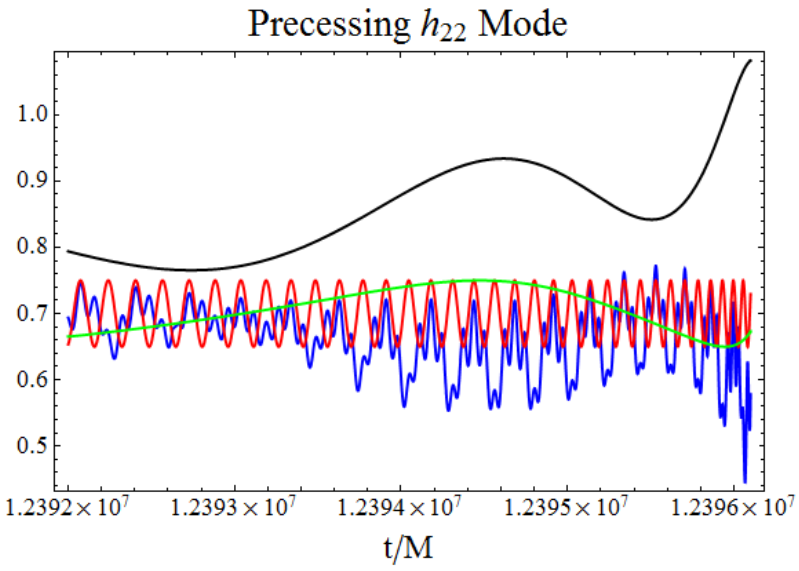

Figure 2.10: Re(h_{22}) mode for a 4:1 mass ratio binary with maximal spins perpendicular to $\mathbf{L}_{\rm N}$ and each other. The blue curve is h_+, the red curve is $\cos 2\Phi$, the green curve is $\cos\alpha$ and the black curve is ι (the latter three scaled to fit the plot). Unlike the polarizations, precessional motion modulates the modes on the orbital time scale because of interference between different harmonics of the orbital phase.

spinning) amplitude term of the polarizations. Note that the angle θ appearing in Eqs. (2.28) and (2.29) is defined by $\cos\theta \equiv \widehat{\mathbf{L}}_{\rm N}\cdot\widehat{\mathbf{N}}$. Precesssion will cause $\widehat{\mathbf{L}}_{\rm N}$ to move relative to $\widehat{\mathbf{N}}$ and thus modulate the amplitude of the waveform. Because this is a modulation of the *leading order* amplitude, and not some higher order correction, the change in amplitude can be quite significant. This modulation occurs on the precessional time scale, and so provides an "envelope function" within which the polarizations oscillate on the more rapid orbital time scale. Note that these modulations will be significantly different depending on the direction at which the binary is observed relative to the precessional cone of the binary. This is illustrated in Fig. 2.9.

We see that precession can significantly modulate the amplitude of the polar-

izations, and that the modulation pattern depends on the observation angle. This would suggest that the harmonic modes would be especially useful for describing waveforms emitted by precessing binaries, since the modes do not depend on the observation angle. However, precession also has a dramatic effect on the harmonic modes. As we noted in Eq. (2.55), if the mode decomposition is performed in a frame in which $\hat{z} \parallel \mathbf{L}_{\mathrm{N}}$, then every $h_{\ell m}$ is proportional to the m^{th} harmonic of the orbital phase. For a precessing binary, there is no inertial frame where this relation holds at all times. As a result, the simple form of the harmonic modes is not preserved, and they will have terms which depend on different harmonics of the orbital phase. These different terms interfere with one another and produce complicated modulation patterns on the *orbital* time scale, rather than the slower *precessional* time scale.

2.3 Applications of analytic waveforms

2.3.1 Matched filter templates

The primary application of the waveforms we have developed so far is to use them as matched filtering templates. This will allow us to use our knowledge of the waveform to extract weak signals from a noisy data stream. That is, we have a data stream from our detector

$$s(t) = \begin{cases} n(t) & \text{no signal present} \\ n(t) + h(t) & \text{signal present} \end{cases} \tag{2.98}$$

which consists of instrumental noise $n(t)$, and possibly a weak gravitational waveform $h(t)$ which we hope is closely matched by one or more of our analytic waveform models for some values of the mass and other parameters. The theory of matched filtering is given a rigorous presentation in a general context in Ref. [93] . Ref. [94] presents the subject in the context of gravitational wave detectors. We will now briefly summarize some of the main points.

In Sec. 2.1.5, we identified some of the principal sources of noise in a laser interferometer and noted that the level of noise varies with frequency. This can be quantified by a (one-sided) power spectral density (PSD or "noise curve") $S_n(f)$ defined for positive f,

$$\langle \tilde{n}(f)\, \tilde{n}^*(f') \rangle = \frac{1}{2}\, S_n(f)\, \delta(f - f') \ , \tag{2.99}$$

where $\tilde{}$ denotes a Fourier transform, * denotes a complex conjugate, and $\langle\ \rangle$ is an ensemble average. The ensemble average can be computed by taking the Fourier transform of a long stretch of data. Formally, if we take noisy data for a duration of time T, then

$$\langle \tilde{n}(f)\, \tilde{n}^*(f') \rangle = \lim_{T\to\infty} \frac{1}{T}\, \tilde{n}(f)\, \tilde{n}^*(f) \ . \tag{2.100}$$

In practice, the PSD is computed over a stretch $T = 2048$s. This is long enough to average out the effect of short, transient disturbances ("glitches"), but short enough not to wash out natural variations in the sensitivity over longer time scales (such as from weather or increased/decreased seismic noise from human activities during

the day/night) [94].

Now, given our (real-valued) time series $s(t)$, we want to pass this data through a (real-valued) filter $K(t)$ such that the output of the filter,

$$z = \int_{-\infty}^{\infty} K(t)\, s(t)\, dt = \int_{-\infty}^{\infty} \tilde{K}(f)\, \tilde{s}^*(f)\, df \tag{2.101}$$

will be large when a signal is present and small when there is no signal. Note that the second equality comes from Parseval's Theorem [95], and means that we can perform the filtering in the frequency domain. It is a well-known result, originally shown by Norbert Wiener, that the optimal[2] (Wiener) filter for detecting a signal $h(t)$ with Fourier transform $\tilde{h}(f)$ in stationary, Gaussian noise is given by

$$\tilde{K}(f) = \frac{\tilde{h}(f)}{S_n(f)} \tag{2.102}$$

(modulo a multiplicative constant) [93]. That is, we simply filter with the signal we are looking for, weighted by the PSD of the instrument. It is convenient to define an *inner product* to describe the matched filtering, and any other integral weighted by the PSD of a detector. Given two real-valued functions $a(t)$ and $b(t)$, their inner product is defined as

$$\begin{aligned} (a|b) &\equiv \int_{-\infty}^{\infty} \frac{\tilde{a}(f)\,\tilde{b}^*(f) + \tilde{a}^*(f)\,\tilde{b}(f)}{S_n(|f|)}\, df = 2\int_0^{\infty} \frac{\tilde{a}(f)\,\tilde{b}^*(f) + \tilde{a}^*(f)\,\tilde{b}(f)}{S_n(f)}\, df \\ &= 4\,\mathrm{Re}\left[\int_0^{\infty} \frac{\tilde{a}(f)\,\tilde{b}^*(f)}{S_n(f)}\, df\right] = 4\,\mathrm{Re}\left[\int_0^{\infty} \frac{\tilde{a}^*(f)\,\tilde{b}(f)}{S_n(f)}\, df\right] . \end{aligned} \tag{2.103}$$

[2]The filter is optimal in the sense that it maximizes the ratio of the filter output when a signal is present to the filter output when there is no signal.

Note that in the first line we have used the fact that for a real-valued function $\tilde{a}(-f) = \tilde{a}^*(f)$ and in the second line we have used that $\left(\tilde{a}(f)\,\tilde{b}^*(f)\right)^* = \tilde{a}^*(f)\,\tilde{b}(f)$. It is straightforward to show that in the absence of a signal, the output of the filter will have mean zero and variance $\sigma^2 = (h|h)$ [93, 94]. It is useful to divide the output of our filter by the variance to get a measure of how much stronger a signal is than what we expect to get from random background noise. Therefore, we define the signal-to-noise ratio (SNR)

$$\rho = \frac{|z|}{\sigma} = \frac{(s|h)}{\sqrt{(h|h)}}\ . \tag{2.104}$$

The SNR is the basic statistic used to rank events. If the SNR crosses a predetermined threshold, then it is considered a trigger. Once a list of such triggers from each interferometer is generated, techniques such as signal-based vetoes and coincidence tests among interferometers are used to determine if the trigger is likely to be a true signal, or caused by noise fluctuations.

2.3.2 A complete search pipeline

In a realistic search pipeline, there are many more steps besides simply computing the SNR of the data relative to a single template. In Ch. 7, we will describe such a search pipeline in more detail. Here we give a broad outline of the steps involved in the pipeline used by the compact binary coalescence (CBC) working group of the LSC for both the "low mass" ($M = (2-35)\,M_\odot$) S5 search efforts [96, 97, 98] and the "high mass" ($M = (25-100)\,M_\odot$) S5 search described in Ch. 7:

- **Data selection:** One must identify the times when the instruments are operating properly and taking good data. Data quality flags are typically used to identify times when there might be excessive noise or problems with the instrument and data should not be analyzed. For information about LIGO methods of data quality control, see Ref. [99].

- **Template bank generation:** It would be impossible to filter with a template for each point in the continuum of parameter space, so one must choose a finite number of templates which adequately cover the parameter space. Templates are placed so that a signal with parameter values falling between templates will only lose an acceptable fraction of its SNR. We refer the reader to Ref. [100] for information about the placement of templates within the parameter space.

- **Matched filtering:** We filter the data against each template in our bank and produce a list of triggers for which the SNR exceeds the threshold. If a certain template crosses the SNR threshold at a certain time, many other nearby times and nearby parameter values will also produce a trigger above threshold. Therefore, clustering over time and parameters is done to find local maxima in the set of triggers, and reduce them to a manageable number. Details of the implementation of the matched filtering in the LAL code can be found in Ref. [101].

- **Signal-based vetoes:** Once we have our clustered list of triggers, signal-based vetoes are used to eliminate or decrease the ranking of triggers which are likely to be caused by background noise. The most important is the χ^2

veto, which determines the goodness-of-fit between signal and template by partitioning the template into several frequency bands which contribute equally to the total SNR. If the power of the signal in each frequency band is close to that of the template, the signal is consistent with the template and χ^2 will be small. If χ^2 is large, it means the power of the signal is distributed differently in frequency from the template and the trigger is likely to be noise. The χ^2 value is used to re-weight the SNR of an event to create an improved detection statistic known as *effective SNR*, denoted $\rho_{\rm eff}$. See Ref. [102] for details about the χ^2 veto.

- **Coincidence:** After signal-based vetoes have been applied, the lists of triggers from each instrument are compared. If two or more instruments have triggers that are within the light travel time between sites and have the same mass parameter values (both within some tolerance), this is counted as a coincidence. We then add in quadrature the effective SNR of the coincident events in each instrument to obtain a *combined effective SNR*, $\rho_{\rm eff,c} = \sqrt{\sum_i \rho^2_{\rm eff,i}}$, which is used to rank coincident events.

- **Followup:** Once we have the list of coincidence events, the most significant events are examined more carefully. This includes further comparisons on the consistency of the raw signals and template waveforms from each interferometer and a detailed look at the state of each interferometer and its environment during the event to see if transient noise glitches were likely to occur. Then, a decision is made as to whether or not there is enough evidence to confidently

claim the event is a true detection.

- **Event rate upper limits:** If a successful detection is not made, then an upper limit is set on the event rate of compact binary coalescences using the approach of Ref. [103]. To do this, one defines a "loudness" statistic which quantifies how likely an event is to be a true signal rather than noise (a higher value meaning it is more likely to be a signal). The trigger with the greatest value of the loudness statistic is called the "loudest event". If one can estimate the efficiency of detecting signals louder than this loudest event and also the background distribution of noise triggers, one can compute a Bayesian posterior probability distribution $p(R|\epsilon, \Lambda)$ for the event rate R given our detection efficiency above the loudest event, ϵ, and the relative likelihood the loudest event was caused by noise versus a true signal, Λ. Then, one can integrate this posterior distribution to a certain confidence level, say 90%, to obtain an upper limit. Therefore, we find the R that satisfies

$$0.9 = \int_0^R p(R'|\epsilon(\rho^*_{\mathrm{eff,c}}), \Lambda(\rho^*_{\mathrm{eff,c}}))\, dR' = 1 - \left[1 + \frac{R\,\epsilon(\rho^*_{\mathrm{eff,c}})\,\Lambda(\rho^*_{\mathrm{eff,c}})}{1 + \Lambda(\rho^*_{\mathrm{eff,c}})}\right] e^{-R\,\epsilon(\rho^*_{\mathrm{eff,c}})}\,. \tag{2.105}$$

This amounts to a statement that "if the event rate were greater than R, there is a 90% chance it would produce a trigger louder than $\rho^*_{\mathrm{eff,c}}$. Since we did not observe such a trigger, we bound the event rate with 90% confidence." For more information about setting upper limits based on the loudest event, see Ref. [103].

In this thesis, we will present two projects which use the EOB waveforms discussed in Sec. 2.2.2 as matched filter templates in such a detection pipeline. In Ch. 5, we present the results of using EOB templates to search for NR waveforms injected into simulated data as part of the Numerical INJection Analysis (NINJA) project [104]. This study used the full pipeline outlined above, except that no upper limit was set, as we did not search real data. It served as a first test of whether the existing matched-filter templates and other search techniques would be able to detect the waveforms predicted by numerical relativity. The author used EOB waveforms for this purpose, while other collaborators used PN waveforms, the so-called phenomenological IMR waveforms of Ref. [105], and unmodelled search techniques, such as those of Refs [106, 107, 108]. As summarized in Table 2.1, the EOB waveforms (denoted "EOBNR" in the table) did quite well, finding the majority of injected signals and finding a few more than similar search pipelines. This NINJA project was somewhat limited in that it used simulated noise rather than real data, the NR waveforms were quite short, and so most could only be injected at very high mass, and no attempt was made to compare the various search pipelines at fixed false alarm rate. However, a second NINJA project has recently begun which aims to improve upon the first NINJA effort by addressing all of these issues as well as including spinning (but non-precessing) NR waveforms. The author of this thesis is involved in this effort, and will once again use an EOB matched filter pipeline to search for the injected waveforms.

The LSC and Virgo collaborations are currently performing a search for binary black hole coalescences with total mass $(25 - 100)\,M_{\odot}$ in the data from LIGO's S5

Template	EOB	EOBNR	Phenom
Freq. Cutoff	Light ring	Full waveform	Full waveform
Filter Start Freq.	40 Hz	30 Hz	30 Hz
Component Mass $M_\odot$	10-60	15-160	20-80
Total Mass $M_\odot$	20-90	30-200	40-160
Minimal Match	0.97	0.99	0.99
Found Single (H1, H2, L1, V1)	91, 64, 82, -	97, 68, 92, 102	92, 61, 87, -
Found Coincidence (LIGO, LV)	83, -	88, 106	81, -
Found Second Coincidence (LIGO, LV)	80, -	85, 102	80, -

Table 2.1: Main results of the NINJA project. There were 126 injections performed into the analysed data. Details and the number of found injections are given for three different search pipelines. "EOB" is a 3PN EOB model which *does not* have a ringdown attached. "EOBNR" is the EOB IMR model described in Sec. 2.2.2 (EOBNR is the name given to its implementation in LAL), and "Phenom" is a phenomenological frequency domain IMR waveform family. H1 and H2 are the 4 km and 2 km LIGO interferometer in Hanford, WA, L1 is the 4 km LIGO interferometer in Livingston, LA and V1 is the Virgo interferometer in Cascina, Italy. On the last two lines, "LIGO" means a coincidence among the LIGO interferometers and "LV" means a coincidence within the full LIGO-Virgo network.

Table 2.2: The 90% confidence upper limit on the merger rate as a function of mass in units of $M_\odot$. The upper limit is reported in two ways. The third column represents the rate in units of mergers $\mathrm{Mpc}^{-3}\,\mathrm{yr}^{-1}$. The fourth column converts this to units of mergers $L_{10}^{-1}\,\mathrm{yr}^{-1}$ by noting that there are 0.0198 L_{10} / Mpc^3 [109].

$\mathbf{m_1}$	$\mathbf{m_2}$	$\mathbf{R_{90\%}}$ **(Mpc^{-3} yr^{-1})**	$\mathbf{R_{90\%}}$ **(L$_{10}$ yr^{-1})**
5	23	3.2e-06	1.6e-04
5	50	5.1e-06	2.6e-04
14	14	1.6e-06	8.0e-05
14	76	1.0e-06	5.3e-05
23	23	1.3e-06	6.7e-05
23	50	4.8e-07	2.4e-05
32	32	4.8e-07	2.4e-05
32	68	2.0e-07	1.0e-05
41	41	2.1e-07	1.1e-05
41	59	1.6e-07	8.0e-06
50	50	1.1e-07	5.5e-06

science run, known as the S5 highmass search. This search is the first attempt to use EOB IMR matched filter templates to search real gravitational wave detector data for gravitational waves from compact binary coalescences. This search is currently undergoing an internal review process to check the methods and computer code used in the search. The final results should be published in the near future. The author of this thesis is one of the corresponding authors of the high-mass S5 paper for the LSC and Virgo collaborations, along with Chad Hanna (Caltech) and Craig Robinson (Cardiff University). The author of this thesis has been involved in implementing the EOB waveforms into the LAL code, running the search on a portion of the data (two months), tuning the χ^2 veto, sanity checking parts of the code, and helping with the review process. While the final results are not yet available, in Ch. 7, we will see some preliminary results from this search. Since these preliminary results have not undergone a full review process, they do not necessarily represent the opinion of the LSC and Virgo collaborations, but only those of this author. Unfortunately, we cannot claim a detection in these preliminary results. However, we can set an upper limit (with 90% confidence) in the rate of coalescences. This upper limit has been calculated for each mass pair within the range of the search. In Table 2.3.2, we present a sampling of these upper limits. A more complete listing (and plot) of the upper limits, as well as methods and other preliminary results of the search are presented in Ch. 7.

2.3.3 Parameter estimation

Once a detection has been made, the next step is to extract the parameters of the waveform to learn as much as possible. This will of course include the masses, sky position and orientation of the binary, and it could also involve testing whether the observed waveform best matches the prediction of general relativity, or an alternative theory of gravity. For example, Refs. [110, 111] considered whether corrections to the waveform phase arising from either Brans-Dicke theory or a massive graviton could be detectable by the Laser Interferometer Space Antenna (LISA).

Markov-chain Monte-Carlo (MCMC) methods have been developed that will be used to estimate the parameters of the waveform for a true detection. For example, Ref. [112] presents such a method for non-spinning binaries, while Ref. [113] builds on this work to develop the technique for spinning binaries. Both of these works used simulated data, while Ref. [114] further refines the method for spinning binaries and is the first published study to apply MCMC techniques to simulated signals injected into real interferometer data. In essence, these MCMC techniques compute the Bayesian likelihood $\mathcal{L}(s|\boldsymbol{\lambda})$ that the data $s(t)$ contains a signal $h(\boldsymbol{\lambda}, t)$ with parameters $\boldsymbol{\lambda}$ by computing the integral

$$\mathcal{L}(s|\boldsymbol{\lambda}) \propto \exp\left[-2\int_0^\infty \frac{|\tilde{s}(f) - \tilde{h}(\boldsymbol{\lambda}, f)|^2}{S_n(f)}\, df\right] = \exp\left[-\frac{1}{2}\,(s - h(\boldsymbol{\lambda})|s - h(\boldsymbol{\lambda}))\right]\,. \tag{2.106}$$

Then, Bayes' Theorem allows one to compute a posterior probability density for the

parameters

$$p(\boldsymbol{\lambda}|s) \propto p(\boldsymbol{\lambda})\, \mathcal{L}(s|\boldsymbol{\lambda}) \ , \tag{2.107}$$

where $p(\boldsymbol{\lambda})$ is the prior distribution of the parameters. Often, this prior is simply the assumption that the parameters have a uniform distribution over some range. One then maps out $p(\boldsymbol{\lambda}|s)$ over the parameter space by repeating the procedure for a very large number of parameter values, with parameter values chosen by some jump criterion so that the parameter space is sampled thoroughly but efficiently.

Because one must generate a waveform and evaluate the inner product integral of Eq. (2.106) very many times, these MCMC parameter estimation techniques are quite computationally expensive. Therefore, because it is much more computationally economical, it has been common practice to use the Fisher matrix formalism to estimate how well one could determine the parameters of a detected gravitational wave signal. See, e.g. Refs. [115, 89, 116, 111, 117, 118] for a cross section of parameter estimation studies using the Fisher matrix, while Ref. [119] discusses some of the problems and limitations of the Fisher matrix formalism. Note that the Fisher matrix only provides an estimate of the precision with which we *could* measure the parameters of a detected signal, it cannot be used to actually extract the parameters once a detection is made. Nonetheless, it is a useful tool in this pre-detection era to answer questions such as "Will adding some physical feature (amplitude corrections, spins, merger-ringdown, etc.) to waveforms improve the parameter estimation?", "Where should a new detector be placed to best improve sky localization?", "How will design choices of proposed advanced detectors affect

parameter estimation?" and many others.

Now, the basic idea of the Fisher matrix is to expand the signal $h(\boldsymbol{\lambda}_0, t)$ with parameters $\boldsymbol{\lambda}_0$ in a Taylor series of derivatives with respect to the parameters

$$h(\boldsymbol{\lambda}, t) = h(\boldsymbol{\lambda}_0, t) + \partial_i h(\boldsymbol{\lambda}_0, t)\, \delta\lambda^i + \ldots \,, \tag{2.108}$$

where $\delta\lambda^i = \lambda^i - \lambda^i_0$ and there is a summation over all of the parameters λ^i. If the SNR is sufficiently large, or if the signal depends linearly on all of its parameters, then it is valid to expand only through the first derivatives, and not include the higher-order parameter derivatives. Then, if we assume a uniform prior distribution for all parameters (over their relevant ranges), from Eqs. (2.106)-(2.107) the posterior probability density is

$$p(\boldsymbol{\lambda}|s) \propto \exp\left[-\frac{1}{2}\,\Gamma_{ij}\,\delta\lambda^i\,\delta\lambda^j\right] \,, \tag{2.109}$$

where

$$\Gamma_{ij} \equiv \left(\frac{\partial h}{\partial\lambda^i}\middle|\,\frac{\partial h}{\partial\lambda^j}\right)\bigg|_{\boldsymbol{\lambda}=\boldsymbol{\lambda}_0} \tag{2.110}$$

is the Fisher information matrix. So, under our assumptions of stationary Gaussian noise and large SNR, we find that $p(\boldsymbol{\lambda}|s)$ has the form of a multivariate Gaussian distribution. Recall that a multivariate Gaussian distribution for a variable $\mathbf{x}$ with mean $\boldsymbol{\mu}$ takes the form

$$p(\mathbf{x}) \propto \exp\left[-\frac{1}{2}\,\left(\Sigma^{-1}\right)_{ij}\,(\mathbf{x}-\boldsymbol{\mu})^i\,(\mathbf{x}-\boldsymbol{\mu})^j\right] \,, \tag{2.111}$$

where Σ is the covariance matrix, which encodes the variance and correlations of all the components of $\mathbf{x}$. Therefore, we see that the covariance matrix must be the inverse of the Fisher matrix,

$$\Sigma_{ij} = \left(\Gamma^{-1}\right)_{ij} \ . \tag{2.112}$$

From the covariance matrix, we can obtain the root mean square parameter errors ($\Delta\lambda_i$) and correlations among parameters (σ_{ij}) as

$$\Delta\lambda_i = \sqrt{\Sigma_{ii}} \ , \tag{2.113}$$

$$\sigma_{ij} = \frac{\Sigma_{ij}}{\sqrt{\Sigma_{ii}\,\Sigma_{jj}}} \ . \tag{2.114}$$

This result is rigorously derived in both frequentist and Bayesian statistical frameworks in Ref. [119]. Intuitively, what we are doing is approximating $p(\boldsymbol{\lambda}|s)$ by a multivariate Gaussian in a region of parameter space around the true parameter values. We evaluate parameter derivatives of the waveform to tell us how sensitive the observed waveform is to changes in that parameter. The larger the derivative, the more steeply the Gaussian will fall off along that parameter direction, and so the more precisely that parameter can be determined. We build a matrix of inner products of these parameters and invert it to obtain the errors and correlations of all the parameters. Now, if the noise is non-Gaussian, the SNR is low, or the dependence on the parameters is highly non-linear, this approximation can break down. As noted in Ref. [119] and others, these assumptions may not necessarily be valid for ground-based GW detectors. However, because one can estimate parameter

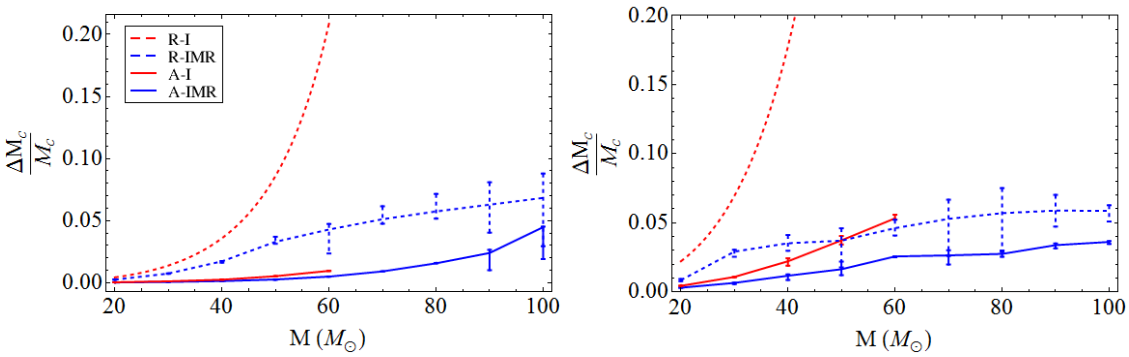

Figure 2.11: We plot the fractional error on $\mathcal{M}_c$ as the total mass is varied for symmetric mass ratio $\nu = 0.05$ (left panel) and $\nu = 0.24$ (right panel) for waveform restricted inspiral-only waveforms (dashed red), restricted IMR waveforms (dashed blue), amplitude-corrected inspiral-only waveforms (solid red) and amplitude-corrected IMR waveforms (solid blue).

errors by evaluating parameter derivatives of the waveform at a single point rather than computing thousands or millions of waveforms and inner products as in the MCMC approach, the Fisher matrix approach has been frequently used in GW parameter estimation studies. Ideally, one might use the Fisher matrix formalism as an initial study, and then attempt to cross-check the results with an MCMC study.

In Ch. 6, we will use the Fisher matrix formalism with restricted and amplitude corrected EOB waveforms to determine whether the inclusion of merger-ringdown and/or amplitude corrections can improve parameter estimation. In short, we find that including both of these features will improve the estimation of the masses and other parameters, particularly for large masses and asymmetric mass ratios. As an example, in Fig. 2.11, we show the error on the chirp mass $\mathcal{M}_c = M\,\nu^{3/5}$ as a function of total mass in initial LIGO at a fixed SNR of 10 for $\nu = 0.05$ (left panel) and $\nu = 0.24$ (right panel). The solid lines contain a merger-ringdown, while the

dashed lines contain only the inspiral. The blue lines are for amplitude-corrected waveforms, while the red lines are for restricted waveforms. We see that both merger-ringdown and amplitude corrections improve the estimation of $\mathcal{M}_c$, especially as the mass increases. The effect is also more pronounced for the highly asymmetric binary (left panel) than for the symmetric binary (right panel). More results, along with a discussion of the methods used (and the difficulties they present) are given in Ch. 6.

Chapter 3

Comparison of post-Newtonian templates for compact binary inspiral signals in gravitational wave detectors

Authors: *Alessandra Buonanno, Bala Iyer, Evan Ochsner, Yi Pan and B. S. Sathyaprakash*[1]

Abstract: The two-body dynamics in general relativity has been solved perturbatively using the post-Newtonian (PN) approximation. The evolution of the orbital phase and the emitted gravitational radiation are now known to a rather high order up to $\mathcal{O}(v^8)$, v being the characteristic velocity of the binary. The orbital evolution, however, cannot be specified uniquely due to the inherent freedom in the choice of parameter used in the PN expansion as well as the method pursued in solving the relevant differential equations. The goal of this paper is to determine the (dis)agreement between different PN waveform families in the context of initial and advanced GW detectors. The waveforms employed in our analysis are those that are currently used by Initial LIGO/Virgo, that is the time-domain PN models TaylorT1, TaylorT2, TaylorT3, the Fourier-domain representation TaylorF2 (or stationary phase approximant, SPA) and the EOB model, and two more recent models, TaylorT4 and TaylorEt. For these models we examine their overlaps with one another for a number of different binaries at 2PN, 3PN and 3.5PN orders to quantify

[1]Originally published as Phys. Rev. D **80** 084043 (2009)

their differences. We then study the overlaps of these families with the prototype effective-one-body family, currently used by Initial LIGO, calibrated to numerical relativity simulations to help us decide whether there exist preferred families, in terms of detectability and computational cost, that are the most appropriate as search templates. We conclude that as long as the total mass remains less than a certain upper limit $M_{\rm crit}$, all template families at 3.5PN order (except TaylorT3 and TaylorEt) are equally good for the purpose of detection. The value of $M_{\rm crit}$ is found to be $\sim 12\,M_\odot$ for Initial, Enhanced and Advanced LIGO. From a purely computational point of view we recommend that 3.5PN TaylorF2 be used below $M_{\rm crit}$ and EOB calibrated to numerical relativity simulations be used for total binary mass $M > M_{\rm crit}$.

3.1 Introduction

Sensitivity of several interferometric GW detectors has either already reached, or is close to, the design goals that were set more than a decade ago [120, 121, 122, 123, 124, 125, 126]. Upgrades that are currently underway and planned for the next four to five years, will see their sensitivity improve by factors of a few to an order-of-magnitude [127]. Coalescing binaries consisting of neutron stars and/or black holes are probably the most promising sources for a first direct detection of gravitational waves. At current sensitivities, initial interferometers are capable of detecting binary neutron star inspirals at distances up to 30 Mpc, the range increasing to 60 Mpc for enhanced detectors (circa 2009-2011) and 175 Mpc for advanced detectors (circa 2014+). Binary black holes or a mixed system consisting of a neutron star and a black hole can be detected to a far greater distance depending on the total mass and the mass ratio.

The range of interferometric detectors for coalescing binaries is computed by assuming that one can pull the signal out of noise by matched filtering. This in turn means that one is able to follow the phasing of gravitational waves typically to within a fraction of a cycle over the duration of the signal in band. The reason for this optimism comes from the fact that one knows the phase evolution of the signal to a high order in post-Newtonian (PN) formalism [21]. Several authors have assessed whether the accuracy with which the formalism provides the waveforms is good enough for the purpose of detection and parameter estimation [128, 129, 130, 131, 132, 133, 134, 30, 33, 135, 136, 137, 34, 138, 139, 140]. The problem, as we

shall see below, is complicated since the PN approximation does not lead to a unique model of the phase evolution. Moreover, though PN results are good up to mildly relativistic velocities, the standard PN approximants become less and less accurate in the strongly relativistic regime as one approaches the last stable orbit (LSO). Resummation methods [132] and in particular the EOB [39, 141, 57] extensions of the PN approximants, are needed for analytical treatments close to and beyond the LSO.

The success in numerical-relativity simulations of binary black holes [142, 143, 144, 145, 146] now provides results for gravitational waveforms that can be compared to standard PN results and other resummed extensions. On the one hand, the analytical PN results for the inspiral phase of the evolution are needed to calibrate and interpret the numerical relativity waveforms of coalescence and merger. On the other hand, the numerical relativity results extend the analytical approximations beyond the inspiral phase and provide the important coalescence and merger phases, producing the strongest signals that are crucial for the detection of binary black holes. However, numerical simulations are still computationally expensive and time-consuming and presently only a small region of the parameter space can be explored. Even in the foreseeable future, numerical relativity may not be able to handle the tens of thousands of cycles that are expected from low-mass systems (e.g., a binary neutron star). Analytical models that smoothly go from the inspiral through coalescense to quasi-normal ringing would be needed and this has led to phenomenological templates [105, 147, 148]. and EOB waveforms [149, 147, 150, 54, 151, 152, 153, 154, 155, 156]. In particular, the recent improved

EOB models [155, 156] which also incorporate a multiplicative decomposition of the multipolar waveform into several physically motivated factors supplemented by a suitable hybridisation (using test particle results) [157], and an improved treatment of non-quasi-circular corrections, show evidence of remarkable success in modeling accurately the numerical relativity waveforms for different mass ratios.

The emphasis of this work is different. Recently, there have been investigations [158] on the ability of various standard families of PN templates to detect a specific signal model TaylorEt [35, 36, 37] and the often-used TaylorF2 to detect a complete numerical relativity signal including merger and ringdown [147, 148]. Reference [158] modelled the signal by the TaylorEt approximant at 3.5PN order and looked at the effectualness and systematic biases in the estimation of mass parameters for TaylorT1, TaylorT4 and TaylorF2 templates in the LIGO and Virgo detectors. It also looked into the possibility of improving the effectualness by using unphysical values of ν beyond the maximum value of 0.25. It was found that the overlaps of a TaylorEt signal with TaylorT1, TaylorT4 and TaylorF2 template is smaller than 0.97 and involved for equal-mass systems a large bias in the total mass. For unequal-mass systems higher overlaps can be obtained at the cost of a large bias in mass and symmetric mass ratio ν and which can be further improved by unphysical values of $\nu > 0.25$. The templates are more unfaithful with increasing total mass. To detect optimally the complete numerical-relativity signal, including merger and ringdown, Ref. [147] suggested the possibility of using the TaylorF2 template bank with a frequency cutoff f_c larger than the usual upper cutoff (i.e., the Schwarzschild LSO) and closer to the fundamental quasi-normal mode frequency of the final black

hole. Moreover, they proposed to further improve this family by allowing either for unphysical values of ν or for the inclusion of a pseudo 4PN (p4PN) coefficient in the template phase, calibrated to the numerical simulations. Reference [148] extended the results of Ref. [147] to more accurate numerical waveforms, found that 3.5PN templates *are nearly always better and rarely significantly worse* than the 2PN templates, and proposed simple analytical frequency cutoffs for both Initial and Advanced LIGO — for example for Initial LIGO they recommended a strategy using p4PN templates for $M \leq 35M_{\odot}$ and 3.5PN templates with unphysical values of ν for larger masses. However, we notice that there is no reason for changing the template bank above $35M_{\odot}$. Reference [148] could have used the p4PN templates over the entire mass region, if they had not employed in their analysis the p4PN coefficient used in Ref. [147], but had calibrated it to the highly accurate waveforms used in their paper[2].

In this work our primary focus is on binary systems dominated by early inspiral and on a critical study of the variety of approximants that describe this. Towards this end, in this chapter we will provide a sufficiently exhaustive comparison of different PN models of adiabatic inspiral for an illustrative variety of different systems and quantify how (dis)similar they are for the purpose of detection. The choice of the PN models used in this paper is motivated by the fact that they are available in the LAL code and some of them have been used in the searches by Initial LIGO. We also compare all these PN models with one fiducial EOB model calibrated to

[2]We computed that the p4PN coefficient calibrated to the highly accurate waveforms used in Ref. [148] is $\mathcal{Y} = 3714$, instead of $\mathcal{Y} = 3923$ found in Ref. [147].

numerical-relativity simulations [54] to delineate the range of mass values where one must definitely go beyond the inspiral-dominated PN models to a more complete description including plunge and coalescence. The choice of this fiducial, preliminary EOB model is only motivated by the fact that it is the EOB model available in LAL and it is currently used for searches by Initial LIGO. It will be improved in the future using the recent results in Refs. [155, 156]. We will conclude that for total masses below a certain upper limit $M_{\rm crit}$, all template families at 3.5PN order (except for TaylorT3 and TaylorEt) are equally good for the purpose of detection. $M_{\rm crit}$ is found to be $\sim 12\,M_\odot$ for Initial, Enhanced and Advanced LIGO. Based solely on computational costs, we recommend that 3.5PN TaylorF2 be used below $M_{\rm crit}$ and EOB calibrated to numerical relativity simulations be used for total binary mass $M > M_{\rm crit}$.

The paper is organized as follows. In Sec. 3.2 we summarise the present status of the PN approximation. In Sec. 3.3 we recapitulate for completeness the main PN approximants and try to provide a ready-reckoner for the equations describing them and the relevant initial and termination conditions. In Sec. 3.4 we discuss the frequency evolution in each of these models. In Sec. 3.5 we discuss overlaps and the maximization used in this work. Section 3.6 and 3.7 presents the results of our analysis related to the effectualness, while Sec. 3.8 summarizes the results related to the faithfulness. In Sec. 3.9 we summarize our main conclusions. Readers who are interested in the main results of the paper and want to avoid technical details could skip Secs. 3.2, 3.3, 3.4, and 3.5, read the main results of Secs. 3.6, 3.7 and 3.8, and mainly focus on Sec. 3.9.

3.2 Current status of post-Newtonian approximation

Post-Newtonian approximation computes the evolution of the orbital phase $\phi(t)$ of a compact binary as a perturbative expansion in a small parameter, typically taken as $v = (\pi M F)^{1/3}$ (characteristic velocity in the binary), or $x = v^2$, although other variants exist. Here M is the total mass of the binary and F the GW frequency. In the adiabatic approximation, and for the *restricted* waveform in which case the gravitational wave phase is twice the orbital phase, the theory allows the phasing to be specified by a pair of differential equations $\dot{\phi}(t) = v^3/M$, $\dot{v} = -\mathcal{F}(v)/E'(v)$, where M is the total mass of the system, $\mathcal{F}$ its GW luminosity and $E'(v)$ is the derivative of the binding energy with respect to v. Different PN families arise because one can choose to treat the ratio $\mathcal{F}/E'(v)$ differently while being equivalent with the same PN order [30]. For instance, one can leave the PN expansions of the luminosity $\mathcal{F}(v)$ and $E'(v)$ as they appear (the so-called TaylorT1 model), or expand the rational polynomial $\mathcal{F}(v)/E'(v)$ in v to consistent PN order (the TaylorT4 model), recast as a pair of parametric equations $\phi(v)$ and $t(v)$ (the TaylorT2 model), or the phasing could be written as an explicit function of time $\phi(t)$ (the TaylorT3 model). These different representations are made possible because one is dealing with a perturbative series. Therefore, one is at liberty to "resum" or "reexpand" the series in any way one wishes (as long as one keeps terms to the correct order in the perturbation expansions), or even retain the expression as the quotient of two polynomials and treat them numerically. There is also the freedom of writing the series in a different variable, say (suitably adimensional) E (the so called TaylorEt

model).

In addition to these models, there have been efforts to extend the evolution of a binary beyond what is naturally prescribed by the PN formalism. Let us briefly discuss two reasons why the PN evolution cannot be used all the way up to the merger of the two bodies. PN evolution is based on the so-called adiabatic approximation according to which the fractional change in the orbital frequency $F_{\rm orb}$ over each orbital period is negligibly small, i.e. $\dot{F}_{\rm orb}/F_{\rm orb}^2 \ll 1$. This assumption is valid during most of the evolution, but begins to fail as the system approaches the LSO where $f_{\rm LSO} = (6^{3/2}\pi M)^{-1}$. In some cases, the frequency evolution stops from being monotonic and $\dot{f}$ changes from being positive to negative well before reaching the LSO — an indication of the breakdown of the approximation.

From the view point of maximizing detection potential one is also interested in going beyond the inspiral phase. The merger and ringdown phases of the evolution, when the luminosity is greatest, cannot be modelled by standard PN approximation. The use of resummation techniques more than a decade ago was followed by the construction of the EOB model [39, 141, 57], which has analytically provided the plunge, merger and ringdown phases of the binary evolution. As mentioned before, more recently, these models have been calibrated to numerical relativity simulations [149, 147, 150, 54, 151, 152, 153, 154, 155, 156]. We now have a very reliable EOB model that can be used to model the merger dynamics.

An astronomical binary is characterized by a large number of parameters some of which are intrinsic to the system (e.g., the masses and spins of the component stars and the changing eccentricity of the orbit) and others that are extrinsic (e.g.,

source location and orientation relative to the detector). In this paper we will worry about only the detection problem. Furthermore, we will assume that a coincident detection strategy will be followed so that we do not have to worry about the angular parameters such as the direction to the source, wave's polarization, etc. If binaries start their lives when their separation r is far larger compared to their gravitational radius (i.e., $r \gg GM/c^2$), by the time they enter the sensitivity band of ground-based detectors any initial eccentricity would have been lost due to gravitational radiation reaction, which tends to circularize[3] a binary [15, 16]. Therefore, we shall consider only systems that are on a quasi-circular inspiralling orbit. We shall also neglect spins which means that we have to worry in reality about only the two masses of the component bodies.

Our goal is to explore how (dis)similar the different waveform families are. We do this by computing the (normalized) cross-correlation between signals and templates, maximized either only over the extrinsic parameters of the templates (*faithfulness*) or over the intrinsic and extrinsic parameters of the templates (*effectualness*), the noise power spectral density of the detector serving as a weighting factor in the computation of the correlation (see Sec.3.5). Our conclusions, therefore, will depend on the masses of the compact stars as well as the detector that we hope to observe the signal with.

The overlaps (i.e., the normalized cross-correlation maximized over various parameters and weighted by the noise power spectral density) we shall compute are

[3]Though this assumption is justified for the prototypical binaries we focus on in this work, there exist credible astrophysical scenarios that lead to inspiral signals from binaries with non-negligible eccentricity in the sensitive detector bandwidth. A more involved treatment is then called for and available. See e.g. [159, 160, 161, 162, 163, 164, 165].

sensitive to the shape of the noise spectral density of a detector and not on how deep that sensitivity is. Now, the upgrade from initial to advanced interferometers will see improvements in sensitivity not only at a given frequency but over a larger band. Therefore, the agreement between different PN models will be sensitive to the noise spectral density that is used in the inner product. Thus, we will compare the PN families using power spectral densities of initial and advanced interferometric detectors.

We end this brief overview with the following observation. As mentioned earlier, following all present gravitational wave data analysis pipelines, this paper works only in the restricted wave approximation. This approximation assumes the waveform amplitude to be Newtonian and thus includes only the leading second harmonic of the orbital phase. Higher PN order amplitude terms bring in harmonics of the orbital phase other than the dominant one at twice the orbital frequency. Their effects can be significant [166, 167], especially close to merger [155], and they need to be carefully included in future work.

3.3 The PN approximants

For the convenience of the reader, in this section, we recapitulate the basic formulas for the different PN families from Refs. [30, 33]. While comparing the expressions below to those in Refs. [30, 33] recall $\lambda = -1987/3080$ [168, 169] and $\Theta = -11831/9240$ [32, 170]. In addition to the evolution equations, we shall also provide initial and final conditions. From the perspective of a data analyst, the initial

condition is simply a starting frequency F_0 and phase ϕ_0, which can be translated, with the help of evolution equations, as conditions on the relevant variables. We shall also give explicit expressions for the evolution of the gravitational wave frequency, namely $\dot{F} \equiv dF/dt$, or more precisely, the dimensionless quantity $\dot{F}\, F^{-2}$, in Sec. 3.4, where they will be used to study the rate at which the binary coalesces in different PN families, which will help us understand the qualitative difference between them. The contents of this section should act as a single point of resource for anyone who is interested in implementing the waveforms for the purpose of data analysis and other applications.

The basic inputs for all families are the PN expressions for the conserved 3PN energy (per unit total mass) [168, 169, 171, 172, 173, 174] $E_3(v)$ and 3.5PN energy flux [175, 176, 31, 32, 170] $\mathcal{F}_{3.5}(v)$,

$$\begin{aligned} E_3(v) &= -\frac{1}{2}\nu v^2 \left[1 - \left(\frac{3}{4} + \frac{1}{12}\nu\right) v^2 - \left(\frac{27}{8} - \frac{19}{8}\nu + \frac{1}{24}\nu^2\right) v^4 \right. \\ &\quad \left. - \left\{\frac{675}{64} - \left(\frac{34445}{576} - \frac{205}{96}\pi^2\right)\nu + \frac{155}{96}\nu^2 + \frac{35}{5184}\nu^3\right\} v^6\right], \end{aligned} \tag{3.1}$$

$$\begin{aligned} \mathcal{F}_{3.5}(v) &= \frac{32}{5}\nu^2 v^{10} \left[1 - \left(\frac{1247}{336} + \frac{35}{12}\nu\right) v^2 + 4\pi v^3 - \left(\frac{44711}{9072} - \frac{9271}{504}\nu - \frac{65}{18}\nu^2\right) v^4 \right. \\ &- \left(\frac{8191}{672} + \frac{583}{24}\nu\right)\pi v^5 + \left\{\frac{6643739519}{69854400} + \frac{16}{3}\pi^2 - \frac{1712}{105}\gamma \right. \\ &+ \left.\left(\frac{41}{48}\pi^2 - \frac{134543}{7776}\right)\nu - \frac{94403}{3024}\nu^2 - \frac{775}{324}\nu^3 - \frac{856}{105}\log\left(16v^2\right)\right\} v^6 \\ &- \left.\left(\frac{16285}{504} - \frac{214745}{1728}\nu - \frac{193385}{3024}\nu^2\right)\pi v^7\right], \end{aligned} \tag{3.2}$$

where $\gamma = 0.577216\ldots$ is the Euler constant. In the adiabatic approximation one

assumes that the orbit evolves slowly so that the fractional change in the orbital velocity ω over an orbital period is negligibly small. That is, $\frac{\Delta\omega}{\omega} \ll 1$, or, equivalently, $\frac{\dot{\omega}}{\omega^2} \ll 1$. In this approximation, one expects the luminosity in gravitational waves to come from the change in orbital energy averaged over a period. For circular orbits this means one can use the energy balance equation $\mathcal{F} = -d\mathcal{E}/dt$ where $\mathcal{E} = ME$.

In the adiabatic approximation one can write an equation for the evolution of any of the binary parameters. For instance, the evolution of the orbital separation $r(t)$ can be written as $\dot{r}(t) = \dot{\mathcal{E}}/(d\mathcal{E}/dr) = -\mathcal{F}/(d\mathcal{E}/dr)$. Together with the Kepler's law, the energy balance equation can be used to obtain the evolution of the orbital phase[4]:

$$\frac{d\phi}{dt} - \frac{v^3}{M} = 0, \tag{3.3a}$$

$$\frac{dv}{dt} + \frac{\mathcal{F}(v)}{ME'(v)} = 0, \tag{3.3b}$$

or, equivalently,

$$t(v) = t_{\rm ref} + M\int_v^{v_{\rm ref}} dv\, \frac{E'(v)}{\mathcal{F}(v)}, \tag{3.4a}$$

$$\phi(v) = \phi_{\rm ref} + \int_v^{v_{\rm ref}} dv\, v^3\, \frac{E'(v)}{\mathcal{F}(v)}, \tag{3.4b}$$

where $t_{\rm ref}$ and $\phi_{\rm ref}$ are integration constants and $v_{\rm ref}$ is an arbitrary reference velocity.

[4]Recall that the GW phase is twice the orbital phase for the restricted waveform and leads to differences in factors of 2 between the equations here for the *orbital* phase and those in [30] for the *gravitational-wave* phase.

3.3.1 TaylorT1

The TaylorT1 approximant refers to the choice corresponding to leaving the PN expansions of the luminosity $\mathcal{F}(v)$ and $E'(v)$ as they appear in Eq. (3.3) as a ratio of polynomials and solving the differential equations numerically

$$\frac{d\phi^{(\mathrm{T1})}}{dt} - \frac{v^3}{M} = 0, \tag{3.5a}$$

$$\frac{dv}{dt} + \frac{\mathcal{F}(v)}{ME'(v)} = 0. \tag{3.5b}$$

In the above $v \equiv v^{(\mathrm{T1})}$ but for the sake of notational simplicity we write only v; from the context the meaning should be clear. In the formulas of this section, and in the sections that follow, the expressions for $\mathcal{F}(v)$ ($E(v)$) are to be truncated at relative PN orders 2 (2), 3 (3) and 3.5 (3) to obtain 2PN [28, 29, 23, 30] , 3PN and 3.5PN [31, 32, 33] template or signal models respectively.

To see how to set up initial conditions, refer to Eq. (3.4). Let the initial gravitational wave frequency be F_0 or, equivalently, initial velocity $v_0 = (\pi M F_0)^{1/3}$. One normally chooses $t = 0$ at $v = v_0$. This can be achieved by choosing $v_{\mathrm{ref}} = v_0$ and $t_{\mathrm{ref}} = 0$, in Eq. (3.4). The initial phase ϕ_{ref} is chosen to be either 0 or $\pi/2$ in order to construct two orthogonal templates (see Sec. 3.5.1 for details).

3.3.2 TaylorT4

TaylorT4 was proposed in Ref. [34] and investigated in Refs. [149, 177, 145], thus many years after the other approximants discussed in this paper were pro-

posed (with the exception of TaylorEt, which is even more recent). However, it is a straightforward extension of TaylorT1 and at 3.5PN order by coincidence is found to be in better agreement with numerical simulations of the inspiral phase [149, 147, 177, 145, 151, 36, 153]. The approximant is obtained by expanding the ratio of the polynomials $\mathcal{F}(v)/E'(v)$ to the consistent PN order. The equation for $v^{(\mathrm{T4})}(t) \equiv v(t)$ at 3.5PN order reads,

$$\begin{aligned}
\frac{dv}{dt} &= \frac{32}{5}\frac{\nu}{M}v^9\left[1-\left(\frac{743}{336}+\frac{11}{4}\nu\right)v^2+4\pi v^3+\left(\frac{34103}{18144}+\frac{13661}{2016}\nu+\frac{59}{18}\nu^2\right)v^4\right.\\
&- \left(\frac{4159}{672}+\frac{189}{8}\nu\right)\pi v^5+\left(\frac{16447322263}{139708800}+\frac{16}{3}\pi^2-\frac{1712}{105}\gamma\right.\\
&+ \left.\left(\frac{451}{48}\pi^2-\frac{56198689}{217728}\right)\nu+\frac{541}{896}\nu^2-\frac{5605}{2592}\nu^3-\frac{856}{105}\log(16v^2)\right)v^6\\
&- \left.\left(\frac{4415}{4032}-\frac{358675}{6048}\nu-\frac{91495}{1512}\nu^2\right)\pi v^7\right]. \qquad (3.6)
\end{aligned}$$

The orbital phase $\phi^{(\mathrm{T4})}$ is determined, as in the case of TaylorT1, by Eq. (3.3a) and numerical solution of Eq. (3.6) and (3.3a) yields the TaylorT4 approximant.

Note that although TaylorT1 and TaylorT4 are perturbatively equivalent, the evolution of the phase can be quite different in these two approximations. The asymptotic structure of the approximants are also quite different: while $\dot{v}$ can have a pole (although not necessarily in the region of interest) when using Eq. (3.5b) none is possible when Eq. (3.6) is used. Differences of this kind can, in principle, mean that the various PN families give different phasing of the orbit. The hope is that when the PN order up to which the approximation is known is large, then the difference between the various PN families becomes negligible.

Setting up the initial conditions for TaylorT4 is the same as in the case of

TaylorT1.

3.3.3 **TaylorT2**

TaylorT2 is based on the second form of the phasing relations Eq. (3.4). Expanding the ratio of the polynomials $\mathcal{F}(v)/E'(v)$ in these equations to consistent PN order and integrating them one obtains a pair of parametric equations for $\phi(v)$ and $t(v)$, the TaylorT2 model.

$$\phi^{(\mathrm{T2})}_{n/2}(v) = \phi^{(\mathrm{T2})}_{\mathrm{ref}} + \phi^{v}_{N}(v)\sum_{k=0}^{n}\hat{\phi}^{v}_{k}v^{k}, \tag{3.7a}$$

$$t^{(\mathrm{T2})}_{n/2}(v) = t^{(\mathrm{T2})}_{\mathrm{ref}} + t^{v}_{N}(v)\sum_{k=0}^{n}\hat{t}^{v}_{k}v^{k}. \tag{3.7b}$$

Of all models considered in this study, TaylorT2 is computationally the most expensive. This is because the phase evolution involves solving a pair of transcendental

equations which is very time-consuming.

$$\begin{aligned}
\phi_{3.5}^{(\mathrm{T2})}(v) &= \phi_{\mathrm{ref}}^{(2)} - \frac{1}{32\nu v^5}\left[1 + \left(\frac{3715}{1008} + \frac{55}{12}\nu\right)v^2 - 10\pi v^3\right. \\
&+ \left(\frac{15293365}{1016064} + \frac{27145}{1008}\nu + \frac{3085}{144}\nu^2\right)v^4 + \left(\frac{38645}{672} - \frac{65}{8}\nu\right)\ln\left(\frac{v}{v_{\mathrm{lso}}}\right)\pi v^5 \\
&+ \left\{\frac{12348611926451}{18776862720} - \frac{160}{3}\pi^2 - \frac{1712}{21}\gamma + \left(\frac{2255}{48}\pi^2 - \frac{15737765635}{12192768}\right)\nu\right. \\
&+ \left.\frac{76055}{6912}\nu^2 - \frac{127825}{5184}\nu^3 - \frac{856}{21}\log(16v^2)\right\}v^6 \\
&+ \left.\left(\frac{77096675}{2032128} + \frac{378515}{12096}\nu - \frac{74045}{6048}\nu^2\right)\pi v^7\right], \qquad (3.8a)
\end{aligned}$$

$$\begin{aligned}
t_{3.5}^{(\mathrm{T2})}(v) &= t_{\mathrm{ref}}^{(\mathrm{T2})} - \frac{5M}{256\nu v^8}\left[1 + \left(\frac{743}{252} + \frac{11}{3}\nu\right)v^2 - \frac{32}{5}\pi v^3\right. \\
&+ \left(\frac{3058673}{508032} + \frac{5429}{504}\nu + \frac{617}{72}\nu^2\right)v^4 - \left(\frac{7729}{252} - \frac{13}{3}\nu\right)\pi v^5 \\
&+ \left\{-\frac{10052469856691}{23471078400} + \frac{128}{3}\pi^2 + \frac{6848}{105}\gamma + \left(\frac{3147553127}{3048192} - \frac{451}{12}\pi^2\right)\nu\right. \\
&- \left.\frac{15211}{1728}\nu^2 + \frac{25565}{1296}\nu^3 + \frac{3424}{105}\log(16v^2)\right\}v^6 \\
&+ \left.\left(-\frac{15419335}{127008} - \frac{75703}{756}\nu + \frac{14809}{378}\nu^2\right)\pi v^7\right]. \qquad (3.8b)
\end{aligned}$$

In this case, t_{ref} has to be chosen so that $t = 0$ when $F = F_0$ or $v = v_0$. This can be achieved most simply by solving for t_{ref}, using Eq. (3.8b), substituting $v = v_0$ on the right hand side and putting the left side to zero.

3.3.4 **TaylorT3**

This form of the approximant goes a step further than the previous TaylorT2 approximant. After computing as before a parametric representation of the phasing

formula $\phi(v)$ and $t(v)$, one explicitly inverts $t(v)$ to obtain $v(t)$ and uses it to produce an explicit representation of $\phi(t) \equiv \phi(v(t))$. This is the TaylorT3 approximant:

$$\phi^{(\mathrm{T3})}_{n/2}(t) = \phi^{(\mathrm{T3})}_{\mathrm{ref}} + \phi^t_N \sum_{k=0}^{n} \hat{\phi}^t_k \theta^k, \tag{3.9a}$$

$$F^{(\mathrm{T3})}_{n/2}(t) = F^t_N \sum_{k=0}^{n} \hat{F}^t_k \theta^k, \tag{3.9b}$$

where $\theta = [\nu(t_{\mathrm{ref}} - t)/(5M)]^{-1/8}$ and $F \equiv (2\,d\phi/dt)(2\pi)^{-1} = v^3/(\pi M)$ is the instantaneous GW frequency.

$$\begin{aligned}
\phi^{(\mathrm{T3})}_{3.5}(t) &= \phi^{(\mathrm{T3})}_{\mathrm{ref}} - \frac{1}{\nu\theta^5}\left[1 + \left(\frac{3715}{8064} + \frac{55}{96}\nu\right)\theta^2 - \frac{3\pi}{4}\theta^3\right. \\
&+ \left(\frac{9275495}{14450688} + \frac{284875}{258048}\nu + \frac{1855}{2048}\nu^2\right)\theta^4 + \left(\frac{38645}{21504} - \frac{65}{256}\nu\right)\ln\left(\frac{\theta}{\theta_{\mathrm{lso}}}\right)\pi\theta^5 \\
&+ \left\{\frac{831032450749357}{57682522275840} - \frac{53}{40}\pi^2 + \left(-\frac{126510089885}{4161798144} + \frac{2255}{2048}\pi^2\right)\nu - \frac{107}{56}\gamma\right. \\
&+ \left.\frac{154565}{1835008}\nu^2 - \frac{1179625}{1769472}\nu^3 - \frac{107}{56}\log(2\theta)\right\}\theta^6 \\
&+ \left.\left(\frac{188516689}{173408256} + \frac{488825}{516096}\nu - \frac{141769}{516096}\nu^2\right)\pi\theta^7\right],
\end{aligned} \tag{3.10a}$$

$$\begin{aligned}
F^{(\mathrm{T3})}_{3.5}(t) &= \frac{\theta^3}{8\pi M}\left[1 + \left(\frac{743}{2688} + \frac{11}{32}\nu\right)\theta^2 - \frac{3}{10}\pi\theta^3\right. \\
&+ \left(\frac{1855099}{14450688} + \frac{56975}{258048}\nu + \frac{371}{2048}\nu^2\right)\theta^4 - \left(\frac{7729}{21504} - \frac{13}{256}\nu\right)\pi\theta^5 \\
&+ \left\{-\frac{720817631400877}{288412611379200} + \frac{53}{200}\pi^2 + \frac{107}{280}\gamma + \left(\frac{25302017977}{4161798144} - \frac{451}{2048}\pi^2\right)\nu\right. \\
&- \left.\frac{30913}{1835008}\nu^2 + \frac{235925}{1769472}\nu^3 + \frac{107}{280}\log(2\theta)\right\}\theta^6 \\
&+ \left.\left(-\frac{188516689}{433520640} - \frac{97765}{258048}\nu + \frac{141769}{1290240}\nu^2\right)\pi\theta^7\right].
\end{aligned} \tag{3.10b}$$

The initial conditions in this case is slightly more complicated than the previous cases. Given an initial frequency F_0, one numerically solves Eq. (3.10b) to find the value of $t_{\rm ref}$ at which $F = F_0$ and $t = 0$ (recall that θ involves $t_{\rm ref}$.) Note that as $t \to t_{\rm ref}$, formally $F \to$ diverges.

3.3.5 TaylorEt

The TaylorEt was recently introduced in Ref. [35, 36, 37]. Introducing[5] $\zeta = -2E/\nu$ (recall that our E is conserved energy per total mass), the TaylorEt approximants are obtained starting from Eq. (3.1) for $E(x)$ or $\zeta(x)$ and inverting it to obtain $x(\zeta)$:

$$\begin{aligned} x &= \zeta\left[1+\left(\frac{3}{4}+\frac{1}{12}\nu\right)\zeta+\left(\frac{9}{2}-\frac{17}{8}\nu+\frac{1}{18}\nu^2\right)\zeta^2\right. \\ &+ \left.\left(\frac{405}{16}+\left(\frac{205}{96}\pi^2-\frac{4795}{72}\right)\nu+\frac{55}{64}\nu^2+\frac{35}{1296}\nu^3\right)\zeta^3\right]. \end{aligned} \tag{3.11}$$

With this choice of variable the equation determining the evolution of v, Eq. (3.3b), transforms to the balance equation for E rewritten in terms of the ζ variable:

$$\frac{d\zeta}{dt} = \frac{2\,\mathcal{F}(v(\zeta))}{\nu\,M}. \tag{3.12}$$

There is no difference between T1 and T4 approximants in the Et-parametrisation and the GW phasing equations Eq. (3.3a) and Eq. (3.3b) in terms of ζ become [158],

[5]Note that the ζ in this paper is denoted variously by ζ in [35] but by ξ in e.g. [158].

$$
\begin{aligned}
\frac{d\phi^{(\mathrm{Et})}(t)}{dt} &= \frac{\zeta^{3/2}}{M}\left[1+\left(\frac{9}{8}+\frac{1}{8}\nu\right)\zeta+\left(\frac{891}{128}-\frac{201}{64}\,\nu+\frac{11}{128}\,\nu^2\right)\zeta^2\right.\\
&+ \left.\left\{\frac{41445}{1024}-\left(\frac{309715}{3072}-\frac{205}{64}\,\pi^2\right)\nu+\frac{1215}{1024}\,\nu^2+\frac{45}{1024}\,\nu^3\right\}\zeta^3\right], \quad (3.13a)\\
\frac{d\zeta}{dt} &= \frac{64\nu\zeta^5}{5M}\left[1+\left(\frac{13}{336}-\frac{5}{2}\nu\right)\zeta+4\pi\zeta^{3/2}+\left(\frac{117857}{18144}-\frac{12017}{2016}\nu+\frac{5}{2}\nu^2\right)\zeta^2\right.\\
&+ \left(\frac{4913}{672}-\frac{177}{8}\nu\right)\pi\zeta^{5/2}+\left\{\frac{37999588601}{279417600}+\frac{16}{3}\pi^2-\frac{1712}{105}\gamma\right.\\
&+ \left.\left(\frac{369}{32}\pi^2-\frac{24861497}{72576}\right)\nu+\frac{488849}{16128}\nu^2-\frac{85}{64}\nu^3-\frac{856}{105}\log(16\zeta)\right\}\zeta^3\\
&+ \left.\left(\frac{129817}{2304}-\frac{3207739}{48384}\nu+\frac{613373}{12096}\nu^2\right)\pi\zeta^{7/2}\right]. \quad (3.13b)
\end{aligned}
$$

To set up the initial condition note that $2\pi F = 2\,d\phi/dt$. Given an initial frequency F_0 one finds the initial value ζ_0 of ζ by numerically solving Eq. (3.13a), by setting the left hand side to πF_0.

3.3.6 **TaylorF2**

The most commonly used form of the approximant is the Fourier representation computed using the *stationary phase approximation*. Using the SPA the waveform in the frequency domain may be written as,

$$
\tilde{h}^{\mathrm{spa}}(f) = \frac{a(t_f)}{\sqrt{\dot{F}(t_f)}} e^{i\left[\psi_f(t_f)-\pi/4\right]}, \quad \psi_f(t) \equiv 2\pi f t - 2\,\phi(t), \qquad (3.14)
$$

where t_f is the saddle point defined by solving for t, $d\psi_f(t)/dt = 0$, i.e. the time t_f when the GW frequency $F(t)$ becomes equal to the Fourier variable f. In the adiabatic approximation, (denoting $v_f \equiv (\pi M f)^{1/3}$) the value of t_f and $\psi_f(t_f)$ are

given by the following integrals:

$$t_f = t_{\rm ref} + M\int_{v_f}^{v_{\rm ref}} \frac{E'(v)}{\mathcal{F}(v)}dv, \tag{3.15a}$$

$$\psi_f(t_f) = 2\pi f t_{\rm ref} - \phi_{\rm ref} + 2\int_{v_f}^{v_{\rm ref}} (v_f^3 - v^3)\frac{E'(v)}{\mathcal{F}(v)}dv. \tag{3.15b}$$

As in the time domain case it is more efficient to use the equivalent differential form

$$\frac{d\psi}{df} - 2\pi t = 0, \qquad \frac{dt}{df} + \frac{\pi M^2}{3v^2}\frac{E'(f)}{\mathcal{F}(f)} = 0, \tag{3.16}$$

and this characterizes the TaylorF1 approximant.

The analogue of the TaylorT2 in the frequency domain follows by explicitly truncating the energy and flux functions to consistent post-Newtonian orders and explicating the v- integration in the above. This leads us to a Fourier domain waveform, the TaylorF2, which is the most often employed PN-approximant, given by

$$\tilde{h}(f) = \mathcal{A}f^{-7/6}e^{i\psi(f)}, \tag{3.17}$$

where $\mathcal{A} \propto \mathcal{M}^{5/6}Q(\text{angles})/D$, and D the distance to the binary. To 3.5PN order

the phase of the Fourier domain waveform is given by

$$\begin{aligned}\psi_{3.5}^{(\mathrm{F2})}(f) &= 2\pi f t_c - \phi_c - \frac{\pi}{4} + \frac{3}{128\,\nu\,v^5}\left[1 + \frac{20}{9}\left(\frac{743}{336} + \frac{11}{4}\nu\right)v^2 - 16\pi v^3\right. \\ &+ 10\left(\frac{3058673}{1016064} + \frac{5429}{1008}\,\nu + \frac{617}{144}\,\nu^2\right)v^4 \\ &+ \pi\left(\frac{38645}{756} - \frac{65}{9}\nu\right)\left\{1 + 3\log\left(\frac{v}{v_{\mathrm{lso}}}\right)\right\}v^5 + \left\{\frac{11583231236531}{4694215680}\right. \\ &- \frac{640}{3}\pi^2 - \frac{6848\,\gamma}{21} - \frac{6848}{21}\log(4\,v) + \left(-\frac{15737765635}{3048192} + \frac{2255\,\pi^2}{12}\right)\nu \\ &+ \left.\left.\frac{76055}{1728}\nu^2 - \frac{127825}{1296}\nu^3\right\}v^6 + \pi\left(\frac{77096675}{254016} + \frac{378515}{1512}\,\nu - \frac{74045}{756}\,\nu^2\right)v^7\right], \end{aligned} \tag{3.18}$$

where $v = (\pi M f)^{1/3}$.

In this case one has to specify the constants t_c and ϕ_c and they can be chosen arbitrarily.

3.3.7 The effective-one-body model

In this paper since we are not particularly concerned with the coalescence signal, we employ the less sophisticated earlier version of the EOB model calibrated to numerical-relativity simulations from Ref. [54] (for more sophisticated versions of the EOB model see Refs. [152, 153, 154, 155, 156]). Below we briefly review the EOB model from Ref. [54].

Introducing polar coordinates (r, ϕ) and their conjugate momenta (p_r, p_ϕ), the

EOB effective metric takes the form [39]

$$ds^2_{\rm eff} = -A(r)\,dt^2 + \frac{D(r)}{A(r)}\,dr^2 + r^2\left(d\theta^2 + \sin^2\theta\,d\phi^2\right). \tag{3.19}$$

The EOB Hamiltonian reads

$$H^{\rm real}(r, p_r, p_\phi) \equiv \mu\hat{H}^{\rm real} = M\sqrt{1 + 2\nu\left(\frac{H^{\rm eff} - \mu}{\mu}\right)}, \tag{3.20}$$

with the effective Hamiltonian [39, 57]

$$H^{\rm eff}(r, p_r, p_\phi) \equiv \mu\,\widehat{H}^{\rm eff} = \mu\sqrt{A(r)\left[1 + \frac{A(r)}{D(r)}p_r^2 + \frac{p_\phi^2}{r^2} + 2(4-3\nu)\,\nu\,\frac{p_r^4}{r^2}\right]}. \tag{3.21}$$

The Taylor-approximants to the coefficients $A(r)$ and $D(r)$ can be written as [39, 57]

$$A_k(r) = \sum_{i=0}^{k+1}\frac{a_i(\nu)}{r^i}, \tag{3.22a}$$

$$D_k(r) = \sum_{i=0}^{k}\frac{d_i(\nu)}{r^i}. \tag{3.22b}$$

The functions $A(r)$, $D(r)$, $A_k(r)$ and $D_k(r)$ all depend on the symmetric mass ratio ν through the ν–dependent coefficients $a_i(\nu)$ and $d_i(\nu)$. These coefficients are currently known through 3PN order (i.e. up to $k = 4$) and can be read from Ref. [54]. During the last stages of inspiral and plunge[6], the EOB dynamics can

[6]To deal with the steep rise of various quantities during the plunge, it is advantageous to consider the EOB equations in terms of the tortoise radial coordinate r_* and its conjugate p_{r_*} rather than in terms of the standard radial coordinate r and p_r as above. The form of $H^{\rm eff}$ in the two cases will be different [150]. For the level of accuracy in our present work, this difference is irrelevant.

be adjusted closer to the numerical simulations by including in the radial potential $A(r)$ a p4PN coefficient $a_5(\nu)$ and $a_5(\nu) = \lambda_0\,\nu$, with λ_0 a constant[7]. In order to assure the presence of a horizon in the effective metric (3.19), a zero needs to be factored out from $A(r)$. This is obtained by applying a Padé resummation [57]. The Padé coefficients for the expansion of $A(r)$ and $D(r)$ at p4PN order are denoted $A^1_4(r)$ and $D^0_4(r)$, and their explicit form can be read from Ref. [54].

The EOB Hamilton equations are written in terms of the reduced (i.e., dimensionless) quantities $\widehat{H}^{\rm real}$ [defined in Eq. (3.20)], $\widehat{t} = t/M$, and $\widehat{\omega} = \omega\,M$ [141]:

$$\frac{dr}{d\widehat{t}} = \frac{\partial \widehat{H}^{\rm real}}{\partial p_r}(r, p_r, p_\phi)\,, \tag{3.23a}$$

$$\frac{d\phi}{d\widehat{t}} = \frac{\partial \widehat{H}^{\rm real}}{\partial p_\phi}(r, p_r, p_\phi)\,, \tag{3.23b}$$

$$\frac{dp_r}{d\widehat{t}} = -\frac{\partial \widehat{H}^{\rm real}}{\partial r}(r, p_r, p_\phi)\,, \tag{3.23c}$$

$$\frac{dp_\phi}{d\widehat{t}} = \widehat{\mathcal{F}}_\phi(r, p_r, p_\phi)\,, \tag{3.23d}$$

with the definition $\widehat{\omega} \equiv d\phi/d\widehat{t}$. Another critical input to the EOB model is the form for the radiation reaction force arising from the basic PN expression of the energy flux. Different choices include Padé resummation [132], and the more recent $\rho_{\ell m}$-resummation [157]. It also further includes the introduction of terms describing next-to-quasi-circular effects. Here, for the ϕ component of the radiation-reaction force we use the less sophisticated Keplerian Padé-approximant to the energy flux as given by Eq. (15) of Ref. [54].

[7]Note that λ_0 was denoted λ in Ref. [54], and a_5 in Refs. [150, 151, 153, 154].

The inspiral-plunge EOB waveform at leading order in a PN expansion reads

$$h^{\rm insp-plunge}(t) \equiv \widehat{\omega}^{1/3}\, \cos[2\phi(t)]\,. \tag{3.24}$$

The merger-ringdown waveform in the EOB approach is built as a superposition of quasi-normal modes [141, 47, 149, 54, 150, 151], as

$$h^{\rm merger-RD}(t) = \sum_{n=0}^{N-1} A_n\, e^{-i\sigma_n (t-t_{\rm match})}, \tag{3.25}$$

where n is the overtone number of the Kerr quasi-normal mode, N is the number of overtones included in our model, and A_n are complex amplitudes to be determined by a matching procedure described below. The quantity $\sigma_n = \omega_n - i\alpha_n$, where the oscillation frequencies $\omega_n > 0$ and the inverse decay-times $\alpha_n > 0$, are numbers associated with each quasi-normal mode. The complex frequencies are known functions of the final black-hole mass and spin and can be found in Ref. [178]. The final black-hole masses and spins are obtained from the fitting to numerical results worked out in Ref. [54].

The complex amplitudes A_n in Eq. (3.25) are determined by matching the EOB merger-ringdown waveform with the EOB inspiral-plunge waveform close to the EOB light ring. In particular, in Ref. [54] the matching point is provided analytically by Eq. (37). In order to do this, N independent complex equations are needed. The N equations are obtained at the matching time by imposing continuity

of the waveform and its time derivatives,

$$\frac{d^k}{dt^k} h^{\rm insp-plunge}(t_{\rm match}) = \frac{d^k}{dt^k} h^{\rm merger-RD}(t_{\rm match}) \,, \quad (k = 0, 1, 2, \cdots, N-1) \,. \quad (3.26)$$

In this paper we use N=3. The above matching approach is referred to as *point matching*. It gives better smoothness around the matching time, but it is not very stable numerically when N is large and higher order numerical derivatives are needed. More sophisticated matching procedures have been proposed in the literature to overcome the stability issue. Reference [150] introduced the *comb matching* approach where N equations are obtained at N points evenly sampled in a small time interval $\Delta t_{\rm match}$ centered at $t_{\rm match}$. More recently, to improve the smoothness of the comb matching Ref. [156] introduced the *hybrid comb matching* where one chooses a time interval $\Delta t_{\rm match}$ ending at $t_{\rm match}$, and imposes not only the continuity of the waveform at $N-4$ points evenly sampled from $t_{\rm match} - \Delta t_{\rm match}$ to $t_{\rm match}$, but also requires continuity of the first and second order time derivatives of the waveform at $t_{\rm match} - \Delta t_{\rm match}$ and $t_{\rm match}$.

Finally, the full (inspiral-plunge-merger-ringdown) EOB waveform reads

$$h(t) = h^{\rm insp-plunge}(t)\, \theta(t_{\rm match} - t) + h^{\rm merger-RD}\, \theta(t - t_{\rm match}) \,, \quad (3.27)$$

where we denote with θ the Heaviside step function.

3.3.8 **Waveforms and termination conditions**

Before concluding this Section we note a few other points concerning the generation of the waveform. Since our goal is to study the agreement between different waveforms it is not necessary to separately consider the two different polarizations but only the detector response. For time-domain models TaylorT1, TaylorT2, TaylorT3, TaylorT4 and EOB the waveform is taken as:

$$h_{\rm A}(t) = C\, v_{\rm A}^2\, \sin[2\,\phi_{\rm A}(t)],$$

where $v_{\rm A}$ and $\phi_{\rm A}(t)$ are computed using the relevant formulas corresponding to the approximant A. In the case of TaylorEt the waveform is taken to be

$$h_{\rm Et}(t) = C\, \zeta(t)\, \sin[2\,\phi_{\rm Et}(t)].$$

In all cases the constant C is fixed by demanding that the norm of the signal be unity (cf. Sec. 3.5). The initial phase of the signal is set to 0, while in the case of templates we construct two orthonormal waveforms corresponding to the starting phases of 0 and $\pi/2$.

The waveforms are terminated when v reaches the value quoted in Table I or before, if the frequency evolution is not monotonic (see next Section). For instance, in the case of TaylorT3 at 3.5PN order the approximant has an unusual behaviour whereby the frequency evolution ceases to be monotonic well before v reaches the nominal value of $1/\sqrt{6}$. In the case of TaylorT1, TaylorT2 and TaylorT3, the termi-

Table 3.1: Termination condition for waveform generation is chosen to be either LSO corresponding to Schwarzschild metric $v_S = 6^{-1/2}$, or the extremum defined by the P-approximant of the energy function as in [132] which is v_{P_4} at 2PN and v_{P_6} at 3- and 3.5PN. In the case of TaylorT3 at 3.5PN, as the frequency evolution is not monotonic, the evolution has to be terminated prematurely at v_m such that $\dot{F}(v_m) = 0$.

Order/Approx	T1	T2	T3	T4	Et	F2
2PN	v_S	v_S	v_S	v_{P_4}	v_{P_4}	v_{P_4}
3PN	v_S	v_S	v_S	v_{P_6}	v_{P_6}	v_{P_6}
3.5PN	v_S	v_S	v_m	v_{P_6}	v_{P_6}	v_{P_6}

nation is at the LSO defined by the Schwarzschild metric, namely $v = 1/\sqrt{6}$, at all PN orders, but we also check for monotonicity of the frequency evolution. For other approximants, except EOB, we terminate at the extremum of the P-approximant energy function [132]. In the case of EOB, the waveform is terminated at the end of the quasi-normal ringing.

3.4 Frequency evolution

The quantity that determines the evolution of a binary, its phasing and the duration for which it lasts starting from a particular frequency, is the acceleration of the bodies under radiation reaction. Equivalently, it is the evolution of the derivative of the gravitational wave frequency $\dot{F} = dF/dt$, which determines the phasing of the waves. When the separation between the bodies is large, the frequency evolution is slow and the quantity [30] $\epsilon(t) = \dot{F}F^{-2}$, which measures the fractional change in the frequency over a period, is small: $\dot{F}F^{-2} \ll 1$. As the binary evolves, this

quantity increases but, as seen in numerical evolutions, remains finite and positive all the way up to the merger of the two bodies. In what follows we will explore the behaviour of ϵ as a function of the PN parameter v rather than t, because the former parameter is (mass) scale free, unlike the latter.

Computing the adiabaticity parameter $\epsilon(v)$ in the case of TaylorT1 and TaylorT4 is straightforward using Eqs. (3.5b) and (3.6). In the case of TaylorT2, one differentiates Eq. (3.8b) with respect to v and then takes its reciprocal. Finding $\epsilon(v)$ in the case of TaylorEt is more involved. The frequency F is given by Eq. (3.13a) but the right hand side is a function of ζ. One must, therefore, combine Eqs. (3.13a) and (3.13b) to find the derivative of the frequency:

$$\pi \dot{F} = \pi \frac{dF}{d\zeta} \frac{d\zeta}{dt} = \frac{d}{d\zeta} \left(\frac{d\phi}{dt} \right) \frac{d\zeta}{dt}. \tag{3.28}$$

The above equation still gives $\dot{F}$ as a function of ζ. One can then use Eq. (3.11) to get $\epsilon(v)$. Consequently, there is no guarantee that v will be monotonic in the region of interest. However, we do find that the function $\epsilon_{\rm Et}(v)$ is positive in the region of interest and therefore v increases monotonically for TaylorEt. To find $\epsilon(v)$ for TaylorT3, $\dot{F}$ is given by differentiating Eq. (3.10b) with respect to t (recall $\theta = \theta(t)$) and then one uses the same equation to find $v = (\pi M F)^{1/3}$ at a given t. It turns out that for TaylorT3 the function $\epsilon_{\rm T3}$ can become negative in the region of interest (exactly when this happens depends on the PN order and mass ratio) and so v does not generally increase monotonically.

Figure 3.1, left panel, plots $\epsilon(v)$ for two values of the mass ratio: $\nu = 0.10$ and

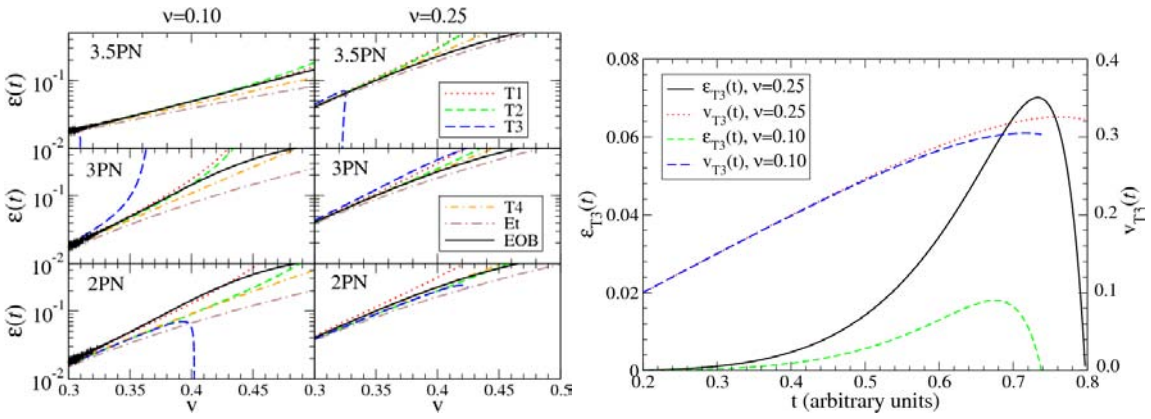

Figure 3.1: On the left hand panel the plots show the evolution of frequency in different PN families. The adiabaticity parameter $\epsilon(t) \equiv F^{-2}\dot{F}$ is essentially the same for all the different approximations at $v \ll 1$ As the binary gets close to coalescence the various approximations begin to differ from each other. The right hand panel shows the adiabaticity parameter for the TaylorT3 model as a function of time t at 3.5PN order. Note that $\epsilon_{\rm T3}(t)$ begins to decrease and even becomes less than zero before v reaches its nominal value of $1/\sqrt{6}$. This leads to waveforms that are significantly shorter in the case of TaylorT3.

$\nu = 0.25$. When v is small ($v \ll 1/\sqrt{6}$) $\epsilon(v)$ for the different approximants is the same. Therefore, in systems for which v remains small when the signal is in band (as, for example, in a binary neutron star), the different approximants, as we shall see in the next Section, agree well with each other. As v approaches $1/\sqrt{6}$, different approximations tend to differ greatly, which means we cannot expect good agreement between the different PN families. Of the approximants considered here, TaylorEt seems to have the smallest value of $\epsilon(v)$ at any given v. Therefore, the evolution will be slower, and the duration of the waveform from a given frequency larger, than the other approximants [37]. TaylorT3 also differs from all others because $\epsilon(v)$ becomes negative before the last stable orbit, and so v does not generally increase monotonically for this approximant. This behavior can be seen at 2PN and 3.5PN orders in the left panel of Fig. 3.1. The reason for this can be seen in Fig. 3.1,

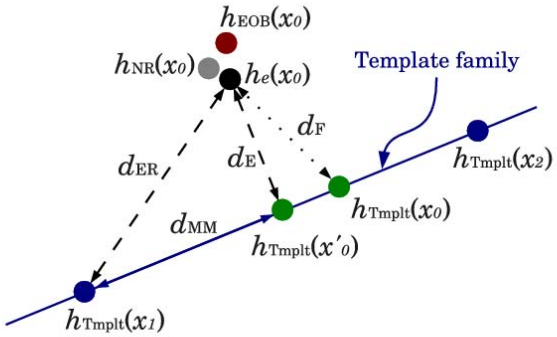

Figure 3.2: Schematic plot of distance (or mismatch) relation between templates and exact, numerical and EOB waveforms.

right panel, where we have shown the time development of $\epsilon_{\rm T3}(t)$ for two values of $\nu = 0.10,\ 0.25$. Since $\dot{F}$ becomes negative before reaching the last stable orbit, the waveform has to be terminated before before v reaches $1/\sqrt{6}$.

3.5 Effectualness

The goal of this study is to compare the different PN approximations by measuring their mutual effectualness (i.e., overlaps maximized over intrinsic and extrinsic parameters) for a number of different mass pairs. To this end it will be very useful to define the scalar product of waveforms. Given waveforms h_k and q_k, $k = 0, \ldots, N-1$, where h_k is the kth sample of the signal $h(t)$ at time $t_k = k\Delta$, $\Delta = 1/f_s$ being the sampling interval corresponding to the sampling rate f_s, their

scalar product is defined by[8]

$$\langle h,\, q\rangle\,(\tau_k) = 2\sum_{m=0}^{N-1}\left[H_m\,Q_m^* + H_m^*\,Q_m\right]\,e^{-2\pi imk/N}\,\frac{\Delta_f}{S_h(f_m)} \tag{3.29}$$

where $\Delta_f = f_s/N$, $f_m = m\Delta_f$, $\tau_k = k\Delta$ is the lag of the template — a measure of the relative time-shift between the template and signal, $H_m = \Delta\sum_{k=0}^{N-1} h_k\,e^{2\pi imk/N}$ is the discrete Fourier transform of $h(t)$ (similarly, Q_m) and $S_h(f_m)$ is the one-sided noise power spectral density of a detector. In comparing two waveforms the overall amplitude is of no interest and we should, therefore, consider waveforms with unit norm, namely $\hat{h} = h/\sqrt{\langle h,\, h\rangle}$. Consequently, the relevant quantity is the scalar product between normalized waveforms defined by

$$\mathcal{O}[h,\, q] = \left\langle \hat{h},\, \hat{q} \right\rangle \tag{3.30}$$

3.5.1 Maximization of the overlaps

The signal and the template both depend on a set of parameters of the source (e.g., masses and initial spins of the component masses) and its orientation relative to the detector. We shall be concerned with binaries with non-spinning components on quasi-circular orbits. Such systems are characterized by two intrinsic parameters, namely the masses m_1 and m_2 of the components, and two extrinsic parameters, namely the time-of-coalescence t_C and the phase of the signal at that time ϕ_c. The

[8]It is conventional to define the scalar product in the continuum limit. Here, however, we have given the definition for a discretely sampled data and this is the expression that is used in computing the overlaps.

overlap integral, therefore, depends on the parameters of the signal and the template and the relevant quantity is the overlap maximized over these parameters.

The data analysis problem is concerned with digging out a specific signal buried in noisy data. This means that the parameters of the signal are fixed but the data analyst is at liberty to maximize over the parameters of the template. In this paper we will explore the effectualness of templates; that is to say the overlap maximized over a template's parameters keeping those of the signal fixed. We will do this for several choices of the component masses of the binary. However, the time-of-coalescence t_C and the phase ϕ_C of the signal at that time, are arbitrarily chosen to be equal to zero. A caveat is in order concerning the value of the effectualness arising as a result of our choice of t_C and ϕ_C : the maximized overlap is not very sensitive to our choice of t_C but it could vary by several percents depending on the choice of a signal's phase, especially when the signal and the template families are not very close in the geometrical sense.

Maximization over a template's masses is carried out using a bank of templates and the template bank is set up such that for all signals of the same family as the template their best overlap with the nearest template is larger than a certain value called the minimal match MM. Our template placement is as in Ref. [179], which is known to produce, with probability close to 1 [179], matches larger than the minimal match for the TaylorT1, TaylorT3, TaylorF2 and EOB families of signals (and templates) for the range of masses considered in this paper. We have checked this to be true also for TaylorEt and TaylorT4 families.

We have used a minimal match of MM = 0.99 in all cases. Maximization over

time-of-coalescence is accomplished by looking at the overlap integral at different lags τ_k. Finally, since our templates are of the form $h_k = A_k \cos(\phi_k + \phi_0)$, where ϕ_0 is an unknown constant phase offset, maximization over ϕ_0 can be achieved by using two quadratures of the template, $h_k^0 = A_k \cos(\phi_k)$ and $h_k^{\pi/2} = A_k \cos(\phi_k + \pi/2)$:

$$\max_{\phi_0} \mathcal{O}[h,\, q] = \left[\left\langle h^0,\, q \right\rangle^2 + \left\langle h^{\pi/2},\, q \right\rangle^2 \right]^{1/2}. \tag{3.31}$$

When the signal and the template belong to the same family the maximized overlap is at least MM. When the waveforms belong to different families the maximized overlap is less than MM.

Our approach to finding the effectualness of a template with a signal of "fixed" parameters is here somewhat different from what is normally followed in the literature, but more appropriate in the context of data analysis. In the literature on the comparisons of different PN models, one normally measures either the *best* or the *minimax* overlap [132]. The best overlap gives the maximum of the overlap over the masses and t_C but maximized over the constant phases of both the signal and the template. On the other hand, the minimax overlap is the overlap maximized over the masses and t_C but minimized over the constant phases of the signal and the template. As mentioned earlier, we fix the phase of the signal to be equal to zero and hence our effectualness is, in principle, smaller than best overlaps but larger than minimax overlaps. The difference between the best and minimax overlaps is tiny when the effectualness is intrinsically large (i.e., close to 1), but could differ by $5 - 8\%$ when the best overlap is ~ 0.8. This should be kept in mind while interpret-

ing our results. Moreover, as mentioned earlier, instead of numerically searching for the maxima of the overlap in the space of masses we just use a grid of templates with a minimal match of MM = 0.99.

We will compute effectualness between every possible template and signal. If our template is the PN approximation A and the signal is the PN approximation B then we are interested in computing the matrix ϵ_{AB} defined by

$$\epsilon_{AB} \equiv \max_{\lambda^A} \mathcal{O}[h_A(\lambda^A),\, h_B(\lambda^B)], \tag{3.32}$$

where λ^A and λ^B are the parameters of the template and the signal, respectively. The overlap is symmetric in its arguments h_A and h_B only if the signal and template, together with their parameters, are interchanged. That is, $\mathcal{O}[h_A(\lambda^A),\, h_B(\lambda^B)] = \mathcal{O}[h_B(\lambda^B),\, h_A(\lambda^A)]$ but, in general, $\mathcal{O}[h_A(\lambda^A),\, h_B(\lambda^B)] \neq \mathcal{O}[h_A(\lambda^B),\, h_B(\lambda^A)]$. Therefore, the maximized overlap ϵ_{AB} *need not* be symmetric. The process of maximization, in which the parameters of the "signal" are kept fixed and those of the "template" are varied, breaks down the symmetry. The lack of symmetry arises primarily because the signal manifolds $\mathcal{M}_{A,B}$ representing the two families are distinct; the nearest "distance" from a coordinate point P on $\mathcal{M}_A$ to a point on $\mathcal{M}_B$ need not be the same as the nearest distance from P on $\mathcal{M}_B$ to a point on $\mathcal{M}_A$.

3.5.2 Effectualness, faithfulness and loss in event rates

A direct measure of the efficiency of a template bank is the loss of event rates due to differences between the template family and the exact signal. The loss

of event rates is determined by two factors: the effectualness of the templates in matching the exact waveforms and the minimal match of the template bank itself. In this section, we will quantify this relation.

In Fig. 3.2 [9] we sketch a portion of the waveform space. The solid line represents the template family subspace. Dots represent various waveforms: (i) $h_{\rm Tmplt}(x_1)$ and $h_{\rm Tmplt}(x_2)$ are two neighboring templates in the template bank with physical parameters x_1 and x_2; (ii) $h_{\rm Tmplt}(x_0)$ and $h_{\rm Tmplt}(x_0')$ are waveforms in the same family as the templates to be chosen as discussed below; (iii) $h_e(x_0)$, $h_{\rm NR}(x_0)$ and $h_{\rm EOB}(x_0)$ are exact, numerical and EOB waveforms of the same physical parameters x_0, respectively. [The EOB waveform is calibrated to the numerical simulation.] We choose x_0' such that the overlap between $h_{\rm Tmplt}(x_1)$ and $h_{\rm Tmplt}(x_0')$ is the minimal match (see below) of the template bank. We choose x_0 such that $h_e(x_0)$ is the exact waveform that has larger overlap with $h_{\rm Tmplt}(x_0')$ than with any other waveforms in the template family. This overlap is larger than the one between $h_e(x_0)$ and $h_{\rm Tmplt}(x_0)$ even though they have the same physical parameters, because of the systematic difference between the family of exact waveforms and the family of templates.

We define the distance in the waveform space between two waveforms h and q by the scalar product $\sqrt{1-\mathcal{O}[h,\,q]}$. For convenience, we define the mismatch to be the square of the distance. The overlap between $h_{\rm Tmplt}(x_1)$ and $h_{\rm Tmplt}(x_0')$ is the minimal match and we denote the corresponding mismatch by $d_{\rm MM} = 1 - {\rm MM}$. Similarly, $1 - d_{\rm E}$ and $1 - d_{\rm F}$ are the effectualness and faithfulness of the template

[9] This figure is very similar to Fig. 3 of Ref. [140].

family with the exact waveform $h_e(x_0)$, respectively. The mismatch between $h_e(x_0)$ and the closest template $h_{\rm Tmplt}(x_1)$ quantifies the reduction in signal-to-noise ratio when the template bank is used to search for the exact waveform. We denote this mismatch by $d_{\rm ER}$. When these mismatches are small, by Pythagorean theorem, we have an the approximate relation $d_{\rm ER} \simeq d_{\rm MM} + d_{\rm E}$. Assuming uniform spatial distribution of sources, the reduction in event rate is $1-(1-d_{\rm ER})^3 \simeq 3d_{\rm ER}$. Therefore, if we want to satisfy the usual requirement of $< 10\%$ loss in event rate, we need $d_{\rm ER} = d_{\rm MM} + d_{\rm E} < 3.5\%$. Typical minimal match adopted in current searches has either $d_{\rm MM} = 3\%$ or $d_{\rm MM} = 1\%$, which means, in the first case, an extremely rigorous requirement on the effectualness: $d_{\rm E} < 0.5\%$, or in the second case, a reasonable requirement of $d_{\rm E} < 2.5\%$. The latter is achievable by PN models. Note that, if both the minimal match of a template bank and the effectualness of the template model are 97%, the loss in event rate rises to 17%.

However, it is not possible to calculate $d_{\rm ER}$ since we do not know the exact waveform $h_e(x_0)$. In this paper, we adopt two strategies to estimate $d_{\rm ER}$: (i) we calculate the mutual effectualness of PN models for low-mass binaries and assume it to be a good representation of their effectualness with exact waveforms; (ii) we approximate $h_e(x_0)$ with the EOB waveform $h_{\rm EOB}(x_0)$ calibrated to the numerical simulations. We can verify the goodness of the latter assumption as follows. The mismatch between the best EOB waveforms [156, 155] and the numerical waveforms is less than 10^{-3}. In Ref. [156], the authors calculated the mismatch among accurate numerical waveforms generated by simulations with different resolutions and/or extraction schemes, as well. They found that the mismatch is less than 10^{-4}. We

consider the latter as an estimate of the mismatch between exact and numerical waveforms. In the worst case, the mismatch between the exact and EOB waveforms with the same physical parameters is roughly $(\sqrt{10^{-3}}+\sqrt{10^{-4}})^2 = 1.7\times10^{-3}$. Therefore, we can conclude that by approximating $h_e(x_0)$ with $h_{\rm EOB}(x_0)$. we underestimate the loss of event rate by at most 0.5%.

Notice that the effectualness result presented in the following sections is slightly different from $1-d_{\rm E}$. It is obtained through discrete searches over template parameters using template banks with MM = 0.99 rather than through continuous searches. Therefore, the mismatch associated with this effectualness result includes already the discreteness effect in the template banks, i.e. a mismatch $d^{(0)}_{\rm MM} = 0.01$. In this case, if a search is carried out with a template bank of a different minimal match, say MM$= 1 - d_{\rm MM} = 0.97$, to calculate the loss of event-rate, a mismatch of $d_{\rm MM} - d^{(0)}_{\rm MM} = 0.02$, instead of $d_{\rm MM}$, needs to be added to the effectualness result in this paper, i.e. $d_{\rm ER} = d_{\rm MM} - d^{(0)}_{\rm MM} + d_{\rm E}$. The only exception in this paper is the effectualness result between EOB models presented in the Conclusions which is obtained through a continuous search.

3.5.3 Choice of binary systems and PN orders

We have chosen three conventional systems, binary neutron stars (BNS), binary black holes (BBH) and binary neutron star-black hole systems, but we have chosen the BNS and BBH systems to be slightly asymmetric, (1.38, 1.42)$M_\odot$ and (9.5, 10.5) $M_\odot$ but NS-BH is chosen to be the conventional (10, 1.4) $M_\odot$ system.

To this we have added another binary with component masses (4.8, 5.2) which lies on the border line between where most PN families are similar to one another and where they begin to differ.

We compute overlaps maximized over a template bank between seven different models (TaylorT1, TaylorT2, TaylorT3, TaylorT4, TaylorF2, TaylorEt, EOB), each at three different PN orders (v^4, v^6, v^7). The results will be presented in the form of a set of Figures. For each mass pair there will be one Figure consisting of 9 panels (one panel for each PN order), each panel containing seven curves (one each for each template family at that order) and each curve with 21 data points corresponding to signals from the seven PN families at each three different PN orders, 2PN, 3PN and 3.5PN.

3.6 Results of the effectualness of PN templates

We will present the results of our investigation in two complementary ways. We will first discuss the effectualness of the different PN families with each other. Such an analysis will help us understand how "close" the various families of PN approximants are at different PN orders in regard to the construction of *detection* templates. We then go on to look at the effectualness of the different approximants with the EOB signal that contains not only the inspiral but also the merger and ringdown parts. The goal of the latter analysis is to identify the region in the parameter space where one can safely use any PN approximant template in a search, without worrying about the loss in signal-to-noise ratio that might arise due to our

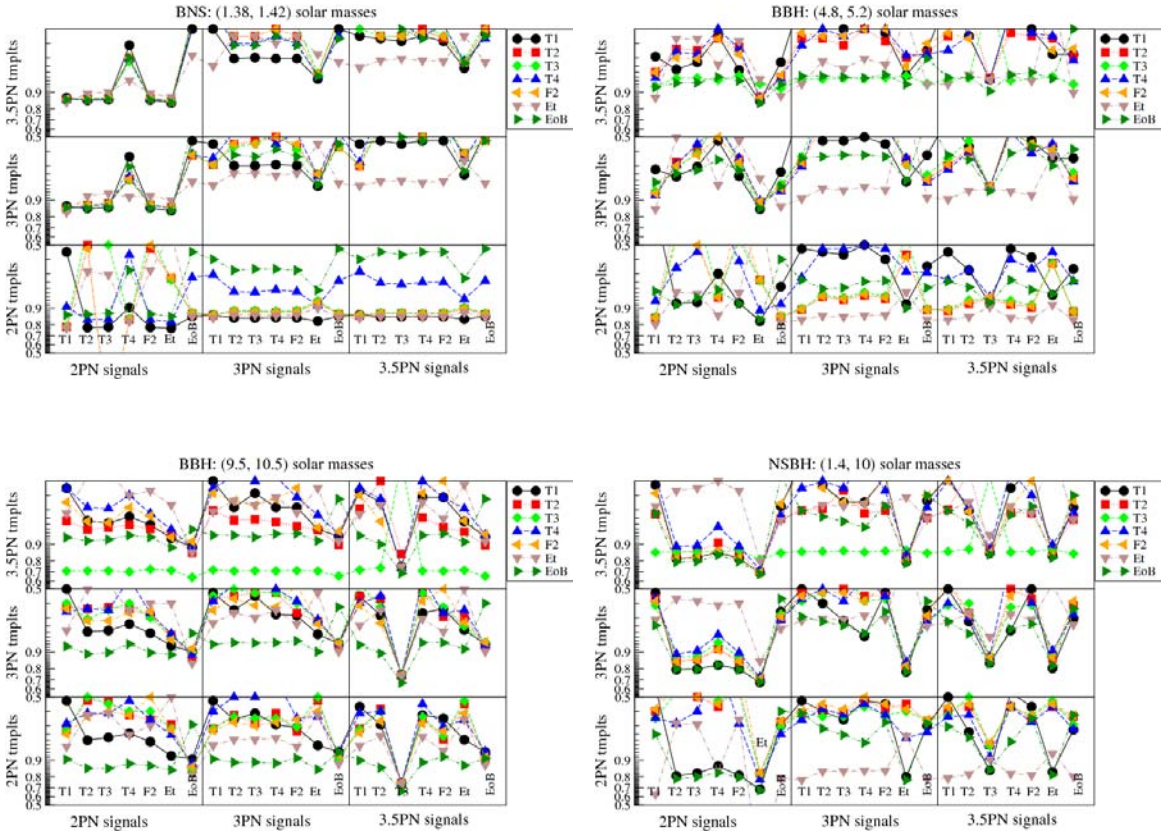

Figure 3.3: The plot shows the effectualness of templates and signals of different post-Newtonian familes and orders for four different binary systems for Initial LIGO. For a template from a given PN approximation (indicated by different line styles and symbols) and order (top panel 3.5PN, middle panel 3PN and bottom panel 2PN) we compute the effectualness of each of the templates with signals from each of the seven families, TaylorT1 (T1), TaylorT2 (T2), TaylorT3 (T3), TaylorT4 (T4), TaylorF2 (F2), TaylorEt (Et) and Effective-One-Body (EOB), at 2PN, 3PN and 3.5PN orders. For instance, solid lines with filled circles give the effectualness of TaylorT1 templates at 3.5PN (top panel), 3PN (middle panel) and 2PN(bottom panel) PN orders, with signals that belong to different PN approximations and orders. In clockwise order the panels from top left correspond to binaries consisting of two neutron stars, with masses 1.38 $M_\odot$ and 1.42 $M_\odot$, two black holes with masses 4.8 $M_\odot$ and 5.2 $M_\odot$, two black holes with masses 9.5 $M_\odot$ and 10.5 $M_\odot$ and, finally, a neutron star and a black hole binary with component masses 1.4 $M_\odot$ and 10 $M_\odot$.

lack of knowledge of the real signal, but without expending undue computational resources. Outside this region, however, one must use template families that are calibrated to waveforms obtained from numerical relativity simulations.

3.6.1 Mutual effectualness of various PN Inspiral template banks

The effectualness of the different PN families with each other is shown in Figs. 3.3 (Initial LIGO) and 3.4 (Advanced LIGO) for four different systems with component masses as indicated at the top of each sub-figure. In each sub-figure, the top panels correspond to the effectualness of different template families at 3.5PN order, middle panels to 3PN order and bottom panels to 2PN order. For each template family considered we find their overlap with signals from different PN orders (as indicated along the x-axis) and approximants (as indicated by the text T1, T2, etc.). Each symbol corresponds to the overlap obtained by a different template family: (black) circles to TaylorT1, (red) squares to TaylorT2, etc., with signals from different PN families. Note that we have used the *logit scale*[10] for the vertical axis. This is so that (minor) disagreements between the different approximants are made clearly visible. Note that since we are considering systems with low total mass, say $\leq 20M_{\odot}$, in this section we use the EOB model terminated at the EOB light ring, that is we do not include the merger and ringdown parts.

Conventionally, one says that two approximants A and B are in close agree-

[10]Recall $\mathrm{logit}(p) = \log\left(\frac{p}{1-p}\right)$.

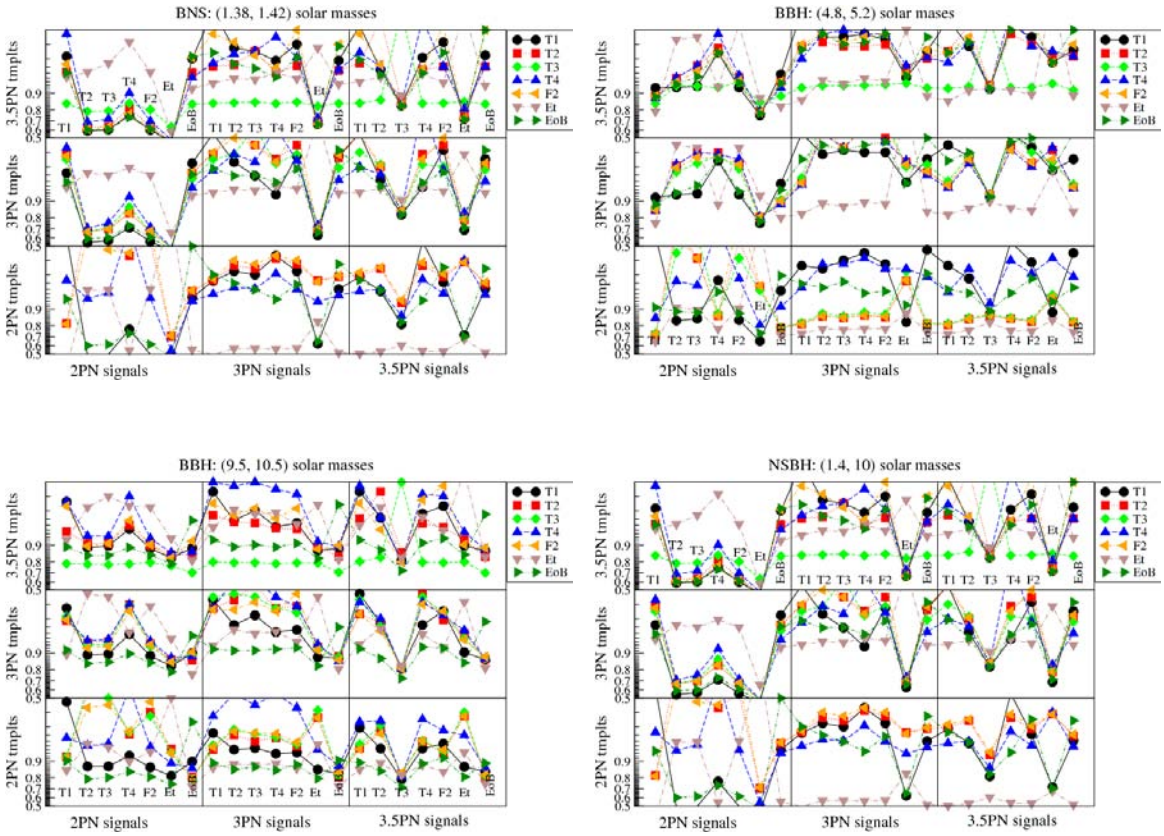

Figure 3.4: Same as Fig. 3.3 but for Advanced LIGO.

ment with each other if their mutual effectualness ϵ_{AB} is 0.965 or greater [30]. Though we shall mildly relax this target a bit to 0.95 for ease of presentation, we shall also indicate in Sec. 3.7, the region of the parameter space where the effectualness is better than 0.965, but we shall also quote regions where the effectualness drops to a low value of 0.9. The latter should be helpful for data analysis pipelines that employ a multi-stage hierarchical search, the first stage of which deploys a coarse grid of templates.

These figures reveal many different aspects of the (dis)agreements between the different approximants at PN orders 2PN, 3PN and 3.5PN and we shall principally highlight in our discussion the "diagonal" behaviour, i.e. overlaps of each template family with a signal family from the same PN order. Focusing first on the Initial LIGO results (Fig. 3.3), we see the evidence for the clustering of the various approximants at 3PN and 3.5PN orders for systems with a smaller total mass. In the case of BNS with component masses $(1.38, 1.42)\,M_\odot$, 2PN "diagonal" overlaps are dispersed between 0.74 to 1, 3PN and 3.5PN overlaps are all above 0.95, with TaylorEt having the smallest overlaps.

In the case of BBH with component masses $(4.8, 5.2)\,M_\odot$, 2PN overlaps are between 0.8 and 1, 3PN overlaps are all greater than 0.95 except TaylorEt, 3.5PN overlaps are greater than 0.95 for all except TaylorEt, TaylorT3 and EOB. There are several important points to note: As discussed in Sec. 3.4, TaylorT3 terminates somewhat prematurely before reaching the last stable orbit. Therefore, one expects to have poorer overlaps for all templates if TaylorT3 signal terminates in band, which will be the case for systems with a total mass greater than about $10\,M_\odot$.

The asymmetry in the overlaps mentioned in Sec. 3.5.1 is apparent in the case of TaylorEt: The overlaps of all templates with TaylorEt signal is greater than the converse, namely the overlaps of the TaylorEt templates with other signals. The smaller overlaps of the EOB templates (terminated at the light ring) is not surprising given the very different termination frequencies of the two families and the fact that the EOB waveform has power in the band beyond the last stable orbit.

In the case of NS-BH with component masses (1.4, 10) $M_\odot$, 2PN "diagonal" overlaps are distributed between 0.6 and 1, 3PN and 3.5PN overlaps are consistently above 0.95 except for TaylorEt signals (both orders) and TaylorT3 (at 3.5PN).

In the case of BBH with component masses (9.5, 10.5) $M_\odot$, there is no agreement between approximants irrespective of the PN order. In this sense, one cannot trust using any particular approximant as a search template.

Let us now turn to Fig. 3.4 which depicts the results for Advanced LIGO noise power spectral density. In the case of BNS with component masses (1.38, 1.42) $M_\odot$, the 2PN "diagonal" overlaps are between 0.4 and 1 (note that some of the data points are below the scale of 0.5 that we employ). The 3PN (except TaylorEt signal) and 3.5PN (except TaylorT3 template and TaylorT3 and TaylorEt signals) overlaps are uniformly larger than 0.95. The effectualness of all templates with TaylorEt signal is generally smaller (0.6-0.8) than the effectualness with a TaylorEt template. In the case of BBH with component masses (4.8, 5.2) $M_\odot$, the 2PN overlaps could be as small as 0.65. At 3PN, all approximants (except TaylorEt templates) and 3.5PN (except TaylorEt and TaylorT3 templates) the overlaps are 0.95 or greater. In the case of NS-BH with component masses (1.4, 10) $M_\odot$, the 2PN overlaps are as low

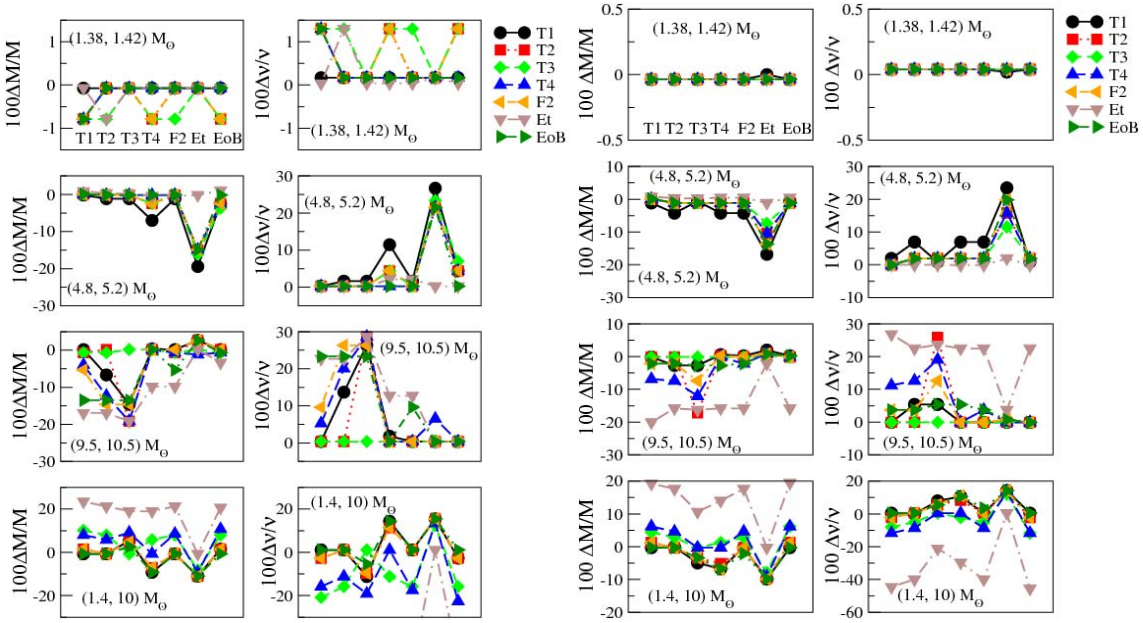

Figure 3.5: Percentage bias in the estimation of the total mass M and symmetric mass ratio ν at 3.5PN order. Left two columns are for Initial LIGO and the right two for Advanced LIGO. The bias $\Delta M/M$ is defined as $\Delta M = (1 - M_{\rm Tmplt}/M_{\rm Sgnl})$, where $M_{\rm Sgnl}$ and $M_{\rm Tmplt}$ denote the total mass corresponding to the signal and the template that obtained the maximum effectualness, respectively (and similarly for ν). What is plotted is percentage bias. The bias arises because the template family (as indicated in the key) is different from that of the signal family (as indicated in the top left panel as T1, T2, etc.).

as 0.4. At 3PN and 3.5PN, the overlaps are larger than 0.95 except in the case of TaylorEt signals (3PN, 3.5PN) and TaylorT3 templates (3.5PN). In the case of BBH with component masses (9.5, 10.5) $M_\odot$, the 2PN overlap could be as low as 0.7. The overlaps are larger than 0.95 at 3PN except in the case of EOB templates and TaylorEt and EOB signals. Finally, at 3.5PN order the different approximants are seen not to agree with each other very well. The cause of these features is the same as our discussion for Initial LIGO.

We conclude with some brief remarks on the "non-diagonal" cases displayed in the two figures. The asymmetric roles of signal and template arising from the

maximisation is obvious from the different panels. From the panels for 2PN signals and 3PN (3.5PN) templates for systems involving neutron stars it is interesting to see that higher PN order approximant templates do not necessarily lead to higher effectualness. One can also read off whether 3PN templates are as effective as the 3.5PN templates for various systems and various detectors. The figures condense a variety of such insights and may be useful to look at specific issues when required.

3.6.2 Discussion

In the case of binary neutron stars, the merger occurs far outside the sensitive band of the detector and even the late stages of inspiral is out of band. Binary neutron stars will very much be in the adiabatic regime as the signal sweeps through the band and a good test of the PN approximation is to ask how well the different waveforms agree with one another in this regime. The finite bandwidth of the detector essentially probes this regime for binary neutron stars. Note that the effectualness amongst different PN families at 2PN order is pretty poor but greater than 0.95 (with the exceptions discussed earlier) at 3PN and 3.5PN orders. In the case of Advanced LIGO (cf. Fig. 3.4), the lower frequency cutoff used in computing the overlap integrals is 20 Hz and a binary neutron star spends more than 750 cycles in band. Effectualness of 0.95 or greater means that the waveforms remain in phase over the entire duration of the signal. Of course, in reality the parameters of the signal and the template are not the same, but even so this is a remarkable success of the PN scheme.

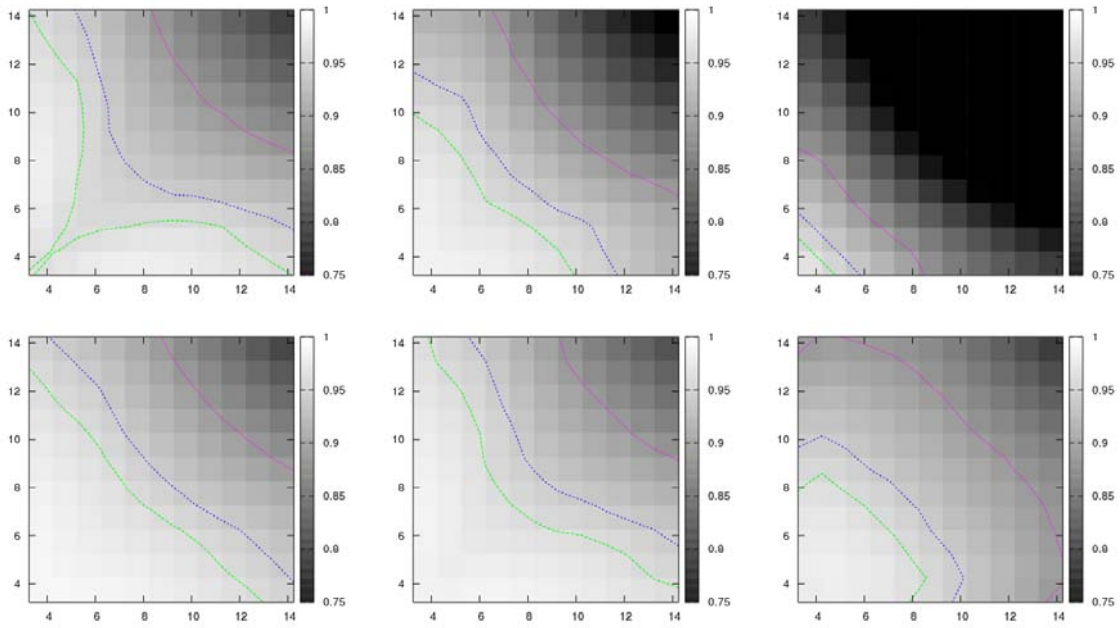

Figure 3.6: Overlaps of different 3.5PN approximants with the EOB inspiral-merger-ringdown signal in Initial LIGO in the $(m_1 - m_2)M_\odot$ plane. The approximants considered from left-to-right are TaylorT1, TaylorT2, TaylorT3 (top panels), and TaylorT4, TaylorF2, TaylorEt (bottom panels). The contours correspond to overlaps of 0.75, 0.9, 0.95 and 0.965.

For a BBH system with masses (4.8, 5.2) $M_\odot$, we see that 2PN and 3PN order templates are qualitatively similar to the binary neutron star case. However, we can see a marked deterioration of the effectualness at 3.5PN order. For a system of total mass of $10\,M_\odot$, the Schwarzschild LSO occurs at $\sim$ 440 Hz and the detector is sensitive to the late stages of the inspiral phase. It is not entirely surprising, therefore, that different PN orders do not agree with each other to the same extent as in the binary neutron star case. However, note that, with the exception of TaylorT3, which terminates at a frequency somewhat lower than others, and TaylorEt, all other templates have effectualness of 0.95 or better with each other. Among approximants that agree with each other, EOB has the smallest effectualness. This is because the latter model contains the plunge phase of the coalescence with ending frequencies

far higher than the LSO while other approximants do not have the plunge phase.

The LSO of a BBH with component masses (9.5, 10.5) $M_\odot$, is at $\sim$ 220 Hz and the plunge phase spans 220 Hz to about 600 Hz. Therefore, the detector is pretty sensitive to the late phases of the coalescence. We see deterioration of the effectualness, both at 3PN and 3.5PN orders. Apart from TaylorT3, whose poor overlaps at 3.5PN are explained by the early termination of the signal, the EOB stands out by achieving overlaps as low as 0.92 with other families.

As a final example, the effectualness of templates for a signal from a neutron star-black hole binary of masses (1.4, 10) $M_\odot$, we see that the different PN families, including the EOB, are in good agreement with each other, with the sole exception of TaylorEt. In fact, the closeness amongst different families seems to be somewhat better than the BBH system of component masses (9.5, 10.5) $M_\odot$.

At this juncture, it is worth pointing out that our numerical results for effectualness in the subset of cases where TaylorEt is chosen as the signal model, are consistent with those in Ref. [158], which investigated the *fitting factors* to ascertain if 3.5PN TaylorEt *signals* could be effectually and faithfully searched by TaylorT1, TaylorT4 and TaylorF2 templates. There is agreement too on the general features of our results with regard to systematic biases, the dependence on the total mass and qualitative factors underlying them. However, this agreement of numerical results for faithfulness and effectualness in no way extends to the general motivation and claims regarding the TaylorEt approximants [35, 158, 37] and, hence, are worth clarifying.

Indeed, there is no basis to refer to the x-based orbital phasing equation

Eq. (3.5a) as Newtonian [37], since the ω here is nPN accurate (depending on the PN-generation order one is working at) and *implicitly* incorporates conservative contributions to GW phase evolution at various PN orders. It is incorrect to claim [158] that conservative contributions to the GW phase evolution do not appear in the standard approximants, or that the TaylorEt-based scheme treats conservative and radiation-reaction contributions more equitably than the standard x-based approximants. It is misleading [158] to refer to *only* TaylorEt-based approximants as "fully gauge invariant in contrast to EOB" (especially in the circular orbit case). All x-based schemes are also fully gauge invariant. Finally, one may work in specific convenient coordinate systems as do EOB and numerical relativity simulations, as long as one deals with and compares gauge invariant quantities at the end.

In our view, the very different behaviour of the TaylorEt approximant relative to the standard x-based approximants may be traced to the manner in which the orbital phasing is "packaged" in the two schemes. In the x-based schemes the orbital phasing is implicitly in a resummed form, since the phasing is written in an appropriate PN-accurate angular velocity $\omega_{n\mathrm{PN}}$ ($n = 2, 3$ for 2PN, 3PN templates). On the other hand, the representation in terms of ζ, relative to the x schemes, is a re-expanded form. And indeed, based on the comparison between analytical schemes and numerical relativity simulations, the ζ schemes do relatively worse. The feature related to the monotonic-convergence of the TaylorEt scheme is of secondary importance in comparison to the main requirement of high phasing accuracy of an analytical model with numerical relativity simulations over all mass-ratios.

A few general comments are in order before we conclude this Section. We

do not believe that at present there are convincing theoretical reasons to consider any one particular PN family of inspiral models to be a privileged signal model. Consequently, the best that one can do is to examine the mutual closeness of these various inspiral models, as we have done, and work at the PN order where these various template families display the greatest agreement. It is precisely in this regard that the viewpoint we present here differs from those in [35, 158, 37] which assumes primacy for one specific approximant, namely the TaylorEt approximant, based on theoretical motivations that at present do not appear to be fundamental or compelling. Consequently, though there is no difference in the numerical results in the subset of cases that are common in our investigations, there is a big difference in the conclusions that we believe can be inferred. For instance, before one can legitimately decide on the inability of standard template banks in the gravitational data pipeline to detect signals from binaries with eccentricity [37], it is necessary to first fold in the differences in the simpler quasi-circular case arising on account of different parametrizations. Similar considerations should be borne in mind when dealing with analogous problems in the spinning case.

Based on the analysis presented heretofore, we conclude that the mutual effectualness of different families of PN approximants are close to each other (i.e. more strongly clustered) at 3PN and 3.5PN orders[11], as long as the total mass is less than about $12\,M_\odot$ (with the exceptions discussed in the previous Section).

[11] We find that the overlaps of the full EOB model obtained with the Virgo design PSD are very similar to those obtained for Advanced LIGO PSD for all Taylor models. The only differences are in the case of the EOB model cutoff at light ring where overlaps obtained with the Virgo PSD are smaller by a few percent. Needless to add, that the situation for a space detector like LISA can be expected to be even more different and interesting to study.

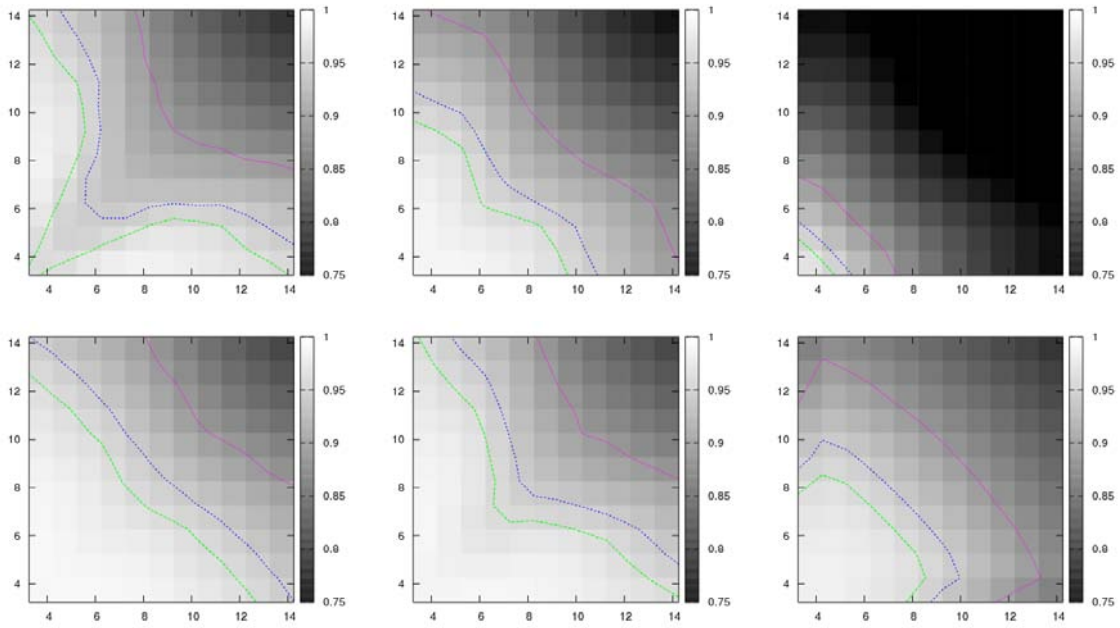

Figure 3.7: Same as Fig. 3.6 except that the noise spectral density is that of Advanced LIGO. The contours correspond to overlaps of 0.9, 0.95 and 0.965.

For heavier binaries, the approximants begin to differ considerably, and this is almost entirely because the adiabatic approximation begins to breakdown and the plunge and the merger phases become more and more important. Hence, in the next Section we will supplement the present analysis by looking more precisely into the overlaps of the different PN templates with a prototype of the more complete signal model, namely the EOB model, including the merger and ringdown parts.

3.6.3 Biases in the estimation of parameters

Recall that, in the computation of the effectualness one maximizes the scalar product of a (normalized) signal with a template over the parameters of the template keeping those of the signal fixed. Therefore, one can get an idea of how dissimilar the parameters of an approximant need to be in order to match a given signal.

This is a systematic effect that leads to a bias in the estimation of parameters if the template approximant is not the same as the signal approximant. Let the total mass of the signal and template waveforms be, respectively, $M_{\rm Sgnl}$ and $M_{\rm Tmplt}$, when the scalar product is maximized. The percentage bias ΔM in the total mass is defined as $\Delta M = 100(1 - M_{\rm Tmplt}/M_{\rm Sgnl})$, and similarly for the symmetric mass ratio ν.

For a given binary, the biases are qualitatively similar for Initial and Advanced LIGO noise power spectral densities. In general, the biases are appreciably smaller at 3PN and 3.5PN orders than at 2PN order and progressively increase with the total mass, although they are far larger than the statistical errors computed using the Fisher information matrix [138]. Figs. 3.5 plots the percentage biases in the total mass M and symmetric mass ratio ν at 3.5PN order. The left two (right two) columns use the Initial LIGO (Advanced LIGO) noise spectral density. For the four systems considered, namely $(1.38\,,1.42)\,M_\odot$, $(4.5\,,5.2)\,M_\odot$, $(1.4\,,10)\,M_\odot$, and $(9.5\,,10.5)\,M_\odot$ binaries, the largest bias in the total mass M is 1%, 20%, 20% and 20%, respectively, and the symmetric mass ratio ν is 1%, 25%, 70% and 25%, respectively.

3.7 Results of the effectualness of PN templates with the full waveform

Having established the mutual closeness of the different families of PN approximants at 3PN and 3.5PN orders (for determining effectual templates for detection) in the regime where the approximation is expected to be valid, let us now examine

the region in the parameter space where PN families can be used as search templates. To achieve this goal we will use the EOB model calibrated to numerical relativity simulations [54]. For brevity, we have omitted plots of the effectualness of the 3PN approximants with this EOB model; they are quite similar to the 3.5PN plots.

Although Ref. [54] explored the agreement between the EOB model and numerical simulations for several modes, in this study we will work with only the dominant harmonic (i.e., the h_{22} mode) at leading PN order. Higher-order amplitude corrections are known to be important for parameter estimation [166, 167] and a future study must repeat this investigation with the full waveforms.

Fig. 3.6 shows the effectualness of the six PN families TaylorT1, TaylorT2, TaylorT3 (top panels, respectively from left to right), TaylorT4, TaylorF2, and TaylorEt (bottom panels, respectively from left to right) for Initial LIGO noise power spectral density. Fig. 3.7 shows the same but for Advanced LIGO noise power spectral density. The effectualness was computed using a hexagonal template bank [179] and is shown as a gray-scale map in the space of the component masses that are taken to vary from $3\,M_\odot$ to $14.5\,M_\odot$. For all the maps we have chosen the gray-scale to vary from 0.76 to 1. The dotted contours show effectualness at three values: 0.965, 0.95 and 0.90.

The trends of the overlaps is rather similar irrespective of which noise power spectral density we use, although the actual overlaps are systematically smaller in the case of Advanced LIGO as compared to Initial LIGO. This is due to the broader frequency sensitivity of the former in relation to the latter. The following discussion

is, therefore, applicable in both cases.

Let us first note some peculiarities. TaylorT3 at 3.5PN leads to particularly ineffectual templates. As mentioned before, TaylorT3 at 3.5PN terminates rather prematurely. The LSO defined by the Schwarzschild potential is at $f_{\rm LSO} \sim (440/10\,M_\odot)\,$Hz, but TaylorT3 at 3.5PN approximants terminate at $\sim (220/10\,M_\odot)\,$Hz. This discrepancy is so large that even with the biases in the component masses allowed in the computation of the effectualness (recall that we maximize the overlap over template masses), which, in principle, makes it possible for a template of a lower mass to match a signal of a higher mass, TaylorT3 is unable to achieve good overlaps. This is because a mismatch in the component masses can make a template more, or less, asymmetric than the signal, which has the effect of increasing, or decreasing, the duration of the template relative to the signal. While small differences in the ending frequencies can be achieved by a mismatch in the total mass without affecting the signal duration too greatly, large differences cannot be compensated by such a mismatch in the parameters.

At 3PN and 3.5PN the effectualness of TaylorEt with a EOB signal for a binary of component masses $(3,\,10)\,M_\odot$ [respectively, $(10,\,10)\,M_\odot$] is 0.83 and 0.90 [respectively, 0.87 and 0.89]. This is because amongst all PN approximants TaylorEt seems to converge far slower than any other. Further, an examination of the coefficients in the PN terms of the phasing formulas in Eqs. (3.13) indicates that higher order PN terms have increasingly greater coefficients. In general, it has been observed that the appearance of such larger coefficients in higher order terms of an approximant scheme inevitably worsens its convergence and the present instance

may be no exception to this case[12].

A final observation: some of the models, TaylorT1 in particular, have lower overlaps along the $m_1 = m_2$ or $\nu = 1/4$ line. A similar feature has been observed in other cases in the past [147] and can be traced to more limited possibilities in maximisation over ν in the equal mass case. For unequal mass systems one can explore template ν values both *smaller and larger* than the signal ν values. Certain template families might agree better with the "exact" signal only for template ν values larger than the signal ν value. However, for equal mass configurations we are already on the boundary $\nu = 1/4$ and if we are constrained to only physical values of template ν, one can only admit values of ν *smaller* than 1/4.

With the exception of the peculiarities noted above, we see that all approximants do progressively better at higher PN orders. Conclusions drawn in the previous Section with regard to the mutual closeness of the different families of PN approximants are further corroborated here where we have measured the overlaps with a signal that is matched to numerical relativity simulation, which can, therefore, be taken to be close to what a real signal might be.

Computationally, TaylorF2, with its phasing formulas given explicitly in the Fourier domain, is the least expensive. This is because matched filtering is most easily carried out in the Fourier domain, which means that a time-domain approximant must be Fourier transformed before computing the cross correlation. By employing TaylorF2 models one can avoid one forward Fourier transform. Moreover, TaylorF2

[12]While comparing the coefficients it may be useful to note that $v \simeq 1/\sqrt{6}$ corresponds to ζ in the range of 0.136-0.138 depending on the symmetric mass ratio ν and the PN order.

offers the flexibility in the choice of the ending frequency. Unlike the time-domain models, which have either a natural ending frequency defined by the extremum of the binding energy or the frequency evolution stops before reaching LSO, TaylorF2 has no such restriction. In fact, as obtained in Refs. [147, 148], by extending the upper cutoff beyond the usual upper cutoff (i.e., the Schwarzschild LSO), the TaylorF2 model matches remarkably well with numerical relativity waveforms for a far greater range of masses. However, as noted in Ref. [148] the ending frequency that must be employed in order to achieve the best match with numerical-relativity waveforms depends on the noise power spectral density. This could turn out to be an unnecessary computational burden in a data analysis pipeline. The alternative is to choose the upper frequency cutoff as an additional search parameter or allow unphysical values of $\nu > 0.25$ [147, 158, 148] or to include a p4PN term in the template phase and calibrate it to numerical simulations [147]. The first two choices would result in an unwarranted increase in the computational cost of a search as also in the false alarm rate, and we advice against it. The third choice could be pursued, but it should be augmented by a more complete description of the merger/ringdown signal — for example by introducing a slope break in the waveform amplitude and a superposition of Lorentzians [147, 105]

If a search requires the minimal match to be much smaller than 0.95 (as, for example, in a hierarchical search) one can extend a search with TaylorF2 to a total mass of $20\,M_\odot$ with effectualness of 0.90.

Before advanced detectors begin to operate, there will be a period when LIGO and Virgo will operate with sensitivities slightly larger than, but bandwidths similar

to initial detectors – the so-called Enhanced LIGO and Virgo+. Since Virgo and Virgo+ are expected to have a sensitivity bandwidth similar to Advanced LIGO the results presented in this paper are qualitatively similar to in those cases too. Moreover, as our results are only sensitive to the bandwidth, conclusions drawn by using the noise spectral density of Initial LIGO will also be valid for Enhanced LIGO.

All approximants (no exceptions) achieve an effectualness of 0.95 or better at 3PN and 3.5PN orders, for binaries whose total mass is less than about $\sim 12\,M_{\odot}$. From the view point of effectualness alone, we conclude that searches for binary black holes, in Initial, Enhanced and Advanced LIGO, could employ any of the 3PN or 3.5PN families as long as the total mass is smaller than about $\sim 12\,M_{\odot}$. The final choice of the PN family should be based on other criteria. If it is desired that the minimal match of a template bank is 0.965 or greater, then the best strategy would be to use the full EOB waveform calibrated to numerical relativity.

Another criteria to be considered is the computational cost. A typical matched filter search in LIGO data must compute thousands of template signals for every 2048 second data segment. This can be a heavy burden if it takes a significant amount of time to compute each template. The EOB templates are computed in the time domain by solving a set of differential equations, and the frequency domain signal is then computed via Fourier transform. For low-mass systems this cost can become significant and will of course vary depending on the implementation and hardware used.

We have estimated the cost to compute TaylorF2 and EOB templates using

their implementation in the LAL code used for matched filtering searches in LIGO data. We find that for a total mass $\geq 40\,M_\odot$, the EOB templates take a factor of 2 longer to generate than the same TaylorF2 signals. For a (10, 10) $M_\odot$, (5, 5) $M_\odot$ and (1.4, 1.4) $M_\odot$ binary, the EOB templates take about a factor of 3, 7 and 20, longer to generate, respectively. We tested the waveform generation on a high performance computer with 32 2.7 GHz CPUs and 132 GB of RAM. On this system, EOB templates with a total mass $\geq 40\,M_\odot$ can be generated in about 0.1s, while the (10, 10) $M_\odot$ EOB template could be generated in about 0.5s. Since LIGO searches employ thousands of CPUs, this is feasible. However, for lower mass signals, the time needed grows rather quickly and about 4s are needed to compute the (1.4, 1.4) $M_\odot$ EOB template. It may be possible to reduce the computational cost somewhat by optimizing the EOB waveform generation code, but the lowest mass templates would almost certainly still have a significant computational cost. Thus, the increased computational cost must be weighed against the benefit of increased effectualness for lower mass signals.

3.8 **Faithfulness**

For completeness, we also report on the faithfulness of the different PN approximants with respect to one another. The faithfulness is the overlap between normalized template and signal approximants when maximizing only over the time and phase at coalescence, t_C and ϕ_C. In Tables 3.2 and 3.3, we list the faithfulness for each pair of PN approximants at their highest PN order, that is 3.5PN order,

Table 3.2: Faithfulness of different approximants for $(1.42, 1.38)\,M_\odot$ (top panel) and $(5.2, 4.8)\,M_\odot$ (bottom panel) binaries. The rows label template approximant, while the columns label signal approximant. For each pair, the top number is Initial LIGO while the bottom number is Advanced LIGO. All approximants are at 3.5PN order, except our EOB model which has a p4PN coefficient.

	EOB	T1	T2	T3	T4	Et	F2
EOB	1	.969	.994	.997	.990	.970	.994
	1	.971	.996	.998	.991	.974	.996
T1	.969	1	.982	.981	.987	.928	.982
	.971	1	.984	.983	.990	.920	.984
T2	.994	.982	1	.998	.999	.958	1.00
	.996	.984	1	.999	.999	.961	1.00
T3	.997	.981	.998	1	.997	.959	.998
	.998	.983	.999	1	.998	.961	.999
T4	.990	.987	.999	.997	1	.950	.999
	.991	.990	.999	.998	1	.949	.999
Et	.970	.928	.958	.959	.950	1	.958
	.974	.920	.961	.961	.949	1	.961
F2	.994	.982	1.000	.998	.999	.958	1
	.996	.984	1.000	.999	.999	.961	1

	EOB	T1	T2	T3	T4	Et	F2
EOB	1	.916	.974	.938	.981	.888	.970
	1	.877	.973	.928	.978	.841	.968
T1	.916	1	.974	.926	.964	.784	.975
	.877	1	.955	.892	.947	.653	.957
T2	.974	.974	1	.949	.993	.861	.993
	.973	.955	1	.932	.994	.775	.995
T3	.938	.926	.949	1	.943	.925	.944
	.928	.892	.932	1	.926	.876	.930
T4	.981	.963	.993	.943	1	.854	.995
	.978	.947	.994	.926	1	.766	.996
Et	.888	.785	.861	.925	.854	1	.852
	.841	.653	.775	.876	.767	1	.770
F2	.970	.975	.993	.944	.995	.853	1
	.968	.957	.995	.930	.996	.770	1

except for the EOB model which uses a p4PN order coefficient, for both Initial and Advanced LIGO and for each of our reference binaries.

In the first row and column of the left panel of Table 3.2, notice that every approximant has an overlap of at least 0.97 with the EOB model for both Initial and Advanced LIGO. That all approximants have good agreement for a low mass binary without searching over mass parameters is further evidence that the 3.5PN approximants are rather close to one another during the adiabatic inspiral. Note that the T2, T3, T4 and F2 approximants all have a faithfulness ≥ 0.99 with the EOB model, while the T1 and Et approximants have somewhat worse agreement at about 0.97. For each pair, the faithfulness for Initial and Advanced LIGO are quite similar for these low mass binaries.

In the right panel of Table 3.2, we increase the total mass to $10M_{\odot}$ while keeping the mass ratio nearly equal. The faithfulness drops for every pair of approximants as the merger begins to enter the sensitive band. Recall that for these masses, all pairs of approximants can achieve an effectualness of at least 0.95 by searching over the mass parameters. When we fix the masses, the T2, T4 and F2 approximants still have very good agreement with the EOB model, with faithfulness of $0.97 - 0.98$. The EOB-T3 faithfulness has degraded somewhat to $0.93 - 0.94$, and the Et and T1 approximants have rather poor agreement with the EOB model with faithfulness in the range $0.84 - 0.92$. Note that the faithfulness is typically lower for Advanced LIGO than for Initial LIGO. We attribute this to the signals having a longer duration (and thus more time to accumulate a phase difference) in Advanced LIGO's wider sensitivity band.

In the left panel of Table 3.3, we increase the total mass to $20M_{\odot}$ while again keeping the mass ratio nearly equal. Once again, the faithfulness drops for all cases as the merger and ringdown become more important. The T4 and F2 approximants have the best agreement with EOB, they are the only approximants to achieve an overlap greater than 0.9 with EOB. The overlap between T3 and EOB has dropped dramatically to 0.65 and 0.72 for Initial and Advanced LIGO respectively.

The right panel of Table 3.3 gives the faithfulness for each approximant pair for an asymmetric $(10,\ 1.4)\,M_{\odot}$ binary. The EOB-F2 faithfulness is very good at 0.99. The T1 and T2 approximants also have good agreement with the EOB model with faithfulness $0.96 - 0.98$. The T3 and T4 have poor agreement with the EOB model with faithfulness $0.80 - 0.86$. For this mass pair, the Et approximant has very poor agreement with all of the others, the faithfulness is ≤ 0.60 for every approximant except T3.

We see a clear trend of decreasing faithfulness as the total mass of the binary increases. This is due to the late inspiral, merger and ringdown moving into the sensitive band and becoming more important for higher mass binaries. The faithfulness is typically lower for Advanced LIGO than Initial LIGO due to its broader sensitive band. The faithfulness can vary with mass ratio. For example, for the $(10,\ 1.4)\,M_{\odot}$ binary, the T1 and T2 approximants have a better faithfulness with the EOB model than the T4 approximant. However, for the nearly equal mass binaries, the T4 approximant has the greater faithfulness with the EOB model. The TaylorF2 approximant is generally the most faithful to the EOB aproximant, with one of the highest overlaps in each case. This is another argument for using Tay-

Table 3.3: Same as Table 3.2 but for $(10.5, 9.5)\,M_\odot$ (top panel) and $(10, 1.4)\,M_\odot$ (bottom panel) binaries.

	EOB	T1	T2	T3	T4	Et	F2
EOB	1	.877	.882	.650	.923	.860	.910
	1	.811	.864	.721	.910	.775	.889
T1	.877	1	.972	.712	.970	.817	.982
	.811	1	.955	.785	.943	.638	.966
T2	.882	.972	1	.742	.968	.886	.959
	.864	.955	1	.831	.969	.784	.959
T3	.650	.712	.742	1	.707	.716	.709
	.721	.785	.831	1	.794	.782	.790
T4	.923	.971	.968	.707	1	.906	.986
	.910	.943	.970	.794	1	.785	.988
Et	.859	.817	.886	.716	.906	1	.845
	.776	.639	.784	.783	.785	1	.707
F2	.909	.982	.959	.708	.985	.846	1
	.889	.967	.959	.790	.988	.706	1

	EOB	T1	T2	T3	T4	Et	F2
EOB	1	.977	.973	.817	.859	.526	.990
	1	.959	.972	.801	.797	.413	.993
T1	.977	1	.972	.796	.805	.508	.991
	.959	1	.954	.753	.691	.398	.978
T2	.973	.972	1	.835	.894	.543	.980
	.972	.954	1	.820	.834	.430	.976
T3	.817	.796	.835	1	.851	.778	.818
	.801	.753	.820	1	.841	.631	.798
T4	.859	.805	.894	.851	1	.595	.852
	.797	.691	.834	.841	1	.456	.779
Et	.526	.508	.543	.778	.595	1	.525
	.413	.398	.430	.631	.456	1	.411
F2	.990	.991	.980	.818	.852	.525	1
	.993	.978	.976	.799	.779	.411	1

lorF2 templates in the mass regime where EOB templates are too computationally expensive to be employed in a matched filtering search.

3.9 Conclusions

In this paper we have examined the mutual effectualness of the different families of PN approximants with the view to validating their closeness for use in the construction of search templates for compact binaries in Initial, Enhanced and Advanced LIGO. We considered seven different approximants, each at three different PN orders, a total of 21 waveforms in all. We computed the effectualness of each of the waveforms with every other at 2PN, 3PN and 3.5PN orders by using a template bank constructed with a minimal match of 0.99 and Initial and Advanced LIGO noise power spectral densities. Our results from a sample of four binaries show that different PN approximations are consistent with one another at 3PN and 3.5PN order. They begin to differ only when the mass becomes so large that the plunge phase, not contained in standard PN waveforms in the adiabatic approximation, enters the detector band.

The above conclusion is best summarized by Fig. 3.8, where we plot the effectualness of the various PN approximants (except for TaylorT3 and TaylorEt that we recommend be discarded, since we have shown that not only do they differ considerably from the others but importantly have poorer overlaps with EOBNR waveforms) with an EOB inspiral-merger-ringdown signal as a function of the total mass of the binary. These plots are convenient for identifying the $M_{\rm crit}$ above which

the PN approximants begin to differ with one another. We find that any of the above approximants could be used as detection templates with less than a 10% loss in event rate up to a total mass of $12\,M_\odot$ for both Initial and Advanced LIGO. Note that this value of $M_{\rm crit}$ is limited by the equal-mass case, as the value of $M_{\rm crit}$ corresponding to a 10% loss in event rate is somewhat greater for mass ratios of 4:1 and 10:1.4. We attribute this result to asymmetric binaries accumulating more signal at low frequencies than in the equal-mass case. Thus, for a fixed total mass, the merger and ringdown are less important for asymmetric binaries than for equal-mass binaries. Therefore, we conclude that we can safely use any of the above 3.5PN families as search templates to detect binaries whose total mass is less than about $12\,M_\odot$. However, purely from the point of view of computational burden TaylorF2 is the least expensive and we recommend that TaylorF2 at 3.5 PN order be deployed as search templates below a total mass of $12\,M_\odot$. It is quite remarkable to note that up to a total mass of $30M_\odot$, the *uncalibrated* EOB model at 3.5PN order is rather close to the calibrated EOB inspiral-merger-ringdown signal. In fact, Ref. [154] found a phase difference of *only* 0.05 rads after 30 GW cycles, at roughly 3 GW cycles before merger between the EOB at 3.5PN order and the highly accurate equal-mass numerical waveform of Caltech/Cornell collaboration.

For systems with total mass larger than about $12\,M_\odot$, TaylorF2 at 3.5PN might be effectual if the upper cutoff frequency is artificially extended to a higher frequency. However, this might require a tweaking of the upper frequency cutoff depending on the noise spectral density of the detector [148] and the mass ratio of the system, and either the extension to unphysical values of ν [147, 148] or the inclusion of

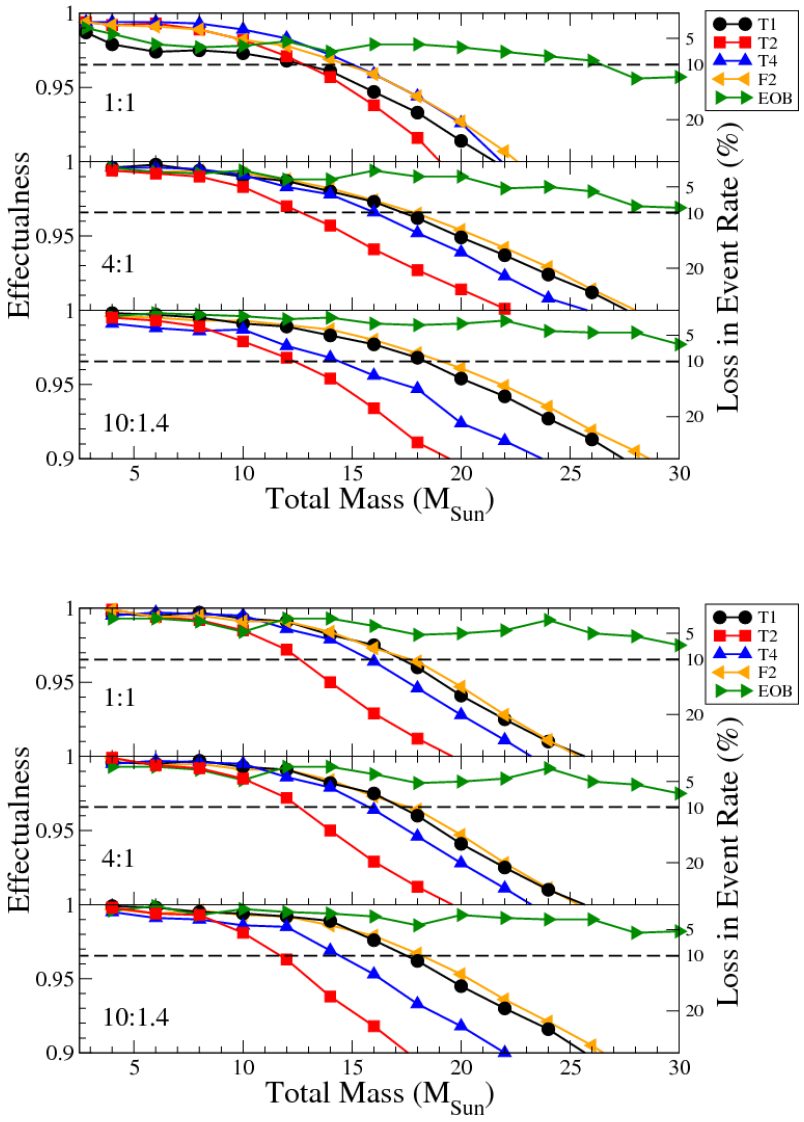

Figure 3.8: Effectualness (left y-axis) and the corresponding loss in event rate (right y-axis) of 3.5PN approximants with the EOB inspiral-merger-ringdown signal calibrated to numerical relativity in Initial LIGO (top panel) and Advanced LIGO (bottom panel) as a function of total mass for 1:1, 4:1 and 10:1.4 mass ratios. The EOB curve is the effectualness between the *uncalibrated* 3.5PN EOB model containing only the inspiral and the *calibrated* inspiral-merger-ringdown EOB signal. Note that any of these approximants are suitable for detection templates below a total mass of about $12\,M_\odot$ for both Initial LIGO and Advanced LIGO, provided a 10% loss of event rate is deemed acceptable.

a p4PN term in the template phase [147] calibrated to the numerical simulations. We believe that a better alternative for heavier systems are the EOB templates calibrated to numerical relativity simulations [149, 147, 150, 54, 151, 152, 153, 154, 155, 156]. The most recent EOB models are in near perfect agreement with the most accurate numerical simulations to date, although only a small number of systems corresponding to different mass ratios have been studied so far. Nevertheless, a physical model with physically meaningful parameters is a far safer bet as search templates unless, of course, if the model in question is not in agreement with the waveform predicted by numerical relativity. So far, the EOB is the best physical model we have and this is what we recommend be used to search for binaries with masses greater than about $12\,M_{\odot}$.

In this paper we adopted the preliminary, fiducial EOB model of Ref. [54], because it is the EOB model currently available in LAL and it is used for searches by Initial LIGO. For completeness, here we quantify the closeness between the EOB model used in this paper and a most recent improved version of the EOB model [156] (which is similar to the one of Ref. [155]). The latter was calibrated to longer and more accurate numerical waveforms generated by the Caltech/Cornell pseudo-spectral code [180]. Reference [156] found that the faithfulness of the improved EOB model to these highly accurate numerical waveforms is better than 0.999. In Table 3.4, we show both the faithfulness and the effectualness of the EOB model [54] to the improved EOB model [156] using noise spectral densities of Initial LIGO, as well as the bias in the parameters M and ν when achieving the effectualness. The search for effectualness in this test is done continuously in the parameter space, instead

Table 3.4: Effectualness and faithfulness of the EOB fiducial model [54] used in this paper (and currently employed by Initial LIGO) to the most recently improved EOB model [156]. We also show the bias in the parameters M and ν when achieving the effectualness. For each pair, the top number is Initial LIGO while the bottom number is Advanced LIGO. The sign of the bias is such that in all cases the fiducial EOB templates slightly overestimate the total mass M and underestimate the mass ratio ν of the improved EOB signal.

	Effectualness	$\Delta M/M$	$\Delta\nu/\nu$	Faithfulness
$(1.4, 1.4)M_\odot$	0.999	0.98%	-1.63%	0.992
	0.999	0.98%	-1.63%	0.995
$(1.38, 1.42)M_\odot$	0.999	0.96%	-1.60%	0.992
	0.999	0.89%	-1.49%	0.995
$(5, 5)M_\odot$	0.997	1.32%	-2.12%	0.973
	0.999	2.06%	-3.47%	0.976
$(4.8, 5.2)M_\odot$	0.999	2.42%	-4.08%	0.973
	0.999	2.11%	-3.54%	0.976
$(10, 10)M_\odot$	0.999	2.70%	-4.62%	0.974
	0.999	2.59%	-4.39%	0.962
$(9.5, 10.5)M_\odot$	0.998	1.40%	-1.94%	0.974
	0.997	2.67%	-4.54%	0.964
$(15, 15)M_\odot$	0.995	4.80%	-9.98%	0.987
	0.999	2.49%	-4.23%	0.973
$(25, 25)M_\odot$	0.995	4.95%	-12.6%	0.982
	0.994	3.00%	-5.56%	0.985

of using a template bank. Although there is some systematic trend in the numbers due to the difference in the EOB models, the main result is that the faithfulness and the effectualness are always better than 0.97 and 0.995, respectively. Assuming the numerical waveforms of Ref. [156] are exact, the EOB model of Ref. [54] used in this paper is accurate for detection purpose with a loss of event rates of $\sim 10\%$, and may cause $\sim 10\%$ bias in estimating the mass parameters.

In this study we considered PN waveforms in the so-called restricted PN ap-

proximation. Restricted waveforms contain only the second harmonic of the orbital frequency. Inclusion of other harmonics is necessary, especially when a binary is arbitrarily oriented with respect to a detector and the component masses are dissimilar. Recent studies [166, 167] have shown the tremendous advantage of including these other harmonics in the GW templates. Therefore, it is necessary that a future effort undertakes a study similar to this, but includes all the amplitude corrections. Furthermore, Ref. [157] has shown that by supplementing the PN results by the available test particle results up to 5.5PN improves the match between the EOB models and numerical relativity simulations. This can be expected to lead to further improvements in the results obtained here in the future.

Chapter 4

Higher-order spin effects in the amplitude and phase of gravitational waveforms emitted by inspiralling compact binaries: Ready-to-use gravitational waveforms

Authors: *K.G. Arun, Alessandra Buonanno, Guillaume Faye and Evan Ochsner*[1]

Abstract: We provide ready-to-use *time-domain* gravitational waveforms for spinning compact binaries with precession effects through 1.5PN order in amplitude and compute their mode decomposition using spin-weighted -2 spherical harmonics. In the presence of precession, the gravitational-wave modes (ℓ, m) contain harmonics originating from combinations of the orbital frequency and precession frequencies. We find that the gravitational radiation from binary systems with large mass asymmetry and large inclination angle can be distributed among several modes. For example, during the last stages of inspiral, for some maximally spinning configurations, the amplitude of the $(2,0)$ and $(2,1)$ modes can be comparable to the amplitude of the $(2,2)$ mode. If the mass ratio is not too extreme, the $\ell = 3$ and $\ell = 4$ modes are generally one or two orders of magnitude smaller than the $\ell = 2$ modes. Restricting ourselves to spinning, non-precessing compact binaries, we apply the stationary-phase approximation and derive the *frequency-domain* gravitational wave-

[1]Originally published as Phys. Rev. D **79** 104023 (2009)

forms including spin-orbit and spin(1)-spin(2) effects through 1.5PN and 2PN order respectively in amplitude, and 2.5PN order in phase. Since spin effects in the amplitude through 2PN order affect only the first and second harmonics of the orbital phase, they do not extend the mass reach of gravitational-wave detectors. However, they can interfere with other harmonics and lower or raise the signal-to-noise ratio depending on the spin orientation. These ready-to-use waveforms could be employed in the data-analysis of the spinning, inspiralling binaries as well as in comparison studies at the interface between analytical and numerical relativity.

4.1 Introduction

Coalescing compact binaries made of neutron stars and/or black holes can produce gravitational waves (GW) strong enough to be detected by ground-based interferometers, such as LIGO [181], Virgo [182] and GEO [183], operating in the frequency range 10–10^4 Hz. Moreover, supermassive BH binaries could be observed at lower frequencies 10^{-5}–10^{-1} Hz and up to cosmological distances by the proposed laser space-based antenna LISA [184]. For detection purposes, matched filtering is applied to noisy data in order to extract any signals that match members of the template bank [185, 186, 187].

Gravitational waves produced during the long inspiral phase can accurately be modeled by the post-Newtonian (PN) approximation to general relativity [188]. As the BHs approach each other and their velocities increase, the PN expansion is expected to become less and less reliable. Late in the evolution, non-perturbative information contained in NR simulations and PN-resummed methods [40], as well as perturbation theory need to be taken into account in building analytical templates for inspiral, merger, and ringdown. In this chapter we shall limit the discussion to the inspiral phase of coalescing BHs.

In constructing templates for detecting inspiralling signals, it is recommended to account for all physical effects which contribute significantly to the gravitational waveform. Those produced by the spins of the binary constituents are among the most important ones, especially for asymmetric compact binaries [189], such as NS-BH binaries [190], and BH-BH binaries with component masses $(m_1, m_2) \in$

$[5, 15]M_\odot \times [1, 5]M_\odot$. For detecting such systems, one may be able to employ phenomenological methods which capture the essential features of spinning, precessing waveforms [59]. However, parameter extraction [89, 90, 191] would warrant the inclusion of as much information about the spins of the binaries as possible, so that one should employ physical templates [192, 193, 78] at the highest PN order for this purpose.

For non-spinning compact binaries, the GW phase evolution has been computed through 3.5PN order [194, 195, 196, 24, 197] and the h_+ and $h_\times$ polarizations are available through 3PN order [198, 199, 200, 201, 27]. For spinning, precessing binaries, the GW phase evolution is known through 2.5PN order [85, 86] for spin-orbit couplings, and through 2PN order [202] for spin-spin couplings (spin(1)-spin(1) and spin(2)-spin(2) contributions have been obtained in Refs. [87, 88]). Spin-orbit and spin(1)-spin(2) effects in the h_+ and $h_\times$ polarizations were computed through 1.5PN and 2PN order, respectively, in Refs. [83, 84]. [2] More recently, the spin(1)-spin(2) contributions at 3PN order in the conservative two-body dynamics were found employing either effective-field theory techniques [204, 205, 206, 207] or the Hamiltonian formalism of Arnowitt, Deser and Misner [208, 209, 210]. Now, spin(1)-spin(1) and spin(2)-spin(2) effects at 3PN order in the conservative two-body dynamics are also available [211]. For including those higher-order spin effects in the GW phase evolution and polarizations, the results [211, 206, 207, 208, 210] need to be extended to the non-conservative dynamics, notably to the GW energy flux.

[2]Note that spin-orbit effects through 2PN order in the h_+ and $h_\times$ polarizations were calculated in Ref. [203]. However, Ref. [86] pointed out that a few multipole moments were computed incorrectly there.

The importance of using templates that have amplitude corrections beyond the leading PN order (henceforth referred to as Newtonian approximation [3]) was emphasized by different authors in the context of ground-based [212, 213, 214, 116] and space-based detectors [215, 216, 217, 218, 219, 220, 221], both for detection and parameter estimation. So far, the effect of spins and precession on parameter estimation was studied in Refs. [222, 223, 224, 191], but those studies were limited to non-spinning and Newtonian GW polarizations [198, 199, 200].

In this chapter we provide ready-to-use h_+ and $h_\times$ polarizations in time domain for spinning, precessing binaries through 1.5PN order. The actual computation of the gravitational waveform h_{ij} through 1.5PN order was done by Kidder [83], as well as Will and Wiseman [84], but the ready-to-use h_+ and $h_\times$ polarizations at 1.5PN order were only written explicitly for strictly circular orbits for which spins are aligned with the orbital angular momentum. Recently, Ref. [225] has obtained the time-domain GW polarizations for generic orbits through 1.5PN order in the binary's comoving frame. The h_+ and $h_\times$ polarizations derived in the present paper for spinning, precessing binaries through 1.5PN order reduces to that of Refs. [84, 83] in the aligned case except for a few typographical errors which we correct.

In view of future studies at the interface between analytical and numerical relativity [48, 226, 227, 228, 229, 230, 231, 62, 60, 61, 63, 232] we decompose the time-domain h_+ and $h_\times$ polarizations in spin-weighted -2 spherical harmonics and compute the modes, $h_{\ell m}$, to 1.5PN order. We then consider spinning, non-precessing

[3]Note that the leading PN order in the polarization amplitude is proportional to $1/c^4$ when one turns the fundamental constants on. However, being the leading term in a PN expansion, it is has become common to call it Newtonian.

binaries for which we derive the Fourier domain representation of the generated gravitational waveform within the stationary phase approximation. We provide a very compact way of writing the Fourier transforms of h_+ and $h_\times$ which can readily be used for data analysis, for comparisons with numerical simulations, or for building analytical frequency-domain templates including inspiral, merger and ringdown [233, 234]. The impact of spinning, precessing waveforms for parameter estimation will be investigated in a future paper.

The remainder of the paper is organized in the following way. In Sec. 4.2 we draw the source and detector frames, and introduce conventions and notations. In Sec. 4.3 we provide ready-to-use h_+ and $h_\times$ polarizations in time domain for nearly circular orbits. The polarization modes $h_{\ell m}$ with respect to the spin-weighted -2 spherical harmonics are derived in Sec. 4.4. The features of the modes when spins are present is then discussed in Sec. 4.5. Section 4.6 focuses on spinning, non-precessing binaries. We compute there the Fourier domain waveforms with spin effects through 2PN order in the amplitude and 2.5PN order in the phase before discussing the main features caused by higher harmonics. Finally, we summarize in Sec. 4.7 our main conclusions. Appendices A and B present the GW polarizations and modes for precessing binaries on nearly circular orbits through 1.5PN order for generic inclination angles, whereas Appendix C shows the PN coefficients of the center-of-mass energy and radiative energy flux for non-precessing, spinning binaries. Appendix D gives explicitly the frequency domain amplitude coefficients with non-spin terms to 2.5PN and spin terms to 2PN order.

4.2 Source frame, polarization and parameter conventions

To obtain the GW polarizations, it is useful to express the gravitational strain tensor, h_{ij}, in an appropriate source frame. Next, one specifies an orthonormal polarization triad composed of the direction of propagation $\widehat{\mathbf{N}}$ and two polarization vectors $\widehat{\mathbf{P}}$ and $\widehat{\mathbf{Q}}$ which are used to construct the GW polarizations from the strain tensor [5]:

$$h_+ = \frac{1}{2}(P^i\,P^j - Q^i\,Q^j)\,h_{ij}\,, \tag{4.1}$$

$$h_\times = \frac{1}{2}(P^i\,Q^j + Q^i\,P^j)\,h_{ij}\,. \tag{4.2}$$

The gravitational strain measured by a detector is then given by

$$h_{\rm strain}(t) = F_+\,h_+(t) + F_\times\,h_\times(t)\,, \tag{4.3}$$

where F_+ and $F_\times$ are the antenna response functions that describe the detector's sensitivity to the two different polarizations. For laser interferometers with arms at a right angle, such as the LIGO and Virgo detectors, the antenna response functions for a GW coming from the sky location $(\bar{\theta}, \bar{\phi})$ in the spherical coordinate grid built from the arm basis, with polarization angle $\bar{\psi}$, are [5]

$$F_+ = \frac{1}{2}(1+\cos^2\bar{\theta})\,\cos 2\bar{\phi}\,\cos 2\bar{\psi} - \cos\bar{\theta}\,\sin 2\bar{\phi}\,\sin 2\bar{\psi}\,, \tag{4.4}$$

$$F_\times = \frac{1}{2}(1+\cos^2\bar{\theta})\,\cos 2\bar{\phi}\,\sin 2\bar{\psi} + \cos\bar{\theta}\,\sin 2\bar{\phi}\,\cos 2\bar{\psi}\,. \tag{4.5}$$

Note that the strain measured in a given instrument, $h_{\rm strain}(t)$, is the same regardless of convention, whereas the wave polarizations depend on the choice of polarization vectors. Different choices of $\widehat{\mathbf{P}}$ and $\widehat{\mathbf{Q}}$ give different polarizations, but there is a compensating rotation of the polarization angle $\bar{\psi}$ so that $h_{\rm strain}(t)$ is unchanged[4]. Here, we follow the convention of Refs. [84, 199], in which

$$\widehat{\mathbf{P}} = \frac{\widehat{\mathbf{N}} \times \mathbf{J}_0}{|\widehat{\mathbf{N}} \times \mathbf{J}_0|}\,, \qquad \widehat{\mathbf{Q}} = \widehat{\mathbf{N}} \times \widehat{\mathbf{P}}\,, \tag{4.6}$$

where $\mathbf{J}_0$ is the unit vector along the initial total angular momentum of the binary. In the absence of precession, the Newtonian orbital angular momentum $\mathbf{L}_N = \mu \mathbf{r} \times \mathbf{v}$ (with $\mathbf{r}$, $\mathbf{v}$, and μ being the binary separation vector, velocity, and reduced mass, respectively) is parallel to $\mathbf{J}_0$. In this case, $\widehat{\mathbf{P}}$ coincides with the *ascending node* where the orbital separation vector crosses the plane of the sky from below. In the presence of precession, $\widehat{\mathbf{P}}$ is still defined as $\widehat{\mathbf{N}} \times \mathbf{J}_0 / |\widehat{\mathbf{N}} \times \mathbf{J}_0|$, but it is not in general the point where the orbital separation vector ascends through the plane of the sky[5].

For our source frame, we construct an adapted orthonormal basis $(\hat{\mathbf{x}}, \hat{\mathbf{y}}, \hat{\mathbf{z}})$ (see Fig. 4.1). We take the z-axis to be along $\mathbf{J}_0$ and the direction of GW propagation, $\widehat{\mathbf{N}}$, to lie in the x–z plane, tilted by an angle θ from the z-axis towards the x-axis. We describe the direction of the Newtonian orbital angular momentum with the

[4]This can be seen explicitly from the relation linking $h_{\rm strain}(t)$ to the complex polarization $h(t)$ introduced in Eq. (4.40): $h_{\rm strain} = \Re\Big[h\, e^{2i\bar{\Psi}}(e^{2i\bar{\phi}} \cos^4(\bar{\theta}/2) + e^{-2i\bar{\phi}} \sin^4(\bar{\theta}/2))\Big]$. The reader can easily check the equivalence with Eqs. (4.3), (4.4) and (4.5).

[5]Note that Ref. [83] chooses polarization vectors rotated by $\pi/2$ relative to ours. This results in an overall sign difference from our polarizations, as can be seen by making the substitutions $\widehat{\mathbf{P}} \to \widehat{\mathbf{Q}}$ and $\widehat{\mathbf{Q}} \to -\widehat{\mathbf{P}}$, or by noting that GWs are spin-2 objects and flip sign under a $\pi/2$ rotation. As mentioned, the polarization angle of this convention is then rotated by $\pi/2$ relative to ours. This flips the sign of the antenna response functions as well, and so the same strain (4.3) is measured by either convention.

spherical coordinate angles (ι, α), where ι denotes the angle between the orbital angular momentum and the z-axis while α is the angle between the x-axis and the projection of the orbital angular momentum onto the x–y plane. For precessing binaries, as these angles vary in time, one must solve the precession equations to find their evolution. Notice that this source frame is the same as used in Ref. [83], and depicted in Fig. 2 of that paper.

We also find it useful to define basis vectors for the instantaneous orbital plane. These vectors have an implicit time dependence through the angles (ι, α), and rotate about $\widehat{\mathbf{L}}_N$ as it precesses. Here are their components in the $(\hat{\mathbf{x}}, \hat{\mathbf{y}}, \hat{\mathbf{z}})$ source basis:

$$\hat{\mathbf{x}}_L = \frac{\mathbf{J}_0 \times \widehat{\mathbf{L}}_{\rm N}}{|\mathbf{J}_0 \times \widehat{\mathbf{L}}_{\rm N}|} = (-\sin\alpha\ ,\ \cos\alpha\ ,\ 0\ )\ , \tag{4.7}$$

$$\hat{\mathbf{y}}_L = \widehat{\mathbf{L}}_{\rm N} \times \hat{\mathbf{x}}_L = (-\cos\iota\,\cos\alpha\ , -\cos\iota\,\sin\alpha\ ,\ \sin\iota\ )\ . \tag{4.8}$$

As an initial condition, we take the orbital separation vector $\hat{\mathbf{n}}$ to lie along $\hat{\mathbf{x}}_L$ at initial time, i.e., $\hat{\mathbf{n}}(t=0) = \hat{\mathbf{x}}_L(t=0)$. Then, we define the phase $\Phi(t)$ to be the cumulative angle between $\hat{\mathbf{x}}_L(t)$ and $\hat{\mathbf{n}}(t)$.

$$\hat{\mathbf{n}}(t) = \hat{\mathbf{x}}_L(t)\,\cos\Phi(t) + \hat{\mathbf{y}}_L(t)\,\sin\Phi(t)\,, \tag{4.9}$$

$$\hat{\boldsymbol{\lambda}}(t) = -\hat{\mathbf{x}}_L(t)\,\sin\Phi(t) + \hat{\mathbf{y}}_L(t)\,\cos\Phi(t)\,. \tag{4.10}$$

We thus see that the phase $\Phi(t)$ measures how $\hat{\mathbf{n}}$ has rotated relative to the vector $\hat{\mathbf{x}}_L$. However, for a precessing binary, $\hat{\mathbf{x}}_L$ is itself rotating about $\widehat{\mathbf{L}}_{\rm N}$. This means that the total rotation of $\hat{\mathbf{n}}$ about $\widehat{\mathbf{L}}_{\rm N}$ can be decomposed as a rotation of $\hat{\mathbf{n}}$ in the

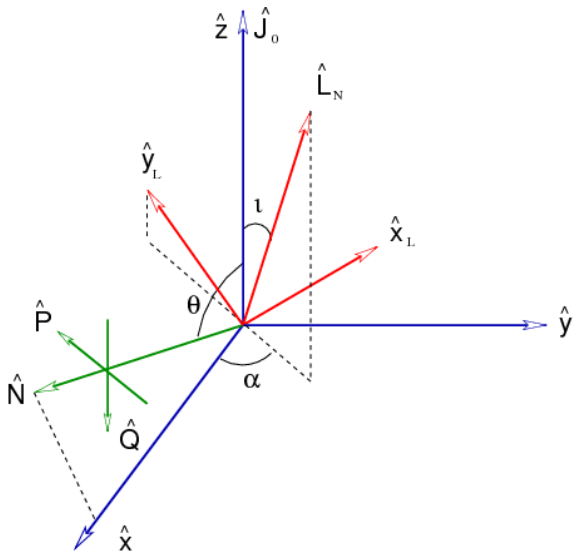

Figure 4.1: We show (i) our source frame defined by the orthonormal basis $(\hat{\mathbf{x}}, \hat{\mathbf{y}}, \hat{\mathbf{z}})$, (ii) the instantaneous orbital plane which is described by the orthonormal basis $(\hat{\mathbf{x}}_{\rm L}, \hat{\mathbf{y}}_{\rm L}, \widehat{\mathbf{L}}_{\rm N})$, (iii) the polarization triad $(\widehat{\mathbf{N}}, \widehat{\mathbf{P}}, \widehat{\mathbf{Q}})$, and (iv) the direction of the total angular momentum at initial time $\mathbf{J}_0$. Dashed lines show projections into the x–y plane.

comoving basis parametrized by $\Phi(t)$ times a rotation parametrized by a *precession phase* due to the movement of the orbital plane itself. In the non-precessing case we have $\mathbf{J}_0 \,||\, \widehat{\mathbf{L}}_{\rm N}$ and $\Phi(t)$ is expected to become the standard orbital phase whose time derivative is the orbital frequency. However, when $\mathbf{J}_0 \,||\, \widehat{\mathbf{L}}_{\rm N}$ holds, we cannot define $\Phi = 0$ for $\hat{\mathbf{n}} = \mathbf{J}_0 \times \widehat{\mathbf{L}}_{\rm N}/|\mathbf{J}_0 \times \widehat{\mathbf{L}}_{\rm N}|$, and we set $\Phi = 0$ at the ascending node $\widehat{\mathbf{N}} \times \widehat{\mathbf{L}}_{\rm N} = \widehat{\mathbf{P}}$, where the orbital separation crosses the plane of the sky from below. Now, $\Phi = 0$ at the ascending node is achieved for $\hat{\mathbf{x}}_L = \hat{\mathbf{n}}$ and $\widehat{\mathbf{P}} = \hat{\mathbf{n}}$, hence $\alpha = \pi$, so that the non-precessing regime is reached in the limit where $\iota = 0$ and $\alpha = \pi$ for all time. This is applicable when the spins of the bodies are aligned or anti-aligned with the orbital angular momentum (or in the non-spinning limit). The waveforms are then greatly simplified.

We define the following mass parameters

$$
\begin{aligned}
M &= m_1 + m_2\,, && (4.11)\\
\nu &= \frac{m_1\, m_2}{(m_1+m_2)^2}\,, && (4.12)\\
\mathcal{M} &= M\,\nu^{3/5}\,, && (4.13)\\
\delta &= \frac{m_1 - m_2}{m_1+m_2}\,, && (4.14)\\
\nu &= \frac{1}{4}(1-\delta^2). && (4.15)
\end{aligned}
$$

They are the total mass M, the symmetric mass ratio ν, the fractional mass difference δ, the chirp mass $\mathcal{M}$. The symmetric mass ratio is bounded according to $0 < \nu \leq 1/4$ and the fractional mass difference satisfies $-1 < \delta < 1$.

The spin of a rotating compact body is of the order $S \sim m\, l\, v_{\rm spin}$ with $l \sim G\, m/c^2$. If the compact body is *maximally* rotating, then $v_{\rm spin} \sim c$ and $S \sim \chi\, G\, m^2/c$. In words, from the PN point of view, the spin is formally of order 0.5PN. By contrast, if the compact body is *slowly* rotating, then $v_{\rm spin} \ll c$, and the spin is formally of higher PN order, $S \sim \chi\, G\, m^2\, v_{\rm spin}/c^2 \sim 1/c^2$. Throughout the paper, we use geometrical units where $G = c = 1$. Henceforth, we shall work with the spin vectors normalized by the component masses as

$$
\boldsymbol{\chi}_n = \frac{\mathbf{S}_n}{m_n^2}\,, \quad n = 1, 2\,, \tag{4.16}
$$

so that $|\boldsymbol{\chi}_n| \leq 1$ for objects that obey the Kerr bound on rotational angular momentum. We also define symmetric and anti-symmetric spin combinations as in

Ref. [84],

$$\boldsymbol{\chi}_s = \frac{1}{2}\left(\boldsymbol{\chi}_1 + \boldsymbol{\chi}_2\right), \tag{4.17}$$

$$\boldsymbol{\chi}_a = \frac{1}{2}\left(\boldsymbol{\chi}_1 - \boldsymbol{\chi}_2\right). \tag{4.18}$$

4.3 Ready-to-use gravitational-wave polarizations for precessing binaries on circular orbits through 1.5PN order: Small inclination angles

The expression of the strain tensor h_{ij} for generic orbits through 1.5PN order was derived in Refs. [194, 84] and is given by Eq. (6.11) of Ref. [84]. In this section we compute ready-to-use polarizations in time domain through 1.5PN order within the *adiabatic* regime where the binary inspiral is modeled as a quasi-stationary sequence of orbits assumed to be nearly circular. By nearly circular, we essentially mean an orbit that would be exactly circular, with separation vector $\mathbf{r}_0$ of constant radius r_0, in the absence of spins and gravitational radiation. The perturbation of the separation δr of such a motion is assumed to remain small with respect to r_0 on timescales on which the radiation-reaction effects can be neglected. This can only happen when the precession angles are at most of the same order of magnitude as the relative corrections induced by the spins in the dynamical quantities. Now, the evolution of δr is governed by the radial part of the 1.5PN perturbation of the force per mass unit given in Eq. (2.1) of Ref. [83]. It turns out that this perturbation depends on the spin exclusively through the two projections $(\mathbf{S}_n \cdot \widehat{\mathbf{L}}_{\rm N})$ with $n = 1, 2$

which are almost constant apart from remainders that will contribute at higher orders in our weak precession hypothesis. In order to write the equation for δr, we project the relative acceleration $\mathbf{a}$ in the basis $\{\hat{\mathbf{n}}, \hat{\boldsymbol{\lambda}}, \widehat{\mathbf{L}}_{\rm N}\}$. For the sake of convenience, we introduce an "orbital"-like frequency $\omega_{\rm orb}$, defined as $\omega_{\rm orb} = (\mathbf{v}\cdot\hat{\boldsymbol{\lambda}})/r$. The closure relation yields the following decomposition for $\mathbf{v}$ and $\mathbf{a}$:

$$\begin{aligned}
\mathbf{v} &= \dot{r}\hat{\mathbf{n}} + \omega_{\rm orb} r \hat{\boldsymbol{\lambda}}\,,\\
\mathbf{a} &= (\ddot{r} - r\omega_{\rm orb}^2)\hat{\mathbf{n}} + (r\dot{\omega}_{\rm orb} + 2\dot{r}\omega_{\rm orb})\hat{\boldsymbol{\lambda}} - r\omega_{\rm orb}\left(\hat{\boldsymbol{\lambda}}\cdot\frac{d\widehat{\mathbf{L}}_{\rm N}}{dt}\right)\widehat{\mathbf{L}}_{\rm N}\,,
\end{aligned} \tag{4.19}$$

with $\dot{r} \equiv dr/dt$. Splitting $\mathbf{a}$ into an unperturbed part $\mathbf{a}_0$ plus a perturbation $\delta\mathbf{a}$ and using the equations of motion, we find finally that δr satisfies the equation $\delta\ddot{r} + \omega_0^2\delta r = \text{const.}$ where ω_0 is the constant angular frequency of the background motion. A particular solution is given by a constant perturbation, $\delta r = \text{const.}$, whereas the homogeneous solution satisfies an harmonic oscillator equation independent of the spin.

By making the particular choice of a zero homogeneous solution, we can always eliminate the oscillations of r that are not directly linked to the non-zero spins of the BHs. Based on these observations, we shall *define* precisely a nearly circular motion to be *a perturbed circular motion whose homogeneous radial perturbation solution* $(\delta r)_{\rm hom}$ *is zero, as it would be for an exactly circular motion*[6]. Assuming such a dynamics for our binary system implies that both δr and $r = r_0 + \delta r$ must be constant, provided we neglect higher order spin terms and radiative effects. We

[6]Though this type of motion can exist and is more general than the spin-aligned or anti-aligned case, it does not necessarily represent yet the most likely evolution to be observed.

can generalize nearly circular motions to the case where spin precession angles are arbitrary in the absence of spin-spin interactions. This is achieved by introducing the concept of spherical motion *defined* as a motion *having a constant separation* r. It immediately follows from Eq. (4.19) that the full (conservative) acceleration is still of the form $-\omega_{\rm orb}^2 r\mathbf{n}$. Moreover, when radiation-reaction effects are neglected, the orbital frequency computed from the 1.5PN equations of motion keeps being almost constant [202, 83], even for precession angles that are no longer small. This can be seen [85] by noticing that the only possible non-constant terms in $\omega_{\rm orb}$ at the 1.5PN order come from the leading spin contribution of the equations of motion, and thus, are of the form $(\mathbf{S}_n{\cdot}\widehat{\mathbf{L}}_{\rm N})$. Their time derivative reads $(d\widehat{\mathbf{L}}_{\rm N}/dt{\cdot}\mathbf{S}_n)+(\widehat{\mathbf{L}}_{\rm N}{\cdot}d\mathbf{S}_n/dt)$. The first term is zero due to the precession equation $d\mathbf{S}_n/dt = \mathbf{\Omega}_n \times \mathbf{S}_n$, while the second term is a higher order correction quadratic in spins because of the approximate conservation of $\widehat{\mathbf{L}}_N$. The treatment of the spin-spin dynamics is more delicate. A possible way to proceed consists in averaging the time dependent spin contributions in $\omega_{\rm orb}$ over one orbital period [83, 235].

Introducing the invariant velocity,

$$v \equiv (M\omega_{\rm orb})^{1/3}\,, \tag{4.20}$$

we reduce Eq. (6.11) of Ref. [84] to nearly circular orbits and expand it in powers of v with the help of the relativistic extension of Kepler's law linking $\omega_{\rm orb}$ and M/r

provided by Eq. (7.1) of Ref. [84]. Schematically, we obtain

$$\begin{aligned} h_{ij} &= \frac{2\,M\,\nu\,v^2}{D_L}\left[\mathrm{Q}_{ij} + \mathrm{P}^{1/2}\mathrm{Q}_{ij}\;v + \left(\mathrm{P}^{1}\mathrm{Q}_{ij} + \mathrm{P}^{1}\mathrm{Q}^{\mathrm{SO}}_{ij}\right)\;v^2\right. \\ &+ \left.\left(\mathrm{P}^{3/2}\mathrm{Q}_{ij} + \mathrm{P}^{3/2}\mathrm{Q}^{\mathrm{tail}}_{ij} + \mathrm{P}^{3/2}\mathrm{Q}^{\mathrm{SO}}_{ij}\right)\;v^3\right]_{\mathrm{TT}}\,, \end{aligned} \tag{4.21}$$

where SO indicates the spin-orbit terms; the tail integral $\mathrm{P}^{3/2}\mathrm{Q}^{\mathrm{tail}}_{ij}$ given by Eq. (6.11e) of Ref. [84] reads

$$\mathrm{P}^{3/2}\mathrm{Q}^{\mathrm{tail}}_{ij} = 4\left[\pi(\hat{\lambda}^i\hat{\lambda}^j - \hat{n}^i\hat{n}^j) + 12\ln\left(\frac{v}{v_0}\right)\hat{\lambda}^{(i}\hat{n}^{j)}\right]_{\mathrm{TT}}\,, \tag{4.22}$$

v_0 being an arbitrary numerical constant reflecting the freedom in the choice of the radiative time origin. The symbol TT on the square bracket indicates the transverse trace-free projection in the plane orthogonal to the direction $\widehat{\mathbf{N}}$ of the observer. We remind the reader that the non-spinning contributions to Eq. (4.21) are known through 3PN order [201, 27].

Apart from the spins, there are four vectors that appear in the expressions for the $\mathrm{P}^n\mathrm{Q}_{ij}$'s in Eq. (4.21). In the source frame constructed in Sec. 4.3, they have the following (x, y, z) components

$$\hat{\mathbf{n}} = (-\sin\alpha\,\cos\Phi - \cos\iota\,\cos\alpha\,\sin\Phi\,,\,\cos\alpha\,\cos\Phi - \cos\iota\,\sin\alpha\,\sin\Phi\,,\,\sin\iota\,\sin\Phi)\,, \tag{4.23}$$

$$\hat{\boldsymbol{\lambda}} = (\sin\alpha\,\sin\Phi - \cos\iota\,\cos\alpha\,\cos\Phi\,,\,-\cos\alpha\,\sin\Phi - \cos\iota\,\sin\alpha\,\cos\Phi\,,\,\sin\iota\,\cos\Phi)\,, \tag{4.24}$$

$$\widehat{\mathbf{N}} = (\sin\theta\,,\,0\,,\,\cos\theta)\;, \tag{4.25}$$

$$\widehat{\mathbf{L}}_{\rm N} = (\sin\iota\,\cos\alpha\,,\,\sin\iota\,\sin\alpha\,,\,\cos\iota)\;, \tag{4.26}$$

where Φ is the phase defined in Eq. (4.9) that measures how $\hat{\mathbf{n}}$ has rotated relative to the vector $\hat{\mathbf{x}}_L$. As $\hat{\mathbf{x}}_L$ is itself rotating about $\widehat{\mathbf{L}}_{\rm N}$ for a precessing binary, the orbital frequency, or the total angular velocity of $\hat{\mathbf{n}}$ about $\widehat{\mathbf{L}}_{\rm N}$, is the angular velocity of the motion of the binary within its instantaneous orbital plane, plus a precession velocity due to the movement of the orbital plane itself. To derive the relationship between the phase $\Phi(t)$ and the orbital phase (or *carrier phase*), we compute the derivative of $\hat{\mathbf{n}}(t)$ by means of Eqs. (4.7), (4.9), obtaining

$$\frac{d\hat{\mathbf{n}}}{dt} = \left(\frac{d\Phi}{dt} + \cos\iota\,\frac{d\alpha}{dt}\right)\,\hat{\boldsymbol{\lambda}} + \left(\frac{d\iota}{dt}\,\sin\Phi - \sin\iota\,\cos\Phi\,\frac{d\alpha}{dt}\right)\,\widehat{\mathbf{L}}_{\rm N}\,. \tag{4.27}$$

By imposing $\widehat{\mathbf{L}}_{\rm N} = \hat{\mathbf{n}}\times\mathbf{v}/|\hat{\mathbf{n}}\times\mathbf{v}| = \hat{\mathbf{n}}\times d\hat{\mathbf{n}}/dt/|\hat{\mathbf{n}}\times d\hat{\mathbf{n}}/dt|$, and using Eq. (4.23) as well as Eq. (4.26), we find that the term proportional to $\widehat{\mathbf{L}}_{\rm N}$ in Eq. (4.27) must be zero. Thus, we have $d\hat{\mathbf{n}}/dt = \dot{r}\mathbf{r}/r^2 + \dot{\mathbf{r}}/r \equiv (\mathbf{v}\cdot\hat{\boldsymbol{\lambda}})\hat{\boldsymbol{\lambda}}$, where $\mathbf{v}\cdot\hat{\boldsymbol{\lambda}}$ is the orbital frequency $\omega_{\rm orb}$ defined before Eq. (4.19), which may be now interpreted as the angular velocity with which $\hat{\mathbf{n}}$ rotates about $\widehat{\mathbf{L}}_{\rm N}$. Identification with Eq. (4.27) leads to the relation

$$\omega_{\rm orb} = \dot{\Phi} + \cos\iota\,\dot{\alpha}\,; \tag{4.28}$$

the phase $\Phi(t)$ being simply the integral

$$\Phi(t) = \int_0^t \left[\omega_{\rm orb}(t') - \cos\iota(t')\,\dot{\alpha}(t')\right]\,dt'\,. \tag{4.29}$$

Due to the freedom in the choice of the time origin by the radiative observer, h_{ij} depends on an undetermined time scale or, equivalently, on an arbitrary reference orbital frequency ω_0. The constant ω_0 is actually associated to the presence of gravitational-wave tails and appears solely in logarithms of the form $\ln(\omega_{\rm orb}/\omega_0)$. Such contributions may be absorbed in the orbital phase by a redefinition of Φ into a shifted phase Ψ [198]. Through 1.5PN order in the shift, we can pose $\Psi = \Phi - 2v^3\,\ln(\omega_{\rm orb}/\omega_0)$. By plugging Eqs. (4.23)–(4.26) into Eq. (4.21), taking the combinations given in Eq. (4.1), and collecting terms by powers in v, we obtain the waveform polarizations

$$h_{+,\times} \;=\; \frac{2\,M\,\nu\,v^2}{D_L}\,\left[H^{(0)}_{+,\times} + H^{(1/2)}_{+,\times} + H^{(1/2,{\rm SO})}_{+,\times} + H^{(1)}_{+,\times} + H^{(1,{\rm SO})}_{+,\times} + H^{(3/2)}_{+,\times} + H^{(3/2,{\rm SO})}_{+,\times}\right]\,. \tag{4.30}$$

The Newtonian, 0.5PN and 1PN order terms were already computed explicitly in Refs. [83, 84] [see in particular Eqs. (B2), (B3) of Ref. [83]], but as a series expansion of M/r rather than v. Let us list for the reader convenience a few typographical errors we found there. In Eq. (4.9d) of Ref. [83], the factor of $(1/6)(149-6\nu)$ has to be replaced with $(1/6)(149-36\nu)$; in Eq. (B2c) Q_+ must be changed to $-Q_+$; in Eq. (B3c) the right parenthesis is missing in the expression $(\cos^2 i\,\sin^2\alpha + \cos^2\alpha)$; at last, in Eq. (B3j) $c\,d$ should be read as $-c\,d$. In Ref. [84], Eq. (F14b) must be

multiplied by 3ν; in Eq. (F20) -3ν has to be replaced with $+3\nu$; there should be an overall minus sign in front of Eq. (F25c). If we re-expand Kidder's polarizations in v, and correct all the previous typos, we obtain complete agreement with both results through 1PN order[7].

The lengthy expression for the GW polarizations can be reduced to a much more compact form by noticing (see also Sec. IVD in Ref. [83]) that in the limit $S \ll L$ the angle ι can be considered a 0.5PN order correction. This can be seen from

$$\sin\iota = \frac{|\mathbf{J}_0 \times \mathbf{L}|}{J_0\, L}\,, \tag{4.31}$$

if we neglect radiation reaction effects, i.e., we assume $\mathbf{J}_0 = \mathbf{J}$, and use $\mathbf{J} = \mathbf{L}+\mathbf{S}_1+\mathbf{S}_2$ and $\mathbf{S}_n = \mathcal{O}(1/c)$. We may then replace $\sin\iota$ and $\cos\iota$ in $h_{+,\times}$ with their Taylor series expansions in ι,

$$\sin\iota = \iota - \frac{\iota^3}{6} + \mathcal{O}(\iota^5)\,, \tag{4.32}$$

$$\cos\iota = 1 - \frac{\iota^2}{2} + \mathcal{O}(\iota^4)\,. \tag{4.33}$$

However, the assumption $S \ll L$ becomes less and less reliable for smaller mass ratio binaries. In fact, as a first approximation, we have $S_n/L = (m_n/M)^2\,\chi_n\, v/\nu$ with $v = (GM\omega_{\rm orb}/c^3)^{1/3}$. Thus, even if $S_n \sim \mathcal{O}(1/c)$, L can become comparable to S_n when ν is sufficiently small. Moreover, we have assumed $\mathbf{J}_0 = \mathbf{J}$ in Eq. (4.31), but

[7]It is also worth noting that Ref. [83] sets the origin of phase to be at a point referred to as the ascending node and defined to be the point where the orbital separation crosses the x–y plane. This is in fact the same as our phase origin, $\widehat{\mathbf{x}}_L = \mathbf{J}_0 \times \hat{\mathbf{L}}_{\rm N}/|\mathbf{J}_0 \times \hat{\mathbf{L}}_{\rm N}|$, but to reduce the possibility of confusion, we do not call this point the ascending node. We reserve this term to mean the point where the separation vector crosses *the plane of the sky* from below.

the latter is not exact when radiation reaction is included, and it can be strongly violated in presence of transitional precession [236]. For these reasons, though we have decided to list in this section the GW polarizations expanded in ι, we display in Appendix A the full expressions for generic inclination angles. For the ι-expanded polarizations, we find

$$H_+^{(0)} = -\left(c_\theta{}^2 + 1\right)\cos 2(\alpha+\Psi)\,, \tag{4.34a}$$

$$H_+^{(1/2)} = v\,\delta\,s_\theta\left[\left(\frac{c_\theta{}^2}{8}+\frac{5}{8}\right)\cos(\alpha+\Psi) - \frac{9}{8}\left(c_\theta{}^2+1\right)\cos 3(\alpha+\Psi)\right], \tag{4.34b}$$

$$\begin{aligned} H_+^{(1)} = v^2\Bigg[&\left(-\frac{c_\theta{}^4}{3}+\frac{3c_\theta{}^2}{2}+\frac{19}{6}+\left(c_\theta{}^4+\frac{11c_\theta{}^2}{6}-\frac{19}{6}\right)\nu\right)\cos 2(\alpha+\Psi)\\ &+\frac{4}{3}\left(1-c_\theta{}^4\right)\left(3\nu-1\right)\cos 4(\alpha+\Psi)\Bigg], \end{aligned} \tag{4.34c}$$

$$\begin{aligned} H_+^{(3/2)} = v^3\Bigg[&\delta\,s_\theta\left(\frac{c_\theta{}^4}{192}-\frac{5c_\theta{}^2}{16}-\frac{19}{64}+\left(-\frac{c_\theta{}^4}{96}-\frac{c_\theta{}^2}{8}+\frac{49}{96}\right)\nu\right)\cos(\alpha+\Psi)\\ &-2\pi(c_\theta{}^2+1)\cos 2(\alpha+\Psi)+\delta\,s_\theta\left(\left(-\frac{81c_\theta{}^4}{128}+\frac{45c_\theta{}^2}{16}+\frac{657}{128}\right)\right.\\ &\left.+\left(\frac{81c_\theta{}^4}{64}+\frac{9c_\theta{}^2}{8}-\frac{225}{64}\right)\nu\right)\cos 3(\alpha+\Psi)\\ &+\delta\,s_\theta\,\frac{625}{384}\left(1-c_\theta{}^4\right)\left(2\nu-1\right)\cos 5(\alpha+\Psi)\Bigg], \end{aligned} \tag{4.34d}$$

$$H_+^{(1/2,\mathrm{SO})} = -2\iota\,c_\theta s_\theta\cos(\alpha+2\Psi)\,, \tag{4.34e}$$

$$\begin{aligned} H_+^{(1,\mathrm{SO})} = v^2&\left[\left(c_\theta\left(\chi_a^x+\delta\chi_s^x\right)-s_\theta\left(\chi_a^z+\delta\chi_s^z\right)\right)\cos(\alpha+\Psi)-c_\theta\left(\chi_a^y+\delta\chi_s^y\right)\sin(\alpha+\Psi)\right]\\ &+v\,\iota\,\delta\,c_\theta\left[\frac{1}{4}s_\theta{}^2\cos\Psi-\left(\frac{c_\theta{}^2}{8}+\frac{5}{8}\right)\cos(2\alpha+\Psi)+\left(-\frac{9}{8}+\frac{27c_\theta{}^2}{8}\right)\cos(2\alpha+3\Psi)\right]\\ &+\iota^2\left[-\frac{3}{2}s_\theta{}^2\cos 2\Psi+\frac{1}{2}(c_\theta{}^2+1)\cos 2(\alpha+\Psi)\right], \end{aligned} \tag{4.34f}$$

$$
\begin{aligned}
H_{+}^{(3/2,\mathrm{SO})} &= v^3\Bigg[s_\theta\, c_\theta \left(2\delta\, \chi_a^x + (2-\nu)\, \chi_s^x\right) + \Bigg(\frac{4}{3}\,(1+{c_\theta}^2)\,\delta\,\chi_a^z \\
&+ \frac{4}{3}\left((1+{c_\theta}^2) + \nu\,(1-5{c_\theta}^2)\right)\chi_s^z - s_\theta\, c_\theta\left(2\delta\,\chi_a^x + (2+7\nu)\,\chi_s^x\right)\Bigg)\,\cos 2(\alpha+\Psi) \\
&- s_\theta\, c_\theta\left(2\delta\,\chi_a^y + (2-\nu)\,\chi_s^y\right)\,\sin 2(\alpha+\Psi)\Bigg] \\
&+ v^2\iota\, s_\theta\Bigg[c_\theta\left(-{c_\theta}^2 + 4 + \left(3{c_\theta}^2 + \frac{2}{3}\right)\nu\right)\cos(\alpha+2\Psi) \\
&+ c_\theta\left(-\frac{{c_\theta}^2}{3} - 1 + \left({c_\theta}^2+3\right)\nu\right)\cos(3\alpha+2\Psi) + c_\theta^3\left(\frac{16}{3} - 16\nu\right)\cos(3\alpha+4\Psi) \\
&- (\chi_a^y + \delta\chi_s^y)\sin\Psi\Bigg] + v\,\iota^2 s_\theta\,\delta\Bigg[\left(-\frac{3{c_\theta}^2}{16} + \frac{9}{16}\right)\cos(\alpha-\Psi) \\
&- \left(\frac{11{c_\theta}^2}{32} + \frac{23}{32}\right)\cos(\alpha+\Psi) + \frac{27}{32}\left({c_\theta}^2+1\right)\cos 3(\alpha+\Psi) \\
&- \frac{1}{32}({c_\theta}^2+1)\cos(3\alpha+\Psi) + \left(-\frac{45}{32} + \frac{135{c_\theta}^2}{32}\right)\cos(\alpha+3\Psi)\Bigg] \\
&+ \iota^3 c_\theta s_\theta\left[\frac{1}{2}\cos(\alpha-2\Psi) + \frac{5}{6}\cos(\alpha+2\Psi)\right] \qquad (4.34g)
\end{aligned}
$$

$$
H_{\times}^{(0)} = -2c_\theta \sin 2(\alpha+\Psi)\,, \qquad (4.35a)
$$

$$
H_{\times}^{(1/2)} = v\,\delta\, c_\theta s_\theta\left[-\frac{9}{4}\sin 3(\alpha+\Psi) + \frac{3}{4}\sin(\alpha+\Psi)\right], \qquad (4.35b)
$$

$$
\begin{aligned}
H_{\times}^{(1)} &= v^2 c_\theta\Bigg[\left(-\frac{4{c_\theta}^2}{3} + \frac{17}{3} + \left(-\frac{13}{3} + 4{c_\theta}^2\right)\nu\right)\sin 2(\alpha+\Psi) \\
&+ {s_\theta}^2\left(-\frac{8}{3} + 8\nu\right)\sin 4(\alpha+\Psi)\Bigg], \qquad (4.35c)
\end{aligned}
$$

$$
\begin{aligned}
H_{\times}^{(3/2)} &= v^3 c_\theta\Bigg[\delta\, s_\theta\left(\left(-\frac{21}{32} + \frac{5{c_\theta}^2}{96}\right) + \left(-\frac{5{c_\theta}^2}{48} + \frac{23}{48}\right)\nu\right)\sin(\alpha+\Psi) \\
&- 4\pi\sin 2(\alpha+\Psi) + \delta\, s_\theta\left(\left(-\frac{135{c_\theta}^2}{64} + \frac{603}{64}\right) +\right.
\end{aligned}
$$

$$\left(-\frac{171}{32} + \frac{135{c_\theta}^2}{32} \right)\nu \Bigg) \sin 3(\alpha+\Psi) + \delta\, s_\theta \left(\frac{625}{192}\,(2\nu-1)\,{s_\theta}^2 \right) \sin 5(\alpha+\Psi) \Bigg], \tag{4.35d}$$

$$H_\times^{(1/2,\mathrm{SO})} = -2\iota\, s_\theta \sin(\alpha+2\Psi)\,, \tag{4.35e}$$

$$\begin{aligned} H_\times^{(1,\mathrm{SO})} &= v^2 \left[(\chi_a^y + \delta\chi_s^y)\cos(\alpha+\Psi) + c_\theta \left(c_\theta(\chi_a^x + \delta\chi_s^x) - s_\theta\,(\chi_a^z + \delta\chi_s^z) \right) \sin(\alpha+\Psi) \right] \\ &\quad + \iota\, v\, \delta \left[{s_\theta}^2 \sin\Psi - \left(\frac{{c_\theta}^2}{2} + \frac{1}{4} \right) \sin(2\alpha+\Psi) + \left(-\frac{9}{4} + \frac{9{c_\theta}^2}{2} \right) \sin(2\alpha+3\Psi) \right] \\ &\quad + \iota^2\, c_\theta \sin 2(\alpha+\Psi)\,, \end{aligned} \tag{4.35f}$$

$$\begin{aligned} H_\times^{(3/2,\mathrm{SO})} &= v^3 \Bigg[s_\theta \left(2\delta\chi_a^y + (2-\nu)\,\chi_s^y \right) \left(1 + \cos 2(\alpha+\Psi) \right) \\ &\quad + \left(\frac{8}{3}\, c_\theta\, \delta\, \chi_a^z + c_\theta \left(\frac{8}{3} - (\frac{4}{3} + 4c_\theta^2)\nu \right) \chi_s^z \right. \\ &\quad \left. - s_\theta \left(2\delta\, \chi_a^x + \left(2 + (3 + 4{c_\theta}^2)\nu \right) \chi_s^x \right) \right) \sin 2(\alpha+\Psi) \Bigg] \\ &\quad + \iota\, v^2\, s_\theta \Bigg[\left(c_\theta\,(\chi_a^x + \delta\chi_s^x) - s_\theta(\chi_a^z + \delta\chi_s^z) \right) \sin\Psi \\ &\quad + \left(\left(-3{c_\theta}^2 + 6 \right) + \left(-\frac{16}{3} + 9{c_\theta}^2 \right)\nu \right) \sin(\alpha+2\Psi) \\ &\quad + \left(-\left({c_\theta}^2 + \frac{1}{3} \right) + \left(3{c_\theta}^2 + 1 \right)\nu \right) \sin(3\alpha+2\Psi) \\ &\quad + \left(\left(-\frac{8}{3} + 8{c_\theta}^2 \right) + \left(-24{c_\theta}^2 + 8 \right)\nu \right) \sin(3\alpha+4\Psi) \Bigg] \\ &\quad + \iota^2 v\, \delta\, c_\theta s_\theta \left[\frac{3}{8}\sin(\alpha-\Psi) - \frac{17}{16}\sin(\alpha+\Psi) + \frac{27}{16}\sin 3(\alpha+\Psi) \right. \\ &\quad \left. - \frac{1}{16}\sin(3\alpha+\Psi) + \frac{45}{16}\sin(\alpha+3\Psi) \right] \\ &\quad + \iota^3 \left[\frac{1}{2} s_\theta \sin(\alpha-2\Psi) + \frac{5}{6} s_\theta \sin(\alpha+2\Psi) \right], \end{aligned} \tag{4.35g}$$

where s_θ and c_θ are shorthand notations for $\sin\theta$ and $\cos\theta$ respectively. In Sec. 4.4

(see Fig. 4.2), we shall discuss typical variations of the inclination angle ι depending on spin orientations and binary mass ratios. Note that whereas the terms of $H^{(1,\mathrm{SO})}_{+,\times}$ linear in $\boldsymbol{\chi}_n$ depend on the first harmonic of the orbital frequency, those of $H^{(3/2,\mathrm{SO})}_{+,\times}$ depend on its zeroth and second harmonic, and so do the terms of $H^{(2,\mathrm{SS})}_{+,\times}$ quadratic in the spin components, although we do not use them here. We include these 2PN SS polarization corrections when constructing frequency-domain waveforms for binaries having their spins aligned or anti-aligned with the orbital angular momentum in Sec. 4.6. The harmonic dependence of the polarization corrections produced by the spins can be understood from the explicit expression for h_{ij} shown in Eqs. (4.9c) and (4.9d) of Ref. [83] or Eqs. (F15a)-(F15c) of Ref. [84]. The 1PN SO contributions are proportional to the components of the orbital separation vector, $\hat{\mathbf{n}}$, which are themselves proportional to $\sin\Phi$ and $\cos\Phi$, so that $H^{(1,\mathrm{SO})}_{+,\times}$ depend on the first harmonic of the orbital phase. Next, the 1.5PN SO and 2PN SS contributions are proportional to products of the orbital separation or instantaneous velocity unit vectors, $\hat{\mathbf{n}}$ or $\hat{\boldsymbol{\lambda}}$, and to products of $\sin\Phi$ or $\cos\Phi$. These can be re-expressed in terms of $\sin 2\Phi$, $\cos 2\Phi$ or constant quantities independent of Φ, so that $H^{(3/2,\mathrm{SO})}_{+,\times}$ and $H^{(2,\mathrm{SS})}_{+,\times}$ depend on the zeroth and second harmonics of the orbital phase. Because the expressions for h_{ij} in Refs. [83, 84] are expanded in (M/r), while we use an expansion in $v = (M\omega_{\mathrm{orb}})^{1/3}$, one has to convert from one expansion to the other by using Eqs. (7.1) and (F20) of Ref. [84]. In doing so, the v-expansion gains additional 1.5PN SO and 2PN SS corrections proportional to the Newtonian order term depending on the second harmonic of the orbital phase. The 1PN SO term is left unchanged.

Ready-to-use time-domain GW polarizations for spinning, precessing binaries through 1.5PN order in phase and amplitude can be obtained by solving numerically the following equations: (i) The spin precession equations [85, 86]

$$\frac{d\mathbf{S}_1}{dt} = \mathbf{\Omega}_1 \times \mathbf{S}_1 \,, \tag{4.36a}$$

$$\frac{d\mathbf{S}_2}{dt} = \mathbf{\Omega}_2 \times \mathbf{S}_2 \,, \tag{4.36b}$$

where at 1.5PN order

$$\mathbf{\Omega}_{1,2} = \omega_{\rm orb}^{5/3} \left(\frac{3}{4} + \frac{\nu}{2} \mp \frac{3}{4}\delta \right) \widehat{\mathbf{L}}_{\rm N} \,; \tag{4.37}$$

(ii) The evolution equation for the Newtonian angular momentum

$$\dot{\widehat{\mathbf{L}}}_{\rm N} = -\frac{v}{\nu} \left(\dot{\mathbf{S}}_1 + \dot{\mathbf{S}}_2 \right) ; \tag{4.38}$$

(iii) The equation for the orbital frequency

$$\begin{aligned} \frac{\dot{\omega}_{\rm orb}}{\omega_{\rm orb}^2} &= \frac{96}{5}\,\nu\, v^5 \Bigg\{ 1 - \left(\frac{743}{336} + \frac{11}{4}\nu \right) v^2 \\ &+ \left[\left(\frac{19}{3}\,\nu - \frac{113}{12} \right) \boldsymbol{\chi}_s \cdot \widehat{\mathbf{L}}_{\rm N} - \frac{113}{12}\,\delta\, \boldsymbol{\chi}_a \cdot \widehat{\mathbf{L}}_{\rm N} \right] v^3 + 4\pi v^3 \Bigg\} . \end{aligned} \tag{4.39}$$

Integrating $\omega_{\rm orb}$ yields the orbital phase $\Phi_{\rm orb}(t) \equiv \int_0^t \omega_{\rm orb}(t')dt'$. The GW polarizations (4.30) through 1.5PN order in phase and amplitude are computed by solving numerically Eqs. (4.29), (4.36), (4.38), and (4.39). In order to compute the GW

polarizations (4.30) through 1.5PN order in amplitude, but at the highest available PN order in phase, one should replace Eqs. (4.36), (4.38) with Eq. (7.5) in Ref. [86] and Eq. (32) in Ref. [48], respectively.

4.4 Gravitational-wave modes for precessing binaries on nearly circular orbits through 1.5PN order: Small inclination angles

Due to the spin-2 nature of GWs, it is convenient to decompose the waveform components in the dyad $\{(\widehat{\mathbf{P}}+i\widehat{\mathbf{Q}})/\sqrt{2},(\widehat{\mathbf{P}}-i\widehat{\mathbf{Q}})/\sqrt{2}\}$ with respect to an orthonormal basis of spin ± 2 functions that are defined on the 2-sphere and belong to an irreducible representation of SO(3). Most commonly, the complex polarization

$$h = h_{jk}\frac{P^j - iQ^j}{\sqrt{2}}\frac{P^k - iQ^k}{\sqrt{2}} = h_+ - ih_\times\,, \tag{4.40}$$

is expanded into the set of spin-weighted -2 spherical harmonics. Like the standard spherical harmonics, these functions of the two angles of spherical coordinates are labeled by a pair of integers, say (ℓ, m), with $\ell \geq 2$ and $m \leq |\ell|$. The spin-weighted $-s$ spherical harmonics associated to any such pair are given by [8] [237]

$${}_{-s}Y^{\ell m}(\theta,\phi) = (-1)^s\sqrt{\frac{2\ell+1}{4\pi}}\,d^{\ell}_{sm}(\theta)\,e^{im\phi}\,, \tag{4.41}$$

[8] Our definition of ${}_{-s}Y^{\ell m}(\theta,\phi)$ differs from that of Ref. [237] by a factor $(-1)^m$ so that ${}_0Y^{\ell m}(\theta,\phi)$ coincides with the most broadly used definition of $Y^{\ell m}(\theta,\phi)$; for the d-matrix $d^{\ell}_{m'm}(\theta)$, we adopt the same convention as Landau-Lifshitz [238].

with

$$d^{\ell}_{sm}(\theta) = \sum_{k=\max(0,m-s)}^{\min(\ell+m,\ell-s)} \frac{(-1)^k}{k!} \frac{\sqrt{(\ell+m)!(\ell-m)!(\ell+s)!(\ell-s)!}}{(k-m+s)!(\ell+m-k)!(\ell-k-s)!} \times \left(\cos\frac{\theta}{2}\right)^{2\ell+m-2k-s} \left(\sin\frac{\theta}{2}\right)^{2k-m+s}, \tag{4.42}$$

and the orthogonality relation holds

$$\int d\Omega \, {}_{-s}Y^{\ell m}(\theta,\phi) \, {}_{-s}Y^{\ell' m' *}(\theta,\phi) = \delta^{\ell\ell'}\delta^{mm'}, \tag{4.43}$$

where $d\Omega = \sin\theta \, d\theta \, d\phi$ denotes the element of solid angle and $\delta^{\ell\ell'}$ is the Kronecker symbol. The integration is performed over the unit sphere, so that $0 \leq \theta \leq \pi$ and $0 \leq \phi \leq 2\pi$. The mode expansion of the complex polarization (4.40) is then of the form

$$h(\theta,\phi) = \sum_{\ell=2}^{+\infty} \sum_{m=-\ell}^{\ell} h_{\ell m} \, {}_{-2}Y^{\ell m}(\theta,\phi). \tag{4.44}$$

The GW modes $h_{\ell m}$ are extracted using the orthogonality property (4.43) by means of the surface integral

$$h_{\ell m} = \int d\Omega \, h(\theta,\phi) \, {}_{-2}Y^{\ell m *}(\theta,\phi), \tag{4.45}$$

where the star on the spin-weighted -2 harmonic indicates the complex conjugation. Therefore, the calculation of $h_{\ell m}$ requires the knowledge of the polarizations h_+ and $h_\times$ for an arbitrary value of the azimuthal angle ϕ of the direction $\widehat{\mathbf{N}}$. In Sec. 4.3 we have computed h_+ and $h_\times$ only for $\phi = 0$; however, a specific choice of the x-axis

orientation *cannot* be responsible for any information loss. Thus, we must be able to recover $h(\theta,\phi)$ from the expression of $h(\theta,0)$ alone.

The quantity h at a given point depends on a number of parameters, such as ι or the spin variables, and can actually be regarded as a function of θ, ϕ as well as a function of the whole set of parameters that possess a geometrical character. More precisely, we may write $h(\theta,\phi) = \overline{h}(\theta,\phi,\iota,\alpha,\Phi,\chi_n^x,\chi_n^y,\chi_n^z)$. Let us now introduce the projection basis $(\hat{\mathbf{x}}',\hat{\mathbf{y}}',\hat{\mathbf{z}}'=\hat{\mathbf{z}})$ obtained by applying a rotation of angle ϕ about the z-axis on the vectors of the original basis $(\hat{\mathbf{x}},\hat{\mathbf{y}},\hat{\mathbf{z}})$. Let us also associate to each variable of $\overline{h}$ a primed counterpart, which is defined in the same way as the unprimed variable but refers to the new basis rather than the original one. For instance, α' denotes the azimuthal angle of the orbital angular momentum measured from the fixed vector $\hat{\mathbf{x}}'$ instead of $\hat{\mathbf{x}}$. In particular, we have $\theta'=\theta$, $\phi'=0$, $\iota'=\iota$, $\alpha'=\alpha-\phi$. The phase Φ, defined as the angle $(\widehat{\mathbf{L}}_{\rm N}\times\hat{\mathbf{z}},\hat{\mathbf{n}}) = (\widehat{\mathbf{L}}_{\rm N}\times\hat{\mathbf{z}}',\hat{\mathbf{n}})$, is not affected by the transformation: $\Phi'=\Phi$. The x' and y' spin components can be obtained from the 2-dimensional formula for a passive rotation of angle ϕ, that is

$$\chi'^x_n = \chi^x_n\cos\phi + \chi^y_n\sin\phi\,, \tag{4.46}$$

$$\chi'^y_n = -\chi^x_n\sin\phi + \chi^y_n\cos\phi\,, \tag{4.47}$$

while the third component is left unchanged. With our conventions, the polarization vectors in the new basis remain equal to $\widehat{\mathbf{P}}$ and $\widehat{\mathbf{Q}}$ respectively. Therefore, the complex polarization is identical to that of the old frame. Moreover, by construction of the primed variables, the functional dependence of h is the same as before,

meaning that $h = \overline{h}(\theta, \phi, \iota, \alpha, \Phi, \chi_n^x, \chi_n^y, \chi_n^z) = \overline{h}(\theta', \phi', \iota', \alpha', \Phi', \chi'^x_n, \chi'^y_n, \chi'^z_n)$. Hence the important relation

$$\begin{aligned} h &\equiv \overline{h}(\theta, \phi, \iota, \alpha, \Phi, \chi_n^x, \chi_n^y, \chi_n^z) \\ &= \overline{h}(\theta, 0, \iota, \alpha - \phi, \Phi, \cos\phi\chi_n^x + \sin\phi\chi_n^y, -\sin\phi\chi_n^x + \cos\phi\chi_n^y, \chi_n^z)\,, \end{aligned} \quad (4.48)$$

where the function $\overline{h}(\theta, 0, \iota, \alpha, \chi_n^x, \chi_n^y, \chi_n^z)$ is given by Eqs. (4.34), (4.35) for the ι-expanded expressions or by Eqs. (A.2), (A.3) for the full ones.

At 1.5PN order, the GW polarizations decompose into a sum of 3 terms, $h_0(\theta, \iota, \alpha, \Phi) + \sum_{n=1,2} \boldsymbol{\chi}_n.\mathbf{h}_n(\theta, \iota, \alpha, \Phi)$, which shows that h may be written as

$$\begin{aligned} h_0(\theta, \iota, \alpha - \phi, \Phi) &+ \sum_{n=1,2} \big[e^{i\phi}\zeta_n^* k_n(\theta, \iota, \alpha - \phi, \Phi) \\ &+ e^{-i\phi}\zeta_n k_n^*(\theta, \iota, \alpha - \phi, \Phi) + \chi_n^z h_n^z(\theta, \iota, \alpha - \phi, \Phi)\big]\,, \end{aligned} \quad (4.49)$$

with $\zeta_n = (\chi_n^x + i\chi_n^y)/\sqrt{2}$ and $k_n = (h_n^x + ih_n^y)/\sqrt{2}$. Each mode $h_{\ell m}$ splits accordingly into 7 contributions: the spin-free term and 6 terms proportional to each of the spin variable components. These contributions are parametrized by a vector weight $m' = -1, 0, 1$, as well as the body label $n = 1, 2$ of the spins; $n = 0$ refers to quantities entering the spin-free part of h for which we also set $m' = 0$. As a result, for precessing binaries, the integral to compute $h_{\ell m}$ takes the form:

$$h_{\ell m} = \sum_{m'=-1}^{1} \sum_{n=1}^{2} X_{m',n} \int d\Omega\, K_{m',n}(\theta, \iota, \alpha - \phi, \Phi) e^{i(-m'-m)\phi}\, {}_{-2}Y^{\ell m *}(\theta, 0)\,, \quad (4.50)$$

where $X_{0,0} = 1$, $X_{0,n'} = \chi^z_{n'}$ (for $n' = 1, 2$), $X_{-1,n'} = \zeta^*_{n'}$, $X_{1,n'} = \zeta_{n'}$, $K_{0,0} = h_0$, $K_{0,n'} = h^z_{n'}$, $K_{-1,n'} = k_{n'}$ and $K_{1,n'} = k^*_{n'}$. By means of the change of variable $\phi \to \phi + \alpha$, we are able to factor out a complex exponential $e^{-i(m+m')\alpha}$ which contain all the dependence in α. Let us now focus henceforth on the case where the waveform has been expanded in powers of ι. As we shall explicitly see below, [see Eq. (4.56)], the $h_{\ell m}$'s are then made of: (i) a spin-free piece proportional to $e^{-im\alpha}$, (ii) two spin pieces proportional to $e^{-i(m-1)\alpha}$ and to ζ^*_1 or ζ^*_2 respectively, (iii) two spin pieces proportional to $e^{-i(m+1)\alpha}$ and to ζ_1 or ζ_2 respectively, (iv) two spin pieces proportional to $e^{-im\alpha}$ and to χ^z_1 or χ^z_2 respectively. In contrast to what happens in the non-spinning case, $h_{\ell m}$ is not in general proportional to $e^{-im\Phi}$ except for the terms that are free of ι, since both $\hat{\mathbf{n}}$ and $\hat{\boldsymbol{\lambda}}$ reduce to trigonometric functions of $\Phi + \alpha$ as $\iota \to 0$. The contributions to the polarization modes that are linear in ι involve couplings of the type $e^{-i(m+m')(\Phi+\alpha)} \cos\Phi$ or $e^{-i(m+m')(\Phi+\alpha)} \sin\Phi$ because the terms of first order in ι entering $\hat{\mathbf{n}}$ and $\hat{\boldsymbol{\lambda}}$ can only be linear combinations of $\iota \cos\Phi$ or $\iota \sin\Phi$ (or equivalently $\iota e^{\pm i\Phi}$). Couplings like $e^{-i(m+m')(\Phi+\alpha)} \cos^a\Phi \sin^b\Phi$, with $a, b \in \mathbb{N}$, arise at higher orders making the dependence in Φ more complicated. A close inspection to the results below [see Eqs. (4.56a)–(4.56r) with $\Psi \to \Phi$] confirm these expectations. Beware that our mode normalization is tuned to factor out the exponential factors $e^{-im\alpha}$.

The structure of the modes is much more complicated for precessing binaries than for non-precessing binaries. When the orbital angular momentum is aligned with the total angular momentum ($\iota = 0, \alpha = \pi$), note that a rotation by ϕ about the z-axis produces an offset in the orbital phase angle, so that

$$\overline{h}(\theta, \phi, \Phi) = \overline{h}(\theta, 0, \Phi - \phi)\,. \tag{4.51}$$

This ensures that only terms proportional to $e^{-im\Phi}$ contribute to the integral over ϕ to compute $h_{\ell m}$. In the precessing case, a rotation by ϕ produces an offset in the α angle, and so terms with different powers of $e^{-i\Phi}$ can contribute to the same $h_{\ell m}$ mode. As we will see below, these terms with different powers of $e^{-i\Phi}$ interfere to produce rather complicated modulations to the modes on the *orbital* time scale. Since the precessional motion is typically much slower than the orbital motion (several orbital cycles are completed in any precessional cycle for the systems we consider), it may be surprising that the relatively slow precessional motion can produce such rapid oscillations in the modes. This is simply a breakdown of the nice structure (i.e. that $h_{\ell m} \propto e^{-im\Phi}$) of the $h_{\ell m}$ modes in the precessing case. Note however, that what is actually observed are the gravitational wave *polarizations*. In the polarizations, precessional effects are indeed on a slower time scale than the orbital motion. They modulate the "envelope" of the waveform, rather than create orbital timescale interference.

A useful property of $\overline{h}$ coming from the arbitrariness of the body labeling is that it must be invariant in the exchange of particles 1 and 2: $m_1 \leftrightarrow m_2$, $\chi_1 \leftrightarrow \chi_2$, $\mathbf{n} \to -\mathbf{n}$, $\mathbf{v} \to -\mathbf{v}$. Under this transformation, the direction of the angular momentum $\widehat{\mathbf{L}}$ remains invariant hence $\boldsymbol{\lambda} \to -\boldsymbol{\lambda}$. The orbital frequency $\omega_{\rm orb} = (\mathbf{v} \cdot \boldsymbol{\lambda})$ is unchanged as well as the direction of the total angular momentum, due to its structure and parity. Therefore, the phase Φ becomes $(\hat{\mathbf{x}}_L, -\hat{\mathbf{n}}) = \Phi + \pi$ whereas the angles α and

ι are unaffected. This yields the relation

$$\overline{h}(\theta,\phi,\iota,\alpha,\Phi,\chi_1^x,\chi_2^x,\chi_1^y,\chi_2^y,\chi_1^z,\chi_2^z) = [\overline{h}(\theta,\phi,\iota,\alpha,\Phi+\pi,\chi_2^x,\chi_1^x,\chi_2^y,\chi_1^y,\chi_2^z,\chi_1^z)]_{\delta\to-\delta}\,. \tag{4.52}$$

The previous identity may be supplemented by another one which originates from the classical parity invariance of physics: for any given time instant t, the waveform resulting from the stress-energy tensor parametrized by the world-lines $\mathbf{x}_n$ and the spins $\boldsymbol{\chi}_n$ must have the same value at point $\mathbf{x}$ as the waveform resulting from $-\mathbf{x}_n$ and $+\boldsymbol{\chi}_n$ at point $-\mathbf{x}$. Taking into account the transformation of the polarization vectors under parity, this means for the function $\overline{h}$:

$$\overline{h}(\theta,\phi,\iota,\alpha,\Phi,\chi_n^x,\chi_n^y,\chi_n^z) = \overline{h}^*(\pi-\theta,\phi+\pi,\iota,\alpha,\Phi+\pi,\chi_n^x,\chi_n^y,\chi_n^z)\,. \tag{4.53}$$

The above formula allows us to express the modes $h_{\ell m}$ in terms of the modes $h_{\ell\,-m}$ by performing the change of variable $\theta\to\pi-\theta$ and $\phi\to\phi+\pi$ in Eq. (4.45). The first factor of the integrand can be then rewritten as $\overline{h}^*(\theta,\phi,\iota,\alpha,\Phi+\pi,\chi_n^x,\chi_n^y,\chi_n^z)$ making use of Eq. (4.53). The second factor ${}_{-2}Y^{\ell m*}(\pi-\theta,\phi+\pi)$ may be transformed by means of two important symmetry properties of the spin-weighted spherical harmonics: ${}_{-2}Y^{\ell m}(\pi-\theta,\phi+\pi) = (-1)^\ell\,{}_{+2}Y^{\ell m}(\theta,\phi)$ and ${}_{+2}Y^{\ell m}(\theta,\phi) = (-1)^m\,{}_{-2}Y^{\ell\,-m*}(\theta,\phi)$, which leads to the new expression $(-1)^{m+\ell}\,{}_{-2}Y^{\ell\,-m}(\theta,\phi)$ for this factor. As a consequence, the link between $h_{\ell m}(\Phi)\equiv\int d\Omega\,\overline{h}(\theta,\phi,\iota,\alpha,\Phi,\chi_n^x,\chi_n^y,\chi_n^z)\,{}_{-2}Y^{\ell\,m*}(\theta,\phi)$ and

$h_{\ell\,-m}(\Phi)$ is given by

$$\begin{aligned} h_{\ell m}(\Phi) &= (-1)^{m+\ell} \int d\Omega\, \overline{h}^{*}(\theta,\phi,\iota,\alpha,\Phi+\pi,\chi_n^x,\chi_n^y,\chi_n^z)\, {}_{-2}Y^{\ell\,-m}(\theta,\phi) \\ &= (-1)^{\ell+m} h^{*}_{\ell\,-m}(\Phi+\pi) \end{aligned} \tag{4.54}$$

The explicit expressions for the modes $h_{\ell m}$ are obtained by inserting Eq. (4.48) into the surface integral (4.43). We normalize them in such a way that the leading order mode starts with coefficient 1. Posing

$$h_{\ell m} = -\frac{(2M\nu v^2)}{D_L}\sqrt{\frac{16\pi}{5}}\, e^{-im(\Psi+\alpha)}\, \hat{h}_{\ell m}\,, \tag{4.55}$$

and expanding in the inclination angle ι, we arrive at [9]

$$\begin{aligned} \hat{h}_{22} &= 1 + \frac{1}{3}e^{i\Psi}\delta v\iota + v^2\left\{\frac{1}{42}(-107+55\nu) - \frac{1}{2}e^{i(\alpha+\Psi)}\Big[\chi_a^x - i\chi_a^y + \delta(\chi_s^x - i\chi_s^y)\Big]\right\} \\ &\quad - \frac{\iota^2}{2} + v^3\left[2\pi - \frac{4\delta\chi_a^z}{3} + \frac{4}{3}(-1+\nu)\chi_s^z\right] + \mathcal{O}\left(\frac{1}{c^4}\right)\,, \end{aligned} \tag{4.56a}$$

$$\begin{aligned} \hat{h}_{21} &= -\frac{\delta v}{3} + e^{-i\Psi}\iota + \frac{v^2}{2}(\chi_a^z + \delta\chi_s^z) + \delta\,\iota^2\, v\left(\frac{5}{12} - \frac{1}{4}e^{2i\Psi}\right) \\ &\quad + v^3\Bigg\{ - e^{i(\alpha+\Psi)}\left[\delta\,(\chi_a^x - i\chi_a^y) + \left(1-\frac{\nu}{2}\right)(\chi_s^x - i\chi_s^y)\right] \\ &\quad + e^{-i(\alpha+\Psi)}\left[\delta(\chi_a^x + i\chi_a^y) + \left(1+\frac{5}{6}\nu\right)(\chi_s^x + i\chi_s^y)\right] + \frac{\delta}{84}(17-20\nu)\Bigg\} \\ &\quad + v^2\iota\left\{\frac{e^{-i\Psi}}{42}(-107+55\nu) + \frac{1}{4}\Big(\chi_a^x - i\chi_a^y + \delta(\chi_s^x - i\chi_s^y)\Big)e^{i\alpha}\Big(-1+e^{2i\Psi}\Big)\right\} \\ &\quad + \frac{\iota^3}{4}\left(-\frac{5}{3}e^{-i\Psi} - e^{3i\Psi}\right) + \mathcal{O}\left(\frac{1}{c^4}\right)\,, \end{aligned} \tag{4.56b}$$

[9] In the case of spins aligned or anti-aligned with the Newtonian angular momentum, the modes $(2,2)$, $(2,1)$ and $(3,2)$ were also computed in Ref. [232]. We fully agree with their results.

$$\hat{h}_{20} = \frac{1}{2}\sqrt{\frac{3}{2}}\Big\{\frac{v^2}{3}\Big[-e^{i(\alpha+\Psi)}\Big(\chi_a^x - i\chi_a^y + \delta(\chi_s^x - i\chi_s^y)\Big)$$
$$+ e^{-i(\alpha+\Psi)}\Big(\chi_a^x + i\chi_a^y + \delta(\chi_s^x + i\chi_s^y)\Big)\Big] + \frac{4i}{3}v\,\iota\,\delta\sin\Psi + 2\iota^2\cos 2\Psi$$
$$- \frac{4i}{3}v^2\iota\sin\Psi(\chi_a^z + \delta\chi_s^z)\Big\} + \mathcal{O}\left(\frac{1}{c^4}\right), \tag{4.56c}$$

$$\hat{h}_{33} = -\frac{3}{4}\sqrt{\frac{15}{14}}\Big\{\delta v + v^3\Big[2\delta(-2+\nu) + \frac{16}{9}e^{i(\alpha+\Psi)}\nu(\chi_s^x - i\chi_s^y)\Big]$$
$$- \frac{4}{9}e^{i\Psi}\iota v^2(-1+3\nu) + \frac{\delta v\iota^2}{4}\Big(-3 + \frac{e^{2i\Psi}}{9}\Big)\Big\} + \mathcal{O}\left(\frac{1}{c^4}\right), \tag{4.56d}$$

$$\hat{h}_{32} = -\frac{9}{8}\sqrt{\frac{5}{7}}\Big[\frac{8}{27}v^2(-1+3\nu) + \delta v\iota\Big(e^{-i\Psi} - \frac{e^{i\Psi}}{27}\Big) - \frac{32}{27}v^3\nu\chi_s^z\Big] + \mathcal{O}\left(\frac{1}{c^4}\right), \tag{4.56e}$$

$$\hat{h}_{31} = -\frac{1}{12\sqrt{14}}\Big\{\delta v + v^3\Big[-\frac{2}{3}\delta(4+\nu) - 16e^{-i(\alpha+\Psi)}\nu(\chi_s^x + i\chi_s^y)\Big]$$
$$+ 20v^2\iota(-1+3\nu)e^{-i\Psi} + \frac{\delta v\iota^2}{2}\Big(-\frac{11}{2} + \frac{135}{2}e^{-2i\Psi} - 3e^{2i\Psi}\Big)\Big\} + \mathcal{O}\left(\frac{1}{c^4}\right), \tag{4.56f}$$

$$\hat{h}_{30} = -\frac{1}{2\sqrt{42}}\delta v\iota\cos\Psi + \mathcal{O}\left(\frac{1}{c^4}\right), \tag{4.56g}$$

$$\hat{h}_{44} = \frac{8}{9}\sqrt{\frac{5}{7}}v^2(1-3\nu) + \mathcal{O}\left(\frac{1}{c^4}\right), \tag{4.56h}$$

$$\hat{h}_{43} = \frac{8}{9}\sqrt{\frac{10}{7}}\Big[\frac{81}{320}v^3\delta(-1+2\nu) + v^2\iota(1-3\nu)\Big(e^{-i\Psi} - \frac{e^{i\Psi}}{16}\Big)\Big] + \mathcal{O}\left(\frac{1}{c^4}\right), \tag{4.56i}$$

$$\hat{h}_{42} = \frac{\sqrt{5}}{63}v^2(1-3\nu) + \mathcal{O}\left(\frac{1}{c^4}\right), \tag{4.56j}$$

$$\hat{h}_{41} = \frac{1}{21}\sqrt{\frac{5}{2}}\Big[\frac{\delta v^3}{20}(-1+2\nu) + v^2\iota(1-3\nu)e^{-i\Psi}\Big] + \mathcal{O}\left(\frac{1}{c^4}\right), \tag{4.56k}$$

$$\hat{h}_{40} = \mathcal{O}\left(\frac{1}{c^4}\right), \tag{4.56l}$$

$$\hat{h}_{55} = -\frac{625}{96\sqrt{66}}\delta v^3(1-2\nu) + \mathcal{O}\left(\frac{1}{c^4}\right), \tag{4.56m}$$

$$\hat{h}_{54} = \mathcal{O}\left(\frac{1}{c^4}\right), \tag{4.56n}$$

$$\hat{h}_{53} = -\frac{9}{32}\sqrt{\frac{3}{110}}v^3\delta(1-2\nu) + \mathcal{O}\left(\frac{1}{c^4}\right) , \tag{4.56o}$$

$$\hat{h}_{52} = \mathcal{O}\left(\frac{1}{c^4}\right) , \tag{4.56p}$$

$$\hat{h}_{51} = -\frac{1}{288\sqrt{385}}\delta v^3(1-2\nu) + \mathcal{O}\left(\frac{1}{c^4}\right) , \tag{4.56q}$$

$$\hat{h}_{50} = \mathcal{O}\left(\frac{1}{c^4}\right) . \tag{4.56r}$$

In Appendix B we display the modes h_{22}, h_{33}, and h_{21} for generic inclination angle ι. The modes $\hat{h}_{\ell m}$ for $m < 0$ are derived from Eq. (4.56) by means of the relation $\hat{h}_{\ell -m}(\Phi) = (-1)^\ell \hat{h}^*_{\ell m}(\Phi+\pi)$. The non-precessing expressions are obtained by setting $\iota = 0$ and $\alpha = \pi$. Notice that when $h_{\ell m}(\Phi)$ does not depend on Φ, we have simply $\hat{h}_{\ell -m} = (-1)^\ell \hat{h}^*_{\ell m}$. For comparison with the modes of Refs. [201, 27] in the non-spinning case, it is important to be aware that the origin of the azimuthal angle there differs from ours by $-\pi/2$, which produces an extra factor $(-i)^m$ (respectively i^m) with respect to us in the modes (respectively in the spin-weighted spherical harmonics).

Finally, let us emphasize that the (ℓ, m) modes defined by Eq. (4.44) depend on the particular choice of the source frame. In fact, they are functions of the spin and angular momentum components with respect to the $(\hat{\mathbf{x}}, \hat{\mathbf{y}}, \hat{\mathbf{z}})$ basis introduced in Sec. 4.2. As there is no canonical way to fix the reference frame for precessing binaries because of the secular but perpetual variation of the direction $\mathbf{J}/|\mathbf{J}|$, it is important to be able to relate the $\hat{h}_{\ell m}$'s given in Eq. (4.56) to the polarization modes $h'_{\ell m}$ computed in another frame with different polarization vectors. Under a passive

rotation

$$R^{i}{}_{j}(A,B,\Gamma) = \begin{pmatrix} \cos A & -\sin A & 0 \\ \sin A & \cos A & 0 \\ 0 & 0 & 1 \end{pmatrix} \begin{pmatrix} \cos B & 0 & \sin B \\ 0 & 1 & 0 \\ -\sin B & 0 & \cos B \end{pmatrix} \begin{pmatrix} \cos\Gamma & -\sin\Gamma & 0 \\ \sin\Gamma & \cos\Gamma & 0 \\ 0 & 0 & 1 \end{pmatrix},$$

the (ℓ, m) modes transform in the same way as they would in the case of a standard spherical harmonics decomposition [239, 240]. In fact, the spin-weighted -2 spherical harmonics are precisely devised to ensure this property for the modes of a spin-weighted -2 object [237]. The law of transformation for the $h_{\ell m}$'s is given by

$$h'_{\ell m}(\Phi', \alpha', \iota', \chi_n'^{x'}, \chi_n'^{y'}, \chi_n'^{z'}) = \sum_{m=-\ell}^{\ell} D^{*\ell}_{mm'}(A,B,\Gamma)\, h_{\ell m}(\Phi, \alpha, \iota, \chi_n^x, \chi_n^y, \chi_n^z)\,, \quad (4.57)$$

where the primed quantities refer to the new frame and where $D^{\ell}_{m'm}$ is the unitary Wigner matrix [237]

$$D^{\ell}_{m'm}(A,B,\Gamma) = (-1)^{m'} \sqrt{\frac{4\pi}{2\ell+1}}\, {}_{-m'}Y^{\ell m}(B,A)\, e^{im'\Gamma} \quad (4.58)$$

with the convention of Landau-Lifshitz [238]. The new angles read

$$\iota' = \arccos\Big[\cos B\cos\iota - \cos(\Gamma+\alpha)\sin B\sin\iota\Big]\,, \quad (4.59a)$$

$$\begin{aligned}\alpha' &= \arccos\cos\alpha' \\ &= \arccos\frac{\cos A\big[\cos\iota\sin B + \cos B\cos(\Gamma+\alpha)\sin\iota\big] - \sin A\sin\iota\sin(\Gamma+\alpha)}{\sqrt{1-\big(\cos B\cos\iota - \cos(\Gamma+\alpha)\sin B\sin\iota\big)^2}}\end{aligned}$$

$$\text{if}\cos\iota\sin A\sin B+\sin\iota\big[\cos B\cos(\Gamma+\alpha)\sin A+\cos A\sin(\Gamma+\alpha)\big]\geq 0\,, \tag{4.59b}$$

$$\alpha'=2\pi-\arccos\cos\alpha'\quad\text{otherwise}\,, \tag{4.59c}$$

$$\begin{aligned}\Phi' &= \arccos\cos\Phi'\\ &= \arccos\Bigg[\Bigg(\cos B\cos\Phi\sin\iota-\sin B\sin\Gamma\left(\cos\iota\cos\Phi\sin\alpha+\cos\alpha\sin\Phi\right)+\\ &\quad\cos\Gamma\sin B\left(\cos\iota\cos\alpha\cos\Phi-\sin\alpha\sin\Phi\right)\Bigg)\\ &\quad/\sqrt{1-\left(\cos B\cos\iota-\cos(\Gamma+\alpha)\sin B\sin\iota\right)^2}\Bigg]\\ &\quad\text{if}\cos\Phi\sin B\sin(\Gamma+\alpha)+\left(\cos\iota\cos(\Gamma+\alpha)\sin B+\cos B\sin\iota\right)\sin\Phi\geq 0\,,\end{aligned} \tag{4.59d}$$

$$\Phi'=2\pi-\arccos\cos\Phi'\quad\text{otherwise}\,. \tag{4.59e}$$

When the direction of the total angular momentum used to built the new frame coincides with that of $\mathbf{J}_0$, which results in the equality $\hat{\mathbf{z}}'=\hat{\mathbf{z}}$, the Euler angle B vanishes. Then, it can be checked from Eqs. (4.59d) and (4.59e) that $\Phi'=\Phi$ as expected.

4.5 Features of gravitational-wave modes for precessing binaries on nearly circular orbits

We now study how spin effects change the waveform modes for generic precessing binaries. We consider two maximally spinning configurations with mass ratios 1:1 and 4:1. We label the spin configurations with the angles $\{\theta_1,\phi_1,\theta_2,\phi_2\}$, where

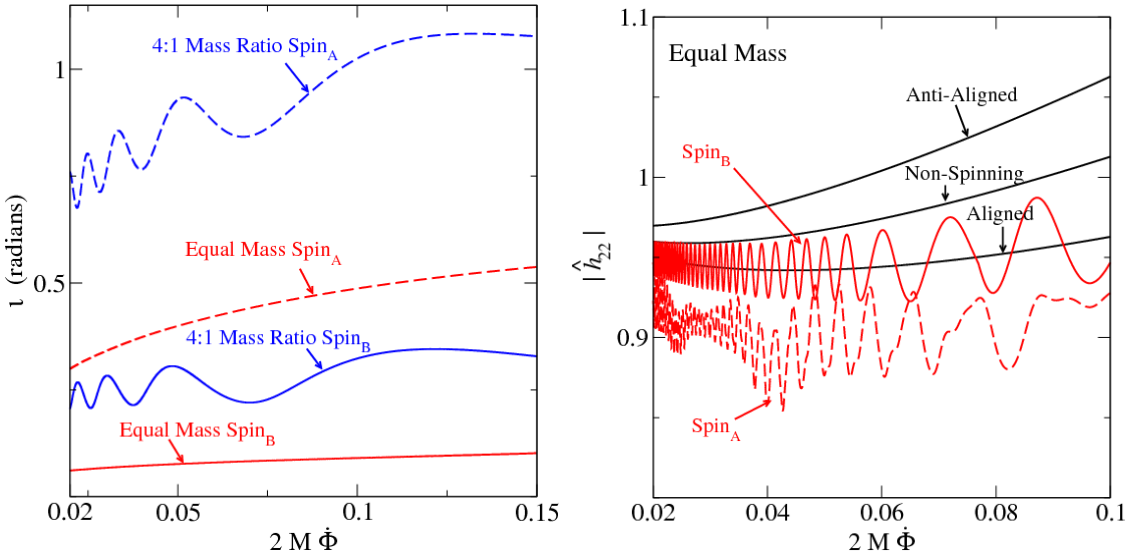

Figure 4.2: The left panel shows the inclination angle of the orbital angular momentum relative to the total angular momentum, ι, as a function of $2M\dot{\Phi}$ for binaries with mass ratios 1:1 and 4:1, having initial spin orientations relative to the orbital angular momentum: $\mathrm{Spin_A} = \{\theta_1 = \pi/2, \phi_1 = 0, \theta_2 = \pi/2, \phi_2 = \pi/2\}$ and $\mathrm{Spin_B} = \{\theta_1 = \pi/6, \phi_1 = \pi/4, \theta_2 = \pi/6, \phi_2 = \pi\}$. The right panel compares the modulus of h_{22} for the two precessing spin configurations with the non-spinning, aligned and anti-aligned cases for equal masses. The computations use waveforms accurate to 1.5PN in amplitude and phase evolved with the precession equations at 1.5PN order [see Eqs. (4.29), (4.36), (4.38), and (4.39)]. Note that these plots (and those of Figs. 3 and 4) begin at $2\,M\,\dot{\Phi} = 0.02$ which is approximately where the dominant second harmonic from a binary of total mass $16\,M_\odot$ enters the LIGO band at 40 Hz and where the second harmonic from a binary of total mass $6.5 \times 10^6\,M_\odot$ enters the LISA band at 10^{-4} Hz.

$\{\theta_i, \phi_i\}$ describe the orientation of the spin vector of the $i^{\rm th}$ body relative to the orbital angular momentum in the initial configuration, which we take to be a circular orbit with $M\omega_{\rm orb} = 0.001$. We use the full expressions for the $h_{\ell m}$'s (i.e., the expressions that have not been expanded in ι) as given in Appendix B and normalized following Eq. (4.55), but we replace Ψ with Φ.

After evolving through 1.5PN order all dynamical quantities they depend on [see Eqs. (4.29), (4.36), (4.38), and (4.39)], we compute the modulus — more often referred to as the absolute value — of a sample of modes. Considering the complicated structure of the $h_{\ell m}$'s, their qualitative behavior in the presence of spins is discussed here in terms of the ι-expanded formulae (4.56). Let us focus on two spin configurations. The configuration $\text{Spin}_{\rm A} = \{\pi/2, 0, \pi/2, \pi/2\}$ has both spin vectors in the orbital plane, meaning a relatively large inclination angle. The configuration $\text{Spin}_{\rm B} = \{\pi/6, \pi/4, \pi/6, \pi\}$ has a smaller component of total spin transverse to the orbital angular momentum, hence a smaller inclination angle. In Figs. 4.3 and 4.4 we plot the amplitude of the $\hat{h}_{\ell m}$ over the frequency range $2\,M\,\dot{\Phi} = 0.02$–0.15, the upper frequency being reached roughly 2 cycles before merger, for an equal-mass, non-spinning binary [63]. For a binary of total mass $16\,M_\odot$, the dominant second harmonic varies over the frequency range 40–300 Hz. For a $6.5 \times 10^6\,M_\odot$ binary, this range is shifted to 10^{-4}–7.5×10^{-4} Hz.

The left panel of Fig. 4.2 shows the inclination angle ι as a function of the dimensionless frequency $2\,M\,\dot{\Phi}$. We see that the inclinations are much larger in the case of 4:1 mass-ratio than for equal masses. Moreover, the inclination increases monotonically in the equal-mass case, whereas the 4:1 mass ratio exhibits nutation,

since the inclination oscillates, but grows on average. These observations can be explained as follows. At early times, when the binary has a large orbital separation, we have $|\mathbf{L}| \gg |\mathbf{S}|$, where $\mathbf{S} = \mathbf{S}_1 + \mathbf{S}_2$ is the total spin, so that $\mathbf{J} = \mathbf{L} + \mathbf{S}$ and $\mathbf{L}$ are nearly aligned. Radiation reaction causes $|\mathbf{L}|$ to decrease, making $\mathbf{J}$ move away from $\mathbf{L}$ and toward $\mathbf{S}$. This is why the inclination angle, ι, grows on average as the frequency increases. The absence of oscillations for the inclination angle ι in the equal-mass case can be explained by the fact that we are evolving the dynamics, in particular the precession equations (4.36), through 1.5PN order, i.e., we are neglecting spin-spin effects. Due to the equality $\mathbf{\Omega}_1 = \mathbf{\Omega}_2$ at this accuracy level, the precession equations simplify then to a single equation of the form $d\mathbf{S}/dt = \mathbf{\Omega} \times \mathbf{S}$. In the absence of radiation reaction, $\mathbf{S}$ precesses around a fixed direction with a constant frequency, and the inclination is constant (apart from the increase produced by radiation reaction). For unequal masses this symmetry does not exist, with the consequence that one must solve two coupled equations for $\mathbf{S}_1$, $\mathbf{S}_2$ instead of a single equation for $\mathbf{S}$. The motion of the spin vectors is thus more complicated. Schematically, they rotate about a fixed direction while also bobbing up and down [241].

The right panel of Fig. 4.2 plots, for the case of equal masses, the absolute value of the h_{22} mode normalized to its Newtonian order expression, $\hat{h}_{22}$, for both precessing spin configurations as well as the non-spinning, aligned and anti-aligned cases. One interesting feature is that the aligned and anti-aligned cases do not bound the absolute value of the modes for generic spin configurations. This and other features of the plot can be understood from the ι expansion (4.56a) of $\hat{h}_{22}$,

which contains four spin corrections. The first correction, $-\iota^2/2$, is zero for the aligned and anti-aligned cases, while it decreases the absolute value of the $\hat{h}_{22}$ mode for all other spin configurations. If ι is comparable to 1 radian, it can be a significant correction. The second correction, $(1/3)e^{i\Psi}\delta v\iota$, vanishes for equal masses. For unequal masses, it interferes with the non-spinning terms and, because it has a different dependence on the orbital phase, produces oscillations in the absolute value of $\hat{h}_{22}$. Next, the 1PN order spin correction, $-(v^2/2)e^{i(\alpha+\Psi)}[\chi_a^x - i\chi_a^y + \delta(\chi_s^x - i\chi_s^y)]$, generates oscillations that depend on the spin vector components transverse to the total angular momentum. Finally, the 1.5PN order spin correction, $v^3[-4\delta\chi_a^z/3 + (4/3)(-1+\nu)\chi_s^z]$, lowers (raises) the absolute value of $\hat{h}_{22}$ for spins aligned (anti-aligned) with the total angular momentum. It is solely responsible for the spread between the aligned and anti-aligned cases, as the other corrections all vanish then.

A similar analysis can be applied to understand the behavior of the other modes. As an illustration, we plot in Fig. 4.3 all of the $\ell = 2$ modes for mass ratios 1:1 and 4:1. The $\hat{h}_{21}$ mode (4.56b) is zero for non-spinning equal mass binaries. However, it contains several spin corrections and can have significant amplitude for precessing binaries, particularly for large ι. It can exhibit complicated modulation, as its different spin corrections interfere with one another. The $\hat{h}_{20}$ mode (4.56c) also has several spin corrections, most notably $2\,\iota^2\,\cos\Psi$. This correction is responsible for the large oscillations in the absolute value of $\hat{h}_{20}$. Note that in the late stages of the inspiral evolution for the 4:1 mass-ratio case, where $\iota \sim 1$ radian, these oscillations in the absolute value of $\hat{h}_{20}$ peak near the absolute value of $\hat{h}_{22}$. The other spin corrections in $\hat{h}_{20}$ are responsible for the further modulations of the absolute

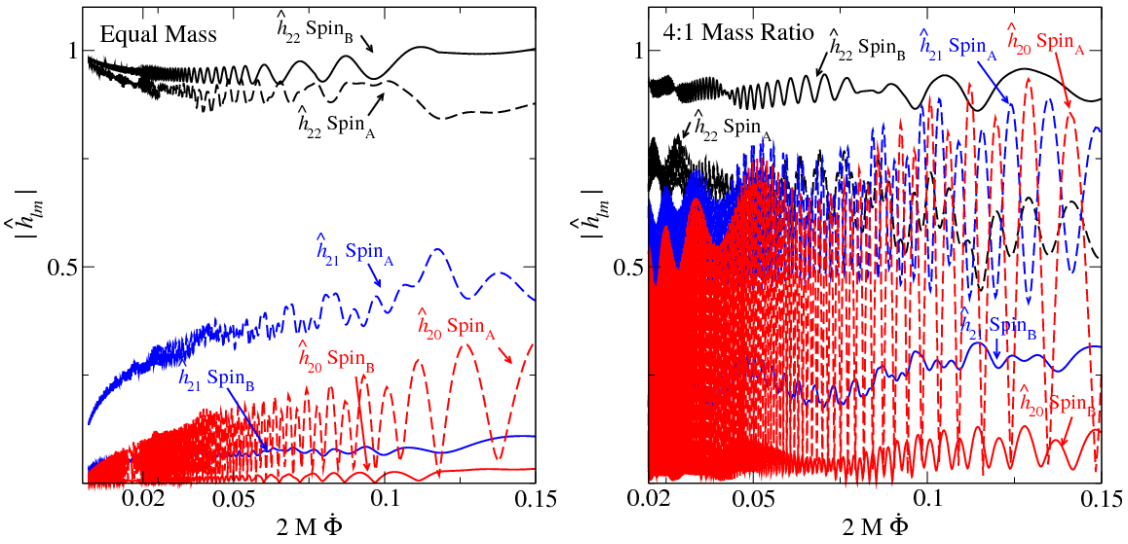

Figure 4.3: We plot the modulus of the $\ell = 2$ modes for mass ratios 1:1 (left panel) and 4:1 (right panel) with the spin configurations described in Fig. 4.2. The computations use waveforms accurate to 1.5PN order in amplitude and phase evolved with precession equations at 1.5PN order. The dashed lines are the larger ι configuration (Spin_A) and the solid lines are the smaller ι configuration (Spin_B). We see that as ι increases, the modulus of $\hat{h}_{22}$ decreases while the modulus of the other $\ell = 2$ modes increases. This effect becomes more pronounced when the mass ratio is more extreme.

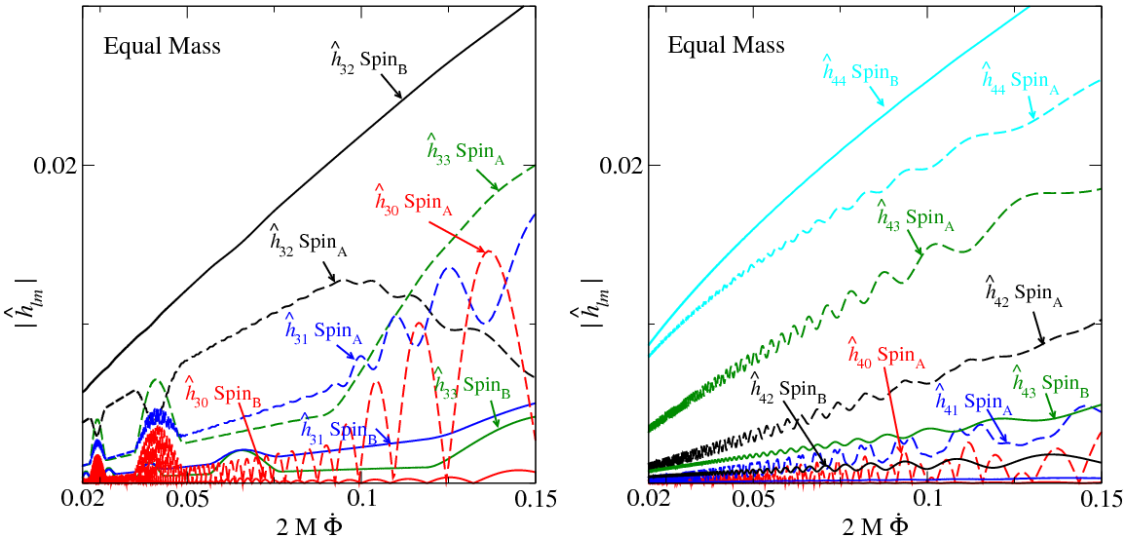

Figure 4.4: We plot the modulus of the $\ell = 3$ modes (left panel) and $\ell = 4$ modes (right panel) for equal masses with the spin configurations described in Fig. 4.2. The computations use waveforms accurate to 1.5PN order in both amplitude and phase evolved by means of the 1.5PN precession equations. The dashed lines refer to the larger ι configuration (Spin_A), the solid lines to the smaller iota configuration (Spin_B). We see a redistribution of power among the modes similar to Fig. 4.3. As ι increases, the largest modes for the non-precessing cases ($|\hat{h}_{32}|$ and $|\hat{h}_{44}|$) become smaller, while the other modes become larger.

value.

Figure 4.4 plots the absolute value of the $\ell = 3$ and $\ell = 4$ modes for equal masses. Note that these modes are about two orders of magnitude smaller than the $\ell = 2$ modes. This remains true in the non-spinning case for the mass ratios we consider. In the case of non-spinning, equal mass binaries, for $\ell = 3$ only the $\hat{h}_{32}$ mode (4.56e) is non-zero. The 1.5PN order spin correction decreases (increases) this mode's absolute value if the spins are aligned (anti-aligned) with the total angular momentum, in a similar way as in the $\hat{h}_{22}$ mode. For unequal masses, the $\hat{h}_{32}$ mode (4.56e) also has an interference term proportional to ι. The other $\ell = 3$ modes are non-zero for generic precessing binaries, and generally have larger absolute values

for larger inclinations. In the left panel of Fig. 4.4, we indeed observe that $|\hat{h}_{33}|$, $|\hat{h}_{31}|$, and $|\hat{h}_{30}|$ are greater for the configuration Spin_A than for Spin_B. For $\ell = 4$, only the $\hat{h}_{44}$ and $\hat{h}_{42}$ modes (4.56h), (4.56j) are non-zero for non-spinning, equal-mass binaries, with $\hat{h}_{44}$ being the largest. Though the ι-expanded form of the $\hat{h}_{44}$, $\hat{h}_{42}$ and $\hat{h}_{40}$ modes in Eq. (4.56) do not have any spin corrections through $\mathcal{O}(1/c^3)$, we do see spin effects in all of the $\ell = 4$ modes when we plot the full expressions accurate through v^3. The v^2 and v^3 coefficients in the full expressions for the $\hat{h}_{44}$, $\hat{h}_{42}$ and $\hat{h}_{40}$ modes depend on the inclination ι but *not* on the spin vector components and this dependence is such that if we treat ι as a $1/c$ correction by performing a Taylor expansion in powers of ι, then the spin terms are proportional to $v^2\,\iota^2$, $v^3\,\iota$ and higher order in ι. They are thus considered as higher order corrections in the ι expansion, though they are present when we expand only in powers of v. None of the $\ell = 4$ modes contain any spin corrections proportional to the spin vector components through order v^3. Those corrections would appear only at higher order in v.

While we have plotted the $\ell = 3$ and $\ell = 4$ modes solely for equal masses, we have also studied these modes for 4:1 mass-ratio binaries. We find that they are affected by the change of mass ratio in much the same way as the $\ell = 2$ modes: the redistribution of signal among the $\ell = 3$ and $\ell = 4$ modes is more pronounced for asymmetric binaries than for equal mass binaries. However, even for 4:1 binaries with large ι (Spin_A) spin configuration, all of the $\ell = 3$ and $\ell = 4$ modes are still one or two orders of magnitude smaller than $\hat{h}_{22}$, whereas the $\hat{h}_{21}$ and $\hat{h}_{20}$ modes can be comparable to $\hat{h}_{22}$. The reason is essentially that $\hat{h}_{21}$ and $\hat{h}_{20}$ have ι corrections at

leading order in v, while ι corrections to the $\ell = 3$ and $\ell = 4$ modes all appear at higher order, and so they do not have as strong an effect as for $\hat{h}_{21}$ and $\hat{h}_{20}$.

By examining the absolute values of the $\hat{h}_{\ell m}$ modes for precessing binaries, we see that they can be significantly altered by the motion of the orbital plane relative to the frame used to perform the mode decomposition and the signal may be redistributed among the modes as observed in Ref. [240]. This suggests that *all* modes, not just the dominant ones for non-spinning binaries, are needed to accurately describe the waveforms emitted from precessing binary systems, especially for asymmetric binaries and binaries with large inclinations where this redistribution of signal among the modes is most dramatic.

Let us close this section with a few comments about the applicability of the full and ι-expanded expressions for the modes and the possibility of combining them with higher order non-spinning corrections. We find that the absolute values of the full and ι-expanded $\hat{h}_{\ell m}$ modes are often quite close to each other for relatively small ι. For inclinations less than half a radian (30°), the difference in $|\hat{h}_{22}|$ is typically of a few percent. For ι comparable to or larger than a radian (60°), significant differences between the full and ι-expanded modes develop and the absolute values may differ by $\sim$ 10–100% when $\iota \geq 1$ radian. Nonetheless, the ι-expanded modes are very useful in understanding the qualitative behavior of precessing binaries, even for inclinations ~ 1 radian, albeit they should not be used for precise quantitative studies of binaries with large inclination angles.

In Refs. [201, 27], expressions of the modes are given to 3PN order for non-spinning binaries. We have compared their absolute values to that of the corre-

sponding quantities truncated at 1.5PN order, which has shown us that they typically differ by $\sim$ 1–10%. For example, the absolute value of the 1.5PN and 3PN order h_{22} modes for equal-mass binaries differ by less than 1% at $2M\,\dot{\Phi} = 0.01$ and by about 3% at $2M\,\dot{\Phi} = 0.05$ or $2M\,\dot{\Phi} = 0.12$. The other modes typically have a larger difference. The 1.5PN order and highest known order absolute values for h_{32}, h_{44} and h_{42} differ by about 5–15% over this same frequency range for equal mass binaries. For 4:1 mass ratio binaries, the differences in absolute value are similar.

Known higher-order non-spinning terms can actually be included in the amplitude if enough care is taken. In the non-precessing case, the modes $h_{\ell m}$ are proportional to $e^{-i\,m\,\Psi}$, as in the non-spinning case, because $\hat{\mathbf{n}}$ and $\hat{\boldsymbol{\lambda}}$ appearing in the strain tensor h_{ij} are trigonometric functions of the orbital phase Φ. In constructing the $h_{\ell m}$'s from h_{ij}, they generate an exponential dependence on multiples of Φ. However, for the case of a precessing binary with small ι, $\hat{\mathbf{n}}$ and $\hat{\boldsymbol{\lambda}}$ are trigonometric functions of $\Phi + \alpha$. Thus, the $h_{\ell m}$'s contain then all of the non-spinning terms, but with the substitution $\Psi \to \Psi + \alpha$. The situation is different for the general precessing case. The vectors $\hat{\mathbf{n}}$ and $\hat{\boldsymbol{\lambda}}$ depend on Φ, α, and ι, and the resulting $h_{\ell m}$ have a complicated dependence on all three of these quantities that cannot be simply related to the non-spinning case. These considerations show that it is only for binaries with a small inclination (or no inclination) that we can readily construct the $h_{\ell m}$'s with spin effects up to 1.5PN order and non-spinning corrections up to 3PN order. For spins (anti-)aligned it is trivial to add the higher-order non-spinning corrections of Refs. [201, 27] to the $h_{\ell m}$ given in Eq. (4.56). For precessing binaries with small inclinations, they can be added to our expressions in Eq. (4.56) with

the substitution $\Psi \to \Psi + \alpha$. For general precessing binaries, it is not so simple to include higher-order non-spinning corrections to the full expressions for the $h_{\ell m}$ given in Appendix B. To do this properly, we would need the spin terms at the same order as the non-spinning terms and repeat the derivation of the $h_{\ell m}$ to a higher order.

4.6 Ready-to-use frequency-domain templates for spinning, non-precessing binaries

4.6.1 Gravitational-wave polarizations in time domain

In the non-precessing case, the orbital angular momentum points in a fixed direction which we take to be the z-axis (see Fig. 4.1) and the spins are either aligned or anti-aligned with it. The basis vectors of the orbital plane, $\hat{\mathbf{x}}_L(t)$ and $\hat{\mathbf{y}}_L(t)$, are constant in time. They can be freely chosen to be any pair of orthogonal unit vectors in the x–y plane. Here, following the convention of Ref. [199], we choose $\hat{\mathbf{x}}_L = \widehat{\mathbf{P}} = \widehat{\mathbf{N}} \times \widehat{\mathbf{L}}_{\rm N}/|\widehat{\mathbf{N}} \times \widehat{\mathbf{L}}_{\rm N}|$, so that the phase is zero at the ascending node (where the orbital separation vector crosses the plane of the sky from below). This is equivalent to setting $\iota = 0$ and $\alpha = \pi$ in Eqs. (4.30), (A.2), and (A.3). Note also that since the orbital plane remains fixed, the phase Φ defined through Eq. (4.28) coincides with the standard definition of the orbital phase, that is

$$\omega_{\rm orb} = \dot{\Phi}\,. \tag{4.60}$$

In the non-precessing case, the vectors in terms of which the GW polarizations are expressed originally take the simpler form

$$\hat{\mathbf{n}} = (\sin\Phi\,,\,-\cos\Phi\,,\,0)\ , \tag{4.61}$$

$$\hat{\boldsymbol{\lambda}} = (\cos\Phi\,,\,\sin\Phi\,,\,0)\ , \tag{4.62}$$

$$\widehat{\mathbf{N}} = (\sin\theta\,,\,0\,,\,\cos\theta)\ , \tag{4.63}$$

$$\widehat{\mathbf{L}}_{\rm N} = (0\,,\,0\,,\,1)\ . \tag{4.64}$$

By plugging the expressions (4.61)–(4.64) into Eq. (4.21) and taking the combinations given in Eq. (4.1), we obtain an equation similar to Eq. (4.30). The spin-dependent 1PN, 1.5PN and 2PN order polarization coefficients read

$$H_{+}^{(1,{\rm SO})} = v^2 s_\theta\,\cos\Psi\,\left[\boldsymbol{\chi}_a\cdot\widehat{\mathbf{L}}_{\rm N} + \delta\,\boldsymbol{\chi}_s\cdot\widehat{\mathbf{L}}_{\rm N}\right]\ , \tag{4.65a}$$

$$H_{+}^{(3/2,{\rm SO})} = v^3\cos 2\Psi\,\frac{4}{3}\,\left[(1+c_\theta^2)\left(\boldsymbol{\chi}_s\cdot\widehat{\mathbf{L}}_{\rm N} + \delta\,\boldsymbol{\chi}_a\cdot\widehat{\mathbf{L}}_{\rm N}\right) + \nu\,(1-5c_\theta^2)\,\boldsymbol{\chi}_s\cdot\widehat{\mathbf{L}}_{\rm N}\right]\ , \tag{4.65b}$$

$$H_{+}^{(2,{\rm SS})} = -v^4\,2\,\nu\,(1+c_\theta^2)\left(\boldsymbol{\chi}_s^2 - \boldsymbol{\chi}_a^2\right)\,\cos 2\Psi\,, \tag{4.65c}$$

$$H_{\times}^{(1,{\rm SO})} = v^2 s_\theta\,c_\theta\,\sin\Psi\,\left[\boldsymbol{\chi}_a\cdot\widehat{\mathbf{L}}_{\rm N} + \delta\,\boldsymbol{\chi}_s\cdot\widehat{\mathbf{L}}_{\rm N}\right]\ , \tag{4.65d}$$

$$H_{\times}^{(3/2,{\rm SO})} = v^3\sin 2\Psi\,\frac{4}{3}\,c_\theta\,\left[2\left(\boldsymbol{\chi}_s\cdot\widehat{\mathbf{L}}_{\rm N} + \delta\,\boldsymbol{\chi}_a\cdot\widehat{\mathbf{L}}_{\rm N}\right) - \nu\,(1+3c_\theta^2)\,\boldsymbol{\chi}_s\cdot\widehat{\mathbf{L}}_{\rm N}\right]\ , \tag{4.65e}$$

$$H_{\times}^{(2,{\rm SS})} = -v^4\,4\,\nu\,c_\theta\,\left(\boldsymbol{\chi}_s^2 - \boldsymbol{\chi}_a^2\right)\,\sin 2\Psi\,, \tag{4.65f}$$

where SS labels the spin(1)-spin(2) contributions[10]. In the equations above, we use the shorthand $c_\theta = \cos\theta$ and $s_\theta = \sin\theta$. Note also that the phase Ψ is the shifted orbital phase that relates to Φ at our accuracy level as

$$\Psi = \Phi - 2\,v^3\,\left(1 - \frac{\nu}{2}\,v^2\right)\,\ln\left(\frac{\omega_{\rm orb}}{\omega_0}\right)\,, \tag{4.65g}$$

where ω_0 can be chosen arbitrarily. Expressed in terms of the orbital phase Φ, the GW polarizations would contain terms logarithmic in $\omega_{\rm orb}$, arising from the propagation of the tails. However, introducing the phase (4.65g), they are all absorbed (up to the 2.5PN order we are considering) into the phase variable [199].

The spin-dependent polarizations (4.65a)–(4.65f) were derived in Ref. [84] [see Eqs. (F24a)–(F25c) in that paper], although the 1.5PN and 2PN order cross polarizations had an erroneous sign, which is corrected here.

4.6.2 Spin-orbit effects at 1.5PN order and spin-spin effects at 2PN order in the frequency-domain gravitational-wave amplitude

Writing $h(t) = h_+\,F_+ + h_\times\,F_\times$ and collecting terms by PN order and by sines or cosines of harmonics of the orbital frequency, we can write the time-domain strain

[10]We remind that spin(1)-spin(1) and spin(2)-spin(2) effects in the waveform polarizations are currently unknown.

in the compact form:

$$
\begin{aligned}
h(t) &= \frac{2\,M\,\nu}{D_L}\sum_{n=0}^{5}\sum_{k=1}^{7} V_k^{2+n}\,\Big[\alpha_k^{(n)}\,\cos(k\,\Psi(t)) + \beta_k^{(n)}\,\sin(k\,\Psi(t))\Big] + \mathcal{O}(v^8)\,, \\
&= \frac{2\,M\,\nu}{D_L}\sum_{n=0}^{5}\sum_{k=1}^{7} V_k^{2+n}\,\Big[\alpha_k^{(n)}\,\cos(k\,\Psi(t)) + \beta_k^{(n)}\,\cos(k\,\Psi(t) - \frac{\pi}{2})\Big] + \mathcal{O}(v^8)\,,
\end{aligned}
\tag{4.66}
$$

where $n/2$ is the PN order and k labels the harmonics of the orbital phase. The PN expansion parameter is defined as $V = (2\pi MF)^{1/3}$, with $F = \omega_{\rm orb}/(2\pi)$. We shall denote the GW frequency by f. For the $k^{\rm th}$ harmonic, we have then the relation $f = f_k \equiv kF$, so that

$$
V_k = \left(2\,\pi\,M\,\frac{f_k}{k}\right)^{1/3}\,. \tag{4.67}
$$

Given a function of the form $h(t) = A(t)\cos\phi(t)$, where $\phi(t)$ is a monotonically increasing function satisfying $d\mathrm{lnA(t)}/dt \ll d\phi(t)/dt$, we can compute its Fourier transform by applying the SPA:

$$
\tilde{h}(f) \simeq \frac{1}{2}\,A(t(f))\,\sqrt{\frac{2\,\pi}{\ddot{\phi}(t(f))}}\,e^{i(2\,\pi\,f\,t(f) - \phi(t(f)) - \pi/4)}\,, \tag{4.68}
$$

$t(f)$ being defined here for each frequency f as the value of t for which $(d\phi/dt)(t) = 2\pi f$. In a similar manner, we apply the SPA to each term in the sum of Eq. (4.66). Moreover, for each harmonic of the orbital phase, we expand the factor inversely proportional to the second time derivative of the orbital phase entering Eq. (4.68)

in a PN series of the form

$$\sqrt{\frac{2\,\pi}{k\,\ddot{\phi}}} = \left(k\,\frac{dF}{dt}\right)^{-1/2} = \sqrt{\frac{5\,\pi}{k\,48\,\nu}}\,M\,V_k^{-11/2} \times \left[1 + \mathcal{S}_2\,V_k^2 + \mathcal{S}_3\,V_k^3 + \mathcal{S}_4\,V_k^4 + \mathcal{S}_5\,V_k^5 + \mathcal{O}(V_k^6)\right] , \tag{4.69}$$

with

$$\begin{aligned}
\mathcal{S}_2 &= \frac{743}{672} + \frac{11}{8}\,\nu\,, \\
\mathcal{S}_3 &= -2\pi + \left(\frac{113}{24} - \frac{19}{6}\,\nu\right)\,\boldsymbol{\chi}_s\cdot\widehat{\mathbf{L}}_{\rm N} + \frac{113}{24}\,\delta\,\boldsymbol{\chi}_a\cdot\widehat{\mathbf{L}}_{\rm N}\,, \\
\mathcal{S}_4 &= \frac{7266251}{8128512} + \frac{18913}{16128}\,\nu + \frac{1379}{1152}\,\nu^2 \\
&- \nu\left(\frac{721}{96}\left(\left(\boldsymbol{\chi}_s\cdot\widehat{\mathbf{L}}_{\rm N}\right)^2 - \left(\boldsymbol{\chi}_a\cdot\widehat{\mathbf{L}}_{\rm N}\right)^2\right) - \frac{247}{96}\left(\boldsymbol{\chi}_s^2 - \boldsymbol{\chi}_a^2\right)\right)\,, \\
\mathcal{S}_5 &= \pi\left(-\frac{4757}{1344} + \frac{57}{16}\,\nu\right)\,.
\end{aligned} \tag{4.70}$$

The expansion (4.69) *without* spin corrections in the amplitude was first given in Ref. [116]. We have added to it the leading order SO corrections through 1.5PN order and the spin(1)-spin(2) SS corrections appearing at 2PN order. In principle, SO corrections at 2.5PN order and spin(1)-spin(1), spin(2)-spin(2) SS corrections at 2PN arising from the spin contribution to the orbital frequency are also present. However, when calculating spin terms in the frequency-domain amplitude, we neglect them because they have not been calculated yet beyond the 1.5PN order in the time domain amplitude. The spin contribution at 2PN and 2.5PN order to the Fourier domain amplitude is not complete unless we take both into account.

Defining the frequency-dependent SPA phase as

$$\Psi_{\rm SPA}(f) = 2\pi\, f\, t(f) - \Psi(f)\,, \tag{4.71}$$

the frequency domain waveform with amplitude corrections containing SO effects through 1.5PN order and spin(1)-spin(2) effects through 2PN order is

$$\begin{aligned}
\tilde{h}(f) &= \frac{M\,\nu}{D_L}\sum_{n=0}^{5}\sum_{k=1}^{7} V_k^{2+n}\,\left(k\,\frac{dF}{dt}\right)^{-1/2} \\
&\quad\times\left(\alpha_k^{(n)}\,e^{i\,(2\,\pi\,f\,t(F)-k\,\Psi(F)\,-\,\pi/4)} + \beta_k^{(n)}\,e^{i(2\,\pi\,f\,t(F)\,-(k\,\Psi(F)-\pi/2)-\pi/4)}\right)\,, \\
&= \frac{M\,\nu}{D_L}\sum_{n=0}^{5}\sum_{k=1}^{7} V_k^{n-\frac{7}{2}}\,\sqrt{\frac{5\,\pi}{k\,48\,\nu}}\,M\,\left(1+\mathcal{S}_2\,V_k^2+\mathcal{S}_3\,V_k^3+\mathcal{S}_4\,V_k^4+\mathcal{S}_5\,V_k^5\right) \\
&\quad\times(\alpha_k^{(n)}+e^{i\,\pi/2}\,\beta_k^{(n)})e^{i\,(k\,\Psi_{\rm SPA}(f/k)-\pi/4)}\,, \\
&= \frac{M^2}{D_L}\sqrt{\frac{5\,\pi\,\nu}{48}}\sum_{n=0}^{5}\sum_{k=1}^{7}\,V_k^{n-\frac{7}{2}}\,\mathcal{C}_k^{(n)}e^{i\,(k\,\Psi_{\rm SPA}(f/k)-\pi/4)}\,.
\end{aligned} \tag{4.72}$$

with

$$\mathcal{C}_k^{(n)} = \frac{1}{\sqrt{k}}\,\left(\alpha_k^{(n)}+i\,\beta_k^{(n)}\right) + \sum_{m=2}^{n}\frac{\mathcal{S}_m}{\sqrt{k}}\,\left(\alpha_k^{(n-m)}+i\,\beta_k^{(n-m)}\right)\,, \tag{4.73}$$

where the index n denotes the PN order and the index k the harmonics. Explicit expressions for the $\mathcal{C}_k^{(n)}$ can be found in Appendix D. The non-spinning terms in the amplitude agree with Ref. [214], although we have written them in a different, more explicit manner. Notice that recently the non-spinning amplitude corrections were calculated through 3PN order [27], but in this paper we restricted the computation to 2.5PN order.

4.6.3 Spin-orbit effects at 2.5PN order in the frequency-domain gravitational-wave phase

For matched filtering, it is best to know the GW phasing at the highest PN order. We now derive the SO contributions to the SPA phase through 2.5PN and the SS contributions (*including* spin(1)-spin(1) and spin(2)-spin(2) contributions) to the SPA phase through 2PN order.

The PN expansion of the SPA phase $\Psi_{\rm SPA}(F)$ can be obtained from the PN expansions of the binary center-of-mass energy, E, and GW flux, F, via the energy balance equation

$$-\frac{dE}{dt} = \mathcal{F}\,. \tag{4.74}$$

Using $d\Psi/dt = 2\,\pi\,F = v^3/M$, we can re-write the energy balance equation as the differential equations

$$dt = -\frac{dE}{dv}\,\frac{1}{\mathcal{F}}\,dv\,, \tag{4.75}$$

and

$$d\Psi = -\frac{dE}{dv}\,\frac{1}{\mathcal{F}}\,\frac{v^3}{M}\,dv\,. \tag{4.76}$$

The quantities E and $\mathcal{F}$ are known as power series in $v = (2\pi\,M\,F)^{1/3}$. The non-spinning terms in the expansions of E and $\mathcal{F}$ have been calculated by Refs. [242, 243, 244, 245, 56, 85], while the spin contributions to these quantities through 2.5PN order were derived by Refs. [83, 84, 235, 24, 197, 86]. The center-of-mass energy

and the flux read

$$E(v) = E_{\rm Newt}\, v^2 \left(1 + \sum_{i=2}^{6} E_i v^i\right), \tag{4.77}$$

$$\mathcal{F}(v) = F_{\rm Newt}\, v^{10} \left(1 + \sum_{i=2}^{7} F_i v^i\right), \tag{4.78}$$

where the coefficients E_i and F_i are explicitly given in Appendix C. By inserting Eqs. (4.77), (4.78) into Eqs. (4.75), (4.76), we obtain rational function approximations to the integrands. We then find the Taylor series of the rational functions and integrate up to some reference frequency, often chosen to be the time of coalescence, when the orbital frequency formally diverges. Thus, we obtain PN approximations of the form

$$t(v) = t_c - \int_{v_c}^{v} \frac{E_{\rm Newt}}{F_{\rm Newt}} \left(2v^{-9} + \sum_{j=2}^{7} t_j\, v^{j-9}\right), \tag{4.79}$$

$$\Psi(v) = \Psi_c - \frac{1}{M} \int_{v_c}^{v} \frac{E_{\rm Newt}}{F_{\rm Newt}} \left(2v^{-6} + \sum_{j=2}^{7} t_j\, v^{j-6}\right), \tag{4.80}$$

where the t_j coefficients are linear combinations of products of the E_i and F_i. Plugging Eqs. (4.79), (4.80) into Eq. (4.71), we obtain the following expression for the SPA phase through 2.5PN order [11]

$$\Psi_{\rm SPA}(F) = 2\pi\, F\, t_c - \Psi_c + \frac{3}{256} (2\pi \mathcal{M} F)^{-5/3} \left\{1 + \left(\frac{3715}{756} + \frac{55}{9}\nu\right) (2\pi M F)^{2/3}\right.$$

[11] The non-spinning terms in the SPA phase through 3.5PN order can be found in Ref. [246].

$$+ \quad (4\,\beta - 16\pi)\,(2\pi MF)\left(\frac{15293365}{508032} + \frac{27145}{504}\nu + \frac{3085}{72}\nu^2 - 10\,\sigma\right) \times (2\pi MF)^{4/3} + \left(\frac{38645}{756}\pi - \frac{65}{9}\pi\,\nu - \gamma\right)(1 + 3\log(v)) \times (2\pi MF)^{5/3}\Bigg\}\,, \tag{4.81}$$

where the 1.5PN SO phase corrections are contained in β, the 2PN SS corrections are contained in σ, and the 2.5PN SO corrections are contained in γ. Note that β and the spin(1)-spin(2) contributions to σ were previously known [89, 90], while we have calculated the spin(1)-spin(1) and spin(2)-spin(2) contributions to σ and the 2.5PN SO corrections to the SPA phase using the results for the center-of-mass energy and GW flux of Refs. [235, 86, 85, 88]. Explicitly, these corrections are

$$\beta = \left(\frac{113}{12} - \frac{19}{3}\,\nu\right)\boldsymbol{\chi}_s \cdot \widehat{\mathbf{L}}_{\rm N} + \frac{113}{12}\,\delta\,\boldsymbol{\chi}_a \cdot \widehat{\mathbf{L}}_{\rm N}\,, \tag{4.82}$$

$$\begin{aligned}\sigma &= \nu\left\{\frac{721}{48}\left[\left(\boldsymbol{\chi}_s \cdot \widehat{\mathbf{L}}_{\rm N}\right)^2 - \left(\boldsymbol{\chi}_a \cdot \widehat{\mathbf{L}}_{\rm N}\right)^2\right] - \frac{247}{48}\left(\boldsymbol{\chi}_s^2 - \boldsymbol{\chi}_a^2\right)\right\} \\ &+ (1 - 2\nu)\left\{\frac{719}{96}\left[\left(\boldsymbol{\chi}_s \cdot \widehat{\mathbf{L}}_{\rm N}\right)^2 + \left(\boldsymbol{\chi}_a \cdot \widehat{\mathbf{L}}_{\rm N}\right)^2\right] - \frac{233}{96}\left(\boldsymbol{\chi}_s^2 + \boldsymbol{\chi}_a^2\right)\right\} \\ &+ \delta\left[\frac{719}{48}\left(\boldsymbol{\chi}_s \cdot \widehat{\mathbf{L}}_{\rm N}\right)\left(\boldsymbol{\chi}_a \cdot \widehat{\mathbf{L}}_{\rm N}\right) - \frac{233}{48}\,\boldsymbol{\chi}_s \cdot \boldsymbol{\chi}_a\right],\end{aligned} \tag{4.83}$$

$$\begin{aligned}\gamma &= \left(-\frac{732985}{2268} + \frac{24260}{81}\,\nu + \frac{340}{9}\,\nu^2\right)\boldsymbol{\chi}_s \cdot \widehat{\mathbf{L}}_{\rm N} \\ &- \left(\frac{732985}{2268} + \frac{140}{9}\,\nu\right)\delta\,\boldsymbol{\chi}_a \cdot \widehat{\mathbf{L}}_{\rm N}\,.\end{aligned} \tag{4.84}$$

We note that these expressions are only valid when both component spins are aligned or anti-aligned with the orbital angular momentum. The spin(1)-spin(1) and spin(2)-spin(2) contributions to σ were also derived in Refs. [87, 88] and we found full agreement with them.

4.6.4 Features of frequency-domain non-precessing waveforms with higher harmonics

We now discuss some interesting features of the *spinning, non-precessing* waveforms derived in Sec. 4.6.2. Several papers have studied the effect of higher harmonics in the amplitude corrections of *non-spinning* binaries observable by ground- and space-based detectors [214, 116, 218, 219, 220, 247].

One important feature of the amplitude-corrected waveforms is that higher harmonics can increase the mass reach of a detector [218]. This is because high-mass binaries whose dominant second harmonic is not in the detector's sensitive band can have higher harmonics in band and therefore become visible to the detector. A closer look at Eq. (4.73) and Appendix D shows that spin corrections through 2PN order appear only in the first and second harmonics. In particular, the only SPA amplitude coefficients with spin dependence are $\mathcal{C}_1^{(2)}$, $\mathcal{C}_2^{(3)}$ and $\mathcal{C}_2^{(4)}$ given in Appendix D. Thus, in the non-precessing case spin corrections through 2PN order in the waveform amplitude do not affect the mass reach of the detector, and only affect binaries whose second harmonic appears in band.

Another important feature of the amplitude-corrected waveforms is that the next-to-leading-order correction to the dominant second harmonic has the opposite sign from the leading order term, and thus decreases the strength of the second harmonic. For binaries where the second harmonic is in the sensitive band, this effect tends to decrease the signal to noise ratio (SNR) [214, 218, 220]. As we shall study in detail in this section, the spin corrections to the second harmonic can either

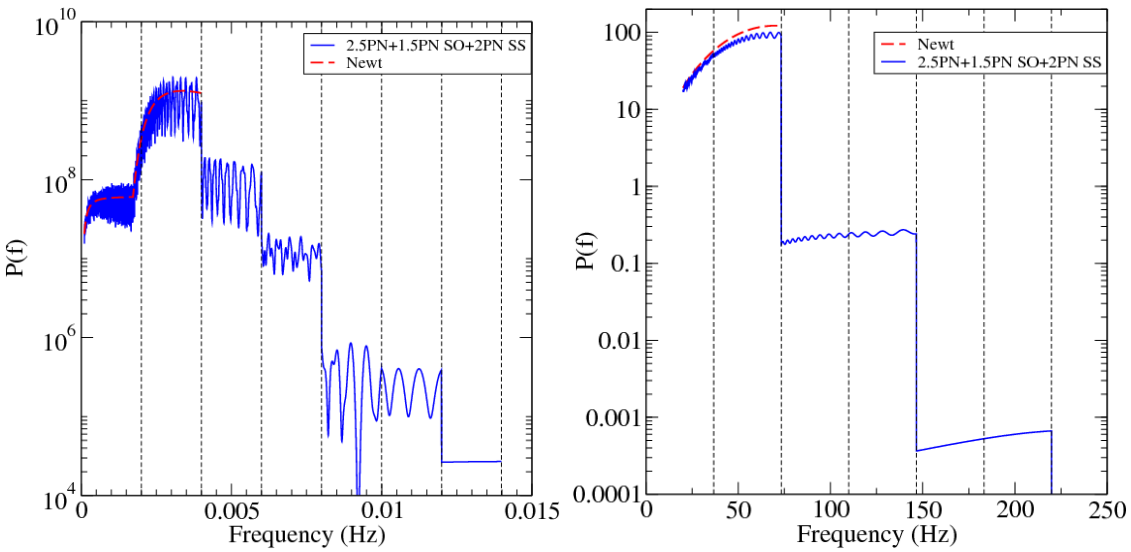

Figure 4.5: We compare the power spectra computed with the Newtonian amplitude waveform (red dashed line) and the 2.5PN waveform with 1.5PN SO and 2PN SS effects included (blue, continuous line). In the left panel we consider a typical source for LISA, a binary with total mass $(10^6 + 10^5)M_\odot$, and spins maximal and aligned with the orbital angular momentum. In the right panel we consider a typical source for Advanced LIGO, a binary of total mass $(30+30)M_\odot$ with spins $\chi_1 = 1$, $\chi_2 = 0.5$ aligned with the orbital angular momentum. Note that the $k^{\rm th}$ harmonic ends at $k\,F_{\rm LSO}$, and these frequencies are marked by the vertical dashed lines on the graph. The spectrum of the 2.5PN waveform is much simpler in the equal-mass case than unequal mass case because in the former case all non-spinning odd harmonics are suppressed.

raise or lower the SNR depending on the spin orientations.

We define the power spectrum, $P(f)$, as

$$P(f) = \frac{|\tilde{h}(f)|^2}{S_n(f)}\,, \tag{4.85}$$

and the *optimal* SNR, ρ, as

$$\rho^2 = 4\int_{f_s}^{7F_{\rm LSO}} \frac{|\tilde{h}(f)|^2}{S_n(f)} df\,, \tag{4.86}$$

where f_s is the low frequency seismic cutoff of the detector, and the upper frequency

cutoff is taken to be the highest harmonic of the orbital frequency at the last stable orbit (LSO) which for simplicity we choose to be the LSO of a test particle in Schwarzschild,

$$F_{\rm LSO} = \frac{1}{2\pi 6^{3/2} M} \,. \tag{4.87}$$

Note that the $k^{\rm th}$ harmonic ends at $kF_{\rm LSO}$ as enforced by a step function $\theta(kF_{\rm LSO}-f)$ [see Eqs. (D.1)–(D.21) in Appendix D]. In Eqs. (4.85), (4.86), we denote with $S_n(f)$ the noise power spectral density of the detector. For Advanced LIGO, we take the spectral density to be Eq. (4.3) of Ref. [116] and fix $f_s = 20$ Hz. For LISA, we use the so-called *effective* non-sky-averaged spectral density given in Eqs. (2.28)–(2.32) of Ref. [248]. We do not consider the orbital motion of the LISA spacecraft [249] and consider only the single detector configuration [12]. In the presence of higher harmonics, the lower and upper cut-off frequencies are chosen following Sec. IIIA of Ref. [218]. For LISA we assume an observation time of one year, and the orbital frequency at the beginning of observation to be Eq. (3.3) of Ref. [218]. As explained in Ref. [218], this can be implemented by multiplying the $k^{\rm th}$ harmonic by the step function $\theta(f - kF_{in})$ where F_{in} is the orbital frequency at the beginning of observation. Finally, because of the 60° angle between LISA's arms, we use $\tilde{h}(f) \to (\sqrt{3}/2)\,\tilde{h}(f)$ in Eqs. (4.85), (4.86) in the case of LISA.

All tables and figures in this section, refer to a binary with orbital angular momentum inclined relative to the line of sight by $\theta = \pi/3$, sky location $\bar{\theta} = \bar{\phi} = \pi/6$ and polarization angle $\bar{\psi} = \pi/4$ [see Eqs. (4.4), (4.5)]. We have verified, by

[12] It should be noted that in our model, though we do not perform an average over the antenna pattern functions, we do not account for the orbital motion of LISA either. In this sense, our model falls in between the *pattern averaged* and *non-pattern averaged* cases described in Ref. [248]

considering random values for the four angles, that the qualitative trends reported in this section are generic and do not depend on the specific values of them (see a detailed discussion at the end of this section). Regardless of the PN order of the amplitude, all waveforms use the SPA phase with non-spinning terms up to 3.5PN order [246], and spin terms up to 2.5PN order, as given in Eqs. (4.81)–(4.84). In the case of Advanced LIGO (LISA) we consider binaries at a distance of 100 Mpc (3 Gpc). Moreover, all masses and distances refer to the redshifted quantities.

The effect of amplitude corrections can be seen in Fig. 4.5. The Newtonian waveform's power spectrum is simply proportional to $f^{-7/3}/S_n(f)$. The higher harmonics present in the 2.5PN waveform create oscillations in the power spectrum. The higher-order corrections to the second harmonic tend to decrease the power spectrum, because they have the opposite sign of the leading-order term. Notice that although the higher harmonics extend the observable frequency band significantly, the power beyond the cutoff of the second harmonic, being at a higher PN order, is suppressed by one or several orders of magnitude. These features explain why the SNR listed in Tables 4.1, 4.2 tends to decrease as the PN order increases for the range of masses we consider. For equal-mass binaries, all non-spinning odd harmonic corrections are suppressed because the latter are proportional to δ which is zero for equal masses [see Eqs. (D.1)–(D.21) in Appendix D]. This is not true of spin-dependent amplitude corrections. For example, the first harmonic has a spin dependent amplitude correction at 1PN order which does not vanish for equal mass systems unless spins are equal and aligned with one another [see Eq. (4.65a)].

Tables 4.1, 4.2 show the SNR for the case of maximal spins both aligned or

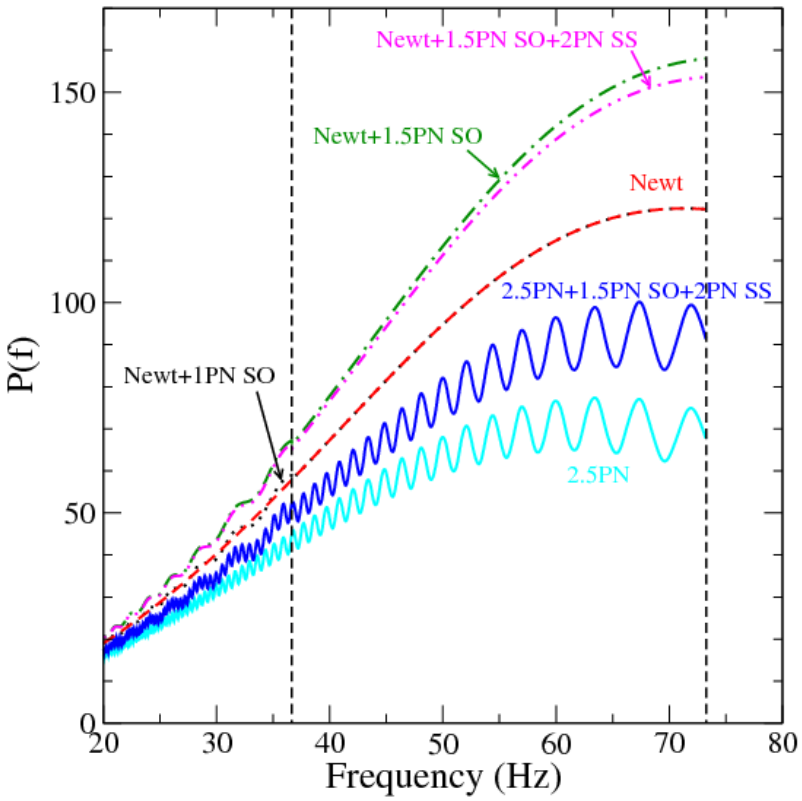

Figure 4.6: For a binary of total mass $(30 + 30)M_\odot$ with spins $\chi_1 = 1, \chi_2 = 0.5$ aligned with the orbital angular momentum (the same binary of the right panel of Fig. 4.5), we show the power spectra up to $2F_{\rm LSO}$. We plot the power spectrum for the waveform through 2.5 PN order with no spin corrections (cyan solid line) and with SO corrections through 1.5PN (that is, 1PN and 1.5PN) and SS corrections at 2PN order (dark blue solid line). We also plot power spectra for the waveform with Newtonian amplitude (red dashed line), Newtonian amplitude plus the 1PN SO correction (black dotted line), Newtonian amplitude plus SO effects through 1.5PN (green,dot dashed line), and Newtonian amplitude plus SO corrections through 1.5PN and the 2PN SS correction (magenta, double-dot-dashed line). The 1.5PN SO and 2PN SS effects raise and lower the power in the dominant harmonic while the 1PN SO effect merely changes the modulation pattern up to its cutoff frequency of $F_{\rm LSO}$. Vertical dashed lines mark the frequencies $F_{\rm LSO}$ and $2\,F_{\rm LSO}$.

anti-aligned with the orbital angular momentum. From the bottom three rows of Tables 4.1, 4.2, we see that, depending on the spin orientation, the 2.5PN amplitude corrections with spins can have SNR $\sim 10\%$ higher or lower than the 2.5PN amplitude corrections without spins. We caution that this $\sim 10\%$ change in the SNR from spin corrections is only meant as a bound on spin effects for spinning, *non-precessing* binaries. As we have seen in Sec. 4.5, the affect of spin corrections on precessing binaries is not bounded by the cases of maximal spins aligned and anti-aligned with the orbital angular momentum.

	Advanced LIGO SNR			
	$(50+5)M_\odot$		$(30+30)M_\odot$	
	$(1,1)$	$(-1,-1)$	$(1,1)$	$(-1,-1)$
Newt	76.4	76.4	131.1	131.1
0.5PN	84.9	82.3	131.1	131.1
1PN	74.2	71.9	116.9	115.8
1PN + 1PN SO	74.1	72.1	116.9	115.8
1.5PN	69.2	67.6	116.9	115.8
1.5PN + 1.5PN SO	79.7	58.1	134.2	98.8
2PN + 1.5PN SO	75.8	55.1	123.1	88.3
2PN + 1.5PN SO + 2PN SS	75.3	54.7	120.3	85.6
2.5PN	64.0	62.6	106.3	105.3
2.5PN + 1.5PN SO	74.2	53.6	123.5	88.5
2.5PN + 1.5PN SO + 2PN SS	73.7	53.2	120.6	85.8

Table 4.1: For several binary configurations observable by Advanced LIGO we list the SNR as the PN order of the amplitude corrections is varied. In each column we show the component spins $(\boldsymbol{\chi}_1 \cdot \widehat{\mathbf{L}}_{\rm N}, \boldsymbol{\chi}_2 \cdot \widehat{\mathbf{L}}_{\rm N})$. We include all non-spinning, SO and SS corrections up to the orders given in the first column. For example, 2.5PN + 1.5PN SO + 2PN SS means we include non-spinning amplitude corrections from Newtonian to 2.5PN order, 1PN and 1.5PN SO corrections, and the 2PN SS correction. Regardless of the PN order of the amplitude, we always use the SPA phase with non-spinning terms up to 3.5PN order, and spin terms up to 2.5PN order, as given in Eqs. (4.81)–(4.84). The binary is at a distance of 100 Mpc with orbital angular momentum inclined relative to the line of sight by $\theta = \pi/3$, sky location $\bar{\theta} = \bar{\phi} = \pi/6$ and polarization angle $\bar{\psi} = \pi/4$ [see Eqs. (4.4),(4.5)].

	LISA SNR			
	$(2\times10^6+10^4)M_\odot$		$(10^6+10^6)M_\odot$	
	$(1,1)$	$(-1,-1)$	$(1,1)$	$(-1,-1)$
Newt	382.6	382.6	2764.3	2764.3
0.5PN	598.5	598.6	2764.3	2764.3
1PN	620.2	621.5	2510.0	2469.7
1PN + 1PN SO	620.0	621.7	2510.0	2469.7
1.5PN	512.3	517.0	2510.0	2469.7
1.5PN + 1.5PN SO	551.8	484.2	2876.0	2118.2
2PN + 1.5PN SO	523.6	457.5	2608.5	1870.5
2PN + 1.5PN SO + 2PN SS	523.4	457.4	2546.7	1814.7
2.5PN	479.4	481.2	2280.3	2242.0
2.5PN + 1.5PN SO	516.4	451.6	2639.2	1901.9
2.5PN + 1.5PN SO + 2PN SS	516.3	451.6	2578.2	1847.5

Table 4.2: For several binary configurations observable by LISA we list the SNR as the PN order of the amplitude corrections is varied. In each column we show the component spins $(\boldsymbol{\chi}_1\cdot\widehat{\mathbf{L}}_{\rm N},\boldsymbol{\chi}_2\cdot\widehat{\mathbf{L}}_{\rm N})$. We include all non-spinning, SO and SS corrections up to the orders given in the first column. Regardless of the PN order of the amplitude, we always use the SPA phase with non-spinning terms up to 3.5PN order, and spin terms up to 2.5PN order, as given in Eqs. (4.81)–(4.84). The binary is at a distance of 3 Gpc with the same orientation as in Table 4.1. The binary masses and distances refer to the redshifted quantities.

Quite interestingly, the 1.5PN SO and 2PN SS corrections are far more important than the 1PN SO correction in terms of their effect on the power spectrum and the SNR. Notice that in Tables 4.1, 4.2 the 1PN SO term always has little or no effect, while the 1.5PN SO term changes the SNR by $\sim 10\%$, and the 2PN SS term changes the SNR for the equal-mass binary. The reason the 1PN SO term is less important is that the 1.5PN SO and 2PN SS terms are corrections to the second harmonic, so they increase or decrease the power in the dominant term. On the other hand, the 1PN SO term is a correction to the first harmonic. Thus, it is merely a perturbation to the dominant signal, and only in the lowest part of the spectrum where the first harmonic is observable. This is illustrated in Fig. 4.6, where

we plot the power spectrum as a function of frequency (up to $2F_{\rm LSO}$) for different spin contributions for the $(30+30)M_\odot$ binary system. We see that the 1.5PN SO and 2PN SS corrections add or subtract their power coherently with the dominant second harmonic. Their net effect is to shift the power spectrum of the full waveform upward without changing its shape. On the other hand, the 1PN SO correction, which is proportional to the (sine or cosine of) half the dominant harmonic, simply changes the modulation pattern of the full waveform up to $F_{\rm LSO}$ (37 Hz). It should however be noted that the structures in the power spectra could be more complicated for asymmetric systems where the non-spinning terms proportional to $\cos\Psi$ and $\sin\Psi$ are not suppressed.

	Advanced LIGO SNR $(60+40)M_\odot$			
	$(1,-1)$	$(0.8,-0.8)$	$(0.5,-0.5)$	$(0.2,-0.2)$
2.5PN	81.0	80.5	80.8	81.8
2.5PN + 1.5PN SO	84.4	83.3	82.5	82.5
2.5PN + 1.5PN SO + 2PN SS	86.7	84.8	83.0	82.6

Table 4.3: For a typical binary observable by Advanced LIGO, we compare the SNR obtained using the 2.5PN amplitude corrected waveform without spin effects, with spin-orbit effects, and with spin-orbit and spin-spin effects. In each column we show the component spins $(\boldsymbol{\chi}_1\cdot\widehat{\mathbf{L}}_{\rm N}, \boldsymbol{\chi}_2\cdot\widehat{\mathbf{L}}_{\rm N})$. In all cases we use the SPA phase with non-spinning terms up to 3.5PN order, and spin terms up to 2.5PN order, as given in Eqs. (4.81)–(4.84). The binary is at a distance of 100 Mpc with the same orientation as in Table 4.1.

The 1.5PN SO term is typically the most important of the spin terms. This term is linearly proportional to the spins of the two bodies, as can be seen in Eq. (D.8). If the spins are aligned with the orbital angular momentum it increases the SNR. If the spin terms are anti-aligned with the orbital angular momentum it

decreases the SNR. If one spin is aligned with $\widehat{\mathbf{L}}_{\rm N}$ and the other anti-aligned, the body with the greater spin $\mathbf{S}_i = m_i^2\,\boldsymbol{\chi}_i$, which is typically the larger body, dominates. Thus, the large body dictates whether the SO effect increases or decreases the SNR, unless the spin of the smaller body is much greater than the spin of the large body. This is illustrated in Table 4.4, where the mass ratio $m_1 : m_2 = 10 : 1$. The spin of the larger body is aligned with $\widehat{\mathbf{L}}_{\rm N}$ and tends to increase the SNR while the spin of the smaller body is anti-aligned with $\widehat{\mathbf{L}}_{\rm N}$ and tends to decrease the SNR. For a spin ratio $\chi_1 : \chi_2 = 1 : 1$ there is a large increase in SNR due the larger BH. For a spin ratio 1:10, the larger BH still dominates and we get a small increase in SNR. For the spin ratios of 1:100 and 1:1000, the smaller BH is now able to overcome the larger BH and produce a net decrease in the SNR.

	LISA SNR $(10^6 + 10^5)M_\odot$			
	$(1, -1)$	$(0.1, -1)$	$(0.01, -1)$	$(0.001, -1)$
2.5PN	2538.7	2570.4	2522.2	2572.4
2.5PN + 1.5PN SO	2917.5	2583.8	2500.6	2546.7
2.5PN + 1.5PN SO + 2PN SS	2938.5	2585.8	2500.8	2546.7

Table 4.4: For a typical binary observable by LISA, we compare the SNR obtained using the 2.5PN waveform without spin effects, with spin-orbit effects, and with spin-orbit and spin-spin effects. In each column we show the component spins $(\boldsymbol{\chi}_1 \cdot \hat{\mathbf{L}}_{\rm N}, \boldsymbol{\chi}_2 \cdot \hat{\mathbf{L}}_{\rm N})$. In all cases we use the SPA phase with non-spinning terms up to 3.5PN order, and spin terms up to 2.5PN order, as given in Eqs. (4.81)–(4.84). The binary is at a distance of 3 Gpc with the same orientation as in Table 4.1. The binary masses and distances refer to the redshifted quantities.

The 2PN SS term decreases the power spectrum and SNR when the component spins are aligned with one another, and increases the power spectrum and SNR when they are anti-aligned with one another. The 2PN SS term has a greater effect on

the SNR and power spectrum than the 1PN SO term, but is less important than the 1.5PN SO term. This is because it is suppressed relative to the 1.5PN SO term by a factor of v/c and it is quadratic in the spins and proportional to the symmetric mass-ratio ν. Thus, the 2PN SS term are most important for binaries with two large component spins and comparable masses. From Tables 4.1, 4.3, we can see that the 2PN SS term has little or no effect on binaries with a mass ratio greater than 10:1. In Tables 4.1, 4.2, for the columns with equal masses and spins aligned with one another, the 2PN SS term decreases the SNR by a few percent. For the binary in Table 4.3, we see that the 2PN SS term increases the SNR by an amount comparable to the SO terms when the spins are maximal. As we decrease the spin magnitude, the SS effect is suppressed faster than the SO effect because it is quadratic in the spins while the SO effect is linear.

Before ending this section we study how different values of the source position and inclination angle can affect the SNR trends shown in Table 4.1. For $(5+50)M_\odot$ and $(30+30)M_\odot$ systems we calculated the SNRs at different PN orders in amplitude for various random realizations of $\bar{\theta}, \bar{\phi}, \bar{\psi}$ and θ and for the spinning and non-spinning cases. For the spinning cases, when all the known spin effects are included at different PN orders, the trends across different orders remains the same for all the random realizations except between the Newtonian and 0.5PN order. Though on most of the occasions, the SNR increases from Newtonian to 0.5PN order, there are cases when it decreases, albeit slightly. All these cases where the SNR decreases have inclination angle θ very close to zero or π. For these cases, the third harmonic, which is proportional to $\sin\theta$, is largely suppressed and the spin-dependent interference

accounts for the small drop in SNR. This drop is observed for systems for which $\chi_1 = \chi_2 = -1$ whereas the non-spinning and $\chi_1 = \chi_2 = 1$ cases consistently showed the increase in SNR between Newtonian and 0.5PN order. To further assert this, we fix the inclination angle to a value very close to zero and π and randomly varied the other three angles. We find that for all the realizations the SNR decreases in going from Newtonian to 0.5PN order. In brief, the trends shown in Table 4.1 is quite general except for inclination angles close to zero or π. We however note that the trends of Table 4.1 need not be same for much higher masses when the leading harmonic approaches the lower cut-off frequency of the detector ($2F_{\rm LSO} \simeq f_s$). We have not done a thorough analysis for the whole mass range.

4.7 Conclusions

The ongoing search for GWs from compact binaries with the network of interferometers LIGO, Virgo and GEO, and the work at the interface between analytical and numerical relativity aimed at providing accurate templates for the search, has made it urgent to include higher-order PN effects in the theoretical predictions of the waveforms. This paper is a step forward in this direction.

We provided ready-to-use time-domain waveforms for spinning, precessing binaries moving on nearly circular orbits through 1.5PN order and decompose those waveforms in spin-weighted -2 spherical harmonics [see Appendices A and B]. Neglecting radiation-reaction effects and assuming $S \ll L$, we found that the inclination angle ι between the total angular momentum and the Newtonian orbital angular

momentum (see Fig. 4.1) is a 0.5PN correction. Motivated by this, we expanded the GW polarizations and spin-weighted spherical harmonic modes in a Taylor series in ι [see Eqs. (4.34), (4.35) and Eqs. (4.56a)–(4.56r)]. Their expressions become much simpler and allow one to extract interesting physical features of the gravitational waves from precessing binaries.

We found that, in contrast to what happens in the non-spinning case, the $h_{\ell m}$'s are not in general proportional to $e^{-im\Psi}$. They also depend on the angles ι and α, where ι is the inclination angle of the Newtonian orbital momentum relative to the total angular momentum and α is the angle between the x-axis and the projection of the Newtonian orbital angular momentum onto the x–y plane (see Fig. 4.1). For example, the terms independent of ι are proportional to $e^{-im(\Psi+\alpha)}$, the terms that are linear in ι are proportional to $e^{-i(m+m')(\Psi+\alpha)}\cos\Psi$ or $e^{-i(m+m')(\Psi+\alpha)}\sin\Psi$, while higher-order contributions in ι involve terms of the form $e^{-i(m+m')(\Psi+\alpha)}\cos^a\Psi\,\sin^b\Psi$, where $a, b \in \mathbb{N}$ and $m' \in -1, 0, 1$. In the presence of precession, the angles ι and α vary in time and the different harmonics present in each of the modes interfere, causing a strong modulation of the mode amplitudes. We also found that, in contrast to what happens in the non-spinning case, the signal can be largely distributed among modes (ℓ, m) other than the $(2, 2)$ mode. With our choice of the source frame, when spins are maximal and the binary system has significant mass asymmetry and/or a large inclination angle, we found that the amplitude of the $(2, 0)$ and $(2, 1)$ modes can be comparable to the amplitude of the $(2, 2)$ mode, especially during the last stages of inspiral. For the mass ratios we considered, we found that the $\ell = 3$ and $\ell = 4$ modes are generally one or two orders of magnitude smaller

than the $\ell = 2$ modes. These results are summarized in Figs. 4.2, 4.3 and 4.4, for binaries with mass ratio 1:1 and 4:1, and for two maximal spin configurations having a small or large inclination angle ι. The ready-to-use time-domain waveforms for spinning, precessing binaries can be employed for accurate comparisons with numerical simulations of binary BHs [250, 251, 252, 253, 254, 231, 240] and for designing time-domain [228, 62, 61, 63] analytical templates.

Restricting ourselves to spinning, non-precessing binaries, we computed ready-to-use frequency-domain waveforms in the stationary-phase approximation. We derived 1PN and 1.5PN order spin-orbit effects, and 2PN order spin-spin (spin(1)-spin(2) only) effects in the frequency-domain GW amplitude [see Eq. (4.73), and Eqs.(D.1)–(D.21) in Appendix D]. We also calculated the 2PN spin-spin (*including* spin(1)-spin(1) and spin(2)-spin(2) effects), and the 2.5PN order spin-orbit effects in the frequency-domain GW phase [see Eqs. (4.81), (4.84) and (4.83)]. For the 2PN spin-spin terms, we found agreement with Refs. [87, 88]. We wrote the frequency-domain waveforms in a rather compact way, so that they can be easily used for data analysis and for building analytical frequency-domain [233, 234] templates.

In the non-precessing case, we found that, through 2PN order, spin effects in the amplitude affect only the PN corrections to the first and second harmonics. Thus, through 2PN order, spin effects do not *yet* extend the mass reach of GW detectors. However, as seen in Figs. 4.5, 4.6, they can interfere with other harmonics and, depending on the spin orientation, lower or raise the signal-to-noise ratio of ground-based (see Tables 4.1, 4.3) and space-based detectors (see Tables 4.2, 4.4). We also expect that those spin terms will help in localizing the binary source in

the sky. We leave to a future publication the use of the waveforms derived in this paper to extend parameter-estimation predictions [246, 212, 248, 213, 214, 116, 215, 216, 217, 218, 219, 220, 222, 223, 224, 191, 221] of ground-based and space-based detectors to spinning, precessing binaries.

Finally, we notice that the gravitational polarizations computed in this paper do not include the modification of the orbital phase evolution at the relative 2.5PN order induced by the flow of energy into the black hole horizons as explicitly computed in Ref. [255]. As summarized in Table IV of Ref. [255], this effect can cause a variation of the number of GW cycles at the Schwarzschild ISCO of 3%–24% depending on the binary mass ratio. We postpone to a future publication the inclusion of those effects.

Chapter 5

Testing gravitational-wave searches with numerical relativity waveforms: Results from the first Numerical INJection Analysis (NINJA) project

Authors: *Benjamin Aylott et al*[1]

Abstract: The Numerical INJection Analysis (NINJA) project is a collaborative effort between members of the numerical relativity and gravitational-wave data analysis communities. The purpose of NINJA is to study the sensitivity of existing gravitational-wave search algorithms using numerically generated waveforms and to foster closer collaboration between the numerical relativity and data analysis communities. We describe the results of the first NINJA analysis which focused on gravitational waveforms from binary black hole coalescence. Ten numerical relativity groups contributed numerical data which were used to generate a set of gravitational-wave signals. These signals were injected into a simulated data set, designed to mimic the response of the Initial LIGO and Virgo gravitational-wave detectors. Nine groups analysed this data using search and parameter-estimation pipelines. Matched filter algorithms, un-modelled-burst searches and Bayesian parameter-estimation and model-selection algorithms were applied to the data. We report the efficiency of these search methods in detecting the numerical waveforms and measuring

[1]Excerpt from the original article Class. Quant. Grav. **26** 165008 (2009). The author of this thesis is principally responsible for the material in Sec. 5.2.3 of this chapter.

their parameters. We describe preliminary comparisons between the different search methods and suggest improvements for future NINJA analyses.

5.1 Introduction

Binary systems of compact objects, i.e., black holes and neutron stars, are among the most important objects for testing general relativity and studying its astrophysical implications [256]. The general solution of the binary problem in Newtonian gravity is given by the Keplerian orbits. In general relativity, the Keplerian orbits for a bound system decay due to the emission of gravitational radiation, leading eventually to the merger of the two compact objects and to a single final remnant [8, 15, 257]. The decay of the orbits is due to the emission of gravitational waves and these waves carry important information about the dynamics of the binary system. In particular, the waves produced during the merger phase contain important non-perturbative general relativistic effects potentially observable by gravitational-wave detectors. Gravitational waves could be detectable by the current generation of gravitational wave detectors such as LIGO and Virgo [258, 259], and detection is very likely with future generations of these detectors.

Two important advances have occurred in recent years that have brought us closer to the goal of observing and interpreting gravitational waves from coalescing compact objects. The first is the successful construction and operation of a world-wide network of large interferometric GW detectors; these include the three LIGO detectors in the United States, Virgo in Italy, TAMA in Japan [260] and the GEO600 detector in Germany [261]. The TAMA detector was the first interferometric detector to achieve its design goals, and it collected science data between 1999 and 2003 [260]. The LIGO detectors started observations in 2002 [121]. From 2005

to 2007 these detectors operated at design sensitivity collecting more than a year of coincident data from the three LIGO detectors; these observations are referred to as S5 [262]. The Virgo detector is also close to achieving its design goals and collected six months of data coincident with the last six months of the LIGO S5 run (referred to as VSR1) [263]. The GEO600 detector has been operating since 2002 in coincidence with the LIGO instruments [261]. The two 4km LIGO detectors are currently being upgraded to improve their sensitivity by a factor of 2–3 (Enhanced LIGO [264]) and will resume observations in 2009. Upgrades to the Virgo detectors to yield comparable sensitivity to Enhanced LIGO are proceeding on a similar schedule. During this time, the GEO600 and the LIGO Hanford 2km detector continue to make best-effort observations (called "astro-watch") to capture any possible strong events, such as a galactic supernova. Following the Enhanced LIGO and Virgo observations, the Advanced LIGO [265] and Virgo [266] upgrades will improve detector sensitivities by a factor of ~ 10 above the Initial LIGO detectors; these upgrades are expected to be complete by 2014. There are also plans to build a second-generation cryogenic detector in Japan known as LCGT [267]. Searching data from these detectors for weak gravitational wave signals over a vast parameter space is a challenging task. The gravitational-wave community has invested significant resources in this effort. A number of searches on S5/VSR1 data for un-modelled bursts and binary coalescence are in progress and many results, including those from previous science runs, have already been reported [268, 269, 270, 271, 272, 273, 274, 275, 276, 277, 278].

The second important advance has been the impressive success of numerical relativity in simulating the merger phase of BBH coalescence. The first break-

throughs occurred in 2005 with simulations by Pretorius [279], closely followed by the independent Goddard and Brownsville (now at RIT) results [143, 144]. Since then, a number of numerical relativity groups around the world have successfully evolved various configurations starting from the inspiral phase all the way through the merger to the final remnant black hole (for recent overviews on the field see e.g. [146, 280, 281]). This has led to important new physical insights in BBH mergers. These include the prediction of large recoil velocities produced by asymmetric emission of gravitational radiation during the merger process [282, 283, 284, 285, 286, 287, 288, 289, 290, 291, 292, 293, 49, 294, 295, 296, 297, 298, 299] and the prediction of the parameters of the remnant Kerr hole for a wide class of initial states [300, 284, 301, 302, 303, 304, 305, 306, 305, 307, 308, 309, 310, 311, 312]. Since the inspiral, merger and coalescence of black holes are also among the most important targets of GW detectors, we expect that the detailed information provided by numerical simulations can be used to increase the reach and to quantify the efficacy of data analysis pipelines. Indeed the driving motivation of research on numerical simulations of black-hole binaries over the last few decades has been their use in GW observations.

Thus far, most searches for gravitational waves from BBH mergers have relied on post-Newtonian results, which are valid when the black holes are sufficiently far apart. Within its range of validity, post-Newtonian theory provides a convenient analytic description of the expected signals produced by binary systems. The numerical relativity results, on the other hand, have not yet been synthesised into an analytic model for the merger phase covering a broad range of parameters, i.e., a

wide range of mass ratios, spins and if necessary, eccentricity; there has however been significant progress for the non-spinning case [313, 302, 105, 147, 54, 145, 314, 151, 152, 153, 315, 148]. Similarly, despite significant progress, there is not yet a complete detailed description over the full parameter space of how post-Newtonian and numerical simulations are to be matched with each other. On the data analysis side, many pipelines, especially ones that rely on a detailed model for the signal waveform, have made a number of choices based on post-Newtonian results, and it is important to verify that these choices are sufficiently robust. More generally, it is necessary to quantify the performance of these data analysis pipelines for both detection and parameter estimation. This is critical for setting astrophysical upper limits in case no detection has been made, for following up interesting detection candidates, and of course for interpreting direct detections. Work on this to date has primarily used post-Newtonian waveforms. Numerical relativity now provides an important avenue for extending this to the merger phase.

There are significant challenges to be overcome before numerical relativity results can be fully exploited in data-analysis pipelines. The NINJA project was started in the spring of 2008 with the aim of addressing these challenges and fostering close collaboration between numerical relativists and data analysts. Participation in NINJA is open to all scientists interested in numerical simulations and GW data analysis. NINJA is the first project of its kind that attempts to form a close working collaboration between the numerical relativity and data analysis communities. Several decisions were made that restrict the scope of the results reported here: we consider only BBH simulations and have not used results from supernova sim-

ulations or simulations containing neutron stars; the waveform data comes purely from numerical simulations and we do not attempt to extend numerical data using post-Newtonian waveforms; the NINJA data set is constructed using Gaussian noise to model the response of the Initial LIGO and Virgo detectors – no attempt has been made to include non-Gaussian noise transients found in real detector data. The comparisons and conclusions reported here are thus necessarily limited, and in many cases are only the first steps towards fully understanding the sensitivity of data-analysis pipelines to black hole signals. Further studies are needed regarding the accuracy and comparison of numerical waveforms, and of how systematic errors in these waveforms can affect parameter estimation. Some analyses of numerical waveforms with regard to gravitational-wave detection have already been performed [316, 317, 147, 148], accuracy standards have been developed for use of numerical waveforms in data analysis [140] and a detailed comparison of some of the waveforms used in the NINJA project was performed in the related Samurai project [318]. We expect that subsequent NINJA analyses will build on these results to address these issues.

Despite the limited scope of the first NINJA project, we are able to draw the following broad conclusions from this work. Our first conclusion is that the current data analysis pipelines used to search LIGO, Virgo and GEO600 data for black hole coalescence are able to detect numerical waveforms injected into the NINJA data set at the expected sensitivities. Indeed, several of these pipelines are able to detect signals that lie outside the parameter space that they target. This is a non-trivial statement since most detectability estimates to date for these sources have

relied on post-Newtonian waveforms, which are valid only when the black holes are sufficiently far apart. For many of these pipelines, this is the first time they have been tested against numerical waveforms. It should be noted, however, that the NINJA data set does not contain non-stationary noise transients so more work is needed to understand how detection performance is affected by the noise artifacts seen in real GW detector data. Our second conclusion is that significant work is required to understand and improve the measurement of signal parameters. For instance, among the pipelines used in this first NINJA analysis only the Markov-chain Monte-Carlo algorithm attempted to estimate the spins of the individual black holes, and the estimation of the component masses by the detection pipelines is poor in most cases. Improvement in this area will be crucial for bridging the gap between gravitational wave observations and astrophysics. NINJA has proven to be extremely valuable at framing the questions that need to be answered.

5.2 Search pipelines using modelled waveforms

When the waveform of the target signal is known, matched filtering is the optimal search technique for recovering signals buried in stationary noise [319, 320]. This section describes the results of filtering the NINJA data with matched-filter based analysis pipelines. Results are given for waveforms that span only the inspiral signal, the ringdown alone, and the full inspiral, merger and ringdown. Although the morphologies of these waveforms differ, the underlying analysis techniques are similar in all cases. All the contributions in this section use a pipeline developed

by the LSC and Virgo Collaboration to search for gravitational waves from binary neutron stars and black holes in a network of detectors [321, 272]. We first describe the features of this pipeline common to all the contributed matched-filter analyses before presenting the results of searching the NINJA data using different matched-filter templates.

The LSC-Virgo search pipeline performs a series of hierarchical operations in order to search for real signals buried in the detector noise: Given a desired search parameter space and waveform model, a "bank" of templates is created to cover the parameter space such that the fractional loss in signal-to-noise ratio (SNR) between any signal and the nearest template is less than a specified value (typically 3%). All the NINJA inspiral searches use a non-spinning template bank parametrised by the two component masses of the binary [322, 323, 179]. It has been found that inspiral searches for spinning binaries using waveforms which neglect the effect of spin are reasonably effective in most cases [321, 324]. Ringdown searches use a two parameter template bank parametrised by the frequency and quality factor of the signal constructed to cover the desired range of mass and spin [325]. Data from each of the detectors is separately match filtered against this bank of waveforms [101, 325] and a "trigger" is produced whenever the SNR exceeds the desired threshold. All the analyses used a threshold of 5.5. A test is then performed which discards triggers which do not have coincident parameters in two or more detectors (time and masses for inspiral searches, and time, mass and spin for ringdown searches) [326, 327]. These coincident triggers provide the GW candidates for the ringdown analysis. The triggers are ranked by a detection statistic ρ_c constructed from the SNRs of the

$N \geq 2$ individual triggers in a coincidence by $\rho_{\rm c} = (\sum_{i=1}^{N} \rho_i^2)^{1/2}$. Coincident inspiral triggers are subject to a second stage of filtering in which "signal-based vetoes" are also calculated, which aim to separate true signals from noise fluctuations. These include the χ^2 [328] and r^2 [329] tests. Signal-based vetoes could also be employed for ringdown searches, but at present they are not implemented in the pipeline. For each trigger, we construct an effective SNR $\rho_{\rm eff}$, which combines the matched-filter SNR and the value of the χ^2 signal based veto [328]. Explicitly, the effective SNR is defined as [321, 272]

$$\rho_{\rm eff}^2 = \rho^2 / \sqrt{\left(\frac{\chi^2}{\rm DOF}\right)\left(1 + \frac{\rho^2}{250}\right)}\,. \tag{5.1}$$

where DOF signifies the number of degrees of freedom in the χ^2 test. For signals of moderate SNR, which are a good match to the template waveform, the expected value of the χ^2 is unity per degree of freedom and consequently the effective SNR is approximately equal to the SNR. Non-stationarities in the data typically have large values of χ^2 and consequently the effective SNR is significantly lower than the SNR. A second test is then performed to discard coincidences in which signal-based vetoes reduce the number of triggers to less than two. These coincidences provide the candidate gravitational wave signals for the inspiral-based pipelines and they are ranked by the combined effective SNR $\rho_{\rm eff} = (\sum_{i=1}^{N} \rho_{{\rm eff}\ i}^2)^{1/2}$. To evaluate the sensitivity of the analyses, we compare the list of GW candidates generated by filtering the NINJA data to the parameters of the inject numerical relativity signals.

Six groups contributed matched-filter results to this analysis and the results

can be roughly divided into three categories based on the waveform templates used: (i) searches based on the stationary-phase approximation to the inspiral signal, which are designed to capture various stages of the inspiral, merger and ringdown, (ii) searches which use waveforms designed to model the full inspiral-merger-ringdown signal, (iii) searches using ringdown-only waveforms obtained from black hole perturbation theory. Within these categories, different parameter choices were made in order to investigate the ability of the pipeline to detect the numerical relativity simulations. Each of these three approaches is described independently in the following sections.

5.2.1 Stationary phase inspiral templates

The workhorse template of the LSC-Virgo search pipeline is based on the stationary-phase approximation to the Fourier transform of the non-spinning post-Newtonian inspiral [133, 101]. This waveform (referred to as SPA or TaylorF2) has been used in the search for binary neutron stars [269, 270, 272, 268], sub-solar mass black holes [271, 272, 268] and stellar mass black holes [268]. The TaylorF2 waveform is parametrised by the binary's component masses m_1 and m_2 (or equivalently the total mass $M = m_1 + m_2$ and the symmetric mass ratio $\eta = m_1 m_2 / M^2$) and an upper frequency cutoff f_c. Amplitude evolution is modelled to leading order and phase evolution is modelled to a specified post-Newtonian order. In this section we investigate the performance of TaylorF2-based searches on the three simulated LIGO detectors. Results which include the simulated Virgo detector are described in

the next section. Several analyses were performed which test the ability of TaylorF2 waveforms to detect numerical relativity signals. The analyses differed in the way the TaylorF2 waveforms or the template bank were constructed. The results of these searches are summarised in Table 5.1, each column giving the results from a different search with a summary of the chosen parameters. We first describe the parameters varied between these analyses and then present a more detailed discussion of the results.

All TaylorF2 NINJA analyses used restricted templates (i.e. the amplitude is calculated to leading order), however the phase was calculated to various different post-Newtonian orders [330]. Phases were computed to either two [331, 332] or three point five post-Newtonian order [176, 333, 32] since these are, respectively, the order currently used in LSC-Virgo searches [268] and the highest order at which post-Newtonian corrections are known. After choosing a post-Newtonian order, one chooses a region of mass-parameter space to cover with the template bank. Figure 5.1 shows the boundaries of the template banks used in the analyses. One search used the range used by the LSC-Virgo "low-mass" search [268] ($m_1, m_2 \geq 1M_\odot, M \leq 35M_\odot$) and all other searches used templates with total masses in the range $20M_\odot \leq M \leq 90M_\odot$. These boundaries were chosen since there were no signals in the NINJA data with mass smaller than $36M_\odot$ and there is little, if any, inspiral power in the sensitive band of the NINJA data for signals with $M \gtrsim 100M_\odot$. The standard LSC-Virgo template bank generation code [323] restricts template generation to signals with $\eta \leq 0.25$, since it is not possible to invert M and η to obtain real-valued component masses for $\eta > 0.25$. All but one of the searches

enforced this constraint, with the $0.03 \leq \eta \leq 0.25$ for the low-mass CBC search and $0.1 \leq \eta \leq 0.25$ for the other "physical-η" searches. It is, however, possible to generate TaylorF2 waveforms with "unphysical" values of $\eta > 0.25$. In two separate studies using Goddard and Pretorius waveforms [147], and Caltech-Cornell waveforms [148] it was observed that match between numerical signals and TaylorF2 templates could be increased by relaxing the condition $\eta \leq 0.25$. One NINJA contribution uses a template bank with $0.1 \leq \eta \leq 1.0$ to explore this.

Finally, it is necessary to specify a cutoff frequency at which to terminate the TaylorF2 waveform. In the LSC-Virgo analyses, this is chosen to be the ISCO frequency for a test mass in a Schwarzschild spacetime

$$f_{\rm ISCO} = \frac{c^3}{6\sqrt{6}\pi GM}. \tag{5.2}$$

This cutoff was chosen as the point beyond which the TaylorF2 waveforms diverge significantly from the true evolution of the binary [330]. More recently, comparisons with numerical relativity waveforms have shown that extending the waveforms up to higher frequencies improves the sensitivity of TaylorF2 templates to higher mass signals [147, 148]. The NINJA TaylorF2 analyses use templates terminated at the ISCO frequency and two additional cut-off frequencies: the effective ringdown (ERD) frequency and a weighted ringdown ending (WRD) frequency. The ERD frequency was obtained by comparing post-Newtonian models to the Pretorius and Goddard waveforms [147]. The ERD almost coincides with the fundamental quasi-normal mode frequency of the black hole formed by the merger of an equal-mass

Analysis	(1)	(2)	(3)	(4)	(5)	(6)
Freq. Cutoff	ISCO	ISCO	ERD	ERD	WRD	WRD
PN Order	2 PN	2 PN	2 PN	3.5 PN	3.5 PN	3.5 PN
Total Mass $M_\odot$	2–35	20–90	20–90	20–90	20–90	20–90
η range	0.03–0.25	0.10–0.25	0.10–0.25	0.10–0.25	0.10–0.25	0.10–1
Found Single (H1, H2, L1)	69, 66, 75	72, 43, 66	83, 51, 81	91, 56, 87	90, 55, 88	90, 56, 88
Found Coincidence	49	59	79	82	82	84
Found Second Coincidence	48	59	77	81	81	81

Table 5.1: **Results of inspiral searches using TaylorF2 templates.** There were 126 injections performed into the data. The table above shows the number of injections which were recovered from the three simulated LIGO detectors (H1, H2 and L1) using various different waveform families, termination frequencies $f_{\rm ISCO}$, $f_{\rm ERD}$ and $f_{\rm WRD}$ (as described in the text), and post-Newtonian orders.

non-spinning black-hole binary. The WRD frequency lies between ISCO and ERD, and was obtained by comparing TaylorF2 waveforms to the Caltech-Cornell numerical signals [148].

The results of these searches are reported in Table 5.1. The principal result is the number of injected signals detected by the search. For simplicity, we define a detected signal as one for which there is a candidate GW signal observed within 50 ms of the coalescence time of the injection, determined by the maximum GW strain of the injected signal. We do not impose any additional threshold on the measured SNR or effective SNR of the candidate. For a single detector, this will

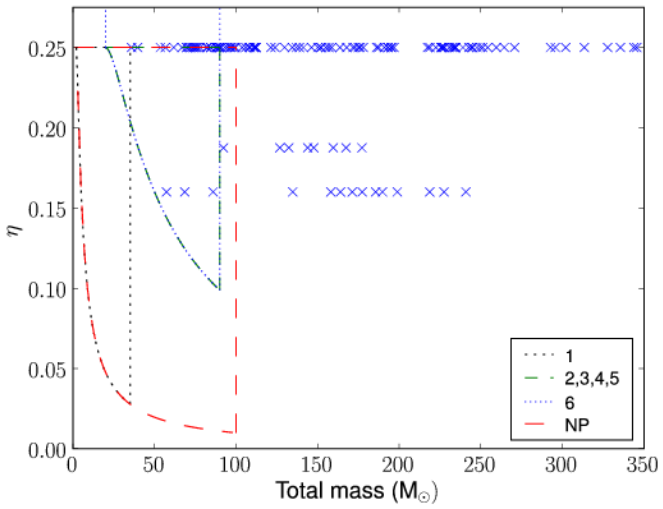

Figure 5.1: **Boundaries of the template banks used in inspiral searches** as a function of total mass M and symmetric mass ratio η. The crosses show the location of the injections in the NINJA data set. The numbers in the legend correspond to entries in table 5.1. Bank 6 extends in a rectangle up to $\eta = 1.00$, as indicated by the arrows. NP is the bank used in the Neyman-Pearson analysis described in Section 5.2.2.

lead to a small number of falsely identified injections, but for coincidence results the false alarm rate is so low that we can be confident that the triggers are associated with the injection. We now describe these results in the order that they appear in Table 5.1.

Search (1) used second order post-Newtonian templates terminated at $f_{\rm ISCO}$ with a maximum mass of $M \leq 35M_{\odot}$. Despite the fact that no NINJA injections had a mass within the range of this search, a significant number of signals were still recovered in coincidence both before and after signal consistency tests. Although the templates are not a particularly good match to the injected signals, they are still similar enough to produce triggers at the time of the injections. Search (2) changed the boundary of the template bank to $20M_{\odot} \leq M \leq 90M_{\odot}$, but left all

other parameters unchanged. The number of detected signals increases significantly as more signals now lie within the mass range searched.

Search (3) extended the upper cutoff frequency of the waveforms to $f_{\rm ERD}$. The number of signals detected increased from 59 to 77, as expected since these waveforms can detect some of the power contained in the late inspiral or early merger part of the signal [147, 148]. Search (4) extends the post-Newtonian order to 3.5 PN, slightly increasing the number of detected signals to 81. With the limited number of simulations performed in this first NINJA analysis, it is difficult to draw a strong conclusion, although there does seem to be evidence that the higher post-Newtonian order waveforms perform better, consistent with previous comparisons of post-Newtonian and numerical relativity waveforms [147, 177, 334, 315, 148]. Search (5) uses an upper-frequency cutoff of $f_{\rm WRD}$ for the templates. The number of injections found in coincidence for this search is the same as the search using 3.5 order templates with a cutoff of $f_{\rm ERD}$, although there are slight differences in the number of found injections at the single detector level.

Search (6) extends the template bank of search (5) to unphysical values of the symmetric mass ratio. Extending the bank to $\eta \leq 1$ increases the number of templates in the bank by a factor of ~ 2. The original and modified template banks are shown in Figure 5.2. With the extended template bank the number of injections found in coincidence remains the same as search (5) after signal-based vetoes are applied. However, many of the injections are recovered at a higher SNR, particular the low-mass signals, as shown in Figure 5.2. Some injections show a reduction in SNR; more work is needed to understand this effect.

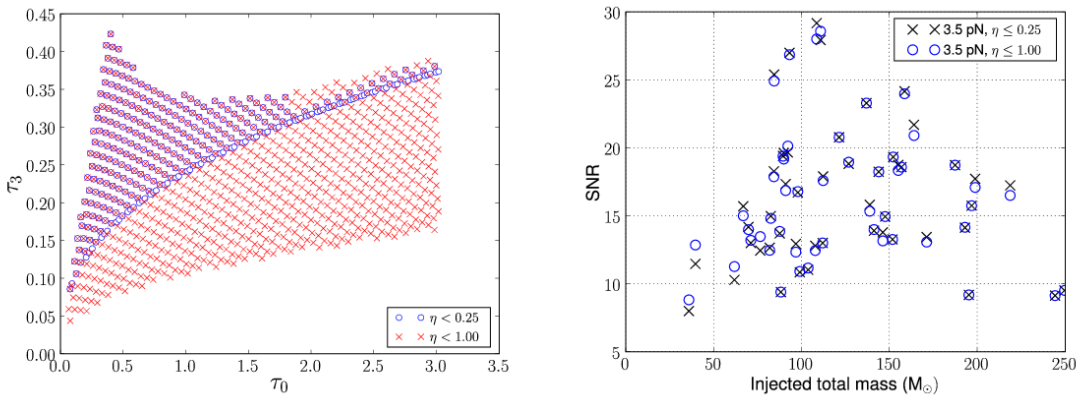

Figure 5.2: **Results from the extended template bank. Left:** The template bank generated by the LSC-Virgo search pipeline (circles) and the bank obtained by extending to $\eta \leq 1.00$ (crosses). In this figure the bank is parametrised by τ_0 and τ_3 which are related to the binary masses by $\tau_0 = 5M/(256\eta v_0^8)$ and $\tau_3 = \pi M/(8\eta v_0^5)$, where $v_0 = (\pi M f_0)^{1/3}$ is a fiducial velocity parameter corresponding to a fiducial frequency $f_0 = 40.0Hz$. **Right:** The signal-to-noise (SNR) ratio at which NINJA injections were recovered using the $\eta \leq 0.25$ bank (squares) and the $\eta \leq 1$ extended bank (circles) in the Hanford detectors, given by $\rho = (\rho_{\rm H1}^2 + \rho_{\rm H2}^2)^{1/2}$. The SNR of the signal recovered using the extended bank shows with significant ($> 10\%$) increases over the standard bank for certain injections.

Finally, we note that the majority of signals passed the χ^2 signal-based veto with the thresholds used in the LSC-Virgo pipeline. The last two lines of Table 5.1 show the number of recovered signals before and after these signal-based vetoes are performed. The post-Newtonian templates and numerical relativity signals are similar enough that virtually all of the injected signals survive the signal based vetoes.

To illustrate the results of these analyses in more detail, Figure 5.3 shows which signals were detected and which were missed by the 3.5 order post-Newtonian TaylorF2 templates terminated at $f_{\rm ERD}$, as a function of injected total mass and effective distance of the binary (a measure of the amplitude of the signal in the

detector), defined by [101]

$$D_{\rm eff} = d \Big/ \sqrt{F_+^2 (1+\cos^2\iota)^2/4 + F_\times^2 \cos^2\iota}\,, \tag{5.3}$$

where d is the luminosity distance of the binary.

One signal, with total mass of $110 M_\odot$ and effective distance ~ 200 Mpc, was missed while others with similar parameters were found. This signal was one of the Princeton waveforms for which the maximum amplitude occurs at the start of the waveform rather than at coalescence[2], rendering our simple coincidence test invalid. The injection finding algorithm compares the peak time to the trigger time and, even though triggers are found at the time of the simulation, there are no triggers within the 50 ms window used to locate detected signals.

Figure 5.4 shows the accuracy with which the total mass and coalescence time of the binary are recovered when using the 3.5 post-Newtonian order Taylor F2 templates. The total mass fraction difference is computed as $(M_{\rm injected} - M_{\rm detected})/M_{\rm injected}$. For lower mass signals, the end time is recovered reasonably accurately, with accuracy decreasing for the high mass systems. The total mass recovery is poor for the majority of signals, with good parameter estimation for only a few of the lowest mass simulations.

[2]That the maximum occurs at the start of the waveform is in part an "artifact" of the double-time integration from the Newman-Penrose scalar ψ_4 to the metric perturbation h, and in part a coordinate artifact. The two integration constants were chosen to remove a constant and linear-in-time piece for h, however, there is still a non-negligible quadratic component; we *suspect* this is purely gauge, though lacking a better understanding of this it was not removed from the waveform.

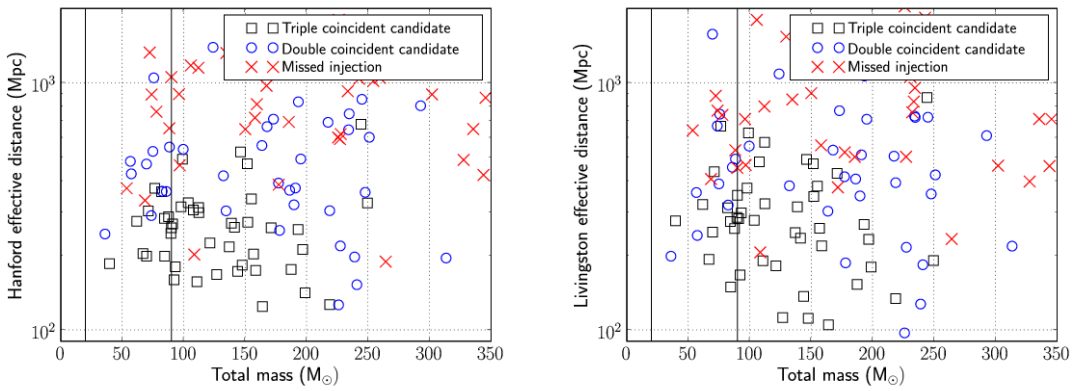

Figure 5.3: **Found and missed injections using TaylorF2 templates terminated at ERD**, plotted as a function of the injected effective distance in Hanford (left) and Livingston (right) and the total mass of the injection. Since the LIGO Observatories are not exactly aligned, the effective distance of a signal can differ, depending on the sky location of the signal. The vertical bars mark the limits of the template bank used in the search. For the lower masses, we see that the majority of the closer injections are found in coincidence in all three of the detectors. There is then a band of injections which are found only in two detectors – H1 and L1 and not the less sensitive H2 detector. For higher masses, the results are less meaningful as the template bank was only taken to a total mass of $90M_{\odot}$.

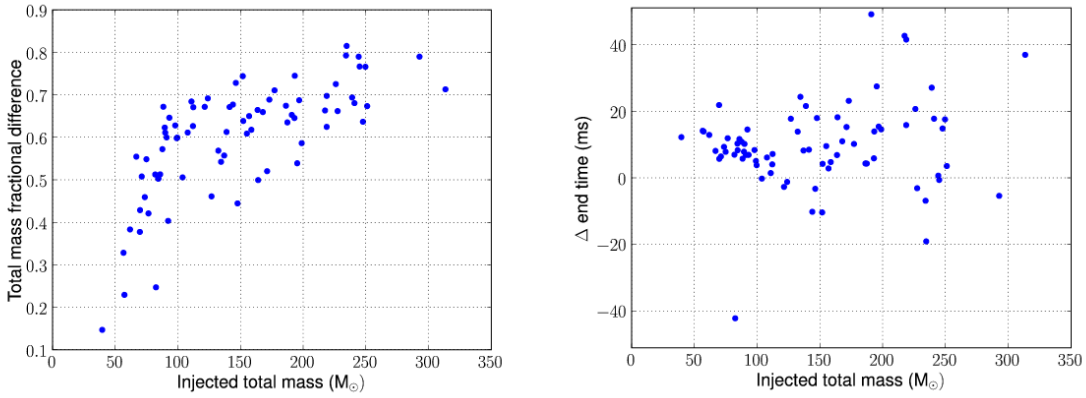

Figure 5.4: **Parameter accuracy using TaylorF2 templates terminated at ERD.Left:** Accuracy with which the total mass is recovered. The template bank covers the region $20M_{\odot} \leq M \leq 90M_{\odot}$, hence the mass of injections with $M > 90M_{\odot}$ are always underestimated. Even within the region covered by the bank, the TaylorF2 templates systematically underestimate the mass of the injected signals and the total mass is recovered accurately only for a few injections. The vast majority of recovered signals have an error of 40% or greater. **Right:** Accuracy of determining the coalescence time of the injections. The end time is not recovered accurately, the timing error can become as large as 50ms, the limits of the injection window.

5.2.2 Four-detector inspiral search

The inspiral analysis described in Section 5.2.1 considered data from the three simulated LIGO detectors. We now extend the analysis to include data from the simulated Virgo detector. In addition, we impose an alternative criterion, based on the Neyman-Pearson formalism [320], to determine those injections which were detected by the pipeline. In the previous section an injection was classified as found by the search if a GW candidate existed within 50 ms of the peak time of the numerical data. Here, we consider a signal to be found is there is an associated candidate whose significance exceeds a predetermined threshold. Specifically, we require the candidate to have a significance greater than *any* candidate arising due to noise alone. This allows us to probe in more detail the effect of signal-based vetoes and the efficaciousness of the effective SNR statistic in analysis of the NINJA data.

Data from all four simulated NINJA detectors was analysed using the CBC pipeline as described in column (1) of Table 5.1. In addition, a second analysis was performed with that the template bank extended to cover the region from $2M_{\odot} \leq M \leq 100M_{\odot}$, with all other parameters unchanged. The search can therefore be though of as the simplest extension of the standard LSC-Virgo "low mass" CBC search [268]. The boundary of the template bank used is shown in Figure 5.1.

In this analysis, we choose a detection statistic and claim that a GW candidate is present if the value of this statistic exceeds a predetermined threshold. All candidates are considered detections. The threshold is chosen so that the false alarm probability—the probability that a noise event will be mistaken for a real

signal—is tolerable. The efficiency of this method depends on how close the chosen statistic is to the optimal detection statistic. It is well known that the matched filter SNR is the optimal statistic for known signals in a single detector *if the noise is stationary* [319, 320]. For a network of detectors containing stationary noise, the optimal statistic is the coherent signal-to-noise ratio ρ_{coherent} [335]. At the time of this analysis, calculation of ρ_{coherent} was not available in the CBC pipeline, so we instead compute a combined SNR from the i detectors, $\rho_{\mathrm{c}} = (\sum_{i=1}^{N} \rho_i^2)^{1/2}$, as a simple alternative. In the presence of non-Gaussian noise, the effective SNR, described in Section 5.2, has shown to be an effective detection statistic [272]. In this analysis, we also consider the combined effective SNR $\rho_{\mathrm{eff}} = (\sum_{i=1}^{N} \rho_{\mathrm{eff}\ i}^2)^{1/2}$.

We investigate three choices of detection statistic: (i) the combined matched filter SNR of coincident candidates before signal-based vetoes are applied ($\rho_{\mathrm{c}}^{\mathrm{first}}$), (ii) the combined matched filter signal-to-noise ratio *after* the χ^2 signal-based veto has been applied applied to coincidences ($\rho_{\mathrm{c}}^{\mathrm{second}}$), (iii) the combined effective SNR ($\rho_{\mathrm{eff}}^{\mathrm{second}}$). This statistic is only available after the second coincidence stage, since it is a function of matched filter SNR and the χ^2 statistic for a candidate. To set a threshold for each statistic we choose the highest value of that statistic NINJA data containing only noise. To do this, we discard all triggers within 5 s of an injected signal; the remaining triggers will be due to the simulated noise alone (we note that this approach is not possible in real data where the locations of the signals are unknown). This crude method of background estimation should provide us with consistent criteria for elimination of spurious detections. Therefore, we mark an injection as found only if it resulted in a trigger with statistic higher then any

Bank mass range	$2M_\odot \leq M \leq 35M_\odot$		$2M_\odot \leq M \leq 100M_\odot$	
Statistic	Statistic Threshold	Found Injections	Statistic Threshold	Found Injections
ρ_c^{first}	9.18	73	9.8	91
ρ_c^{second}	9.18	69	9.8	93
$\rho_{\text{eff}}^{\text{second}}$	10.05	27	10.05	85

Table 5.2: **Number of injections found as determined by the Neyman-Pearson criteria** for different choices of detection statistic Λ and threshold Λ^*. The mass range of the template bank is shown in the first row, all other parameters of the search as the same as those described in column (1) of Table 5.1.

background trigger found in the data.

Table 5.2 shows the threshold and the number of triggers found for each choice of statistic. It is interesting to compare the results for the low-mass search when we threshold on ρ_c^{second}, rather than using a 50 ms time window to determine detected signals. When using the time-window method, the number of injections found by the low-mass search is 51, but this increases to 69 when using the threshold method. Since all the injected signals lie outside the boundary of the low-mass bank, the coalescence time of the signals will be poorly estimated. This will result in triggers outside the 50 ms window, which are nevertheless are loud enough to lie above the background.

Signal-based vetoes are applied at the second stage of the inspiral pipeline and are used to compute ρ_{eff}. By comparing the number of triggers found before and after signal-based vetoes are applied, we can evaluate their effect on the sensitivity of the search. Note that we observe the same threshold for both ρ_c^{first} and ρ_c^{second}. However, the number of detected signals in the low-mass search is reduced by 4 as

the χ^2 veto has removed triggers where the templates are not a good match for the signals. More intriguing is a slight increase in the number of detected signals after the χ^2 veto in the bank with the extended mass range (from 91 to 93). Additional investigations revealed that, despite having fewer triggers in each detector after the χ^2 test has been applied, the total number of coincident triggers actually increases. This is due to the fact that the signal-based vetoes cause the time of the signal to be measured more accurately in the detectors; more triggers therefore survive the coincidence test. We do not observe this in the case of the low mass search.

Finally, we turn our attention to the effective SNR statistic, defined in equation (5.1). Since the NINJA detector noise is stationary and Gaussian, the expected value of the χ^2 is one per degree of freedom. Therefore, we do not expect that the effective SNR will be useful in reducing the significance of loud background triggers. This is borne out by the fact that the statistic threshold actually increases slightly when using effective SNR. For the low mass search the number of signals found by thresholding on ρ_{eff} is significantly less than when using the combined SNR statistic. This is to be expected as the simulated signals do not match well with the templates. Although the low mass templates produce candidates, these will have large values of χ^2 since signal and template do not match well. Thus, the effective SNR will be smaller than the original SNR and fewer signals will be recovered above the threshold. This effect is less significant for the second search with a larger mass range as the templates provide a better match to the simulated signals. Since effective SNR has been a powerful statistic in real detector data, this highlights the need for further NINJA studies using data containing non-stationary noise transients.

5.2.3 Inspiral-merger-ringdown templates

The calculation of the full binary binary black hole coalescence waveform accessible to ground-based detectors requires numerical methods. At the moment, it is not possible to accurately model a coalescing binary over hundreds of orbits due to the computational cost of evolutions. Furthermore, it is not necessary to model the entire waveform, since post-Newtonian gives a valid description of the system when the black holes are sufficiently separated. During their final orbits before merger the black holes' velocities increase and the post-Newtonian expansion becomes less reliable. At this stage the non-perturbative information contained in numerical simulations is required. A successful approach has been to combine analytical and numerical results to obtain full waveform templates. Two different families of such waveforms have been used to analyse the NINJA data: the EOB [336, 141, 337, 57] and phenomenological [105, 314] models.

By combining together results from post-Newtonian theory and perturbation theory, the EOB model [336, 141] predicts the full inspiral, merger and ringdown waveform. More recently, the non-spinning EOB model has been further improved by calibrating it to NR results, achieving high overlaps without the need to maximise the intrinsic mass parameters of the binary [313, 147, 54, 151, 152, 153, 315]. The LSC Algorithm Library (LAL) [338] contains two implementations of the effective one body template: one (called EOB) which only evolves the waveform to the light-ring frequency

$$f_{\mathrm{LR}} = \frac{c^3}{3\sqrt{3}\pi GM}, \tag{5.4}$$

and a second (called EOBNR) which implements the full EOB waveform described in [54]. This template which was constructed to match the NASA-Goddard binary black hole simulations with mass ratios m_1:m_2 = 1:1, 3:2, 2:1 and 4:1, however LAL waveforms do not yet implement higher harmonics of the signal. Both of these implementations were used to search for black hole binary signals in NINJA data.

Another approach for constructing the full waveform is to "stitch" together the results of post-Newtonian and numerical relativity calculations. The model presented in [105, 314, 339] consists of matching the post-Newtonian and numerical waveforms in an appropriate matching regime (where both are sufficiently accurate) to obtain a "hybrid" waveform. This hybrid is then fit by a phenomenological model in the frequency domain determined entirely by the physical parameters of the system. This procedure has been carried out for non-spinning black holes and a two-dimensional template family of waveforms that attempts to model the inspiral, merger and ringdown stages for non-spinning binary black holes has been obtained. Each waveform is parametrised by the physical parameters of the system, i.e., the masses m_1 and m_2 of the black holes.

Since the EOBNR and phenomenological models provide complete waveforms, the search was performed to higher masses ($200M_\odot$ and $160M_\odot$ respectively) than for inspiral only searches. In principle, the search could be extended to even higher masses, but technical issues with the current waveform generation procedures prevent this. The minimum component mass was also increased, in an effort to reduce the size of the template bank by limiting the number of highly asymmetric signals. Finally, the template bank for all these searches was constructed using the standard

Template	EOB	EOBNR	Phenom
Freq. Cutoff	Light ring	Full waveform	Full waveform
Filter Start Freq.	40 Hz	30 Hz	30 Hz
Component Mass $M_\odot$	10-60	15-160	20-80
Total Mass $M_\odot$	20-90	30-200	40-160
Minimal Match	0.97	0.99	0.99
Found Single (H1, H2, L1, V1)	91, 64, 82, -	97, 68, 92, 102	92, 61, 87, -
Found Coincidence (LIGO, LV)	83, -	88, 106	81, -
Found Second Coincidence (LIGO, LV)	80, -	85, 102	80, -

Table 5.3: **Results of the search for NINJA signals using IMR template banks.** There were 126 injections performed into the analysed data. The signal-based vetoes have little influence in the rejection of triggers, confirming their efficiency in separating inspiral-like signals from other kind of glitches.

second order post-Newtonian metric, and hexagonal placement algorithm [179]. At high masses, the parameter space metric for the full waveforms will differ significantly from the standard second-order post-Newtonian metric. However, the current template bank placement suffices for detection purposes, although probably not for good parameter estimation.

The parameters of the NINJA analyses using the EOB, EOBNR and phenomenological waveforms are also given in Table 5.3. Again, the primary result is the number of GW candidates found to be coincident with an injected signal. For the EOB model truncated at light ring, the parameters were chosen to match the TaylorF2 analyses described in Section 5.2.1. Therefore, it is unsurprising that the results are very similar to the TaylorF2 search extended to ERD (the fourth column of Table 5.1). Further details of the EOB search, and a comparison to TaylorF2 results are available in The EOBNR results show some improvement for detecting

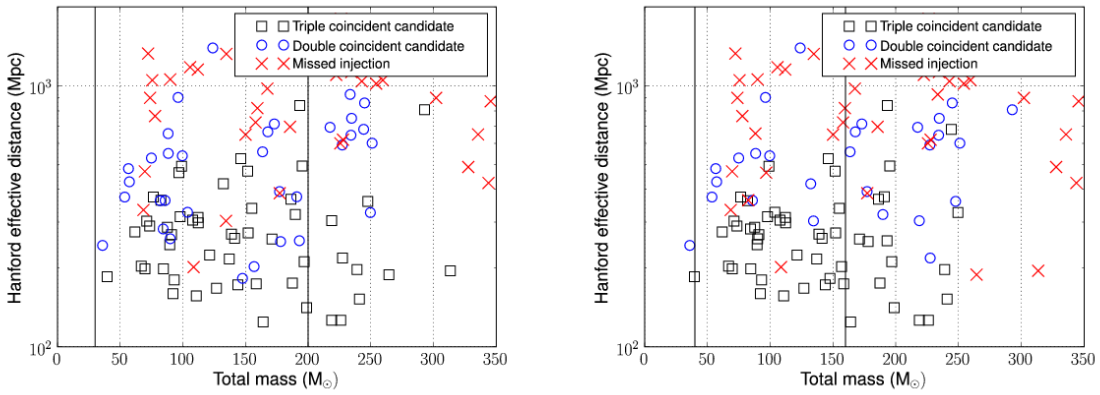

Figure 5.5: **Found and missed injections for the EOBNR and Phenomenological templates.** The figures shows found and missed injections as a function of the injected effective distance in Hanford and the total mass. **Left:** Results for the EOBNR search. **Right:** Results for the search with phenomenological waveforms. The vertical bars mark the limits of the template bank used in the search.

the numerical relativity signals over the usual post-Newtonian or EOB waveforms. For the phenomenological waveforms, time windows of 120ms in single detector and 80ms in coincidence have been used to associate triggers to injections. These parameters differ from those employed in other searches to compensate for a relatively large observed error in the estimation of the coalescence time. By comparing the results with the standard post-Newtonian analyses presented in Section 5.2.1, we conclude that in the present case the phenomenological waveforms [105, 314] do not seem to provide a clear benefit over the usual post-Newtonian waveforms extended to higher cutoff frequency and/or to unphysical regions of the parameter space [147, 148]. For an extended description of the search with phenomenological waveforms see [340]. In all cases, the signal-based vetoes have little influence in the rejection of triggers, confirming their efficiency in separating inspiral-like signals from other kind of glitches.

Plots of found and missed injections for the searches are shown in Figure 5.5. For the most part, simulated signals in the mass range covered by the template banks are well recovered. Some of the missed signals at lower distance correspond to waveforms from simulations of spinning black holes. Since all searches make use of non-spinning waveforms this drop is expected. Finally, we turn to parameter estimation. Figures 5.6 and 5.7 show the parameter recovery accuracies for the EOBNR and phenomenological searches respectively. In both cases, the accuracy of recovering the total mass of the simulations is greatly improved over TaylorF2 waveforms shown in Figure 5.4. This is likely related to the increased mass range of the searches, as well as the use of full waveforms. The timing accuracy for EOBNR is comparable with the TaylorF2 results, while for the phenomenological waveforms, the known timing bias affects the results.

Both the EOBNR and phenomenological models will be improved in the future. Further accurate EOBNR models have already appeared in the literature [54, 151, 152, 153, 315] since the time the EOBNR model used in this analysis was implemented, and extensions to include spin and eccentricity are under development. There are a number of obvious improvements in the phenomenological waveforms that can be made: Calculating the parameter space metric for the phenomenological waveforms would enable the use of an optimal template bank and allow for improved coincidence algorithms. The construction of the phenomenological waveform model can itself be significantly improved by extending the fitting to higher mass ratios and spins, quantifying the error on the phenomenological parameters, matching to post-Newtonian theory as early as possible and including higher

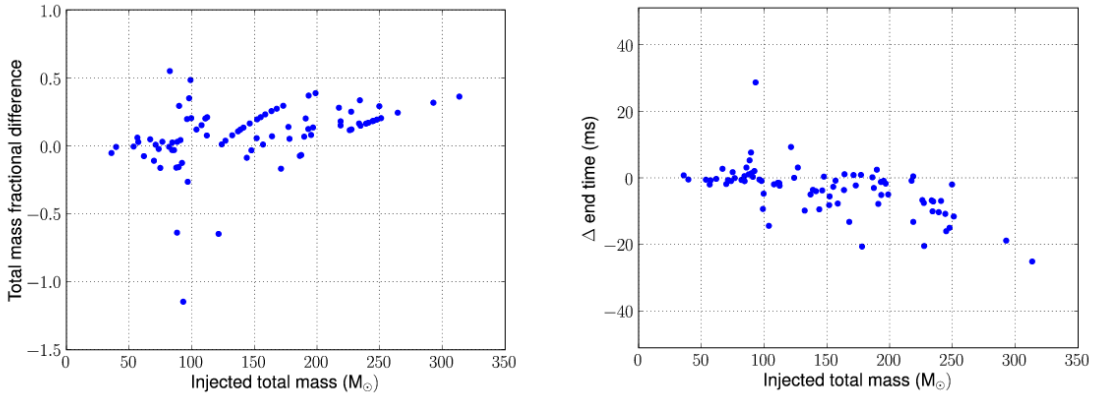

Figure 5.6: **Parameter accuracy for EOBNR templates. Left:** Accuracy with which the total mass is recovered. The template bank covers the region $30M_\odot \leq M \leq 200M_\odot$, hence the mass of injections with $M > 200M_\odot$ are always underestimated. Most of the injections with total mass less than 200 $M_\odot$ were recovered with a mass accurate within to a few tens of percent, demonstrating that the EOBNR templates are more faithful to the injected signal than the TaylorF2 templates shown in Figure 5.4. Higher mass injections are necessarily recovered with underestimated total mass, because the template bank did not cover the entire simulation region. **Right:** Accuracy of determining the coalescence time of the injections. The end time for injections with total mass less than 200 $M_\odot$ was typically recovered to within a few milliseconds. The end time for injections with total mass above 200 $M_\odot$ (outside the range of the template bank) was typically recovered to within 10 or 20 milliseconds.

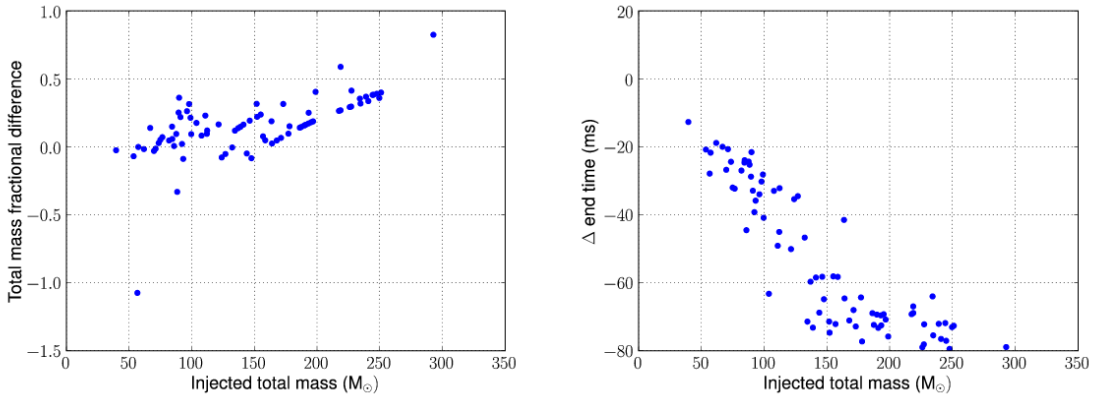

Figure 5.7: **Parameter accuracy for phenomenological templates. Left:** Accuracy with which the total mass is recovered. The total mass is typically recovered within 20%, for signals within the template space. For higher mass injections, there is an inevitable underestimation of the mass due to the limited reach of the template bank. **Right:** Accuracy of determining the coalescence time of the injections. The timing plot shows the systematic offset discussed in the text.

order modes in the waveform. The results of the NINJA analysis also demonstrate a clear need to improve accuracy in measuring the end time of the signal. This is not straightforward, however, since there is no clear definition of the time of merger for the phenomenological waveforms or the numerical signals [318]. Work on the improvements to both the EOBNR and phenomenological searches are being made, and will be applied in and guided by future NINJA projects.

5.2.4 **Ringdown templates**

As described in section 5.2, ringdown templates can be computed using black hole perturbation theory and so matched filtering can be used to search for these signals. Ringdown templates are exponentially damped sinusoids parametrised by the ringdown frequency f and quality factor Q. The LSC ringdown search pipeline [327] has been used to filter the NINJA data against a bank of ringdown templates with frequencies between 50 Hz and 2 kHz, and quality factors between 2 and 20. The bank had a maximum mismatch of 3% and contained 583 templates. A lower-frequency cutoff of 45 Hz was applied when filtering the NINJA data generated with the LIGO noise curves and 35 Hz for data with the Virgo noise curve. The goals of these analyses were to ascertain the detectability of the injected numerical waveforms using ringdown templates at single and coincident detector levels and the accuracy with which the final black hole parameters can be estimated. The current searches use single-mode templates. The waveforms described in this paper are known to contain higher order multipoles. The potential effects of ignoring these

in the search are discussed in Ref. [341] (see in particular Fig. 8 in there).

An injection is defined as found if a set of coincident triggers lies within 10 ms of the peak time of the injection (as specified in the contributed numerical data). If more than one set of coincident triggers satisfies this criterion, that with the largest value of $\sum_i \rho_i^2$ is selected, where ρ_i is the signal to noise ratio in the i^{th} detector. Of the 126 injections made into the three simulated LIGO detectors, 45 were found in triple coincidence, 24 in H1 and L1 (only), and 7 in H1 and H2 (only). Figure 5.8 shows the distribution of found and missed injections for this analysis. The ringdown frequency and quality is computed via the Echeverria formulae [342]:

$$f = \frac{1}{2\pi}\frac{c^3}{GM}\left[1 - 0.63\,(1-a)^{\frac{3}{10}}\right] \tag{5.5}$$

$$Q = 2\,(1-a)^{-\frac{9}{20}}\,. \tag{5.6}$$

More recent and accurate fits for a variety of modes are listed in the Appendices of Ref. [178]. The final black hole mass M and spin a can be computed from the component masses and spins of the numerical simulation, as described in [54] and [343], respectively. See also Refs. [302, 344] for a discussion and comparison of different numerical techniques to perform the necessary fits.

As expected, we see that in general, the closest injections (measured by effective distance D_{eff}), defined in equation 5.3) were found in triple coincidence, those with a large Livingston effective distance were found in H1 and H2 only, while those with a large Hanford effective distance were not found in H2, and the furthest injections were missed in at least two detectors. The plots show that there are three

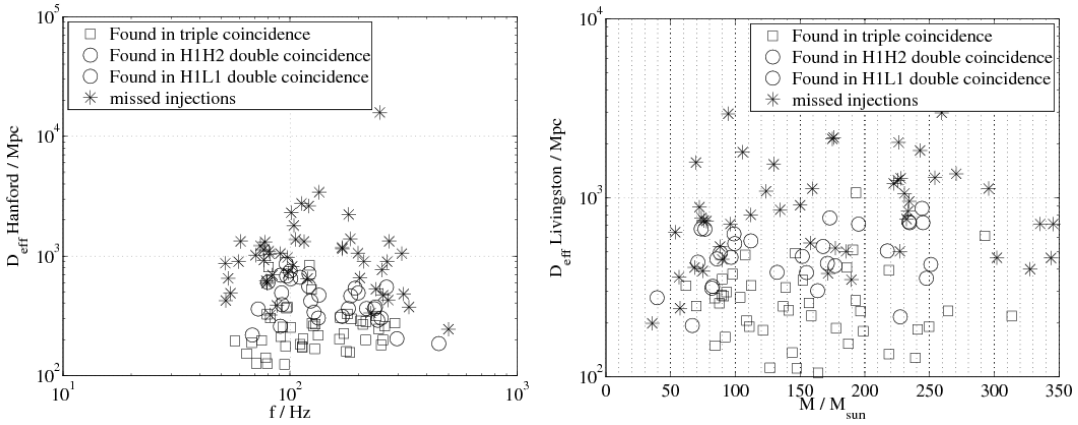

Figure 5.8: **Distribution of injections found and missed by the ringdown pipeline.** The left figure shows the effective distance of the injected signal in the LIGO Hanford Observatory as a function of the predicted ringdown frequency. The right figure shows the effective distance of the injected signal in the LIGO Livingston Observatory as a function of the total initial mass of the signal. The figures show signals found in triple coincidence (blue crosses), in double coincidence in H1H2 (green stars), in double coincidence in H1L1 (cyan stars), and missed (red circles).

missed injections which, given their frequencies and effective distances, we would have expected to find. However, all three of these are (non-spinning) injections with mass ratio of 4:1, and thus the energy emitted in the ringdown is less than would be emitted by a binary of the same total mass but with a mass ratio of 1 [302]. This is not taken into account in the calculation of effective distance.

Equations (5.5) and (5.6) can be inverted to calculate M and a from the template parameters f and Q of a given GW candidate. Figure 5.9 shows the accuracy with which the ringdown search measures the mass and peak time of the injected signals. Given that mass is radiated during the ringdown phase (the exact amount depends on the initial mass ratio) one would expect the measured mass to underestimate the mass of the signal, and hence the data points would lie below the diagonal. However, the recovered frequency is systematically underestimated due

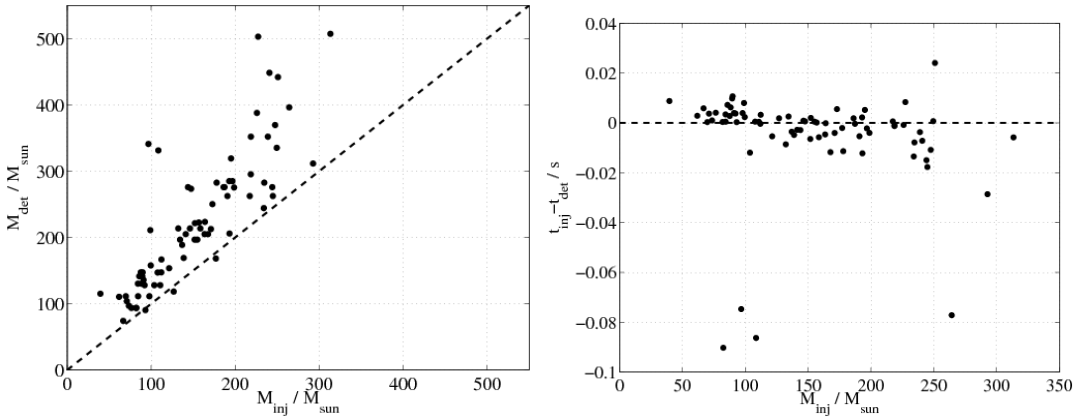

Figure 5.9: **Accuracy of measuring the ringdown parameters.** The left figure shows the detected ringdown mass versus total injected mass for all found injections. The right figure shows the difference between the time of injected waveform peak amplitude and the start time of the ringdown as found by the search.

to the presence of the preceding inspiral, leading to an overestimation of the mass. The peak time of the signal is measured with similar accuracies to the coalescence time measured by the TaylorF2 templates described in Section 5.2.1. The three data points with a large time difference and masses lying in the range 80 and 110 $M_{\odot}$ are part of the `PU_T52W` non-spinning, equal mass group where the peak amplitude occurred early in the waveform (i.e prior to the merger).

5.3 Conclusions

The NINJA project was conceived as a first step towards a long-term collaboration between numerical relativists and data analysts with the goal of using numerical waveforms to enhance searches for gravitational waves. NINJA is unique in that it focused on running existing GW search algorithms on data containing waveforms obtained from numerical simulations. Since this constitutes the first such analysis,

the scope of the project was deliberately kept somewhat modest: restrictions were placed on the number of waveforms to be submitted by each numerical group, no attempt was made to include transient noise sources in the data and only a limited number of simulated signals were produced for the data analysis. This helped to encourage significant involvement from both the numerical relativity and data analysis communities, with ten numerical relativity groups providing waveforms and data-analysis contributions from nine different groups.

Communication between the data analysis and numerical communities has been smooth and fluent during the course of the NINJA project. The format described in [345] provided a good starting point from which to interchange data between the communities. As the project was being developed, several improvements were made to the format, which we expect will continue evolving as more experience is gained with a broader family of waveforms, including those containing matter.

The limited number of signals in the NINJA data makes it dangerous to draw strong conclusions from the comparison of different waveform families and different search methods. Overall, it is clear that many of the data analysis methods were capable of detecting a significant fraction of the simulated waveforms. This is immediately significant as several of the analyses performed are routinely used in searches of the LIGO and Virgo data. However, since the NINJA data set did not include the type of non-Gaussian transients seen in real GW detector data, it is difficult to translate the efficiencies observed here into statements about LIGO or Virgo sensitivity.

NINJA has demonstrated that more work is required to measure the parameters of signals in detector data. Parameter estimation is poor for most pipelines, and several methods tend to associate a candidate event to that part of the waveform which lies in the most sensitive band of the detector. For example, in a search with inspiral only templates, the ringdown of a high mass black hole which occurs at around 100 Hz might be picked up. This will lead to poor estimation of both the binary's mass and coalescence time. Similarly, the un-modelled burst searches will correctly identify the signal but, without knowing which part of the coalescence it corresponds to, have difficulty providing accurate parameters. There is some evidence that using full inspiral-merger-ringdown waveform templates alleviates this problem, as well as evidence that estimation of the sky location of the signal is largely independent of the mismatches between simulated and template waveform. These are all issues which warrant further investigation.

We hope that this work will provide a foundation for future analyses, and plans are envisioned to continue and extend the NINJA project. Several suggestions have been made to broaden this work and make it more systematic: in addition to expanding the parameter space explored by numerical simulations, two crucial steps will be to construct hybrid analytic-numerical waveforms (which will allow a lower range of masses to be injected) and to consider data containing non-stationary noise. It would also be natural to include other waveform families, such as supernovae or binary mergers comprising one or two neutron stars. Subsequent NINJA projects could provide a noise-free data set for tuning parameter estimation and measurement pipelines and release "training" and "challenge" data sets, as has proven success-

ful in the Mock LISA Data Challenges [346, 347], in which the parameters of the waveforms are known and unknown to the analysts, respectively. The numerical data sets may also be useful for efforts aimed at using the best-available waveforms to explore and develop LISA data analysis approaches and in evaluating parameter estimation accuracy for LISA. These efforts, as carried out by the Mock LISA Data Challenge Task Force and the LISA Parameter Estimation Task Force, are summarised in Ref. [348, 349].

However future analyses progress, it is clear that a significant amount remains to be learned from collaborations between the numerical relativity and gravitational-wave data analysis communities.

Chapter 6

Improvements in parameter estimation of gravitational wave signals in ground-based detectors with amplitude-corrected inspiral-merger-ringdown waveforms

6.1 Introduction

If a gravitational wave is detected by ground-based laser interferometers such as LIGO or Virgo (or by any other experiment), it will be a very exciting confirmation of the predictions of general relativity. Beyond simply confirming this basic prediction, one would also like to extract as much scientific information as possible. To do this, one must determine the parameters which characterize the waveform as accurately as possible. This includes parameters describing the source, such as the masses, spins, location and orientation of the source. One could potentially deduce a wealth of astrophysical information from these source parameters, particularly if many detections are made. For example, one might learn how common compact binaries are and how they are distributed in space, if they are likely to be higher or lower mass, have large or small spins, and whether they form in galaxies or globular clusters. One could also extract information of a more cosmological or theoretical nature. For example, if an electromagnetic counterpart to a binary coalescence is observed along with a gravitational wave signal, one would have inde-

pendent measurements of the redshift and the luminosity distance [115, 5, 350, 351]. This would allow one to measure the rate of expansion of the Universe and Hubble's constant rather precisely [7]. One could also parametrize the effects alternative theories of gravity would have on the waveform and attempt to measure these parameters to test general relativity and constrain alternative theories, as studied in Refs. [110, 352, 111, 353, 354], for example.

So far, very many studies have been done on the parameter estimation capabilities of current and future GW detectors (a sample of these studies were listed in Sec. 2.3.3). Most of these studies have used restricted, adiabatic PN waveforms. A few notable exceptions for ground-based detectors are Ref. [116], which used amplitude-corrected PN waveforms of inspiralling binaries with spin-corrections in the phase (but *not* the amplitude), Ref. [117], which used so-called phenomenological (restricted) IMR waveforms, and for space-based detectors Ref. [118], which used EOB IMR waveforms with and without amplitude corrections. Such improved waveform models (relative to the restricted PN waveforms) have the potential to improve parameter estimation capabilities and will likely be employed in future searches and parameter extraction methods for gravitational wave detectors, so it is important to understand just what effect these improved waveform models will have. In the context of advanced ground-based detectors, Ref. [116] found that a single detector using amplitude-corrected PN waveforms could estimate the mass and spin parameters, the time of coalescence and the binary inclination with good accuracy. These errors were significantly better than when using restricted PN waveforms, especially for large total mass and for asymmetric binaries. In the context of initial

and advanced ground-based detectors, Ref. [117] found that the phenomenological waveforms gave improvements in parameter estimation relative to PN waveforms due to the inclusion of a merger-ringdown signal. This improvement was greatest for masses $\gtrsim 100\,M_{\odot}$. This study was limited to mass ratios in the range 1:1 - 4:1, because NR simulations were not available to calibrate the phenomenological waveforms outside this range, and consequently the phenomenological waveforms become unreliable at more extreme mass ratios. In the context of the space-based LISA, Ref. [118] found that both the merger-ringdown and amplitude corrections could offer improvements to parameter estimation. The merger-ringdown was found to be especially important for determining the sky position of the source. This work considered mass ratios 1:1 - 10:1, although it did not attempt to estimate the mass ratio, but treated it as though it were known exactly.

In this work, we would like to confirm and build upon these results by studying the parameter estimation capabilities of EOB IMR waveforms with (and without) amplitude corrections. One improvement is that we will not assume the mass ratio is known or restrict ourselves to comparable masses. In this work, we will consider mass ratios as extreme as $\nu = 0.04$ (roughly a 23:1 component mass ratio). Unfortunately, due to concerns over the accuracy and robustness of our results, we find it necessary to restrict ourselves to total mass $\leq 100\,M_{\odot}$ and a single initial LIGO detector (but in the future we plan to extend our results to total mass $\gtrsim 100\,M_{\odot}$ and a network of advanced detectors, where we expect the merger-ringdown and amplitude corrections to have the most significant impact). One positive note is that our extreme mass ratio results are just as robust as our comparable mass results, so we cover some

new ground relative to the works mentioned above.

The rest of this chapter is organized as follows: in Sec. 6.2, we will review the methods used in this study, including the waveforms and how the errors can be estimated using the Fisher matrix formalism and how we have implemented the waveforms and Fisher matrix calculation. In Sec. 6.3, we explain some of the difficulties faced in performing these Fisher matrix calculations accurately, and the many tests we have done to check the robustness of our results. In Sec. 6.4, we present the main results of this chapter and plot parameter errors as we vary the total mass, symmetric mass ratio and binary inclination. In Sec. 6.5, we summarize our results.

6.2 Methods

6.2.1 Waveform models

For this study, we use the EOB model described in Sec. 2.2.2. This will include a *restricted* version, which is a Newtonian amplitude waveform in which only the $(2, \pm 2)$ mode is present, and an *amplitude-corrected* version, which is a 0.5PN amplitude in which the $(2, \pm 2)$, $(3, \pm 3)$, $(2, \pm 1)$ and $(3, \pm 1)$ modes are present. In either case, the dynamical variables are evolved in the same way, according to Eqs. (2.69)-(2.72). The only difference is which set of harmonic modes the orbital phase Φ and frequency $\omega_{\rm orb}$ are plugged into. The ringdown attachment procedure is the same for all modes, as outlined in Sec. 2.2.2.3, and is always done at the same orbital frequency, the $\omega_{\rm match}$ of Eq. (2.89). The polarizations are obtained from the

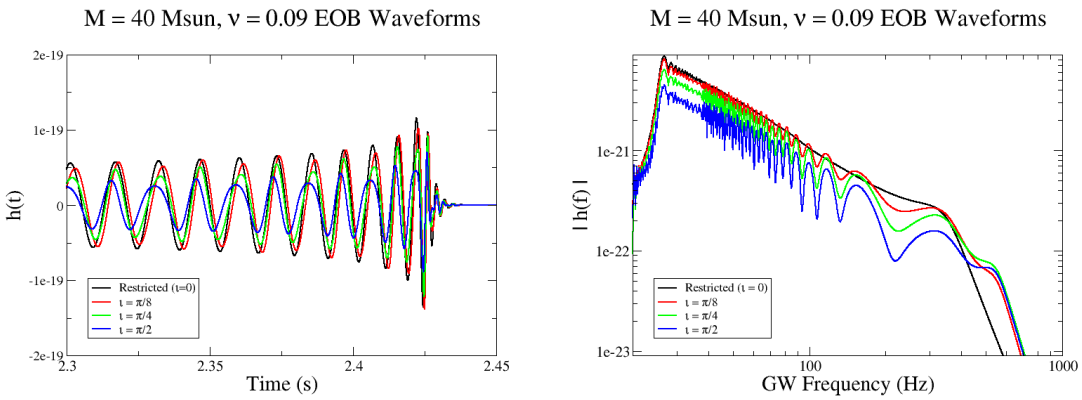

Figure 6.1: We plot restricted (or, equivalently amplitude-corrected with $\iota = 0$) and amplitude-corrected EOB waveforms for several choices of ι for an $M = 40\,M_\odot$, $\nu = 0.09$ binary in the time-domain (left panel) and frequency-domain (right panel).

modes with Eq. (2.53), and the strain measured by a detector, $h(t)$ is then

$$h(t) = F_+\ h_+(t) + F_\times\ h_\times(t)\ , \tag{6.1}$$

where the antenna pattern functions F_+ and $F_\times$ are functions of the sky position (θ, ϕ) and polarization angle ψ of the source relative to the detector. Recall that for an interferometer with right angle arms, the antenna functions are given by

$$\begin{aligned} F_+(\theta,\phi,\psi) &= \frac{1}{2}\left(1+\cos^2\theta\right)\,\cos 2\phi\,\cos 2\psi - \cos\theta\,\sin 2\phi\,\sin 2\psi\,, \\ F_\times(\theta,\phi,\psi) &= \frac{1}{2}\left(1+\cos^2\theta\right)\,\cos 2\phi\,\sin 2\psi + \cos\theta\,\cos 2\phi\,\sin 2\psi\ . \end{aligned} \tag{6.2}$$

In Fig. 6.1, we plot the restricted waveform and the amplitude-corrected waveform (for a few different binary inclinations ι) for a binary with total mass $M = 40\,M_\odot$ and symmetric mass ratio $\nu = 0.09$ in the time-domain and frequency-domain. Note that the 1^{st} and 3^{rd} harmonics (the modes with $m = \pm 1\,,\,3$ respec-

tively) modulate the waveform in the time-domain. In the frequency-domain, the different harmonics interfere with one another (mostly destructively), and the 3^{rd} harmonic extends the frequency band of the signal relative to the restricted waveform. The odd harmonics are all proportional to $\sin\iota$ and $\delta = (m_1 - m_2)/M$, so their effect is most noticeable for large inclinations and extreme mass ratios.

6.2.1.1 Restricted waveform

For the restricted waveform, the GW polarizations for a non-spinning binary are given by

$$\begin{aligned} h_+(t) &= -\frac{2\,M\,\nu\,v^2}{D_L}\,\left(1+\cos^2\iota\right)\,\cos 2\Phi(t)\ , \\ h_\times(t) &= -\frac{2\,M\,\nu\,v^2}{D_L}\,2\cos\iota\,\sin 2\Phi(t)\ , \end{aligned} \tag{6.3}$$

where $M = m_1 + m_2$ is the total mass, $\nu = m_1\,m_2/M^2$ is the symmetric mass ratio, $\Phi(t)$ is the binary orbital phase, $v = (M\,\omega_{\rm orb})^{1/3}$ is a PN expansion parameter, $D_L = D\,(1+z)$ is the redshifted distance, and ι is the inclination angle between the binary's orbital angular momentum, $\mathbf{L}$ and the direction of propagation, $\widehat{\mathbf{N}}$, or $\cos\iota = \widehat{\mathbf{N}}\cdot\widehat{\mathbf{L}}$. It is common to define the *effective distance* as

$$D_{\rm eff} = \frac{D_L}{\sqrt{F_+^2\,\left(1+\cos^2\iota\right)^2 + F_\times^2\,4\,\cos^2\iota}}\ . \tag{6.4}$$

For restricted waveforms, any binary at an arbitrary sky location with an arbitrary orientation is equivalent to one which is optimally located (directly overhead) and

optimally oriented ("face-on") at distance $D_{\rm eff}$. In addition, one can define an angle

$$\varphi_0 = \tan^{-1}\left(\frac{F_\times\, 2\, \cos\iota}{F_+\, (1+\cos^2\iota)}\right) \ , \tag{6.5}$$

which can be absorbed into the orbital phase and thus simplify the waveform

$$\begin{aligned} h(t) &= -\frac{2\,M\,\nu\,v^2}{D_{\rm eff}}\,\left[\cos\varphi_0\,\cos 2\Phi(t-t_{\rm ref}) + \sin\varphi_0\,\sin 2\Phi(t-t_{\rm ref})\right] \\ &= -\frac{2\,M\,\nu\,v^2}{D_{\rm eff}}\,\cos\left[2\Phi(t-t_{\rm ref}) - \varphi_0\right] \ . \end{aligned} \tag{6.6}$$

Therefore, the restricted waveform can be described in terms of 5 parameters: Two mass parameters, one parameter for the overall amplitude or effective distance, and two parameters which specify a reference time of the waveform, and the phase at that reference time. However, as noted in Refs. [89, 119], in a Fisher matrix calculation, the amplitude (or $D_{\rm eff}$) parameter does not correlate with the others, which are determined from the waveform phasing. Therefore, the Fisher matrix is block-diagonal, and one finds that the fractional error on the amplitude (or $D_{\rm eff}$) of the restricted waveform is simply the inverse of the SNR, $1/\rho$. Therefore, for the purposes of the Fisher matrix calculation, the parameter set for the restricted waveform is

$$\{\mathcal{M}_c, \nu, t_{\rm ref}, \phi_{\rm ref}\} \ , \tag{6.7}$$

where $\mathcal{M}_c = M\,\nu^{3/5}$ is the so-called "chirp mass" (this mass parameter can be determined more precisely than other mass parameters because the phase of the frequency-domain waveform $\propto \mathcal{M}_c^{-5/3}$ at leading-order), $t_{\rm ref}$ is the time at which

the waveform reaches some reference point, and $\phi_{\rm ref} = 2\,\Phi(t_{\rm ref})$ is the GW phase at the reference point.

6.2.1.2 Amplitude-corrected waveform

Once amplitude corrections are added to the restricted waveform, it is no longer true that any arbitrarily oriented binary is equivalent to an optimally located and oriented binary at distance $D_{\rm eff}$. The amplitude-corrected waveform has the same dependence on the sky position and polarization angle as the restricted waveform. However, the amplitude corrections have a different dependence on the binary inclination from the leading order amplitude term. In fact, the 1st and 3rd harmonics of the orbital phase that appear at 0.5PN order (and all odd harmonics) are proportional to $\sin\iota$, and so vanish when $\iota = 0$. The 0.5PN order amplitude strain is given as

$$\begin{aligned} h(t) &= -\frac{2\,M\,\nu\,v^2}{D_L}\left\{F_+\left[\left(1+c_\iota^2\right)\,\cos 2\Phi(t)\right.\right. \\ &+ v\,\delta\,s_\iota\left(\frac{5}{8}+\frac{1}{8}c_\iota^2\right)\,\cos\Phi(t) - v\,\delta\,s_\iota\left(\frac{9}{8}+\frac{9}{8}c_\iota^2\right)\,\cos 3\Phi(t)\Big] \\ &+ \left.\left. F_\times\left[2c_\iota\,\sin 2\Phi(t) + \frac{3}{4}v\,\delta\,s_\iota\,c_\iota\,\sin\Phi(t) - \frac{9}{4}v\,\delta\,s_\iota\,c_\iota\,\sin 3\Phi(t)\right]\right\}\,, \end{aligned} \tag{6.8}$$

where $\delta = (m_1 - m_2)/M = \sqrt{(1-4\,\nu)}$ and c_ι and s_ι are shorthand for $\cos\iota$ and $\sin\iota$ respectively.

Note that a binary for which $\iota \neq 0$ is not equivalent to any optimally oriented ($\iota = 0$) binary, because the former contains three harmonics, while the latter will

have only the 2nd harmonic present. With this more complicated structure, one cannot absorb everything into a single overall amplitude parameter and phase offset. Our amplitude-corrected waveform has 9 physically meaningful parameters,

$$\{\mathcal{M}_c, \nu, t_{\rm ref}, \phi_{\rm ref}, \iota, D_L, \theta, \phi, \psi\} \ . \tag{6.9}$$

In principle, a single detector could measure ι, because the harmonic content of the waveform will vary as ι varies, but in practice it is poorly determined because of degeneracies with other angular parameters. Note that the strain depends on the sky position and polarization angle only through the antenna pattern functions, so that one can immediately reduce the number of parameters by one

$$\{\mathcal{M}_c, \nu, t_{\rm ref}, \phi_{\rm ref}, \iota, D_L, F_+, F_\times\} \ . \tag{6.10}$$

Furthermore, one can map F_+, $F_\times$ and $D_{\rm L}$ onto an overall amplitude and angle giving the ratio of antenna pattern functions,

$$\mathcal{A} = {\rm sign}(F_+) \frac{\sqrt{F_+^2 + F_\times^2}}{D_{\rm L}} \ , \tag{6.11}$$

$$\alpha = \tan^{-1}\left(\frac{F_\times}{F_+}\right) \ . \tag{6.12}$$

These parameters may be thought of as the "antenna amplitude" and "antenna angle", respectively. Thus, we can reduce the total number of parameters to seven,

i.e.

$$\{\mathcal{M}_c, \nu, t_{\rm ref}, \phi_{\rm ref}, \iota, \mathcal{A}, \alpha\} \ . \tag{6.13}$$

Therefore, in terms of these seven parameters, the amplitude-corrected strain is

$$\begin{aligned} h(t) &= -2\,\mathcal{M}_c\,\nu^{2/5}\,v^2\,\mathcal{A}\Bigg\{\cos\alpha\left[\left(1+c_\iota^2\right)\,\cos 2\Phi(t)\right. \\ &+ \left. v\,\delta\,s_\iota\left(\frac{5}{8}+\frac{1}{8}c_\iota^2\right)\cos\Phi(t) - v\,\delta\,s_\iota\left(\frac{9}{8}+\frac{9}{8}c_\iota^2\right)\cos 3\Phi(t)\right] \\ &+ \sin\alpha\left[2c_\iota\,\sin 2\Phi(t) + \frac{3}{4}v\,\delta\,s_\iota\,c_\iota\,\sin\Phi(t) - \frac{9}{4}v\,\delta\,s_\iota\,c_\iota\,\sin 3\Phi(t)\right]\Bigg\}\ , \end{aligned} \tag{6.14}$$

where for brevity we use $\delta = \sqrt{1-4\,\nu}$.

6.2.2 Choice of reference point

For the waveform parameters $t_{\rm ref}$ and $\phi_{\rm ref}$, one is free to choose any reference point in the waveform one wants, such as the "time of arrival" when the waveform enters the band of the detector, the time it reaches a certain frequency, or the time when the waveform reaches its peak amplitude. However, by far the most common choice has been the time at which the frequency formally diverges in the PN adiabatic approximation, which is called the "time of coalescence"[1]. The vast majority of Fisher matrix studies have also used SPA (TaylorF2) waveforms. The only exceptions of which I am aware are Ref. [117], which used phenomenological waveforms (frequency-domain IMR waveforms which are an extension of the SPA waveform) and Ref. [118], which used EOB IMR waveforms similar to the model used

[1]This is something of an abuse of the language, as the frequency does not become infinite when the two bodies coalesce.

here but with a merger-ringdown generated using the so-called "implicit rotating source" model (also ν was assumed to be known exactly and not included as a parameter in the Fisher matrix) in the context of LISA.

For all of the studies with SPA waveforms (and also the phenomenological waveforms of Ref. [117]), the frequency-domain phase takes the form of Eq. (3.18) *only if* the reference point is the "time of coalescence". If the reference point occurs at any other frequency, one must subtract the phase evaluated at the reference point,

$$\Psi(f) \to \Psi(f) - \Psi(f_{\rm ref}) \ . \tag{6.15}$$

However, these phase terms evaluated at $f_{\rm ref}$ have been largely ignored and rarely if ever appear in formulas for the SPA phase in the literature. This may partly explain why nearly every Fisher matrix study has used the "time of coalescence" as the reference point. The choice of reference point does more than simplify the SPA phase, however. The time and phase can be measured more precisely at some reference points than others. For example, Ref. [355] showed that the "time of coalescence" can be measured more precisely than the time of arrival. To understand intuitively why this is, note that the frequency changes slowly early on and rises much faster at the end. Therefore, the waveform is at approximately the arrival frequency for a relatively long time, but chirps up to its final frequency in a much shorter time. Later, Ref. [356] showed that an even better estimation can be obtained by choosing the time at which the waveform frequency reaches the most sensitive frequency of the detector. While a clever choice of reference point can improve the

precision with which the reference time and phase are measured, the errors on the other parameters should be the same for any reference point (as we will see, this is one way to test the robustness of Fisher matrix results).

For EOB waveforms, the frequency never diverges, so there is no such thing as the "time of coalescence" in the sense of the PN adiabatic waveforms and one must choose another reference point. Since EOB waveforms are generated by numerically integrating a set of evolution equations, we can directly control the phase only at the start of the evolution. Therefore, a convenient choice would be to choose the reference time as the start of the evolution. However, as we have already noted, this will give larger errors on the reference time and phase than a later reference point. More importantly, as we will see in Sec. 6.3, the Fisher matrix results for this reference point are not very robust for high masses. One could also choose a particular frequency as the reference point, as in Ref. [356], but again we find our results are not very robust. Lastly, one could choose some physical feature of the waveform, such as the peak of the waveform amplitude, as was done with the EOB waveforms of Ref. [118]. For a coalescing waveform the peak of the waveform is quite close to the peak of the radiated energy and also the formation of a common apparent horizon in NR simulations, and so it is a very natural definition of "time of coalescence". In a private communication, the primary author of Ref. [118] explained the peak was chosen as the reference point both because it is a real, physically observable feature of the waveform and because the Fisher matrix errors were more robust with this choice of reference point. Indeed, as we will see in Sec. 6.3, we also find this reference point to be more robust than others.

6.2.3 Computing the Fisher matrix

To compute the Fisher matrix, one must first compute the parameter derivatives of the waveform,

$$h_i(t) \equiv \frac{\partial h(\boldsymbol{\lambda}, t)}{\partial \lambda^i} = \lim_{\delta\lambda^i \to 0} \frac{h(\lambda^i + \delta\lambda^i, t) - h(\lambda^i - \delta\lambda^i, t)}{2\,\delta\lambda^i} \tag{6.16}$$

for each parameter λ^i. Then, the Fisher matrix is constructed by computing the inner products of the parameter derivatives,

$$\Gamma_{ij} = (h_i | h_j) \ . \tag{6.17}$$

Here "(|)" is the inner product of Eq. (2.103). Now, formally this inner product is an integral over the infinite frequency range $[0, \infty)$, but in practice we can compute it over a finite range. First of all, real ground-based interferometers have a "seismic wall" at some frequency $f_{\rm low}$ and below that frequency $S_n(f)$ is very large and any contribution to the inner product would be negligible. At the upper end, the waveform may end at some frequency. For example, PN waveforms, which assume an adiabatic inspiral, are typically cut at the frequency of the ISCO for a test particle orbiting a Schwarzschild black hole, since inside the ISCO there are no circular orbits, and the adiabatic assumption breaks down. For EOB and other IMR waveforms, the waveform extends past the ISCO and reaches the ringdown. The ringdown will peak at the frequency of the dominant QNM and then decay as a Lorentzian at higher frequencies. Therefore, one could cut IMR waveforms at, say

twice the frequency of the $(2, 2, 0)$ QNM mode to capture all of the non-negligible signal. Alternatively, note that any interferometer will produce discretely sampled data, and so it cannot resolve any signal at frequencies higher than the Nyquist frequency (half the sampling frequency) and so the Nyquist frequency could always be used as the upper frequency cutoff. Therefore, we will compute the Fisher matrix elements as the integral

$$\Gamma_{ij} = 4\,\mathrm{Re}\left[\int_{f_{\rm low}}^{f_{\rm cut}} \frac{\tilde{h}_i(f)\,\tilde{h}_j^*(f)}{S_n(f)}\,df\right] \ , \tag{6.18}$$

where $f_{\rm low}$ is the low frequency seismic cutoff of the interferometer, and $f_{\rm cut}$ can be the ISCO frequency, twice the $(2, 2, 0)$ QNM frequency, or the Nyquist frequency.

6.2.4 Implementations

To integrate Hamilton's equations, we use an adaptive step size fourth-order Runge-Kutta routine adapted from the functions `odeint`, `rkck` and `rkqs` from Ref. [357]. With this routine, one specifies an accuracy goal, ϵ. At each step, one estimates the error on each of the variables, requires that each is within the accuracy goal, and adjusts the step size appropriately to try to reach this goal. This can be either an absolute accuracy or a fractional accuracy. We enforce a fractional accuracy on r, p_r and p_ϕ, but an absolute accuracy on ϕ. The Runge-Kutta integration routine provides us with a time series for ϕ and the other variables sampled at uneven times. We use a cubic spline interpolation routine based on the functions `spline` and `splint` from Ref. [357]. This routine fits a cubic polynomial between

adjacent raw data points for ϕ, and the fitted polynomial is evaluated at each desired sample point, $\phi(k\,\Delta t)$, where Δt is the sampling interval, and k is an integer labeling each sample. To get the time series for $\omega_{\rm orb}(k\,\Delta t)$, we take the derivative of the fitted polynomial and evaluate it at each sample. One could also obtain $\omega_{\rm orb}$ by storing the right hand side of Hamilton's equation for $d\phi/dt$ at each step of the Runge-Kutta routine, and interpolating that data directly. The two methods agree very well.

The parameter derivatives are computed by finite difference in the time domain. Fourier transforms of the waveform and parameter derivatives are computed using the routines of the "fastest Fourier transforms in the West" (FFTW) package [358, 359], which is very widely used and tested. We have checked the FFTW routines by comparing with *Mathematica* and find agreement to within machine precision (fractional errors $\simeq 10^{-16}$). We have also checked that the parameter derivative and Fourier transform operations commute. That is, one can compute the finite difference in the time domain and then Fourier transform the difference, or one can take the finite difference between two Fourier transformed waveforms. The two approaches give identical parameter derivative spectra, Fisher matrices and parameter errors to within machine precision. Taking the finite difference in the time domain is slightly faster, as one computes a single Fourier transform of the finite difference, rather than Fourier transforming two perturbed waveforms.

The inner products of the Fisher matrix are all computed as finite sums

$$(h_i|h_j) = \int_{f_{\rm low}}^{f_{\rm cut}} \frac{\tilde{h}_i(f)\,\tilde{h}_j^*(f)}{S_n(f)}\,df = \sum_{k=f_{\rm low}/\Delta f}^{f_{\rm cut}/\Delta f} \frac{\tilde{h}_i(k\,\Delta f)\,\tilde{h}_j^*(k\,\Delta f)}{S_n(k\,\Delta f)}\,\Delta f\ , \tag{6.19}$$

where the frequency step size Δf is determined by the length of the time domain waveform. The time series of the waveform and its derivatives are padded with zeroes to a power of 2, so the fast Fourier transform routines are as efficient as possible. We have changed the amount of padding to change the step size Δf, and find that the finite sum of Eq. (6.19) is consistent for different Δf.

Once the Fisher matrix is computed, we invert it to obtain the covariance matrix using the matrix inversion routine of the Newmat package [360]. This routine has been checked against the *Mathematica* matrix inversion routine, and the results agree to within machine precision.

6.3 Difficulties of the Fisher matrix with time-domain waveforms

As noted in Ref. [119], there are several potential pitfalls with the Fisher matrix formalism. First of all, the result is derived under the assumption of stationary Gaussian noise, while real interferometer data can have non-stationary, non-Gaussian "glitches". Second, (first generation) ground-based interferometers expect to make detections at SNR ~ 10, and it is not clear that this qualifies as the limit of "high SNR". These two points are fundamental limitations of the Fisher matrix, and

there is nothing we can do within the Fisher matrix formalism to remedy them. We simply have to consider our results to be rough estimates of the expected parameter errors. If a more accurate result is needed, we must resort to more sophisticated methods, such as including higher order corrections to the parameter space probability density or performing MCMC studies. Furthermore, we can use the Fisher matrix in situations where the SNR is larger, to alleviate the second concern. It is likely that the Advanced LIGO and Virgo detectors will make many detections at SNR ~ 10, although they may also make some detections at SNR ~ 100. Furthermore, the proposed third generation Einstein telescope (ET) would likely make many detections at SNR $\gtrsim 100$, and so the Fisher matrix would be better suited to studies of these advanced detectors. These advanced detectors will have sensitivity down to lower frequencies, potentially down to 10 Hz for Advanced LIGO and Virgo and perhaps even down to 1 Hz for ET, and so the waveforms will be much longer for these instruments. Unfortunately, at the present time we have some difficulty getting robust Fisher matrix results for these longer waveforms, so we will focus primarily on initial LIGO, although in the future we hope to obtain results for the advanced detectors.

Another issue is the possibility of an "ill-conditioned" Fisher matrix, which means that the ratio of the largest and smallest eigenvalues of the matrix is quite large. As pointed out in Refs. [115, 119], if the ratio of the largest to smallest eigenvalues of the Fisher matrix is κ, and the Fisher matrix elements are computed to within some numerical error $\delta\Gamma$, then the error on the covariance matrix *can be* magnified by κ. That is, $\delta\Sigma \leq \kappa\, \delta\Gamma$. This is an upper bound for the error on Σ, and

we may not hit this bound in practice. However, since the ratio of eigenvalues for the Fisher matrices in this study are typically $\gtrsim 10^{12}$, even if we are several orders of magnitude away from this upper bound, we will still lose several digits of precision. This is a reason for concern and we must take care to compute the Fisher matrix accurately and check the result for robustness.

An effort has been made to understand and test the precision of each step of the Fisher matrix calculation. As already noted, we have tested our `C++` matrix inversion and fast Fourier transform routines by comparing them with *Mathematica* routines. Both of the `C++` routines agree with their *Mathematica* counterparts to within machine precision. We have also tested the robustness of computing the inner product as a finite sum by changing the frequency step size (via the amount of zero-padding of the time-domain waveforms). While the results do not agree down to the level of machine precision, the parameter errors (i.e. the results *after* the matrix inversion) typically vary by less than a few percent. We consider this adequate, since we only trust the Fisher matrix results to the level of about one significant digit due to their fundamental limitations (non-Gaussianities and low SNR). Furthermore, we have tested all of these routines by computing the Fisher matrix with SPA waveforms with analytic parameter derivatives and comparing the results against published results such as Refs. [89, 90, 111]. In all cases, we can reproduce the published results to the number of significant digits provided in those papers. Furthermore, we have compared against the same references using SPA waveforms with derivatives computed by finite difference. We are able to reproduce the published results to within 1% for a range of parameter step sizes spanning

many orders of magnitude. Therefore, we are confident that the matrix inversion, fast Fourier transform, inner product and finite difference routines are sufficiently precise and robust.

However, while we find that the finite difference routine is quite robust when used on SPA waveforms, this is not the case for our time-domain EOB waveforms. Actually, for the EOB waveforms, the finite difference is still robust for the parameters $t_{\rm ref}$, $\phi_{\rm ref}$, ι, $\mathcal{A}$ and α for step sizes spanning many orders of magnitude. It is only the mass parameters $\mathcal{M}_c$ and ν which are less robust. Therefore, one must take care to check that the mass parameter derivatives have "converged", i.e. that the final results do not vary much as the finite difference step size is changed.

The difficulty with taking the mass parameter derivatives does not lie with the finite difference routine itself, but rather with the fact that our time-domain EOB waveforms are computed by numerically solving evolution equations, while the SPA waveforms are given by an analytic formula. This means our time-domain EOB waveforms will have some numerical error associated with them that is not present in the SPA waveforms. Let us take the finite difference between two perturbed waveforms, $h(\lambda^i \pm \delta\lambda^i, t)$ with numerical errors $\delta h_\pm(t)$ respectively. Then, our finite difference parameter derivative

$$h_i(t) \equiv \frac{\partial h(\boldsymbol{\lambda}, t)}{\partial \lambda^i} \simeq \frac{(h(\lambda^i + \delta\lambda^i, t) + \delta h_+(t)) - (h(\lambda^i - \delta\lambda^i, t) + \delta h_-(t))}{2\,\delta\lambda^i} \tag{6.20}$$

will have an error $(\delta h_+(t) - \delta h_-(t)) \,/\, (2\,\delta\lambda^i)$ resulting from the numerical error in our numerically-computed waveforms. Note this is in addition to the error from

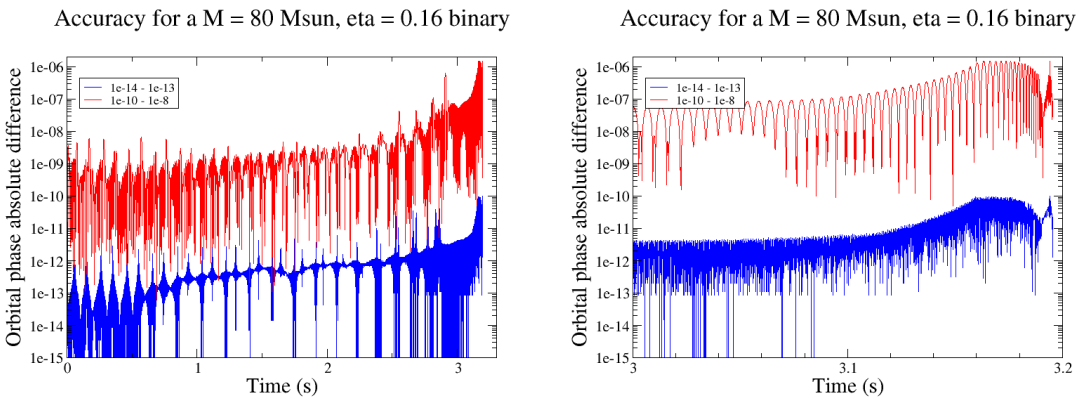

Figure 6.2: We plot the absolute difference in orbital phase for different choices of the integration accuracy goal, $|\Phi(\epsilon_1, t) - \Phi(\epsilon_2, t)|$ for an $M = 80\,M_\odot$, $\nu = 0.16$ binary. We compare $\epsilon_1 = 10^{-8}$, $\epsilon_2 = 10^{-10}$ (red curve) and $\epsilon_1 = 10^{-13}$, $\epsilon_2 = 10^{-14}$ (blue curve). The right panel is a zoom on the end of the left panel. We see that the difference in phase (and thus the waveform error) rises at late times.

approximating a derivative (a limit as the step size goes to zero) by a finite difference.

This numerical error term, $(\delta h_+(t) - \delta h_-(t)) \,/\, (2\,\delta\lambda^i)$ does not exist for SPA waveforms. Furthermore, for the parameters $t_{\rm ref}$, $\phi_{\rm ref}$, ι, $\mathcal{A}$ and α of our EOB waveform this error term will be zero. The reason is that these are *extrinsic* parameters which describe the position, orientation and reference point of our waveform. They will not affect the evolution of our binary. We simply numerically solve our evolution equations once to get the orbital phase $\Phi(t)$ and frequency $\omega_{\rm orb}(t)$ and plug the same time series into waveforms of Eq. (6.14) or Eq. (6.6) with different extrinsic parameters. Therefore, the two perturbed waveforms will have the *same* numerical errors and they will cancel, $\delta h_+(t) = \delta h_-(t)$. If we perturb the mass parameters, the two perturbed waveforms will have different evolutions, so when they are computed they will have different numerical errors, $\delta h_+(t) \neq \delta h_-(t)$. The numerical errors do not cancel and in fact get magnified by a factor $(2\,\delta\lambda^i)^{-1}$.

We do have some control over the numerical error associated with the waveform generation through the accuracy goal, ϵ, of the Runge-Kutta integration routine. To generate waveforms for matched filtering templates, it should be sufficient to choose an accuracy goal of, say $\epsilon \sim \mathcal{O}\left(10^{-8}\right)$. With this choice, the routine can take rather large steps over most of the waveform, and take smaller steps over the more delicate end of the waveform. For this accuracy goal, the waveforms considered here can typically be generated in a few seconds. However, since the numerical error on the derivatives can be $\sim \left(\delta\lambda^i\right)^{-1}$ larger than the numerical error on the waveforms, we must enforce a higher precision. For all of the Fisher matrix calculations presented here, we will use $\epsilon = 10^{-14}$ as our accuracy goal. This is a rather lofty goal, as it is approaching the machine precision. To try and reach this goal, the Runge-Kutta routine will typically take many more steps than for $\epsilon = 10^{-8}$. For the waveforms considered here, it can take tens of minutes to generate a waveform. In Figs 6.2 and 6.3, we check whether the orbital phase and frequency are really accurate to within the accuracy goal by comparing the time series for different ϵ. We see that the difference is comparable to the accuracy goal for most of the evolution, but that the difference rises rather sharply at the end and becomes larger than the accuracy goal. We typically find that our Fisher matrix results are less robust for higher masses than lower masses. This may be at least partially explained by the rise in numerical error at the end of the waveforms, as this part of the waveform will be at frequencies where the detectors have little sensitivity for low masses, but it will dominate the observable portion of higher mass signals. Note that because our Runge-Kutta integration routine uses adaptive step sizes, it will produce time series

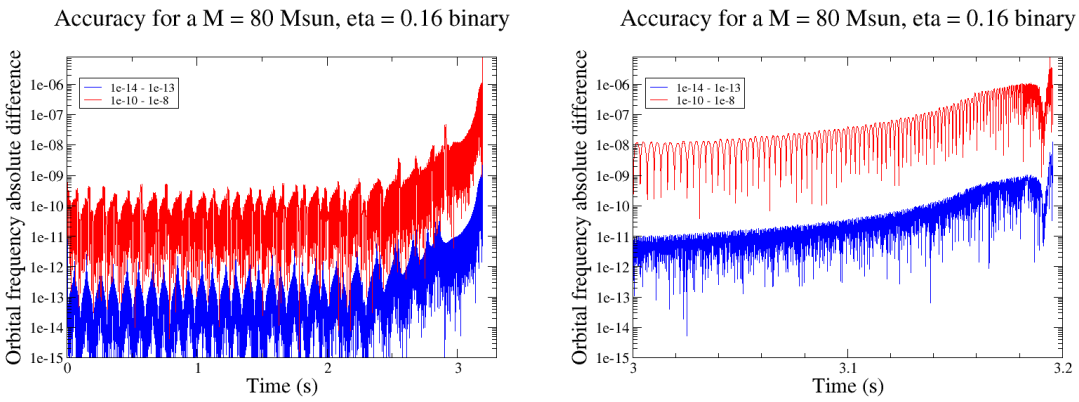

Figure 6.3: We plot the absolute difference in orbital frequency for different choices of the integration accuracy goal, $|\omega_{\rm orb}(\epsilon_1, t) - \omega_{\rm orb}(\epsilon_2, t)|$ for an $M = 80\,M_\odot$, $\nu = 0.16$ binary. We compare $\epsilon_1 = 10^{-8}$, $\epsilon_2 = 10^{-10}$ (red curve) and $\epsilon_1 = 10^{-13}$, $\epsilon_2 = 10^{-14}$ (blue curve). The right panel is a zoom on the end of the left panel. We see that the difference in omega (and thus the waveform error) rises at late times.

at irregular intervals which will be different for different ϵ. So, we must compare the orbital phase and frequency after we have used the cubic spline interpolation routine to produce evenly sampled time series. This means that Figs 6.2 and 6.3 are a measure of the combined numerical error from the Runge-Kutta integrator *and* the spline interpolation. It is not clear if the rising numerical error at the end of the waveform is a failure of one or both of these routines. This is worth investigating in the future, possibly by using a fixed step size integration routine, as in Ref. [118], to disentangle the errors from the integrator and the interpolator.

Now, since the derivative is a limit as the step size approaches zero, a finite difference will approximate the derivative most accurately when the step size $\delta\lambda^i$ is small. However, the numerical error in the waveforms creates a numerical error in the derivatives which scales as the inverse of the step size and so becomes larger for smaller step sizes. Therefore, one must choose step sizes which are neither too

large nor too small so that both types of errors are manageable. Generally, we try varying both mass parameter step sizes $\delta\mathcal{M}_c$ and $\delta\nu$ over a range $\sim 10^{-4} - 10^{-10}$ and compare the parameter errors for hundreds of pairs of step sizes in this range. If we see a flat region in the $\delta\mathcal{M}_c$–$\delta\nu$ plane, this suggests that the parameter derivatives have "converged", and the result is likely to be trustworthy. If we get convergent results for multiple reference points, we also check that the mass errors agree for different reference points. In Fig. 6.4, we show examples of our "convergence tests" when the reference point is at the start of the evolution. We show plots only for the error on $\mathcal{M}_c$, but we also check the same plots for other parameters and they typically converge (or not) in the same regions. It is clear that the parameter errors converge for the two lower mass binaries but not the highest mass binary. We find this is a general trend when aligning at the beginning of the evolution: It exhibits good convergence for low mass binaries, but poorer convergence as the total mass increases. In Fig. 6.5, we plot the convergence tests when the reference point is the peak of the waveform for the poorly converging binary in the right panel of Fig. 6.4. We perform the inner product integrals of Eq. (6.19) up to the ISCO frequency, twice the ringdown frequency or the Nyquist frequency.

When applicable, we also compare to Fisher matrix errors for 3.5PN SPA waveforms. If we integrate the inner product integrals of Eq. (6.19) up to the Nyquist or twice the ringdown frequency, we do not expect EOB waveforms to agree with the SPA results[2]. However, if we integrate only up to the ISCO frequency, then

[2]Except possibly for lower masses when the merger-ringdown signal is at high frequencies where the interferometers have very little sensitivity.

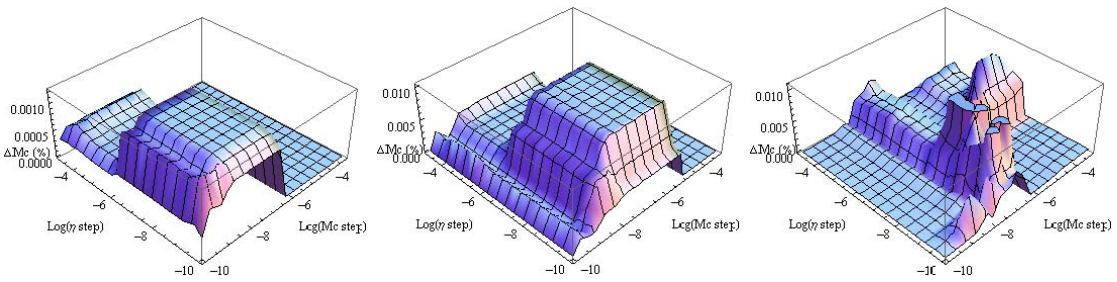

Figure 6.4: Fractional error on $\mathcal{M}_c$ as a function of mass parameter step sizes for a binary with total mass $M = 20\,M_\odot$ (left), $M = 60\,M_\odot$ (center) and $M = 80\,M_\odot$ (right). In all cases, $\nu = 0.16$, the SNR = 10 in initial LIGO, the upper limit of the inner product frequency integrals is the ISCO and the reference point is the start of the evolution at 25 Hz. The lower mass systems ($20\,M_\odot$ and $60\,M_\odot$) exhibit convergence

the EOB and SPA results should be closer together. They need not be exactly the same, of course, because they are two different waveform models. Furthermore, the SPA waveforms assume adiabaticity throughout the evolution, so it is always exactly true that $\tilde{h}^{\rm SPA} \propto f^{-7/6}$. For EOB waveforms, which do not assume adiabaticity, at early times this $f^{-7/6}$ power law is true to a very good approximation, but the slope starts to deviate from this even before the ISCO. Therefore, even when integrating only up to the ISCO, we expect the difference between the SPA and EOB results to grow as the total mass is increased, and the non-adiabatic portion falls in the most sensitive band of the interferometers.

Another potential danger of using time-domain waveforms comes from sharp "edges" or "kinks" in the time-domain waveform. It is a well-known result that if one Fourier transforms a time series which abruptly starts or ends, this will create unphysical noise in the frequency-domain spectrum. This issue is discussed in detail in Ref. [361], and the authors suggest applying a tapering function to the beginning and end of time-domain inspiral waveforms. The idea is that if the beginning (end) of

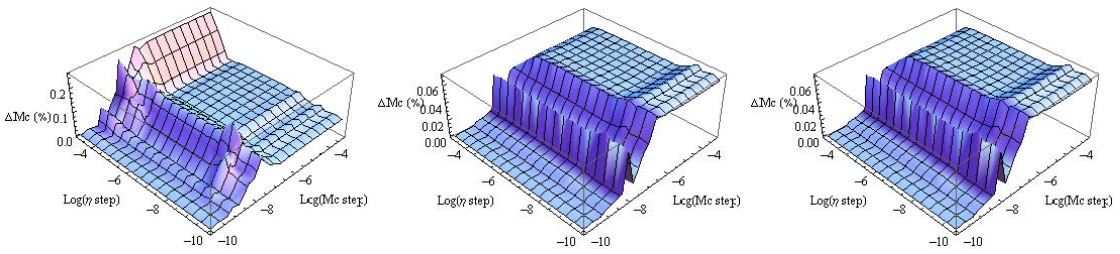

Figure 6.5: Fractional error on $\mathcal{M}_c$ as a function of mass parameter step sizes for an $M = 80\,M_\odot$, $\nu = 0.16$ binary with SNR $= 10$ in initial LIGO with the reference point as the peak waveform amplitude. The upper limit of the inner product frequency integrals is the ISCO (left), twice the $(2, 2, 0)$ ringdown frequency (center) or the Nyquist frequency (right). All three frequency cutoffs exhibit convergence, and the last two are consistent with one another and have smaller errors than the first, as expected.

a time-domain waveforms has an "edge" from an abrupt start (stop), one multiplies the beginning (end) of the waveform by a smooth function which varies between 0 and 1 in some finite interval. This ensures the waveform does not abruptly start or stop, but smoothly increases from zero to full strength over the finite interval. For inspiral-only time-domain waveforms, it is appropriate to taper both the beginning and end of the waveform. However, the end of our EOB IMR waveforms are naturally tapered, because they decay exponentially as a superposition of damped sinusoidal QNMs. Therefore, we taper only the beginning with Eq. (7) of Ref. [361] as our tapering function, and the interval is defined as the first N local maxima of the waveform. In this work, we choose $N = 10$, and we have checked that the results are robust for other choices of N.

Quite similar to the "edges" from an abrupt start or stop, we may also encounter "kinks" that arise from the discreteness of our time series. Let us suppose that we choose our reference point as the start of evolution, and we want to compute the $\mathcal{M}_c$ derivative, so we evolve the perturbed inspiral waveforms $h^{\rm insp}_{\pm}(\mathcal{M}_c \pm \delta\mathcal{M}_c, t)$.

Now, to each of these waveforms we attach a ringdown waveform at the $\omega_{\rm match}$ of Eq. (2.89). However, because the waveforms are discretely sampled, we will not have a sample at precisely this $\omega_{\rm match}$, but rather at nearby frequencies $\omega^{\pm}_{\rm match}$, and it will generally be true that $\omega^{+}_{\rm match} \neq \omega^{-}_{\rm match}$. The two perturbed waveforms will of course have some difference in their ringdown waveforms, since they have slightly different mass parameters. However, the difference in their matching points will create an extra, unphysical difference between them that is really a type of numerical error. This numerical error in the perturbed waveforms arising from attaching the ringdown at a slightly incorrect matching point is not so large. However, taking the finite difference leads to an error in the parameter derivative which is magnified by a factor $(2\,\delta\lambda^i)^{-1}$. For even modest differences in the matching point, this can create a huge error in the parameter derivatives. In some instances, the time series of the $\mathcal{M}_c$ derivative will be quite smooth throughout the inspiral, and then the amplitude will suddenly jump several orders of magnitude at the ringdown attachment point. This creates a "kink" in the waveform, and much like an edge at the beginning/end of the waveform, this will create unphysical noise in the parameter derivative's frequency spectrum. For large kinks, this noise will be found over the entire frequency range and can completely ruin the parameter derivative spectra.

Fortunately, we have found a procedure to alleviate this problem. First, we generate the dynamical variables $\Phi(t)$ and $\omega_{\rm orb}(t)$ for each of our perturbed waveforms. Next, we use a root-finding routine (based on the routine `zbrent` from Ref. [357]) to find precisely the time at which the orbital frequency reaches $\omega_{\rm match}$ for each perturbed waveform. Generally, this time will lie some $\delta t_{\pm}$ from the nearest

discrete sample. Then, we use our cubic spline interpolation routine to resample the dynamical variables so that they will have a sample at precisely the matching point,

$$\Phi(t) \longrightarrow \Phi(t + \delta t_{\pm}) \ , \tag{6.21}$$

$$\omega_{\rm orb}(t) \longrightarrow \omega_{\rm orb}(t + \delta t_{\pm}) \ . \tag{6.22}$$

We now generate our perturbed waveforms from the time-shifted dynamical variables as usual. By construction, the two waveforms will attach their ringdown at exactly the same point, so we will not have a kink in the finite difference at the ringdown attachment.

Now, just as we took care to ensure the two perturbed waveforms each have a sample at exactly their ringdown attachment point, we will use essentially the same technique to ensure they have a sample at exactly their reference point before taking the finite difference. This is important because the parameter derivatives are supposed to be taken while the other parameters (including $t_{\rm ref}$ and $\Phi_{\rm ref}$) are held fixed. So, we need to ensure the two perturbed waveforms are properly aligned at the reference point. Therefore, we use our root-finding routine to find $t_{\rm ref}$, which will generally lie some $\delta\tau_{\pm}$ from the nearest sample. Then, we use our spline interpolation routine to resample the waveform time series[3], so that they have a sample at precisely the reference point,

$$h(t) \longrightarrow h(t + \tau_{\pm}) \ . \tag{6.23}$$

[3]Strictly speaking, we actually resample time series of the waveform amplitude and complex argument, $|(h_+ - i\,h_\times)(t)|$ and $\mathrm{Arg}\,[(h_+ - i\,h_\times)(t)]$

After performing this time shift, we also apply a constant phase shift to ensure that we have the proper orbital phase at the matching point, $\Phi(t_{\rm ref}) = \phi_{\rm ref}/2$. This method of ensuring proper alignment of perturbed waveforms at the ringdown attachment and reference point (via two time shifts and a phase shift) could be used for any choice of the reference point. For the results of the next section, we will use this technique with the reference point chosen as the peak waveform amplitude.

We have taken great care to compute Fisher matrix results which are as accurate as possible by sanity checking every piece of code, enforcing a high precision in solving the evolution equations and resampling waveforms twice to ensure proper alignment of the perturbed waveforms used in finite differences. Even so, a loss of precision and unreliable results are still an ever-present threat. Recall that we use mass parameter step sizes $\delta\lambda^i \sim 10^{-4} - 10^{-10}$, which can lead to numerical errors in the mass parameter derivatives of order $\sim (\delta\lambda^i)^{-1}$, and that inverting the Fisher matrix to obtain the covariance matrix can amplify numerical errors by up to the ratio of largest to smallest eigenvalues, $\kappa \gtrsim 10^{12}$. So, even though we enforce an accuracy of $\epsilon \sim 10^{-14}$ in evolving the waveforms, this could potentially lead to an error in our covariance matrix of

$$\delta\Sigma \sim \epsilon \ \left(\delta\lambda^i\right)^{-1} \ \kappa \sim 10^{-16} - 10^{-22} \ . \tag{6.24}$$

Although this is an upper bound, and not a guarantee of the actual amount of error, the potential for loss of precision is quite alarming. Therefore, we will apply the Fisher matrix to EOB waveforms only in regimes where the results are robust.

6.4 Results

We would like to use our Fisher matrix formalism in the context of advanced ground-based detectors, such as Advanced LIGO and Virgo or ET. These detectors are expected to have low-frequency seismic cutoffs of 10 Hz or even 1 Hz. Note that because the amplitude-corrected waveforms contain a third harmonic of the orbital frequency, to use the Fisher matrix for these instruments we must start evolving the EOB waveforms at an orbital frequency below one third of the seismic cutoff to capture all of the in-band signal. This would mean starting the evolution at orbital frequencies of ~ 3 Hz or ~ 0.3 Hz for the advanced detectors and generating very long waveforms. Unfortunately, at the present time we are unable to get robust results when starting at such low frequencies. We either do not find a flat region of convergence for a wide range of parameter step sizes, or else low mass EOB waveforms integrated up to the ISCO give parameter errors an order of magnitude better than the 3.5PN SPA result. It is possible this last feature may be a real result, but it would be rather surprising, and we will not trust it unless it is verified by other methods.

We would also like to apply the formalism to high mass binaries. For high mass binaries, both the merger-ringdown and the extra frequency band provided by the third harmonic would lie in the sensitive band of the detectors, and so these binaries should have the greatest improvement in parameter estimation from both the merger-ringdown and the higher harmonics. Unfortunately, at the present time our results become less robust as we go to higher masses.

Because of these concerns over the robustness of results, we will restrict our discussion to initial LIGO and to binaries which merge in the detector bandwidth but have total masses $M \leq 100\,M_\odot$. We will plot the parameter errors for four different types of waveforms:

- **Restricted inspiral-only (R-I):** Denoted by a dashed red line in all plots. This is the Newtonian-amplitude restricted TaylorF2 (SPA) waveform with 3.5PN phasing described in Sec. 3.3.6. These waveforms and their parameter derivatives are computed analytically. The inner product integrals are performed up to the Schwarzschild ISCO frequency.

- **Restricted IMR (R-IMR):** Denoted by a dashed blue line in all plots. This is the Newtonian-amplitude restricted EOB waveform described in Sec. 6.2.1.1. The inner product integrals are performed up to twice the frequency of the $(2, 2, 0)$ QNM, so that the full IMR signal contributes to the Fisher matrix.

- **Amplitude-corrected inspiral-only (A-I):** Denoted by a solid red line in all plots. This is the Newtonian-amplitude restricted EOB waveform described in Sec. 6.2.1.2. Note that we generate the full IMR waveform, but the inner product integrals are performed only up to the Schwarzschild ISCO frequency, so that only the inspiral portion contributes to the Fisher matrix.

- **Amplitude-corrected IMR (A-IMR):** Denoted by a solid blue line in all plots. This is the Newtonian-amplitude restricted EOB waveform described in Sec. 6.2.1.2. The inner product integrals are performed up to twice the

frequency of the $(2, 2, 0)$ QNM, so that the full IMR signal contributes to the Fisher matrix.

In the next subsections, we will plot the parameter errors of the Fisher matrix formalism for each of these types of waveforms as the total mass (Sec. 6.4.1), symmetric mass ratio (Sec. 6.4.2) and binary inclination to line of sight (Sec. 6.4.3) are varied in the context of initial LIGO. By comparing the various curves, we will understand how much the inclusion of amplitude corrections and merger-ringdown can improve the parameter estimation. In an attempt to get more robust results, we have averaged the parameter errors over many different $\mathcal{M}_c$ and ν finite difference step sizes. To do this, for each data point we first compute the errors for several hundred choices of step sizes and plot the parameter errors as in Figs. 6.4-6.5. Then, we attempt to identify a "region of convergence" in these plots and lay out a finer grid of ~ 100 step size pairs in this region of convergence. Each parameter error reported in the plots below is the mean value in this region of convergence, with error bars determined by the minimum and maximum parameter error in this region. Note that these error bars are a measure of the numerical error which arises from taking a finite difference of numerically-computed time-domain waveforms. They do not account for other potential errors, such as non-Gaussian detector noise and low SNR. The plots for the R-I waveforms do not have these error bars, as the parameter derivatives are taken analytically.

For all of the results presented here, we assume the binary has sky location and polarization angles of $\theta = \phi = \psi = \pi/4$. By comparing parameter errors for

90 different configurations chosen uniformly in the sky and in the angle ψ, we have verified that the resulting parameter errors have very little variation for different choices of these angles (except the errors on $\mathcal{A}$ and α, but these parameters are very poorly determined anyway). We will choose a binary inclination of $\iota = \pi/3$ in all cases, except in Sec. 6.4.3, where we vary the inclination. All of the comparisons are done at a fixed SNR = 10. This means that when we vary M, we are in effect comparing distant high mass binaries to closer low mass binaries (and similarly for the comparisons varying ν and ι). Now, one might argue that it would be more appropriate to do these comparisons at a fixed distance. However, we feel that fixed SNR is appropriate, especially for initial LIGO, because one is most likely to make most detections near the detection threshold (which is roughly SNR $\sim$ 10). So, if a low mass (or asymmetric or edge-on) binary is detected it will likely be at a closer distance than a detected high mass (or symmetric or face-on) binary, and the fixed SNR comparison takes this into account. At any rate, the parameter errors produced by the Fisher matrix scale as the inverse of SNR, so one could rescale the results if one knows the ratio of SNRs for two configurations.

6.4.1 **Varying total mass**

We now consider the parameter errors as a function of total mass, and the improvements provided by the merger-ringdown and amplitude corrections. In Fig. 6.6, we vary the total mass over the range $(20 - 100)\, M_\odot$ and display the errors on $\mathcal{M}_c$, ν and $t_{\rm ref}$ for the various waveform models. Plots for a highly asymmetric system

with $\nu = 0.05$ (or approximately an 18:1 component mass ratio) are in the left column, while plots for a nearly symmetric system with $\nu = 0.24$ (or approximately a 1.5:1 component mass ratio) are in the right column. Note that the inspiral-only waveforms are only plotted up to a total mass $60\,M_{\odot}$, which corresponds to an ISCO frequency of $\simeq 73$ Hz. At higher masses, there is almost no inspiral signal in band and the R-I parameter errors become extremely large, while the A-I results become erratic and untrustworthy.

For the amplitude-corrected waveform models, we find that $\phi_{\rm ref}$, $\mathcal{A}$ and α are very poorly determined in all cases, and in effect cannot be measured by a single detector. The binary inclination ι is very poorly determined for all total masses in the $\nu = 0.24$ case, while for the $\nu = 0.05$ case we have $\Delta\iota \simeq 0.45 \pm 0.1$ radians across the total mass range, whether including the full IMR signal or cutting at the ISCO.

To get a sense of the importance of merger-ringdown, one should compare the red and blue curves with the same dashing pattern in each panel of Fig. 6.6. Merger-ringdown provides more improvement to parameter accuracy for higher total mass binaries, which should not be surprising, as the merger-ringdown will be closer to the peak sensitivity and contribute a greater portion of the observed signal for higher masses. Comparing the left and right columns, we see that the merger-ringdown provides a greater improvement to the mass parameter errors for symmetric binaries than asymmetric ones. This is also quite reasonable, as the amplitude of the ringdown waveform is greater for symmetric binaries than for asymmetric ones. In the first two rows of the left column, the A-I (solid red) and A-IMR (solid blue) curves are quite close together, which illustrates that including the merger-ringdown does

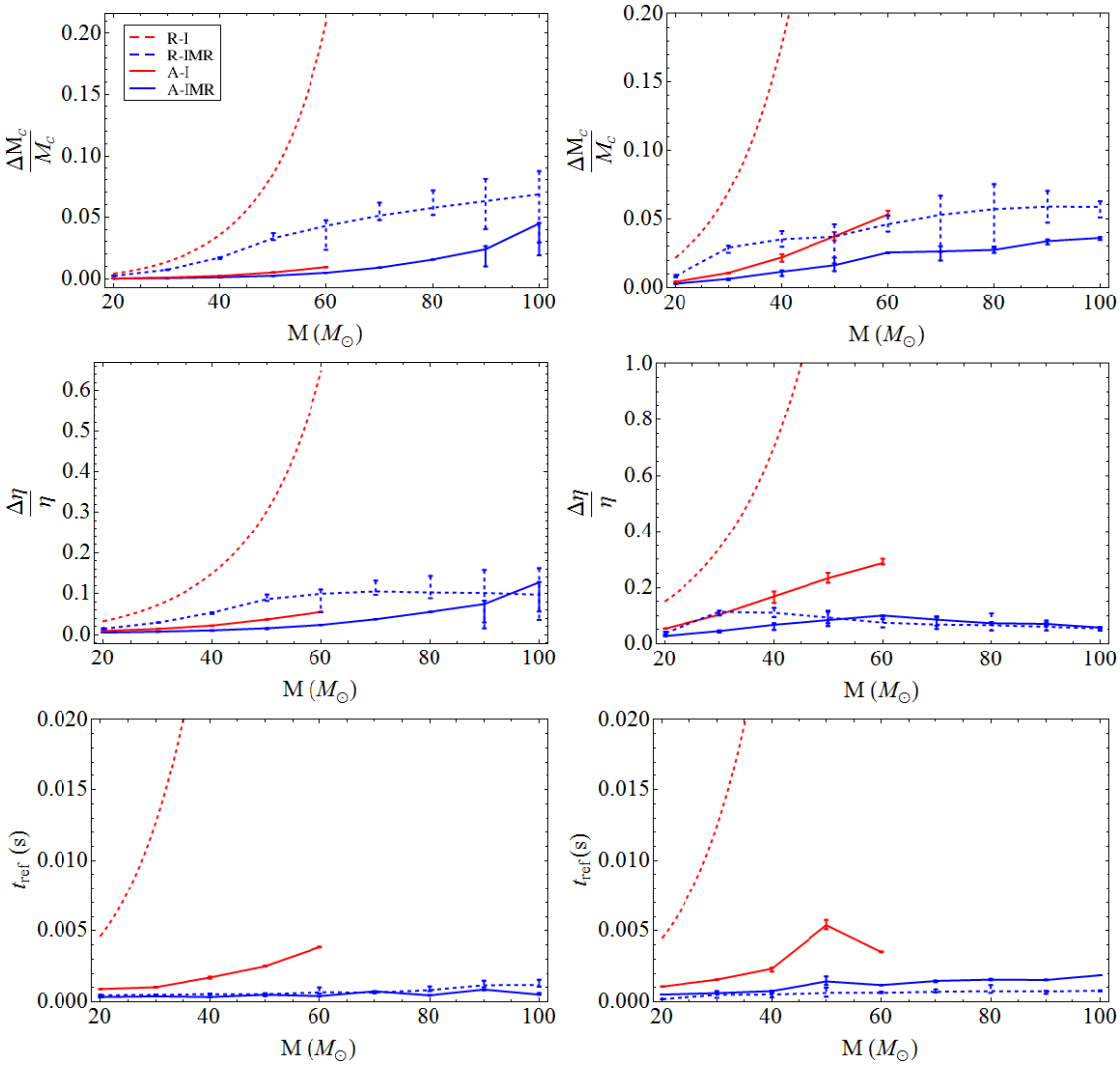

Figure 6.6: We plot the fractional error on $\mathcal{M}_c$ (top row), the fractional error on ν (center row) and the error on $t_{\rm ref}$ (bottom row) as the total mass is varied for symmetric mass ratio $\nu = 0.05$ (left column) and $\nu = 0.24$ (right column) for waveform models R-I (dashed red), R-IMR (dashed blue), A-I (solid red) and A-IMR (solid blue).

very little to improve the estimation of these parameters for the amplitude-corrected waveforms. Contrast this with the right column, where these same two curves differ by a factor two in $\Delta\mathcal{M}_c$ and a factor three in $\Delta\nu$ at $60\,M_\odot$. The merger-ringdown seems to provide a significant improvement to the timing accuracy regardless of the total mass or mass ratio. The A-IMR and R-IMR models (blue curves) have a timing accuracy $t_{\rm ref} \simeq 1$ ms across a wide range of total mass and mass ratio, while the A-I model (solid red) has timing accuracies $t_{\rm ref} \simeq 2-10$ ms and the timing accuracy for the R-I model rises very rapidly with the total mass, approaching ~ 100 ms at $60\,M_\odot$. Note that the R-I (i.e. the SPA waveform) uses the "time of coalescence" as $t_{\rm ref}$, while all the other models use the peak of the waveform amplitude. In all cases, we find the timing accuracy is significantly better when the reference point is the peak of the amplitude than when it is the "time of coalescence".

To understand the importance of amplitude corrections, one should compare solid and dashed curves of the same color in each plot. We note that the amplitude corrections significantly improve all of the parameter errors for the inspiral-only waveform models in all cases. However, note that we are comparing SPA waveforms with analytic derivatives to EOB waveforms with finite difference derivatives, so this comparison is potentially more error-prone than the others. In the case of the IMR waveforms, from the first row of Fig. 6.6, we see that the amplitude corrections improve the error on $\mathcal{M}_c$ by a factor ~ 2 across a range of total masses and mass ratios. From the second row, we see that the amplitude corrections improve the error on ν at low and intermediate masses, but that at high masses there is little if any improvement. Again, the effect is reasonably similar for the highly asymmetric

and nearly symmetric binaries. From the last row, we see the effect of amplitude corrections on the timing accuracy. Note that amplitude corrections do not significantly improve $\Delta t_{\rm ref}$ for IMR waveforms. Furthermore, the A-I model (which uses the same definition of $t_{\rm ref}$ but does not include merger-ringdown) has $\Delta t_{\rm ref}$ a factor of a few larger than the A-IMR and R-IMR models. This suggests that the inclusion of merger-ringdown is much more important than the inclusion of amplitude corrections for obtaining a good timing accuracy.

Now, a word about how our results compare to those of Ref. [117]. To make a direct comparison, one should compare the right column of our Fig. 6.6 to Fig. 7 of Ref. [117]. The authors of Ref. [117] consider three different mass ratios, ($\nu = 0.25,\ 0.2222,\ 0.16$), but their results are quite similar for any of these mass ratios. In Ref. [117], the dashed curves represent 3.5PN SPA waveforms (the same model as our dashed red curves) and the solid lines represent phenomenological IMR waveforms, which were fit to restricted amplitude hybrid waveforms and are rather analogous to our R-IMR (dashed blue) model. Reassuringly, our 3.5PN SPA results agree with theirs.

Comparing their phenomenological errors to our R-IMR errors, the errors on $\mathcal{M}_c$ and ν are rather consistent (the log scale of Ref. [117] makes a precise comparison difficult, but the mass parameter errors seem to agree to within a factor of 2 or better) up to total mass $\sim 60\,M_\odot$. However, our mass errors stay rather constant beyond this up to total masses of $100\,M_\odot$, while the mass errors in Ref. [117] rise rather sharply, reaching $\Delta\mathcal{M}_c,\ \Delta\nu \simeq 50\%$ at $M = 100\,M_\odot$. It is known that the EOB and phenomenological waveform models considered here and in Ref. [117]

have some differences, particularly in the merger-ringdown (with the EOB generally having a larger amplitude during merger-ringdown). It is possible that this extra power in the EOB merger-ringdown accounts for the improved parameter estimation at higher masses, although MCMC studies (or other more sophisticated tests) should be done to confirm this result.

As for the timing accuracy, we note that our R-IMR model uses the peak of the waveform amplitude as $t_{\rm ref}$, while the phenomenological IMR model of Ref. [117] uses the "time of coalescence" in the adiabatic PN sense. Therefore, we do not necessarily expect consistency in $\Delta t_{\rm ref}$. At a total mass of $20\,M_\odot$, the $\Delta t_{\rm ref}$ of Ref. [117] seems to be rather consistent with our result. However, our timing accuracy is quite flat, and we have $\Delta t_{\rm ref} \simeq 1$ ms all the way out to $100\,M_\odot$, while in Ref. [117] $\Delta t_{\rm ref}$ rises with the total mass, reaching $\Delta t_{\rm ref} \simeq 50$ ms or so at $100\,M_\odot$. Since we have noted that the merger-ringdown seems to play an important role in determining the timing accuracy, the improved timing accuracy of the EOB model may be partly due to the excess power in the merger-ringdown. However, it seems very likely that part or all of the improvement in timing accuracy comes from the definition of $t_{\rm ref}$, as we have found the peak of waveform amplitude can be measured significantly more accurately than the "time of coalescence" even for low total mass and asymmetric binaries. Once again, MCMC studies would be useful to confirm our results.

6.4.2 **Varying mass ratio**

We now consider the parameter errors as a function of symmetric mass ν, and the improvements provided by the merger-ringdown and amplitude corrections. In Fig. 6.7, we vary ν over the range $0.04 - 0.24$ and display the errors on $\mathcal{M}_c$, ν and ι for the various waveform models. Plots for a lower mass binary ($M = 20\,M_\odot$) are in the left column, while plots for a higher mass binary ($M = 40\,M_\odot$) are in the right column.

We once again find that $\phi_{\rm ref}$, $\mathcal{A}$ and α are very poorly determined. The error on $t_{\rm ref}$ is nearly constant as ν is varied, and the values of $\Delta t_{\rm ref}$ here are consistent with the values at $20\,M_\odot$ and $40\,M_\odot$ in the bottom row of Fig. 6.6.

The plots of Fig. 6.7 exhibit some of the same basic trends on the importance of merger-ringdown and amplitude corrections as the plots of Fig. 6.6. The errors on the mass parameters are roughly an order of magnitude larger for the higher mass binary of the right column than for the lower mass binary of the left column, although both exhibit similar trends as the mass ratio is varied. For the binaries considered here, we find that typically the amplitude corrections provide a greater improvement to the mass parameter errors than is provided by the merger-ringdown. This can be seen because the errors on the A-I (solid red) model typically lie below the errors of the R-IMR (dashed blue) model. The only exception is at $\nu = 0.24$, where the opposite is true for the errors on ν, and the errors on $\mathcal{M}_c$ are comparable for the higher mass binary of the right column. This trend is consistent with Fig. 6.6, where we observed that merger-ringdown improved the mass parameter errors for

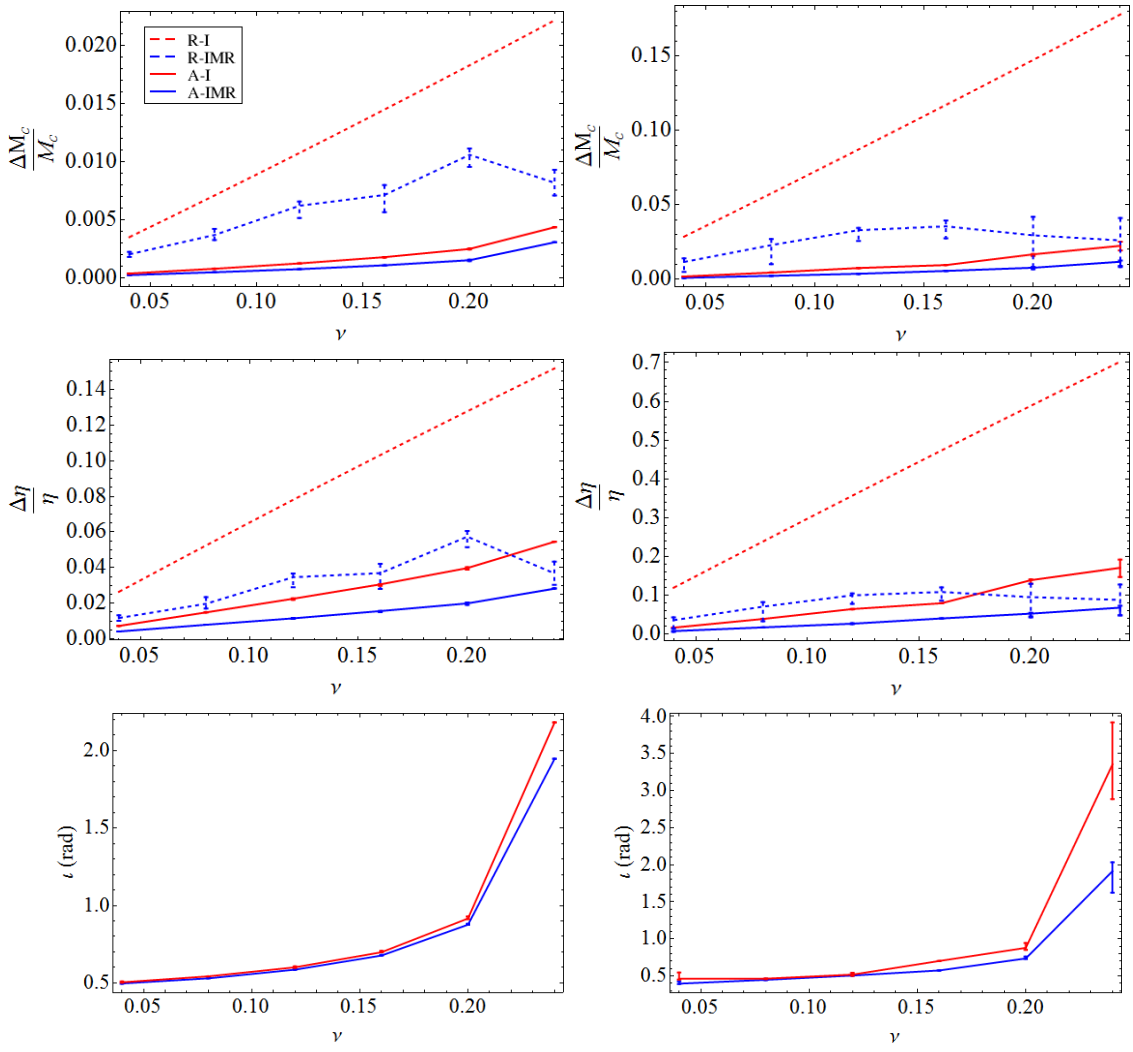

Figure 6.7: We plot the fractional error on $\mathcal{M}_c$ (top row), the fractional error on ν (center row) and the error on ι (bottom row) as ν is varied for total mass $M = 20\,M_\odot$ (left column) and $M = 40\,M_\odot$ (right column) for waveform models R-I (dashed red), R-IMR (dashed blue), A-I (solid red) and A-IMR (solid blue).

symmetric binaries, but gave very little improvement to highly asymmetric binaries.

The bottom row of Fig. 6.7 displays the error on the binary inclination ι. Note that it contains curves for the A-IMR and A-I models, but not R-IMR and R-I, because ι is not a parameter of the restricted waveform, but is instead absorbed into an overall amplitude. Recall that in Sec. 6.4.1, we did not plot the error on ι, but noted that it was quite large for the $\nu = 0.24$ binary, and we had $\Delta\iota \sim 0.5$ rad for the $\nu = 0.05$ binary. In either case, this error was reasonably flat as the total mass was varied. We see a similar trend in the bottom row of Fig. 6.7. We again find $\Delta\iota \sim 0.5$ for $\nu = 0.04$, and $\Delta\iota$ rises as ν increases, especially as we approach $\nu = 0.25$. The errors are rather similar in the left and right columns, although they are slightly larger for the higher mass system of the right column. One interesting feature is that the merger-ringdown does very little to improve the estimation of ι. This means that the information about the inclination as primarily accumulated during the inspiral. For either total mass, the red and blue curves are quite close to each other throughout the plot, separating a bit at the symmetric mass ratio end. In the right column, we see a large separation between the curves at $\nu = 0.24$, but this is a bit misleading, because we have $\Delta\iota \sim 2$ or 3.5 radians, so ι (which has the range $[0, \pi]$) is really essentially undetermined in either case. We can determine ι to a higher precision for asymmetric binaries because the different harmonics of the orbital frequency have a different dependence on ι. From Eq. (6.14), we see the odd harmonics which appear in the 0.5PN amplitude are $\propto \delta = \sqrt{1 - 4\,\nu}$, and so they will be most significant for asymmetric binaries.

6.4.3 **Varying binary inclination**

We now consider the parameter errors as a function of binary inclination to line of sight ι, and the improvements provided by the merger-ringdown and amplitude corrections. In Fig. 6.8, we vary ι over the range $0 - \pi$ for a binary with $\nu = 0.09$ and $M = 20\,M_\odot$ (left column) or $M = 60\,M_\odot$ (right column) and display the errors on $\mathcal{M}_c$, ν and ι for the amplitude-corrected waveform models A-IMR (blue curve) and A-I (red curve). For the restricted waveform models R-IMR and R-I, changing ι would simply change the effective distance. For our comparisons at fixed SNR, this would have no effect on the parameter errors.

Note that the plots in this section do not contain error bars, because we did not perform the same averaging over mass parameter step sizes as in the previous two subsections. We consider this reasonable because here we are fixing the masses and varying an *extrinsic* parameter. Therefore, if a certain pair of step sizes works well for one value of ι, we expect them to work well for all values of ι. So, we simply identified a single point in the center of our "region of convergence" and used those step sizes in all cases. In Fig. 6.8, the plots take much finer steps along the x-axis than the other figures and the fact that we get smooth curves suggests that this approach has worked.

In the first two rows of Fig. 6.8, we plot the errors on $\mathcal{M}_c$ and ν, respectively. Note that (for fixed SNR) these parameters are best determined for "edge-on" binaries, for which $\iota \simeq \pi/2$. These parameter errors are relatively flat across a wide range of values of ι, with the errors first rising slowly as one moves away from $\iota = \pi/2$,

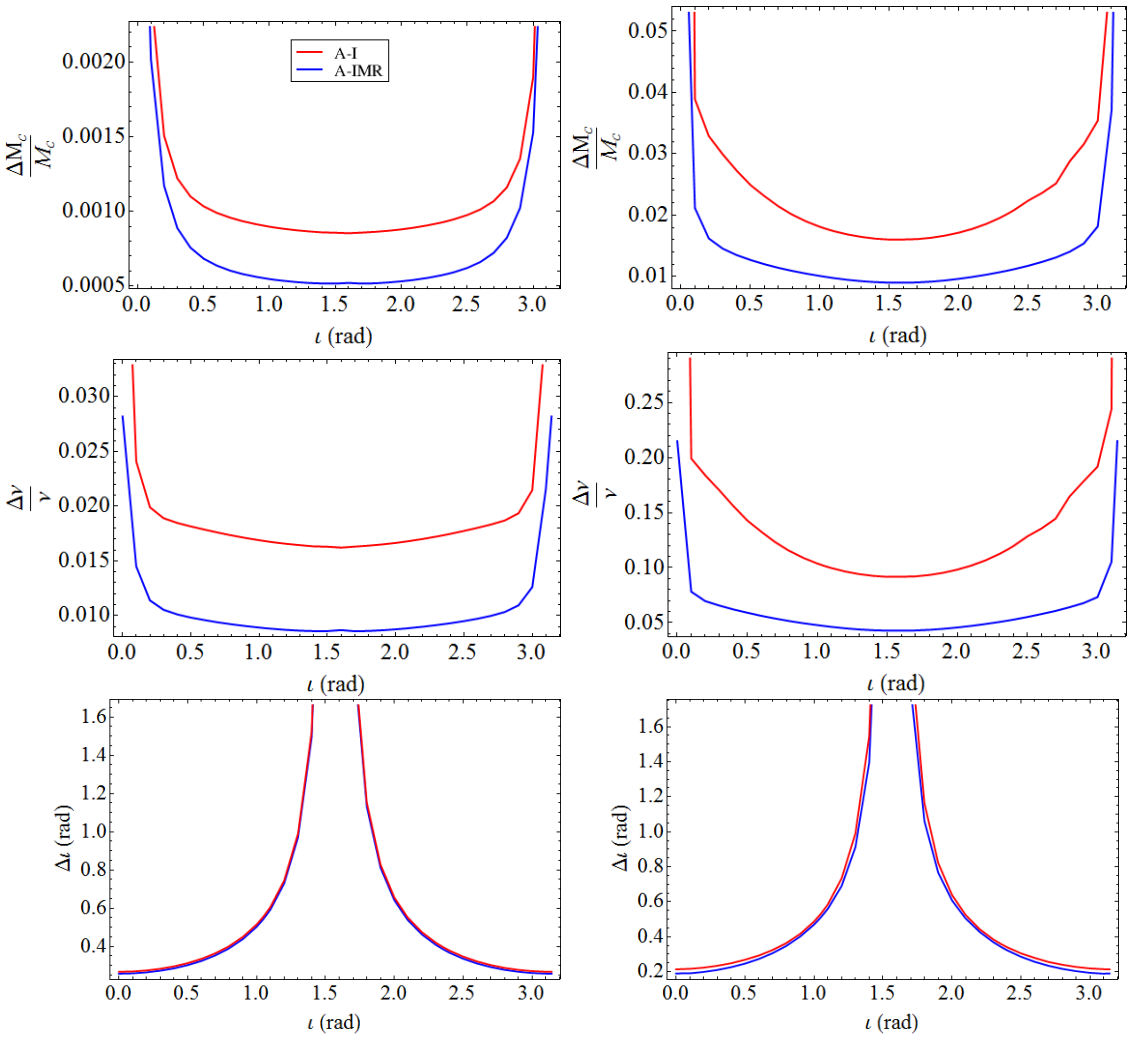

Figure 6.8: We plot the fractional error on $\mathcal{M}_c$ (top row), the fractional error on ν (center row) and the error on ι (bottom row) as ι is varied for symmetric mass ratio $\nu = 0.09$ and total mass $M = 20\,M_\odot$ (left column) and $M = 60\,M_\odot$ (right column) for waveform models A-I (solid red) and A-IMR (solid blue).

but then rising sharply as one approaches $\iota \to 0, \pi$. From Eq. (6.14), we see that this happens because the amplitude corrections are $\propto \sin\iota$, and so they vanish when $\iota = 0, \pi$ and one loses the information contained in the amplitude corrections. For both plots, we see that the merger-ringdown provides some improvement to the mass parameter errors, and that this level of improvement does not depend very strongly on the binary inclination.

In the bottom row of Fig. 6.8, we plot the error on ι. These plots exhibit the opposite behavior from the other two rows. First of all, in either column the inclusion of merger-ringdown has essentially no effect on the determination of ι (consistent with what we found in Fig. 6.7). More interestingly, we find ι is best determined when the binary is "face-on" ($\iota \simeq 0, \pi$), and the error rises sharply as one approaches "edge-on" ($\iota \to \pi/2$). If the binary is nearly edge-on, ι will essentially be undetermined, but if it is nearly face-on, it will be rather well-determined, as even a single detector can measure it to within a few tenths of a radian according to these results. This may seem counter-intuitive, because we have noted that the amplitude corrections are $\propto \sin\iota$ and thus vanish in the face-on case. However, it may be that their absence is precisely what allows for the precise determination. From Eq.(6.14), we see that if a detection is made in which the odd harmonics are not present (or are negligibly small), this means either $\iota = 0, \pi$ or $\nu = 0.25$ (or both). So long as ν is determined to within an error that excludes $\nu = 0.25$ (which is the case in Fig. 6.8), then this gives a rather tight constraint on the value of ι. On the other hand, if we do measure non-negligible odd harmonics, then the form of those odd harmonics depends on $\delta = \sqrt{1 - 4\,\nu}$, ι and also the antenna pattern functions

F_+ and $F_\times$, and so ι could be poorly determined due to correlations with other parameters. In any case, this general trend on $\Delta\iota$ appears for many different binary configurations, and so it seems to be a real feature in estimating the parameters of an amplitude-corrected waveform.

6.5 Conclusions and future work

We have investigated how accurately the parameters of a gravitational wave could be measured by using the Fisher matrix formalism with EOB waveforms. In particular, we have attempted to understand what improvements could be obtained by using waveforms with amplitude corrections and/or merger-ringdown. We have restricted ourselves to a single initial LIGO detector and binaries with a total mass $\leq 100\,M_\odot$. This was necessary because we find that the Fisher matrix formalism is quite susceptible to numerical errors which arise from taking the finite difference of numerically-computed time-domain waveforms.

We find that the inclusion of merger-ringdown can significantly improve the mass parameter errors for binaries with large total mass and comparable component masses, which is in qualitative agreement with Ref. [117]. However, we find significant quantitative differences from Ref. [117] in the estimation of mass parameters for total masses in the range $M \sim (50 - 100)\,M_\odot$. It is possible that differences in the waveform models could account for this difference, but MCMC studies would be useful to confirm our results. Unlike Ref. [117], we also considered very asymmetric binaries and we find that the merger-ringdown is far less important in determining

the mass parameters of these binaries. We do find that merger-ringdown is quite important in improving the timing accuracy for any mass ratio and any total mass in the range $M = (20 - 100)\, M_\odot$, in qualitative agreement with Refs. [117, 118]. For most of the binaries we have studied, the time of the peak waveform amplitude can be measured to within $\simeq 1$ ms, and we find that it can always be measured more accurately than the "time of coalescence" that is used as a reference time for PN waveforms. The merger-ringdown does not seem to be important in determining the binary inclination, with IMR and inspiral-only amplitude-corrected waveforms giving essentially the same error on ι.

We find that amplitude corrections provide a significant improvement to the error on $\mathcal{M}_c$ for a wide range of total masses and mass ratios. We find that amplitude corrections provide an improvement to the error on ν for lower total mass ($\lesssim 50\, M_\odot$), but that as one goes to higher mass, restricted and amplitude-corrected EOB IMR waveforms have similar errors on ν. This does not agree with Ref. [116], which found that the improvement on the errors of mass parameters $\mathcal{M}_c$ and $\delta = \sqrt{1 - 4\,\nu}$ from amplitude corrections rises dramatically as the total mass is increased. Since we use different waveform models from Ref. [116], there could be differences in our results, but our result seems to be rather counterintuitive. More sophisticated studies such as MCMC methods could be used to resolve this issue.

We find that the mass parameter errors of amplitude-corrected waveforms do not depend very strongly on the binary inclination, so long as $\iota \neq 0, \pi$, in which case the amplitude-corrections vanish and the mass parameter errors increase. We find that the binary inclination can be measured most precisely (errors of $\Delta\iota \simeq 0.1 - 0.2$

rad for a single detector) for binaries which are "face-on" ($\iota \simeq 0,\ \pi$) but that ι cannot be accurately determined if the binary is "edge-on" ($\iota \simeq \pi/2$).

We have also seen that there are significant difficulties in applying the Fisher matrix formalism to EOB waveforms (and generally to numerically-computed time-domain waveforms). The Fisher matrix is known to have potential pitfalls in that it assumes Gaussian detector noise and high SNR signals and inverting the Fisher matrix can cause a loss of precision, but it has been widely used (with analytic, frequency-domain SPA waveforms) for parameter estimation studies because it is simple to implement and computationally inexpensive. However, because one must generate waveforms at a very high precision, take care in how the parameter derivatives are calculated, perform the calculation many times to ensure robustness, and still be cautious about the possibility of large numerical errors, the Fisher matrix may be of limited use with EOB waveforms. It is still computationally cheaper than MCMC methods (but not so dramatically as with SPA waveforms), but the MCMC results will be much more reliable.

Chapter 7

Preliminary results from the search for high mass compact binary coalescences in LIGO's fifth science run

7.1 Introduction

In this thesis we have presented analytic waveforms to describe the radiation emitted by compact binary coalescences and applied them to test the robustness of the PN formalism, study how spins affect the waveforms, test whether they can recover NR waveforms in simulated noise, and study how well we might be able to extract the parameters of a detected signal. Now, we culminate these efforts by using the waveforms to search for true gravitational wave signals in real data.

We will analyze the data taken during LIGO's S5 science run and use the EOB IMR waveforms presented in Sec. 2.2.2 as matched filter templates to search for coalescing compact binaries with a total mass $25\,M_\odot \leq M \leq 100\,M_\odot$ and component masses $1\,M_\odot \leq m_1, m_2 \leq 99\,M_\odot$. This search effort is notable in that it is the first to use waveforms which model the entire coalescence through inspiral, merger and ringdown. For the mass range considered here, the merger occurs in the most sensitive band of the LIGO detectors, and so it is crucial to model the merger-ringdown portion of the signal rather than just the inspiral.

The LIGO S5 data was taken between November 4, 2005 and September 30,

2007 and includes more than one year worth of triple-coincident data with the three interferometers operating at or near their design sensitivity. Starting May 18, 2007 the Virgo detector started taking its first science data (VSR1) and the LSC and Virgo collaborations agreed to share data and operate a joint four-detector network. Results from "low mass" searches for signals with total mass $2\,M_\odot \leq M \leq 35\,M_\odot$ have been published for the LIGO-only S5 data [96, 97], and for joint S5/VSR1 LIGO and Virgo data [98]. They did not make a detection, but set upper limits on the rate of coalescences in their mass range. This effort, dubbed the "high mass" search, will search the entire LIGO S5 data for gravitational wave signals, but will not analyze any Virgo data. This is because the Virgo detector had excessive noise at low frequencies during VSR1, which greatly limits its sensitivity to high mass signals. Since the LSC and Virgo collaborations have agreed to share data, and since Virgo collaboration members have contributed to the data analysis, this is a joint LIGO-Virgo search effort.

This search is the result of a collaborative effort by many people. The author of this thesis has contributed to that effort by implementing the EOB waveforms into the LAL code, running the search on a portion of the data, tuning the χ^2 veto, sanity checking parts of the code, helping to review the search methods and results, and helping to write up the results for publication. We emphasize that the results here are *preliminary*, as the search methods and results have not completed an internal review. The final results should appear in the near future in a publication for which the author of the present thesis, Chad Hanna (Caltech) and Craig Robinson (Cardiff University) will be the corresponding authors for the LSC and Virgo collaborations.

7.1.1 Motivation to search for high mass binary black holes

While there is direct observational evidence for neutron star binaries, which are a source for the low mass searches, the populations—and even the existence—of sources for the high mass searches are rather uncertain. Black holes have been observed in X-ray binaries and typically have masses $\lesssim 20\,M_\odot$ [362, 363], although a recent observation suggests a BH with mass $\gtrsim 24\ M_\odot$ [364]. This suggests the BH-BH binaries which form as the end product of a binary star system would likely have total masses $\lesssim 40\,M_\odot$.

However, other scenarios have been suggested to which could lead to more massive BH-BH binaries. For example, a number of studies have suggested the possibility of forming BH-BH binaries through dynamical capture in dense stellar environments such as globular clusters [17, 18, 365, 366, 367, 368]. Mass segregation would cause the most massive black holes to sink to the center of a cluster, so that if a binary forms near the center, it may favor the larger black holes. Also, as suggested in Ref. [17], in many of these mergers, the remnant black hole will not receive a large enough kick to be ejected from the cluster. Therefore, it could remain in the center to form an ever-larger black hole through additional coalescences. This could lead to binaries with larger total masses.

It has been suggested that a somewhat larger class of black holes with masses in the range $\sim (50 - 500)\,M_\odot$, dubbed intermediate-mass black holes (IMBHs) may exist, perhaps forming through several mergers of stellar-scale ($M \lesssim 20\,M_\odot$) black holes in globular clusters. Observational evidence supporting the existence of these

objects is still under debate (see reviews in Refs. [369, 370] for additional details), although Ref. [371] represents a possible recent detection of an IMBH. If they do exist, IMBHs could capture other IMBHs or stellar-scale BHs to form binaries with total masses $\sim (100 - 1000)\, M_\odot$ [372, 373, 374, 375] which could potentially be observable by ground-based detectors or LISA.

Therefore, it is worthwhile to search for compact binaries with as large a mass as possible. Since this is the first search effort to use IMR template waveforms calibrated to numerical relativity, we had some concerns (such as template placement and the performance of signal-based vetoes) about using these templates for total mass $\geq 100\, M_\odot$. However, as we will see in the next section, there are "ringdown" search efforts which will cover higher mass binaries. For these reasons, we define the range of our search as a total mass $25\, M_\odot \leq M \leq 100\, M_\odot$ and component masses $1\, M_\odot \leq m_1, m_2 \leq 99\, M_\odot$.

7.1.2 Numerical relativity breakthrough

Numerically solving for the inspiral, merger and ringdown of two black holes in full general relativity without resorting to perturbative or approximate methods has proven to be an exceptionally difficult problem. Hahn and Lindquist first tried to simulate two colliding black holes more than four decades ago [376]. It was not until 2005 that the final few orbits, merger and ringdown were successfully simulated by Pretorius [279]. This was quickly followed by successful simulations from other groups using different methods [143, 144]. Now, there are many groups which are

able to produce NR simulations which continue to become more accurate, longer and span a greater portion of the parameter space (see, e.g. [146, 280, 281, 377] for recent overviews on the field, and Sec. 2 of [104] for a compact summary). These NR simulations have facilitated the development of analytic waveforms which model the full inspiral, merger and ringdown waveforms. This includes the EOB waveforms, which we have already discussed in detail in Ch. 2, and also the so-called phenomenological IMR waveforms which we discuss below. This search effort will use both families of IMR waveforms.

7.1.3 IMR waveforms calibrated to numerical relativity

The high mass search uses EOB waveforms as matched filter templates to search for gravitational radiation from compact binary coalescences. As explained in Sec. 7.2.9, we also need waveforms to inject into the data and attempt to recover them via matched filtering to test the detection efficiency of our search pipeline, and we use EOB waveforms for this purpose as well. These EOB waveforms were described in detail in Sec. 2.2.2, and the equations needed to generate the particular EOB model used in this search were given in Sec. 2.2.2.5. However, the EOB formalism is not the only one which can be used to generate analytic IMR waveforms. Another approach, proposed in Ref. [105], can be used to generate so-called *phenomenological* IMR waveforms. While we do not use these waveforms as matched filters, we do inject them into the data and attempt to recover them with EOB templates. This serves as a useful sanity check that our templates can recover sig-

nals which are not exactly identical to the templates, because the EOB (and the phenomenological) IMR waveforms will not exactly match a true IMR signal from a binary black hole coalescence. We now give a brief description of the phenomenological IMR waveforms.

Because of computational expense, NR simulations can only feasibly simulate the last orbits before merger, currently roughly ≤ 30 GW cycles. However, longer IMR signals can be created by stitching PN adiabatic inspiral waveforms together with NR simulations of the last few orbits, merger and ringdown. These stitched-together waveforms are referred to as hybrid waveforms. Note that they are not analytic, as the last portion is an NR waveform. Therefore, we cannot generate them for an arbitrary mass ratio, but only for the mass ratios which have been simulated. The phenomenological approach first creates these hybrid waveforms, and then fits a purely-analytical ansatz waveform to the hybrid waveforms. Once they are fit to the hybrid waveforms, these analytical *phenomenological* waveforms can be evaluated for any mass parameters, to effectively interpolate between the available hybrid waveforms.

To construct the hybrid waveforms, the 3.5PN order TaylorT1 approximant was used to generate the PN inspiral waveforms, which were matched to NR waveforms produced using the `BAM` NR code [378]. Then, an ansatz of the form

$$\tilde{h}(f) \equiv A_{\rm eff}\, e^{{\rm i}\Psi_{\rm eff}(f)}$$

$$
\begin{aligned}
A_{\rm eff}(f) &\equiv C \begin{cases} (f/f_{\rm merg})^{-7/6} & \text{if } f < f_{\rm merg} \\ (f/f_{\rm merg})^{-2/3} & \text{if } f_{\rm merg} \leq f < f_{\rm ring} \\ w\,\mathcal{L}(f, f_{\rm ring}, \sigma) & \text{if } f_{\rm ring} \leq f < f_{\rm cut}, \end{cases} \\
\Psi_{\rm eff}(f) &\equiv \frac{1}{\eta} \sum_{k=0}^{7} (x_k\,\nu^2 + y_k\,\nu + z_k)\,(\pi M f)^{(k-5)/3} + 2\pi f t_0 + \varphi_0
\end{aligned}
\tag{7.1}
$$

is fit to the hybrid waveforms, where C is a numerical waveform amplitude constant which depends on the location and orientation of the binary as well as the mass parameters, $\mathcal{L}(f, f_{\rm ring}, \sigma)$ is a Lorentzian function that has a width σ, and that is centered around the frequency $f_{\rm ring}$. The parameter w is chosen so that $A_{\rm eff}(f)$ is continuous across the "transition" frequency $f_{\rm ring}$. The parameter $f_{\rm merg}$ is another transition frequency at which the power-law changes from $f^{-7/6}$ to $f^{-2/3}$ to mark the end of the *adaibatic* inspiral and the beginning of the merger. The phenomenological parameters $\mu_j \equiv \{f_{\rm merg}, f_{\rm ring}, \sigma, f_{\rm cut}\}$ are given in terms of the mass parameters of the binary as: $\pi M \mu_j = a_j\,\nu^2 + b_j\,\nu + c_j$. The coefficients $a_j, b_j, c_j,\ j = 0...3$ and $x_k, y_k, z_k,\ k = 0, 2, 3, 4, 6, 7$ are chosen to maximize the overlap between the hybrid waveforms and the ansatz phenomenological waveforms. They are tabulated in Table I of [339]. The phenomenological waveforms are generated in the Fourier domain but can be converted to time domain for injections by means of an inverse Fourier transform.

We note that this approach is in a sense an evolution of the BCV phenomenological waveforms of Ref. [379]. Those BCV waveforms assumed an ansatz frequency-

domain waveform based on the SPA, but with undetermined phase coefficients which were allowed to vary freely. The reasoning was that the PN formalism gave an incomplete picture of the waveform, and that allowing the coefficients to vary freely could effectively mimic higher-order corrections and other unknown physical effects. For the phenomenological waveforms used here, we again have an ansatz frequency-domain waveform based on the SPA with undetermined parameters, this time in the amplitude as well as the phase. However, instead of allowing the undetermined coefficients to take any value, we now use the insights of numerical relativity to fix them to values which make the ansatz waveform match the NR simulations as closely as possible.

It is worth mentioning that there are some limitations in using the phenomenological IMR waveforms in the search. Those waveforms were built by matching them against NR simulations with mass ratios between 1:1 and 4:1, and the phenomenological coefficients that are fixed through this matching do not reduce to the PN coefficients at low frequencies. If we attempt to push the waveforms to very extreme mass ratios, they will produce very unrealistic waveforms. Said another way, the phenomenological IMR waveforms *interpolate* between NR simulations quite effectively, but one should be careful about using them to *extrapolate* very far beyond the parameter space of the simulations. For this reason, we will only use phenomenological IMR waveforms with component mass ratios less than or equal to 10:1. In addition, the choice of the time interval for matching PN and NR waveforms is somewhat *ad hoc*, being chosen so as to maximize the fit of PN and NR waveforms. Finally, *restricted* (Newtonian-order amplitude) PN waveforms were used to con-

struct the hybrid waveforms and the amplitude of the NR waveforms was scaled to match the PN waveforms. This creates a systematic bias of $\sim 10\%$ in the phenomenological waveforms. However, improved phenomenological IMR waveforms which address these issues have already been constructed [380].

7.1.4 Other search efforts for inspiralling binary black holes in LIGO and Virgo

There have been previous search efforts to detect binary black holes in earlier LIGO data sets which covered a portion of the parameter space searched here, none of which made a successful detection. First, the S2 data set, which contained ~ 386 hours of data, was searched for binaries with a total mass in the range $(3-20)\,M_{\odot}$. This search had sensitivity out to a distance of about 1 Mpc and the results are reported in Ref. [381]. The results of a search of S3 and S4 data are reported in Ref. [382]. S3 consisted of ~ 788 hours of data and was searched with templates up to a total mass of $40\,M_{\odot}$, while S4 consisted of ~ 576 hours of data and was searched with templates up to total mass $80\,M_{\odot}$. These S2, S3 and S4 search efforts used the so-called BCV phenomenological waveforms proposed in Ref. [379]. These waveforms take the form of the (non-spinning) TaylorF2 (or SPA) PN waveforms, except that coefficients appearing in the complex phase of the frequency-domain waveforms are not assumed to take the values predicted by PN theory, but are allowed to vary as free parameters. In addition, another search was performed on the S3 data which used inspiral waveforms with spin effects [59] and component

masses in the range $m_1 = [1, 3]\, M_\odot$ and $m_2 = [12, 20]\, M_\odot$ with the results reported in Ref. [383].

Besides these inspiral searches, there has also been an effort to detect ringdown waveforms. For binaries with total masses $\gtrsim 100\, M_\odot$, little if any of the inspiral signal will be inband and the ringdown will dominate the observable signal. A ringdown search was performed on the S4 data to search for the remnant of binaries with total mass in the range $(85 - 390)\, M_\odot$ [327, 384].

Lastly, the low mass search of the LIGO S5 and Virgo VSR1 data reported in Refs. [96, 97, 98] searched for binaries with a total mass up to $35\, M_\odot$, and so overlaps with the low mass end of this search.

7.2 The data analysis pipeline

The method to analyze the interferometer data to search for signals, estimate background rates and set an upper limit in the absence of a detection is referred to as a data analysis pipeline. The search pipeline used for the S5 high mass search described here is the same pipeline used for the S5 low mass ($M = (2 - 35)\, M_\odot$) search efforts described in Refs. [96, 97, 98], except for the choice of template and injection waveforms, the way in which the χ^2 signal-based veto is applied, and the way in which the upper limit on the event rate is reported. We now describe the various steps of this data analysis pipeline.

7.2.1 Data selection and data quality vetoes

If the Fabry-Perot cavities which make up the the interferometer arms and the power recycling cavity are near resonance, then the signal at the dark port (the photosensor monitoring the signal leaving the beam splitter) will respond linearly to displacements of the mirrors, and the whole system will be stable. When this happens, the interferometer is said to be "in lock" and data can be taken. If the optical cavities are away from resonance, the system will generally not be stable against mirror displacements, high quality data cannot be taken, and the interferometer is said to be "out of lock".

The three LIGO interferometers did not operate continuously during the S5 science run. The interferometers would often lose lock due to earthquakes, passing trains or airplanes, and many other types of environmental disturbances. From time to time they were also intentionally taken out of lock to perform maintenance and tuning. Data from the interferometers is recorded when the instrument is in a stable lock. This is referred to as *science mode*, and the times when the data are recorded are referred to as *science time*. Not all science time is created equally. In some cases, even though the interferometer is locked, there may be excessive noise. If this noise is likely to cause an excessive number of triggers, or excessively loud triggers, one may not want to analyze the data at all, or one may want to exclude it from the upper limit calculation, but still search it to be sure an exceptional detection candidate is not missed. To partition the science times into categories of various quality, a set of data quality (DQ) flags have been created.

The most basic DQ flags are denoted category 1. These simply flag all times during which the interferometers are not in science mode. Any time with a category 1 flag will not be analyzed. The remaining DQ flags are defined by monitoring auxiliary channels to identify times which are likely to have significant environmental noise. For example, an accelerometer is placed near each of the mirrors in the interferometer to monitor local vibrations. One could flag all times when the accelerometer readings are above a certain level, and in this way veto times when there is elevated seismic activity. Hundreds of such DQ flags monitoring hundreds of auxiliary channels have been defined in this way and are grouped into categories 2, 3 and 4.

While data with a category 1 flag is never analyzed, the remaining DQ vetoes are actually applied downstream in the pipeline. That is, data which has a DQ flag other than category 1 will proceed through the pipeline and be matched filtered to produce a list of triggers. However, a "DQ veto" will be applied to the list of triggers, and those which occur during flagged times will be excluded from the final list. This is done downstream (rather than at the beginning of the pipeline) so that the effectiveness of various DQ flags can be evaluated and so the DQ flags can be assigned to the appropriate category. In essence, one wants to apply DQ vetoes which will remove many loud noise triggers while vetoing as little time as possible to retain as much high quality data as possible. Category 2 DQ flags are those which veto the greatest number of loud triggers while vetoing the least amount of science time. The origin of noise sources and their coupling to the signal at the dark port are typically well understood for category 2 flags. Category 3 DQ flags

veto fewer loud triggers and/or veto more science time than category 2. The origins of this noise and its correlation to the signal at the dark port is typically less well understood. Triggers with category 2 or 3 flags are vetoed and not considered as detection candidates, nor used in setting upper limits. Category 4 DQ flags typically veto more science time and/or have weaker correlation to the signal at the dark port. Triggers with a category 4 flag are not considered when setting upper limits, but are checked as viable detection candidates.

7.2.2 Template bank generation

It would be impossible to filter with a template for each point in the continuum of parameter space, so one must choose a finite number of templates which adequately cover the parameter space. Typically, one chooses a mismatch MM and requires that the normalized inner product between any two adjacent templates h_1 and h_2 satisfy $(h_1|h_2) \geq 1 - \mathrm{MM}$, so that the loss of SNR (and thus the decrease in maximum observable distance) for a signal that falls between templates will be no more than MM. Since the event rate scales as the observable volume, which scales as the cubic of the observable distance, the loss in event rate due to the discreteness of the template bank will be $1 - (1 - \mathrm{MM})^3$. A common choice of mismatch (and the value used in this search) is $\mathrm{MM} = 3\%$, so that the loss of event rate will be less than 10%.

The template placement algorithm used in the LAL code is described in detail in Ref. [100]. As we will see, it is possible to maximize analytically over the extrinsic

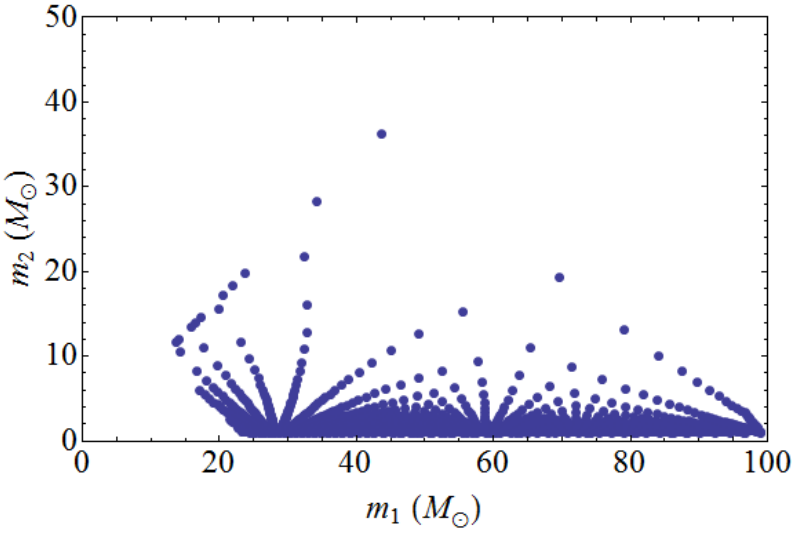

Figure 7.1: A typical template bank in the m_1-m_2 plane covering the region $M = (25-100)\,M_\odot$ with component mass $(1-99)\,M_\odot$ for a 2048 s stretch of LIGO data.

parameters $t_{\rm ref}$ and $\phi_{\rm ref}$, so that we do not have to create templates with different values of these parameters. We simply need to lay out templates in the 2-D space of mass parameters. In the LAL code, this is done in terms of so-called "chirp time" parameters defined as

$$\tau_0 = \frac{5}{256\,\pi\,\nu\,f_{\rm low}}\,(\pi\,M\,f_{\rm low})^{-5/3} \qquad \tau_3 = \frac{1}{8\,\nu\,f_{\rm low}}\,(\pi\,M\,f_{\rm low})^{-2/3}\,, \tag{7.2}$$

where $f_{\rm low}$ is the low-frequency cutoff of the interferometer. While the placement is computed in terms of the chirp time parameters, there is a one-to-one mapping with other pairs of mass parameters, such as (m_1, m_2), (M, ν), etc. Table 7.2.2 plots a typical template bank used in this search in the m_1-m_2 plane.

The high mass search places templates according to an analytic metric on the parameter space derived for 2PN order TaylorF2 (SPA) waveforms, as described

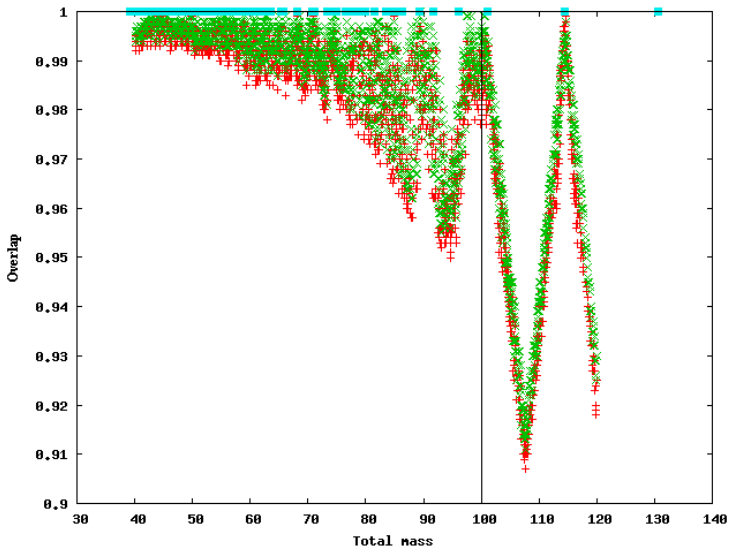

Figure 7.2: EOB waveforms are injected into data and recovered with EOB templates placed according to a 2PN order SPA waveform metric. The cyan squares at the top of the plot represent the total mass of the template waveforms. If the EOB signals (denoted by red and green points) fall at masses between templates, the overlap will drop. The vertical line at $100\,M_\odot$ represents the upper total mass boundary of this search.

in Refs. [385, 322, 100]. This metric quantifies the "distance", or mismatch, between template waveforms with different mass parameters. Templates are placed until, according to the metric, any point in the mass range of the search will be within MM of at least one template. Although the metric is derived for 2PN order SPA waveforms, while in this search we use EOB templates, we find that it does approximate the distance between EOB signals well for low masses. As one approaches the high mass end of our search ($M \sim 100\,M_\odot$), however, the 2PN SPA metric underestimates the distance between EOB waveforms somewhat and places fewer templates than are needed. In Fig. 7.2, we test the template placement by injecting many EOB signals and computing their overlap with the template bank. We see that the overlap drops below our goal of 97% at the high mass end, but

Detector Bank	$\bar{N}$	σ
H1 First Bank	1568.4	201.6
H1 Second Bank	404.8	395.5
H2 First Bank	1315.1	88.7
H2 Second Bank	208.1	241.4
L1 First Bank	1963.3	305.9
L1 Second Bank	709.7	468.6

Table 7.1: The choice of templates depends on the time-dependent PSD of the detectors. This table outlines the average number of templates required in the first and second bank stages as well as the standard deviation.

we still have overlaps $\geq 95\%$ for the entire mass range. We consider this adequate for this first search effort with IMR templates, but in the future the placement of IMR templates should be improved. Because the distance between waveforms is defined by a noise-weighted inner product, if the instrument noise changes, this will affect template placement. Therefore, we compute a template bank for every 2048 s of data. In Table 7.2.2, we give the standard deviation and average number of templates per 2048 s chunk for each interferometer for both first- and second-stage filtering (explained in Sec. 7.2.6).

7.2.3 Filtering the data

For each interferometer, we filter the data against each template in our bank and produce a list of triggers for which the SNR exceeds some predetermined threshold (chosen as $\rho \geq 5.5$ in this search). In Eqs. (2.103)-(2.104) of Ch. 2, we saw how the SNR could be defined in terms of a real-valued inner product. It turns out that one can maximize over the extrinsic parameters $t_{\rm ref}$ and $\phi_{\rm ref}$ by defining a

complex-valued inner product

$$z(t) = \langle s|h\rangle\,(t) \equiv 4\int_0^\infty \frac{\tilde{s}(f)\,\tilde{h}^*(f)}{S_n(f)}\,e^{2\pi i f t}\,df\ , \tag{7.3}$$

where we have used angular brackets to distinguish this inner product from the real-valued inner product of Eq. (2.103). Then, changing $\phi_{\rm ref}$ will simply cause a rotation of the complex argument of $z(t)$. So, $|z(t)$ will be the value of the (complex- or real-valued) inner product maximized over $\phi_{\rm ref}$. Therefore, we simply find the time $t_{\rm ref}$ which maximizes $|z(t)|$ to perform the maximization over the extrinsic parameters. Thus, we define the SNR (maximized over $t_{\rm ref}$ and $\phi_{\rm ref}$) as

$$\rho = \frac{|z(t)|}{\sigma} = \frac{|\,\langle s|h\rangle\,(t)|}{\sqrt{(h|h)}}\ . \tag{7.4}$$

Now, if a certain template crosses the SNR threshold at a certain time, many other nearby times and nearby parameter values will also produce a trigger above threshold. Therefore, clustering over time and parameters is done to find local maxima in the set of triggers, and reduce them to a manageable number. A more detailed description of the implementation of matched filtering in LAL can be found in Refs. [101, 94].

7.2.4 The χ^2 consistency test

To help distinguish between obvious background noise events and viable detection candidates, signal-based vetoes are used to eliminate or decrease the ranking

of triggers which are likely to be caused by background noise. The most important of these is the χ^2 consistency test, which determines the goodness-of-fit between signal and template. In this test, each template is broken into p (in this search we use $p = 10$) non-overlapping frequency bands, $\tilde{h}(f) = \sum_i^p \tilde{u}_i(f)$, such that each one contributes an equal portion to the signal strength, $(u_i|u_j) = \delta_{ij}\,\sigma^2/p$ (δ_{ij} is the Kronecker-delta). We matched filter against each of the $\tilde{u}_i(f)$ to find their contribution to the SNR,

$$\rho_i(t) = \frac{\sqrt{p}}{\sqrt{(h|h)}}\ \langle s|u_i\rangle\,(t)\ . \tag{7.5}$$

Then, we define

$$\chi^2 = \sum_{i=1}^{p} \left| \frac{\rho(t)}{p} - \rho_i(t) \right|^2\ . \tag{7.6}$$

Note that because it depends on the complex inner product with real and imaginary parts, this χ^2 will have $N = 2(p-1)$ degrees of freedom. If the power of the signal in each frequency band is close to that of the template, the signal is consistent with the template and χ^2 will be small. If χ^2 is large, it means the power of the signal is distributed differently in frequency from the template and the trigger is likely to be noise. See Ref. [102] for details about the χ^2 consistency test.

In this search, the χ^2 value is used to re-weight the SNR of an event to create an improved detection statistic known as *effective SNR* and defined as

$$\rho_{\text{eff}} = \frac{\rho}{\left[(1+\rho^2/C)(\chi^2/N)\right]^{1/4}}\ , \tag{7.7}$$

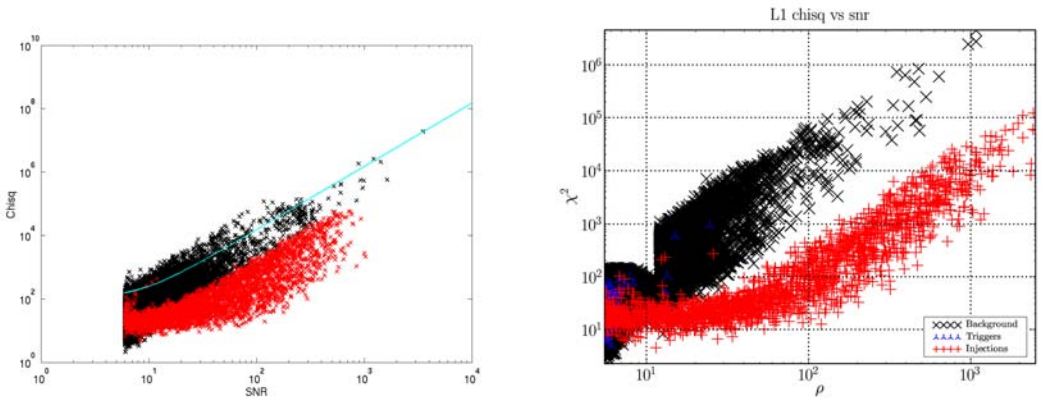

Figure 7.3: Plots of χ^2 vs SNR with EOB inspiral-only template and injected waveforms (left panel) and with EOB template and injected waveforms (right panel). In either case, background triggers (generated with time slides) are denoted with black markers, while triggers from injected waveforms are denoted with red markers. We see that the full IMR signal has a better separation of background from injections.

where $N = 2(p-1) = 18$ is the number of degrees of freedom, and $C = 50$ is a tunable parameter.

7.2.5 Coincidence test

Once we have a list of triggers for each interferometer, those lists of triggers are compared to identify coincident events. If two or more instruments have triggers at nearly the same time (within some tolerance to account for the light travel time between sites and errors on the reference time) and have similar mass parameters, then they are counted as a coincidence. The same metric used to place templates is also used to determine if the triggers from two different interferometers are sufficiently close in time and masses to be considered a coincident event. As we noted, this metric was derived for 2PN SPA waveforms, while we are using EOB template waveforms. For this reason, the coincidence window is chosen to be looser than for

previous search efforts. The coincidence window seems to work well. For example, simulated waveforms injected into multiple detectors can be recovered as coincident events. However, this could be improved in the future with the use of an IMR metric. For our list of coincident events, we add the effective SNR from the triggers in each interferometer in quadrature to compute a *combined effective SNR*,

$$\rho_{\mathrm{eff,c}} = \sqrt{\sum_i \rho^2_{\mathrm{eff,i}}} \, . \tag{7.8}$$

7.2.6 Hierarchical filtering and coincidence

Now, it turns it is rather computationally expensive to compute the χ^2 value of a trigger. For example, note that we must determine the frequency bands which contribute $1/p$ to the total SNR, break our template waveform into p sub-templates, and then filter the data against each sub-template. For this reason, we employ a hierarchical pipeline which performs the filtering and coincidence test twice so that the χ^2 is computed only for the subset of templates which produce coincident triggers.

In the first stage of the hierarchical pipeline, one performs the filtering as described in Sec. 7.2.3 for each interferometer using the full template bank computed according to Sec. 7.2.2. Using this list of triggers from each interferometer, one makes a list of all coincident events. Then, one makes a second-stage template bank for each interferometer which includes only the templates that appear in the coincident event list. The data is filtered a second time using the second-stage

template bank, and this time the χ^2 is also computed for every template and the effective SNR is tabulated. Then, a coincidence test is performed a second time and the combined effective SNR of each coincident event is recorded. Note that this hierarchical approach is applied only to reduce the number of times χ^2 must be computed to speed up the analysis. In Table 7.2.2, we show the average number of templates for each interferometer and stage of the hierarchical pipeline. Note that the first stage has thousands of templates, while the second stage is reduced to hundreds of templates.

7.2.7 How to estimate the background

To understand how likely a coincident event is to be a true gravitational wave, we need to understand how likely it is to have random, coincident noise fluctuations create a coincident event of the same "loudness" (e.g. the same combined effective SNR). To this end, we perform a series of "time slides" — we shift the data streams from interferometers at different sites relative to one another by 5 second increments. Then, the time-shifted data is run through exactly the same hierarchical filtering and coincidence pipeline as the unshifted, or so-called "zero lag" data. Because 5 seconds is much greater than the light travel time between LIGO sites ($\sim$ 10 ms), any coincident events found in the time-shifted data must be caused by random noise triggers. 100 such times slides are performed, and this gives us 100 independent background trials, as we do not expect any correlations in noise between the widely separated LIGO sites.

Now, because H1 and H2 are co-located, we expect them to have correlated noise from local environmental disturbances. Therefore, this time slide procedure will not accurately model the coincident event rate for the detector pair H1H2. In fact, for this search we do not have a reliable way of estimating the H1H2 background rate, and so we do not consider events which are coincident in only H1 and H2. The time slide procedure does allow us to estimate the background rate for all other interferometer combinations. Note that for the H1H2L1 triple coincident background we slide H1 and H2 together relative to L1. During times when all three interferometers are operating, we do not consider events which coincident in H2L1, because of H2 has a trigger from a true signal, the more sensitive H1 should also have a trigger. We do, however, consider H2L1 coincident events if H1 is not operating.

7.2.8 How to rank events

The ranking of events which emerge from the hierarchical pipeline will depend on how loud the signals are (SNR) and also on the goodness of fit (χ^2) which are encoded in the effective SNR formula of Eq. (7.7). Since we require coincidence between multiple detectors, it is natural to rank coincident events according to the combined effective SNR of Eq. (7.8). However, while it is relatively common for two interferometers to experience random noise triggers at coincident times, it is much rarer to have three interferometers experience coincident random noise triggers. Therefore, if we have a triple-coincident candidate event and a double-

coincident candidate event with the same effective SNR, the triple-coincident event will have a much lower background rate and is the more interesting event. In addition, we find that noise fluctuations tend to match some templates much more frequently than others. In particular, templates with a high total mass have a much higher background trigger rate than low total mass templates. Therefore, if we have a low mass candidate event and a high mass candidate event with the same combined effective SNR, the low mass candidate will be more interesting due its lower background rate.

To take these issues into account, we will not use the combined effective SNR as our final ranking statistic, but will rather define a false alarm rate for the event. This false alarm rate will depend on the set of interferometers that were operating, the set of interferometers which had a coincident trigger and the masses of the template waveforms. The mass dependence of the false alarm rate is addressed by partitioning the candidate events into three total mass bins with boundaries $[25, 50)$, $[50, 85)$, $[85, 100]$. We also divide the list of candidates according to coincidence type. These are "H1H2L1 triggers in H1H2L1 time", "H1L1 triggers in H1H2L1 time", "H1L1 triggers in H1L1 time" and "H2L1 triggers in H2L1 time". The first set of interferometer abbreviations denotes which ones had a coincident trigger, while the second denotes which ones were operating. Note that H2L1 and H1H2 triggers in H1H2L1 time are excluded because the former should have an H1 trigger for a real event, and we cannot estimate the background of the latter.

For the candidate events in each of these categories defined by a total mass range and coincident type, we compare the combined effective SNR of the candidate

to the combined effective SNRs of the background events (produced by time slides) in this category and count the number of background events which match or exceed the combined effective SNR of the candidate. To compare events across different categories, we divide the number of louder background events by some standard unit of time (such as a year). In this way, we assign a false alarm rate to each candidate coincident event. We define our ranking statistic as the inverse false alarm rate (IFAR), ξ^{-1} (the IFAR is used as the ranking statistic rather than the false alarm rate so that a higher value means a more interesting signal, corresponding to the intuitive notion of "loudness" of an event).

7.2.9 Assessing detection efficiency with injections

To gauge the detection efficiency of our search pipeline, we inject many simulated waveforms into the data and attempt to detect them with our search pipeline. By "inject", we mean that we record the data time series from each detector and use software to add to it the time series of a gravitational wave (with a time, amplitude and phasing in each detector that is consistent with a certain sky location and orientation). We then analyze this data with the same pipeline used to do the actual search and to estimate background via time slides. To measure the detection efficiency, we consider an injection found if it has a lower false alarm rate (or higher IFAR) than the loudest event of our search.

Recall that we estimate the noise PSD of the interferometers in 2048 s blocks. Now, if we injected many loud signals into these blocks, the excess power from the

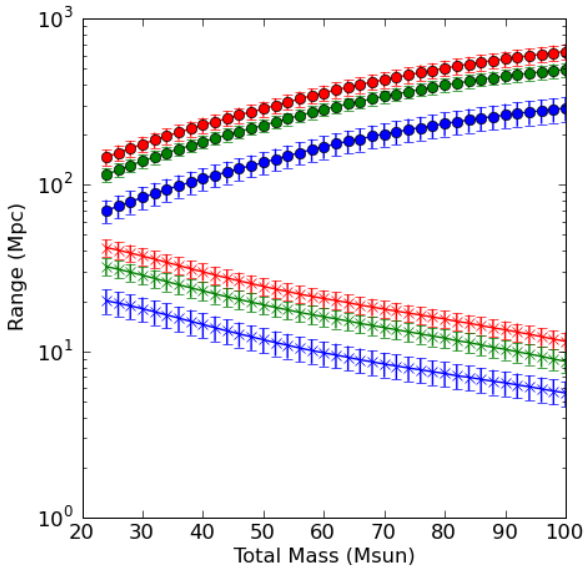

Figure 7.4: A plot of horizon distance as a function of the total mass of the system for the H1, H2 and L1 detectors (red, blue and green lines respectively). The upper lines are for systems with equal component masses. The lower lines are for asymmetric systems with component masses $(1, M_{total} - 1)M_{\odot}$.

injections would significantly alter the noise curve of the instrument. It has been found that we can inject $\sim$ 1 waveform per 2048 s block without ruining the computation of the PSD, so this limits somewhat the number of injections we can perform into our data. However, we can get more injection trials by injecting a set of waveforms into the data and analyzing it, then repeating this procedure with another set of injections with different parameters at different times. In this search we perform 10 such injection runs, which allows us to analyze $\sim 10^6$ injected waveforms. For seven of these runs, we injected EOB waveforms over the whole mass range of the search (total mass $(25 - 100)\, M_{\odot}$ and component masses $(1 - 99)\, M_{\odot}$). For the other three sets, we injected phenomenological IMR waveforms, but we restricted their range so that the ratio of component masses is never greater than 10:1. As

explained above, this was done because the phenomenological IMR waveforms were found to be unrealistic for more extreme mass ratios. For all of these injection sets, the waveforms were injected at physical distances between $1 - 750$ Mpc uniform in the logarithm of distance and with a random, uniform distribution of sky location and binary inclination. They were intended to be injected with a random, uniform distribution in the polarization angle ψ as well, *but due to a software bug discovered during the review of this search, in the results reported here all injections were made with* $\psi = 0$. Preliminary investigations suggest that this will not significantly affect the results of this search, but a rerun of the search with the bug fixed is underway and nearly completed. The final published results will use the correct distribution of injections to analyze the data.

In Fig. 7.4, we plot the *horizon distance* for the injected waveforms, which is the maximum *effective distance* (or the physical distance for an optimally located and oriented binary) to which we find injections. The upper curves plot the horizon distance for equal mass binaries as a function of total mass. The lower curves plot the horizon distance for the most asymmetric binary at a given total mass, the pair $(1, M - 1)\, M_\odot$. For a given total mass, the equal mass binaries have a greater amplitude than the asymmetric binaries, and so can be detected out to much greater distances.

7.2.10 Tuning the search pipeline

Before we perform our final analysis, we would like to ensure that we have not made any mistakes and that we are satisfied with the signal-based vetoes and detection statistics we have defined. Therefore, we will allow ourselves to look at data from timeslides and injections, but we will not allow ourselves to look at the "zero lag" data that will be used to set our upper limit. Looking at the zero lag data would unblind the search effort, and if we tune the search pipeline according to this data, we could introduce bias. We do, however, set aside 10% of the zero lag data, called "playground data" which we are allowed to analyze along with the injections and time slides to attempt to optimize the signal-based vetoes and detection statistics in our pipeline. To avoid bias, this playground data is not used in setting an event rate upper limit. However, if we find a very credible detection candidate in the playground data, we will still allow ourselves to claim a detection.

Much of our "tuning" efforts focused on the χ^2 consistency test. There were previous attempts to perform the S5 high mass analysis using 3PN order EOB inspiral-only template waveforms. However, it was found that the χ^2 test performed very poorly in this case. Note the left panel of Fig. 7.5, where we plot the distribution of time slide triggers (black) and EOB inspiral-only injections recovered with EOB inspiral-only templates (red). Note that the two distributions are right on top of one another, so the χ^2 is a poor discriminator of signal from background. The cyan line represents a proposed χ^2 cut which would retain all but a few injections if these inspiral-only waveforms were to be used as detection templates. Note that a wide

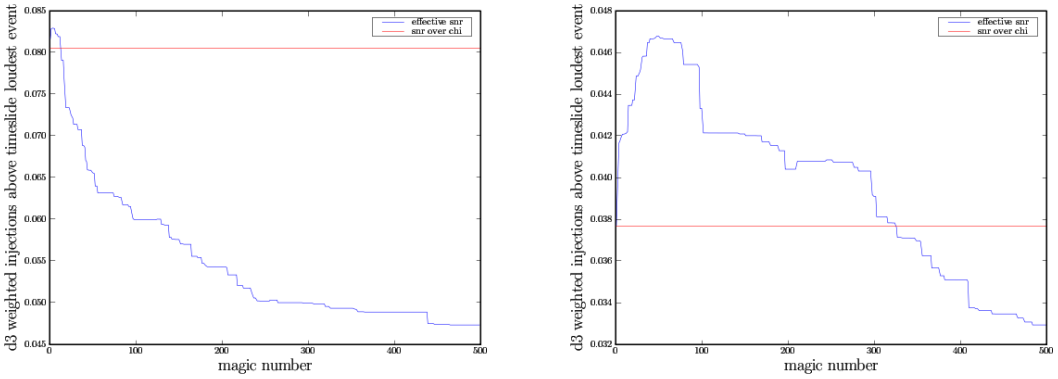

Figure 7.5: Plots of detection efficiency (weighted by the signal distance cubed) versus the "magic number" appearing in the effective SNR definition of Eq. (7.7) for H1 (left panel) and L1 (right panel) during a subset of the S5 data. The horizontal red line is the efficiency when defining $\rho_{\rm eff} = \rho/\chi$. There is a clear trend that smaller values of C give a greater detection efficiency, and $C = 50$ was found to be the best value over all interferometers and all data considered.

majority of background events would pass this cut.

In the early part of 2008, the EOB waveforms described in Sec. 2.2.2, were implemented into the LAL code by the author of this thesis along with Yi Pan and B.S. Sathyaprakash. It became quite clear that the χ^2 consistency test performed much better with full EOB waveforms than with inspiral-only EOB waveforms. We see this in the right panel, which is the same as the left panel, except that the red denotes EOB injections recovered with EOB templates. We obtain a much better separation of signal and background making the χ^2 much more useful. Furthermore, it was decided not to use perform a hard cut on the χ^2 veto (meaning that a trigger would either pass the veto and be retained or fail it and be discarded), but rather to use the χ^2 consistency test to re-weight the significance of an event by defining an *effective SNR* which depends on χ^2. Therefore, all triggers would be retained, but their ranking would increase or decrease depending on their χ^2 value.

We attempted to further optimize the effectiveness of the χ^2 by tuning the definition of the effective SNR. Notice that the effective SNR formula of Eq. (7.7) has a free parameter, C, which is colloquially referred to as the "magic number". Each value of ρ_{eff} labels a certain contour in the ρ-χ^2 plane (these contours move towards the lower right corner of Fig. 7.3 as ρ_{eff} increases). Now, in essence, one wants to choose a value of C so that the contours of constant ρ_{eff} conform to the lower right edge of the black distribution as closely as possible. Then, the contour which passes through the loudest background event will have as many injected signals as possible lying at higher ρ_{eff}, and so this will maximize the detection efficiency. All other things being equal, we would rather tune our ρ_{eff} definition to find low SNR signals rather than high SNR signals. This is because there will be many more low SNR (i.e. large distance) signals than high SNR (i.e. small distance) signals (assuming the signals are distributed roughly uniform in volume) and also because the low SNR signals will be more difficult to detect. For this reason, in optimizing the value of C in the ρ_{eff} definition, we count the fraction of injections with ρ_{eff} larger than the loudest background event, and we weight each injection by its distance cubed (to account for the fact that there will be more signals at larger distances in a uniform-in-volume distribution).

The three corresponding authors for the search computed ρ and χ^2 for the injections and time slides of the final 6 calendar months (months 19-24) and performed a study of how many injections (weight by their distance cubed) had a greater ρ_{eff} than the background as the value of C was varied. We plotted these results for each interferometer and each two-month pair. The results for H1 and L1 in months 19-20

(which were analyzed by the author of this thesis) are plotted in Fig. 7.5. Across all months and all interferometers, there was a clear trend that smaller values of C gave higher efficiencies. Based on these plots, we chose $C = 50$, which gave a high efficiency in all cases.

In addition to the χ^2 veto, we also considered a so-called effective distance cut. Two interferometers at widely separate locations (such as H1 and L1) can measure very different effective distances for the same source, because that source will be located and oriented differently relative to each interferometer. However, because the H1 and H2 interferometers are co-located, they should measure the same effective distance to a source. Therefore, for coincident events which include H1 and H2 triggers, we could require that they report the same effective distance to within some tolerance and veto the event if they do not. However, we found that H1 and H2 would often recover injections with quite different effective distances (due to differences in the template mass parameters for each interferometer). Therefore, even if the tolerance was set quite loose ($\gtrsim 50\%$ difference in effective distance), this test would veto a significant number of injections. Setting a very loose tolerance also limited the ability to veto background triggers. So, it was decided not to use an effective distance cut in this search.

7.2.11 **Setting upper limits on coalescence rates**

If a successful detection is not made, then we use the non-playground zero lag data to set an upper limit on the event rate of compact binary coalescences using

the approach of Ref. [103]. To do this, we rank all coincident events by IFAR, ξ^{-1}, according to the procedure in Sec. 7.2.8 and identify the loudest event with false alarm rate ξ_*, i.e. IFAR ξ_*^{-1}. Then, with a knowledge of the detection efficiency above the loudest event and the relative likelihood the loudest event was caused by a background noise trigger, one can compute a Bayesian posterior probability distribution for the rate of compact binary coalescences. Then, one integrates this distribution over all possible rates (starting at a rate of 0) up to a value R where one reaches a certain confidence level, which we choose to be 90% in this search. This amounts to making the statement "if the event rate were greater than R, there is a 90% chance it would produce a trigger louder than ξ_*. Since we did not observe such a trigger, we conclude with 90% confidence that the event rate must be less than R."

In this search, we bin the mass plane into a discrete set of (m_1, m_2) mass pair bins and compute an event rate upper limit for each mass pair. To do this, we first define for each mass pair a detection efficiency

$$\epsilon_i(\xi_*, \mathbf{x}, m_1, m_2) = \frac{N_f(\xi_*, \mathbf{x}, m_1, m_2)}{N_t(\mathbf{x}, m_1, m_2)} \ , \tag{7.9}$$

where ξ_* denotes the loudest event, $\mathbf{x} = \{D, \theta, \phi, \iota, \psi\}$ denotes the physical location and orientation of the source binary, N_f is the number of found injections in the mass pair bin at that location and orientation, N_t is the total number of such injections, and i labels the coincidence-type (e.g. which detectors were operating and which had a trigger). Computing an efficiency for each coincidence-type is

necessary because our ranking statistic is IFAR, which depends on the background rate of that particular coincidence-type. With this efficiency, one integrates over space and orientation angles to obtain an observed volume,

$$V_i(\xi_*, m_1, m_2) = \int d\mathbf{x}\ \epsilon_i(\xi_*, \mathbf{x}, m_1, m_2)\ . \tag{7.10}$$

with units of Mpc^3. We can get an estimate of the uncertainty on this volume by varying the boundaries of the mass pair bins, recomputing the observed volume, and taking the variance of such values. Therefore, we define an error on the observed volume

$$\sigma_i(\xi_*, m_1, m_2)^2 = \overline{V_i(\xi_*, m_1, m_2)^2} - \left(\overline{V_i(\xi_*, m_1, m_2)}\right)^2\ , \tag{7.11}$$

where an overbar is used to denote the average observed volume of the mass bin as the boundaries are varied. Then, in our notation, Eq. (24) of Ref. [103] gives the Bayesian posterior probability distribution for the event rate for our mass pair

$$\begin{aligned}
p_i(R|m_1, m_2) &= p_i(R|k, \overline{VT}, \Lambda) && (7.12)\\
&= \frac{\overline{VT}}{1+\Lambda}\left[\frac{1}{(1+R\overline{VT}/k)^{k+1}} + \frac{R\overline{VT}\Lambda(1+1/k)}{(1+R\overline{VT}/k)^{k+2}}\right], \\
\overline{VT} &= V_i(\xi_*, \bar{m}_1, m_2)\, T_i, && (7.13)\\
k &= \left[\frac{V_i(\xi_*, \bar{m}_1, m_2)}{\sigma_i(\xi_*, m_1, m_2)}\right]^2, && (7.14)\\
\Lambda &= -\frac{\mathrm{d}\ln\left[V_i(\xi_*, m_1, m_2)\right]}{\mathrm{d}\xi_*}, && (7.15)
\end{aligned}$$

where Λ quantifies the relative likelihood of the loudest event being a true signal

versus a background trigger and the factor k comes from assuming a γ-distribution for the posterior probability, we again refer the reader to Ref. [103] for more details.

The p_i posterior probabilities could be used to determine an upper limit for each mass pair based on observations of one coincident type. We can obtain a posterior probability for all of the observation time by taking the product of the individual posterior probabilities

$$p(R|m_1, m_2) = \prod_i p_i(R|k, V_i(\xi_*, m_1, m_2)T, \Lambda) \ . \tag{7.16}$$

Then, we perform the integral

$$0.9 = \int_0^R p(R^{'}|m_1, m_2)\, dR^{'} \tag{7.17}$$

to find our 90% confidence upper limit, R, on the rate of binary coalescences with masses (m_1, m_2).

7.3 Preliminary search results

The LIGO interferometers took a full year of triple-coincident data, but some of this data ends up being DQ vetoed. The amount of data remaining after category 3 vetoes (i.e. the data searched for detection candidates) is shown in Table 7.2 for each class of coincident time. The S5 data was partitioned into 12 segments which each correspond to roughly two calendar months. Each two-month period was assigned to a different data analyst, who was charged with running the search pipeline to

Detectors	Live time (yr)
H2L1	0.06
H1L1	0.10
H1H2L1	0.62
H1H2	0.00

Table 7.2: The amount of analyzed time surviving the pipeline after category 3 vetoes were applied. Notice that H1H2 times were not analyzed due to the inability to properly estimate the background for co-located detectors.

analyze that two-month period (I analyzed the data from months 19-20). For each two-month period, we rank the events according to their IFAR relative to the data of that two-month period, computed within the mass bin and coincident-type of the event as described in Sec. 7.2.8. The reason the false alarm rate of an event is computed using only the data of a two-month period (rather than the full two calendar years) is to account (in a rather crude way) for different background rates during different portions of S5. For example, the interferometers typically had lower background rates towards the end of S5 compared to the beginning of S5. After each two-month pair has been analyzed, we pool all of the data together to produce a list of the top overall detection candidates and an upper limit based on all of the data.

7.3.1 Detection candidates

Each coincident event is assigned a false alarm rate by comparing it to the distribution of background events within its own mass bin, coincidence type and two-month period. Because the ranking of each event is normalized as a rate per some common unit of time (typically years or seconds), the false alarm rate, or equiv-

alently IFAR, serves as a universal ranking of the coincident events that transcends their categories. Therefore, we all coincident events across categories to study their distribution and produce an overall list of the loudest events.

In Fig. 7.6, we plot a cumulative histogram of the IFAR of coincident events combined over all categories, except for the set of interferometers which were operating. Said another way, the left panel of Fig. 7.6 is the IFAR histogram of all triple- and/or double-coincident events which occurred when H1, H2 and L1 were all operating, from all mass bins and all two-month periods. The center and right panels of Fig. 7.6 are the IFAR histograms of all double-coincident events when their respective pairs of interferometers were operating from all mass bins and all two-month periods. The shaded regions represent standard deviations from the expected background. These plots show that we had two triggers in triple-coincident time with IFARs which significantly above the expectation, and one trigger in H2L1 time significantly above the expectation. These three triggers are in fact the three loudest events of our search. In Table 7.3, we give some information on the ten overall loudest triggers in our search. We now discuss the three loudest events in a bit more detail.

7.3.1.1 **The loudest event**

The loudest event of this search, which was a triple-coincident event at GPS time 825664840.1523, was more significant than any of the 100 background trials performed during the two month period in the triple-coincident H1H2L1 time. Be-

Rank	ξ **(yr**$^{-1}$**)**	ρ_{eff}	**GPS Time**	ρ_{H1}	χ^2_{H1}	$m_{1\,\mathrm{H1}}$	$m_{2\,\mathrm{H1}}$	ρ_{H2}	χ^2_{H2}	$m_{1\,\mathrm{H2}}$	$m_{2\,\mathrm{H2}}$	ρ_{L1}	χ^2_{L1}	$m_{1\,\mathrm{L1}}$	$m_{2\,\mathrm{L1}}$
1	$<$ 4.0e-01	11.6	825664840.1523	5.6	21.5	51.7	1.1	6.2	1.6	50.5	1.1	5.5	39.1	36.2	2.4
2	$<$ 2.0e-01	12.8	848905672.3369	172.0	4060.4	94.0	6.0	24.4	166.1	49.7	17.3	8.3	46.7	95.2	4.8
3	7.1e-01	10.3	842749918.8057	-	-	-	-	5.5	7.8	67.1	2.5	12.2	20.4	83.2	16.8
4	1.4e+00	12.0	830222610.4062	5.5	33.9	98.0	2.0	*	*	*	*	28.8	43.6	91.7	8.3
5	2.1e+00	9.8	827865922.1265	9.2	67.6	37.3	1.2	-	-	-	-	6.8	4.2	31.0	1.5
6	5.4e+00	10.4	850406432.9307	20.1	56.9	65.8	3.2	*	*	*	*	5.9	11.5	70.5	1.0
7	1.2e+01	9.7	849056023.4121	5.7	11.6	29.9	1.3	*	*	*	*	5.6	2.7	23.6	1.8
8	1.2e+01	9.5	836048263.0366	6.2	15.0	52.9	1.4	6.4	14.6	46.7	1.6	5.9	21.3	53.0	1.3
9	1.3e+01	10.8	835998008.6890	23.2	52.3	94.8	5.2	*	*	*	*	5.8	21.2	78.1	1.2
10	1.3e+01	10.7	854487078.6543	6.1	29.3	96.7	3.3	*	*	*	*	18.1	29.8	97.0	3.0

Table 7.3: The loudest events of the search. The coincident events are ranked by their combined false alarm rate ξ. A " - " represents that the detector was not functioning during the time of the event in question. A " * " represents that the detector was functioning but did not produce a trigger above the single detector SNR threshold of 5.5.

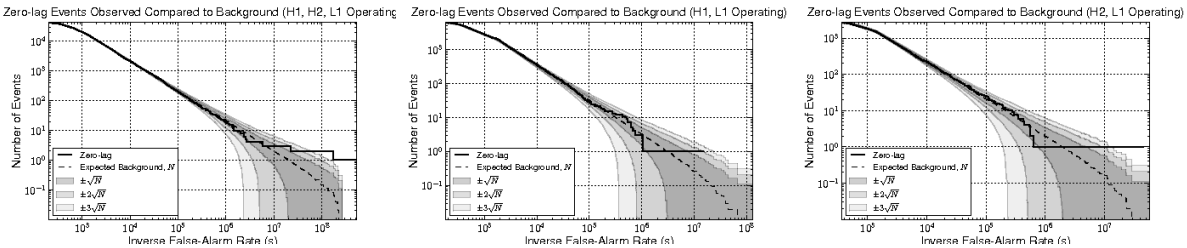

Figure 7.6: The combined IFAR for events ranked in all 12 time periods broken up by the three detector time categories H1H2L1, H1L1, H2L1. The dashed black lines are the expected number of events from background and the shaded regions represent one standard deviation from this expectation. The solid black lines represent the foreground measurement. There is approximately a factor of 10 times more H1H2L1 observation time than H2L1 or H1L1 time. Therefore, deviations from the expectation in the H1H2L1 time category are more significant in terms of IFAR than the other categories. There are three events that stand out above the background. Two of these events occur in H1H2L1 time (shown in the left figure). One event occurs in H2L1 time (shown in the right figure).

cause it is louder than all of our background, we cannot assign it a definite false alarm rate, but we can say that this event should occur no more often than once every 4 years (which is the amount of background time we obtain from time slides for this trigger's category).

The event was found in all three detectors H1, H2, and L1 with SNR only slightly above threshold 5.60, 6.17 and 5.55 respectively. The masses were consistent between the detectors. It is relatively common to get a triple-coincident event in which the SNR is just slightly above threshold in each interferometer. In H1 and L1, the χ^2 of this event was highly consistent with background trials. However, it had an unusually low χ^2 value (0.1 per degree of freedom) in H2 which is quite uncommon. We note that a χ^2 value of less than 0.1 per degree of freedom is no more consistent with signal than with noise (even if the template and signal are identical, one would expect a $\chi^2 \sim 1$ per degree of freedom due to the presence of noise) and that this

fact is borne out by our simulations. No background trials out of $\sim 300,000$ had such a low χ^2 value nor did any of the $\sim 10^6$ simulated signals. So, this event is unlike the background distribution, but also unlike the simulated signals. Therefore, we do not claim this event is a plausible gravitational wave candidate.

7.3.1.2 The second loudest event

The second loudest event of this search, which was a triple-coincident event at GPS time 848905672.3369, was also louder than any of the time slide trials in its category. Again, we cannot assign it a definite false alarm rate, but we can claim it is rarer than the amount of background time we have in its category, two years in this case.

This event was a loud glitch in H1 with a moderate response in H2 coincident with some excess noise in L1. The ratio of SNR measured in H1 and H2 should be equal to the ratio of the sensitivities of H1 and H2 at the time of the event (which should be roughly a factor of 2). The SNR in H2 is too low for this, which makes the event unlikely to be a true signal. The H1 χ^2, although better than most of the time slide trials, still does not lie within the signal distribution. We therefore conclude that this is not a gravitational wave candidate.

7.3.1.3 The third loudest event

The third loudest event of this search, which was at GPS time 842749918.8057, was found in H2L1 (while H1 was not operating). It was also louder than the

time slides. However, there was very little time in this particular category and so its overall significance is quite low. The L1 SNR and χ^2 is consistent with the background in that instrument. The H2 trigger is just above the SNR threshold of 5.5. We conclude that this event is not a gravitational wave candidate.

7.3.2 Preliminary upper limits on black hole coalescences

Since we have not claimed a detection, we will set an upper limit with 90% confidence on the compact binary coalescence event rate as a function of component mass pairs based on our observation of the DQ category 4, non-playground data. These upper limits, expressed as a rate per volume per time in units $\mathrm{Mpc}^{-3}\ \mathrm{yr}^{-1}$, are plotted in the m_1-m_2 plane in Fig. 7.7. They are also tabulated in Table 7.3.2 as a rate per volume per time and as a rate per blue light luminosity per time expressed in units $L_{10}^{-1}\ \mathrm{yr}^{-1}$, where L_{10} is the blue light luminosity of 10^{10} stars (note the Milky Way contains $1.7\,L_{10}$). We note that the upper limits are tightest for binaries with comparable masses which are towards the high total mass end of our parameter space. This is not surprising, as these waveforms from these binaries have the largest amplitudes, and are thus observable over the largest volume.

7.4 Conclusions and future improvements

In this chapter we presented preliminary results from the first search to use IMR waveforms calibrated to numerical relativity simulations to search for gravitational waves from compact binary coalescences with LIGO detectors. This search

$\mathbf{m}_1$	$\mathbf{m}_2$	$\mathbf{R}_{90\%}$ ($\mathbf{Mpc^{-3}\ yr^{-1}}$)	$\mathbf{R}_{90\%}$ ($\mathbf{L_{10}\ yr^{-1}}$)
5	23	3.2e-06	1.6e-04
5	32	3.6e-06	1.8e-04
5	41	3.2e-06	1.6e-04
5	50	5.1e-06	2.6e-04
5	59	3.6e-06	1.8e-04
5	68	5.5e-06	2.8e-04
5	76	8.5e-06	4.3e-04
5	85	1.2e-05	5.9e-04
5	94	8.5e-05	4.3e-03
14	14	1.6e-06	8.0e-05
14	23	1.5e-06	7.3e-05
14	32	1.3e-06	6.5e-05
14	41	1.0e-06	5.2e-05
14	50	9.9e-07	5.0e-05
14	59	8.4e-07	4.2e-05
14	68	1.0e-06	5.3e-05
14	76	1.0e-06	5.3e-05
14	85	2.9e-06	1.5e-04
23	23	1.3e-06	6.7e-05
23	32	7.3e-07	3.7e-05
23	41	5.1e-07	2.6e-05
23	50	4.8e-07	2.4e-05
23	59	3.1e-07	1.6e-05
23	68	3.1e-07	1.6e-05
23	76	4.2e-07	2.1e-05
32	32	4.8e-07	2.4e-05
32	41	3.4e-07	1.7e-05
32	50	2.8e-07	1.4e-05
32	59	2.8e-07	1.4e-05
32	68	2.0e-07	1.0e-05
41	41	2.1e-07	1.1e-05
41	50	2.0e-07	9.9e-06
41	59	1.6e-07	8.0e-06
50	50	1.1e-07	5.5e-06

Table 7.4: The 90% confidence upper limit on the merger rate as a function of mass in units of $M_\odot$. The upper limit is reported in two ways. The third column represents the rate in units of mergers $Mpc^{-3}\ yr^{-1}$. The fourth column converts this to units of mergers $L_{10}^{-1}\ yr^{-1}$ by noting that there are 0.0198 L_{10} / Mpc^3 [109].

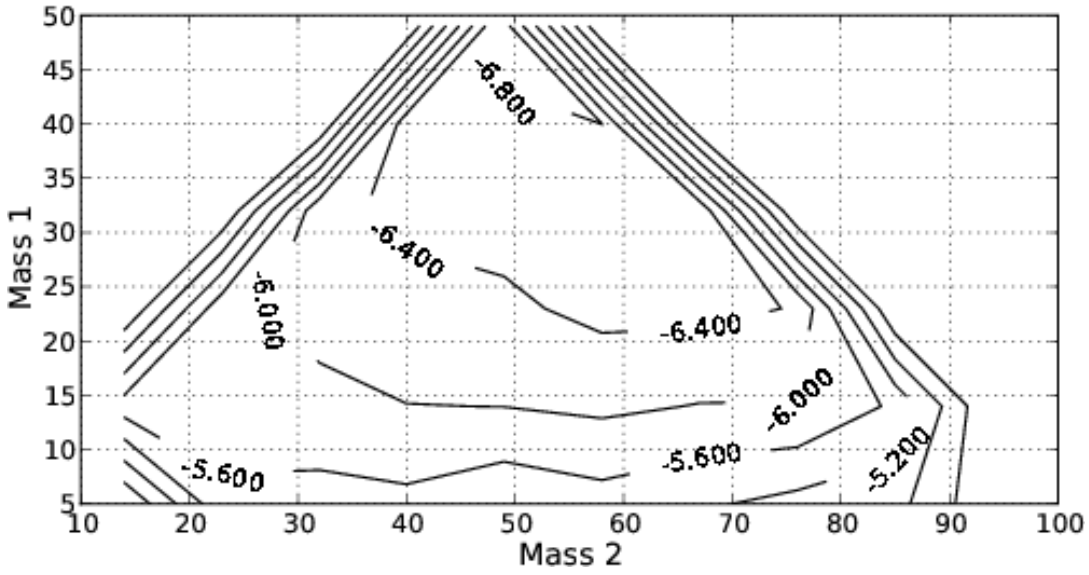

Figure 7.7: The logarithm (base 10) 90% confidence upper limit on merger rate as a function of component mass in mergers / Mpc^3 / yr. Here the upper limit is represented as a contour plot in order to visualize the variation in the mass plane. The values are available in table 7.3.2.

targeted binaries with total masses between 25–100 $\mathrm{M}_\odot$ and component masses between 1–99 $\mathrm{M}_\odot$ with negligible spins. We analyzed data taken during the LIGO S5 science run, which spanned approximately two years from fall 2005 to fall 2007 and included a year of triple-coincident data.

We did not detect any plausible gravitational-wave candidates in this search. However, by estimating our search sensitivity, we were able to constrain the merger rate of compact binary coalescences in the nearby Universe for all possible component mass pairs in our targeted range. For example, we established to 90% confidence that the merger rate of black holes with component masses of (23,23) $\mathrm{M}_\odot$ is less than 1.3×10^{-6} Mpc^{-3} yr^{-1}.

While this search effort is notable in its application of IMR template waveforms, there are still a number of limitations to this search which will be addressed

in the future. Perhaps the most important limitation is that the template waveforms neglect the effects of spin. While the statistical distribution of the spins of black holes in binaries is not well known [19], there are examples of black holes in X-ray binaries which have been observed to have a large spin [20]. If one or both of the objects in a binary has a non-negligible spin, this can affect the observed gravitational waveform in a number of ways. First, it can increase or decrease the length of the observable signal depending on the orientation(s) of the spin(s). It will also affect the final spin of the remnant black hole, which will affect the ringdown waveform. If the spins are not aligned with the orbital angular momentum, the orbital plane will precess, which will modulate the observed waveform in amplitude and phase. At the time this search effort began, analytic IMR waveforms which included spin effects were not available. However, NR simulations of spinning binaries have been performed, and both the EOB [65] and phenomenological [386] waveforms have been improved and calibrated to NR simulations of non-precessing spinning binaries. Effort is also underway to create analytic IMR waveforms which are valid for precessing binaries, notably through the NR-AR collaboration [82]. Therefore, future searches will likely use spinning IMR waveforms.

Errors in the waveform amplitudes are another limitation which affects the reported upper limits, but not our ability to make a detection. Note that the first EOB and phenomenological waveform models calibrated to NR waveforms focused on modeling the waveform *phase* as accurately as possible, and did not attempt to obtain amplitude agreement to the same high accuracy. In particular, we used *restricted* EOB waveforms, and the phenomenological waveforms were calibrated to

restricted hybrid waveforms. This means that both of our IMR waveform families can have amplitude errors $\sim 10\%$ (relative to the NR simulations and to each other) during the inspiral and even larger differences during the merger-ringdown. Since we filter with *normalized* templates, this will not affect our ability to make a detection, but it will introduce a rather large errors into the observable volume and thus the upper limits, particularly for higher mass systems. The preliminary results presented here do not attempt to account for or correct this error on the upper limits, but this issue is currently being addressed within the LSC and Virgo collaborations, and the final results will properly account for this error. Furthermore, the improved EOB and phenomenological IMR models in Refs. [65, 386] include amplitude-corrections, and could be used in future search efforts.

Chapter 8

Conclusions and future work

In the introductory chapter, we have briefly reviewed some of the basic properties of gravitational waves and the principles of detecting them. We have described how analytic template waveforms for one of the most promising types of sources, the inspiral, merger and ringdown of two compact objects, can be constructed. The PN formalism can be used to construct waveforms during an adiabatic inspiral, when the shrinking of the radius caused by the emission of gravitational waves is much slower than the orbital motion, but this approach becomes inadequate during the late inspiral as the adiabatic assumption and the low-velocity approximation break down. We have introduced the EOB formalism, which improves upon the PN formalism and provides analytic waveforms through all phases of the coalescence, the inspiral, merger and ringdown, which have been calibrated to obtain excellent agreement with NR waveforms. We have also explained how spin effects can be included in PN waveforms and noted some of the consequences these spin effects have on the waveforms. Lastly, we have introduced some of the basic concepts needed to apply these analytic waveform models to data analysis tasks, such as using them as matched filter templates to search for real signals and to estimate the accuracy with which those signals might be detected. The remaining chapters of this thesis presented the details of several projects undertaken by the author and collaborators

which apply these waveforms to various data analysis tasks.

In Ch. 3, we have done a detailed comparison of various types of PN waveforms and identified the regime in which they are adequate as search templates for realistic IMR signals. We find them to be adequate below a total mass of $\sim 12\,M_{\odot}$, while above that mass we recommend using IMR templates such as the EOB waveforms.

In Ch. 4, we derived ready-to-use expressions for spinning PN waveforms for a generic spin configuration and presented a detailed study of the spin effects in these waveforms. One striking feature is that while the $(2, 2)$ harmonic mode is truly the dominant mode (it is much larger than any of the other modes) for a non-precessing binary, this is not necessarily the case for a precessing binary. If the precessional motion is rather large, which occurs for large spins and asymmetric binaries, then much of the signal formerly contained in the $(2, 2)$ mode is re-distributed among other modes. In addition, the modes exhibit rapid, complicated oscillations on an orbital time scale due to the precessional motion. The actual, physically-observable signal is described by the waveform polarizations, which experience an amplitude modulation on the slower precessional time scale, rather than the rapid oscillations. However, for building EOB waveforms and comparing to NR simulations, one typically uses the harmonic mode decomposition, so when building precessing EOB models and comparing to precessing NR waveforms, one will likely have to include a greater number of modes, and ensure that the techniques used are robust against the more complicated structure of the harmonic modes. The ongoing NR-AR collaboration [82] seeks to create precessing IMR template waveforms by comparing to NR simulations and will have to confront these issues.

In Ch. 5, we presented the results of the first effort to use EOB waveforms as matched-filter templates as part of the NINJA project. In this effort, NR waveforms were injected into simulated data, and a number of search techniques including matched filter searches with inspiral templates, ringdown templates, and IMR templates as well as unmodelled searches were tasked with attempting to recover the injections. The EOB matched filter templates performed well in this situation, recovering a majority of the injected signals and a few more than similar search efforts. A second NINJA project is underway which will provide a more realistic challenge with longer injected signals, real detector data, and comparisons of search techniques at fixed false alarm rates. I will again be part of the effort to search with EOB templates within this project.

In Ch. 6, we investigated how well the parameters of a true signal might be recovered the LIGO detectors with EOB templates through the Fisher matrix formalism. In particular, we sought to understand how merger-ringdown and higher harmonics of the orbital frequency can improve the estimation of parameters. We find that both features do provide improvement to the parameter estimation. The merger-ringdown provides the greatest improvement for binaries with comparable component masses and high total mass, while the amplitude corrections provide the greatest improvement for asymmetric binaries and high total mass. These general trends are in qualitative agreement with other works on the subject, Refs. [116, 117, 118]. We have also discussed in detail the difficulties of using numerically-computed time-domain waveforms (such as the EOB) within the Fisher matrix formalism. These difficulties forced us to limit the scope of this project for the time being, as

we restricted to a single initial LIGO detector and total mass $\leq 100\,M_{\odot}$, although we plan to improve upon this study in the future. The difficulties also suggest that more sophisticated techniques, such as MCMC methods, could be especially useful in this case.

In Ch. 7, we presented preliminary results from the first effort to use EOB IMR templates to search for real signals in real interferometer data, the LIGO S5 highmass search. These are not the official results of the search endorsed by the LSC and Virgo collaborations, because the search is currently undergoing an internal review, but they illustrate the search techniques used and preliminary observational results. There were no viable detection candidates in this search, but we set upper limits on the event rates for binary coalescences as a function of binary mass pairs. The EOB matched filter templates will be used in future searches, including LIGO's S6 data and Virgo's VSR2 data. This data is currently being taken and analyzed. For this data, the LIGO interferometers are operating in their so-called "enhanced" configuration, which includes some improvements to the inteferometer, principally a more powerful laser. This has improved the detector performance at high frequencies (which are limited by photon shot noise), but the noise level at lower frequencies is comparable to S5, and so the LIGO sensitivity to high mass signals during S6 is rather similar to the sensitivity in S5. However, Virgo data will also be analyzed during the S6/VSR2 highmass search, which will improve the overall sensitivity relative to the preliminary S5 search presented here. In the future, LIGO and Virgo will operate in their "advanced" configurations, which should provide about an order of magnitude improvement in the sensitivity of each instrument, which will greatly

improve the chances of a detection.

Going forward, Advanced LIGO and Virgo have been funded and should start taking data in about five years. The cryogenic LCGT will soon begin construction as well. Beyond that, the space-based LISA mission will hopefully launch and observe the gravitational wave spectrum in a new, lower frequency band allowing us to observe compact binary coalescences of a galactic scale. The third generation ET is also being designed and promises to take data at an unprecedented sensitivity in the future. The coming years should prove to be very exciting for gravitational-wave physics. To fully take advantage of the data these advanced instruments will collect, it will be important to continually improve the data analysis techniques needed to analyze their data and inform their design. To this end, improving analytic waveform models will be very important. This can be done through improved theoretical techniques and, importantly, comparisons with more accurate, longer and more numerous NR simulations. In the near term, I will contribute to the NR-AR collaboration to work towards the goal of creating the first accurate, analytic models of precessing IMR waveforms. Furthermore, I plan to undertake studies of what science the advanced detectors will be capable of, and how this will be affected by design choices. The Fisher matrix, MCMC techniques and studies like the NINJA project(s) can help address these questions. Lastly, I would like to improve various aspects of data analysis pipelines to be used during the Advanced LIGO/Virgo era. This could include filtering with improved waveforms with amplitude-corrections and spin effects, improving template bank placement and improving signal-based vetoes.

Appendix A

Ready-to-use gravitational-wave polarizations for precessing binaries on nearly circular orbits through 1.5PN order: generic inclination angles

In Sec. 4.3 we wrote the GW polarizations

$$\begin{aligned} h_{+,\times} &= \frac{2\,M\,\nu\,v^2}{D_L}\,\Big[\hat{h}^{(0)}_{+,\times} + \Big(\hat{h}^{(1/2)}_{+,\times} + \hat{h}^{(1/2,\mathrm{SO})}_{+,\times}\Big)\,v \\ &+ \Big(\hat{h}^{(1)}_{+,\times} + \hat{h}^{(1,\mathrm{SO})}_{+,\times}\Big)\,v^2 + \Big(\hat{h}^{(3/2)}_{+,\times} + \hat{h}^{(3/2,\mathrm{SO})}_{+,\times}\Big)\,v^3\Big]\,, \end{aligned} \tag{A.1}$$

expanded in the inclination angle ι. Here we give the full expressions. The Newtonian, 0.5PN and 1PN order coefficients were computed explicitly in Ref. [83], the 1.5PN order coefficients, are computed for the first time in this paper. They read

$$\begin{aligned} \hat{h}^{(0)}_{+} &= \Big(-\frac{3}{2}-\frac{c_{2\theta}}{2}\Big)c^4_{\frac{\iota}{2}}\cos(2\alpha+2\Psi) - 2c^3_{\frac{\iota}{2}}\cos(\alpha+2\Psi)s_{2\theta}s_{\frac{\iota}{2}} + 2\cos(\alpha-2\Psi) \\ &\times s_{2\theta}c_{\frac{\iota}{2}}s^3_{\frac{\iota}{2}} + \Big(-\frac{3}{2}-\frac{c_{2\theta}}{2}\Big)\cos(2\alpha-2\Psi)s^4_{\frac{\iota}{2}} - \frac{3}{2}\cos(2\Psi)s^2_\theta s^2_\iota\,, \end{aligned} \tag{A.2a}$$

$$\begin{aligned} \hat{h}^{(1/2)}_{+} &= \delta\Bigg[c^6_{\frac{\iota}{2}}\cos(3\alpha+3\Psi)\Big(-\frac{45s_\theta}{32}-\frac{9s_{3\theta}}{32}\Big) + c^2_{\frac{\iota}{2}}\cos(\alpha+\Psi) \\ &\times\Bigg(-\frac{175s_\theta}{256} + c_\iota\Big(\frac{87s_\theta}{64}-\frac{5s_{3\theta}}{64}\Big) + c_{2\iota}\Big(-\frac{5s_\theta}{256}+\frac{15s_{3\theta}}{256}\Big) + \frac{13s_{3\theta}}{256}\Bigg) \\ &+ \cos(\alpha-\Psi)\Bigg(\frac{175s_\theta}{256} + c_\iota\Big(\frac{87s_\theta}{64}-\frac{5s_{3\theta}}{64}\Big) + c_{2\iota}\Big(\frac{5s_\theta}{256}-\frac{15s_{3\theta}}{256}\Big) - \frac{13s_{3\theta}}{256}\Bigg)s^2_{\frac{\iota}{2}} \\ &+ c^4_{\frac{\iota}{2}}\cos(3\alpha+\Psi)\Big(-\frac{5s_\theta}{32}-\frac{s_{3\theta}}{32}\Big)s^2_{\frac{\iota}{2}} + c^4_{\frac{\iota}{2}}\cos(\alpha+3\Psi)\Big(-\frac{45s_\theta}{32}+\frac{135s_{3\theta}}{32}\Big)s^2_{\frac{\iota}{2}} \end{aligned}$$

$$
\begin{aligned}
&+ c_{\frac{\iota}{2}}^2 \cos(\alpha - 3\Psi)\Big(\frac{45 s_\theta}{32} - \frac{135 s_{3\theta}}{32}\Big) s_{\frac{\iota}{2}}^4 + c_{\frac{\iota}{2}}^2 \cos(3\alpha - \Psi)\Big(\frac{5 s_\theta}{32} + \frac{s_{3\theta}}{32}\Big) s_{\frac{\iota}{2}}^4 \\
&+ \Big(\frac{27}{16} + \frac{9 c_{2\theta}}{16}\Big) \cos(3\alpha - 3\Psi) s_\theta s_{\frac{\iota}{2}}^6 + \frac{45}{16} c_\theta \cos(3\Psi) s_\theta^2 s_\iota^3 + \cos(2\alpha + \Psi) \\
&\times \bigg(\Big(-\frac{85 c_\theta}{256} - \frac{1}{128} c_\theta c_{2\theta} - \frac{1}{32} c_\theta c_{2\theta} c_\iota - \frac{3}{128} c_\theta c_{2\theta} c_{2\iota}\Big) s_\iota - \frac{11}{64} c_\theta s_{2\iota} - \frac{1}{256} c_\theta s_{3\iota}\bigg) \\
&+ \cos(2\alpha + 3\Psi)\bigg(\Big(\frac{45 c_\theta}{256} + \frac{81}{128} c_\theta c_{2\theta} + \frac{27}{32} c_\theta c_{2\theta} c_\iota + \frac{27}{128} c_\theta c_{2\theta} c_{2\iota}\Big) s_\iota + \frac{9}{64} c_\theta s_{2\iota} \\
&+ \frac{9}{256} c_\theta s_{3\iota}\bigg) + \cos(2\alpha - \Psi)\bigg(\Big(-\frac{85 c_\theta}{256} + \frac{1}{256} c_\theta c_{2\theta}\Big) s_\iota + \Big(\frac{11 c_\theta}{64} + \frac{1}{64} c_\theta c_{2\theta}\Big) s_{2\iota} \\
&+ \Big(-\frac{c_\theta}{256} - \frac{3}{256} c_\theta c_{2\theta}\Big) s_{3\iota}\bigg) + \cos(2\alpha - 3\Psi)\bigg(\Big(\frac{45 c_\theta}{256} + \frac{135}{256} c_\theta c_{2\theta}\Big) s_\iota \\
&+ \Big(-\frac{9 c_\theta}{64} - \frac{27}{64} c_\theta c_{2\theta}\Big) s_{2\iota} + \Big(\frac{9 c_\theta}{256} + \frac{27}{256} c_\theta c_{2\theta}\Big) s_{3\iota}\bigg) \\
&+ \cos(\Psi)\Big(\frac{1}{64} c_\theta s_\theta^2 s_\iota + \frac{5}{64} c_\theta s_\theta^2 s_{3\iota}\Big)\bigg], \qquad \text{(A.2b)}
\end{aligned}
$$

$$
\begin{aligned}
\hat{h}_+^{(1)} = &\bigg[c_{\frac{\iota}{2}}^4\bigg(\frac{59}{16} + \frac{5 c_{2\theta}}{2} - \frac{3 c_{4\theta}}{16} + \Big(\frac{5}{24} - \frac{11 c_{2\theta}}{6} + \frac{7 c_{4\theta}}{24}\Big) c_\iota + \Big(-\frac{5}{48} - \frac{c_{2\theta}}{12} \\
&- \frac{7 c_{4\theta}}{48}\Big) c_{2\iota}\bigg) + \nu c_{\frac{\iota}{2}}^4\Big(-\frac{25}{16} - \frac{13 c_{2\theta}}{3} + \frac{9 c_{4\theta}}{16} + \Big(-\frac{5}{8} + \frac{11 c_{2\theta}}{2} - \frac{7 c_{4\theta}}{8}\Big) c_\iota \\
&+ \Big(\frac{5}{16} + \frac{c_{2\theta}}{4} + \frac{7 c_{4\theta}}{16}\Big) c_{2\iota}\Big)\bigg] \cos(2\alpha + 2\Psi) + \cos(4\alpha + 4\Psi)\bigg(\Big(-2 - \frac{2 c_{2\theta}}{3}\Big) \\
&\times c_{\frac{\iota}{2}}^8 s_\theta^2 + \nu\Big(6 + 2 c_{2\theta}\Big) c_{\frac{\iota}{2}}^8 s_\theta^2\bigg) + \cos(3\alpha + 4\Psi)\Big(\frac{32}{3} c_\theta^3 c_{\frac{\iota}{2}}^7 s_\theta s_{\frac{\iota}{2}} - 32\nu c_\theta^3 c_{\frac{\iota}{2}}^7 s_\theta s_{\frac{\iota}{2}}\Big) \\
&+ \cos(3\alpha + 2\Psi)\bigg[c_{\frac{\iota}{2}}^5\bigg(\Big(-\frac{5}{6} + \frac{c_{2\theta}}{6}\Big) s_{2\theta} - \frac{2}{3} c_\theta^2 c_\iota s_{2\theta}\bigg) s_{\frac{\iota}{2}} + \nu c_{\frac{\iota}{2}}^5\bigg(\Big(\frac{5}{2} - \frac{c_{2\theta}}{2}\Big) s_{2\theta} \\
&+ 2 c_\theta^2 c_\iota s_{2\theta}\bigg) s_{\frac{\iota}{2}}\bigg] + \cos(2\alpha + 4\Psi)\bigg(\Big(-\frac{10}{3} - \frac{8 c_{2\theta}}{3} - \frac{14 c_{4\theta}}{3}\Big) c_{\frac{\iota}{2}}^6 s_{\frac{\iota}{2}}^2 \\
&+ \nu\Big(10 + 8 c_{2\theta} + 14 c_{4\theta}\Big) c_{\frac{\iota}{2}}^6 s_{\frac{\iota}{2}}^2\bigg) + \cos(4\alpha + 2\Psi)\bigg(\Big(-\frac{1}{2} - \frac{c_{2\theta}}{6}\Big) c_{\frac{\iota}{2}}^6 s_\theta^2 s_{\frac{\iota}{2}}^2 \\
&+ \nu\Big(\frac{3}{2} + \frac{c_{2\theta}}{2}\Big) c_{\frac{\iota}{2}}^6 s_\theta^2 s_{\frac{\iota}{2}}^2\bigg) + \cos(\alpha + 4\Psi)\bigg(\Big(\frac{8}{3} - \frac{56 c_{2\theta}}{3}\Big) c_{\frac{\iota}{2}}^5 s_{2\theta} s_{\frac{\iota}{2}}^3 \\
&+ \nu\Big(-8 + 56 c_{2\theta}\Big) c_{\frac{\iota}{2}}^5 s_{2\theta} s_{\frac{\iota}{2}}^3\bigg) + \cos(\alpha - 2\Psi)\bigg[\nu\bigg(c_{\frac{\iota}{2}}\Big(\frac{16 s_{2\theta}}{3} + \frac{31}{4} c_\iota s_{2\theta} \\
&+ \frac{1}{4} c_{2\iota} s_{2\theta} - \frac{19 s_{4\theta}}{16}\Big) - \frac{7}{8} c_{\frac{3\iota}{2}} s_{4\theta} - \frac{7}{16} c_{\frac{5\iota}{2}} s_{4\theta}\bigg) s_{\frac{\iota}{2}}^3 + \bigg(c_{\frac{\iota}{2}}\Big(-6 s_{2\theta} - \frac{31}{12} c_\iota s_{2\theta}
\end{aligned}
$$

$$
\begin{aligned}
&- \frac{1}{12}c_{2\iota}s_{2\theta} + \frac{19s_{4\theta}}{48}\Big) + \frac{7}{24}c_{\frac{3\iota}{2}}s_{4\theta} + \frac{7}{48}c_{\frac{5\iota}{2}}s_{4\theta}\Big)s_{\frac{\iota}{2}}^3\Big] + \cos(2\alpha - 2\Psi)\\
&\times \Big[\Big(\frac{59}{16} + \frac{5c_{2\theta}}{2} - \frac{3c_{4\theta}}{16} + \Big(- \frac{5}{24} + \frac{11c_{2\theta}}{6} - \frac{7c_{4\theta}}{24}\Big)c_\iota + \Big(- \frac{5}{48} - \frac{c_{2\theta}}{12}\\
&- \frac{7c_{4\theta}}{48}\Big)c_{2\iota}\Big)s_{\frac{\iota}{2}}^4 + \nu\Big(- \frac{25}{16} - \frac{13c_{2\theta}}{3} + \frac{9c_{4\theta}}{16} + \Big(\frac{5}{8} - \frac{11c_{2\theta}}{2} + \frac{7c_{4\theta}}{8}\Big)c_\iota\\
&+ \Big(\frac{5}{16} + \frac{c_{2\theta}}{4} + \frac{7c_{4\theta}}{16}\Big)c_{2\iota}\Big)s_{\frac{\iota}{2}}^4\Big] + \cos(\alpha - 4\Psi)\Big(\nu\Big(8 - 56c_{2\theta}\Big)c_{\frac{\iota}{2}}^3 s_{2\theta}s_{\frac{\iota}{2}}^5\\
&+ \Big(- \frac{8}{3} + \frac{56c_{2\theta}}{3}\Big)c_{\frac{\iota}{2}}^3 s_{2\theta}s_{\frac{\iota}{2}}^5\Big) + \cos(3\alpha - 2\Psi)\Big[c_{\frac{\iota}{2}}\Big(\Big(\frac{5}{6} - \frac{c_{2\theta}}{6}\Big)s_{2\theta}\\
&- \frac{2}{3}c_\theta^2 c_\iota s_{2\theta}\Big)s_{\frac{\iota}{2}}^5 + \nu c_{\frac{\iota}{2}}\Big(\Big(- \frac{5}{2} + \frac{c_{2\theta}}{2}\Big)s_{2\theta} + 2c_\theta^2 c_\iota s_{2\theta}\Big)s_{\frac{\iota}{2}}^5\Big] + \cos(2\alpha - 4\Psi)\\
&\times \Big(\Big(- \frac{10}{3} - \frac{8c_{2\theta}}{3} - \frac{14c_{4\theta}}{3}\Big)c_{\frac{\iota}{2}}^2 s_{\frac{\iota}{2}}^6 + \nu\Big(10 + 8c_{2\theta} + 14c_{4\theta}\Big)c_{\frac{\iota}{2}}^2 s_{\frac{\iota}{2}}^6\Big)\\
&+ \cos(4\alpha - 2\Psi)\Big(\Big(- \frac{1}{2} - \frac{c_{2\theta}}{6}\Big)c_{\frac{\iota}{2}}^2 s_\theta^2 s_{\frac{\iota}{2}}^6 + \nu\Big(\frac{3}{2} + \frac{c_{2\theta}}{2}\Big)c_{\frac{\iota}{2}}^2 s_\theta^2 s_{\frac{\iota}{2}}^6\Big)\\
&+ \cos(3\alpha - 4\Psi)\Big(- \frac{32}{3}c_\theta^3 c_{\frac{\iota}{2}}s_\theta s_{\frac{\iota}{2}}^7 + 32\nu c_\theta^3 c_{\frac{\iota}{2}}s_\theta s_{\frac{\iota}{2}}^7\Big) + \cos(4\alpha - 4\Psi)\\
&\times \Big(\Big(- 2 - \frac{2c_{2\theta}}{3}\Big)s_\theta^2 s_{\frac{\iota}{2}}^8 + \nu\Big(6 + 2c_{2\theta}\Big)s_\theta^2 s_{\frac{\iota}{2}}^8\Big) + \cos(2\Psi)\Big[\Big(\Big(\frac{349}{96}\\
&- \frac{25c_{2\theta}}{96}\Big)s_\theta^2 + \Big(- \frac{25}{96} - \frac{35c_{2\theta}}{96}\Big)c_{2\iota}s_\theta^2\Big)s_\iota^2 + \nu\Big(\Big(- \frac{45}{32} + \frac{25c_{2\theta}}{32}\Big)s_\theta^2\\
&+ \Big(\frac{25}{32} + \frac{35c_{2\theta}}{32}\Big)c_{2\iota}s_\theta^2\Big)s_\iota^2\Big] + \cos(4\Psi)\Big(\Big(- \frac{25}{12} - \frac{35c_{2\theta}}{12}\Big)s_\theta^2 s_\iota^4 + \nu\Big(\frac{25}{4} +\\
&\frac{35c_{2\theta}}{4}\Big)s_\theta^2 s_\iota^4\Big) + \cos(\alpha + 2\Psi)\Big[c_{\frac{\iota}{2}}^3\Big(6s_{2\theta} - \frac{31}{12}c_\iota s_{2\theta} + \frac{1}{12}c_{2\iota}s_{2\theta} - \frac{19s_{4\theta}}{48}\Big)s_{\frac{\iota}{2}}\\
&+ \frac{7}{24}c_{\frac{\iota}{2}}^3 s_{4\theta}s_{\frac{3\iota}{2}} - \frac{7}{48}c_{\frac{\iota}{2}}^3 s_{4\theta}s_{\frac{5\iota}{2}} + \nu\Big(c_{\frac{\iota}{2}}^3\Big(- \frac{16s_{2\theta}}{3} + \frac{31}{4}c_\iota s_{2\theta} - \frac{1}{4}c_{2\iota}s_{2\theta}\\
&+ \frac{19s_{4\theta}}{16}\Big)s_{\frac{\iota}{2}} - \frac{7}{8}c_{\frac{\iota}{2}}^3 s_{4\theta}s_{\frac{3\iota}{2}} + \frac{7}{16}c_{\frac{\iota}{2}}^3 s_{4\theta}s_{\frac{5\iota}{2}}\Big)\Big]\,, \qquad \text{(A.2c)}
\end{aligned}
$$

$$
\begin{aligned}
\hat{h}_+^{(3/2)} &= \Big(- 3\pi - \pi c_{2\theta}\Big)c_{\frac{\iota}{2}}^4\cos(2\alpha + 2\Psi) - 4\pi c_{\frac{\iota}{2}}^3\cos(\alpha + 2\Psi)s_{2\theta}s_{\frac{\iota}{2}}\\
&+ 4\pi\cos(\alpha - 2\Psi)c_{\frac{\iota}{2}}s_{2\theta}s_{\frac{\iota}{2}}^3 + \Big(- 3\pi - \pi c_{2\theta}\Big)\cos(2\alpha - 2\Psi)s_{\frac{\iota}{2}}^4\\
&- 3\pi\cos(2\Psi)s_\theta^2 s_\iota^2 + \delta\Big[\cos(5\alpha + 5\Psi)\Big(\Big(- \frac{625}{256} - \frac{625c_{2\theta}}{768}\Big)c_{\frac{\iota}{2}}^{10}s_\theta^3
\end{aligned}
$$

$$+\nu\Big(\frac{625}{128}+\frac{625c_{2\theta}}{384}\Big)c_{\frac{\iota}{2}}^{10}s_\theta^3\Big)+\cos(\alpha+\Psi)\times\Big[\nu c_{\frac{\iota}{2}}^2\Big(-\frac{7449s_\theta}{16384}-\frac{331s_{3\theta}}{32768}$$
$$+c_{2\iota}\Big(\frac{337s_\theta}{12288}-\frac{47s_{3\theta}}{8192}-\frac{21s_{5\theta}}{8192}\Big)+c_{4\iota}\Big(\frac{7s_\theta}{49152}+\frac{7s_{3\theta}}{32768}-\frac{35s_{5\theta}}{32768}\Big)$$
$$+c_{3\iota}\Big(-\frac{59s_\theta}{6144}-\frac{91s_{3\theta}}{4096}+\frac{7s_{5\theta}}{4096}\Big)+c_\iota\Big(\frac{1873s_\theta}{2048}+\frac{19s_{3\theta}}{4096}+\frac{35s_{5\theta}}{12288}\Big)$$
$$-\frac{155s_{5\theta}}{98304}\Big)+c_{\frac{\iota}{2}}^2\Big(\frac{43723s_\theta}{98304}-\frac{9653s_{3\theta}}{65536}+c_\iota\Big(-\frac{10675s_\theta}{12288}+\frac{1901s_{3\theta}}{8192}$$
$$-\frac{35s_{5\theta}}{24576}\Big)+c_{3\iota}\Big(\frac{59s_\theta}{12288}+\frac{91s_{3\theta}}{8192}-\frac{7s_{5\theta}}{8192}\Big)+c_{4\iota}\Big(-\frac{7s_\theta}{98304}-\frac{7s_{3\theta}}{65536}$$
$$+\frac{35s_{5\theta}}{65536}\Big)+c_{2\iota}\Big(\frac{1103s_\theta}{24576}-\frac{2833s_{3\theta}}{16384}+\frac{21s_{5\theta}}{16384}\Big)+\frac{155s_{5\theta}}{196608}\Big)\Big]$$
$$+\cos(3\alpha+3\Psi)\Big[c_{\frac{\iota}{2}}^6\Big(\frac{39249s_\theta}{8192}+\frac{38331s_{3\theta}}{16384}+c_{2\iota}\Big(-\frac{1701s_\theta}{8192}-\frac{3159s_{3\theta}}{16384}$$
$$-\frac{3645s_{5\theta}}{16384}\Big)+c_\iota\Big(\frac{2403s_\theta}{2048}-\frac{6399s_{3\theta}}{4096}+\frac{2187s_{5\theta}}{4096}\Big)-\frac{5751s_{5\theta}}{16384}\Big)$$
$$+\nu c_{\frac{\iota}{2}}^6\Big(-\frac{4689s_\theta}{4096}-\frac{24507s_{3\theta}}{8192}+c_\iota\Big(-\frac{2403s_\theta}{1024}+\frac{6399s_{3\theta}}{2048}-\frac{2187s_{5\theta}}{2048}\Big)$$
$$+c_{2\iota}\Big(\frac{1701s_\theta}{4096}+\frac{3159s_{3\theta}}{8192}+\frac{3645s_{5\theta}}{8192}\Big)+\frac{5751s_{5\theta}}{8192}\Big)\Big]+\cos(4\alpha+5\Psi)$$
$$\times\Big(\nu\Big(-\frac{11875c_\theta}{384}-\frac{3125c_{3\theta}}{384}\Big)c_{\frac{\iota}{2}}^9s_\theta^2s_{\frac{\iota}{2}}+\Big(\frac{11875c_\theta}{768}+\frac{3125c_{3\theta}}{768}\Big)c_{\frac{\iota}{2}}^9s_\theta^2s_{\frac{\iota}{2}}\Big)$$
$$+\cos(4\alpha+3\Psi)\Big[c_{\frac{\iota}{2}}^7\Big(\Big(-\frac{351c_\theta}{256}+\frac{243}{256}c_\theta c_{2\theta}\Big)s_\theta^2+\Big(-\frac{567c_\theta}{256}$$
$$-\frac{405}{256}c_\theta c_{2\theta}\Big)c_\iota s_\theta^2\Big)s_{\frac{\iota}{2}}+\nu c_{\frac{\iota}{2}}^7\Big(\Big(\frac{351c_\theta}{128}-\frac{243}{128}c_\theta c_{2\theta}\Big)s_\theta^2+\Big(\frac{567c_\theta}{128}$$
$$+\frac{405}{128}c_\theta c_{2\theta}\Big)c_\iota s_\theta^2\Big)s_{\frac{\iota}{2}}\Big]+\cos(5\alpha+3\Psi)\Big(\Big(-\frac{243}{256}-\frac{81c_{2\theta}}{256}\Big)c_{\frac{\iota}{2}}^8s_\theta^3s_{\frac{\iota}{2}}^2$$
$$+\nu\Big(\frac{243}{128}+\frac{81c_{2\theta}}{128}\Big)c_{\frac{\iota}{2}}^8s_\theta^3s_{\frac{\iota}{2}}^2\Big)+\cos(\alpha-\Psi)\Big[\Big(-\frac{43723s_\theta}{98304}+\frac{9653s_{3\theta}}{65536}$$
$$+c_\iota\Big(-\frac{10675s_\theta}{12288}+\frac{1901s_{3\theta}}{8192}-\frac{35s_{5\theta}}{24576}\Big)+c_{2\iota}\Big(-\frac{1103s_\theta}{24576}+\frac{2833s_{3\theta}}{16384}$$
$$-\frac{21s_{5\theta}}{16384}\Big)+c_{3\iota}\Big(\frac{59s_\theta}{12288}+\frac{91s_{3\theta}}{8192}-\frac{7s_{5\theta}}{8192}\Big)+c_{4\iota}\Big(\frac{7s_\theta}{98304}+\frac{7s_{3\theta}}{65536}-\frac{35s_{5\theta}}{65536}\Big)$$
$$-\frac{155s_{5\theta}}{196608}\Big)s_{\frac{\iota}{2}}^2+\nu\Big(\frac{7449s_\theta}{16384}+\frac{331s_{3\theta}}{32768}+c_{4\iota}\Big(-\frac{7s_\theta}{49152}-\frac{7s_{3\theta}}{32768}+\frac{35s_{5\theta}}{32768}\Big)$$
$$+c_{3\iota}\Big(-\frac{59s_\theta}{6144}-\frac{91s_{3\theta}}{4096}+\frac{7s_{5\theta}}{4096}\Big)+c_{2\iota}\Big(-\frac{337s_\theta}{12288}+\frac{47s_{3\theta}}{8192}+\frac{21s_{5\theta}}{8192}\Big)$$

$$+ c_\iota\Big(\frac{1873s_\theta}{2048} + \frac{19s_{3\theta}}{4096} + \frac{35s_{5\theta}}{12288}\Big) + \frac{155s_{5\theta}}{98304}\Big)s_{\frac{\iota}{2}}^2\Big] + \cos(3\alpha + \Psi)$$
$$\times \Big[c_{\frac{\iota}{2}}^4\Big(\frac{1675s_\theta}{4096} + \frac{825s_{3\theta}}{8192} + c_{2\iota}\Big(-\frac{7s_\theta}{4096} - \frac{13s_{3\theta}}{8192} - \frac{15s_{5\theta}}{8192}\Big) + c_\iota\Big(\frac{27s_\theta}{1024}$$
$$- \frac{151s_{3\theta}}{2048} + \frac{3s_{5\theta}}{2048}\Big) - \frac{13s_{5\theta}}{8192}\Big)s_{\frac{\iota}{2}}^2 + \nu c_{\frac{\iota}{2}}^4\Big(\frac{245s_\theta}{2048} - \frac{57s_{3\theta}}{4096} + c_\iota\Big(-\frac{27s_\theta}{512}$$
$$+ \frac{151s_{3\theta}}{1024} - \frac{3s_{5\theta}}{1024}\Big) + c_{2\iota}\Big(\frac{7s_\theta}{2048} + \frac{13s_{3\theta}}{4096} + \frac{15s_{5\theta}}{4096}\Big) + \frac{13s_{5\theta}}{4096}\Big)s_{\frac{\iota}{2}}^2\Big]$$
$$+ \cos(3\alpha + 5\Psi)\Big(c_{\frac{\iota}{2}}^8\Big(-\frac{4375s_\theta}{1024} - \frac{8125s_{3\theta}}{2048} - \frac{9375s_{5\theta}}{2048}\Big)s_{\frac{\iota}{2}}^2 + \nu c_{\frac{\iota}{2}}^8\Big(\frac{4375s_\theta}{512}$$
$$+ \frac{8125s_{3\theta}}{1024} + \frac{9375s_{5\theta}}{1024}\Big)s_{\frac{\iota}{2}}^2\Big) + \cos(\alpha + 3\Psi)\Big[c_{\frac{\iota}{2}}^4\Big(\frac{20475s_\theta}{4096} - \frac{149391s_{3\theta}}{8192}$$
$$+ c_\iota\Big(\frac{2187s_\theta}{1024} + \frac{10017s_{3\theta}}{2048} - \frac{1701s_{5\theta}}{2048}\Big) + \frac{7371s_{5\theta}}{8192} + c_{2\iota}\Big(-\frac{567s_\theta}{4096}$$
$$- \frac{1701s_{3\theta}}{8192} + \frac{8505s_{5\theta}}{8192}\Big)\Big)s_{\frac{\iota}{2}}^2 + \nu c_{\frac{\iota}{2}}^4\Big(-\frac{3195s_\theta}{2048} + \frac{45711s_{3\theta}}{4096} + c_{2\iota}\Big(\frac{567s_\theta}{2048}$$
$$+ \frac{1701s_{3\theta}}{4096} - \frac{8505s_{5\theta}}{4096}\Big) - \frac{7371s_{5\theta}}{4096} + c_\iota\Big(-\frac{2187s_\theta}{512} - \frac{10017s_{3\theta}}{1024}$$
$$+ \frac{1701s_{5\theta}}{1024}\Big)\Big)s_{\frac{\iota}{2}}^2\Big] + \cos(2\alpha + 5\Psi)\Big(\nu\Big(-\frac{4375c_\theta}{192} - \frac{625c_{3\theta}}{128}$$
$$- \frac{3125c_{5\theta}}{128}\Big)c_{\frac{\iota}{2}}^7 s_{\frac{\iota}{2}}^3 + \Big(\frac{4375c_\theta}{384} + \frac{625c_{3\theta}}{256} + \frac{3125c_{5\theta}}{256}\Big)c_{\frac{\iota}{2}}^7 s_{\frac{\iota}{2}}^3\Big) + \cos(4\alpha + \Psi)$$
$$\times \Big[c_{\frac{\iota}{2}}^5\Big(\Big(-\frac{37c_\theta}{384} + \frac{1}{384}c_\theta c_{2\theta}\Big)s_\theta^2 + \Big(-\frac{7c_\theta}{384} - \frac{5}{384}c_\theta c_{2\theta}\Big)c_\iota s_\theta^2\Big)s_{\frac{\iota}{2}}^3$$
$$+ \nu c_{\frac{\iota}{2}}^5\Big(\Big(\frac{37c_\theta}{192} - \frac{1}{192}c_\theta c_{2\theta}\Big)s_\theta^2 + \Big(\frac{7c_\theta}{192} + \frac{5}{192}c_\theta c_{2\theta}\Big)c_\iota s_\theta^2\Big)s_{\frac{\iota}{2}}^3\Big] + \cos(5\alpha + \Psi)$$
$$\times \Big(\Big(-\frac{1}{128} - \frac{c_{2\theta}}{384}\Big)c_{\frac{\iota}{2}}^6 s_\theta^3 s_{\frac{\iota}{2}}^4 + \nu\Big(\frac{1}{64} + \frac{c_{2\theta}}{192}\Big)c_{\frac{\iota}{2}}^6 s_\theta^3 s_{\frac{\iota}{2}}^4\Big) + \cos(3\alpha - \Psi)$$
$$\times \Big[\nu c_{\frac{\iota}{2}}^2\Big(-\frac{245s_\theta}{2048} + \frac{57s_{3\theta}}{4096} + c_{2\iota}\Big(-\frac{7s_\theta}{2048} - \frac{13s_{3\theta}}{4096} - \frac{15s_{5\theta}}{4096}\Big)$$
$$+ c_\iota\Big(-\frac{27s_\theta}{512} + \frac{151s_{3\theta}}{1024} - \frac{3s_{5\theta}}{1024}\Big) - \frac{13s_{5\theta}}{4096}\Big)s_{\frac{\iota}{2}}^4 + c_{\frac{\iota}{2}}^2\Big(-\frac{1675s_\theta}{4096} - \frac{825s_{3\theta}}{8192}$$
$$+ c_\iota\Big(\frac{27s_\theta}{1024} - \frac{151s_{3\theta}}{2048} + \frac{3s_{5\theta}}{2048}\Big) + c_{2\iota}\Big(\frac{7s_\theta}{4096} + \frac{13s_{3\theta}}{8192} + \frac{15s_{5\theta}}{8192}\Big) + \frac{13s_{5\theta}}{8192}\Big)s_{\frac{\iota}{2}}^4\Big]$$
$$+ \cos(\alpha + 5\Psi)\Big(\nu c_{\frac{\iota}{2}}^6\Big(\frac{4375s_\theta}{768} + \frac{4375s_{3\theta}}{512} - \frac{21875s_{5\theta}}{512}\Big)s_{\frac{\iota}{2}}^4 + c_{\frac{\iota}{2}}^6\Big(-\frac{4375s_\theta}{1536}$$

$$
- \frac{4375s_{3\theta}}{1024} + \frac{21875s_{5\theta}}{1024}\Big)s_{\frac{\iota}{2}}^4\Big) + \cos(\alpha - 3\Psi)\Big[c_{\frac{\iota}{2}}^2\Big(- \frac{20475s_\theta}{4096} + \frac{149391s_{3\theta}}{8192}
$$

$$
+ c_{2\iota}\Big(\frac{567s_\theta}{4096} + \frac{1701s_{3\theta}}{8192} - \frac{8505s_{5\theta}}{8192}\Big) + c_\iota\Big(\frac{2187s_\theta}{1024} + \frac{10017s_{3\theta}}{2048} - \frac{1701s_{5\theta}}{2048}\Big)
$$

$$
- \frac{7371s_{5\theta}}{8192}\Big)s_{\frac{\iota}{2}}^4 + \nu c_{\frac{\iota}{2}}^2\Big(\frac{3195s_\theta}{2048} - \frac{45711s_{3\theta}}{4096} + \frac{7371s_{5\theta}}{4096} + c_\iota\Big(- \frac{2187s_\theta}{512}
$$

$$
- \frac{10017s_{3\theta}}{1024} + \frac{1701s_{5\theta}}{1024}\Big) + c_{2\iota}\Big(- \frac{567s_\theta}{2048} - \frac{1701s_{3\theta}}{4096} + \frac{8505s_{5\theta}}{4096}\Big)\Big)s_{\frac{\iota}{2}}^4\Big]
$$

$$
+ \cos(4\alpha - \Psi)\Big[\nu c_{\frac{\iota}{2}}^3\Big(\Big(\frac{37c_\theta}{192} - \frac{1}{192}c_\theta c_{2\theta}\Big)s_\theta^2 + \Big(- \frac{7c_\theta}{192} - \frac{5}{192}c_\theta c_{2\theta}\Big)c_\iota s_\theta^2\Big)s_{\frac{\iota}{2}}^5
$$

$$
+ c_{\frac{\iota}{2}}^3\Big(\Big(- \frac{37c_\theta}{384} + \frac{1}{384}c_\theta c_{2\theta}\Big)s_\theta^2 + \Big(\frac{7c_\theta}{384} + \frac{5}{384}c_\theta c_{2\theta}\Big)c_\iota s_\theta^2\Big)s_{\frac{\iota}{2}}^5\Big]
$$

$$
+ \cos(5\alpha - \Psi)\Big(\nu\Big(- \frac{1}{64} - \frac{c_{2\theta}}{192}\Big)c_{\frac{\iota}{2}}^4 s_\theta^3 s_{\frac{\iota}{2}}^6 + \Big(\frac{1}{128} + \frac{c_{2\theta}}{384}\Big)c_{\frac{\iota}{2}}^4 s_\theta^3 s_{\frac{\iota}{2}}^6\Big)
$$

$$
+ \cos(3\alpha - 3\Psi)\Big[\nu\Big(\Big(\frac{14067}{4096} + \frac{4689c_{2\theta}}{1024} - \frac{5751c_{4\theta}}{4096}\Big)s_\theta + \Big(- \frac{297}{1024}
$$

$$
+ \frac{1053c_{2\theta}}{256} - \frac{2187c_{4\theta}}{1024}\Big)c_\iota s_\theta + \Big(- \frac{5103}{4096} - \frac{1701c_{2\theta}}{1024} - \frac{3645c_{4\theta}}{4096}\Big)c_{2\iota}s_\theta\Big)s_{\frac{\iota}{2}}^6
$$

$$
+ \Big(\Big(- \frac{55539}{8192} - \frac{8145c_{2\theta}}{2048} + \frac{5751c_{4\theta}}{8192}\Big)s_\theta + \Big(\frac{297}{2048} - \frac{1053c_{2\theta}}{512} + \frac{2187c_{4\theta}}{2048}\Big)c_\iota s_\theta
$$

$$
+ \Big(\frac{5103}{8192} + \frac{1701c_{2\theta}}{2048} + \frac{3645c_{4\theta}}{8192}\Big)c_{2\iota}s_\theta\Big)s_{\frac{\iota}{2}}^6\Big] + \cos(\alpha - 5\Psi)\Big(c_{\frac{\iota}{2}}^4\Big(\frac{4375s_\theta}{1536}
$$

$$
+ \frac{4375s_{3\theta}}{1024} - \frac{21875s_{5\theta}}{1024}\Big)s_{\frac{\iota}{2}}^6 + \nu c_{\frac{\iota}{2}}^4\Big(- \frac{4375s_\theta}{768} - \frac{4375s_{3\theta}}{512} + \frac{21875s_{5\theta}}{512}\Big)s_{\frac{\iota}{2}}^6\Big)
$$

$$
+ \cos(2\alpha - 5\Psi)\Big(\nu\Big(- \frac{4375c_\theta}{192} - \frac{625c_{3\theta}}{128} - \frac{3125c_{5\theta}}{128}\Big)c_{\frac{\iota}{2}}^3 s_{\frac{\iota}{2}}^7 + \Big(\frac{4375c_\theta}{384}
$$

$$
+ \frac{625c_{3\theta}}{256} + \frac{3125c_{5\theta}}{256}\Big)c_{\frac{\iota}{2}}^3 s_{\frac{\iota}{2}}^7\Big) + \cos(4\alpha - 3\Psi)\Big[\nu c_{\frac{\iota}{2}}\Big(\Big(\frac{351c_\theta}{128} - \frac{243}{128}c_\theta c_{2\theta}\Big)s_\theta^2
$$

$$
+ \Big(- \frac{567c_\theta}{128} - \frac{405}{128}c_\theta c_{2\theta}\Big)c_\iota s_\theta^2\Big)s_{\frac{\iota}{2}}^7 + c_{\frac{\iota}{2}}\Big(\Big(- \frac{351c_\theta}{256} + \frac{243}{256}c_\theta c_{2\theta}\Big)s_\theta^2
$$

$$
+ \Big(\frac{567c_\theta}{256} + \frac{405}{256}c_\theta c_{2\theta}\Big)c_\iota s_\theta^2\Big)s_{\frac{\iota}{2}}^7\Big] + \cos(5\alpha - 3\Psi)\Big(\nu\Big(- \frac{243}{128} - \frac{81c_{2\theta}}{128}\Big)c_{\frac{\iota}{2}}^2 s_\theta^3 s_{\frac{\iota}{2}}^8
$$

$$
+ \Big(\frac{243}{256} + \frac{81c_{2\theta}}{256}\Big)c_{\frac{\iota}{2}}^2 s_\theta^3 s_{\frac{\iota}{2}}^8\Big) + \cos(3\alpha - 5\Psi)\Big(\nu c_{\frac{\iota}{2}}^2\Big(- \frac{4375s_\theta}{512} - \frac{8125s_{3\theta}}{1024}
$$

$$
- \frac{9375s_{5\theta}}{1024}\Big)s_{\frac{\iota}{2}}^8 + c_{\frac{\iota}{2}}^2\Big(\frac{4375s_\theta}{1024} + \frac{8125s_{3\theta}}{2048} + \frac{9375s_{5\theta}}{2048}\Big)s_{\frac{\iota}{2}}^8\Big) + \cos(4\alpha - 5\Psi)
$$

$$\times \Big(\nu\Big(-\frac{11875c_\theta}{384}-\frac{3125c_{3\theta}}{384}\Big)c_{\frac{\iota}{2}}s_\theta^2 s_{\frac{\iota}{2}}^9+\Big(\frac{11875c_\theta}{768}+\frac{3125c_{3\theta}}{768}\Big)c_{\frac{\iota}{2}}s_\theta^2 s_{\frac{\iota}{2}}^9\Big)$$
$$+\cos(5\alpha-5\Psi)\Big(\nu\Big(-\frac{625}{128}-\frac{625c_{2\theta}}{384}\Big)s_\theta^3 s_{\frac{\iota}{2}}^{10}+\Big(\frac{625}{256}+\frac{625c_{2\theta}}{768}\Big)s_\theta^3 s_{\frac{\iota}{2}}^{10}\Big)$$
$$+\cos(3\Psi)\Big[\nu\Big(\Big(\frac{10197c_\theta}{2048}-\frac{3969c_\theta c_{2\theta}}{2048}\Big)s_\theta^2+\Big(-\frac{1701c_\theta}{2048}$$
$$-\frac{5103c_\theta c_{2\theta}}{2048}\Big)c_{2\iota}s_\theta^2\Big)s_\iota^3+\Big(\Big(-\frac{44757c_\theta}{4096}+\frac{3969c_\theta c_{2\theta}}{4096}\Big)s_\theta^2+\Big(\frac{1701c_\theta}{4096}$$
$$+\frac{5103c_\theta c_{2\theta}}{4096}\Big)c_{2\iota}s_\theta^2\Big)s_\iota^3\Big]+\cos(5\Psi)\Big(\nu\Big(-\frac{21875c_\theta}{2048}-\frac{13125c_{3\theta}}{2048}\Big)s_\theta^2 s_\iota^5$$
$$+\Big(\frac{21875c_\theta}{4096}+\frac{13125c_{3\theta}}{4096}\Big)s_\theta^2 s_\iota^5\Big)+\cos(2\alpha+3\Psi)\Big[\Big(-\frac{37071c_\theta c_{2\theta}}{16384}$$
$$+c_\theta\Big(-\frac{7641}{8192}+\frac{567c_{4\theta}}{32768}\Big)+\Big(-\frac{10917c_\theta}{8192}-\frac{2835c_\theta c_{2\theta}}{1024}\Big)c_\iota+\Big(-\frac{10089c_\theta}{16384}$$
$$+\frac{135c_\theta c_{2\theta}}{8192}\Big)c_{2\iota}+\frac{513c_\theta c_{3\iota}}{8192}+\frac{567c_\theta c_{4\iota}}{32768}\Big)s_\iota-\frac{81c_\theta c_{4\theta}s_{2\iota}}{8192}+\frac{1053c_\theta c_{4\theta}s_{3\iota}}{65536}$$
$$+\Big(\frac{2565c_{3\theta}}{32768}+\frac{729c_{5\theta}}{32768}\Big)s_{4\iota}+\Big(\frac{243c_{3\theta}}{131072}+\frac{1215c_{5\theta}}{131072}\Big)s_{5\iota}+\nu\Big[\Big(\frac{5967c_\theta c_{2\theta}}{8192}$$
$$+c_\theta\Big(\frac{2457}{4096}-\frac{567c_{4\theta}}{16384}\Big)+\Big(\frac{4005c_\theta}{4096}+\frac{243}{512}c_\theta c_{2\theta}\Big)c_\iota+\Big(\frac{6633c_\theta}{8192}$$
$$-\frac{5319c_\theta c_{2\theta}}{4096}\Big)c_{2\iota}-\frac{513c_\theta c_{3\iota}}{4096}-\frac{567c_\theta c_{4\iota}}{16384}\Big)s_\iota+\frac{81c_\theta c_{4\theta}s_{2\iota}}{4096}-\frac{1053c_\theta c_{4\theta}s_{3\iota}}{32768}$$
$$+\Big(-\frac{2565c_{3\theta}}{16384}-\frac{729c_{5\theta}}{16384}\Big)s_{4\iota}+\Big(-\frac{243c_{3\theta}}{65536}-\frac{1215c_{5\theta}}{65536}\Big)s_{5\iota}\Big]\Big]+$$
$$\cos(2\alpha-3\Psi)\Big[\Big(-\frac{18603c_\theta c_{2\theta}}{8192}+c_\theta\Big(-\frac{20475}{32768}+\frac{567c_{4\theta}}{32768}\Big)\Big)s_\iota+\Big(\frac{2835c_\theta c_{2\theta}}{2048}$$
$$+c_\theta\Big(\frac{5715}{8192}+\frac{81c_{4\theta}}{8192}\Big)\Big)s_{2\iota}+\Big(\frac{135c_\theta c_{2\theta}}{16384}+c_\theta\Big(-\frac{20745}{65536}+\frac{1053c_{4\theta}}{65536}\Big)\Big)s_{3\iota}$$
$$+\Big(-\frac{513c_\theta}{16384}-\frac{2565c_{3\theta}}{32768}-\frac{729c_{5\theta}}{32768}\Big)s_{4\iota}+\Big(\frac{567c_\theta}{65536}+\frac{243c_{3\theta}}{131072}+\frac{1215c_{5\theta}}{131072}\Big)s_{5\iota}$$
$$+\nu\Big[\Big(\frac{5643c_\theta c_{2\theta}}{4096}+c_\theta\Big(\frac{3195}{16384}-\frac{567c_{4\theta}}{16384}\Big)\Big)s_\iota+\Big(-\frac{243c_\theta c_{2\theta}}{1024}$$
$$+c_\theta\Big(-\frac{2259}{4096}-\frac{81c_{4\theta}}{4096}\Big)\Big)s_{2\iota}+\Big(-\frac{5319c_\theta c_{2\theta}}{8192}+c_\theta\Big(\frac{13833}{32768}-\frac{1053c_{4\theta}}{32768}\Big)\Big)s_{3\iota}$$
$$+\Big(\frac{513c_\theta}{8192}+\frac{2565c_{3\theta}}{16384}+\frac{729c_{5\theta}}{16384}\Big)s_{4\iota}+\Big(-\frac{567c_\theta}{32768}-\frac{243c_{3\theta}}{65536}-\frac{1215c_{5\theta}}{65536}\Big)s_{5\iota}\Big]\Big]$$

$$
\begin{aligned}
&+\cos(2\alpha+\Psi)\Bigg[\Bigg(\frac{319c_\theta c_{2\theta}}{24576}+c_\theta\Big(\frac{871}{4096}+\frac{c_{4\theta}}{49152}\Big)+\Big(\frac{933c_\theta}{4096}+\frac{133c_\theta c_{2\theta}}{1536}\Big)c_\iota\\
&+\Big(\frac{625c_\theta}{24576}+\frac{211c_\theta c_{2\theta}}{4096}\Big)c_{2\iota}-\frac{11c_\theta c_{3\iota}}{12288}-\frac{7c_\theta c_{4\iota}}{49152}\Bigg)s_\iota-\frac{c_\theta c_{4\theta}s_{2\iota}}{12288}+\frac{c_\theta c_{4\theta}s_{3\iota}}{32768}\\
&+\Big(-\frac{45c_{3\theta}}{16384}-\frac{c_{5\theta}}{16384}\Big)s_{4\iota}+\Big(-\frac{c_{3\theta}}{65536}-\frac{5c_{5\theta}}{65536}\Big)s_{5\iota}+\nu\Bigg[\Bigg(\frac{257c_\theta c_{2\theta}}{12288}\\
&+c_\theta\Big(-\frac{1493}{6144}-\frac{c_{4\theta}}{24576}\Big)+\Big(-\frac{1391c_\theta}{6144}+\frac{11}{768}c_\theta c_{2\theta}\Big)c_\iota\\
&+\Big(-\frac{49c_\theta}{12288}+\frac{77c_\theta c_{2\theta}}{2048}\Big)c_{2\iota}+\frac{11c_\theta c_{3\iota}}{6144}+\frac{7c_\theta c_{4\iota}}{24576}\Bigg)s_\iota+\frac{c_\theta c_{4\theta}s_{2\iota}}{6144}-\frac{c_\theta c_{4\theta}s_{3\iota}}{16384}\\
&+\Big(\frac{45c_{3\theta}}{8192}+\frac{c_{5\theta}}{8192}\Big)s_{4\iota}+\Big(\frac{c_{3\theta}}{32768}+\frac{5c_{5\theta}}{32768}\Big)s_{5\iota}\Bigg]\Bigg]+\cos(2\alpha-\Psi)\\
&\times\Bigg[\Bigg(-\frac{157c_\theta c_{2\theta}}{12288}+c_\theta\Big(\frac{9827}{49152}+\frac{c_{4\theta}}{49152}\Big)\Bigg)s_\iota+\Bigg(-\frac{133c_\theta c_{2\theta}}{3072}\\
&+c_\theta\Big(-\frac{1405}{12288}+\frac{c_{4\theta}}{12288}\Big)\Bigg)s_{2\iota}+\Bigg(\frac{211c_\theta c_{2\theta}}{8192}+c_\theta\Big(\frac{419}{32768}+\frac{c_{4\theta}}{32768}\Big)\Bigg)s_{3\iota}\\
&+\Big(\frac{11c_\theta}{24576}+\frac{45c_{3\theta}}{16384}+\frac{c_{5\theta}}{16384}\Big)s_{4\iota}+\Big(-\frac{7c_\theta}{98304}-\frac{c_{3\theta}}{65536}-\frac{5c_{5\theta}}{65536}\Big)s_{5\iota}\\
&+\nu\Bigg[\Bigg(\frac{13c_\theta c_{2\theta}}{6144}+c_\theta\Big(-\frac{5923}{24576}-\frac{c_{4\theta}}{24576}\Big)\Bigg)s_\iota+\Bigg(-\frac{11c_\theta c_{2\theta}}{1536}+c_\theta\Big(\frac{701}{6144}\\
&-\frac{c_{4\theta}}{6144}\Big)\Bigg)s_{2\iota}+\Bigg(\frac{77c_\theta c_{2\theta}}{4096}+c_\theta\Big(-\frac{35}{16384}-\frac{c_{4\theta}}{16384}\Big)\Bigg)s_{3\iota}+\Big(-\frac{11c_\theta}{12288}\\
&-\frac{45c_{3\theta}}{8192}-\frac{c_{5\theta}}{8192}\Big)s_{4\iota}+\Big(\frac{7c_\theta}{49152}+\frac{c_{3\theta}}{32768}+\frac{5c_{5\theta}}{32768}\Big)s_{5\iota}\Bigg]\Bigg]+\cos(\Psi)\\
&\times\Bigg[\Big(-\frac{341c_\theta}{8192}+\frac{c_\theta c_{2\theta}}{8192}\Big)s_\theta^2 s_\iota+\Big(-\frac{3411c_\theta}{16384}+\frac{7c_\theta c_{2\theta}}{16384}\Big)s_\theta^2 s_{3\iota}+\Big(\frac{35c_\theta}{32768}\\
&+\frac{21c_{3\theta}}{32768}\Big)s_\theta^2 s_{5\iota}+\nu\Bigg(\Big(-\frac{43c_\theta}{4096}-\frac{c_\theta c_{2\theta}}{4096}\Big)s_\theta^2 s_\iota+\Big(-\frac{429c_\theta}{8192}-\frac{7c_\theta c_{2\theta}}{8192}\Big)s_\theta^2 s_{3\iota}\\
&+\Big(-\frac{35c_\theta}{16384}-\frac{21c_{3\theta}}{16384}\Big)s_\theta^2 s_{5\iota}\Bigg)\Bigg]\Bigg], \qquad \text{(A.2d)}
\end{aligned}
$$

$$
\begin{aligned}
\hat{h}_+^{(1,\mathrm{SO})} &= \cos(\alpha+\Psi)\Big(\chi_a^x c_\theta c_{\frac{\iota}{2}}^2-\chi_a^z c_{\frac{\iota}{2}}^2 s_\theta\Big)+\cos(\alpha-\Psi)\Bigg(\chi_a^x\Big(\frac{c_\theta}{2}-\frac{c_\theta c_\iota}{2}\Big)-\chi_a^z s_\theta s_{\frac{\iota}{2}}^2\Bigg)\\
&-\chi_a^y c_\theta s_{\frac{\iota}{2}}^2\sin(\alpha-\Psi)-\chi_a^y s_\theta s_\iota\sin(\Psi)-\chi_a^y c_\theta c_{\frac{\iota}{2}}^2\sin(\alpha+\Psi)+\delta\Bigg[\cos(\alpha+\Psi)\\
&\times\Big(\chi_s^x c_\theta c_{\frac{\iota}{2}}^2-\chi_s^z c_{\frac{\iota}{2}}^2 s_\theta\Big)+\cos(\alpha-\Psi)\Bigg(\chi_s^x\Big(\frac{c_\theta}{2}-\frac{c_\theta c_\iota}{2}\Big)-\chi_s^z s_\theta s_{\frac{\iota}{2}}^2\Bigg)
\end{aligned}
$$

$$- \chi_s^y c_\theta s_{\frac{\iota}{2}}^2 \sin(\alpha - \Psi) - \chi_s^y s_\theta s_\iota \sin(\Psi) - \chi_s^y c_\theta c_{\frac{\iota}{2}}^2 \sin(\alpha + \Psi)\Big], \tag{A.2e}$$

$$\begin{aligned}
\hat{h}_+^{(3/2,\mathrm{SO})} &= \chi_s^x\Big(2c_\theta c_\iota^3 s_\theta - \nu c_\theta c_\iota^3 s_\theta\Big) + \cos(2\alpha + 2\Psi)\Big[\chi_s^z\Big[\nu c_{\frac{\iota}{2}}^4\Big(-\frac{5}{2} - \frac{7c_{2\theta}}{2} \\
&+ \Big(\frac{1}{2} + \frac{c_{2\theta}}{6}\Big)c_\iota\Big) + c_{\frac{\iota}{2}}^4\Big(-3 - c_{2\theta} + \Big(5 + \frac{5c_{2\theta}}{3}\Big)c_\iota\Big)\Big] + \chi_s^x\Big(c_{\frac{\iota}{2}}^4\Big(\frac{7s_{2\theta}}{3} \\
&- \frac{10}{3}c_\iota s_{2\theta}\Big) + \nu c_{\frac{\iota}{2}}^4\Big(-\frac{19s_{2\theta}}{6} - \frac{1}{3}c_\iota s_{2\theta}\Big)\Big)\Big] + \chi_s^x\cos(3\alpha + 2\Psi) \\
&\times \Big(\nu\Big(\frac{1}{2} + \frac{c_{2\theta}}{6}\Big)c_{\frac{\iota}{2}}^5 s_{\frac{\iota}{2}} + \Big(5 + \frac{5c_{2\theta}}{3}\Big)c_{\frac{\iota}{2}}^5 s_{\frac{\iota}{2}}\Big) + \chi_s^x\cos(3\alpha - 2\Psi) \\
&\times \Big(\nu\Big(\frac{1}{2} + \frac{c_{2\theta}}{6}\Big)c_{\frac{\iota}{2}} s_{\frac{\iota}{2}}^5 + \Big(5 + \frac{5c_{2\theta}}{3}\Big)c_{\frac{\iota}{2}} s_{\frac{\iota}{2}}^5\Big) + \cos(\alpha + 2\Psi) \\
&\times \Big[\chi_s^x\Big[\nu c_{\frac{\iota}{2}}^3\Big(-\frac{17}{4} + \frac{79c_{2\theta}}{12} + \Big(-\frac{1}{4} + \frac{7c_{2\theta}}{12}\Big)c_\iota\Big)s_{\frac{\iota}{2}} + c_{\frac{\iota}{2}}^3\Big(\frac{3}{2} - \frac{13c_{2\theta}}{6} \\
&+ \Big(-\frac{5}{2} + \frac{35c_{2\theta}}{6}\Big)c_\iota\Big)s_{\frac{\iota}{2}}\Big] + \chi_s^z\Big(\nu c_{\frac{\iota}{2}}^3\Big(-7s_{2\theta} + \frac{2}{3}c_\iota s_{2\theta}\Big)s_{\frac{\iota}{2}} \\
&+ c_{\frac{\iota}{2}}^3\Big(-2s_{2\theta} + \frac{20}{3}c_\iota s_{2\theta}\Big)s_{\frac{\iota}{2}}\Big)\Big] + \cos(\alpha - 2\Psi)\Big[\chi_s^x\Big[c_{\frac{\iota}{2}}\Big(\frac{3}{2} - \frac{13c_{2\theta}}{6} \\
&+ \Big(\frac{5}{2} - \frac{35c_{2\theta}}{6}\Big)c_\iota\Big)s_{\frac{\iota}{2}}^3 + \nu c_{\frac{\iota}{2}}\Big(-\frac{17}{4} + \frac{79c_{2\theta}}{12} + \Big(\frac{1}{4} - \frac{7c_{2\theta}}{12}\Big)c_\iota\Big)s_{\frac{\iota}{2}}^3\Big] \\
&+ \chi_s^z\Big(c_{\frac{\iota}{2}}\Big(-2s_{2\theta} - \frac{20}{3}c_\iota s_{2\theta}\Big)s_{\frac{\iota}{2}}^3 + \nu c_{\frac{\iota}{2}}\Big(-7s_{2\theta} - \frac{2}{3}c_\iota s_{2\theta}\Big)s_{\frac{\iota}{2}}^3\Big)\Big] \\
&+ \cos(2\alpha - 2\Psi)\Big[\chi_s^z\Big[\nu\Big(\frac{5}{2} + \frac{7c_{2\theta}}{2} + \Big(\frac{1}{2} + \frac{c_{2\theta}}{6}\Big)c_\iota\Big)s_{\frac{\iota}{2}}^4 + \Big(3 + c_{2\theta} \\
&+ \Big(5 + \frac{5c_{2\theta}}{3}\Big)c_\iota\Big)s_{\frac{\iota}{2}}^4\Big] + \chi_s^x\Big(\Big(-\frac{7s_{2\theta}}{3} - \frac{10}{3}c_\iota s_{2\theta}\Big)s_{\frac{\iota}{2}}^4 + \nu\Big(\frac{19s_{2\theta}}{6} \\
&- \frac{1}{3}c_\iota s_{2\theta}\Big)s_{\frac{\iota}{2}}^4\Big)\Big] + \chi_s^z\Big(-3c_\iota s_\theta^2 s_\iota^2 + \frac{3}{2}\nu c_\iota s_\theta^2 s_\iota^2\Big) + \chi_s^x\cos(3\alpha) \\
&\times \Big(\nu\Big(-\frac{3}{8} - \frac{c_{2\theta}}{8}\Big)s_\iota^3 + \Big(\frac{3}{4} + \frac{c_{2\theta}}{4}\Big)s_\iota^3\Big) + \cos(2\Psi)\Big(\chi_s^x\Big(\frac{10}{3}c_\theta c_\iota s_\theta s_\iota^2 \\
&+ \frac{1}{3}\nu c_\theta c_\iota s_\theta s_\iota^2\Big) + \chi_s^z\Big(5c_\iota s_\theta^2 s_\iota^2 + \frac{1}{2}\nu c_\iota s_\theta^2 s_\iota^2\Big)\Big) + \cos(2\alpha)\Big[\chi_s^z\Big(\nu\Big(-\frac{3}{4} \\
&- \frac{c_{2\theta}}{4}\Big)c_\iota s_\iota^2 + \Big(\frac{3}{2} + \frac{c_{2\theta}}{2}\Big)c_\iota s_\iota^2\Big) + \chi_s^x\Big(-c_\iota s_{2\theta} s_\iota^2 + \frac{1}{2}\nu c_\iota s_{2\theta} s_\iota^2\Big)\Big] \\
&+ \cos(\alpha)\Big[\chi_s^x\Big(-\frac{11}{16}c_{2\theta} s_\iota - \frac{3s_\iota^3}{4} - \frac{7}{16}c_{2\theta} s_{3\iota} + \nu\Big(\frac{11}{32}c_{2\theta} s_\iota + \frac{3s_\iota^3}{8}\Big)\Big)\Big]
\end{aligned}$$

$$+\frac{7}{32}c_{2\theta}s_{3\iota}\Big)\Big)+\chi_s^z\Big(\frac{1}{2}s_{2\theta}s_\iota-\frac{1}{2}s_{2\theta}s_{3\iota}+\nu\Big(-\frac{1}{4}s_{2\theta}s_\iota+\frac{1}{4}s_{2\theta}s_{3\iota}\Big)\Big)\Big]$$
$$+\chi_s^y\Big[\Big(\frac{15}{8}-\frac{3c_{2\theta}}{8}+\Big(\frac{9}{8}-\frac{5c_{2\theta}}{8}\Big)c_{2\iota}\Big)s_\iota+\nu\Big(-\frac{15}{16}+\frac{3c_{2\theta}}{16}+\Big(-\frac{9}{16}$$
$$+\frac{5c_{2\theta}}{16}\Big)c_{2\iota}\Big)s_\iota\Big]\sin(\alpha)+\chi_s^y\Big(-2c_\theta c_\iota s_\theta s_\iota^2+\nu c_\theta c_\iota s_\theta s_\iota^2\Big)\sin(2\alpha)$$
$$+\chi_s^y\Big(\nu\Big(-\frac{3}{8}-\frac{c_{2\theta}}{8}\Big)s_\iota^3+\Big(\frac{3}{4}+\frac{c_{2\theta}}{4}\Big)s_\iota^3\Big)\sin(3\alpha)+\chi_s^y\Big[c_{\frac{\iota}{2}}\Big(\frac{5}{2}-\frac{11c_{2\theta}}{6}$$
$$+\Big(\frac{15}{2}-\frac{25c_{2\theta}}{6}\Big)c_\iota\Big)s_{\frac{\iota}{2}}^3+\nu c_{\frac{\iota}{2}}\Big(\frac{1}{4}-\frac{31c_{2\theta}}{12}+\Big(\frac{3}{4}-\frac{5c_{2\theta}}{12}\Big)c_\iota\Big)s_{\frac{\iota}{2}}^3\Big]\sin(\alpha-2\Psi)$$
$$+\chi_s^y\Big(\Big(-\frac{7s_{2\theta}}{3}-\frac{10}{3}c_\iota s_{2\theta}\Big)s_{\frac{\iota}{2}}^4+\nu\Big(-\frac{5s_{2\theta}}{6}-\frac{1}{3}c_\iota s_{2\theta}\Big)s_{\frac{\iota}{2}}^4\Big)\sin(2\alpha-2\Psi)$$
$$+\chi_s^y\Big(\nu\Big(\frac{1}{2}+\frac{c_{2\theta}}{6}\Big)c_{\frac{\iota}{2}}s_{\frac{\iota}{2}}^5+\Big(5+\frac{5c_{2\theta}}{3}\Big)c_{\frac{\iota}{2}}s_{\frac{\iota}{2}}^5\Big)\sin(3\alpha-2\Psi)$$
$$+\chi_s^y\Big(-\frac{1}{3}c_\theta s_\theta s_\iota^2-\frac{11}{6}\nu c_\theta s_\theta s_\iota^2\Big)\sin(2\Psi)+\chi_s^y\Big[\nu c_{\frac{\iota}{2}}^3\Big(\frac{1}{4}-\frac{31c_{2\theta}}{12}+\Big(-\frac{3}{4}$$
$$+\frac{5c_{2\theta}}{12}\Big)c_\iota\Big)s_{\frac{\iota}{2}}+c_{\frac{\iota}{2}}^3\Big(\frac{5}{2}-\frac{11c_{2\theta}}{6}+\Big(-\frac{15}{2}+\frac{25c_{2\theta}}{6}\Big)c_\iota\Big)s_{\frac{\iota}{2}}\Big]\sin(\alpha+2\Psi)$$
$$+\chi_s^y\Big(c_{\frac{\iota}{2}}^4\Big(\frac{7s_{2\theta}}{3}-\frac{10}{3}c_\iota s_{2\theta}\Big)+\nu c_{\frac{\iota}{2}}^4\Big(\frac{5s_{2\theta}}{6}-\frac{1}{3}c_\iota s_{2\theta}\Big)\Big)\sin(2\alpha+2\Psi)$$
$$+\chi_s^y\Big(\nu\Big(\frac{1}{2}+\frac{c_{2\theta}}{6}\Big)c_{\frac{\iota}{2}}^5s_{\frac{\iota}{2}}+\Big(5+\frac{5c_{2\theta}}{3}\Big)c_{\frac{\iota}{2}}^5s_{\frac{\iota}{2}}\Big)\sin(3\alpha+2\Psi)$$
$$+\delta\Big[2\chi_a^xc_\theta c_\iota^3s_\theta+\cos(2\alpha+2\Psi)\Big[\chi_a^zc_{\frac{\iota}{2}}^4\Big(-3-c_{2\theta}+\Big(5+\frac{5c_{2\theta}}{3}\Big)c_\iota\Big)$$
$$+\chi_a^xc_{\frac{\iota}{2}}^4\Big(\frac{7s_{2\theta}}{3}-\frac{10}{3}c_\iota s_{2\theta}\Big)\Big]+\chi_a^x\Big(5+\frac{5c_{2\theta}}{3}\Big)c_{\frac{\iota}{2}}^5s_{\frac{\iota}{2}}\cos(3\alpha+2\Psi)$$
$$+\chi_a^x\Big(5+\frac{5c_{2\theta}}{3}\Big)c_{\frac{\iota}{2}}s_{\frac{\iota}{2}}^5\cos(3\alpha-2\Psi)+\cos(\alpha+2\Psi)\Big[\chi_a^xc_{\frac{\iota}{2}}^3\Big(\frac{3}{2}-\frac{13c_{2\theta}}{6}$$
$$+\Big(-\frac{5}{2}+\frac{35c_{2\theta}}{6}\Big)c_\iota\Big)s_{\frac{\iota}{2}}+\chi_a^zc_{\frac{\iota}{2}}^3\Big(-2s_{2\theta}+\frac{20}{3}c_\iota s_{2\theta}\Big)s_{\frac{\iota}{2}}\Big]+\cos(\alpha-2\Psi)$$
$$\times\Big[\chi_a^xc_{\frac{\iota}{2}}\Big(\frac{3}{2}-\frac{13c_{2\theta}}{6}+\Big(\frac{5}{2}-\frac{35c_{2\theta}}{6}\Big)c_\iota\Big)s_{\frac{\iota}{2}}^3+\chi_a^zc_{\frac{\iota}{2}}\Big(-2s_{2\theta}-\frac{20}{3}c_\iota s_{2\theta}\Big)s_{\frac{\iota}{2}}^3\Big]$$
$$+\cos(2\alpha-2\Psi)\Big[\chi_a^z\Big(3+c_{2\theta}+\Big(5+\frac{5c_{2\theta}}{3}\Big)c_\iota\Big)s_{\frac{\iota}{2}}^4+\chi_a^x\Big(-\frac{7s_{2\theta}}{3}$$
$$-\frac{10}{3}c_\iota s_{2\theta}\Big)s_{\frac{\iota}{2}}^4\Big]-3\chi_a^zc_\iota s_\theta^2s_\iota^2+\chi_a^x\Big(\frac{3}{4}+\frac{c_{2\theta}}{4}\Big)\cos(3\alpha)s_\iota^3+\cos(2\Psi)$$

$$
\begin{aligned}
&\times \Big(\frac{10}{3}\chi_a^x c_\theta c_\iota s_\theta s_\iota^2 + 5\chi_a^z c_\iota s_\theta^2 s_\iota^2\Big) + \cos(2\alpha)\bigg(\chi_a^z\Big(\frac{3}{2}+\frac{c_{2\theta}}{2}\Big)c_\iota s_\iota^2 - \chi_a^x c_\iota s_{2\theta} s_\iota^2\bigg)\\
&+ \cos(\alpha)\bigg(\chi_a^x\Big(-\frac{11}{16}c_{2\theta}s_\iota - \frac{3s_\iota^3}{4} - \frac{7}{16}c_{2\theta}s_{3\iota}\Big) + \chi_a^z\Big(\frac{1}{2}s_{2\theta}s_\iota - \frac{1}{2}s_{2\theta}s_{3\iota}\Big)\bigg)\\
&+ \chi_a^y\bigg(\frac{15}{8} - \frac{3c_{2\theta}}{8} + \Big(\frac{9}{8} - \frac{5c_{2\theta}}{8}\Big)c_{2\iota}\bigg)s_\iota \sin(\alpha) - 2\chi_a^y c_\theta c_\iota s_\theta s_\iota^2 \sin(2\alpha)\\
&+ \chi_a^y\Big(\frac{3}{4}+\frac{c_{2\theta}}{4}\Big)s_\iota^3 \sin(3\alpha) + \chi_a^y c_{\frac{\iota}{2}}\bigg(\frac{5}{2} - \frac{11c_{2\theta}}{6} + \Big(\frac{15}{2} - \frac{25c_{2\theta}}{6}\Big)c_\iota\bigg)s_{\frac{\iota}{2}}^3\\
&\times \sin(\alpha - 2\Psi) + \chi_a^y\Big(-\frac{7s_{2\theta}}{3} - \frac{10}{3}c_\iota s_{2\theta}\Big)s_{\frac{\iota}{2}}^4 \sin(2\alpha - 2\Psi)\\
&+ \chi_a^y\Big(5 + \frac{5c_{2\theta}}{3}\Big)c_{\frac{\iota}{2}}s_{\frac{\iota}{2}}^5 \sin(3\alpha - 2\Psi) - \frac{1}{3}\chi_a^y c_\theta s_\theta s_\iota^2 \sin(2\Psi)\\
&+ \chi_a^y c_{\frac{\iota}{2}}^3\bigg(\frac{5}{2} - \frac{11c_{2\theta}}{6} + \Big(-\frac{15}{2} + \frac{25c_{2\theta}}{6}\Big)c_\iota\bigg)s_{\frac{\iota}{2}} \sin(\alpha + 2\Psi)\\
&+ \chi_a^y c_{\frac{\iota}{2}}^4\Big(\frac{7s_{2\theta}}{3} - \frac{10}{3}c_\iota s_{2\theta}\Big)\sin(2\alpha + 2\Psi)\\
&+ \chi_a^y\Big(5 + \frac{5c_{2\theta}}{3}\Big)c_{\frac{\iota}{2}}^5 s_{\frac{\iota}{2}} \sin(3\alpha + 2\Psi)\bigg], \qquad \text{(A.2f)}
\end{aligned}
$$

$$
\begin{aligned}
\hat{h}_\times^{(0)} &= 4c_{\frac{\iota}{2}}s_\theta s_{\frac{\iota}{2}}^3 \sin(\alpha - 2\Psi) - 2c_\theta s_{\frac{\iota}{2}}^4 \sin(2\alpha - 2\Psi)\\
&\quad - 4c_{\frac{\iota}{2}}^3 s_\theta s_{\frac{\iota}{2}} \sin(\alpha + 2\Psi) - 2c_\theta c_{\frac{\iota}{2}}^4 \sin(2\alpha + 2\Psi)\,, \qquad \text{(A.3a)}\\
\hat{h}_\times^{(1/2)} &= \delta\bigg[-\frac{45}{8}c_{\frac{\iota}{2}}^2 s_{2\theta}s_{\frac{\iota}{2}}^4 \sin(\alpha - 3\Psi) + \frac{9}{2}c_{2\theta}c_{\frac{\iota}{2}}s_{\frac{\iota}{2}}^5 \sin(2\alpha - 3\Psi)\\
&\quad + \frac{9}{8}s_{2\theta}s_{\frac{\iota}{2}}^6 \sin(3\alpha - 3\Psi) + \Big(-\frac{1}{64}c_\theta s_\theta + \frac{43}{128}c_\theta c_\iota s_\theta - \frac{23}{128}c_{2\iota}s_{2\theta}\\
&\quad + \frac{5}{256}c_{3\iota}s_{2\theta}\Big)\sin(\alpha - \Psi) + \bigg(\Big(-1 - \frac{c_{2\theta}}{4}\Big)c_{\frac{\iota}{2}} + \frac{1}{4}c_{2\theta}c_{\frac{\iota}{2}}c_\iota\bigg)\\
&\quad \times s_{\frac{\iota}{2}}^3 \sin(2\alpha - \Psi) + \frac{1}{8}c_{\frac{\iota}{2}}^2 s_{2\theta}s_{\frac{\iota}{2}}^4 \sin(3\alpha - \Psi) + \frac{1}{2}s_\theta^2 s_{2\iota}\sin(\Psi)\\
&\quad + \Big(\frac{c_\theta s_\theta}{64} + \frac{43}{128}c_\theta c_\iota s_\theta + \frac{23}{128}c_{2\iota}s_{2\theta} + \frac{5}{256}c_{3\iota}s_{2\theta}\Big)\sin(\alpha + \Psi)\\
&\quad + \bigg(\Big(-1 - \frac{c_{2\theta}}{4}\Big)c_{\frac{\iota}{2}}^3 - \frac{1}{4}c_{2\theta}c_{\frac{\iota}{2}}^3 c_\iota\bigg)s_{\frac{\iota}{2}} \sin(2\alpha + \Psi)
\end{aligned}
$$

$$
\begin{aligned}
&- \frac{1}{8}c_{\frac{\iota}{2}}^4 s_{2\theta} s_{\frac{\iota}{2}}^2 \sin(3\alpha+\Psi) + \frac{45}{8}c_{\frac{\iota}{2}}^4 s_{2\theta} s_{\frac{\iota}{2}}^2 \sin(\alpha+3\Psi) \\
&+ \frac{9}{2}c_{2\theta}c_{\frac{\iota}{2}}^5 s_{\frac{\iota}{2}} \sin(2\alpha+3\Psi) - \frac{9}{8}c_{\frac{\iota}{2}}^6 s_{2\theta}\sin(3\alpha+3\Psi)\Big], \qquad \text{(A.3b)}
\end{aligned}
$$

$$
\begin{aligned}
\hat{h}_{\times}^{(1)} = &\Big(\nu c_{\frac{\iota}{2}}^3\Big(-12s_\theta - 28s_{3\theta}\Big)s_{\frac{\iota}{2}}^5 + c_{\frac{\iota}{2}}^3\Big(4s_\theta + \frac{28s_{3\theta}}{3}\Big)s_{\frac{\iota}{2}}^5\Big)\sin(\alpha-4\Psi) \\
&+ \Big(\Big(-\frac{4c_\theta}{3} - \frac{28c_{3\theta}}{3}\Big)c_{\frac{\iota}{2}}^2 s_{\frac{\iota}{2}}^6 + \nu\Big(4c_\theta + 28c_{3\theta}\Big)c_{\frac{\iota}{2}}^2 s_{\frac{\iota}{2}}^6\Big)\sin(2\alpha-4\Psi) \\
&+ \Big(c_{\frac{\iota}{2}}\Big(\frac{4s_\theta}{3} - 4s_{3\theta}\Big)s_{\frac{\iota}{2}}^7 + \nu c_{\frac{\iota}{2}}\Big(-4s_\theta + 12s_{3\theta}\Big)s_{\frac{\iota}{2}}^7\Big)\sin(3\alpha-4\Psi) \\
&+ \Big(-\frac{8}{3}c_\theta s_\theta^2 s_{\frac{\iota}{2}}^8 + 8\nu c_\theta s_\theta^2 s_{\frac{\iota}{2}}^8\Big)\sin(4\alpha-4\Psi) + \Big[c_{\frac{\iota}{2}}\Big(-\frac{79s_\theta}{8} \\
&+ c_\iota\Big(\frac{3s_\theta}{4} - \frac{19s_{3\theta}}{12}\Big) + c_{2\iota}\Big(\frac{s_\theta}{8} + \frac{7s_{3\theta}}{24}\Big) - \frac{3s_{3\theta}}{8}\Big)s_{\frac{\iota}{2}}^3 + \nu c_{\frac{\iota}{2}}\Big(\frac{103s_\theta}{24} \\
&+ c_{2\iota}\Big(-\frac{3s_\theta}{8} - \frac{7s_{3\theta}}{8}\Big) + \frac{9s_{3\theta}}{8} + c_\iota\Big(-\frac{9s_\theta}{4} + \frac{19s_{3\theta}}{4}\Big)\Big)s_{\frac{\iota}{2}}^3\Big]\sin(\alpha-2\Psi) \\
&+ \Big[\Big(\frac{47c_\theta}{8} + \frac{c_{3\theta}}{8} + \Big(\frac{7c_\theta}{6} + \frac{c_{3\theta}}{6}\Big)c_\iota + \Big(-\frac{c_\theta}{24} - \frac{7c_{3\theta}}{24}\Big)c_{2\iota}\Big)s_{\frac{\iota}{2}}^4 \\
&+ \nu\Big(-\frac{119c_\theta}{24} - \frac{3c_{3\theta}}{8} + \Big(-\frac{7c_\theta}{2} - \frac{c_{3\theta}}{2}\Big)c_\iota + \Big(\frac{c_\theta}{8} + \frac{7c_{3\theta}}{8}\Big)c_{2\iota}\Big)s_{\frac{\iota}{2}}^4\Big] \\
&\times \sin(2\alpha-2\Psi) + \Big[c_{\frac{\iota}{2}}\Big(\frac{4s_\theta}{3} + \Big(-\frac{1}{3} - c_{2\theta}\Big)c_\iota s_\theta\Big)s_{\frac{\iota}{2}}^5 + \nu c_{\frac{\iota}{2}}\Big(-4s_\theta \\
&+ \Big(1 + 3c_{2\theta}\Big)c_\iota s_\theta\Big)s_{\frac{\iota}{2}}^5\Big]\sin(3\alpha-2\Psi) + \Big(-\frac{2}{3}c_\theta c_{\frac{\iota}{2}}^2 s_\theta^2 s_{\frac{\iota}{2}}^6 + 2\nu c_\theta c_{\frac{\iota}{2}}^2 s_\theta^2 s_{\frac{\iota}{2}}^6\Big) \\
&\times \sin(4\alpha-2\Psi) + \Big(-\frac{5}{2}c_\theta c_\iota s_\theta^2 s_\iota^2 + \frac{15}{2}\nu c_\theta c_\iota s_\theta^2 s_\iota^2\Big)\sin(2\Psi) + \Big[c_{\frac{\iota}{2}}^3\Big(\frac{79s_\theta}{8} \\
&+ c_\iota\Big(\frac{3s_\theta}{4} - \frac{19s_{3\theta}}{12}\Big) + c_{2\iota}\Big(-\frac{s_\theta}{8} - \frac{7s_{3\theta}}{24}\Big) + \frac{3s_{3\theta}}{8}\Big)s_{\frac{\iota}{2}} + \nu c_{\frac{\iota}{2}}^3\Big(-\frac{103s_\theta}{24} \\
&+ c_{2\iota}\Big(\frac{3s_\theta}{8} + \frac{7s_{3\theta}}{8}\Big) - \frac{9s_{3\theta}}{8} + c_\iota\Big(-\frac{9s_\theta}{4} + \frac{19s_{3\theta}}{4}\Big)\Big)s_{\frac{\iota}{2}}\Big]\sin(\alpha+2\Psi) \\
&+ \Big[c_{\frac{\iota}{2}}^4\Big(\frac{47c_\theta}{8} + \frac{c_{3\theta}}{8} + \Big(-\frac{7c_\theta}{6} - \frac{c_{3\theta}}{6}\Big)c_\iota + \Big(-\frac{c_\theta}{24} - \frac{7c_{3\theta}}{24}\Big)c_{2\iota}\Big) \\
&+ \nu c_{\frac{\iota}{2}}^4\Big(-\frac{119c_\theta}{24} - \frac{3c_{3\theta}}{8} + \Big(\frac{7c_\theta}{2} + \frac{c_{3\theta}}{2}\Big)c_\iota + \Big(\frac{c_\theta}{8} + \frac{7c_{3\theta}}{8}\Big)c_{2\iota}\Big)\Big] \\
&\times \sin(2\alpha+2\Psi) + \Big[c_{\frac{\iota}{2}}^5\Big(-\frac{4s_\theta}{3} + \Big(-\frac{1}{3} - c_{2\theta}\Big)c_\iota s_\theta\Big)s_{\frac{\iota}{2}}
\end{aligned}
$$

$$
\begin{aligned}
&+ \nu c_{\frac{\iota}{2}}^5\Big(4s_\theta + \Big(1+3c_{2\theta}\Big)c_\iota s_\theta\Big)s_{\frac{\iota}{2}}\Big]\sin(3\alpha+2\Psi) + \Big(-\frac{2}{3}c_\theta c_{\frac{\iota}{2}}^6 s_\theta^2 s_{\frac{\iota}{2}}^2 \\
&+ 2\nu c_\theta c_{\frac{\iota}{2}}^6 s_\theta^2 s_{\frac{\iota}{2}}^2\Big)\sin(4\alpha+2\Psi) + \Big(c_{\frac{\iota}{2}}^5\Big(-4s_\theta - \frac{28s_{3\theta}}{3}\Big)s_{\frac{\iota}{2}}^3 \\
&+ \nu c_{\frac{\iota}{2}}^5\Big(12s_\theta + 28s_{3\theta}\Big)s_{\frac{\iota}{2}}^3\Big)\sin(\alpha+4\Psi) + \Big(\Big(-\frac{4c_\theta}{3} - \frac{28c_{3\theta}}{3}\Big)c_{\frac{\iota}{2}}^6 s_{\frac{\iota}{2}}^2 \\
&+ \nu\Big(4c_\theta + 28c_{3\theta}\Big)c_{\frac{\iota}{2}}^6 s_{\frac{\iota}{2}}^2\Big)\sin(2\alpha+4\Psi) + \Big(\nu\Big(-8-24c_{2\theta}\Big)c_{\frac{\iota}{2}}^7 s_\theta s_{\frac{\iota}{2}} \\
&+ \Big(\frac{8}{3} + 8c_{2\theta}\Big)c_{\frac{\iota}{2}}^7 s_\theta s_{\frac{\iota}{2}}\Big)\sin(3\alpha+4\Psi) \\
&+ \Big(-\frac{8}{3}c_\theta c_{\frac{\iota}{2}}^8 s_\theta^2 + 8\nu c_\theta c_{\frac{\iota}{2}}^8 s_\theta^2\Big)\sin(4\alpha+4\Psi)\,, \qquad \text{(A.3c)}
\end{aligned}
$$

$$
\begin{aligned}
\hat{h}_\times^{(3/2)} &= 8\pi c_{\frac{\iota}{2}} s_\theta s_{\frac{\iota}{2}}^3 \sin(\alpha-2\Psi) - 4\pi c_\theta s_{\frac{\iota}{2}}^4 \sin(2\alpha-2\Psi) \\
&- 8\pi c_{\frac{\iota}{2}}^3 s_\theta s_{\frac{\iota}{2}} \sin(\alpha+2\Psi) - 4\pi c_\theta c_{\frac{\iota}{2}}^4 \sin(2\alpha+2\Psi) \\
&+ \delta\Big[\Big(c_{\frac{\iota}{2}}^4\Big(-\frac{4375s_{2\theta}}{384} - \frac{4375s_{4\theta}}{256}\Big)s_{\frac{\iota}{2}}^6 + \nu c_{\frac{\iota}{2}}^4\Big(\frac{4375s_{2\theta}}{192} \\
&+ \frac{4375s_{4\theta}}{128}\Big)s_{\frac{\iota}{2}}^6\Big)\sin(\alpha-5\Psi) + \Big(\nu\Big(-\frac{625c_{2\theta}}{48} - \frac{625c_{4\theta}}{16}\Big)c_{\frac{\iota}{2}}^3 s_{\frac{\iota}{2}}^7 \\
&+ \Big(\frac{625c_{2\theta}}{96} + \frac{625c_{4\theta}}{32}\Big)c_{\frac{\iota}{2}}^3 s_{\frac{\iota}{2}}^7\Big)\sin(2\alpha-5\Psi) + \Big(\nu c_{\frac{\iota}{2}}^2\Big(\frac{625s_{2\theta}}{128} \\
&- \frac{5625s_{4\theta}}{256}\Big)s_{\frac{\iota}{2}}^8 + c_{\frac{\iota}{2}}^2\Big(-\frac{625s_{2\theta}}{256} + \frac{5625s_{4\theta}}{512}\Big)s_{\frac{\iota}{2}}^8\Big)\sin(3\alpha-5\Psi) \\
&+ \Big(\nu\Big(-\frac{625}{48} - \frac{625c_{2\theta}}{24}\Big)c_{\frac{\iota}{2}} s_\theta^2 s_{\frac{\iota}{2}}^9 + \Big(\frac{625}{96} + \frac{625c_{2\theta}}{48}\Big)c_{\frac{\iota}{2}} s_\theta^2 s_{\frac{\iota}{2}}^9\Big) \\
&\times \sin(4\alpha-5\Psi) + \Big(\frac{625}{192}c_\theta s_\theta^3 s_{\frac{\iota}{2}}^{10} - \frac{625}{96}\nu c_\theta s_\theta^3 s_{\frac{\iota}{2}}^{10}\Big)\sin(5\alpha-5\Psi) \\
&+ \Big[\nu c_{\frac{\iota}{2}}^2\Big(-\frac{4923s_{2\theta}}{512} + c_\iota\Big(\frac{459s_{2\theta}}{128} - \frac{2079s_{4\theta}}{256}\Big) - \frac{945s_{4\theta}}{1024} \\
&+ c_{2\iota}\Big(\frac{567s_{2\theta}}{512} + \frac{1701s_{4\theta}}{1024}\Big)\Big)s_{\frac{\iota}{2}}^4 + c_{\frac{\iota}{2}}^2\Big(\frac{22203s_{2\theta}}{1024} + c_{2\iota}\Big(-\frac{567s_{2\theta}}{1024} \\
&- \frac{1701s_{4\theta}}{2048}\Big) + \frac{945s_{4\theta}}{2048} + c_\iota\Big(-\frac{459s_{2\theta}}{256} + \frac{2079s_{4\theta}}{512}\Big)\Big)s_{\frac{\iota}{2}}^4\Big]\sin(\alpha-3\Psi) \\
&+ \Big[\nu c_{\frac{\iota}{2}}\Big(\frac{27}{16} + \frac{1233c_{2\theta}}{128} + \frac{27c_{4\theta}}{128} + \Big(\frac{27}{8} + \frac{27c_{2\theta}}{16} + \frac{27c_{4\theta}}{16}\Big)c_\iota
\end{aligned}
$$

$$+\Big(-\frac{81c_{2\theta}}{128}-\frac{243c_{4\theta}}{128}\Big)c_{2\iota}\Big)s_{\frac{\iota}{2}}^{5}+c_{\frac{\iota}{2}}\Big(-\frac{27}{32}-\frac{4689c_{2\theta}}{256}-\frac{27c_{4\theta}}{256}$$
$$+\Big(-\frac{27}{16}-\frac{27c_{2\theta}}{32}-\frac{27c_{4\theta}}{32}\Big)c_{\iota}+\Big(\frac{81c_{2\theta}}{256}+\frac{243c_{4\theta}}{256}\Big)c_{2\iota}\Big)s_{\frac{\iota}{2}}^{5}\Big]\sin(2\alpha-3\Psi)$$
$$+\Big[\nu\Big(\Big(\frac{4761}{1024}-\frac{1377c_{2\theta}}{1024}\Big)s_{2\theta}+\Big(\frac{837}{256}-\frac{621c_{2\theta}}{256}\Big)c_{\iota}s_{2\theta}+\Big(\frac{243}{1024}$$
$$-\frac{2187c_{2\theta}}{1024}\Big)c_{2\iota}s_{2\theta}\Big)s_{\frac{\iota}{2}}^{6}+\Big(\Big(-\frac{11673}{2048}+\frac{1377c_{2\theta}}{2048}\Big)s_{2\theta}+\Big(-\frac{837}{512}$$
$$+\frac{621c_{2\theta}}{512}\Big)c_{\iota}s_{2\theta}+\Big(-\frac{243}{2048}+\frac{2187c_{2\theta}}{2048}\Big)c_{2\iota}s_{2\theta}\Big)s_{\frac{\iota}{2}}^{6}\Big]\sin(3\alpha-3\Psi)$$
$$+\Big[\nu c_{\frac{\iota}{2}}\Big(\Big(\frac{81}{32}-\frac{27c_{2\theta}}{16}\Big)s_{\theta}^{2}+\Big(-\frac{81}{32}-\frac{81c_{2\theta}}{16}\Big)c_{\iota}s_{\theta}^{2}\Big)s_{\frac{\iota}{2}}^{7}$$
$$+c_{\frac{\iota}{2}}\Big(\Big(-\frac{81}{64}+\frac{27c_{2\theta}}{32}\Big)s_{\theta}^{2}+\Big(\frac{81}{64}+\frac{81c_{2\theta}}{32}\Big)c_{\iota}s_{\theta}^{2}\Big)s_{\frac{\iota}{2}}^{7}\Big]\sin(4\alpha-3\Psi)$$
$$+\Big(\frac{81}{64}c_{\theta}c_{\frac{\iota}{2}}^{2}s_{\theta}^{3}s_{\frac{\iota}{2}}^{8}-\frac{81}{32}\nu c_{\theta}c_{\frac{\iota}{2}}^{2}s_{\theta}^{3}s_{\frac{\iota}{2}}^{8}\Big)\sin(5\alpha-3\Psi)+\Big[\frac{683c_{\theta}s_{\theta}}{16384}$$
$$+\Big(\frac{557}{4096}-\frac{11c_{2\theta}}{12288}\Big)c_{2\iota}s_{2\theta}+\Big(-\frac{1719}{32768}+\frac{91c_{2\theta}}{32768}\Big)c_{3\iota}s_{2\theta}-\frac{c_{\theta}s_{3\theta}}{16384}$$
$$+c_{\iota}\Big(-\frac{10511c_{\theta}s_{\theta}}{49152}+\frac{173c_{\theta}s_{3\theta}}{49152}\Big)+\nu\Big(\frac{85c_{\theta}s_{\theta}}{8192}+\Big(-\frac{679}{6144}+\frac{11c_{2\theta}}{6144}\Big)c_{2\iota}s_{2\theta}$$
$$+\Big(-\frac{201}{16384}-\frac{91c_{2\theta}}{16384}\Big)c_{3\iota}s_{2\theta}+\frac{c_{\theta}s_{3\theta}}{8192}+c_{\iota}\Big(\frac{6031c_{\theta}s_{\theta}}{24576}-\frac{173c_{\theta}s_{3\theta}}{24576}\Big)$$
$$+c_{5\iota}\Big(-\frac{7s_{2\theta}}{49152}-\frac{7s_{4\theta}}{32768}\Big)+c_{4\iota}\Big(-\frac{37s_{2\theta}}{24576}+\frac{91s_{4\theta}}{16384}\Big)\Big)$$
$$+c_{4\iota}\Big(\frac{37s_{2\theta}}{49152}-\frac{91s_{4\theta}}{32768}\Big)+c_{5\iota}\Big(\frac{7s_{2\theta}}{98304}+\frac{7s_{4\theta}}{65536}\Big)\Big]\sin(\alpha-\Psi)$$
$$+\Big[\nu\Big(\frac{19}{512}c_{4\theta}c_{\frac{3\iota}{2}}+\frac{9}{512}c_{4\theta}c_{\frac{5\iota}{2}}+c_{\frac{\iota}{2}}\Big(-\frac{11}{16}-\frac{35c_{2\theta}}{128}+\frac{79c_{4\theta}}{1536}$$
$$+\Big(\frac{1}{32}-\frac{37c_{2\theta}}{256}\Big)c_{\iota}+\Big(\frac{1}{32}+\frac{3c_{2\theta}}{128}\Big)c_{2\iota}-\frac{1}{768}c_{2\theta}c_{3\iota}\Big)-\frac{1}{512}c_{4\theta}c_{\frac{7\iota}{2}}\Big)s_{\frac{\iota}{2}}^{3}$$
$$+\Big(-\frac{19c_{4\theta}c_{\frac{3\iota}{2}}}{1024}-\frac{9c_{4\theta}c_{\frac{5\iota}{2}}}{1024}+c_{\frac{\iota}{2}}\Big(\frac{19}{32}-\frac{23c_{2\theta}}{768}-\frac{79c_{4\theta}}{3072}+\Big(-\frac{1}{64}$$
$$-\frac{347c_{2\theta}}{512}\Big)c_{\iota}+\Big(-\frac{1}{64}-\frac{3c_{2\theta}}{256}\Big)c_{2\iota}+\frac{c_{2\theta}c_{3\iota}}{1536}\Big)+\frac{c_{4\theta}c_{\frac{7\iota}{2}}}{1024}\Big)s_{\frac{\iota}{2}}^{3}\Big]\sin(2\alpha-\Psi)$$
$$+\Big[c_{\frac{\iota}{2}}^{2}\Big(-\frac{355s_{2\theta}}{1024}+c_{\iota}\Big(-\frac{13s_{2\theta}}{256}-\frac{11s_{4\theta}}{512}\Big)+c_{2\iota}\Big(-\frac{s_{2\theta}}{1024}+\frac{9s_{4\theta}}{2048}\Big)$$

$$
\begin{aligned}
&- \frac{5s_{4\theta}}{2048}\Big)s_{\frac{\iota}{2}}^4 + \nu c_{\frac{\iota}{2}}^2\Big(- \frac{29s_{2\theta}}{512} + c_{2\iota}\Big(\frac{s_{2\theta}}{512} - \frac{9s_{4\theta}}{1024}\Big) + c_\iota\Big(\frac{13s_{2\theta}}{128} + \frac{11s_{4\theta}}{256}\Big)\\
&+ \frac{5s_{4\theta}}{1024}\Big)s_{\frac{\iota}{2}}^4\Big]\sin(3\alpha - \Psi) + \Big[\nu c_{\frac{\iota}{2}}^3\Big(\Big(\frac{7}{48} + \frac{c_{2\theta}}{24}\Big)s_\theta^2 + \Big(- \frac{1}{48}\\
&- \frac{c_{2\theta}}{24}\Big)c_\iota s_\theta^2\Big)s_{\frac{\iota}{2}}^5 + c_{\frac{\iota}{2}}^3\Big(\Big(- \frac{7}{96} - \frac{c_{2\theta}}{48}\Big)s_\theta^2 + \Big(\frac{1}{96} + \frac{c_{2\theta}}{48}\Big)c_\iota s_\theta^2\Big)s_{\frac{\iota}{2}}^5\Big]\\
&\times \sin(4\alpha - \Psi) + \Big(\frac{1}{96}c_\theta c_{\frac{\iota}{2}}^4 s_\theta^3 s_{\frac{\iota}{2}}^6 - \frac{1}{48}\nu c_\theta c_{\frac{\iota}{2}}^4 s_\theta^3 s_{\frac{\iota}{2}}^6\Big)\sin(5\alpha - \Psi)\\
&+ \Big[\Big(- \frac{77}{256} + \frac{c_{2\theta}}{256}\Big)s_\theta^2 s_{2\iota} + \Big(\frac{5}{512} + \frac{7c_{2\theta}}{512}\Big)s_\theta^2 s_{4\iota} + \nu\Big(\Big(\frac{45}{128} - \frac{c_{2\theta}}{128}\Big)s_\theta^2 s_{2\iota}\\
&+ \Big(- \frac{5}{256} - \frac{7c_{2\theta}}{256}\Big)s_\theta^2 s_{4\iota}\Big)\Big]\sin(\Psi) + \Big(\nu\Big(- \frac{135}{32} - \frac{189c_{2\theta}}{32}\Big)c_\iota s_\theta^2 s_\iota^3\\
&+ \Big(\frac{135}{64} + \frac{189c_{2\theta}}{64}\Big)c_\iota s_\theta^2 s_\iota^3\Big)\sin(3\Psi) + \Big[- \frac{683c_\theta s_\theta}{16384} + \Big(- \frac{557}{4096}\\
&+ \frac{11c_{2\theta}}{12288}\Big)c_{2\iota}s_{2\theta} + \Big(- \frac{1719}{32768} + \frac{91c_{2\theta}}{32768}\Big)c_{3\iota}s_{2\theta} + \frac{c_\theta s_{3\theta}}{16384}\\
&+ c_\iota\Big(- \frac{10511c_\theta s_\theta}{49152} + \frac{173c_\theta s_{3\theta}}{49152}\Big) + \nu\Big(- \frac{85c_\theta s_\theta}{8192} + \Big(\frac{679}{6144} - \frac{11c_{2\theta}}{6144}\Big)c_{2\iota}s_{2\theta}\\
&+ \Big(- \frac{201}{16384} - \frac{91c_{2\theta}}{16384}\Big)c_{3\iota}s_{2\theta} - \frac{c_\theta s_{3\theta}}{8192} + c_\iota\Big(\frac{6031c_\theta s_\theta}{24576} - \frac{173c_\theta s_{3\theta}}{24576}\Big)\\
&+ c_{4\iota}\Big(\frac{37s_{2\theta}}{24576} - \frac{91s_{4\theta}}{16384}\Big) + c_{5\iota}\Big(- \frac{7s_{2\theta}}{49152} - \frac{7s_{4\theta}}{32768}\Big)\Big) + c_{5\iota}\Big(\frac{7s_{2\theta}}{98304}\\
&+ \frac{7s_{4\theta}}{65536}\Big) + c_{4\iota}\Big(- \frac{37s_{2\theta}}{49152} + \frac{91s_{4\theta}}{32768}\Big)\Big]\sin(\alpha + \Psi) + \Big[c_{\frac{\iota}{2}}^3\Big(\frac{19}{32} - \frac{23c_{2\theta}}{768}\\
&- \frac{79c_{4\theta}}{3072} + \Big(\frac{1}{64} + \frac{347c_{2\theta}}{512}\Big)c_\iota + \Big(- \frac{1}{64} - \frac{3c_{2\theta}}{256}\Big)c_{2\iota} - \frac{c_{2\theta}c_{3\iota}}{1536}\Big)s_{\frac{\iota}{2}}\\
&+ \frac{19c_{4\theta}c_{\frac{\iota}{2}}^3 s_{\frac{3\iota}{2}}}{1024} - \frac{9c_{4\theta}c_{\frac{\iota}{2}}^3 s_{\frac{5\iota}{2}}}{1024} - \frac{c_{4\theta}c_{\frac{\iota}{2}}^3 s_{\frac{7\iota}{2}}}{1024} + \nu\Big(c_{\frac{\iota}{2}}^3\Big(- \frac{11}{16} - \frac{35c_{2\theta}}{128} + \frac{79c_{4\theta}}{1536}\\
&+ \Big(- \frac{1}{32} + \frac{37c_{2\theta}}{256}\Big)c_\iota + \Big(\frac{1}{32} + \frac{3c_{2\theta}}{128}\Big)c_{2\iota} + \frac{1}{768}c_{2\theta}c_{3\iota}\Big)s_{\frac{\iota}{2}} - \frac{19}{512}c_{4\theta}c_{\frac{\iota}{2}}^3 s_{\frac{3\iota}{2}}\\
&+ \frac{9}{512}c_{4\theta}c_{\frac{\iota}{2}}^3 s_{\frac{5\iota}{2}} + \frac{1}{512}c_{4\theta}c_{\frac{\iota}{2}}^3 s_{\frac{7\iota}{2}}\Big)\Big]\sin(2\alpha + \Psi) + \Big[\nu c_{\frac{\iota}{2}}^4\Big(\frac{29s_{2\theta}}{512}\\
&+ c_{2\iota}\Big(- \frac{s_{2\theta}}{512} + \frac{9s_{4\theta}}{1024}\Big) + c_\iota\Big(\frac{13s_{2\theta}}{128} + \frac{11s_{4\theta}}{256}\Big) - \frac{5s_{4\theta}}{1024}\Big)s_{\frac{\iota}{2}}^2 + c_{\frac{\iota}{2}}^4\Big(\frac{355s_{2\theta}}{1024}\\
&+ c_\iota\Big(- \frac{13s_{2\theta}}{256} - \frac{11s_{4\theta}}{512}\Big) + c_{2\iota}\Big(\frac{s_{2\theta}}{1024} - \frac{9s_{4\theta}}{2048}\Big) + \frac{5s_{4\theta}}{2048}\Big)s_{\frac{\iota}{2}}^2\Big]\sin(3\alpha + \Psi)
\end{aligned}
$$

$$+\Big[c_{\frac{\iota}{2}}^{5}\Big(\Big(-\frac{7}{96}-\frac{c_{2\theta}}{48}\Big)s_{\theta}^{2}+\Big(-\frac{1}{96}-\frac{c_{2\theta}}{48}\Big)c_{\iota}s_{\theta}^{2}\Big)s_{\frac{\iota}{2}}^{3}+\nu c_{\frac{\iota}{2}}^{5}\Big(\Big(\frac{7}{48}+\frac{c_{2\theta}}{24}\Big)s_{\theta}^{2}$$
$$+\Big(\frac{1}{48}+\frac{c_{2\theta}}{24}\Big)c_{\iota}s_{\theta}^{2}\Big)s_{\frac{\iota}{2}}^{3}\Big]\sin(4\alpha+\Psi)+\Big(-\frac{1}{96}c_{\theta}c_{\frac{\iota}{2}}^{6}s_{\theta}^{3}s_{\frac{\iota}{2}}^{4}+\frac{1}{48}\nu c_{\theta}c_{\frac{\iota}{2}}^{6}s_{\theta}^{3}s_{\frac{\iota}{2}}^{4}\Big)$$
$$\times\sin(5\alpha+\Psi)+\Big[\nu c_{\frac{\iota}{2}}^{4}\Big(\frac{4923s_{2\theta}}{512}+c_{\iota}\Big(\frac{459s_{2\theta}}{128}-\frac{2079s_{4\theta}}{256}\Big)$$
$$+c_{2\iota}\Big(-\frac{567s_{2\theta}}{512}-\frac{1701s_{4\theta}}{1024}\Big)+\frac{945s_{4\theta}}{1024}\Big)s_{\frac{\iota}{2}}^{2}+c_{\frac{\iota}{2}}^{4}\Big(-\frac{22203s_{2\theta}}{1024}$$
$$+c_{2\iota}\Big(\frac{567s_{2\theta}}{1024}+\frac{1701s_{4\theta}}{2048}\Big)-\frac{945s_{4\theta}}{2048}+c_{\iota}\Big(-\frac{459s_{2\theta}}{256}+\frac{2079s_{4\theta}}{512}\Big)\Big)s_{\frac{\iota}{2}}^{2}\Big]$$
$$\times\sin(\alpha+3\Psi)+\Big[\nu c_{\frac{\iota}{2}}^{5}\Big(\frac{27}{16}+\frac{1233c_{2\theta}}{128}+\frac{27c_{4\theta}}{128}+\Big(-\frac{27}{8}-\frac{27c_{2\theta}}{16}$$
$$-\frac{27c_{4\theta}}{16}\Big)c_{\iota}+\Big(-\frac{81c_{2\theta}}{128}-\frac{243c_{4\theta}}{128}\Big)c_{2\iota}\Big)s_{\frac{\iota}{2}}+c_{\frac{\iota}{2}}^{5}\Big(-\frac{27}{32}-\frac{4689c_{2\theta}}{256}$$
$$-\frac{27c_{4\theta}}{256}+\Big(\frac{27}{16}+\frac{27c_{2\theta}}{32}+\frac{27c_{4\theta}}{32}\Big)c_{\iota}+\Big(\frac{81c_{2\theta}}{256}+\frac{243c_{4\theta}}{256}\Big)c_{2\iota}\Big)s_{\frac{\iota}{2}}\Big]$$
$$\times\sin(2\alpha+3\Psi)+\Big[c_{\frac{\iota}{2}}^{6}\Big(\frac{11673s_{2\theta}}{2048}+c_{2\iota}\Big(\frac{243s_{2\theta}}{2048}-\frac{2187s_{4\theta}}{4096}\Big)$$
$$+c_{\iota}\Big(-\frac{837s_{2\theta}}{512}+\frac{621s_{4\theta}}{1024}\Big)-\frac{1377s_{4\theta}}{4096}\Big)+\nu c_{\frac{\iota}{2}}^{6}\Big(-\frac{4761s_{2\theta}}{1024}$$
$$+c_{\iota}\Big(\frac{837s_{2\theta}}{256}-\frac{621s_{4\theta}}{512}\Big)+\frac{1377s_{4\theta}}{2048}+c_{2\iota}\Big(-\frac{243s_{2\theta}}{1024}+\frac{2187s_{4\theta}}{2048}\Big)\Big)\Big]$$
$$\times\sin(3\alpha+3\Psi)+\Big[c_{\frac{\iota}{2}}^{7}\Big(\Big(-\frac{81}{64}+\frac{27c_{2\theta}}{32}\Big)s_{\theta}^{2}+\Big(-\frac{81}{64}-\frac{81c_{2\theta}}{32}\Big)c_{\iota}s_{\theta}^{2}\Big)s_{\frac{\iota}{2}}$$
$$+\nu c_{\frac{\iota}{2}}^{7}\Big(\Big(\frac{81}{32}-\frac{27c_{2\theta}}{16}\Big)s_{\theta}^{2}+\Big(\frac{81}{32}+\frac{81c_{2\theta}}{16}\Big)c_{\iota}s_{\theta}^{2}\Big)s_{\frac{\iota}{2}}\Big]\sin(4\alpha+3\Psi)$$
$$+\Big(-\frac{81}{64}c_{\theta}c_{\frac{\iota}{2}}^{8}s_{\theta}^{3}s_{\frac{\iota}{2}}^{2}+\frac{81}{32}\nu c_{\theta}c_{\frac{\iota}{2}}^{8}s_{\theta}^{3}s_{\frac{\iota}{2}}^{2}\Big)\sin(5\alpha+3\Psi)+\Big(\nu c_{\frac{\iota}{2}}^{6}\Big(-\frac{4375s_{2\theta}}{192}$$
$$-\frac{4375s_{4\theta}}{128}\Big)s_{\frac{\iota}{2}}^{4}+c_{\frac{\iota}{2}}^{6}\Big(\frac{4375s_{2\theta}}{384}+\frac{4375s_{4\theta}}{256}\Big)s_{\frac{\iota}{2}}^{4}\Big)\sin(\alpha+5\Psi)$$
$$+\Big(\nu\Big(-\frac{625c_{2\theta}}{48}-\frac{625c_{4\theta}}{16}\Big)c_{\frac{\iota}{2}}^{7}s_{\frac{\iota}{2}}^{3}+\Big(\frac{625c_{2\theta}}{96}+\frac{625c_{4\theta}}{32}\Big)c_{\frac{\iota}{2}}^{7}s_{\frac{\iota}{2}}^{3}\Big)$$
$$\times\sin(2\alpha+5\Psi)+\Big(c_{\frac{\iota}{2}}^{8}\Big(\frac{625s_{2\theta}}{256}-\frac{5625s_{4\theta}}{512}\Big)s_{\frac{\iota}{2}}^{2}+\nu c_{\frac{\iota}{2}}^{8}\Big(-\frac{625s_{2\theta}}{128}$$
$$+\frac{5625s_{4\theta}}{256}\Big)s_{\frac{\iota}{2}}^{2}\Big)\sin(3\alpha+5\Psi)+\Big(\nu\Big(-\frac{625}{48}-\frac{625c_{2\theta}}{24}\Big)c_{\frac{\iota}{2}}^{9}s_{\theta}^{2}s_{\frac{\iota}{2}}$$

$$+\Big(\frac{625}{96}+\frac{625c_{2\theta}}{48}\Big)c_{\frac{\iota}{2}}^{9}s_{\theta}^{2}s_{\frac{\iota}{2}}\Big)\sin(4\alpha+5\Psi)$$
$$+\Big(-\frac{625}{192}c_{\theta}c_{\frac{\iota}{2}}^{10}s_{\theta}^{3}+\frac{625}{96}\nu c_{\theta}c_{\frac{\iota}{2}}^{10}s_{\theta}^{3}\Big)\sin(5\alpha+5\Psi)\Big], \tag{A.3d}$$

$$\hat{h}_{\times}^{(1,\mathrm{SO})}=\chi_{a}^{y}\Big(\frac{1}{2}+\frac{c_{\iota}}{2}\Big)\cos(\alpha+\Psi)+\chi_{a}^{y}\cos(\alpha-\Psi)s_{\frac{\iota}{2}}^{2}+\Big(\chi_{a}^{x}\Big(\frac{c_{\theta}^{2}}{2}-\frac{1}{2}c_{\theta}^{2}c_{\iota}\Big)$$
$$+\chi_{a}^{z}\Big(-\frac{1}{2}c_{\theta}s_{\theta}+\frac{1}{2}c_{\theta}c_{\iota}s_{\theta}\Big)\Big)\sin(\alpha-\Psi)+\Big(\chi_{a}^{x}c_{\theta}s_{\theta}s_{\iota}-\chi_{a}^{z}s_{\theta}^{2}s_{\iota}\Big)\sin(\Psi)$$
$$+\Big(\chi_{a}^{x}\Big(\frac{c_{\theta}^{2}}{2}+\frac{1}{2}c_{\theta}^{2}c_{\iota}\Big)+\chi_{a}^{z}\Big(-\frac{1}{2}c_{\theta}s_{\theta}-\frac{1}{2}c_{\theta}c_{\iota}s_{\theta}\Big)\Big)\sin(\alpha+\Psi)$$
$$+\delta\Big[\chi_{s}^{y}\Big(\frac{1}{2}+\frac{c_{\iota}}{2}\Big)\cos(\alpha+\Psi)+\chi_{s}^{y}\cos(\alpha-\Psi)s_{\frac{\iota}{2}}^{2}+\Big(\chi_{s}^{x}\Big(\frac{c_{\theta}^{2}}{2}-\frac{1}{2}c_{\theta}^{2}c_{\iota}\Big)$$
$$+\chi_{s}^{z}\Big(-\frac{1}{2}c_{\theta}s_{\theta}+\frac{1}{2}c_{\theta}c_{\iota}s_{\theta}\Big)\Big)\sin(\alpha-\Psi)+\Big(\chi_{s}^{x}c_{\theta}s_{\theta}s_{\iota}-\chi_{s}^{z}s_{\theta}^{2}s_{\iota}\Big)\sin(\Psi)$$
$$+\Big(\chi_{s}^{x}\Big(\frac{c_{\theta}^{2}}{2}+\frac{1}{2}c_{\theta}^{2}c_{\iota}\Big)+\chi_{s}^{z}\Big(-\frac{1}{2}c_{\theta}s_{\theta}-\frac{1}{2}c_{\theta}c_{\iota}s_{\theta}\Big)\Big)\sin(\alpha+\Psi)\Big], \tag{A.3e}$$

$$\hat{h}_{\times}^{(3/2,\mathrm{SO})}=\chi_{s}^{y}\Big(2c_{\iota}^{3}s_{\theta}-\nu c_{\iota}^{3}s_{\theta}\Big)+\chi_{s}^{y}\cos(2\alpha+2\Psi)\Big(\nu c_{\frac{\iota}{2}}^{4}\Big(-\frac{5s_{\theta}}{3}+\frac{2c_{\iota}s_{\theta}}{3}\Big)$$
$$+c_{\frac{\iota}{2}}^{4}\Big(-\frac{14s_{\theta}}{3}+\frac{20c_{\iota}s_{\theta}}{3}\Big)\Big)+\chi_{s}^{y}\cos(3\alpha+2\Psi)\Big(-\frac{20}{3}c_{\theta}c_{\frac{\iota}{2}}^{5}s_{\frac{\iota}{2}}-\frac{2}{3}\nu c_{\theta}c_{\frac{\iota}{2}}^{5}s_{\frac{\iota}{2}}\Big)$$
$$+\chi_{s}^{y}\cos(\alpha+2\Psi)\Big(\nu c_{\frac{\iota}{2}}^{3}\Big(\frac{7c_{\theta}}{3}+\frac{c_{\theta}c_{\iota}}{3}\Big)s_{\frac{\iota}{2}}+c_{\frac{\iota}{2}}^{3}\Big(-\frac{2c_{\theta}}{3}+\frac{10c_{\theta}c_{\iota}}{3}\Big)s_{\frac{\iota}{2}}\Big)$$
$$+\chi_{s}^{y}\cos(\alpha-2\Psi)\Big(c_{\frac{\iota}{2}}\Big(-\frac{2c_{\theta}}{3}-\frac{10c_{\theta}c_{\iota}}{3}\Big)s_{\frac{\iota}{2}}^{3}+\nu c_{\frac{\iota}{2}}\Big(\frac{7c_{\theta}}{3}-\frac{c_{\theta}c_{\iota}}{3}\Big)s_{\frac{\iota}{2}}^{3}\Big)$$
$$+\chi_{s}^{y}\cos(2\alpha-2\Psi)\Big(\nu\Big(\frac{5s_{\theta}}{3}+\frac{2c_{\iota}s_{\theta}}{3}\Big)s_{\frac{\iota}{2}}^{4}+\Big(\frac{14s_{\theta}}{3}+\frac{20c_{\iota}s_{\theta}}{3}\Big)s_{\frac{\iota}{2}}^{4}\Big)$$
$$+\chi_{s}^{y}\cos(3\alpha-2\Psi)\Big(-\frac{20}{3}c_{\theta}c_{\frac{\iota}{2}}s_{\frac{\iota}{2}}^{5}-\frac{2}{3}\nu c_{\theta}c_{\frac{\iota}{2}}s_{\frac{\iota}{2}}^{5}\Big)+\chi_{s}^{y}\cos(2\alpha)$$
$$\times\Big(2c_{\iota}s_{\theta}s_{\iota}^{2}-\nu c_{\iota}s_{\theta}s_{\iota}^{2}\Big)+\chi_{s}^{y}\cos(2\Psi)\Big(\frac{10}{3}c_{\iota}s_{\theta}s_{\iota}^{2}+\frac{1}{3}\nu c_{\iota}s_{\theta}s_{\iota}^{2}\Big)$$
$$+\chi_{s}^{y}\cos(3\alpha)\Big(-c_{\theta}s_{\iota}^{3}+\frac{1}{2}\nu c_{\theta}s_{\iota}^{3}\Big)+\chi_{s}^{y}\cos(\alpha)\Big(-\frac{5}{4}c_{\theta}s_{\iota}-\frac{1}{4}c_{\theta}s_{3\iota}$$
$$+\nu\Big(\frac{5c_{\theta}s_{\iota}}{8}+\frac{1}{8}c_{\theta}s_{3\iota}\Big)\Big)+\Big[\chi_{s}^{x}\Big(\Big(-\frac{3c_{\theta}}{2}-\frac{1}{2}c_{\theta}c_{2\iota}\Big)s_{\iota}+\nu\Big(\frac{3c_{\theta}}{4}+\frac{1}{4}c_{\theta}c_{2\iota}\Big)s_{\iota}\Big)$$
$$+\chi_{s}^{z}\Big(-2c_{2\iota}s_{\theta}s_{\iota}+\nu c_{2\iota}s_{\theta}s_{\iota}\Big)\Big]\sin(\alpha)+\Big(\chi_{s}^{z}\Big(2c_{\theta}c_{\iota}s_{\iota}^{2}-\nu c_{\theta}c_{\iota}s_{\iota}^{2}\Big)$$

$$
\begin{aligned}
&+ \chi_s^x\Big(- 2c_\iota s_\theta s_\iota^2 + \nu c_\iota s_\theta s_\iota^2\Big)\Big)\sin(2\alpha) + \chi_s^x\Big(c_\theta s_\iota^3 - \frac{1}{2}\nu c_\theta s_\iota^3\Big)\sin(3\alpha)\\
&+ \Bigg[\chi_s^x\Bigg(c_{\frac{\iota}{2}}\Big(- \frac{2c_\theta}{3} - \frac{10c_\theta c_\iota}{3}\Big)s_{\frac{\iota}{2}}^3 + \nu c_{\frac{\iota}{2}}\Big(- \frac{5c_\theta}{3} + 4c_{3\theta} - \frac{c_\theta c_\iota}{3}\Big)s_{\frac{\iota}{2}}^3\Bigg)\\
&+ \chi_s^z\Bigg(c_{\frac{\iota}{2}}\Big(- 4s_\theta - \frac{40c_\iota s_\theta}{3}\Big)s_{\frac{\iota}{2}}^3 + \nu c_{\frac{\iota}{2}}\Big(- 2s_\theta - \frac{4c_\iota s_\theta}{3} - 4s_{3\theta}\Big)s_{\frac{\iota}{2}}^3\Bigg)\Bigg]\\
&\times \sin(\alpha - 2\Psi) + \Bigg[\chi_s^z\Bigg(\nu\Big(5c_\theta + c_{3\theta} + \frac{2c_\theta c_\iota}{3}\Big)s_{\frac{\iota}{2}}^4 + \Big(4c_\theta + \frac{20c_\theta c_\iota}{3}\Big)s_{\frac{\iota}{2}}^4\Bigg)\\
&+ \chi_s^x\Bigg(\Big(- \frac{14s_\theta}{3} - \frac{20c_\iota s_\theta}{3}\Big)s_{\frac{\iota}{2}}^4 + \nu\Big(\frac{10s_\theta}{3} - \frac{2c_\iota s_\theta}{3} + s_{3\theta}\Big)s_{\frac{\iota}{2}}^4\Bigg)\Bigg]\\
&\times \sin(2\alpha - 2\Psi) + \chi_s^x\Big(\frac{20}{3}c_\theta c_{\frac{\iota}{2}} s_{\frac{\iota}{2}}^5 + \frac{2}{3}\nu c_\theta c_{\frac{\iota}{2}} s_{\frac{\iota}{2}}^5\Big)\sin(3\alpha - 2\Psi)\\
&+ \Bigg[- 6\nu\chi_s^z c_\theta s_\theta^2 s_\iota^2 + \chi_s^x\Bigg(\frac{1}{3}s_\theta s_\iota^2 + \nu\Big(- \frac{7}{6} + 3c_{2\theta}\Big)s_\theta s_\iota^2\Bigg)\Bigg]\sin(2\Psi)\\
&+ \Bigg[\chi_s^x\Bigg(\nu c_{\frac{\iota}{2}}^3\Big(- \frac{5c_\theta}{3} + 4c_{3\theta} + \frac{c_\theta c_\iota}{3}\Big)s_{\frac{\iota}{2}} + c_{\frac{\iota}{2}}^3\Big(- \frac{2c_\theta}{3} + \frac{10c_\theta c_\iota}{3}\Big)s_{\frac{\iota}{2}}\Bigg)\\
&+ \chi_s^z\Bigg(c_{\frac{\iota}{2}}^3\Big(- 4s_\theta + \frac{40c_\iota s_\theta}{3}\Big)s_{\frac{\iota}{2}} + \nu c_{\frac{\iota}{2}}^3\Big(- 2s_\theta + \frac{4c_\iota s_\theta}{3} - 4s_{3\theta}\Big)s_{\frac{\iota}{2}}\Bigg)\Bigg]\\
&\times \sin(\alpha + 2\Psi) + \Bigg[\chi_s^z\Bigg(\nu c_{\frac{\iota}{2}}^4\Big(- 5c_\theta - c_{3\theta} + \frac{2c_\theta c_\iota}{3}\Big) + c_{\frac{\iota}{2}}^4\Big(- 4c_\theta\\
&+ \frac{20c_\theta c_\iota}{3}\Big)\Bigg) + \chi_s^x\Bigg(c_{\frac{\iota}{2}}^4\Big(\frac{14s_\theta}{3} - \frac{20c_\iota s_\theta}{3}\Big) + \nu c_{\frac{\iota}{2}}^4\Big(- \frac{10s_\theta}{3} - \frac{2c_\iota s_\theta}{3} - s_{3\theta}\Big)\Bigg)\Bigg]\\
&\times \sin(2\alpha + 2\Psi) + \chi_s^x\Big(\frac{20}{3}c_\theta c_{\frac{\iota}{2}}^5 s_{\frac{\iota}{2}} + \frac{2}{3}\nu c_\theta c_{\frac{\iota}{2}}^5 s_{\frac{\iota}{2}}\Big)\sin(3\alpha + 2\Psi)\\
&+ \delta\Bigg[2\chi_a^y c_\iota^3 s_\theta + \chi_a^y c_{\frac{\iota}{2}}^4\cos(2\alpha + 2\Psi)\Big(- \frac{14s_\theta}{3} + \frac{20c_\iota s_\theta}{3}\Big)\\
&+ \chi_a^y c_{\frac{\iota}{2}}^3\Big(- \frac{2c_\theta}{3} + \frac{10c_\theta c_\iota}{3}\Big)\cos(\alpha + 2\Psi)s_{\frac{\iota}{2}} - \frac{20}{3}\chi_a^y c_\theta c_{\frac{\iota}{2}}^5 s_{\frac{\iota}{2}}\cos(3\alpha + 2\Psi)\\
&+ \chi_a^y c_{\frac{\iota}{2}}\Big(- \frac{2c_\theta}{3} - \frac{10c_\theta c_\iota}{3}\Big)\cos(\alpha - 2\Psi)s_{\frac{\iota}{2}}^3 + \chi_a^y\cos(2\alpha - 2\Psi)\\
&\times \Big(\frac{14s_\theta}{3} + \frac{20c_\iota s_\theta}{3}\Big)s_{\frac{\iota}{2}}^4 - \frac{20}{3}\chi_a^y c_\theta c_{\frac{\iota}{2}}\cos(3\alpha - 2\Psi)s_{\frac{\iota}{2}}^5 + 2\chi_a^y c_\iota\cos(2\alpha)s_\theta s_\iota^2\\
&+ \frac{10}{3}\chi_a^y c_\iota\cos(2\Psi)s_\theta s_\iota^2 - \chi_a^y c_\theta\cos(3\alpha)s_\iota^3 + \chi_a^y\cos(\alpha)\Big(- \frac{5}{4}c_\theta s_\iota - \frac{1}{4}c_\theta s_{3\iota}\Big)\\
&+ \Bigg(\chi_a^x\Big(- \frac{3c_\theta}{2} - \frac{1}{2}c_\theta c_{2\iota}\Big)s_\iota - 2\chi_a^z c_{2\iota} s_\theta s_\iota\Bigg)\sin(\alpha)\\
&+ \Big(2\chi_a^z c_\theta c_\iota s_\iota^2 - 2\chi_a^x c_\iota s_\theta s_\iota^2\Big)\sin(2\alpha) + \chi_a^x c_\theta s_\iota^3\sin(3\alpha)
\end{aligned}
$$

$$
\begin{aligned}
&+\left(\chi_a^x c_{\frac{\iota}{2}}\Big(-\frac{2c_\theta}{3}-\frac{10c_\theta c_\iota}{3}\Big)s_{\frac{\iota}{2}}^3+\chi_a^z c_{\frac{\iota}{2}}\Big(-4s_\theta-\frac{40c_\iota s_\theta}{3}\Big)s_{\frac{\iota}{2}}^3\right)\\
&\times\sin(\alpha-2\Psi)+\left(\chi_a^z\Big(4c_\theta+\frac{20c_\theta c_\iota}{3}\Big)s_{\frac{\iota}{2}}^4+\chi_a^x\Big(-\frac{14s_\theta}{3}-\frac{20c_\iota s_\theta}{3}\Big)s_{\frac{\iota}{2}}^4\right)\\
&\times\sin(2\alpha-2\Psi)+\frac{20}{3}\chi_a^x c_\theta c_{\frac{\iota}{2}}s_{\frac{\iota}{2}}^5\sin(3\alpha-2\Psi)+\frac{1}{3}\chi_a^x s_\theta s_\iota^2\sin(2\Psi)\\
&+\left(\chi_a^x c_{\frac{\iota}{2}}^3\Big(-\frac{2c_\theta}{3}+\frac{10c_\theta c_\iota}{3}\Big)s_{\frac{\iota}{2}}+\chi_a^z c_{\frac{\iota}{2}}^3\Big(-4s_\theta+\frac{40c_\iota s_\theta}{3}\Big)s_{\frac{\iota}{2}}\right)\\
&\times\sin(\alpha+2\Psi)+\left(\chi_a^z c_{\frac{\iota}{2}}^4\Big(-4c_\theta+\frac{20c_\theta c_\iota}{3}\Big)+\chi_a^x c_{\frac{\iota}{2}}^4\Big(\frac{14s_\theta}{3}-\frac{20c_\iota s_\theta}{3}\Big)\right)\\
&\times\sin(2\alpha+2\Psi)+\frac{20}{3}\chi_a^x c_\theta c_{\frac{\iota}{2}}^5 s_{\frac{\iota}{2}}\sin(3\alpha+2\Phi)\Big]. \qquad \text{(A.3f)}
\end{aligned}
$$

where s_X and c_X are shorthand for $\sin X$ and $\cos X$, respectively, with $X=\theta,\iota,\ldots$.

Appendix B

Gravitational-wave modes for precessing binaries on nearly circular orbits through 1.5PN order: generic inclination angles

In Sec. 4.4 we wrote the gravitational-wave modes expanded in the inclination angle ι. Here we give the full expression of the h_{22}, h_{33} and h_{21} modes. They read

$$
\begin{aligned}
h_{22} \;=\; & -\frac{2\,M\,\nu\,v^2}{D_L}\,e^{-2i\,(\alpha+\Psi)}\frac{3}{2}\sqrt{\frac{\pi}{5}}\left\{\frac{1}{6}e^{-2i\iota}\left(e^{4i\Psi}\left(-1+e^{i\iota}\right)^4+\left(1+e^{i\iota}\right)^4\right)\right.\\
& +\frac{1}{9}ie^{-i(2\iota-\Psi)}\left[e^{2i\Psi}\left(-1+e^{i\iota}\right)^3\left(1+e^{i\iota}\right)-\left(-1+e^{i\iota}\right)\left(1+e^{i\iota}\right)^3\right]v\,\delta\\
& +v^2\left[\frac{1}{252}e^{-2i\iota}\left(-107e^{4i\Psi}\left(-1+e^{i\iota}\right)^4-107\left(1+e^{i\iota}\right)^4\right)\right.\\
& +\frac{55}{252}e^{-2i\iota}\left(e^{4i\Psi}\left(-1+e^{i\iota}\right)^4+\left(1+e^{i\iota}\right)^4\right)\eta+\frac{1}{3}e^{i(\alpha-\iota+\Psi)}\left(e^{2i\Psi}\left(-1+e^{i\iota}\right)^2\right.\\
& \left.-\left(1+e^{i\iota}\right)^2\right)\chi_a^x+\frac{1}{3}e^{i(\alpha-\iota+\Psi)}\left(e^{2i\Psi}\left(-1+e^{i\iota}\right)^2-\left(1+e^{i\iota}\right)^2\right)\delta\chi_s^x\\
& +i\left(\frac{1}{3}e^{i(\alpha-\iota+\Psi)}\left(-e^{2i\Psi}\left(-1+e^{i\iota}\right)^2+\left(1+e^{i\iota}\right)^2\right)\chi_a^y\right.\\
& \left.\left.+\frac{1}{3}e^{i(\alpha-\iota+\Psi)}\left(-e^{2i\Psi}\left(-1+e^{i\iota}\right)^2+\left(1+e^{i\iota}\right)^2\right)\delta\chi_s^y\right)\right]\\
& +v^3\left[\frac{1}{3}e^{-2i\iota}\left(e^{4i\Psi}\left(-1+e^{i\iota}\right)^4+\left(1+e^{i\iota}\right)^4\right)\pi+\delta\left(\frac{1}{36}e^{-i(\alpha+3\iota)}\right.\right.\\
& \times\left(-5\left(-1+e^{i\iota}\right)\left(1+e^{i\iota}\right)^5+e^{2i\alpha}\left(1+e^{i\iota}\right)^3\left(-5+7e^{i\iota}-7e^{2i\iota}+5e^{3i\iota}\right)\right.\\
& +e^{4i\Psi}\left(-1+e^{i\iota}\right)^3\left(1+e^{i\iota}\right)\left(-5+5e^{2i\alpha}+5e^{2i\iota}\left(-1+e^{2i\alpha}\right)\right.\\
& \left.\left.+2e^{i\iota}\left(5+e^{2i\alpha}\right)\right)+6e^{2i\Psi}\left(\left(-1+e^{2i\iota}\right)^3-e^{2i\alpha}\left(-1-5e^{2i\iota}+5e^{4i\iota}\right.\right.\right.
\end{aligned}
$$

$$+e^{6i\iota}\big)\big)\big)\,\chi_a^y+\frac{1}{18}e^{-3i\iota}\Big(6e^{2i\Psi}\left(-1+e^{2i\iota}\right)^2\left(1+e^{2i\iota}\right)-\left(1+e^{i\iota}\right)^4$$
$$\times\left(5-6e^{i\iota}+5e^{2i\iota}\right)-e^{4i\Psi}\left(-1+e^{i\iota}\right)^4\left(5+6e^{i\iota}+5e^{2i\iota}\right)\Big)\,\chi_a^z\Big)$$
$$+\frac{1}{36}e^{-i(\alpha+3\iota)}\Big(-5\left(-1+e^{i\iota}\right)\left(1+e^{i\iota}\right)^5+e^{2i\alpha}\left(1+e^{i\iota}\right)^3\left(-5+7e^{i\iota}\right.$$
$$\left.-7e^{2i\iota}+5e^{3i\iota}\right)+e^{4i\Psi}\left(-1+e^{i\iota}\right)^3\left(1+e^{i\iota}\right)\left(-5+5e^{2i\alpha}\right.$$
$$\left.+5e^{2i\iota}\left(-1+e^{2i\alpha}\right)+2e^{i\iota}\left(5+e^{2i\alpha}\right)\right)+6e^{2i\Psi}\Big(\left(-1+e^{2i\iota}\right)^3$$
$$-e^{2i\alpha}\left(-1-5e^{2i\iota}+5e^{4i\iota}+e^{6i\iota}\right)\big)\big)\,\chi_s^y+\frac{1}{18}e^{-3i\iota}\Big(6e^{2i\Psi}\left(-1+e^{2i\iota}\right)^2$$
$$\times\left(1+e^{2i\iota}\right)-\left(1+e^{i\iota}\right)^4\left(5-6e^{i\iota}+5e^{2i\iota}\right)-e^{4i\Psi}\left(-1+e^{i\iota}\right)^4$$
$$\times\left(5+6e^{i\iota}+5e^{2i\iota}\right)\big)\,\chi_s^z+i\Big(\delta\Big(\frac{1}{252}e^{-i(2\iota-\Psi)}\Big(-17e^{2i\Psi}\left(-1+e^{i\iota}\right)^3$$
$$\times\left(1+e^{i\iota}\right)+17\left(-1+e^{i\iota}\right)\left(1+e^{i\iota}\right)^3\Big)+\frac{1}{63}e^{-i(2\iota-\Psi)}\left(5e^{2i\Psi}\right.$$
$$\left.\times\left(-1+e^{i\iota}\right)^3\left(1+e^{i\iota}\right)-5\left(-1+e^{i\iota}\right)\left(1+e^{i\iota}\right)^3\right)\eta+\frac{1}{36}e^{-i(\alpha+3\iota)}$$
$$\times\Big(5\left(-1+e^{i\iota}\right)\left(1+e^{i\iota}\right)^5+e^{2i\alpha}\left(1+e^{i\iota}\right)^3\left(-5+7e^{i\iota}\right.$$
$$\left.-7e^{2i\iota}+5e^{3i\iota}\right)+e^{4i\Psi}\left(-1+e^{i\iota}\right)^3\left(1+e^{i\iota}\right)\Big(5\left(-1+e^{i\iota}\right)^2$$
$$+e^{2i\alpha}\left(5+2e^{i\iota}+5e^{2i\iota}\right)\big)+6e^{2i\Psi}\Big(-\left(-1+e^{2i\iota}\right)^3$$
$$-e^{2i\alpha}\left(-1-5e^{2i\iota}+5e^{4i\iota}+e^{6i\iota}\right)\big)\big)\,\chi_a^x\Big)+\frac{1}{36}e^{-i(\alpha+3\iota)}\left(5\left(-1+e^{i\iota}\right)\right.$$
$$\left.\left(1+e^{i\iota}\right)^5+e^{2i\alpha}\left(1+e^{i\iota}\right)^3\left(-5+7e^{i\iota}-7e^{2i\iota}+5e^{3i\iota}\right)\right.$$
$$+e^{4i\Psi}\left(-1+e^{i\iota}\right)^3\left(1+e^{i\iota}\right)\Big(5\left(-1+e^{i\iota}\right)^2+e^{2i\alpha}\left(5+2e^{i\iota}+5e^{2i\iota}\right)\Big)$$
$$+6e^{2i\Psi}\Big(-\left(-1+e^{2i\iota}\right)^3-e^{2i\alpha}\left(-1-5e^{2i\iota}+5e^{4i\iota}+e^{6i\iota}\right)\Big)\Big)\,\chi_s^x$$
$$+\frac{1}{72}e^{-i(\alpha+3\iota)}\Big(\left(-1+e^{i\iota}\right)\left(1+e^{i\iota}\right)^3\left(1+e^{2i\alpha}+e^{2i\iota}\left(1+e^{2i\alpha}\right)\right.$$
$$\left.-2e^{i\iota}\left(-1+9e^{2i\alpha}\right)\right)+e^{4i\Psi}\left(-1+e^{i\iota}\right)^3\left(1+e^{i\iota}\right)\left(1+e^{2i\alpha}\right.$$
$$\left.+e^{2i\iota}\left(1+e^{2i\alpha}\right)+2e^{i\iota}\left(-1+9e^{2i\alpha}\right)\right)+6e^{2i\Psi}\Big(\left(-1+e^{2i\iota}\right)^3$$

$$
\begin{aligned}
&+e^{2i\alpha}\left(-1-5e^{2i\iota}+5e^{4i\iota}+e^{6i\iota}\right)\Big)\,\eta\chi_s^x\Big)+\eta\left(\frac{1}{72}e^{-i(\alpha+3\iota)}\right.\\
&\times\Big(-\left(-1+e^{i\iota}\right)\left(1+e^{i\iota}\right)^5+e^{2i\alpha}\left(1+e^{i\iota}\right)^3\left(-1+19e^{i\iota}-19e^{2i\iota}+e^{3i\iota}\right)\\
&+e^{4i\Psi}\left(-1+e^{i\iota}\right)^3\left(1+e^{i\iota}\right)\left(-1+e^{2i\alpha}+e^{2i\iota}\left(-1+e^{2i\alpha}\right)\right.\\
&+2e^{i\iota}\left(1+9e^{2i\alpha}\right)\Big)+6e^{2i\Psi}\Big(-\left(-1+e^{2i\iota}\right)^3\\
&+e^{2i\alpha}\left(-1-5e^{2i\iota}+5e^{4i\iota}+e^{6i\iota}\right)\Big)\Big)\,\chi_s^y\\
&+\frac{1}{36}e^{-3i\iota}\Big(-6e^{2i\Psi}\left(-1+e^{2i\iota}\right)^2\left(1+e^{2i\iota}\right)-\left(1+e^{i\iota}\right)^4\left(1-10e^{i\iota}+e^{2i\iota}\right)\\
&\left.-e^{4i\Psi}\left(-1+e^{i\iota}\right)^4\left(1+10e^{i\iota}+e^{2i\iota}\right)\Big)\,\chi_s^z\Big)\right]+\mathcal{O}(v^4)\Bigg\}\,, \qquad \text{(B.1)}
\end{aligned}
$$

$$
\begin{aligned}
h_{21} \;=\; & -\frac{2\,M\,\nu\,v^2}{D_L}\,e^{-i\,(\alpha+\Psi)}i\sqrt{\frac{\pi}{5}}\left\{\frac{1}{2}e^{-i(2\iota+\Psi)}\Big(-e^{4i\Psi}\left(-1+e^{i\iota}\right)^3\left(1+e^{i\iota}\right)\right.\\
&-\left(-1+e^{i\iota}\right)\left(1+e^{i\iota}\right)^3\Big)+\frac{1}{3}ie^{-2i\iota}\Big[1+e^{i\iota}+e^{3i\iota}+e^{4i\iota}\\
&-e^{2i\Psi}\left(-1+e^{i\iota}\right)^2\left(1+e^{i\iota}+e^{2i\iota}\right)\Big]v\delta+v^2\Big[\frac{107}{84}e^{-i(2\iota+\Psi)}\left(-1+e^{i\iota}\right)\\
&\times\left(1+e^{i\iota}\right)\Big(e^{4i\Psi}\left(-1+e^{i\iota}\right)^2+\left(1+e^{i\iota}\right)^2\Big)+\frac{1}{84}e^{-i(2\iota+\Psi)}\\
&\times\Big(-55e^{4i\Psi}\left(-1+e^{i\iota}\right)^3\left(1+e^{i\iota}\right)-55\left(-1+e^{i\iota}\right)\left(1+e^{i\iota}\right)^3\Big)\,\eta\\
&-\frac{1}{2}e^{i(\alpha-\iota)}\left(-1+e^{2i\iota}\right)\left(-1+e^{2i\Psi}\right)\chi_a^x-\frac{1}{2}e^{i(\alpha-\iota)}\left(-1+e^{2i\iota}\right)\\
&\times\left(-1+e^{2i\Psi}\right)\delta\chi_s^x+i\left(\frac{1}{2}e^{i(\alpha-\iota)}\left(-1+e^{2i\iota}\right)\left(-1+e^{2i\Psi}\right)\chi_a^y+\right.\\
&\frac{1}{2}e^{-i\iota}\Big(e^{2i\Psi}\left(-1+e^{i\iota}\right)^2-\left(1+e^{i\iota}\right)^2\Big)\,\chi_a^z+\delta\Big(\frac{1}{2}e^{i(\alpha-\iota)}\left(-1+e^{2i\iota}\right)\\
&\left.\times\left(-1+e^{2i\Psi}\right)\chi_s^y+\frac{1}{2}e^{-i\iota}\Big(e^{2i\Psi}\left(-1+e^{i\iota}\right)^2-\left(1+e^{i\iota}\right)^2\Big)\,\chi_s^z\Big)\Big)\Big]\\
&+v^3\Big[e^{-i(2\iota+\Psi)}\Big(-e^{4i\Psi}\left(-1+e^{i\iota}\right)^3\left(1+e^{i\iota}\right)\pi-\left(-1+e^{i\iota}\right)\left(1+e^{i\iota}\right)^3\pi\Big)\\
&+\delta\Big(\frac{1}{12}e^{-i(\alpha+3\iota+\Psi)}\Big(\left(1+e^{i\iota}\right)^4\left(5-7e^{i\iota}+5e^{2i\iota}\right)-e^{2i\alpha}\left(-1+e^{2i\iota}\right)^2\\
&\times\left(5+e^{i\iota}+5e^{2i\iota}\right)+6e^{2i\Psi}\left(1+e^{2i\iota}\right)\Big(-\left(-1+e^{2i\iota}\right)^2+e^{2i\alpha}\left(1+e^{2i\iota}\right)^2\Big)
\end{aligned}
$$

$$
\begin{aligned}
&+e^{4i\Psi}\left(-e^{2i\alpha}\left(-1+e^{2i\iota}\right)^2\left(5-e^{i\iota}+5e^{2i\iota}\right)+\left(-1+e^{i\iota}\right)^4\right.\\
&\left.\times\left(5+7e^{i\iota}+5e^{2i\iota}\right)\right)\chi_a^y+\frac{1}{6}e^{-i(3\iota+\Psi)}\left(\left(1+e^{i\iota}\right)^3\left(-5+8e^{i\iota}\right.\right.\\
&\left.-8e^{2i\iota}+5e^{3i\iota}\right)+e^{4i\Psi}\left(-1+e^{i\iota}\right)^3\left(5+8e^{i\iota}+8e^{2i\iota}+5e^{3i\iota}\right)\\
&\left.-6e^{2i\Psi}\left(-1+e^{2i\iota}-e^{4i\iota}+e^{6i\iota}\right)\right)\chi_a^z\Big)+\frac{1}{12}e^{-i(\alpha+3\iota+\Psi)}\left(\left(1+e^{i\iota}\right)^4\right.\\
&\left.\times\left(5-7e^{i\iota}+5e^{2i\iota}\right)-e^{2i\alpha}\left(-1+e^{2i\iota}\right)^2\left(5+e^{i\iota}+5e^{2i\iota}\right)\right.\\
&+6e^{2i\Psi}\left(1+e^{2i\iota}\right)\left(-\left(-1+e^{2i\iota}\right)^2+e^{2i\alpha}\left(1+e^{2i\iota}\right)^2\right)+e^{4i\Psi}\left(-e^{2i\alpha}\right.\\
&\left.\left.\times\left(-1+e^{2i\iota}\right)^2\left(5-e^{i\iota}+5e^{2i\iota}\right)+\left(-1+e^{i\iota}\right)^4\left(5+7e^{i\iota}+5e^{2i\iota}\right)\right)\right)\chi_s^y\\
&+\frac{1}{6}e^{-i(3\iota+\Psi)}\left(\left(1+e^{i\iota}\right)^3\left(-5+8e^{i\iota}-8e^{2i\iota}+5e^{3i\iota}\right)+e^{4i\Psi}\left(-1+e^{i\iota}\right)^3\right.\\
&\left.\times\left(5+8e^{i\iota}+8e^{2i\iota}+5e^{3i\iota}\right)-6e^{2i\Psi}\left(-1+e^{2i\iota}-e^{4i\iota}+e^{6i\iota}\right)\right)\chi_s^z\\
&+i\left(\delta\left(\frac{1}{84}e^{-2i\iota}\left(-17+17e^{2i\Psi}\left(-1+e^{i\iota}\right)^2\left(1+e^{i\iota}+e^{2i\iota}\right)-17e^{i\iota}\right.\right.\right.\\
&\left.\times\left(1+e^{2i\iota}+e^{3i\iota}\right)\right)+\frac{5}{21}e^{-2i\iota}\left(1+e^{i\iota}+e^{3i\iota}+e^{4i\iota}-e^{2i\Psi}\left(-1+e^{i\iota}\right)^2\right.\\
&\left.\left.\times\left(1+e^{i\iota}+e^{2i\iota}\right)\right)\eta+\frac{1}{12}e^{-i(\alpha+3\iota+\Psi)}\left(-\left(1+e^{i\iota}\right)^4\left(5-7e^{i\iota}+5e^{2i\iota}\right)\right.\right.\\
&-e^{2i\alpha}\left(-1+e^{2i\iota}\right)^2\left(5+e^{i\iota}+5e^{2i\iota}\right)+6e^{2i\Psi}\left(1+e^{2i\iota}\right)\left(\left(-1+e^{2i\iota}\right)^2\right.\\
&\left.+e^{2i\alpha}\left(1+e^{2i\iota}\right)^2\right)+e^{4i\Psi}\left(-e^{2i\alpha}\left(-1+e^{2i\iota}\right)^2\left(5-e^{i\iota}+5e^{2i\iota}\right)\left(-1+e^{i\iota}\right)^4\right.\\
&\left.\left.\left(5+7e^{i\iota}+5e^{2i\iota}\right)\right)\right)\chi_a^x\Big)+\frac{1}{12}e^{-i(\alpha+3\iota+\Psi)}\left(-\left(1+e^{i\iota}\right)^4\left(5-7e^{i\iota}+5e^{2i\iota}\right)\right.\\
&-e^{2i\alpha}\left(-1+e^{2i\iota}\right)^2\left(5+e^{i\iota}+5e^{2i\iota}\right)+6e^{2i\Psi}\left(1+e^{2i\iota}\right)\left(\left(-1+e^{2i\iota}\right)^2\right.\\
&\left.+e^{2i\alpha}\left(1+e^{2i\iota}\right)^2\right)+e^{4i\Psi}\left(-e^{2i\alpha}\left(-1+e^{2i\iota}\right)^2\left(5-e^{i\iota}+5e^{2i\iota}\right)\right.\\
&\left.\left.-\left(-1+e^{i\iota}\right)^4\left(5+7e^{i\iota}+5e^{2i\iota}\right)\right)\right)\chi_s^x+\frac{1}{24}e^{-i(\alpha+3\iota+\Psi)}\left(-e^{2i\alpha}\left(-1+e^{2i\iota}\right)^2\right.\\
&\left.\times\left(1-13e^{i\iota}+e^{2i\iota}\right)-\left(1+e^{i\iota}\right)^4\left(1+3e^{i\iota}+e^{2i\iota}\right)+6e^{2i\Psi}\left(1+e^{2i\iota}\right)\right.\\
&\left.\times\left(-\left(-1+e^{2i\iota}\right)^2-e^{2i\alpha}\left(1+e^{2i\iota}\right)^2\right)+e^{4i\Psi}\left(-\left(-1+e^{i\iota}\right)^4\right.\right.
\end{aligned}
$$

$$
\begin{aligned}
&\times\left(1-3e^{i\iota}+e^{2i\iota}\right)-e^{2i\alpha}\left(-1+e^{2i\iota}\right)^2\left(1+13e^{i\iota}+e^{2i\iota}\right)\Big)\Big)\,\eta\chi_s^x\Big)\\
&+\eta\left(\frac{1}{24}e^{-i(\alpha+3\iota+\Psi)}\left(-e^{2i\alpha}\left(-1+e^{2i\iota}\right)^2\left(1-13e^{i\iota}+e^{2i\iota}\right)+\left(1+e^{i\iota}\right)^4\right.\right.\\
&\times\left(1+3e^{i\iota}+e^{2i\iota}\right)+6e^{2i\Psi}\left(1+e^{2i\iota}\right)\left(\left(-1+e^{2i\iota}\right)^2-e^{2i\alpha}\left(1+e^{2i\iota}\right)^2\right)\\
&+e^{4i\Psi}\left(\left(-1+e^{i\iota}\right)^4\left(1-3e^{i\iota}+e^{2i\iota}\right)-e^{2i\alpha}\left(-1+e^{2i\iota}\right)^2\right.\\
&\times\left.\left.\left(1+13e^{i\iota}+e^{2i\iota}\right)\right)\right)\chi_s^y+\frac{1}{12}e^{-i(3\iota+\Psi)}\left(\left(1+e^{i\iota}\right)^3\right.\\
&\times\left(-1+6e^{i\iota}-6e^{2i\iota}+e^{3i\iota}\right)+e^{4i\Psi}\left(-1+e^{i\iota}\right)^3\left(1+6e^{i\iota}+6e^{2i\iota}+e^{3i\iota}\right)\\
&\left.+6e^{2i\Psi}\left(-1+e^{2i\iota}-e^{4i\iota}+e^{6i\iota}\right)\right)\chi_s^z\Big)\Big]+\mathcal{O}(v^4)\Big\}\,, \qquad \text{(B.2)}
\end{aligned}
$$

$$
\begin{aligned}
h_{33} \;=\;& \frac{2\,M\,\nu\,v^2}{D_L}\,e^{-3i\,(\alpha+\Psi)}\frac{1}{64}\sqrt{\frac{\pi}{42}}\left\{e^{-3i\iota}\left(9\,e^{6i\Psi}\left(-1+e^{i\iota}\right)^6-e^{4i\Psi}\left(-1+e^{i\iota}\right)^4\right.\right.\\
&\times\left(1+e^{i\iota}\right)^2-e^{2i\Psi}\left(-1+e^{i\iota}\right)^2\left(1+e^{i\iota}\right)^4+9\left(1+e^{i\iota}\right)^6\Big)\,v\,\delta\\
&+i\,v^2\left[e^{-i(3\iota-\Psi)}\left(8\,e^{4i\Psi}\left(-1+e^{i\iota}\right)^5\left(1+e^{i\iota}\right)-8\left(-1+e^{i\iota}\right)\left(1+e^{i\iota}\right)^5\right)\right.\\
&\left.+\;e^{-i(3\iota-\Psi)}\left(-24\,e^{4i\Psi}\left(-1+e^{i\iota}\right)^5\left(1+e^{i\iota}\right)+24\left(-1+e^{i\iota}\right)\left(1+e^{i\iota}\right)^5\right)\eta\right]\\
&+v^3\left[\delta\,\left(\frac{1}{3}\,e^{-3i\iota}\left(-108\,e^{6i\Psi}\left(-1+e^{i\iota}\right)^6+8\,e^{4i\Psi}\left(-1+e^{i\iota}\right)^4\left(1+e^{i\iota}\right)^2\right.\right.\right.\\
&\left.+8\,e^{2i\Psi}\left(-1+e^{i\iota}\right)^2\left(1+e^{i\iota}\right)^4-108\left(1+e^{i\iota}\right)^6\right)\\
&+\frac{1}{3}\,e^{-3i\iota}\left(54\,e^{6i\Psi}\left(-1+e^{i\iota}\right)^6+2\,e^{4i\Psi}\left(-1+e^{i\iota}\right)^4\left(1+e^{i\iota}\right)^2\right.\\
&\left.+2\,e^{2i\Psi}\left(-1+e^{i\iota}\right)^2\left(1+e^{i\iota}\right)^4+54\left(1+e^{i\iota}\right)^6\right)\eta\Big)\\
&+64\,e^{i(\alpha-2\iota+\Psi)}\left(-e^{4i\Psi}\left(-1+e^{i\iota}\right)^4+\left(1+e^{i\iota}\right)^4\right)\eta\chi_s^x\\
&\left.+64i\,e^{i(\alpha-2\iota+\Psi)}\left(e^{4i\Psi}\left(-1+e^{i\iota}\right)^4-\left(1+e^{i\iota}\right)^4\right)\eta\chi_s^y\right]+\mathcal{O}(v^4)\Big\}\,. \qquad \text{(B.3)}
\end{aligned}
$$

Appendix C

Center-of-mass energy and gravitational-wave energy flux

For nearly circular orbits, the center-of-mass energy is known through 2PN order, when spins are present and 3PN order when spins are neglected. The coefficients entering Eq. (4.77) are [83, 84, 235, 242, 243, 244, 245, 56, 85]

$$
\begin{aligned}
E_{\rm Newt} &= -\frac{M}{2}\,\nu\,, && \text{(C.1)}\\
E_2 &= -\frac{3}{4}-\frac{1}{12}\nu\,, && \text{(C.2)}\\
E_3 &= \left[\left(\frac{8}{3}-\frac{4}{3}\,\nu\right)\boldsymbol{\chi}_s\cdot\hat{\mathbf{L}}_{\rm N}+\frac{8}{3}\,\delta\,\boldsymbol{\chi}_a\cdot\hat{\mathbf{L}}_{\rm N}\right]\,, && \text{(C.3)}\\
E_4 &= -\frac{27}{8}+\frac{19}{8}\nu-\frac{1}{24}\nu^2+\nu\left\{(\boldsymbol{\chi}_s^2-\boldsymbol{\chi}_a^2)-3\left[\left(\boldsymbol{\chi}_s\cdot\hat{\mathbf{L}}_{\rm N}\right)^2-\left(\boldsymbol{\chi}_a\cdot\hat{\mathbf{L}}_{\rm N}\right)^2\right]\right\}\\
&+ \left(\frac{1}{2}-\nu\right)\left\{\boldsymbol{\chi}_s^2+\boldsymbol{\chi}_a^2-3\left[\left(\boldsymbol{\chi}_s\cdot\hat{\mathbf{L}}_{\rm N}\right)^2+\left(\boldsymbol{\chi}_a\cdot\hat{\mathbf{L}}_{\rm N}\right)^2\right]\right\}\\
&+ \delta\left\{\boldsymbol{\chi}_s\cdot\boldsymbol{\chi}_a-3\left[\left(\boldsymbol{\chi}_s\cdot\hat{\mathbf{L}}_{\rm N}\right)\left(\boldsymbol{\chi}_a\cdot\hat{\mathbf{L}}_{\rm N}\right)\right]\right\}\,, && \text{(C.4)}\\
E_5 &= \left[\left(8-\frac{121}{9}\,\nu+\frac{2}{9}\,\nu^2\right)\boldsymbol{\chi}_s\cdot\hat{\mathbf{L}}_{\rm N}+\left(8-\frac{31}{9}\,\nu\right)\,\delta\,\boldsymbol{\chi}_a\cdot\hat{\mathbf{L}}_{\rm N}\right]\,, && \text{(C.5)}\\
E_6 &= -\frac{675}{64}+\left(\frac{34445}{576}-\frac{205}{96}\pi^2\right)\nu-\frac{155}{96}\nu^2-\frac{35}{5184}\nu^3\,. && \text{(C.6)}
\end{aligned}
$$

The GW energy flux is known through 2.5PN order for spin effects [86, 85, 87, 88], and 3.5PN order when spin effects are absent [197]. The coefficients in Eq. (4.78) read

$$
F_{\rm Newt} = \frac{32}{5}\nu^2\,, \qquad \text{(C.7)}
$$

$$
\begin{aligned}
F_2 &= -\frac{1247}{336} - \frac{35}{12}\nu\,, && \text{(C.8)}\\
F_3 &= 4\pi - \left[\left(\frac{11}{4} - 3\nu\right)\boldsymbol{\chi}_s\cdot\hat{\mathbf{L}}_{\rm N} + \frac{11}{4}\,\delta\,\boldsymbol{\chi}_a\cdot\hat{\mathbf{L}}_{\rm N}\right]\,, && \text{(C.9)}\\
F_4 &= -\frac{44711}{9072} + \frac{9271}{504}\nu + \frac{65}{18}\nu^2\\
&+ \left(\frac{287}{96} + \frac{\nu}{24}\right)\left(\boldsymbol{\chi}_s\cdot\hat{\mathbf{L}}_{\rm N}\right)^2 - \left(\frac{89}{96} + \frac{7\nu}{24}\right)\boldsymbol{\chi}_s^2\\
&\quad + \left(\frac{287}{96} - 12\,\nu\right)\left(\boldsymbol{\chi}_a\cdot\hat{\mathbf{L}}_{\rm N}\right)^2 + \left(-\frac{89}{96} + 4\,\nu\right)\boldsymbol{\chi}_a^2\\
&\quad + \frac{287}{48}\,\delta\,\left(\boldsymbol{\chi}_s\cdot\hat{\mathbf{L}}_{\rm N}\right)\left(\boldsymbol{\chi}_a\cdot\hat{\mathbf{L}}_{\rm N}\right) - \frac{89}{48}\,\delta\,\left(\boldsymbol{\chi}_s\cdot\boldsymbol{\chi}_a\right)\,, && \text{(C.10)}\\
F_5 &= \left(-\frac{8191}{672} - \frac{583}{24}\nu\right)\pi + \left[\left(-\frac{59}{16} + \frac{227}{9}\,\nu - \frac{157}{9}\,\nu^2\right)\boldsymbol{\chi}_s\cdot\hat{\mathbf{L}}_{\rm N}\right.\\
&\quad \left. + \left(-\frac{59}{16} + \frac{701}{36}\,\nu\right)\,\delta\,\boldsymbol{\chi}_a\cdot\hat{\mathbf{L}}_{\rm N}\right]\,, && \text{(C.11)}\\
F_6 &= \frac{6643739519}{69854400} + \frac{16}{3}\pi^2 - \frac{1712}{105}\gamma_E - \frac{856}{105}\log(16v^2)\\
&\quad + \left(-\frac{134543}{7776} + \frac{41}{48}\pi^2\right)\nu - \frac{94403}{3024}\nu^2 - \frac{775}{324}\nu^3\,, && \text{(C.12)}\\
F_7 &= \left(-\frac{16285}{504} + \frac{214745}{1728}\nu + \frac{193385}{3024}\nu^2\right)\,\pi\,. && \text{(C.13)}
\end{aligned}
$$

Appendix D

Frequency-domain amplitude corrections

We give here the complex coefficients $\mathcal{C}_k^{(n)}$ appearing in the frequency domain non-precessing waveform (4.72). The lower index in $\mathcal{C}_k^{(n)}$ denotes the harmonic of the orbital phase, and the upper index denotes the (half) PN order. Since the different harmonics end at different GW frequencies, the $k^{\rm th}$ harmonic ends at k times the orbital frequency cutoff. Thus, we introduce step functions $\Theta(k\,F_{\rm cut} - f)$ to ensure each harmonic ends at its proper frequency. We derive

$$\mathcal{C}_2^{(0)} = \frac{1}{\sqrt{2}}\left[-(1+c_\theta^2)\,F_+ - 2i\,c_\theta\,F_\times\right]\Theta(2\,F_{\rm cut}-f)\,, \tag{D.1}$$

$$\mathcal{C}_1^{(1)} = s_\theta\,\delta\left[-\left(\frac{5}{8}+\frac{c_\theta^2}{8}\right)\,F_+ - \frac{3}{4}i\,c_\theta\,F_\times\right]\Theta(F_{\rm cut}-f)\,, \tag{D.2}$$

$$\mathcal{C}_3^{(1)} = \frac{1}{\sqrt{3}}\left[\frac{9}{8}\,s_\theta\,\delta\,\left((1+c_\theta^2)\,F_+ + i\,2\,c_\theta\,F_\times\right)\right]\Theta(3\,F_{\rm cut}-f)\,, \tag{D.3}$$

$$\mathcal{C}_1^{(2)} = s_\theta\left(\delta\,\boldsymbol{\chi}_s\cdot\hat{\mathbf{L}}_{\rm N} + \boldsymbol{\chi}_a\cdot\hat{\mathbf{L}}_{\rm N}\right)\,(F_+ + i\,c_\theta\,F_\times)\,\Theta(F_{\rm cut}-f)\,, \tag{D.4}$$

$$\mathcal{C}_2^{(2)} = \frac{1}{\sqrt{2}}\left[\left(\frac{1385}{672}-\frac{109\nu}{24}+\left(\frac{265}{672}+\frac{11\nu}{24}\right)\,c_\theta^2+\left(-\frac{1}{3}+\nu\right)\,c_\theta^4\right)\,F_+\right.$$

$$+i\left(\left(\frac{387}{112}-\frac{85}{12}\nu\right)c_\theta+\left(-\frac{4}{3}+4\nu\right)c_\theta^3\right)F_\times\Bigg]\Theta(2\,F_{\rm cut}-f)\,, \quad \text{(D.5)}$$

$$\mathcal{C}_4^{(2)} = \frac{1}{2}s_\theta^2\left[\frac{4}{3}(3\nu-1)\left((1+c_\theta^2)\,F_+ + i\,2\,c_\theta\,F_\times\right)\right]\Theta(4\,F_{\rm cut}-f)\,, \quad \text{(D.6)}$$

$$\begin{aligned}\mathcal{C}_1^{(3)} &= s_\theta\,\delta\left[\left(-\frac{2119}{5376}-\frac{263\nu}{192}+\left(\frac{937}{5376}-\frac{3\nu}{64}\right)c_\theta^2+\left(-\frac{1}{192}+\frac{\nu}{96}\right)c_\theta^4\right)F_+\right.\\ &\left.+i\left(-\left(\frac{155}{896}+\frac{145\nu}{96}\right)c_\theta+\frac{5}{96}(2\nu-1)\,c_\theta^3\right)F_\times\right]\Theta(F_{\rm cut}-f)\,, \quad \text{(D.7)}\end{aligned}$$

$$\begin{aligned}\mathcal{C}_2^{(3)} &= \frac{1}{\sqrt{2}}\left[\left(-\frac{27}{8}\left(1+c_\theta^2\right)\delta\left(\boldsymbol{\chi}_a\cdot\hat{\mathbf{L}}_{\rm N}\right)+\left(-\frac{27}{8}\left(1+c_\theta^2\right)\right.\right.\right.\\ &\left.\left.+\frac{1}{2}\left(9-7c_\theta^2\right)\nu\right)\left(\boldsymbol{\chi}_s\cdot\hat{\mathbf{L}}_{\rm N}\right)\right)F_+ + i\,c_\theta\left(-\frac{27}{4}\,\delta\left(\boldsymbol{\chi}_a\cdot\hat{\mathbf{L}}_{\rm N}\right)\right.\\ &\left.\left.+\left(-\frac{27}{4}+\left(5-4c_\theta^2\right)\nu\right)\left(\boldsymbol{\chi}_s\cdot\hat{\mathbf{L}}_{\rm N}\right)\right)F_\times\right]\,\Theta(2\,F_{\rm cut}-f)\,,\end{aligned} \quad \text{(D.8)}$$

$$\begin{aligned}\mathcal{C}_3^{(3)} &= \frac{1}{\sqrt{3}}\,s_\theta\,\delta\left[\left(-\frac{6969}{1792}+\frac{81\nu}{16}+\left(-\frac{2811}{1792}+\frac{27\nu}{64}\right)c_\theta^2+\frac{81}{128}(1-2\nu)\,c_\theta^4\right)F_+\right.\\ &\left.+i\left(\left(-\frac{6213}{896}+\frac{135\nu}{16}\right)c_\theta+\frac{135}{64}(1-2\nu)c_\theta^3\right)F_\times\right]\Theta(3\,F_{\rm cut}-f)\,, \quad \text{(D.9)}\end{aligned}$$

$$\mathcal{C}_5^{(3)} = \frac{1}{\sqrt{5}}\,s_\theta^3\,\delta\,(1-2\nu)\left[\frac{625}{384}\left((1+c_\theta^2)\,F_+ + i\,2\,c_\theta\,F_\times\right)\right]\Theta(5\,F_{\rm cut}-f)\,, \quad \text{(D.10)}$$

$$\mathcal{C}_1^{(4)} = s_\theta\,\delta\left[\left(\frac{5\pi}{8}+i\left(\frac{11}{40}+\frac{5\ln 2}{4}\right)+\left(\frac{\pi}{8}+i\left(\frac{7}{40}+\frac{\ln 2}{4}\right)\right)c_\theta^2\right)F_+\right.$$

$$+\left(-\left(\frac{9}{20}+\frac{3\ln 2}{2}\right)+i\,\frac{3\pi}{4}\right)\,c_\theta\,F_\times\Bigg]\,\Theta(F_{\rm cut}-f)\,, \tag{D.11}$$

$$\begin{aligned}
\mathcal{C}_2^{(4)} \;=\; & \frac{1}{\sqrt{2}}\,\Bigg[\Bigg(\frac{113419241}{40642560}+\frac{152987\nu}{16128}-\frac{11099\nu^2}{1152}+\Bigg(\frac{165194153}{40642560}\\
& -\frac{149\nu}{1792}+\frac{6709\nu^2}{1152}\Bigg)\,c_\theta^2+\Bigg(\frac{1693}{2016}-\frac{5723\nu}{2016}+\frac{13\nu^2}{12}\Bigg)\,c_\theta^4\\
& +\Bigg(-\frac{1}{24}+\frac{5\nu}{24}-\frac{5\nu^2}{24}\Bigg)\,c_\theta^6\Bigg)\,F_+ + i\,\Bigg(\Bigg(\frac{114020009}{20321280}+\frac{133411\nu}{8064}\\
& -\frac{7499\nu^2}{576}\Bigg)\,c_\theta+\Bigg(\frac{5777}{2520}-\frac{5555\nu}{504}+\frac{34\nu^2}{3}\Bigg)\,c_\theta^3\\
& +\Bigg(-\frac{1}{4}+\frac{5\nu}{4}-\frac{5\nu^2}{4}\Bigg)\,c_\theta^5\Bigg)\,F_\times+\nu\,\Bigg(\frac{721}{96}\,\Bigg(\Big(\boldsymbol{\chi}_s\cdot\hat{\mathbf{L}}_{\rm N}\Big)^2-\Big(\boldsymbol{\chi}_a\cdot\hat{\mathbf{L}}_{\rm N}\Big)^2\Bigg)\\
& -\frac{439}{96}\,\left(\boldsymbol{\chi}_s^2-\boldsymbol{\chi}_a^2\right)\Bigg)\,\Big((1+c_\theta^2)\,F_+ + i\,2\,c_\theta\,F_\times\Big)\Bigg]\,\Theta(2\,F_{\rm cut}-f)\,,
\end{aligned} \tag{D.12}$$

$$\begin{aligned}
\mathcal{C}_3^{(4)} \;=\; & \frac{1}{\sqrt{3}}\,s_\theta\,\delta\,\Bigg[\Bigg(\frac{9\pi}{8}+i\,\Bigg(-\frac{189}{40}+\frac{27\ln(3/2)}{4}\Bigg)\Bigg)\\
& \times\Big((1+c_\theta^2)\,F_+ + i\,2\,c_\theta\,F_\times\Big)\Bigg]\,\Theta(3\,F_{\rm cut}-f)\,,
\end{aligned} \tag{D.13}$$

$$\begin{aligned}
\mathcal{C}_4^{(4)} \;=\; & \frac{1}{2}\,\Bigg[\Bigg(\frac{16109}{2520}-\frac{13367\nu}{504}+\frac{39\nu^2}{2}+\Bigg(\frac{16}{15}-\frac{16\nu}{3}+\frac{16\nu^2}{3}\Bigg)\\
& \times c_\theta^2\,\left(c_\theta^4-3\right)+\Bigg(-\frac{10733}{2520}+\frac{7991\nu}{504}-\frac{53\nu^2}{6}\Bigg)\,c_\theta^4\Bigg)\,F_+\\
& +i\,\Bigg(\Bigg(\frac{2953}{252}-\frac{12023\nu}{252}+\frac{101\nu^2}{3}\Bigg)\,c_\theta\\
& +\Bigg(-\frac{18797}{1260}+\frac{16055\nu}{252}-\frac{149\nu^2}{3}\Bigg)\,c_\theta^3\\
& +\Bigg(\frac{16}{5}-16\,\nu+16\,\nu^2\Bigg)\,c_\theta^5\Bigg)\,F_\times\Bigg]\,\Theta(4\,F_{\rm cut}-f)\,,
\end{aligned} \tag{D.14}$$

$$\mathcal{C}_6^{(4)} = \frac{1}{\sqrt{6}}\, s_\theta^4 \left[\left(-\frac{81}{40}+\frac{81\nu}{8}-\frac{81\nu^2}{8}\right) \left((1+c_\theta^2)\, F_+ + i\, 2\, c_\theta\, F_\times\right)\right] \Theta(6\, F_{\rm cut} - f)\,, \tag{D.15}$$

$$\begin{aligned}\mathcal{C}_1^{(5)} = {} & s_\theta\, \delta \left[\left(\frac{37533829}{325140480}+\frac{76171\nu}{43008}-\frac{8407\nu^2}{4608}+c_\theta^2\left(-\frac{29850823}{325140480}\right.\right.\right. \\ & \left.+\frac{56543\nu}{129024}+\frac{139\nu^2}{576}\right)+c_\theta^4\left(\frac{255}{14336}-\frac{2659\nu}{64512}+\frac{127\nu^2}{9216}\right) \\ & \left.+c_\theta^6\left(-\frac{1}{9216}+\frac{\nu}{2304}-\frac{\nu^2}{3072}\right)\right)\, F_+ + i\left(c_\theta\left(-\frac{3453823}{54190080}\right.\right. \\ & \left.+\frac{163015\nu}{64512}-\frac{4237\nu^2}{2304}\right)+c_\theta^3\left(\frac{34373}{322560}-\frac{11755\nu}{32256}+\frac{631\nu^2}{2304}\right) \\ & \left.\left.+c_\theta^5\left(-\frac{7}{4608}+\frac{7\nu}{1152}-\frac{7\nu^2}{1536}\right)\right)\, F_\times\right] \Theta(F_{\rm cut} - f)\,, \end{aligned} \tag{D.16}$$

$$\begin{aligned}\mathcal{C}_2^{(5)} = {} & \frac{1}{\sqrt{2}}\left[\left(\frac{85\pi}{64}(1-4\,\nu)+i\left(-\frac{9}{5}+32\nu\right)+c_\theta^2\left(\frac{85\pi}{64}(1-4\,\nu)\right.\right.\right. \\ & \left.\left.+i\,\frac{14}{5}(1+4\,\nu)\right)+i\,c_\theta^4\,\frac{7}{5}(1-4\,\nu)\right)\, F_+ + \left(c_\theta\left(2-\frac{282\nu}{5}\right.\right. \\ & \left.\left.\left.+i\,\frac{85\pi}{32}(1-4\,\nu)\right)+c_\theta^3\left(-\frac{22}{5}+\frac{94\nu}{5}\right)\right)\, F_\times\right] \Theta(2\, F_{\rm cut} - f)\,, \end{aligned} \tag{D.17}$$

$$\begin{aligned}\mathcal{C}_3^{(5)} = {} & \frac{1}{\sqrt{3}}\, s_\theta\, \delta \left[\left(-\frac{8781361}{7225344}-\frac{366781\nu}{17920}+\frac{15193\nu^2}{1280}+c_\theta^2\left(-\frac{238136057}{36126720}\right.\right.\right. \\ & \left.+\frac{37829\nu}{71680}-\frac{7073\nu^2}{1280}\right)+c_\theta^4\left(-\frac{328347}{143360}+\frac{396009\nu}{71680}-\frac{10557\nu^2}{5120}\right) \\ & \left.+c_\theta^6\left(\frac{729}{5120}-\frac{729\nu}{1280}+\frac{2187\nu^2}{5120}\right)\right)\, F_+ + i\left(c_\theta\left(-\frac{63633869}{18063360}\right.\right. \\ & \left.-\frac{89609\nu}{2560}+\frac{697\nu^2}{40}\right)+c_\theta^3\left(-\frac{508689}{71680}+\frac{812727\nu}{35840}-\frac{4707\nu^2}{320}\right) \\ & \left.\left.+c_\theta^5\left(\frac{1701}{2560}-\frac{1701\nu}{640}+\frac{5103\nu^2}{2560}\right)\right)\, F_\times\right] \Theta(3\, F_{\rm cut} - f)\,, \end{aligned} \tag{D.18}$$

$$\mathcal{C}_4^{(5)} = \frac{1}{2}\,s_\theta^2\,\left[\left(\frac{8\pi}{3}(3\,\nu-1)+i\,\left(\frac{56}{5}-\frac{1193\nu}{30}+\frac{32\,\ln 2}{3}(3\,\nu-1)\right)\right)\right.$$
$$\left.\times\Big((1+c_\theta^2)\,F_+ + i\,2\,c_\theta\,F_\times\Big)\right]\,\Theta(4\,F_{\rm cut}-f)\,, \qquad \text{(D.19)}$$

$$\mathcal{C}_5^{(5)} = \frac{1}{\sqrt{5}}\,s_\theta\,\delta\,\left[\left(-\frac{854375}{86016}+\frac{3919375\nu}{129024}-\frac{160625\nu^2}{9216}\right.\right.$$
$$+c_\theta^2\,\left(\frac{40625}{9216}-\frac{40625\nu}{2304}+\frac{40625\nu^2}{3072}\right)+c_\theta^4\,\left(\frac{1863125}{258048}-\frac{2519375\nu}{129024}\right.$$
$$\left.\left.+\frac{85625\nu^2}{9216}\right)+c_\theta^6\,\left(-\frac{15625}{9216}+\frac{15625\nu}{2304}-\frac{15625\nu^2}{3072}\right)\right)\,F_+$$
$$+i\,\left(c_\theta\,\left(-\frac{2388125}{129024}+\frac{3569375\nu}{64512}-\frac{141875\nu^2}{4608}\right)\right.$$
$$+c_\theta^3\,\left(\frac{3000625}{129024}-\frac{1598125\nu}{21504}+\frac{51875\nu^2}{1152}\right)$$
$$\left.\left.+c_\theta^5\,\left(-\frac{21875}{4608}+\frac{21875\nu}{1152}-\frac{21875\nu^2}{1536}\right)\right)\,F_\times\right]\,\Theta(5\,F_{\rm cut}-f)\,, \qquad \text{(D.20)}$$

$$\mathcal{C}_7^{(5)} = \frac{1}{\sqrt{7}}\,s_\theta^5\,\delta\,\left[\left(\frac{117649}{46080}-\frac{117649\nu}{11520}+\frac{117649\nu^2}{15360}\right)\right.$$
$$\left.\times\Big((1+c_\theta^2)\,F_+ + i\,2\,c_\theta\,F_\times\Big)\right]\,\Theta(7\,F_{\rm cut}-f)\,. \qquad \text{(D.21)}$$

Bibliography

[1] R.A. Hulse and J.H. Taylor. Discovery of a pulsar in a binary system. *Astrophys. J.*, 195:L51–L53, 1975.

[2] J. H. Taylor and J. M. Weisberg. A new test of general relativity: Gravitational radiation and the binary pulsar PS R 1913+16. *Astrophys. J.*, 253:908–920, 1982.

[3] J.H. Taylor and J.M. Weisberg. Further experimental tests of relativistic gravity using the binary pulsar psr 1913+16. *Astrophys. J.*, 345:434–450, 1989.

[4] J. M. Weisberg and J. H. Taylor. Relativistic binary pulsar b1913+16: Thirty years of observations and analysis. 2004, astro-ph/0407149 to be published in Binary Radio Pulsars, Proc. Aspen Conference, ASP Conf. Series, eds. F.A. Rasio & I.H. Stairs.

[5] L.S. Finn and D.F. Chernoff. Observing binary inspiral in gravitational radiation: One interferometer. *Phys. Rev. D*, 47:2198–2219, 1993.

[6] Clifford M. Will. The confrontation between general relativity and experiment. *Living Reviews in Relativity*, 9(3), 2006.

[7] B F Schutz. Determining the Hubble constant from gravitational wave observations. *Nature (London)*, 323:310, 1986.

[8] A. Einstein. Approximative Integration of the Field Equations of Gravitation. *Preuss. Akad. Weiss. Berlin*, page 688, 1916.

[9] M. Maggiore. *Gravitational waves: Theory and Experiments*. Oxford University Press, Oxford, U.K., 2007.

[10] R. M. Wald. *General Relativity*. University of Chicago Press, Chicago, U.S., 1984.

[11] Alessandra Buonanno. Gravitational waves. 2007, arXiv:0709.4682.

[12] S. Carroll. *Spacetime and Geometry: An Introduction to General Relativity*. Addison-Wesley, Chicago, U.S., 2003.

[13] B. Abbott et al. LIGO: The Laser Interferometer Gravitational-Wave Observatory. *Rept. Prog. Phys.*, 72:076901, 2009, arXiv:0711.3041.

[14] `http://gw.icrr.u-tokyo.ac.jp/lcgt`.

[15] P.C. Peters and J. Mathews. Gravitational radiation from point masses in a keplerian orbit. *Phys. Rev.*, 131:435–439, 1963.

[16] P.C. Peters. Gravitational radiation and the motion of two point masses. *Phys. Rev.*, 136:B1224–B1232, 1964.

[17] M. C. Miller and D. P. Hamilton. Four-body effects in globular cluster black hole coalescence. *Astrophys. J.*, 576:894–898, September 2002, astro-ph/0202298.

[18] Linqing Wen. On the eccentricity distribution of coalescing black hole binaries driven by the kozai mechanism in globular clusters. *Astrophys. J.*, 598:419, 2003, astro-ph/0211492.

[19] I. Mandel and R. O'Shaughnessy. Compact binary coalescences in the band of ground-based gravitational-wave detectors. *Classical and Quantum Gravity*, 27(11):114007, June 2010, arXiv:0912.1074.

[20] Jeffrey E. McClintock, Rebecca Shafee, Ramesh Narayan, Ronald A. Remillard, Shane W. Davis, and Li-Xin Li. The spin of the near-extreme kerr black hole GRS 1915+105. *Astrophysical Journal* , 652:518, 2006.

[21] L. Blanchet. Gravitational radiation from post-newtonian sources and inspiralling compact binaries. *Living Rev. Relativity*, 9:4, 2006, arXiv:gr-qc/0202016.

[22] K.S. Thorne. Multipole expansions of gravitational radiation. *Rev. Mod. Phys.*, 52:299–339, 1980.

[23] Clifford M. Will and Alan G. Wiseman. Gravitational radiation from compact binary systems: gravitational waveforms and energy loss to second post-Newtonian order. *Phys. Rev. D*, 54:4813–4848, 1996, arXiv:gr-qc/9608012.

[24] Luc Blanchet, Guillaume Faye, Bala R. Iyer, and Benoit Joguet. Gravitational-wave inspiral of compact binary systems to 7/2 post-newtonian order. *Phys. Rev. D*, 65:061501(R), 2002. erratum-ibid D. **71**, 129902(E) (2005).

[25] Luc Blanchet, Thibault Damour, Gilles Esposito-Farèse, and Bala R. Iyer. Gravitational radiation from inspiralling compact binaries completed at the third post-Newtonian order. *Phys. Rev. Lett.*, 93:091101, 2004.

[26] Luc Blanchet, Thibault Damour, Gilles Esposito-Farèse, and Bala R. Iyer. Gravitational radiation from inspiralling compact binaries completed at the third post-Newtonian order. *Phys. Rev. Lett.*, 93:091101, 2004.

[27] Luc Blanchet, Guillaume Faye, Bala R. Iyer, and Siddhartha Sinha. The third post-Newtonian gravitational wave polarisations and associated spherical harmonic modes for inspiralling compact binaries in quasi-circular orbits. *Class. Quantum Grav.*, 25:165003, 2008.

[28] L. Blanchet, T. Damour, B.R. Iyer, C.M. Will, and A.G. Wiseman. Gravitational-radiation damping of compact binary systems to second post-newtonian order. *Phys. Rev. Lett.*, 74:3515, 1995, arXiv:gr-qc/9501027.

[29] Luc Blanchet, Thibault Damour, and Bala R. Iyer. Gravitational waves from inspiralling compact binaries: Energy loss and wave form to second postNewtonian order. *Phys. Rev. D*, 51:5360–5386, 1995, arXiv:gr-qc/9501029.

[30] Thibault Damour, Bala R. Iyer, and B. S. Sathyaprakash. A comparison of search templates for gravitational waves from binary inspiral. *Phys. Rev. D*, 63:044023, 2001. Erratum-ibid. D 72 (2005) 029902.

[31] Luc Blanchet and Bala R. Iyer. Hadamard regularization of the third post-Newtonian gravitational wave generation of two point masses. *Phys. Rev. D*, 71:024004, 2005, arXiv:gr-qc/0409094.

[32] L. Blanchet, T. Damour, G. Esposito-Farese, and B.R. Iyer. Gravitational radiation from inspiralling compact binaries completed at the third post-newtonian order. *Phys. Rev. Lett.*, 93:091101, 2004, arXiv:gr-qc/0406012.

[33] Thibault Damour, Bala R. Iyer, and B. S. Sathyaprakash. A comparison of search templates for gravitational waves from binary inspiral: 3.5-PN update. *Phys. Rev. D*, 66:027502, 2002, arXiv:gr-qc/0207021.

[34] A. Buonanno, Y. Chen, and M. Vallisneri. Detecting gravitational waves from precessing binaries of spinning compact objects: Adiabatic limit. *Phys. Rev. D*, 67(10):104025–+, May 2003, arXiv:gr-qc/0211087.

[35] Achamveedu Gopakumar. New Class of Gravitational Wave Templates for Inspiralling Compact Binaries. 2007, arXiv:0712.3236.

[36] Achamveedu Gopakumar, Mark Hannam, Sascha Husa, and Bernd Brügmann. Comparison between numerical relativity and a new class of post-Newtonian gravitational-wave phase evolutions: the non-spinning equal-mass case. *Phys. Rev. D*, 78:064026, 2008, arXiv:0712.3737.

[37] Manuel Tessmer and Achamveedu Gopakumar. On the ability of various circular inspiral templates to capture inspiral gravitational waves from compact binaries having tiny orbital eccentricities. 2008, arXiv:0812.0549.

[38] Curt Cutler et al. The last three minutes: issues in gravitational wave measurements of coalescing compact binaries. *Phys. Rev. Lett.*, 70:2984–2987, 1993.

[39] A. Buonanno and T. Damour. Effective one-body approach to general relativistic two- body dynamics. *Phys. Rev. D*, 59:084006, 1999.

[40] Alessandra Buonanno and Thibault Damour. Transition from inspiral to plunge in binary black hole coalescences. *Phys. Rev. D*, 62:064015, 2000.

[41] E. Brezin, C. Itzykson, and J. Zinn-Justin. Relativistic balmer formula including recoil effects. *Phys. Rev. D*, 1(8):2349–2355, Apr 1970.

[42] Thibault Damour, Piotr Jaranowski, and Gerhard Schäfer. On the determination of the last stable orbit for circular general relativistic binaries at the third post-newtonian approximation. *Phys. Rev. D*, 62:084011, 2000.

[43] Thibault Damour, Bala R. Iyer, Piotr Jaranowski, and B. S. Sathyaprakash. Gravitational waves from black hole binary inspiral and merger: The span of third post-newtonian effective-one-body templates. *Phys. Rev. D*, 67:064028, 2003, gr-qc/0211041.

[44] C. V. Vishveshwara. *Nature*, 227:936, 1970.

[45] S. Chandrasekhar and S. Detweiler. The quasi-normal modes of the Schwarzschild black hole. *Proc. Roy. Soc. Lond.*, A344:441–452, 1975.

[46] B. F. Schutz and C. M. Will. *Astrophys. J.*, 291:L33–36, 1985.

[47] Thibault Damour and Achamveedu Gopakumar. Gravitational recoil during binary black hole coalescence using the effective one body approach. *Phys. Rev. D*, 73(12):124006, 2006.

[48] Alessandra Buonanno, Gregory B. Cook, and Frans Pretorius. Inspiral, merger and ring-down of equal-mass black-hole binaries. *Phys. Rev. D*, 75:124018, 2007.

[49] Jeremy D. Schnittman et al. Anatomy of the binary black hole recoil: A multipolar analysis. *Phys. Rev.*, D77:044031, 2008, arXiv:0707.0301.

[50] E. Berti, V. Cardoso, and C. M. Will. Gravitational-wave spectroscopy of massive black holes with the space interferometer LISA. *Phys. Rev. D*, 73:064030, March 2006.

[51] M Davis, R Ruffini, W H Press, and R H Price. *Phys. Rev. Lett*, 27:1466, 1971.

[52] Marc Davis, Remo Ruffini, and Jayme Tiomno. Pulses of gravitational radiation of a particle falling radially into a schwarzschild black hole. *Phys. Rev. D*, 5(12):2932–2935, Jun 1972.

[53] A. Buonanno, Y. Chen, and M. Vallisneri. Detection template families for gravitational waves from the final stages of binary black-holes binaries: Non-spinning case. *Phys. Rev. D*, 67:024016, 2003. Erratum-ibid. D 74, 029903(E) (2006).

[54] A Buonanno et al. Toward faithful templates for non-spinning binary black holes using the effective-one-body approach. *Phys. Rev. D*, 76:104049, 2007, arXiv:0706.3732.

[55] T. Damour, B R Iyer, and B S Sathyaprakash. Improved filters for gravitational waves from inspiraling compact binaries. *Phys. Rev. D*, 57:885–907, 1998.

[56] T. Damour, P. Jaranowski, and G. Schäfer. Dimensional regularization of the gravitational interaction of point masses. *Phys. Lett.*, 513B:147–155, 2001.

[57] Thibault Damour, Piotr Jaranowski, and Gerhard Schaefer. On the determination of the last stable orbit for circular general relativistic binaries at the third post-Newtonian approximation. *Phys. Rev.*, D62:084011, 2000, gr-qc/0005034.

[58] C. Bender and S. Orszag. *Advanced Mathematical Methods for Scientists and Engineers: Asymptotic Methods and Perturbation Theory*. Springer-Verlag, New York, 1999.

[59] A. Buonanno, Y. Chen, and M. Vallisneri. Detection template families for precessing binaries of spinning compact binaries: Adiabatic limit. *Phys. Rev. D*, 67:104025, 2003. Erratum-ibid. D 74, 029904(E) (2006).

[60] Thibault Damour, Alessandro Nagar, Ernst Nils Dorband, Denis Pollney, and Luciano Rezzolla. Faithful effective-one-body waveforms of equal-mass coalescing black-hole binaries. *Phys. Rev. D*, 77(8):084017, 2008.

[61] T. Damour, A. Nagar, M. Hannam, S. Husa, and B. Brügmann. Accurate Effective-One-Body waveforms of inspiralling and coalescing black-hole binaries. *Phys. Rev. D*, 78:044039, 2008.

[62] T. Damour and A. Nagar. Comparing Effective-One-Body gravitational waveforms to accurate numerical data. *Phys. Rev. D*, 77:024043, 2008.

[63] M. Boyle, A. Buonanno, L. E. Kidder, A. H. Mroué, Y. Pan, H. P. Pfeiffer, and M. A. Scheel. High-accuracy numerical simulation of black-hole binaries: Computation of the gravitational-wave energy flux and comparisons with post-Newtonian approximants. 2008, arXiv:0804.4184 [gr-qc].

[64] Thibault Damour and Alessandro Nagar. An improved analytical description of inspiralling and coalescing black-hole binaries. *Phys. Rev.*, D79:081503, 2009, 0902.0136.

[65] Y. Pan, A. Buonanno, L.T. Buchman, T. Chu, L.E. Kidder, H.P. Pfeiffer, and M.A. Scheel. Effective-one-body waveforms calibrated to numerical relativity simulations: coalescence of non-precessing, spinning, equal-mass black holes. *Phys. Rev.*, D81:084041, 2010.

[66] Thibault Damour, Bala R. Iyer, and Alessandro Nagar. Improved resummation of post-Newtonian multipolar waveforms from circularized compact binaries. *Phys. Rev.*, D79:064004, 2009, arXiv:0811.2069.

[67] Yi Pan, Alessandra Buonanno, Ryuichi Fujita, Etienne Racine, and Hideyuki Tagoshi. Post-Newtonian factorized multipolar waveforms for spinning, non-precessing black-hole binaries. 2010, arXiv:1006.0431.

[68] Ryuichi Fujita and Bala R. Iyer. Spherical harmonic modes of 5.5 post-Newtonian gravitational wave polarisations and associated factorised resummed waveforms for a particle in circular orbit around a Schwarzschild black hole. 2010, 1005.2266.

[69] Steven Detweiler. A consequence of the gravitational self-force for circular orbits of the Schwarzschild geometry. *Phys. Rev.*, D77:124026, 2008, 0804.3529.

[70] Luc Blanchet, Steven Detweiler, Alexandre Le Tiec, and Bernard F. Whiting. Post-Newtonian and Numerical Calculations of the Gravitational Self-Force for Circular Orbits in the Schwarzschild Geometry. 2009, 0910.0207.

[71] Thibault Damour. Gravitational Self Force in a Schwarzschild Background and the Effective One Body Formalism. *Phys. Rev.*, D81:024017, 2010, 0910.5533.

[72] Leor Barack, Thibault Damour, and Norichika Sago. Precession effect of the gravitational self-force in a Schwarzschild spacetime and the effective one-body formalism. 2010, 1008.0935.

[73] Leor Barack and Norichika Sago. Gravitational self-force correction to the innermost stable circular orbit of a Schwarzschild black hole. *Phys. Rev. Lett.*, 102:191101, 2009, 0902.0573.

[74] Alessandro Nagar, Thibault Damour, and Angelo Tartaglia. Binary black hole merger in the extreme mass ratio limit. *Class. Quant. Grav.*, 24:S109–S124, 2007, gr-qc/0612096.

[75] Thibault Damour and Alessandro Nagar. Faithful effective-one-body waveforms of small-mass-ratio coalescing black hole binaries. *Phys. Rev. D*, 76(6):064028, 2007.

[76] Nicolas Yunes, Alessandra Buonanno, Scott A. Hughes, M. Coleman Miller, and Yi Pan. Modeling Extreme Mass Ratio Inspirals within the Effective-One-Body Approach. *Phys. Rev. Lett.*, 104:091102, 2010, 0909.4263.

[77] Thibault Damour. Coalescence of two spinning black holes: An effective one-body approach. *Phys. Rev. D*, 64(12):124013, Nov 2001.

[78] A. Buonanno, Y. Chen, and T. Damour. Transition from inspiral to plunge in precessing binaries of spinning black holes. *Phys. Rev. D*, 74:104005, 2006.

[79] Thibault Damour, Piotr Jaranowski, and Gerhard Schaefer. Effective one body approach to the dynamics of two spinning black holes with next-to-leading order spin-orbit coupling. *Phys. Rev.*, D78:024009, 2008, 0803.0915.

[80] Enrico Barausse and Alessandra Buonanno. An improved effective-one-body Hamiltonian for spinning black-hole binaries. *Phys. Rev.*, D81:084024, 2010.

[81] Enrico Barausse, Etienne Racine, and Alessandra Buonanno. Hamiltonian of a spinning test-particle in curved spacetime. *Phys. Rev.*, D80:104025, 2009, 0907.4745.

[82] `https://www.ninja-project.org/doku.php?id=nrar:home`.

[83] L.E. Kidder. Coalescing binary systems of compact objects to 5/2-post-newtonian order. v. spin effects. *Phys. Rev. D*, 52:821–847, 1995.

[84] C.M. Will and A.G. Wiseman. Gravitational radiation from compact binary systems: Gravitational waveforms and energy loss to second post-newtonian order. *Phys. Rev. D*, 54:4813–4848, 1996.

[85] Guillaume Faye, Luc Blanchet, and Alessandra Buonanno. Higher-order spin effects in the dynamics of compact binaries. i: Equations of motion. *Phys. Rev. D*, **74**:104033, 2006.

[86] Luc Blanchet, Alessandra Buonanno, and Guillaume Faye. Higher-order spin effects in the dynamics of compact binaries. ii: Radiation field. *Phys. Rev. D*, **74**:104034, 2006. erratum-ibid. D **75**, 049903 (E) (2007).

[87] B. Mikóczi, M. Vasúth, and L. Á. Gergely. Self-interaction spin effects in inspiralling compact binaries. *Phys. Rev. D*, 71:124043, 2005.

[88] Etienne Racine, Alessandra Buonanno, and Lawrence E. Kidder. Recoil velocity at 2PN order for spinning black hole binaries. *Phys. Rev.*, D80:044010, 2009, 0812.4413.

[89] C. Cutler and E.E. Flanagan. Gravitational waves from merging compact binaries: How accurately can one extract the binary's parameters from the inspiral waveform? *Phys. Rev. D*, 49:2658–2697, 1994.

[90] E. Poisson and C.M. Will. Gravitational waves from inspiralling compact binaries - parameter-estimation using second-post-newtonian wave-forms. *Phys. Rev. D*, 52:848–855, 1995.

[91] Theocharis A. Apostolatos, Curt Cutler, Gerald J. Sussman, and Kip S. Thorne. Spin-induced orbital precession and its modulation of the gravitational waveforms from merging binaries. *Phys. Rev. D*, 49:6274, 1994.

[92] Lawrence E. Kidder. Coalescing binary systems of compact objects to $(\text{post})^{5/2}$-Newtonian order. V. Spin effects. *Phys. Rev. D*, 52(2):821–847, Jul 1995.

[93] L A Wainstein and V D Zubakov. *Extraction of Signals from Noise*. Prentice-Hall, Englewood Cliffs, 1962.

[94] Duncan Brown. *Searching for Gravitational Radiation from Binary Black Hole MACHOs in the Galactic Halo*. PhD thesis, University of Wisconsin–Milwaukee, 2004, 0705.1514.

[95] G. Arfken and H. Weber. *Mathematical Methods for Physicists*. Harcourt Academic Press, San Diego, fifth edition, 2001.

[96] B. Abbott et al. Search for Gravitational Waves from Low Mass Binary Coalescences in the First Year of LIGO's S5 Data. *Phys. Rev. D*, 79:122001, 2009, arXiv:0901.0302.

[97] B. Abbott et al. Search for Gravitational Waves from Low Mass Compact Binary Coalescence in 186 Days of LIGO's fifth Science Run. *Phys. Rev. D*, 80:047101, 2009, arXiv:0905.3710.

[98] J. Abadie et al. Search for Gravitational Waves from Compact Binary Coalescence in LIGO and Virgo Data from S5 and VSR1. *Phys. Rev. D*, 82(10):102001, Nov 2010.

[99] J. Slutsky et al. Methods for Reducing False Alarms in Searches for Compact Binary Coalescences in LIGO Data. *Class. Quant. Grav.*, 27:165023, 2010, 1004.0998.

[100] Stas Babak, Balasubramanian, David Churches, Thomas Cokelaer, and B.S. Sathyaprakash. A template bank to search for gravitational waves from inspiralling compact binaries i: physical models. *Class. Quantum Grav.*, 23:5477–5504, 2006, gr-qc/0604037.

[101] Bruce Allen, Warren G. Anderson, Patrick R. Brady, Duncan A. Brown, and Jolien D. E. Creighton. FINDCHIRP: An Algorithm for Detection of Gravitational Waves from Inspiraling Compact Binaries. 2005, arXiv:gr-qc/0509116.

[102] Bruce Allen. A χ^2 time-frequency discriminator for gravitational wave detection. *Phys. Rev. D*, 71:062001, 2005.

[103] Rahul Biswas, Patrick R. Brady, Jolien D. E. Creighton, and Stephen Fairhurst. The Loudest Event Statistic: General Formulation, Properties and Applications. *Class. Quantum Grav.*, 26:175009, 2009, arXiv:0710.0465.

[104] Benjamin Aylott et al. Testing gravitational-wave searches with numerical relativity waveforms: Results from the first Numerical INJection Analysis (NINJA) project. *Class. Quantum Grav.*, 26:165008, 2009, arXiv:0901.4399.

[105] P. Ajith et al. A template bank for gravitational waveforms from coalescing binary black holes: I. non-spinning binaries. *Phys. Rev. D*, 77:104017, 2008, arXiv:0710.2335.

[106] S. Chatterji. *The search for gravitational-wave bursts in data from the second LIGO science run*. PhD thesis, MIT, 2005.

[107] S. Chatterji, L. Blackburn, G. Martin, and E. Katsavounidis. Multiresolution techniques for the detection of gravitational-wave bursts. *Class. Quant. Grav.*, 21:S1809–S1818, 2004, gr-qc/0412119.

[108] Jordan B. Camp, John K. Cannizzo, and Kenji Numata. Application of the Hilbert-Huang transform to the search for gravitational waves. *Phys. Rev.*, D75:061101, 2007, gr-qc/0701148.

[109] Ravi Kumar Kopparapu, Chad Hanna, Vicky Kalogera, Richard O'Shaughnessy, Gabriela Gonzalez, Patrick R. Brady, and Stephen Fairhurst. Host Galaxies Catalog Used in LIGO Searches for Compact Binary Coalescence Events. *Astrophysical Journal* , 675(2):1459–1467, 2008.

[110] Clifford M. Will. Testing scalar - tensor gravity with gravitational wave observations of inspiraling compact binaries. *Phys. Rev.*, D50:6058–6067, 1994, gr-qc/9406022.

[111] Emanuele Berti, Alessandra Buonanno, and Clifford M. Will. Estimating spinning binary parameters and testing alternative theories of gravity with LISA. *Phys. Rev.*, D71:084025, 2005, gr-qc/0411129.

[112] Christian Rover, Renate Meyer, and Nelson Christensen. Coherent Bayesian inference on compact binary inspirals using a network of interferometric gravitational wave detectors. *Phys. Rev.*, D75:062004, 2007, gr-qc/0609131.

[113] Marc van der Sluys et al. Parameter estimation of spinning binary inspirals using Markov-chain Monte Carlo. *Class. Quant. Grav.*, 25:184011, 2008, 0805.1689.

[114] Marc van der Sluys et al. Parameter estimation for signals from compact binary inspirals injected into LIGO data. *Class. Quant. Grav.*, 26:204010, 2009, 0905.1323.

[115] L.S. Finn. Detection, measurement, and gravitational radiation. *Phys. Rev. D*, 46:5236, 1992.

[116] C. Van Den Broeck and A. S. Sengupta. Binary black hole spectroscopy. *Class. Quantum Grav.*, 24:1089–1113, March 2007.

[117] P. Ajith and S. Bose. Estimating the parameters of non-spinning binary black holes using ground-based gravitational-wave detectors: Statistical errors. *Phys. Rev. D*, 79:084032, 2009, arXiv:0901.4936[gr-qc].

[118] Sean T. McWilliams, James Ira Thorpe, John G. Baker, and Bernard J. Kelly. Impact of mergers on LISA parameter estimation for nonspinning black hole binaries. *Phys. Rev.*, D81:064014, 2010, 0911.1078.

[119] Michele Vallisneri. Use and abuse of the Fisher information matrix in the assessment of gravitational-wave parameter-estimation prospects. *Phys. Rev.*, D77:042001, 2008, gr-qc/0703086.

[120] A Abramovici et al. Ligo: The laser interferometer gravitational wave observatory. *Science*, 256:325, 1992.

[121] B. Abbott et al. Detector description and performance for the first coincidence observations between LIGO and GEO. *Nucl. Instrum. Meth.*, A517:154–179, 2004, gr-qc/0308043.

[122] B Caron et al. The virgo interferometer. *Class. Quantum Grav.*, 14:1461, 1997.

[123] F Acernese et al. The virgo status. *Class. Quantum Grav.*, 23:S635–S642, 2006.

[124] H Lück et al. Status of the geo600 detector. *Class. Quantum Grav.*, 23:S71–S78, 2006.

[125] K Tsubono et al. Tama project. In K. Tsubono, M.-K. Fujimoto, and K. Kuroda, editors, *Gravitational Wave Detection*, volume 20 of *Frontiers Science Series*, page 183, Tokyo, Japan, 1997. Universal Academy Press.

[126] J. Hough and S. Rowan. Gravitational wave detection by interferometry (ground and space). *Living Rev. Relativity*, 3, 2000.

[127] J R Smith. The path to the enhanced and advanced LIGO gravitational-wave detectors . 2009, arXiv:0902.0381.

[128] C. Cutler, E. Poisson, G. J. Sussman, and L. S. Finn. Gravitational radiation from a particle in circular orbit around a black hole. 2: Numerical results for the nonrotating case. *Phys. Rev. D*, 47:1511–1518, 1993.

[129] C. Cutler and É.É. Flanagan. Gravitational waves from merging compact binaries: How accurately can one extract the binary's parameters from the inspiral wave form? *Phys. Rev. D*, 49:2658–2697, 1994, arXiv:gr-qc/9402014.

[130] E. Poisson and C.M. Will. Gravitational waves from inspiraling compact binaries: Parameter estimation using second postnewtonian wave forms. *Phys. Rev. D*, 52:848–855, 1995, arXiv:gr-qc/9502040.

[131] Takahiro Tanaka, Hideyuki Tagoshi, and Misao Sasaki. Gravitational waves by a particle in circular orbits around a Schwarzschild black hole: 5.5 post-Newtonian formula. *Prog. Theor. Phys.*, 96:1087–1101, 1996, arXiv:gr-qc/9701050.

[132] T. Damour, B.R. Iyer, and B.S. Sathyaprakash. Improved filters for gravitational waves from inspiraling compact binaries. *Phys. Rev. D*, 57:885–907, 1998, arXiv:gr-qc/9708034.

[133] Serge Droz, Daniel J. Knapp, Eric Poisson, and Benjamin J. Owen. Gravitational waves from inspiraling compact binaries: Validity of the stationary-phase approximation to the Fourier transform. *Phys. Rev. D*, 59:124016, 1999, arXiv:gr-qc/9901076.

[134] Thibault Damour, Bala R. Iyer, and B. S. Sathyaprakash. Frequency-domain P-approximant filters for time-truncated inspiral gravitational wave signals from compact binaries. *Phys. Rev. D*, 62:084036, 2000, arXiv:gr-qc/0001023.

[135] Thibault Damour, Bala R. Iyer, Piotr Jaranowski, and B. S. Sathyaprakash. Gravitational waves from black hole binary inspiral and merger: The span of third post-Newtonian effective-one-body templates. *Phys. Rev. D*, 67:064028, 2003, arXiv:gr-qc/0211041.

[136] P Canitrot. Systematic errors for matched filtering of gravitational waves from inspiraling compact binaries . *Phys. Rev. D*, 63:082005, 2001.

[137] A. Buonanno, Y. Chen, and M. Vallisneri. Detection template families for gravitational waves from the final stages of binary black-hole inspirals: Nonspinning case. *Phys. Rev. D*, 67(2):024016–+, January 2003, arXiv:gr-qc/0205122.

[138] K. G. Arun, Bala R. Iyer, B. S. Sathyaprakash, and Pranesh A. Sundararajan. Parameter estimation of inspiralling compact binaries using 3.5 post-Newtonian gravitational wave phasing: The non-spinning case. *Phys. Rev. D*, 71:084008, 2005, arXiv:gr-qc/0411146.

[139] Parameswaran Ajith, Bala R. Iyer, C. A. K. Robinson, and B. S. Sathyaprakash. New class of post-Newtonian approximants to the waveform templates of inspiralling compact binaries: Test-mass in the Schwarzschild spacetime. *Phys. Rev. D*, 71:044029, 2005, arXiv:gr-qc/0412033.

[140] Lee Lindblom, Benjamin J. Owen, and Duncan A. Brown. Model Waveform Accuracy Standards for Gravitational Wave Data Analysis. *Phys. Rev. D*, 78:124020, 2008, arXiv:0809.3844.

[141] Alessandra Buonanno and Thibault Damour. Transition from inspiral to plunge in binary black hole coalescences. *Phys. Rev. D*, 62:064015, 2000, arXiv:gr-qc/0001013.

[142] Frans Pretorius. Evolution of binary black hole spacetimes. *Phys. Rev. Lett.*, 95:121101, 2005.

[143] M. Campanelli, C.O. Lousto, P. Marronetti, and Y. Zlochower. Accurate evolutions of orbiting black-hole binaries without excision. *Phys. Rev. Lett.*, 96:111101, 2006, arXiv:gr-qc/0511048.

[144] J.G. Baker, J. Centrella, D. Choi, M. Koppitz, and J. van Meter. Gravitational wave extraction from an inspiraling configuration of merging black holes. *Phys. Rev. Lett.*, 96:111102, 2006, arXiv:gr-qc/0511103.

[145] M Boyle et al. High-accuracy comparison of numerical relativity simulations with post-newtonian expansions. *Phys. Rev. D*, 76:124038, 2007, arXiv:0710.0158.

[146] F. Pretorius. Binary black hole coalescence. In M. Colpi, P. Casella, V. Gorini, U. Moschella, and A. Possenti, editors, *Physics of Relativistic Objects in Compact Binaries: From Birth to Coalescence*, volume 359 of *Astrophysics and Space Science Library*. Springer, Berlin; New York, 2009, arXiv:0710.1338.

[147] Y. Pan et al. A data-analysis driven comparison of analytic and numerical coalescing binary waveforms: Nonspinning case. *Phys. Rev. D*, 77:024014, 2008, arXiv:0704.1964.

[148] Michael Boyle, Duncan A. Brown, and Larne Pekowsky. Comparison of high-accuracy numerical simulations of black-hole binaries with stationary phase post-Newtonian template waveforms for Initial and Advanced LIGO. 2009, arXiv:0901.1628.

[149] Alessandra Buonanno, Gregory B. Cook, and Frans Pretorius. Inspiral, merger, and ring-down of equal-mass black-hole binaries. *Phys. Rev. D*, 75(12):124018, 2007, arXiv:gr-qc/0610122.

[150] Thibault Damour and Alessandro Nagar. Faithful Effective-One-Body waveforms of small-mass-ratio coalescing black-hole binaries. *Phys. Rev.*, D76:064028, 2007, 0705.2519.

[151] T. Damour and A. Nagar. Comparing effective-one-body gravitational waveforms to accurate numerical data. *Phys. Rev. D*, 77:024043, 2008, arXiv:0711.2628.

[152] T. Damour, A. Nagar, E. N. Dorband, D. Pollney, and L. Rezzolla. Faithful effective-one-body waveforms of equal-mass coalescing black-hole binaries. *Phys. Rev. D*, 77, 2008, arXiv:0712.3003.

[153] T. Damour, A. Nagar, M. Hannam, S. Husa, and B. Brügmann. Accurate effective-one-body waveforms of inspiralling and coalescing black-hole binaries. *Phys. Rev. D*, 78, 2008, arXiv:0803.3162.

[154] Michael Boyle, Alessandra Buonanno, Lawrence E. Kidder, Abdul H. Mroué, Yi Pan, Harald P. Pfeiffer, and Mark A. Scheel. High-accuracy numerical simulation of black-hole binaries: Computation of the gravitational-wave energy flux and comparisons with post-Newtonian approximants. *Phys. Rev. D*, 78(12):104020, 2008, arXiv:0804.4184.

[155] T. Damour and A. Nagar. An improved analytical description of inspiralling and coalescing black-hole binaries. 2009, arXiv:0902.0136.

[156] Alessandra Buonanno et al. Effective-one-body waveforms calibrated to numerical relativity simulations: coalescence of non-spinning, equal- mass black holes. 2009, arXiv:0902.0790.

[157] T Damour, B R Iyer, and A Nagar. Improved resummation of post-newtonian multipolar waveforms from circularized compact binaries. *Phys. Rev. D*, 79:064004, 2009, arXiv:0811.2069.

[158] Sukanta Bose, Achamveedu Gopakumar, and Manuel Tessmer. Gravitational wave data analysis implications of TaylorEt inspiral approximants for ground-based detectors: the non- spinning case. 2008, arXiv:0807.2400.

[159] Karl Martel and E Poisson. Gravitational waves from eccentric compact binaries: Reduction in signal-to-noise ratio due to nonoptimal signal pr ocessing. *Phys. Rev. D*, 60:124008, 1999, gr-qc/9907006.

[160] Thibault Damour, Achamveedu Gopakumar, and Bala R Iyer. Phasing of gravitational waves from inspiralling eccentric binaries. *Phys. Rev. D*, 70:064028, 2004, gr-qc/0404128.

[161] Christian Konigsdorffer and Achamveedu Gopakumar. Phasing of gravitational waves from inspiralling eccentric binaries at the third-and-a-half post-newtonian order. *Phys. Rev. D*, 73:124012, 2006, gr-qc/0603056.

[162] Manuel Tessmer and Achamveedu Gopakumar. Gravitational waves from compact binaries inspiralling along post-Newtonian accurate eccentric orbits: Data analysis implications. *Phys. Rev.*, D78:084029, 2008, arXiv:0712.3199.

[163] K. G. Arun, Luc Blanchet, Bala R. Iyer, and Moh'd S. S. Qusailah. Tail effects in the 3PN gravitational wave energy flux of compact binaries in quasi-elliptical orbits. 2007, 0711.0250.

[164] K. G. Arun, Luc Blanchet, Bala R. Iyer, and Moh'd S. S. Qusailah. Inspiralling compact binaries in quasi-elliptical orbits: The complete 3PN energy flux. 2007, 0711.0302.

[165] Nicolas Yunes, K. G. Arun, Emanuele Berti, and Clifford M. Will. Post-Circular Expansion of Eccentric Binary Inspirals: Fourier-Domain Waveforms in the Stationary Phase Approximation. 2009, arXiv:0906.0313.

[166] C. Van Den Broeck and A.S. Sengupta. Binary black hole spectroscopy. *Class. Quantum Grav.*, 24:1089–1114, 2007, arXiv:gr-qc/0610126.

[167] C. Van Den Broeck and A.S. Sengupta. Phenomenology of amplitude-corrected post-newtonian gravitational waveforms for compact binary inspiral. i. signal-to-noise ratios. *Class. Quantum Grav.*, 24:155–176, 2007, arXiv:gr-qc/0607092.

[168] Thibault Damour, Piotr Jaranowski, and Gerhard Schäfer. Dimensional regularization of the gravitational interaction of point masses. *Phys. Lett. B*, 513:147–155, 2001, arXiv:gr-qc/0105038.

[169] Luc Blanchet, Thibault Damour, and Gilles Esposito-Farese. Dimensional regularization of the third post-Newtonian dynamics of point particles in harmonic coordinates. *Phys. Rev. D*, 69:124007, 2004, arXiv:gr-qc/0311052.

[170] L. Blanchet, T. Damour, G. Esposito-Farese, and B.R. Iyer. Dimensional regularization of the third post-newtonian gravitational wave generation from two point masses. *Phys. Rev. D*, 71:124004, 2005, arXiv:gr-qc/0503044.

[171] Thibault Damour, Piotr Jaranowski, and Gerhard Schäfer. Equivalence between the ADM-Hamiltonian and the harmonic- coordinates approaches to the third post-Newtonian dynamics of compact binaries. *Phys. Rev. D*, 63:044021, 2001, arXiv:gr-qc/0010040.

[172] Vanessa C. de Andrade, Luc Blanchet, and Guillaume Faye. Third post-Newtonian dynamics of compact binaries: Noetherian conserved quantities and equivalence between the harmonic coordinate and ADM-Hamiltonian formalisms. *Class. Quant. Grav.*, 18:753–778, 2001, arXiv:gr-qc/0011063.

[173] Luc Blanchet and Bala R. Iyer. Third post-Newtonian dynamics of compact binaries: Equations of motion in the center-of-mass frame. *Class. Quant. Grav.*, 20:755, 2003, arXiv:gr-qc/0209089.

[174] Yousuke Itoh and Toshifumi Futamase. New derivation of a third post-Newtonian equation of motion for relativistic compact binaries without ambiguity. *Phys. Rev. D*, 68:121501, 2003, arXiv:gr-qc/0310028.

[175] Luc Blanchet, Bala R. Iyer, and Benoit Joguet. Gravitational waves from inspiralling compact binaries: Energy flux to third post-Newtonian order. *Phys. Rev. D*, 65:064005, 2002, arXiv:gr-qc/0105098.

[176] Luc Blanchet, Guillaume Faye, Bala R. Iyer, and Benoit Joguet. Gravitational-wave inspiral of compact binary systems to 7/2 post-Newtonian order. *Phys. Rev. D*, 65:061501, 2002, arXiv:gr-qc/0105099.

[177] John G. Baker, James R. van Meter, Sean T. McWilliams, Joan Centrella, and Bernard J. Kelly. Consistency of post-Newtonian waveforms with numerical relativity. *Phys. Rev. Lett.*, 99:181101, 2007, arXiv:gr-qc/0612024.

[178] E. Berti, V. Cardoso, and C. M. Will. Gravitational-wave spectroscopy of massive black holes with the space interferometer lisa. *Phys. Rev. D*, 73(6):064030–+, March 2006.

[179] T. Cokelaer. Gravitational waves from inspiralling compact binaries: hexagonal template placement and its efficiency in detecting physical signals. *Phys. Rev. D*, 76, 2007, arXiv:0706.4437.

[180] Mark A. Scheel et al. High-accuracy waveforms for binary black hole inspiral, merger, and ringdown. *Phys. Rev.*, D79:024003, 2009, arXiv:0810.1767.

[181] `http://www.ligo.org`.

[182] `http://www.virgo.infn.it`.

[183] `http://www.geo600.uni-hannover.de`.

[184] `http://lisa.jpl.nasa.gov`.

[185] Bruce Allen et al. Observational limit on gravitational waves from binary neutron stars in the galaxy. *Phys. Rev. Lett.*, 83:1498, 1999.

[186] B. Abbott et al. Search for gravitational waves from galactic and extra-galactic binary neutron stars. *Phys. Rev. D*, 72(8):082001, 2005.

[187] B. Abbott et al. Search for gravitational waves from binary black hole inspirals in ligo data. *Phys. Rev. D*, 73:062001, 2006.

[188] Luc Blanchet. Gravitational radiation from post-newtonian sources and inspiralling compact binaries. *Living Rev. Rel.*, 9:4, 2006.

[189] A. Buonanno, Y. Chen, Y. Pan, H. Tagoshi, and M. Vallisneri. Detecting gravitational waves from precessing binaries of spinning compact objects. II. Search implementation for low-mass binaries. *Phys. Rev. D*, 72:084027, 2005.

[190] Krzysztof Belczynski, Ronald E. Taam, Emmanouela Rantsiou, and Marc van der Sluys. Black hole spin evolution: Implications for short-hard gamma ray bursts and gravitational wave detection. *Astrophys. J.*, 682:474–486, 2007.

[191] M. V. van der Sluys et al. Gravitational-wave astronomy with inspiral signals of spinning compact-object binaries. 2007, arXiv:0710.1897 [astro-ph].

[192] Y. Pan, A. Buonanno, Y. Chen, and M. Vallisneri. Physical template family for gravitational waves from precessing binaries of spinning compact objects: Application to single-spin binaries. *Phys. Rev. D*, 69(10):104017–+, 2004. Erratum-ibid. D 74, 029905(E) (2006).

[193] A. Buonanno, Y. Chen, Y. Pan, and M. Vallisneri. Quasiphysical family of gravity-wave templates for precessing binaries of spinning compact objects: Application to double-spin precessing binaries. *Phys. Rev. D*, 70(10):104003, November 2004. Erratum-ibid. D **74**, 029902(E) (2006).

[194] Luc Blanchet, Thibault Damour, and Bala R. Iyer. Gravitational waves from inspiralling compact binaries: Energy loss and wave form to second post-newtonian order. *Phys. Rev. D*, 51:5360–5386, 1995.

[195] Luc Blanchet, Thibault Damour, Bala R. Iyer, Clifford M. Will, and Alan. G. Wiseman. Gravitational radiation damping of compact binary systems to second post-newtonian order. *Phys. Rev. Lett.*, 74:3515–3518, 1995.

[196] Luc Blanchet. Energy losses by gravitational radiation in inspiralling compact binaries to five halves post-newtonian order. *Phys. Rev. D*, 54:1417–1438, 1996. erratum-ibid. D **71**, 129904(E) (2005).

[197] Luc Blanchet, Thibault Damour, Gilles Esposito-Farèse, and Bala R. Iyer. Gravitational radiation from inspiralling compact binaries completed at the third post-newtonian order. *Phys. Rev. Lett.*, 93:091101, 2004.

[198] Luc Blanchet, Bala R. Iyer, Clifford M. Will, and Alan G. Wiseman. Gravitational wave forms from inspiralling compact binaries to second-post-newtonian order. *Class. Quantum Grav.*, 13:575–584, 1996.

[199] K G Arun, Luc Blanchet, Bala R. Iyer, and Moh'd S S. Qusailah. The 2.5pn gravitational wave polarisations from inspiralling compact binaries in circular orbits. *Class. Quantum Grav.*, 21:3771, 2004. Erratum-ibid. **22**, 3115 (2005).

[200] Lawrence E. Kidder, Luc Blanchet, and Bala R. Iyer. Radiation reaction in the 2.5pn waveform from inspiralling binaries in circular orbits. *Class. Quant. Grav.*, 24:5307, 2007.

[201] L. E. Kidder. Using full information when computing modes of post-Newtonian waveforms from inspiralling compact binaries in circular orbit. *Phys. Rev. D*, 77:044016, 2007.

[202] L.E. Kidder, C.M. Will, and A.G. Wiseman. Spin effects in the inspiral of coalescing compact binaries. *Phys. Rev. D*, 47:R4183–R4187, 1993.

[203] B.J. Owen, H. Tagoshi, and A. Ohashi. Nonprecessional spin-orbit effects on gravitational waves from inspiraling compact binaries to second post-newtonian order. *Phys. Rev. D*, 57:6168–6175, 1998.

[204] R. A. Porto and I. Z. Rothstein. Calculation of the First Nonlinear Contribution to the General-Relativistic Spin-Spin Interaction for Binary Systems. *Phys. Rev. Lett.*, 97:021101, 2006.

[205] R. A. Porto and I. Z. Rothstein. Comment on 'On the next-to-leading order gravitational spin(1)-spin(2) dynamics' by J. Steinhoff et al. 2007, arXiv:0712.2032[gr-qc].

[206] R. A. Porto and I. Z. Rothstein. Spin(1)Spin(2) Effects in the Motion of Inspiralling Compact Binaries at Third Order in the Post-Newtonian Expansion. 2008, arXiv:0802.0720 [gr-qc].

[207] M. Levi. Next to Leading Order gravitational Spin-Spin coupling with Kaluza-Klein reduction. 2008, arXiv:0802.1508 [gr-qc].

[208] Jan Steinhoff, Steven Hergt, and Gerhard Schaefer. On the next-to-leading order gravitational spin(1)-spin(2) dynamics. *Phys. Rev. D*, 77:081501(R), 2008.

[209] Jan Steinhoff, Gerhard Schaefer, and Steven Hergt. ADM canonical formalism for gravitating spinning objects. *Phys. Rev. D*, 77:104018, 2008.

[210] Jan Steinhoff, Steven Hergt, and Gerhard Schafer. Spin-squared Hamiltonian of next-to-leading order gravitational interaction. 2008, arXiv:0809.2200[gr-qc].

[211] R. A. Porto and I. Z. Rothstein. Next to Leading Order Spin(1)Spin(1) Effects in the Motion of Inspiralling Compact Binaries. 2008, arXiv:0804.0260 [astro-ph].

[212] Alicia M Sintes and Alberto Vecchio. Detection of gravitational waves from inspiraling compact binaries using non-restricted post-newtonian approximations. In J. Dumarchez, editor, *Rencontres de Moriond:Gravitational waves and experimental gravity*. Frontires, Paris, 2000, gr-qc/0005058.

[213] Chris Van Den Broeck. Binary black hole detection rates in inspiral gravitational wave searches. *Class. Quantum Grav.*, 23:L51, 2006.

[214] Chris Van Den Broeck and Anand Sengupta. Phenomenology of amplitude-corrected post-newtonian gravitational waveforms for compact binary inspiral. i. signal-to-noise ratios. *Class. Quantum Grav.*, 24:155, 2007.

[215] A. M. Sintes and A. Vecchio. Lisa observations of massive black hole binaries using post-newtonian waveforms. In S. Meshkov, editor, *Third Amaldi conference on Gravitational Waves*, page 403. American Institute of Physics Conference Series, 2000, gr-qc/0005059.

[216] Thomas A Moore and Ronald W Hellings. The angular resolution of space-based gravitational wave detectors. *Phys. Rev. D*, 65:062001, 2002.

[217] Rolan W Hellings and Thomas A Moore. The information content of gravitational wave harmonics in compact binary inspiral. *Class. Quant. Grav.*, 20:S181, 2003.

[218] K. G. Arun, B. R. Iyer, B. S. Sathyaprakash, and S. Sinha. Higher harmonics increase LISA's mass reach for supermassive black holes. *Phys. Rev. D*, 75:124002, 2007.

[219] K. G. Arun, Bala R. Iyer, B. S. Sathyaprakash, Siddhartha Sinha, and Chris Van Den Broeck. Higher signal harmonics, lisa's angular resolution and dark energy. *Phys. Rev. D*, 76:104016, 2007.

[220] Miquel Trias and Alicia M. Sintes. LISA observations of supermassive black holes: parameter estimation using full post-Newtonian inspiral waveforms. *Phys. Rev. D*, 77:024030, 2008.

[221] S. Babak, M. Hannam, S. Husa, and B. Schutz. Resolving Super Massive Black Holes with LISA. 2008, arXiv:0806.1591 [gr-qc].

[222] Alberto Vecchio. Lisa observations of rapidly spinning massive black hole binary systems. *Phys. Rev. D*, 70:042001, 2004.

[223] Ryan N. Lang and Scott A. Hughes. Measuring coalescing massive binary black holes with gravitational waves: The impact of spin-induced precession. *Phys. Rev. D*, 74:122001, 2006. Erratum-ibid. D **75**, 089902 (2007).

[224] Ryan N. Lang and Scott A. Hughes. Localizing coalescing massive black hole binaries with gravitational waves. *Astrophys. J.*, 677:1184, 2007.

[225] J. Majár and M. Vasúth. Gravitational waveforms for spinning compact binaries. *Phys. Rev. D*, 77:104005, 2008.

[226] E. Berti, V. Cardoso, J. A. Gonzalez, U. Sperhake, M. Hannam, S. Husa, and B. Brügmann. Inspiral, merger, and ringdown of unequal mass black hole binaries: A multipolar analysis. *Phys. Rev. D*, 76(6):064034–+, September 2007.

[227] John G. Baker, James R. van Meter, Sean T. McWilliams, Joan Centrella, and Bernard J. Kelly. Consistency of post-newtonian waveforms with numerical relativity. *Phys. Rev. Lett.*, 99:181101, 2007.

[228] Alessandra Buonanno, Yi Pan, John G. Baker, Joan Centrella, Bernard J. Kelly, Sean T. McWilliams, and James R. van Meter. Approaching faithful templates for non-spinning binary black holes using the effective-one-body approach. *Phys. Rev. D*, 76:104049, 2007.

[229] Mark Hannam, Sascha Husa, Ulrich Sperhake, Bernd Brugmann, and Jose A. Gonzalez. Where post-newtonian and numerical-relativity waveforms meet. *Phys. Rev. D*, 77:044020, 2008.

[230] Michael Boyle et al. High-accuracy comparison of numerical relativity simulations with post-newtonian expansions. *Phys. Rev. D*, 76:124038, 2007.

[231] M. Hannam, S. Husa, B. Brügmann, and A. Gopakumar. Comparison between numerical-relativity and post-Newtonian waveforms from spinning binaries: the orbital hang-up case. 2007, arXiv:0712.3787 [gr-qc].

[232] E. Berti, V. Cardoso, J. A. González, U. Sperhake, and B. Brügmann. Multipolar analysis of spinning binaries. *Class. Quant. Grav.*, 25(11):114035, 2008.

[233] P. Ajith, S. Babak, Y. Chen, M. Hewitson, B. Krishnan, A. M. Sintes, J. T. Whelan, B. Brügmann, P. Diener, N. Dorband, J. Gonzalez, M. Hannam, S. Husa, D. Pollney, L. Rezzolla, L. Santamaría, U. Sperhake, and J. Thornburg. Template bank for gravitational waveforms from coalescing binary black holes: Nonspinning binaries. *Phys. Rev. D*, 77(10):104017, May 2008.

[234] Yi Pan, Alessandra Buonanno, John G. Baker, Joan Centrella, Bernard J. Kelly, Sean T. McWilliams, Frans Pretorius, and James R. van Meter. Data-analysis driven comparison of analytic and numerical coalescing binary waveforms: Nonspinning case. *Phys. Rev. D*, 77:024014, 2008.

[235] E. Poisson. Gravitational waves from inspiraling compact binaries: The quadrupole-moment term. *Phys. Rev. D*, 57:5287, 1998.

[236] Theocharis A. Apostolatos, Curt Cutler, Gerald J. Sussman, and Kip S. Thorne. Spin induced orbital precession and its modulation of the gravitational wave forms from merging binaries. *Phys. Rev. D*, 49:6274–6297, 1994.

[237] J. N. Goldberg, A. J. Macfarlane, E. T. Newman, F. Rohrlich, and E. C. G. Sudarshan. Spin-s spherical harmonics and $\eth$. *J. Math. Phys.*, 8:2155, 1967.

[238] L.D. Landau and E.M. Lifshitz. *Quantum Mechanics*. Pergamon, Oxford, 1977.

[239] L. Gualtieri, E. Berti, V. Cardoso, and U. Sperhake. Transformation of the multipolar components of gravitational radiation under rotations and boosts. *Class. Quantum Grav.*, 805, May 2008.

[240] M. Campanelli, C. O. Lousto, H. Nakano, and Y. Zlochower. Comparison of Numerical and Post-Newtonian Waveforms for Generic Precessing Black-Hole Binaries. 2008, arXiv:0808.0713 [gr-qc].

[241] E. Racine. Analysis of spin precession in binary black hole systems including quadrupole-monopole interaction. *Phys. Rev. D*, 78:044021, 2008.

[242] P. Jaranowski and G. Schäfer. Binary black-hole problem at the third post-newtonian approximation in the orbital motion: Static part. *Phys. Rev. D*, 60:124003–1–12403–7, 1999.

[243] P. Jaranowski and G. Schäfer. The binary black-hole dynamics at the third post-newtonian order in the orbital motion. *Ann. Phys. (Berlin)*, 9:378–383, 2000.

[244] V. C. de Andrade, L. Blanchet, and G. Faye. Third post-Newtonian dynamics of compact binaries: Noetherian conserved quantities and equivalence between the harmonic-coordinate and adm-hamiltonian formalisms. *Class. Quantum Grav.*, 18:753–778, 2001.

[245] L. Blanchet and G. Faye. General relativistic dynamics of compact binaries at the third post-Newtonian order. *Phys. Rev. D*, 63:062005, 2001.

[246] K G Arun, B R Iyer, B S Sathyaprakash, and P A Sundararajan. Parameter estimation of inspiralling compact binaries using 3.5 post-newtonian gravitational wave phasing: The non-spinning case. *Phys. Rev. D*, 71:084008, 2005. Erratum-ibid. D **72**, 069903 (2005).

[247] Edward K. Porter and Neil J. Cornish. The Effect of Higher Harmonic Corrections on the Detection of massive black hole binaries with LISA. 2008, arXiv:0804.0332 [gr-qc].

[248] E. Berti, A. Buonanno, and C. M. Will. Estimating spinning binary parameters and testing alternative theories of gravity with lisa. *Phys. Rev. D*, 71(8):084025–+, April 2005.

[249] C Cutler. Angular resolution of the lisa gravitational wave detector. *Phys. Rev. D*, 57:7089, 1998.

[250] M. Campanelli, C. O. Lousto, and Y. Zlochower. Gravitational radiation from spinning-black-hole binaries: The orbital hang up. *Phys. Rev. D*, 74:041501, 2006.

[251] M. Campanelli, C. O. Lousto, and Y. Zlochower. Spin-orbit interactions in black-hole binaries. *Phys. Rev. D*, 74:084023, 2006.

[252] Manuela Campanelli, Carlos O. Lousto, Yosef Zlochower, Badri Krishnan, and David Merritt. Spin flips and precession in black-hole binary mergers. *Phys. Rev. D*, 75:064030, 2007.

[253] F. Herrmann, Ian Hinder, D. Shoemaker, P. Laguna, and Richard A. Matzner. Gravitational recoil from spinning binary black hole mergers. *Astrophys. J.*, 661:430, 2007.

[254] Frank Herrmann, Ian Hinder, Deirdre M. Shoemaker, Pablo Laguna, and Richard A. Matzner. Binary black holes: Spin dynamics and gravitational recoil. *Phys. Rev. D*, 76:084032, 2007.

[255] K. Alvi. Energy and angular momentum flow into a black hole in a binary. *Phys. Rev. D*, 64:104020, 2001.

[256] K S Thorne. Gravitational radiation. In S. W. Hawking and W. Israel, editors, *Three hundred years of gravitation*, chapter 9, pages 330–458. Cambridge University Press, Cambridge, 1987.

[257] P. C. Peters. Gravitational Radiation and the Motion of Two Point Masses. *Phys. Rev.*, 136:B1224–B1232, 1964.

[258] B. C. Barish and R. Weiss. LIGO and the detection of gravitational waves. *Phys. Today*, 52N10:44–50, 1999.

[259] F. Acernese et al. The Virgo detector. *AIP Conf. Proc.*, 794:307–310, 2005.

[260] K. Tsubono. TAMA project. Prepared for 9th Marcel Grossmann Meeting on Recent Developments in Theoretical and Experimental General Relativity, Gravitation and Relativistic Field Theories (MG 9), Rome, Italy, 2-9 Jul 2000.

[261] Benno Willke. GEO600: Status and plans. *Class. Quant. Grav.*, 24:S389–S397, 2007.

[262] B. Abbott et al. LIGO: The Laser Interferometer Gravitational-Wave Observatory. 2007, 0711.3041.

[263] F. Acernese et al. Noise studies during the first Virgo science run and after. *Class. Quant. Grav.*, 25:184003, 2008.

[264] R. Adhikari, P. Fritschel, and S. Waldman. Enhanced LIGO tech. rep. LIGO-T060156-01-I, `http://www.ligo.caltech.edu/docs/T/T060156-01.pdf`. 2006.

[265] Peter Fritschel. Second generation instruments for the Laser Interferometer Gravitational Wave Observatory (LIGO). 2003, gr-qc/0308090.

[266] F. et al Acernese. Advanced Virgo tech. rep. VIR089A08, `https://pub3.ego-gw.it/codifier/index.php?content=show&doc=2110`.

[267] T. Uchiyama et al. Present status of large-scale cryogenic gravitational wave telescope. *Class. Quant. Grav.*, 21:S1161–S1172, 2004.

[268] B. P. Abbott et al. Search for Gravitational Waves from Low Mass Binary Coalescences in the First Year of LIGO's S5 Data. *Phys. Rev.*, D79:122001, 2009, 0901.0302.

[269] B. et al. (LIGO Scientific Collaboration) Abbott. Analysis of ligo data for gravitational waves from binary neutron stars. *Phys. Rev. D*, 69, 2004, arXiv:gr-qc/0308069.

[270] B. et al. (LIGO Scientific Collaboration) Abbott. Search for gravitational waves from galactic and extra- galactic binary neutron stars. *Phys. Rev. D*, 72, 2005, arXiv:gr-qc/0505041.

[271] B. et al. (LIGO Scientific Collaboration) Abbott. Search for gravitational waves from primordial black hole binary coalescences in the galactic halo. *Phys. Rev. D*, 72, 2005, arXiv:gr-qc/0505042.

[272] B. Abbott et al. Search for gravitational waves from binary inspirals in S3 and S4 LIGO data. *Phys. Rev.*, D77:062002, 2008, 0704.3368.

[273] B. et al. (LIGO Scientific Collaboration) Abbott. Search of s3 ligo data for gravitational wave signals from spinning black hole and neutron star binary inspirals. *Phys. Rev. D*, 78, 2008, arXiv:0712.2050.

[274] B. Abbott et al. First upper limits from ligo on gravitational wave bursts. *Phys. Rev.*, D69:102001, 2004, gr-qc/0312056.

[275] B. Abbott et al. Upper limits on gravitational wave bursts in LIGO's second science run. *Phys. Rev.*, D72:062001, 2005, gr-qc/0505029.

[276] B. Abbott et al. Search for gravitational wave bursts in LIGO's third science run. *Class. Quant. Grav.*, 23:S29–S39, 2006, gr-qc/0511146.

[277] B. Abbott et al. Upper limits from the LIGO and TAMA detectors on the rate of gravitational-wave bursts. *Phys. Rev.*, D72:122004, 2005, gr-qc/0507081.

[278] B. et al. (LIGO Scientific Collaboration) Abbott. Search for gravitational-wave bursts in ligo data from the fourth science run. *Class. Quantum Grav.*, 24:5343–5370, 2007, arXiv:0704.0943.

[279] Frans Pretorius. Evolution of binary black hole spacetimes. *Phys. Rev. Lett.*, 95:121101, 2005, gr-qc/0507014.

[280] Sascha Husa. Numerical modeling of black holes as sources of gravitational waves in a nutshell. *Eur. Phys. J. ST*, 152:183–207, 2007, 0812.4395.

[281] Mark Hannam. Status of black-hole-binary simulations for gravitational-wave detection. 2009, arXiv:0901.2931.

[282] F. Herrmann, I. Hinder, D. Shoemaker, and P. Laguna. Unequal Mass Binary Black Hole Plunges and Gravitational Recoil. *Class. Quantum Grav.*, 2007, gr-qc/0601026.

[283] J.G. Baker, J.M. Centrella, D.-I. Choi, M. Koppitz, J.R. van Meter, and M.C. Miller. Getting a kick out of numerical relativity. *Astrophys. J. Lett.*, 653:L93–L96, 2006, arXiv:astro-ph/0603204.

[284] J.A. Gonzalez, U. Sperhake, B. Brügmann, M. Hannam, and S. Husa. Total recoil: the maximum kick from nonspinning black-hole binary inspiral. *Phys. Rev. Lett.*, 98, 2007, arXiv:gr-qc/0610154.

[285] F. Herrmann, I. Hinder, D. Shoemaker, P. Laguna, and R.A. Matzner. Gravitational recoil from spinning binary black hole mergers. *Astrophys. J.*, 661:430–436, 2007, arXiv:gr-qc/0701143.

[286] Michael Koppitz et al. Getting a kick from equal-mass binary black hole mergers. *Phys. Rev. Lett.*, 99:041102, 2007, gr-qc/0701163.

[287] M. Campanelli, C.O. Lousto, Y. Zlochower, and D. Merritt. Large merger recoils and spin flips from generic black-hole binaries. *Astrophys. J.*, 659:L5–L8, 2007, arXiv:gr-qc/0701164.

[288] José A. Gonzalez, Mark D. Hannam, Ulrich Sperhake, Bernd Brügmann, and Sascha Husa. Supermassive kicks for spinning black holes. *Phys. Rev. Lett.*, 98:231101, 2007, gr-qc/0702052.

[289] Wolfgang Tichy and Pedro Marronetti. Binary black hole mergers: Large kicks for generic spin orientations. *Phys. Rev. D*, 76:061502, 2007, gr-qc/0703075.

[290] Manuela Campanelli, Carlos O. Lousto, Yosef Zlochower, and David Merritt. Maximum gravitational recoil. *Phys. Rev. Lett.*, 98:231102, 2007, gr-qc/0702133.

[291] John G. Baker et al. Modeling kicks from the merger of non-precessing black-hole binaries. *Astrophys. J.*, 668:1140–1144, 2007. astro-ph/0702390.

[292] Frank Herrmann, Ian Hinder, Deirdre M. Shoemaker, Pablo Laguna, and Richard A. Matzner. Binary Black Holes: Spin Dynamics and Gravitational Recoil. *Phys. Rev. D*, 76:084032, 2007, 0706.2541.

[293] B. Brügmann, J.A. Gonzalez, M. Hannam, S. Husa, and U. Sperhake. Exploring black hole superkicks. *Phys. Rev. D*, 77, 2008, arXiv:0707.0135.

[294] D. et al. Pollney. Recoil velocities from equal-mass binary black-hole mergers: a systematic investigation of spin-orbit aligned configurations. *Phys. Rev. D*, 76, 2007, arXiv:0707.2559.

[295] Carlos O. Lousto and Yosef Zlochower. Further insight into gravitational recoil. *Phys. Rev. D*, 77:044028, 2008, 0708.4048.

[296] John G. Baker et al. Modeling kicks from the merger of generic black-hole binaries. *Astrophys. J.*, 682:L29, 2008, 0802.0416.

[297] Sergio Dain, Carlos O. Lousto, and Yosef Zlochower. Extra-Large Remnant Recoil Velocities and Spins from Near- Extremal-Bowen-York-Spin Black-Hole Binaries. *Phys. Rev. D*, 78:024039, 2008, 0803.0351.

[298] James Healy, Frank Herrmann, Ian Hinder, Deirdre M. Shoemaker, Pablo Laguna, and Richard A. Matzner. Superkicks in hyperbolic encounters of binary black holes. *Phys. Rev. Lett.*, 102:041101, 2009, arXiv:0807.3292 [gr-qc].

[299] José A. Gonzalez, Ulrich Sperhake, and Bernd Brügmann. Black-hole binary simulations: the mass ratio 10:1. *Phys. Rev. D*, 79:124006, 2009, arXiv:0811.3952 [gr-qc].

[300] Manuela Campanelli, C. O. Lousto, and Yosef Zlochower. Spin-orbit interactions in black-hole binaries. *Phys. Rev. D*, 74:084023, 2006, astro-ph/0608275.

[301] Manuela Campanelli, Carlos O. Lousto, Yosef Zlochower, Badri Krishnan, and David Merritt. Spin Flips and Precession in Black-Hole-Binary Mergers. *Phys. Rev. D*, 75:064030, 2007, gr-qc/0612076.

[302] E. Berti, V. Cardoso, J.A. Gonzalez, U. Sperhake, M. Hannam, S. Husa, and B. Brügmann. Inspiral, merger and ringdown of unequal mass black hole binaries: A multipolar analysis. *Phys. Rev. D*, 76, 2007, arXiv:gr-qc/0703053.

[303] L. Rezzolla, E.N. Dorband, C. Reisswig, P. Diener, D. Pollney, E. Schnetter, and B. Szilágy. Spin diagrams for equal-mass black-hole binaries with aligned spins. *Astrophys. J.*, 679:1422–1426, 2007, arXiv:0708.3999.

[304] Latham Boyle, Michael Kesden, and Samaya Nissanke. Binary black hole merger: symmetry and the spin expansion. *Phys. Rev. Lett.*, 100:151101, 2008, 0709.0299.

[305] Luciano Rezzolla et al. The final spin from the coalescence of aligned-spin black- hole binaries. *Astrophys. J.*, 674:L29–L32, 2008, 0710.3345.

[306] P. Marronetti, W. Tichy, B. Brügmann, J. Gonzalez, and U. Sperhake. High-spin binary black hole mergers. *Phys. Rev. D*, 77, 2008, arXiv:0709.2160.

[307] Ulrich Sperhake et al. Eccentric binary black-hole mergers: The transition from inspiral to plunge in general relativity. *Phys. Rev. D*, 78:064069, 2008, 0710.3823.

[308] Ian Hinder, Birjoo Vaishnav, Frank Herrmann, Deirdre Shoemaker, and Pablo Laguna. Universality and Final Spin in Eccentric Binary Black Hole Inspirals. *Phys. Rev. D*, 77:081502, 2008, 0710.5167.

[309] E. Berti, V. Cardoso, José A. Gonzalez, Ulrich Sperhake, and Bernd Brügmann. Multipolar analysis of spinning binaries. *Class. Quantum Grav.*, 25:114035, 2008, 0711.1097.

[310] Latham Boyle and Michael Kesden. The spin expansion for binary black hole merger: new predictions and future directions. *Phys. Rev. D*, 78:024017, 2008, 0712.2819.

[311] Wolfgang Tichy and Pedro Marronetti. The final mass and spin of black hole mergers. *Phys. Rev. D*, 78:081501, 2008, 0807.2985.

[312] Luciano Rezzolla. Modelling the final state from binary black-hole coalescences. *Class. Quantum Grav.*, 26:094023, 2009, arXiv:0812.2325 [gr-qc]. Proceedings of 7th LISA Symposium, Barcelona June 2008.

[313] Alessandra Buonanno, Gregory B. Cook, and Frans Pretorius. Inspiral, merger and ring-down of equal-mass black-hole binaries. *Phys. Rev. D*, 75:124018, 2007.

[314] P. et al. Ajith. Phenomenological template family for black-hole coalescence waveforms. *Class. Quantum Grav.*, 24:S689–S700, 2007, arXiv:0704.3764.

[315] Michael Boyle et al. High-accuracy numerical simulation of black-hole binaries: Computation of the gravitational-wave energy flux and comparisons with post-Newtonian approximants. *Phys. Rev. D*, 78:104020, 2008, 0804.4184.

[316] Thomas Baumgarte et al. Learning about compact binary merger: The interplay between numerical relativity and gravitational-wave astronomy. *Phys. Rev.*, D77:084009, 2008, gr-qc/0612100.

[317] Birjoo Vaishnav, Ian Hinder, Frank Herrmann, and Deirdre Shoemaker. Matched Filtering of Numerical Relativity Templates of Spinning Binary Black Holes. *Phys. Rev.*, D76:084020, 2007, 0705.3829.

[318] Mark Hannam et al. The Samurai Project: verifying the consistency of black- hole-binary waveforms for gravitational-wave detection. *Phys. Rev.*, D79:084025, 2009, 0901.2437.

[319] L A Wainstein and V D Zubakov. *Extraction of signals from noise*. Prentice-Hall, Englewood Cliffs, NJ, 1962.

[320] C. W. Helmstrom. *Statistical Theory of Signal Detection*. Permagon, London, 1968.

[321] B. Abbott et al. Tuning matched filter searches for compact binary coalescence. Technical Report LIGO-T070109-01, 2007.

[322] B.J. Owen and B.S. Sathyaprakash. Matched filtering of gravitational waves from inspiraling compact binaries: Computational cost and template placement. *Phys. Rev. D*, 60, 1999, arXiv:gr-qc/9808076.

[323] S. Babak, R. Balasubramanian, D. Churches, T. Cokelaer, and B. S. Sathyaprakash. A template bank to search for gravitational waves from inspiralling compact binaries. I: Physical models. *Class. Quant. Grav.*, 23:5477–5504, 2006, gr-qc/0604037.

[324] Chris Van Den Broeck et al. Template banks to search for compact binaries with spinning components in gravitational wave data. *Phys. Rev.*, D80:024009, 2009, 0904.1715.

[325] Jolien D. E. Creighton. Search techniques for gravitational waves from black-hole ringdowns. *Phys. Rev. D*, 60:022001, 1999, gr-qc/9901084.

[326] C.A.K. Robinson, B.S. Sathyaprakash, and A.S. Sengupta. A geometric algorithm for efficient coincident detection of gravitational waves. *Phys. Rev. D*, 78, 2008, arXiv:0804.4816.

[327] L. M. Goggin. *A search for gravitational waves from perturbed black hole ringdowns in LIGO data*. PhD thesis, Caltech, 2008, arXiv:gr-qc/0908.2085.

[328] B. Allen. A chi**2 time-frequency discriminator for gravitational wave detection. *Phys. Rev. D*, 71:062001, 2005, arXiv:gr-qc/0405045.

[329] Andres Rodríguez. Reducing false alarms in searches for gravitational waves from coalescing binary systems. Master's thesis, Louisiana State University, 2007, arXiv:0802.1376.

[330] Luc Blanchet. Gravitational radiation from post-Newtonian sources and inspiralling compact binaries. *Living Rev. Rel.*, 5:3, 2002, arXiv:gr-qc/0202016.

[331] Luc Blanchet, Bala R. Iyer, Clifford M. Will, and Alan G. Wiseman. Gravitational wave forms from inspiralling compact binaries to second-post-Newtonian order. *Class. Quantum Grav.*, 13:575, 1996.

[332] Luc Blanchet, Thibault Damour, Bala R. Iyer, Clifford M. Will, and Alan. G. Wiseman. Gravitational-radiation damping of compact binary systems to second post-Newtonian order. *Phys. Rev. Lett.*, 74:3515–3518, 1995.

[333] Luc Blanchet, Guillaume Faye, Bala R. Iyer, and Benoit Joguet. Erratum: Gravitational-wave inspiral of compact binary systems to 7/2 post-newtonian order [phys. rev. d 65, 061501(r) (2002)]. *Phys. Rev. D*, 71(12):129902, Jun 2005.

[334] Mark Hannam et al. Where post-Newtonian and numerical-relativity waveforms meet. *Phys. Rev. D*, 77:044020, 2008, arXiv:0706.1305.

[335] Sukanta Bose, Archana Pai, and Sanjeev V. Dhurandhar. Detection of gravitational waves from inspiraling compact binaries using a network of interferometric detectors. *Int. J. Mod. Phys.*, D9:325–329, 2000, gr-qc/0002010.

[336] A. Buonanno and T. Damour. Effective one-body approach to general relativistic two- body dynamics. *Phys. Rev.*, D59:084006, 1999, gr-qc/9811091.

[337] Thibault Damour, Bala R. Iyer, and B. S. Sathyaprakash. Improved filters for gravitational waves from inspiralling compact binaries. *Phys. Rev.*, D57:885–907, 1998, gr-qc/9708034.

[338] LSC Algorithm Library software packages LAL, LALWRAPPER, and LALAPPS.

[339] P. Ajith. Gravitational-wave data analysis using binary black-hole waveforms. *Class. Quantum Grav.*, 25:114033, 2008, arXiv:0712.0343.

[340] Lucia Santamaria, Badri Krishnan, and John T. Whelan. Searching for numerically-simulated signals of black hole binaries with a phenomenological template family. *Class. Quant. Grav.*, 26:114010, 2009, 0901.4696.

[341] Emanuele Berti, Jaime Cardoso, Vitor Cardoso, and Marco Cavaglia. Matched-filtering and parameter estimation of ringdown waveforms. *Phys. Rev.*, D76:104044, 2007, 0707.1202.

[342] F. Echeverria. Gravitational wave measurements of the mass and angular momentum of a black hole. *Phys. Rev. D*, 40:3194–3203, 1989.

[343] L. Rezzolla, E. Barausse, E.N. Dorband, D. Pollney, C. Reisswig, J. Seiler, and S. Husa. On the final spin from the coalescence of two black holes. *Phys. Rev. D*, 78, 2007, arXiv:0712.3541.

[344] Emanuele Berti, Vitor Cardoso, Jose A. Gonzalez, and Ulrich Sperhake. Mining information from binary black hole mergers: a comparison of estimation methods for complex exponentials in noise. *Phys. Rev.*, D75:124017, 2007, gr-qc/0701086.

[345] D. Brown et al. Data formats for numerical relativity waves. 2007, 0709.0093.

[346] K. A. Arnaud et al. Report on the first round of the Mock LISA Data Challenges. *Class. Quant. Grav.*, 24:S529–S540, 2007, gr-qc/0701139.

[347] Stanislav Babak et al. Report on the second Mock LISA Data Challenge. *Class. Quant. Grav.*, 25:114037, 2008, 0711.2667.

[348] Stanislav Babak et al. The Mock LISA Data Challenges: from Challenge 1B to Challenge 3. *Class. Quant. Grav.*, 25:184026, 2008, 0806.2110.

[349] K. G. Arun et al. Massive Black Hole Binary Inspirals: Results from the LISA Parameter Estimation Taskforce. *Class. Quant. Grav.*, 26:094027, 2009, 0811.1011.

[350] Dragoljub Markovic. On the possibility of determining cosmological parameters from measurements of gravitational waves emitted by coalescing, compact binaries. *Phys. Rev.*, D48:4738–4756, 1993.

[351] Samaya Nissanke, Scott A. Hughes, Daniel E. Holz, Neal Dalal, and Jonathan L. Sievers. Exploring short gamma-ray bursts as gravitational-wave standard sirens. 2009, 0904.1017.

[352] Clifford M Will. Bounding the mass of the graviton using gravitional-wave observations of inspiralling compact binaries. *Phys. Rev. D*, 57:2061, 1998, gr-qc/9709011.

[353] K. G. Arun and Clifford M. Will. Bounding the mass of the graviton with gravitational waves: Effect of higher harmonics in gravitational waveform templates. *Class. Quant. Grav.*, 26:155002, 2009, 0904.1190.

[354] Adamantios Stavridis and Clifford M. Will. Bounding the mass of the graviton with gravitational waves: Effect of spin precessions in massive black hole binaries. *Phys. Rev.*, D80:044002, 2009, 0906.3602.

[355] R. Balasubramanian, B. S. Sathyaprakash, and S. V. Dhurandhar. Gravitational waves from coalescing binaries: Detection strategies and Monte Carlo estimation of parameters. *Phys. Rev. D*, 53:3033–3055, 1996, gr-qc/9508011.

[356] F. Acernese et al. Improving the timing precision for inspiral signals found by interferometric gravitational wave detectors. *Class. Quant. Grav.*, 24:S617–S625, 2007.

[357] William H. Press, Saul A. Teukolsky, William T. Wetterling, and Brian P. Flannery. *Numerical Recipes in C*. Cambridge University Press, Cambridge, England, second edition, 1992.

[358] `http://www.fftw.org`.

[359] Matteo Frigo and Steven G. Johnson. The design and implementation of FFTW3. *Proceedings of the IEEE*, 93(2):216–231, 2005. Special issue on "Program Generation, Optimization, and Platform Adaptation".

[360] `http://www.robertnz.net/nm_intro.htm`.

[361] D. J. A. McKechan, C. Robinson, and B. S. Sathyaprakash. A tapering window for time-domain templates and simulated signals in the detection of gravitational waves from coalescing compact binaries. *Class. Quant. Grav.*, 27:084020, 2010, 1003.2939.

[362] Ronald A. Remillard and Jeffrey E. McClintock. X-ray properties of black-hole binaries. *Annual Review of Astronomy and Astrophysics*, 44:49, 2006.

[363] J. A. Orosz, J. E. McClintock, R. Narayan, C. D. Bailyn, J. D. Hartman, L. Macri, J. Liu, W. Pietsch, R. A. Remillard, A. Shporer, and T. Mazeh. A 15.65-solar-mass black hole in an eclipsing binary in the nearby spiral galaxy M 33. *Nature* , 449:872–875, October 2007, 0710.3165.

[364] P. A. Crowther, R. Barnard, S. Carpano, J. S. Clark, V. S. Dhillon, and A. M. T. Pollock. NGC 300 X-1 is a Wolf-Rayet/black hole binary. *MNRAS* , pages L11+, January 2010, 1001.4616.

[365] R. M. O'Leary, R. O'Shaughnessy, and F. A. Rasio. Dynamical interactions and the black-hole merger rate of the Universe. *Phys. Rev. D*, 76(6):061504–+, September 2007, astro-ph/0701887.

[366] A. Sadowski, K. Belczynski, T. Bulik, N. Ivanova, F. A. Rasio, and R. O'Shaughnessy. The Total Merger Rate of Compact Object Binaries in the Local Universe. *Astrophysical Journal* , 676:1162–1169, April 2008, 0710.0878.

[367] M. C. Miller and V. M. Lauburg. Mergers of Stellar-Mass Black Holes in Nuclear Star Clusters. *Astrophysical Journal* , 692:917–923, February 2009, 0804.2783.

[368] R. M. O'Leary, B. Kocsis, and A. Loeb. Gravitational waves from scattering of stellar-mass black holes in galactic nuclei. *MNRAS* , 395:2127–2146, June 2009, 0807.2638.

[369] M. C. Miller and E. J. M. Colbert. Intermediate-Mass Black Holes. *International Journal of Modern Physics D*, 13:1–64, January 2004, astro-ph/0308402.

[370] M. Coleman Miller. Intermediate-mass black holes as lisa sources, 2008.

[371] S. A. Farrell, N. A. Webb, D. Barret, O. Godet, and J. M. Rodrigues. An intermediate-mass black hole of over 500 solar masses in the galaxy ESO243-49. *Nature* , 460:73–75, July 2009.

[372] D. A. Brown, J. Brink, H. Fang, J. R. Gair, C. Li, G. Lovelace, I. Mandel, and K. S. Thorne. Prospects for Detection of Gravitational Waves from Intermediate-Mass-Ratio Inspirals. *Phys. Rev. Lett.*, 99(20):201102–+, November 2007, arXiv:gr-qc/0612060.

[373] I. Mandel, D. A. Brown, J. R. Gair, and M. C. Miller. Rates and Characteristics of Intermediate Mass Ratio Inspirals Detectable by Advanced LIGO. *Astrophysical Journal* , 681:1431–1447, July 2008, 0705.0285.

[374] J. M. Fregeau, S. L. Larson, M. C. Miller, R. O'Shaughnessy, and F. A. Rasio. Observing IMBH-IMBH Binary Coalescences via Gravitational Radiation. *Astrophysical Journal* , 646:L135–L138, August 2006, astro-ph/0605732.

[375] P. Amaro-Seoane and M. Freitag. Intermediate-Mass Black Holes in Colliding Clusters: Implications for Lower Frequency Gravitational-Wave Astronomy. *Astrophysical Journal* , 653:L53–L56, December 2006, astro-ph/0610478.

[376] S. G. Hahn and R. W. Lindquist. The two-body problem in geometrodynamics. *Annals of Physics*, 29:304–331, September 1964.

[377] Ian Hinder. The Current Status of Binary Black Hole Simulations in Numerical Relativity. 2010, 1001.5161.

[378] Bernd Bruegmann et al. Calibration of Moving Puncture Simulations. *Phys. Rev.*, D77:024027, 2008, gr-qc/0610128.

[379] Alessandra Buonanno, Yanbei Chen, and Michele Vallisneri. Detection template families for gravitational waves from the final stages of binary-black-hole inspirals: Nonspinning case. *Phys. Rev. D*, 67:024016, 2003. Erratum-ibid. 74 (2006) 029903(E).

[380] P. Ajith, M. Hannam, S. Husa, Y. Chen, B. Bruegmann, N. Dorband, D. Mueller, F. Ohme, D. Pollney, C. Reisswig, L. Santamaria, and J. Seiler. "Complete" gravitational waveforms for black-hole binaries with non-precessing spins. *ArXiv e-prints*, September 2009, 0909.2867.

[381] B. Abbott et al. Search for gravitational waves from binary black hole inspirals in LIGO data. *Phys. Rev. D*, 73:062001, 2006, arXiv:gr-qc/0509129.

[382] B. Abbott et al. Search for gravitational waves from binary inspirals in S3 and S4 LIGO data. *Phys. Rev. D*, 77:062002, 2008, arXiv:0704.3368.

[383] B. Abbott et al. Search of S3 LIGO data for gravitational wave signals from spinning black hole and neutron star binary inspirals. *Phys. Rev. D*, 78:042002, 2008, arXiv:0712.2050.

[384] B. Abbott et al. Search for gravitational wave ringdowns from perturbed black holes in LIGO S4 data. *Phys. Rev. D*, 80:062001, 2009, 0905.1654.

[385] Benjamin J. Owen. Search templates for gravitational waves from inspiraling binaries: Choice of template spacing. *Phys. Rev. D*, 53:6749–6761, 1996.

[386] P. Ajith et al. 'Complete' gravitational waveforms for black-hole binaries with non-precessing spins. 2009, 0909.2867.